UNIVERSIDADE DE BRASÍLIA - UNB
INSTITUTO DE GEOCIÊNCIAS - IG
PROGRAMA DE PÓS-GRADUAÇÃO EM GEOLOGIA

MIGMATITOS E RETROECLOGITOS DO BLOCO ARQUEANO CAMPO GRANDE, PROVÍNCIA BORBOREMA, NE DO BRASIL

Alanielson da Câmara Dantas Ferreira

TESE DE DOUTORADO Nº160

Orientador: Prof. Dr. Elton Luiz Dantas

BRASÍLIA, 2019

UNIVERSIDADE DE BRASÍLIA - UNB
INSTITUTO DE GEOCIÊNCIAS - IG
PÓS-GRADUAÇÃO EM GEOLOGIA

MIGMATITOS E RETROECLOGITOS DO BLOCO ARQUEANO CAMPO GRANDE, PROVÍNCIA BORBOREMA, NE DO BRASIL

Tese de Doutorado

Alanielson da Câmara Dantas Ferreira

Área de Concentração: Geologia Regional

Orientador:
Prof. Dr. Elton Luiz Dantas

Banca Examinadora:

_____
Prof. Dr. Elton Luiz Dantas (IG – UNB)

_____
Prof. Dr. Fátima Bittencourt (IG – UFGRS)

_____
Prof. Dr. Lauro Cézar Montefalco Lira dos Santos (IG-UFPE)

_____
Prof. Dr. Gustavo Viegas (IG – UNB)

Brasília-DF, dezembro de 2019.

Dedicado à Dona Letícia,

e a todos que me permitiram ter esperança.

Agradecimentos

Quatro anos se passaram. Vieram os primeiros cabelos brancos. Não recordo quantas noites ou finais de semanas passei de frente para o computador, mas apesar da angústia, e de certos traumas, foi principalmente gratificante. Nessa jornada, agradeço a minha família que compreendeu os inúmeros momentos de ausência. Aos professores Elton e Fuck pela dedicação e tempo destinado as correções e orientações. De forma mais abrangente, a todos os professores e técnicos que contribuíram para essa pesquisa. Em especial, agradeço aos alunos da Faculdade do Noroeste de Minas pelo reconhecimento e motivação. A Espinoza, Kant e Sartre por me mostrarem que a vida sem filosofia é extremamente ingênua e empobrecida.

SUMÁRIO

ÍNDICE DE FIGURAS

ÍNDICE DE TABELAS

RESUMO

O Bloco Campo Grande (BCG) é constituído por rochas arqueanas de 2,9 Ga e 2,65 Ga retrabalhadas durante eventos orogênicos riacianos (2,2 – 1,95 Ga) e neoproterozoicos (630 – 560 Ma). O bloco compreende uma área de cerca de 1500 km^2, com geometria elipsoidal, eixo SSW-NNE, na porção central do embasamento do Domínio Rio Grande do Norte, Província Borborema. O BCG é constituído por: 1. Complexo gnáissico-migmatito representado por biotita gnaisse bandado, granada-biotita gnaisse lepidogranoblástico e K-feldspato alcali gnaisse porfiroblástico. Os migmatitos são separados em paleossomas tonalíticos de 2,9 Ga, leucossomas *in source* ou *in situ* de composição granítica de 1,95 Ga e leucossomas injetados (veios pegmatíticos) de 580 – 560 Ma, com composição alcalina. 2. Rochas toleíticas ultramáficas de 2.69 – 2.52 Ga, formadas por cumulatos de ortopiroxênio (En 74,9 - 80,9% e 10,7 - 14,1% wt. de FeO) e clinopiroxênio (diopsídio e augita, En 31 - 42% e 9,9 - 16,1% wt. de MgO), parcialmente retrogradados para anfibólios da série cummingtonita (Mg) - grunerita (Fe). 3. Rochas metamáficas, com assembleia mineral formada por Mg-hornblenda, Fe-hornblenda, pargasita, granada, plagioclásio e clinopiroxênio. Neste grupo, enquadra-se sequência de corpos desmembrados (boudinados) constituídos por rutilo-clinopiroxênio-granada anfibolito com textura granoblástica, contendo granada com até 32% da molécula de piropo, crescimento simplectítico de Pl + Cpx e corona de Amph + Pl. As rochas metamáficas possuem protolito magmático de 2,65 Ga e registram dois eventos metamórficos, o primeiro em 2,0 Ga e o segundo no intervalo de 630 – 590 Ma. 4. rochas supracrustais neoproterozoicas, representadas por paragnaisses finamente bandados, granada-biotita xistos e anfibólio-epidoto calciossilicáticas que também ocorrem como lentes concordantes com a foliação principal. Idades modelo T_{DM} e valores positivos e negativos de εNd(t) em rocha total revelam épocas acrescionárias em 3,3 – 3,1 Ga, 2,9 Ga e 2,7 – 2,5 Ga, com aporte de material juvenil e retrabalhamento de fontes mais antigas já no Arqueano. Na porção leste desse núcleo arqueano são mapeados complexos ortognáissicos ricos em K-feldspato, cujos protólitos apresentam idade de cristalização de 2,23 – 2,18 Ga e composição calcioalcalina de alto K. Os ortognaisses possuem T_{DM} entre 2,59 e 2,46 Ga e $\varepsilon_{Nd(t)}$ negativos, suportando acresção por arcos magmáticos durante o Riaciano. Plutons graníticos neoproterozoicos (600 Ma) alojados em zonas de cisalhamento de escala regional delimitam o Bloco Campo Grande a leste e a oeste. Os dados obtidos mostram que a área de estudo apresenta intenso processo de reciclagem crustal e acresção de

arcos magmáticos do Arqueano ao Neoproterozoico, representando assim o primeiro registro, em escala de bloco, dos processos quelogênicos necessários para a diferenciação e o crecimento da crosta continental, anteriormente observado apenas em extensas áreas continentais, com mais de 1.000.000 km^2. Além disso, a geração de crosta continental em 2,9 Ga é rara, com registros de apenas outras duas ocorrências no Gondwana Ocidental, distantes mais de 2000 km da região de Campo Grande.

Palavras chave: crosta continental arqueana, retrabalhamento crustal, processos quelogênicos, Província Borborema.

1. INTRODUÇÃO

1.1 IMPORTÂNCIA DO ESTUDO

Embora o Arqueano represente o principal período de crescimento crustal da história do planeta, poucas áreas preservam rochas com idade superior a 3,5 Ga (e.g. Hawkesworth et al., 2017, 2019), caracterizadas principalmente pelas ocorrências de komatiitos e associações tipo tonalito-trondhjemito-granodiorito (TTG's) (e.g. Martin, 1986; 1994; Nance et al., 2014; Nebel et al., 2018). Portanto, o reconhecimento da crosta arqueana é estratégico para a compreensão dos mecanismos e processos de crescimento e reciclagem crustal (e.g. Holder et al., 2019). A gênese dos TTG's é interpretada como fusão parcial de rochas toleíticas, de idade arqueana, reequilibrados em granada anfibolito ou eclogitos, tendo granada como fase residual (e.g. Barker e Arth, 1976; Condie, 1981; Martin, 1986; 1994), ou representariam fases residuais derivadas de "refusões" de protolitos siálicos alojadas na base da crosta (e.g. Johnston e Wyllie, 1988).

A evolução crustal do Mesoarqueano foi caracterizada pela acresção de crosta juvenil (3,1-3,0 Ga) a núcleos mais antigos (e.g. Toteu et al., 1994; 2001), além da geração de granitos de alto-K em 2,7 Ga (e.g. Moyen e Martin, 2012), estes últimos interpretados como gerados a partir da reciclagem de crosta continental (e.g. Goodwin, 1991; Sylvester, 1994; Moyen e Martin, 2012), ou a partir de fonte manto-derivada, caso da maioria das rochas básicas e intermediárias ricas em K2O, denominados de sanukitoides (e.g. Stern e Hanson, 1991; Smithies e Champion, 2000; Martin et al., 2010) ou granitos tipo closepet (e.g. Jayananda et al., 1995; Martin et al., 2005; Moyen et al., 2001, 2003; Moyen, 2009).

Provavelmente a crosta continental arqueana foi formada a partir da fusão de rochas basálticas (e.g. Rapp e Watson, 1995; Foley et al., 2002; Dantas et al., 2013), como anfibolitos e eclogitos. No entanto, o mecanismo e o ambiente em que essa fusão ocorreu ainda padece de incerteza considerável (e.g., plumas mantélicas vs subducção, ou fusão abaixo de platôs oceânicos espessos vs zonas de subducção da crosta oceânica; Bedard, 2006; Rollinson, 2010). Esses mecanismos tiveram comportamentos distintos dos modernos, uma vez que são inegáveis as diferenças composicionais e térmicas entre a litosfera arqueana e fanerozoica (Griffin et al.,

2009; Herzberg et al., 2010). A geração de eclogitos de 2,7 Ga (cuja assinatura química sugere crosta oceânica como fonte) contemporâneos a magmatismo tonalítico-trondhjemítico-granodiorítico (TTG) suporta um crescimento crustal promovido por zonas de subducção para o Cráton do Atlântico Norte (Groenlândia; Tappe et al., 2011). O Maciço São José do Campestre, Província Borborema, registra sucessivos episódios acrescionários de arcos (3,5 a 2,7 Ga), também indicando a participação de crosta oceânica subductada e cunha mantélica durante a evolução continental Paleo- a Neoarqueana (Dantas et al., 2013).

O Paleoproterozoico (2,5–1,6 Ga) também constitui intervalo estratégico na história da Terra (e.g. Reddy e Evans, 2009). Durante esse éon ocorreram expressiva atividade tectônica, magmatismo característico, processos acrescionários de crosta juvenil e retrabalhada, além de eventos climáticos e bioquímicos diferenciados, resultando em mudanças significativas na configuração do planeta (e.g. Condie, 2000; Condie e O'Neill, 2010; Evans e Mitchell, 2011). Porém, o magmatismo do início do Sideriano foi drasticamente reduzido em resposta a uma menor atividade da tectônica de placas, levando a escassez relativa de idades entre 2,5 e 2,3 Ga em escala global, tanto em cristais magmáticos de zircão, quanto em grãos detríticos desse mineral (e.g. Diwu et al., 2014). Contudo, magmatismo máfico e alcalino (2,50 Ga a 2,39 Ga) é documentado no Escudo Fennoscandian, relacionado a eventos magmáticos bimodais, associados a fases extensionais de áreas estáveis arqueanas (~2,7 Ga; Lauri et al., 2012). Em contraste, o Riaciano (2,2 a 2,1 Ga) é caractizado por intensa geração e retrabalhamento crustal, principalmente relacionados a ambientes de arco magmáticos (Taylor & McLennan, 1985; Brito Neves et al., 2011; Wei et al., 2014), com participação de derivados mantélicos "rasos" (slightly shallow mantle source) durante os processos pós-colisionais (Terentiev et al., 2016) e de granitos cálcio-alcalinos a alcalinos intensamente fracionados (Tipo A; Reddy e Evans, 2009).

Portanto, a crosta continental apresenta crescimento progressivo (e.g. Hurley e Rand, 1969), principalmente ao longo do Arqueano-Paleoproterozoico (Rogers, 1996; Rogers e Santosh, 2002; Flament et al., 2008; Condie e O'Neill, 2010), sendo reconhecidos episódios de rápida expansão lateral (e.g., 2,9, 2,7, 2,1, 1,9, 1,8, 1,2, 0,9 e 0,8 Ga; Condie, 2000; Rollinson, 2006; Reddy e Evans, 2009; Condie e Aster, 2010). Atuação de plumas mantélicas, além dos processos acrescionários em zonas

de subducção, também é considerada para a geração desses eventos de “rápido” crescimento crustal (Albarède, 1998; Condie, 1998; Condie e O’Neill, 2010).

Neste contexto os dados petrológicos, geoquímicos e geocronológicos mostrando geração e reciclagem de crosta nos períodos 3,0–2,9 Ga, 2,7–2,5 Ga, 2,2–2,0 Ga e ca. 600 Ma são registros inéditos na região de Campo Grande e permitem sugerir que esta área pode contribuir para as discussões globais de crescimento e diferenciação da crosta continental.

1.2 CONTEXTO GEOLÓGICO E SELEÇÃO DA ÁREA DE ESTUDO

A Província Borborema (Almeida et al., 1981), Nordeste do Brasil, é uma área-chave para o entendimento da evolução geodinâmica da transição Arqueano/Paleoproterozoico. Apresenta complexa evolução crustal, com registro de rochas arqueanas a neoproterozoicas (e.g. Dantas et al., 2004), além de diversos ciclos orogênicos e tafrogênicos paleoproterozoicos (clímax no Riaciano, 2,25-2,15 Ga) a mesoproterozoicos, com estruturação final no Neoproterozoico, correlata aos sistemas orogênicos brasilianos/pan-africanos, que estabilizaram Gondwana Ocidental (Fig. 1.1A) (e.g. Brito Neves, 1975; 2011; Caby, 1989; Caby et al., 1991; Jardim de Sá, 1994; Van Schmus et al., 1995; 2003; 2011; Santos, 1996; Trompette, 1997; Fetter et al., 2000; Brito Neves et al., 1995; 2000; Souza et al., 2007; 2016; Hollanda et al., 2011; 2015; Dantas et al., 2004; 2008; 2013). A Província Borborema (PB) é compartimentada por complexo sistema de zonas de cisalhamento regionais que separam domínios, maciços e faixas/sequências metasupracrustais neoproterozoicas, além de controlar o alojamento preferencial de plútons graníticos neoproterozoicos (Brito Neves, 1975; Caby et al., 1991; Jardim de Sá, 1994; Vauchez et al., 1995; Santos, 1996; Van Schmus et al., 2011).

O Domínio Rio Grande do Norte (DRGN) (Fig. 1.1B) representa a porção nordeste da Província Borborema (Brito Neves et al., 2000). O DRGN é constituído por sucessivas colagens e amálgamas de distintos fragmentos crustais arqueanos a neoproterozoicos, que evidenciam diferentes processos de geração e reciclagem crustal (e.g. Fetter et al., 2000; Dantas el al., 2004; Souza et al., 2007; Sá et al., 2014; Hollanda et al., 2015). Estudos sistemáticos de U-Pb em grãos de zircão na porção central do DRGN (Fig. 1.1C) revelam idades de 2,16 a 2,13 Ga para ortognaisses e metagabros da região de São Vicente-Florânia (Hackspacher et al.,

1990; Dantas, 1992; Van Schmus et al., 1995), enquanto granitos cálcio-alcalinos e ortognaisses dioríticos da região de Caicó apresentam idades de 2,24-2,25 Ga (Legrand et al., 1991, 1997; Medeiros et al., 2012). Os ortognaisses dessa região (denominado de Complexo Caicó; Ferreira e Albuquerque, 1969) foram gerados a partir de magmatismo granítico cálcio-alcalino de alto-K, com idade entre 2,15 e 2,25 Ga, tendo evoluído por fracionamento intracrustal em baixa pressão, que resultou em líquidos granodioríticos (e.g. Souza et al., 2007; 2016). Na região de Lajes, intrusões de rochas máfico-ultramáficas de 2,19–2,20 Ga são constituídas por wehrlitos, clinopiroxenitos e troctolitos, que revelam características típicas de arcos magmáticos, indicando subducção de crosta oceânica e participação de fontes mantélicas (Ferreira, 2015; Ferreira et al., 2019). Anomalias negativas de high field strength elements e o enriquecimento em large ion lithophile elements sugerem magmatismo básico a partir da fusão parcial do manto metassomatizado em ambiente de zona de subducção para magmatismo cálcio-alcalino (e.g. Souza et al., 2007; Ferreira et al., 2019).

Porém, mesmo frente ao crescente histórico de publicações ao longo de 40 anos, ainda remanescem regiões sem a cobertura petrográfica, geoquímica, geocronológica ou mesmo mapeamento geológico básico, como na porção oeste do DRGN (Fig. 1.1C). Esta região em específico é composicionalmente distinta das demais áreas em que está exposto o embasamento do DRGN (Fig.1.1 C), podendo ser estratégica para a melhor compreensão da evolução geológica do domínio. Trabalhos anteriores no embasamento da região centro-oeste do DRGN abordaram exclusivamente a granitogênese brasiliana (Galindo, 1993; Trindade et al., 1999) e investigações metalogenéticas pontuais (Lima et al., 1980). Nos mapas regionais (Angelim et al., 2006) as rochas dessa área são interpretadas como pertencentes ao contexto evolutivo do Complexo Caicó. Além disso, a área é constituída por migmatitos, característica esta já sugerida por Brito Neves (1975) como indicativa de blocos ou terrenos anteriores ao magmatismo calcioalcalino de alto-K de 2,2 Ga. Assim, foram realizadas etapas de mapeamentos e aquisição de amostras para avaliar de forma preliminar a contribuição da região de Campo Grande, visando melhor entendimento da evolução geodinâmica do embasamento do Domínio Rio Grande do Norte.

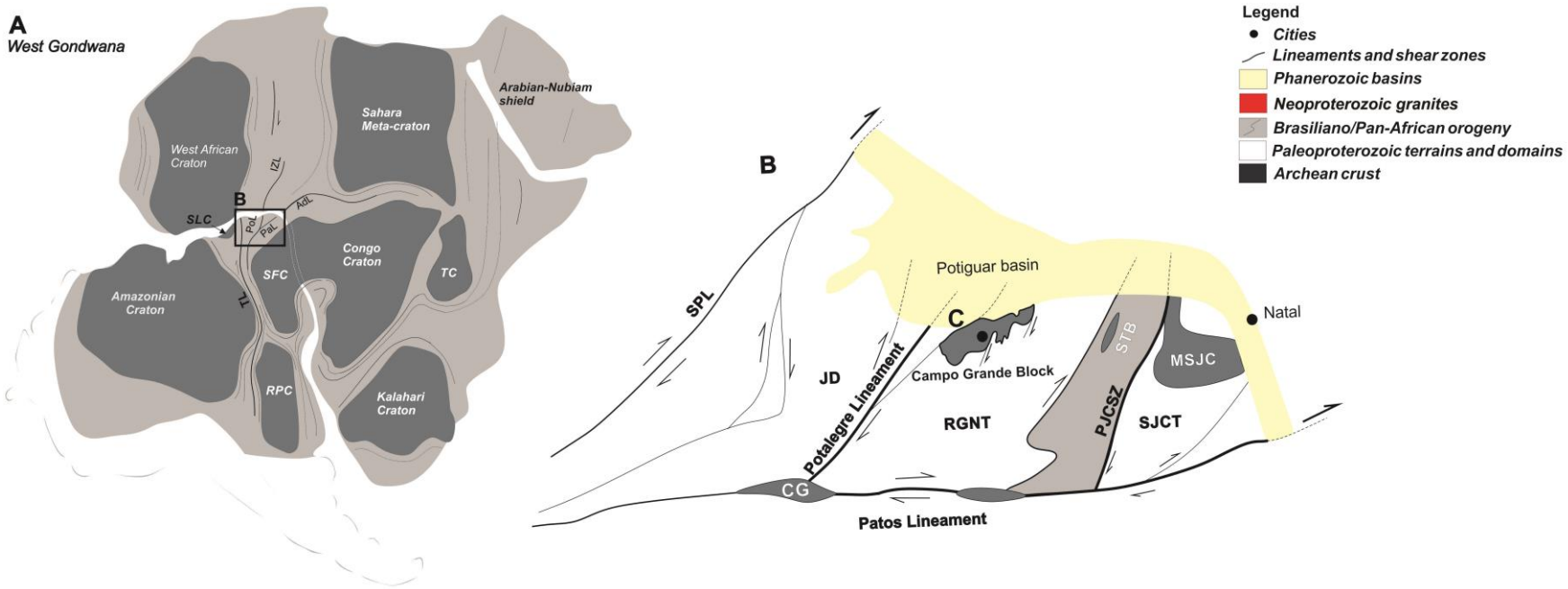

Figura 1.1.Contexto geológico regional. A) Localização da Província Borborema no Gondwana Ocidental. B) Mapa geológico da porção central do Domínio Rio Grande do Norte.

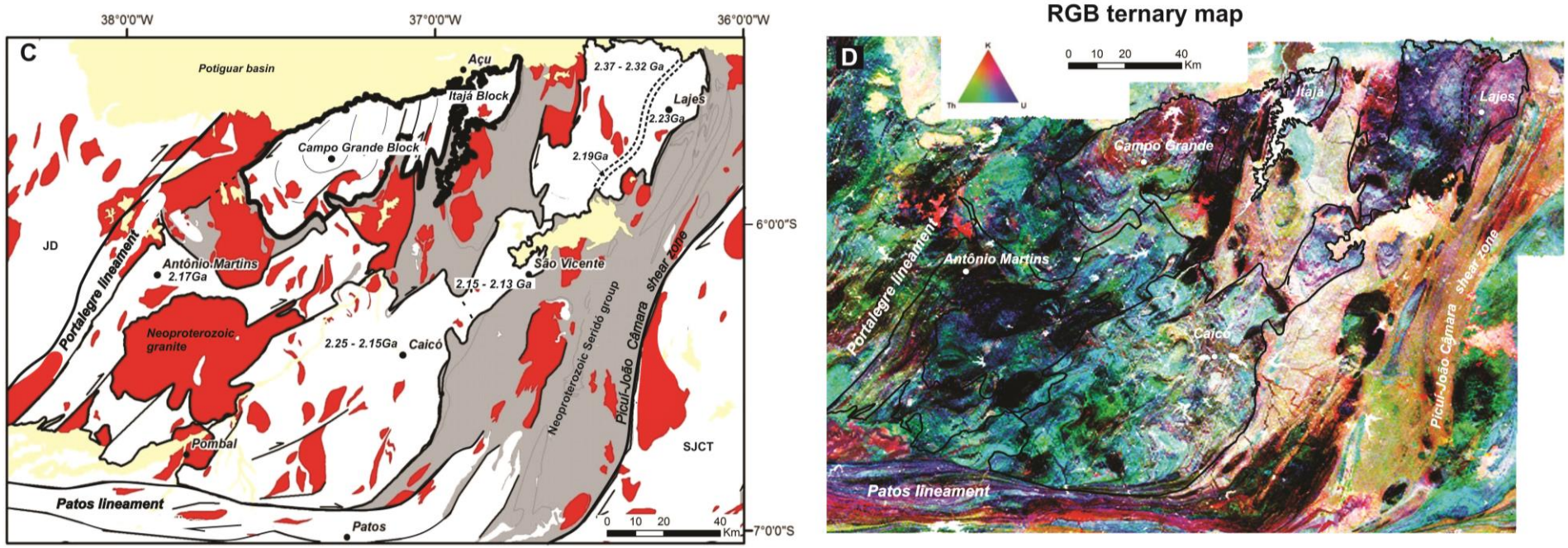

Figura 1.1. Contexto geológico regional. C) Distribuição das idades U-Pb em zircão, e D) Mapa ternário gammaespectrométrico das regiões de Caicó-São Vicente, Lajes, Antônio Martins e Campo Grande-Itajá, nas quais é exposto o embasamento do DRGN. Legenda: RPC – Cráton Rio de La Plata, SFC – Cráton São Francisco, SLC – Cráton São Luiz, TC – Cráton da Tanzânia, IZL – Lineamento Ifewara-Zungeru, PoL – Lineamento Portalegre, PJCSZ – Zona de cisalhamento Picuí-João Câmara, PaL – Lineamento Patos, ADL – Lineamento Adamaoua, JD – Domínio Jaguaribe, SJCT – Terreno São José do Campestre. Idades U-Pb retiradas de Souza et al. (2007), Hollanda et al. (2011) e Ferreira et al. (2019).

1.3 RELEVÂNCIA E OBJETIVOS DA TESE

A proposta central desta tese consiste em descrever a evolução do Bloco Campo Grande, a partir da caracterização petrológica, mineralógica, litogeoquímica, geocronológica e isotópica, com vistas a compreender os processos de crescimento crustal e evolução pré-cambriana e contribuir para o incremento do conhecimento geológico regional. O maior desafio foi definir o arranjo tectono-estratigráfico de área sem estudo prévio, na qual as relações de contato entre as distintas unidades não são muito claras, em vista da superposição de distintos eventos deformacionais.

Por isso, a proposta básica deste projeto consistiu no emprego de diferentes análises (e.g. mapeamento geológico, petrografia, geoquímica, geocronologia, geologia isotópica), visando contribuir para:

a) Melhor compreensão dos processos de geração da crosta continental arqueana e seu retrabalhamento durante o Proterozoico;

b) Estudo do comportamento dos sistemas isotópicos U-Pb, Lu-Hf e Sm-Nd em relação à superposição de eventos (ciclos) magmáticos-deformacionais;

c) Definição dos limites e evolução geodinâmica dos distintos constituintes tectono-estratigráficos do Bloco Campo Grande;

d) Inserção dos resultados nos modelos globais de crescimento e diferenciação da crosta continental.

1.4 LOCALIZAÇÃO E VIAS DE ACESSOS

A área de estudo localiza-se na porção centro-oeste do Estado do Rio Grande do Norte (Fig. 1.2A,B), abrangendo parte dos municípios de Itajá, São Rafael, Paraú, Triunfo Potiguar, Caraúbas, Upanema e tendo Campo Grande como a cidade central. Os acessos principais são por meio da BR-304 (rodovia Natal-Mossoró), em seguida RN-233, e BR-226 (Fig. 1.2C).

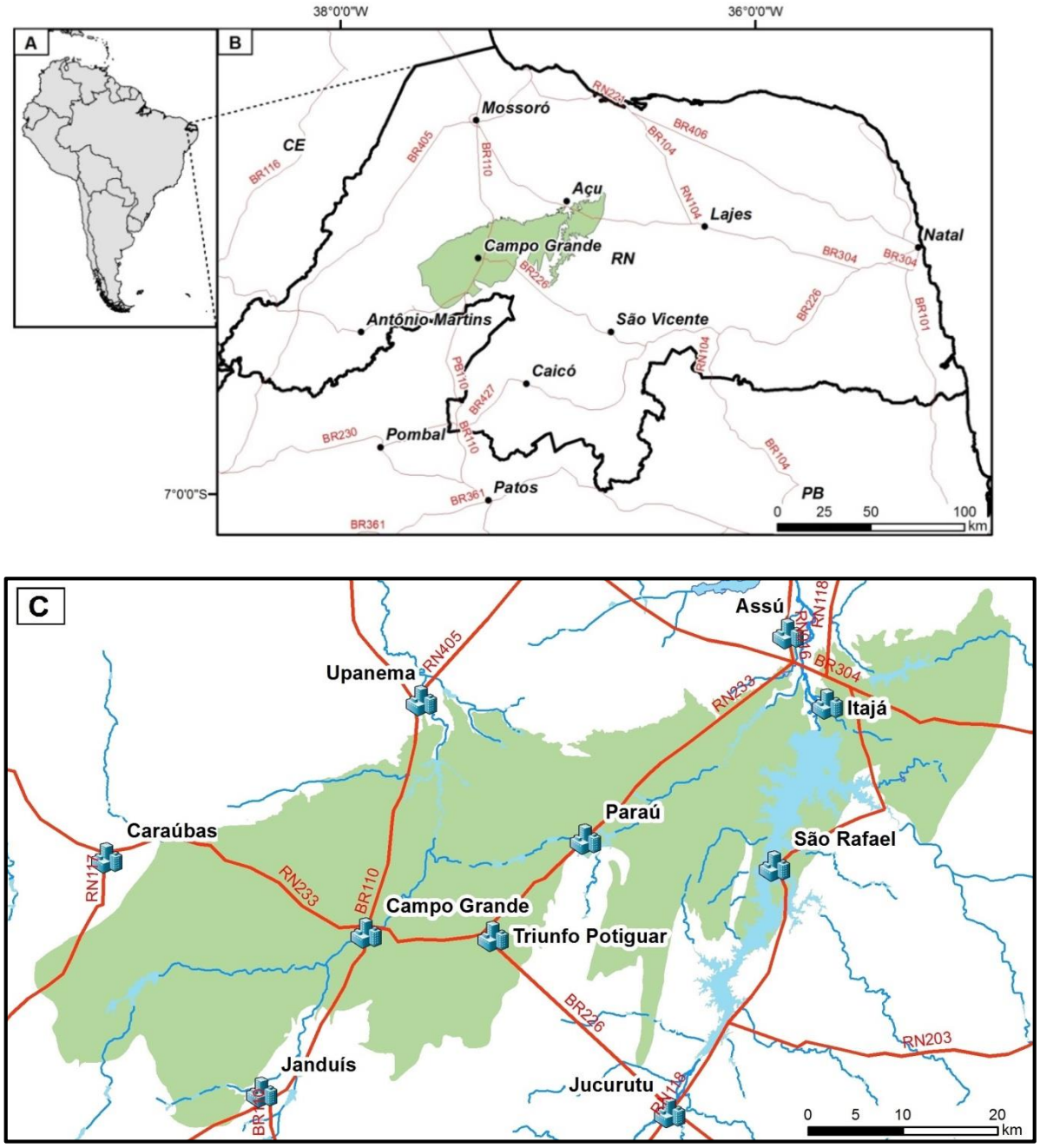

Figura 1.2: Mapa de localização e acesso da área estudada. A) Contorno da América do Sul. B) Contorno do Estado do Rio Grande do Norte. C) Destaque da área de estudo no região oeste do Estado do Rio Grande do Norte.

1.5 ESCOPO DA TESE

A tese apresenta-se estruturada na forma de capítulos. O Capítulo 1, no qual contém as informações gerais da pesquisa: importância do estudo, seleção e histórico da área, relevância e objetivos, localização e este sub-tópico, “Escopo da tese”.

O Capítulo 2 contém o artigo *"Retrograde evolution of eclogites from the Borborema Province in Northeast Brazil: evidence from texture, mineral chemistry and X-ray mapping"*. Este trabalho apresenta os dados petrográficos, texturais, composição mineral e zonação composicional das fases de alto e baixo grau metamórfico, registrados nas rochas metamáficas estudadas.

O Capítulo 3 contém o artigo *"High-pressure metamorphic rocks in the Borborema Province, Northeast Brazil: reworking of Archean oceanic crust during Neoproterozoic orogeny"*, em que são apresentadas e discutidas as assinaturas químicas da fonte e a evolução temporal das rochas metamáficas do Bloco Campo Grande.

O Capítulo 4 contém o artigo *"Multiple migmatite generation and magma differentiation as a crucial factor of Archean to Proterozoic continental evolution in the Borborema Province, Northeast Brazil".* Neste artigo são abordados os múltiplos eventos de reciclagem crustal, determinantes para a diferenciação e crescimento da crosta continental desde 2,9 Ga na área de estudo.

O Capítulo 5 contém o artigo *"The previously missing 2.9 Ga continental crust in West Gondwana revealed in Northeast Brazil"*. Neste trabalho é destacada a geração de crosta continental em 2,9 Ga, um intervalo de tempo considerado de quiescência tectônica com apenas dois registros de atividade magmática entre 3,0 e 2,9 Ga no Gondwana Ocidental.

O Capítulo 6 apresenta o artigo *"Archean to Neoproterozoic arc docking and crustal reworking in Northeast Brazil"*, mostrando que o Bloco Campo Grande representa o primeiro exemplo de processos de crescimento quelogênicos em escala de bloco.

O Capítulo 7 contém uma síntese conclusiva da tese a partir dos dados apresentados nos diferentes artigos, destacando a história evolutiva integrada a partir dos diferentes registros preservados nas rochas que compõem o Bloco Campo Grande.

2. ARTIGO CIENTÍFICO 1: RETROGRADE EVOLUTION OF ECLOGITES FROM THE BORBOREMA PROVINCE IN NORTHEAST BRAZIL: EVIDENCE FROM TEXTURE, MINERAL CHEMISTRY AND X-RAY MAPPING

Alanielson da Câmara Dantas Ferreira[1], Elton Luiz Dantas[1], Ticiano José Saraiva dos Santos[2], Reinhardt A. Fuck[1], Mahyra Tedeschi[3]

[1]Instituto de Geociências, Universidade de Brasília (UnB), 70910-900 Brasília-DF, Brazil

[2]Instituto de Geociências, Universidade Estadual de Campinas (UNICAMP); Departamento de Geologia e Recursos Naturais, 13083-970 Campinas-SP, Brazil

[3]Instituto de Geociências, Universidade Federal de Minas Gerais (UFMG), 31270-901, Belo Horizonte- MG, Brazil

Corresponding author: Alanielson da Câmara Dantas Ferreira (ferreira.acd@gmail.com)

2.1 ABSTRACT

Neoproterozoic retro-eclogites consist of garnet, clinopyroxene, amphibole and plagioclase. Quartz, zircon, ilmenite and rutile are accessory minerals. The data reveal a complex and progressive process of diffusion and migration of Ca, Fe, Mg, Mn, Al and Na between retrograded minerals, Fe-Mn-rich garnet rim + diopside-augite + plagioclase and Ca to Fe amphibole, and the peak metamorphic assemblage of eclogite facies, omphacite + Mg-Ca-rich garnet core. It demonstrates that the range of mineral composition is a function of precursor minerals and textural relationships with distinct metamorphic retrogression phases. X-ray maps show that all the major mineral phases (garnet, clinopyroxene, plagioclase and amphibole) have multiple and compatible progressive growth “zones”, that are the loci of

chemical and diffusive transport through the fluid according to its precursor mineral. Symplectite cores show high-Ca-Mg pyroxene in equilibrium with Ca-rich plagioclase and minor amphibole while its rims exhibit high-Al-Na amphibole in equilibrium with Na-rich plagioclase. Progressive decrease in Na and Al content is marked in clinopyroxene symplectite. Garnet displays decreasing Mg and Ca content from core to rim with Fe-Mn increase in the same direction. Diffusion-controlled chemical and mineral zoning in symplectites are associated with rapid uplift rates and disequilibrium on a micron scale due to greater diffusion of Fe, Al and Na into symplectite during decompression, while Mg and Ca tend to remain fixed. The best tectonic scenary revealed by the textural evidences present in these rocks suggests that retro-eclogite lenses in the northeastern Borborema Province represent relict subducted oceanic crust, which can define a paleosuture zone, and implies that there was submitted to eclogite facies metamorphism during the Neoproterozoic evolution of the Rio Grande do Norte domain. The study of these kinetics and element transport on the scale of mineral assemblage allows a better understanding of the post-orogenic exhumation and metamorphic retrogression of the eclogite facies process in the Borborema Province.

Keywords: retro-eclogite, omphacite and garnet breakdown reaction, corona and symplectite textures, Borborema Province.

2.2 INTRODUCTION

High-pressure (HP) and ultrahigh-pressure (UHP) eclogites are significant in understanding plate subduction and record important information on the dynamics of orogens, as indicators of paleosuture zones and subsequent continent collision. However, the definition and localization of these suture zones are among the most challenging questions in geological research, since HP and UHP mineral assemblages are obliterated by medium- to low-P mineral assemblages due to deformation and retrograde metamorphism (Ernst, 1988; Faryad and Kachlík, 2013). In this context, the fully equilibrated mineral assemblages record a point in the P-T path while partially equilibrated assemblages can record a larger range of their retrograde evolution (Elvevold and Gilotti, 2000; Anderson and Moecher, 2007).

Disequilibrium textures, e.g. compositional zoning, exsolution, symplectites, corona and reaction rims, result from retrogression and provide information on the

decompression P-T path after plate subduction (Johansson et al., 2001). The symplectite-forming reactions are largely isochemical, allowing retrograded assemblages to be used to estimate the original omphacite composition and minimum pressure at the mineral assemblage scale. Clinopyroxene + plagioclase (±Hbl ± Qtz) symplectites are interpreted as decompression result of precursor omphacite generated under eclogite facies conditions or HP metamorphism. Mafic rocks containing such features are reported as relict eclogites (e.g., Eskola, 1921; Vogel, 1966; Holland, 1983; O'Brien et al., 1990; Rubie, 1990; Zhao et al., 2001; Shervais et al., 2003; Anderson and Moecher, 2007). The presence of inclusions in zoned garnet also allows the extraction of information on segments of the prograde and retrograde P-T conditions (O'Brien, 1997; Simakov, 2008).

The Campo Grande block is a basement inleier surrounded by Neoproterozoic supracrustal belts, in northern part of Borborema Province, and presents a complex tectonometamorfic evolution that reflects the development of accretion along its margins since the Archean. We descover new occurrence of mafic rocks as small bodies intrusive in TTG gneiss, which preserved composition and texture of the major mineral phases produced during metamorphic retrogression events, could be interpreted as representing a rare example of partially equilibrated retro-eclogite in this region. Textural relationships and mineral composition are sensitive indicators of metamorphic reactions during PT trajectory. Thus, the purpose of this study is to (1) investigate the composition range of Cpx-Pl-Amph symplectites and corona around garnet in retro-eclogites via mineral chemistry and element X-ray mapping, and (2) provide a better understanding of the diffusion process and element migration of the retrograded assemblage (garnet rim + clinopyroxene + plagioclase and amphibole) after eclogite facies peak metamorphism (omphacite + garnet core + rutile).

2.3 GEOLOGICAL SETTING

The Borborema Province is formed of discontinuous remnants of Archean crust, Paleoproterozoic migmatite-gneiss complexes, Meso- and Neoproterozoic supracrustal rocks and intrusions (Van Schmus et al., 2003; Oliveira and Medeiros, 2018). These units were amalgamated to West Gondwana (Fig. 2.1) during the Brasiliano/Pan-African orogeny that resulted in crust thickening by nappe stacking associated with Neoproterozoic ocean closures (Santos et al., 2009; Ganade de

Araujo et al., 2014; Padilha et al., 2014, 2016, 2017). The main evidences were described in the Central Ceará domain by the occurrence of retro-eclogites in Neoproterozoic suture zones (Santos et al., 2008). Several shear zones represent local adjustments within each terrain, as well as delimit the crustal domains (Caby, 1989; Van Schmus et al., 2008). The major tectonic lineaments extend into the Benin–Nigeria Province in NW Africa (Santos et al., 2008), and contain HP mafic rocks on both continents (Santos et al., 2009; Ganade de Araujo et al., 2014). The Transbrasiliano-Kandi-4°50' Lineament is the most prominent feature (Arthaud et al., 2008).

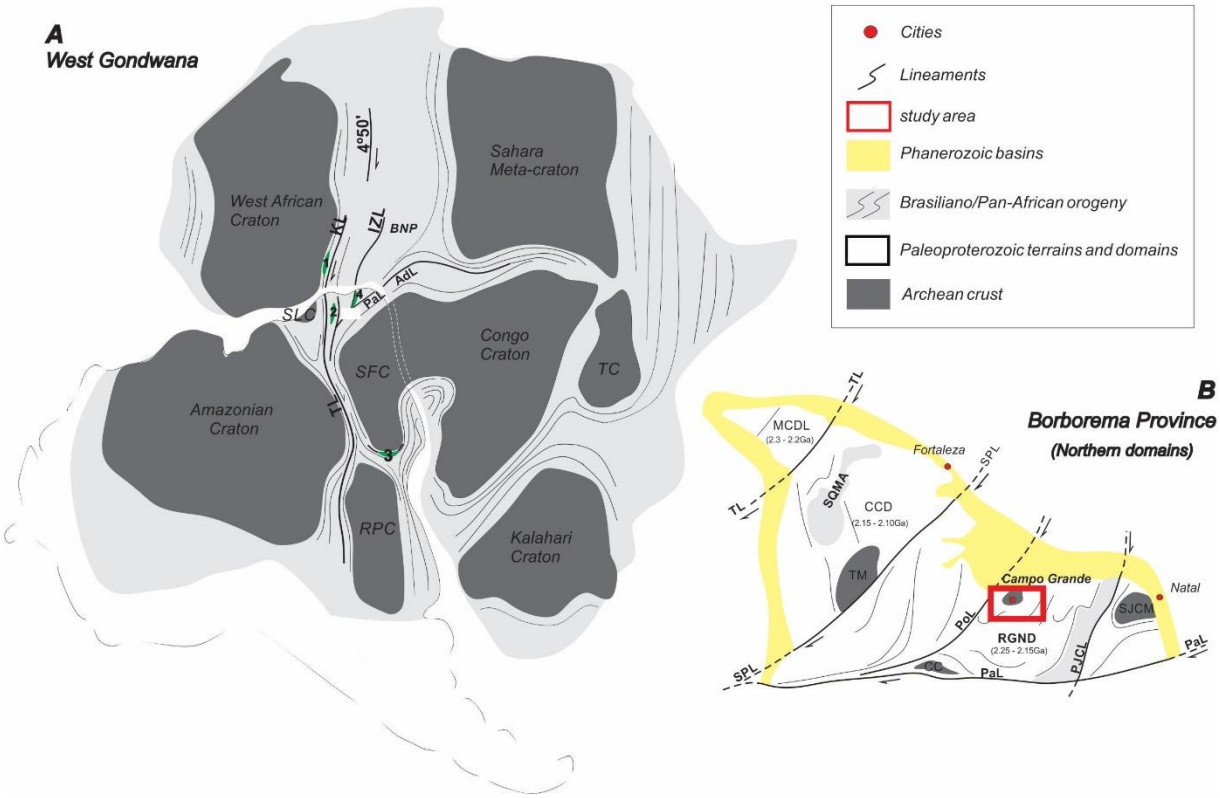

Figure 2.1. Regional geological setting. A) Localization map of the Borborema Province (BP) in West Gondwana. BNP - Benin-Nigeria Province, RPC - Rio de La Plata Craton, SFC - São Francisco Craton, TC - Tanzania Craton. 1 – UHP rocks in the Dahomey belt (Santos et al., 2008), 2 – UHP rocks in the Ceará Central domain (Santos et al., 2009), 3 – HP amphibolite in the Southern Brasília orogen (Tedeschi et al., 2017) and 4 – HP amphibolites from Campo Grande area. B) Geological map of the Northern domain of the Borborema Province modified from Arthaud et al., 2008. MCD - Médio Coreaú domain, CCD - Ceará Central domain and RGND - Rio Grande do Norte domain. TM - Tróia massif, SJCM – São José do Campestre massif and GC - Granjeiro Complex. SQMA - Santa Quitéria magmatic arc. TL - Transbrasiliano Lineament, KL- Kandi Lineament, SPL - Senador Pompeu Lineament, IZL - Ifewara-Zungeru Lineament, PoL - Portalegre Lineament, PJCL – Picuí-João Câmara Lineament, PaL - Patos Lineament, ADL - Adamaoua Lineament.

The Rio Grande do Norte domain (RGND) is located in the northeasternmost Borborema Province and is limited by the Portalegre shear zone correlated probably with the Ifewara-Zungeru fault in Africa, and the Patos-Adamaoua Lineament (Brito Neves et al., 2000; Arthaud et al. 2008). In the central portion, RGND consists of Rhyacian (2.25 to 2.15 Ga) high-K calc-alkaline magmatic rocks (e.g. Caicó Complex; Souza et al., 2007; Hollanda et al., 2011) and Siderian (2.3 Ga) supracrustal rocks (Dantas et al., 2008) form the basement of the Neoproterozoic Seridó Group (Van Schmus et al., 2003; Hollanda et al., 2015). Inserted in the RGND, the Campo Grande area comprises banded migmatites, leucocratic gneisses, and minor ultramafic and amphibolite lenses (Ferreira et al., 2019). These amphibolites are interpreted as retrograde eclogites and form up to 20 km long and 100 m thick (oftenmore of metric dimensions) tabular bodies in the migmatite-gneiss complex, exposed along major shear zones (Fig. 2.2). The 2650 ± 5 Ma U-Pb age of homogeneous, oscillatory-zoned zircon cores is interpreted as the crystallization age of the eclogite protolith. Thin rims of zircon grains were dated at 614 ± 8 Ma, reflecting partial recrystallization at subsolidus conditions during the Neoproterozoic metamorphic peak (Ferreira et al., 2019). We collected samples of these amphibolites and performed spot analyses of mineral chemistry, compositional sections and X-ray maps to describe the chemical transport during the formation of symplectic and corona texture.

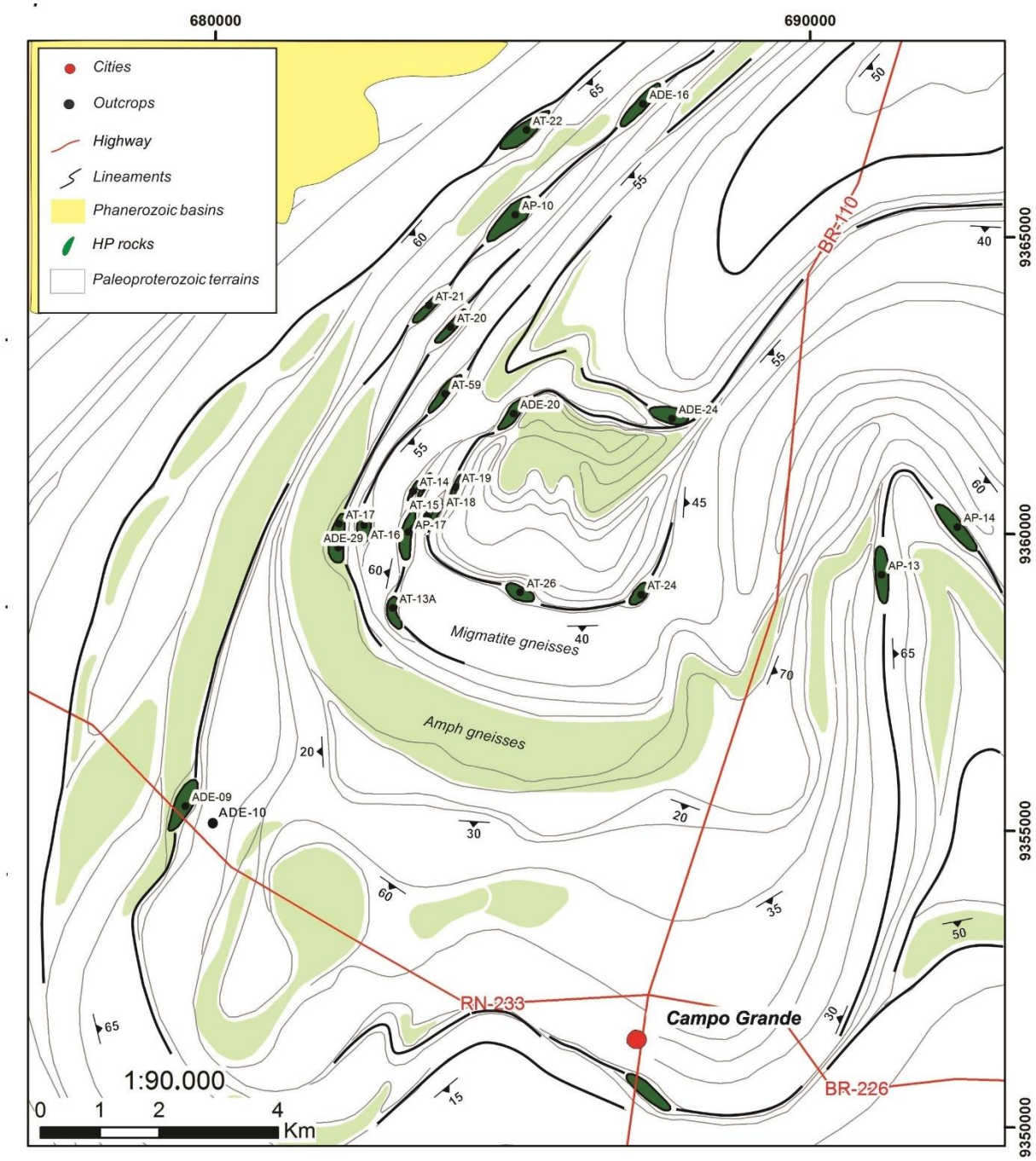

Figure 2.2. Simplified geological map of the Campo Grande area.

2.4 MATERIALS AND METHODS

Geological mapping (1:100.000 scale) in the study area was carried out from 2016 to 2018. Geological sampling was supported by geochemical, geophysical and petrographic surveys. The latter was developed at the Microscopy Laboratory of the Instituto de Geociências of the Universidade de Brasília (Brazil).

Mineral analyses were performed on polished thin section using a JEOL JXA-8230 SuperProbe with 5 wavelengths dispersive (WDS) spectrometers at the Electron Microprobe Laboratory of the Universidade de Brasília (Brazil). Systematic WDS analyses were obtained for garnet, clinopyroxene, plagioclase and amphibole. Operating conditions for the WDS analyses were 15 kV accelerating voltage, with a beam current of 10 nA and probe diameters of 3 μm for all minerals, except for plagioclase (5 μm). Count times on peak and on background were 10s and 5s, respectively. Both synthetic and natural mineral standards were used for the analyses and the same standards and procedure were retained throughout. Fe3+ contents were estimated using site and charge balance calculations on cation-normalized analyses (Droop, 1987). Systematic analyses were obtained from 9 representative samples from amphibolite lenses. Microprobe analysis was used to reintegrate precursor pyroxene compositions. For each estimate, clinopyroxene-plagioclase-amphibole symplectites (and their modal proportions) that occur within the same area or were as close as possible were used.

X-ray compositional maps were acquired by electron probe micro-analyser (EPMA) and standardized in concentration maps of oxide weight percentage using the internal standard technique (Andrade et al., 2005). The analytical conditions of X–ray mapping included a 15 kV accelerating voltage, 50 nA probe current and Dwell of 40 ms. Structural formula maps in atom per formula unit (apfu) were used to investigate the compositional variability of the mineral phases at the thin section scale.

2.5 RESULTS

2.5.1 Field Relationships and Petrography

Metamafic rocks are found at different places and levels in the Campo Grande block. They are mainly smaller amphibolite lenses hosted by migmatites and gneisses or larger exposed bodies. Some retro-eclogite relics are preserved as several-meters-thick pods concordant in the central portions of these amphibolites. The amphibolites occur as lenses or up to 100 m thick tabular bodies, dismembered along a trend of 20 km and parallel to the main foliation and concordant with main shear zones (Fig. 2.2 and Fig. 2.3A). These shear zones contain strong hornblende mineral lineation and an increase in garnet porphyroblasts. The hot emplacement of the Campo

Grande retro-eclogites is coeval with stretching lineations and kinematic criteria that indicate east-west compression with tectonic transport to the east and NNE (Fig. 2.2). Late tourmaline-bearing pegmatite veins and feldspar granite intrusions crosscut the amphibolite lenses and migmatite–gneiss complex.

The retro-eclogites contain mainly massive porfiroblastic garnet (15-25%) and granoblastic amphibole (15-35%) with variable proportions of vermicular fine-grained plagioclase + diopside + clinopyroxene (25-45%), forming a typical symplectitic texture (Fig. 2.3B to F), quartz (1%-5%) and a small amount of zircon, rutile, apatite, spinel, magnetite and ilmenite (<3%). The garnet crystals exhibit irregular shapes with lobate edges, and a composite corona texture is developed at their borders, composed of inner plagioclase and outer amphibole corona (Fig. 2.3C and E).

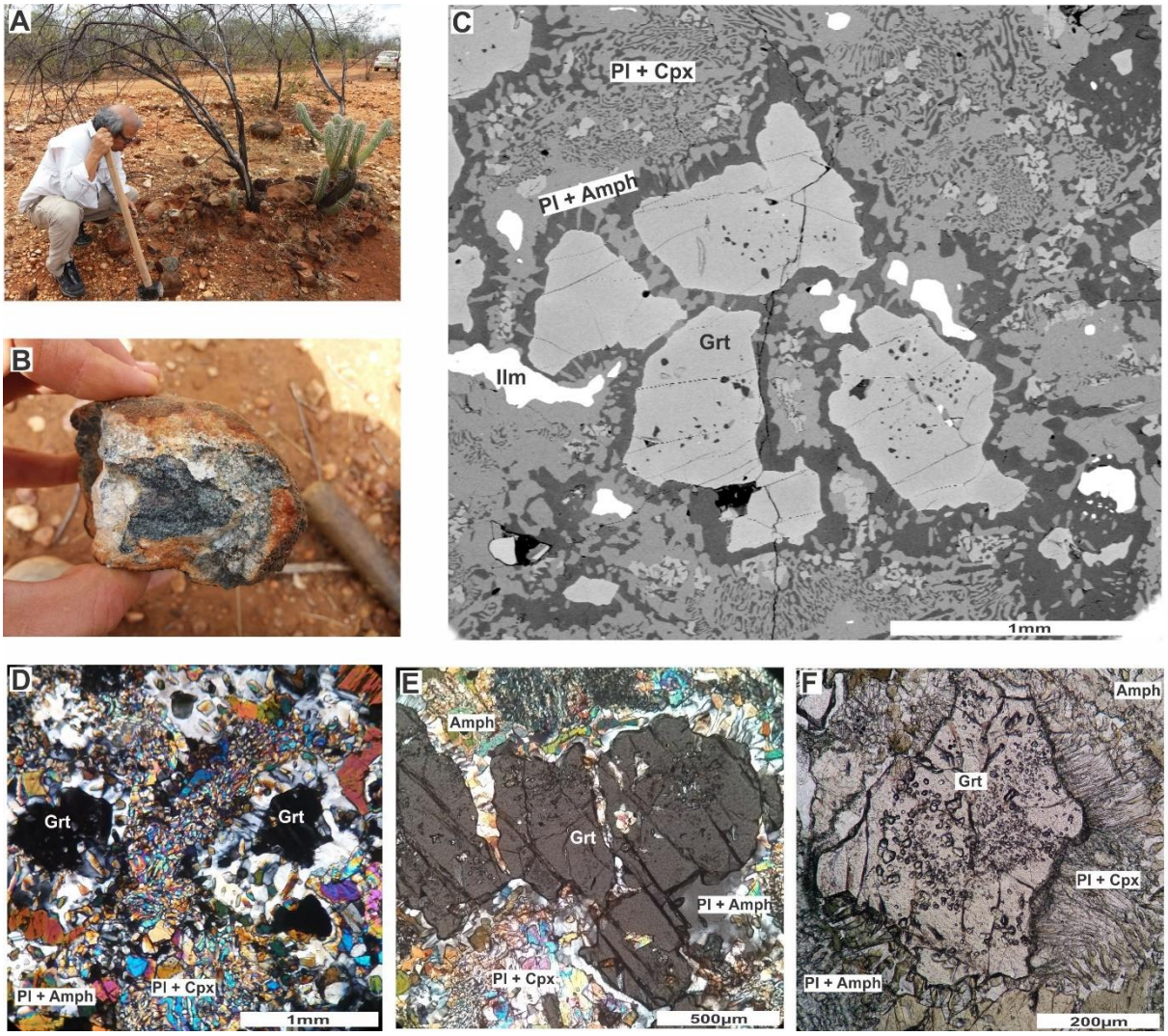

Figure 2.3. Petrographic features of retro-eclogites. A) Outcrop of ADE-09 sample. B) Detail of sample ADE-09. C) Mineral assemblage and texture in scanning electron microscope image of ADE-09 sample. D) Mineral assemblage and texture of ADE-20 sample. E) Mineral assemblage and texture of

ADE-29 sample. F) Mineral assemblage and texture of AT-14 sample. Mineral symbols follow Whitney and Evans (2010).

2.5.2 Mineral Chemistry

Garnet

Garnet forms light red, euhedral-subhedral porphyroblasts (200 µm to 3 mm) displaying abundant inclusions (5 to 30 µm), such as quartz, diopside, rutile, spinel, apatite, plagioclase and amphibole, within cores overgrown by inclusion-free rims (Fig. 2.3C, D and F). Quartz inclusions were examined by Raman spectroscopy, but high-pressure polymorphs (e.g. coesite) were not found.

Garnet grains have chemical compositions with structural formula ranging from $Alm_{(40.9)}Prp_{(32.2)}Grs_{(30.2)}Sps_{(0.8)}Adr_{(0.0)}Uvt_{(0.0)}$ in the crystal core to $Alm_{(65.6)}Prp_{(9.8)}Grs_{(9.8)}Sps_{(4.2)}Adr_{(5.3)}Uvt_{(0.4)}$ in the rim (Supplementary Table 2.1 and Fig. 2.4). These analyses show an increase of Fe (1.26 to 1.95 cations per formula unit - CPFU) and Mn (0.03 to 0.13 CPFU) with a marked decrease in Mg (0.96 to 0.22 CPFU) and Ca (0.90 to 0.29 CPFU) toward the crystal rims. All analyzed garnet crystals display slight and progressive zoning with decreasing pyrope (32 to 9 % mol) and grossular (30 to 9 % mol) and increasing almandine (40 to 65 % mol) from the core to the rim (Fig. 2.4). Most of the garnet analyses plot in the high-pressure eclogite field (C-type) (Fig. 2.5). Strong increase in spessartine (0.8 to 5 % mol) is observed at microfractures and garnet rims (Fig. 2.6C and Fig. 2.15; Mn map).

Garnet grains have their margin retrograded to symplectite of various mineral components, mainly fine-grained vermicular plagioclase, diopside-augite and Ca amphibole, depending on the composition of neighbor minerals (Fig. 2.6A to F). Some garnet crystals are bounded by thin (100 to 200µm) Fe-amphibole and plagioclase symplectite with Fe-amphibole coronae and may contain Ca-amphibole and Al-Ca-rich plagioclase exsolutions (Fig. 2.7A to F).

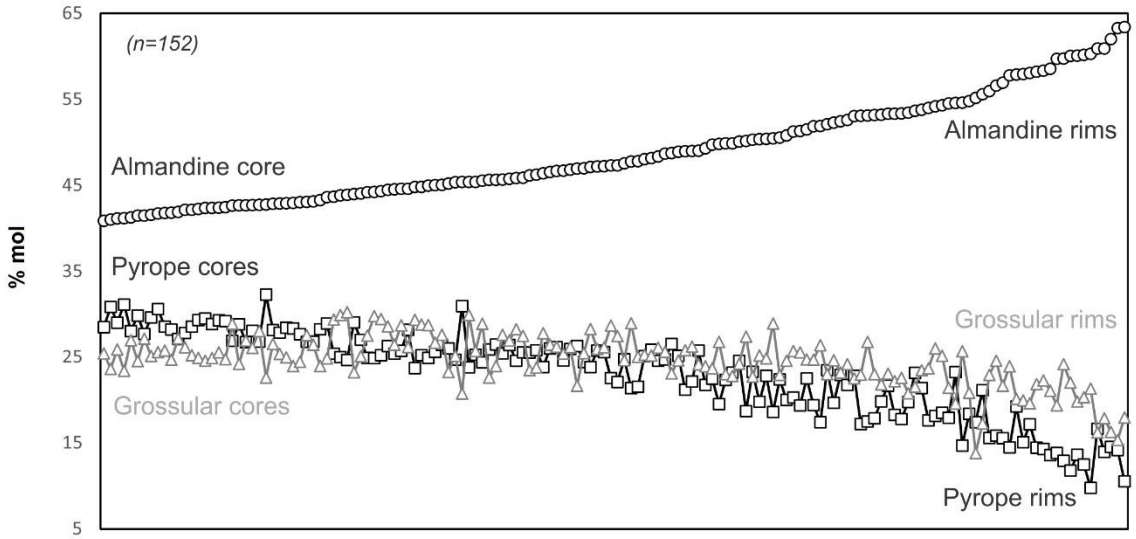

Figure 2.4. Almandine, pyrope and grossular profile of analyzed garnet, indicating changing compositions from core to rim (Supplementary Table 2.1).

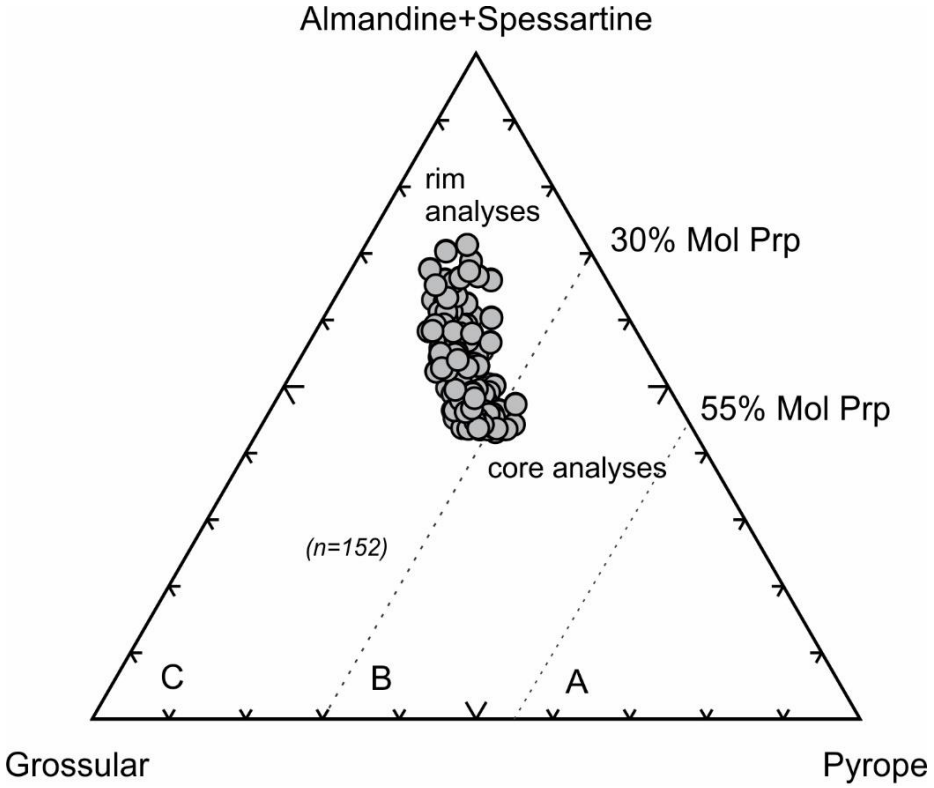

Figure 2.5. Compositional ranges of garnet from retro-eclogites shown in a Alm+Sps–Grs–Prp diagram, indicating changing compositions from rims to cores in all analyses (n=152). Eclogite classification fields follow Coleman et al. (1965): A) eclogite inclusions in mantle rocks; B) eclogite lenses in migmatitic-gneissic terranes (Medium Pressure); and C) eclogite lenses in alpine-type metamorphic rocks (High-pressure) (Supplementary Table 2.1).

Clinopyroxene

The primary omphacite grains were wholly retrograded to relict retrogressive clinopyroxenes with exsolution of plagioclase. Clinopyroxene occurs as subhedral to vermicular fine-grained crystals developing symplectitic texture with plagioclase and amphibole and quite a few grains are bounded by amphibole coronae (Fig. 2.3C to F, Fig. 2.6A and Fig. 2.7A).

Mineral chemistry reveals diopside-augite compositions (Supplementary Table 2.2) with higher CaO, from 19.6 to 23.7 wt.% and lower Na_2O (0.18 to 0.27 wt.%), Al_2O_3 (0.17 to 2.14 wt.%), FeO (7.65 to 12.24 wt.%), TiO_2 (up to 0.41 wt.%), V_2O_3 (0.03-0.07 wt.%) and 0.74 to 9.10 mol% of jadeite for more retrogressive pyroxenes. These low jadeite-containing clinopyroxene occurs in symplectite with plagioclase and amphibole. A few pyroxene grains contain higher Na_2O (0.71 to 0.73 wt.%), Al_2O_3 (4.49 to 5.14 wt.%), FeO (12.15 to 13.88 wt.%; high Fe content discards "contamination" by plagioclase), TiO_2 (0.45-1.09 wt.%), V_2O_3 (0.12 to 0.16 wt.%) with jadeite end member between 17.28 mol% and 20.24 mol% (e.g. sample ADE-20), ploting within the omphacite field (Fig. 2.8A; Morimoto, 1988). These Fe-Na-Al-rich clinopyroxene grains do not present omphacite stoichiometry (Fig. 2.8B), but point to more primitive pyroxene compositions, appearing in symplectite with minor plagioclase and no amphibole.

The Na_2O vs Al_2O_3 diagrams show the retrogression path of HP pyroxenes to retrogressed clinopyroxenes by progressive decrease in Na and Al contents (Fig. 2.8C-D). The pyroxene analyses display XMg ($Mg^{2+}/(Mg^{2+}+Fe^{2+})$) ranging from 0.93 to 0.61, also indicating progressive decrease in Mg from HP mineralogy to more retrogressed assemblages.

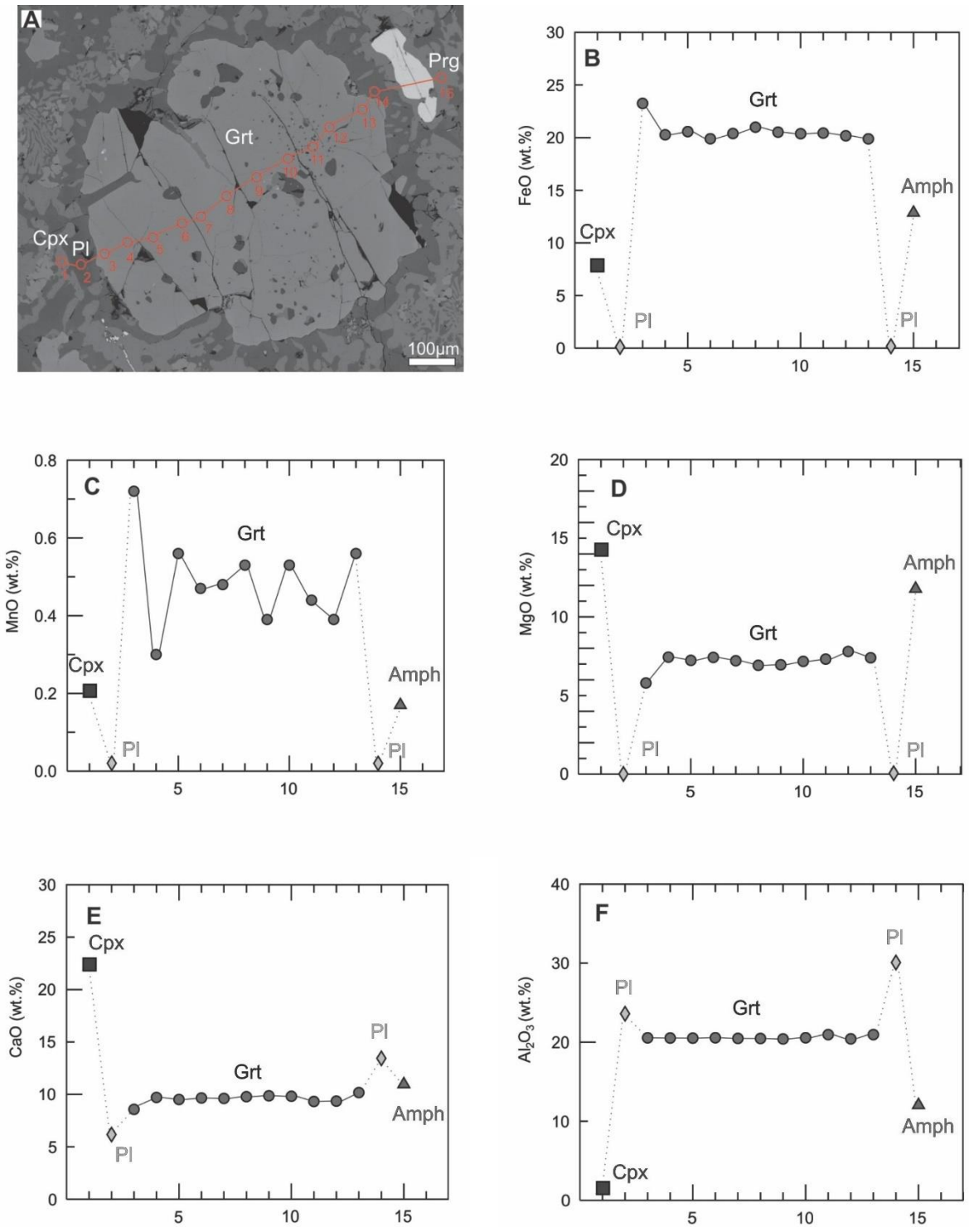

Figure 2.6. Backscattered-Electron (BSE) image and compositional profiles across clinopyroxene-plagioclase symplectite, garnet porphyroblast and amphibole-plagioclase symplectite from sample ADE-09 retro-eclogite (Supplementary Table 2.1 to 2.4).

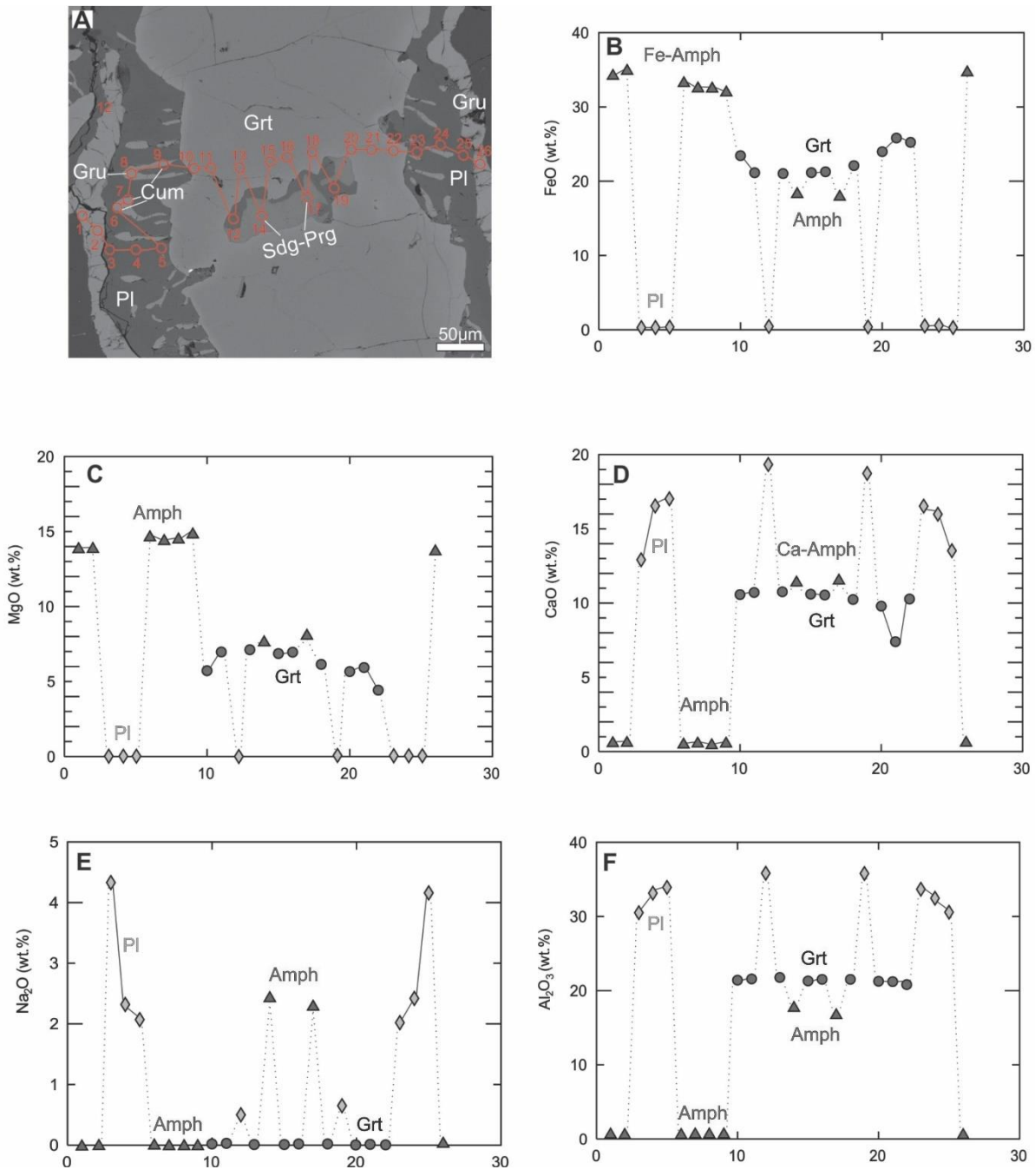

Figure 2.7. Backscattered-Electron (BSE) image and compositional profiles across Fe-amphibolite corona, Fe-amphibolite-plagioclase symplectite, garnet porphyroblast, exsolution Ca-amphibole and plagioclase within garnet crystals, plagioclase symplectite and Fe-amphibolite corona from sample AT-24 retro-eclogite (Supplementary Table 2.1 to 2.4).

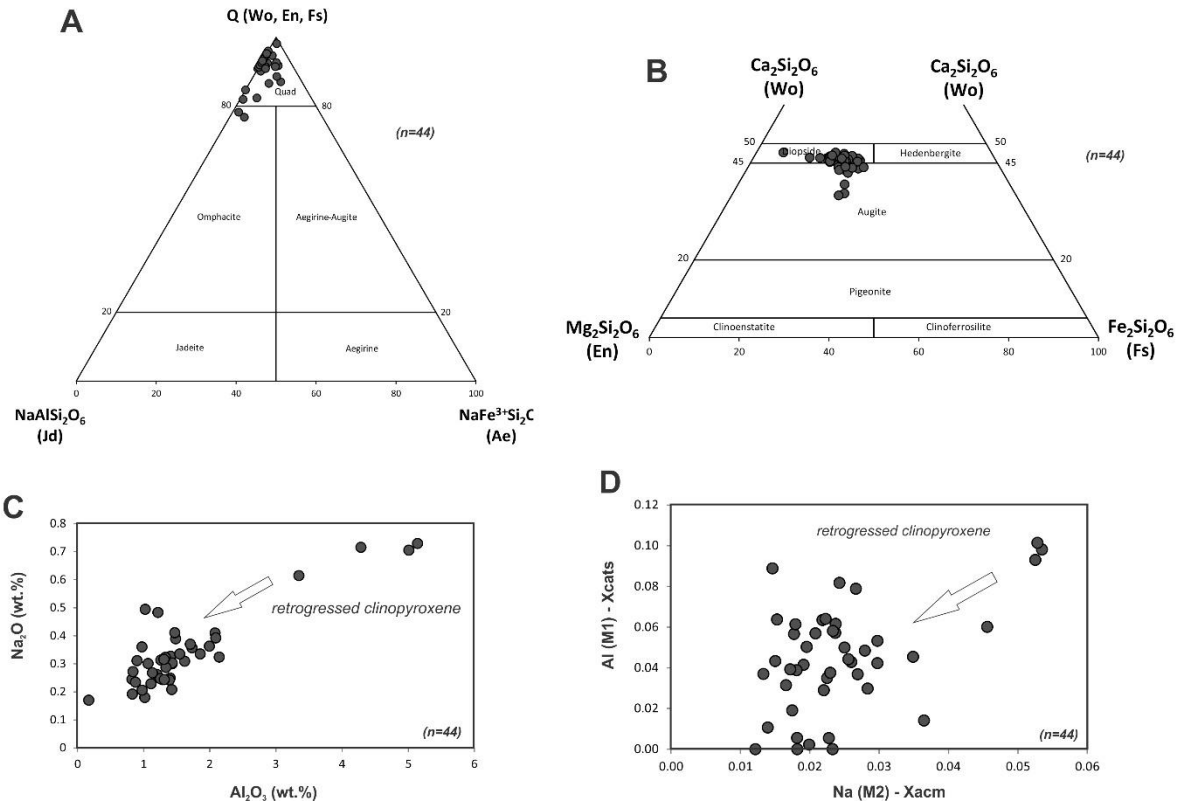

Figure 2-8. A-B) Classification of pyroxenes. C-D) Plot of Al2O3 vs Na2O and Na (Xacm) vs Al (Xcats) content for clinopyroxenes. Nomenclature from Morimoto (1988) (Supplementary Table 2.2). Normalization based on 6 oxygens.

Amphibole

Amphibole occurs by replacing both primary and secondary pyroxene and garnet crystals. Hawthorne et al. (2012) scheme was used for classification and nomenclature of amphibole (Supplementary Table 2.3). Four types of amphibole occurrence and composition are discerned according to textural relationships and metamorphic phase:

i) Na-Al-rich amphibole with compositions from Fe-sadanagaite to pargasite (Al_2O_3 16.6 to 17.6 wt.% and Na_2O 2.28 to 2.42 wt.%) as inclusions (up to 100 µm) in granoblastic garnet (Fig. 2.7A to F);

ii) Ca amphiboles (CaO 9.63-12.12 wt.%; Fig. 2.9A) as vermicular fine-grained crystals in symplectite with compositions varying from Mg-hornblende (higher MgO, 9.04 to 13.43 wt.%, and lower FeO, 1.78 to 16.71 wt.%), tschermakite, hastingsite, pargasite to Fe-hornblende (lower MgO, 6.69-9.06 wt.%, and higher FeO, 17.9 -

22.29 wt.%). The Ca amphiboles have Na2O between 0.67 and 2.50 wt.% (Fig. 2.9C). The Mg-hornblende analyses are mainly recorded in pyroxene-rich samples (e.g. sample ADE-20) and show lower Na_2O (1.07 to 1.22 wt.% with 0.3 apfu Na) and Al_2O_3 (7.7 to 8.9 wt. % with ~1.3 apfu) and higher XMg (0.6 - 0.7). On the other hand, pargasite grains are developed in pyroxene-poor samples (e.g. sample ADE-29) and have higher Na_2O (1.6 to 2.0 wt.% with 0.5 apfu Na) and Al_2O_3 (10.5 to 11.7 wt. % with 1.5–1.8 apfu Al+IV) and lower XMg (0.5). Fe amphibole (cummingtonite) sometimes occurs as irregular medium-grained crystals in the symplectite matrix (Fig. 2.13; Fe-map);

iii) Fe amphiboles medium-grained crystals (retrograde rim) around amphibole-plagioclase symplectites and pyroxene grains, with developed corona texture (Fig. 2.7A) of cummingtonite and mainly grunerite composition with 26 to 34.9 wt.% FeO (Fig. 2.9B) and 12.65 to 18.78 wt.% MgO (Fig. 2.7C).

iv) Mg-Hornblende and pargasite coarse-grained crystals in granoblastic texture. The pargasite grains have higher Na_2O (up to 2.05 wt.%) and Al_2O_3 (up to 11.8 wt.%). Sample AP-14 was used to illustrate the texture difference between symplectite and granoblastic Mg-hornblende (Fig. 2.9D). The vermicular fine grains display lower Na_2O (0.88 to 0.96 wt.% with 0.2 apfu Na) and Al_2O_3 (9.1 to 10.1 wt.% with 1.2 apfu Al^{+IV}), while coarse grains contain higher Na_2O (1 to 1.7 wt.% with 4 apfu Na) and Al_2O_3 (11.3 to 139. wt.% with 1.4-1.8 apfu Al^{+IV}) (Fig. 2.9E).

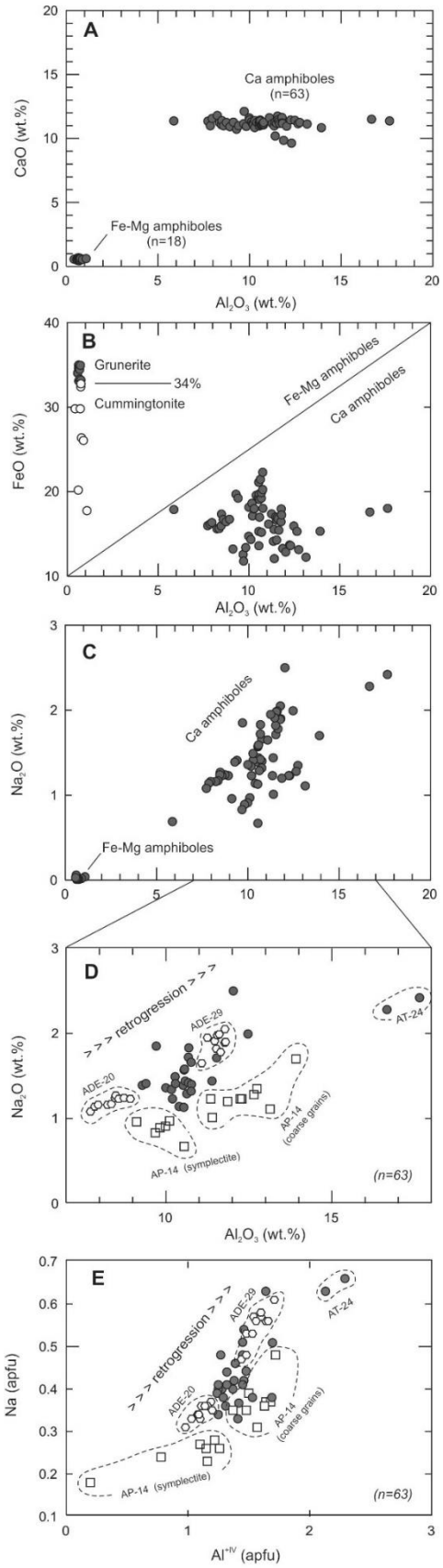

Figure 2.9. A) Plot of Al_2O_3 vs CaO, B) Plot of Al_2O_3 vs FeO, C) Plot of Al_2O_3 vs Na_2O differentiating from Ca to Fe amphiboles. D) Al2O3 vs Na2O and E) Al^{+IV} vs Na content diagrams only of Ca amphiboles. (Supplementary Table 2.3). Normalization based on 23 oxygens.

Plagioclase

Plagioclase analyses (Supplementary Table 2.4) show a wide range of chemical compositions (Fig. 2.10 and Fig. 2.11 A, C and E), which are a function of the textural relationships with distinct phases during metamorphic retrogression. Higher Ca contents (18.73-19.33 wt.% CaO with An94 – 95) are observed as exsolution needles within garnet crystals (Fig. 2.7D). Plagioclase symplectites display a progressive decrease in Ca content and further increase in Na content: bytownite (14.92-17.63 wt.% CaO with An74 – 87) is observed in the symplectite near the garnet rim, when mantling garnet (e.g. sample ADE-20; Fig. 2.11B). Labradorite-andesine (8.29 - 13.66 wt.% CaO with An38–65) is the composition of the symplectite in equilibrium with more amphibole and less or absent pyroxene. Oligoclase-andesine (lower 3.65-7.45 wt.% CaO with An18-36) occurs in the symplectite or corona of plagioclase in equilibrium with amphibole after full retrogression of pyroxene, thus generating Na-rich plagioclase with 7.91 wt.% average and up to 9.35 wt.% Na_2O (e.g. sample ADE-29; Fig. 2.11D and F).

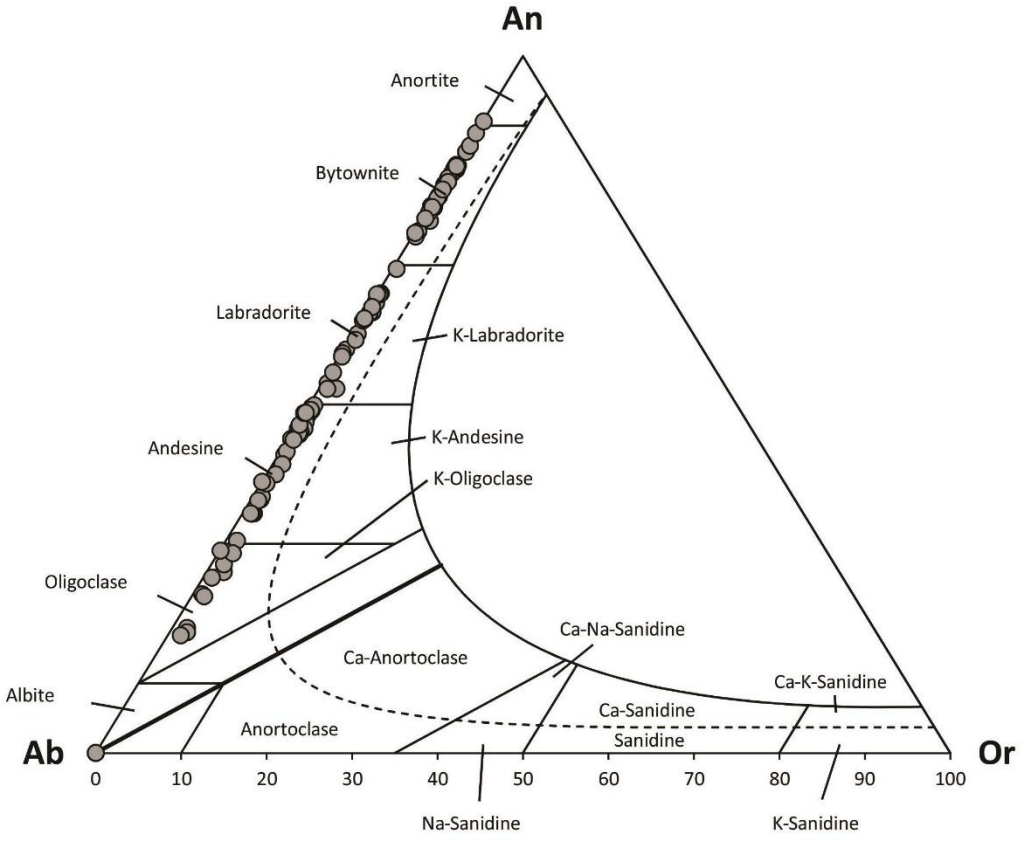

Figure 2.10. Classification of plagioclase grains from the Campo Grande retro-eclogites.

The Al_2O_3 content also reflects the mineral precursor and subsequent elements diffusion and migration process. The higher Al_2O_3 contents (35.82 wt.%, Al 1.95 CPFU with An 94-95) are found in plagioclase exsolution within garnet (20.6 wt.% Al_2O_3 average in analyzed garnet crystals) while the lower Al_2O_3 contents (21.74 wt.%, Al 1.13 CPFU and An 18-36) are related to plagioclase generated from the full retrogression of omphacite. The highest Al_2O_3 and Na_2O values in preserved omphacite reach 10.8 wt.% and 7.9 wt.%, respectively, which supports the HP omphacite as precursor mineral of these plagioclase grains (Xu et al., 2000).

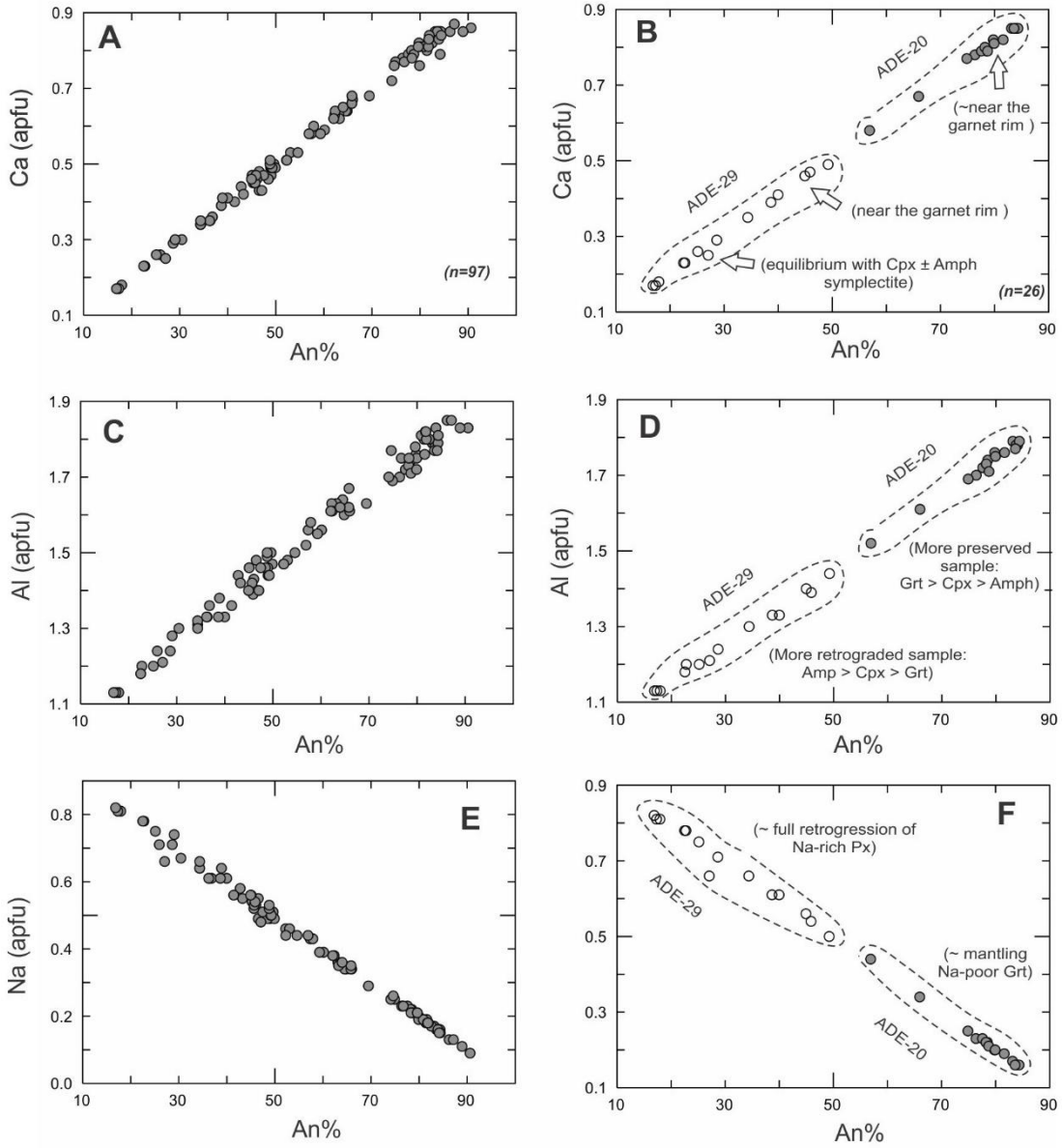

Figure 2.11. A, C and E) Plot of An vs Al, Na and Ca content for plagioclase analyses. B, D and F) Plot of An vs Al, Na and Ca within ADE-20 and ADE-29 sample (Supplementary Table 2.4).

2.5.3 X-ray Mapping

X-ray elemental intensity maps of garnet porphyroblasts reveal a progressive transition from Mg-Ca-Al-rich cores to Fe-Mn-rich rims (Fig. 2.6 and 2.7; Fig. 2.12 to Fig. 2.17). Clinopyroxene, amphibole, plagioclase and mainly quartz inclusions are observed in garnet cores. Strong increase in Mn content is again observed at the garnet rims (Fig. 2.15; Mn-map). Al-rich plagioclase-amphibole symplectites occur as reaction rims surrounding the border (100 to 300 µm) of garnet porphyroblasts (19 to 21 wt.% Al2O3) appear bright in the Al-map (Fig. 2.16).

Clinopyroxene + Na-rich plagioclase + Ca to Fe amphibole symplectites occur as large oikocrystal grains, for which size and shape could indicate the pseudomorph precursor mineral (Fig. 2.3C; Fig. 2.12, Ca-map, and Fig. 2.14, Mg-map). The symplectic texture is zoned with Mg-Ca-rich cores due to the occurrence of clinopyroxene + plagioclase and minor amphibole, and Al-Na-rich rims that are function of amphibole + plagioclase and minor clinopyroxene assemblages. The maps of Ca, Al and Na prove that symplectic clinopyroxenes adjacent to plagioclase and minor amphibole are Ca-rich (21-22 wt. % CaO) and depleted in Al (up to 5.14 wt.% Al_2O_3) and Na (up to 0.73 wt.% Na_2O) contents (Fig. 2.12, 2.16 and 2.17).

Irregular cummingtonite grains occur in the Cpx + Pl + Ca-Amph symplectites (Fig. 2.7A) and as rims surrounding clinopyroxene crystals (Fig. 2.12 and 2.13). In the latter, the cummingtonite grains are surrounded by Na-rich plagioclase (Fig. 2.17). Fe-amphibole exsolutions appear to be coeval with the growth of Cpx + Pl + Mg-Ca-amphibole needles and prior to Na-rich plagioclase coronae. Ilmenite exsolutions (Supplementary Table 2.5) appear to be subsequent to the growth of clinopyroxene + Na-rich plagioclase + Ca to Fe amphibole symplectite, and coeval to Al-rich plagioclase + Na-rich amphibole symplectite (Fig. 2.13; Fe-map).

Compositional trends in symplectic plagioclase show higher Na (up to 9.62 wt.% Na_2O) when in equilibrium with Na-poor pyroxene, suggesting a Na-rich mineral precursor (estimated composition between 6 and 8 wt.% Na_2O) for these plagioclase grains (Fig. 2.17; Na-map). Symplictite plagioclase also displays high Na content (4.82 to 8.32 wt. % Na_2O) when in equilibrium with Ca amphibole (0.9 to 2.5 wt. % Na_2O), and lower Na (0.50 to 4.37 wt. % Na_2O) when in reaction with the Na-poor garnet rim (up to 0.05 wt.% Na_2O) (Fig. 2.7C and Fig. 2.17).

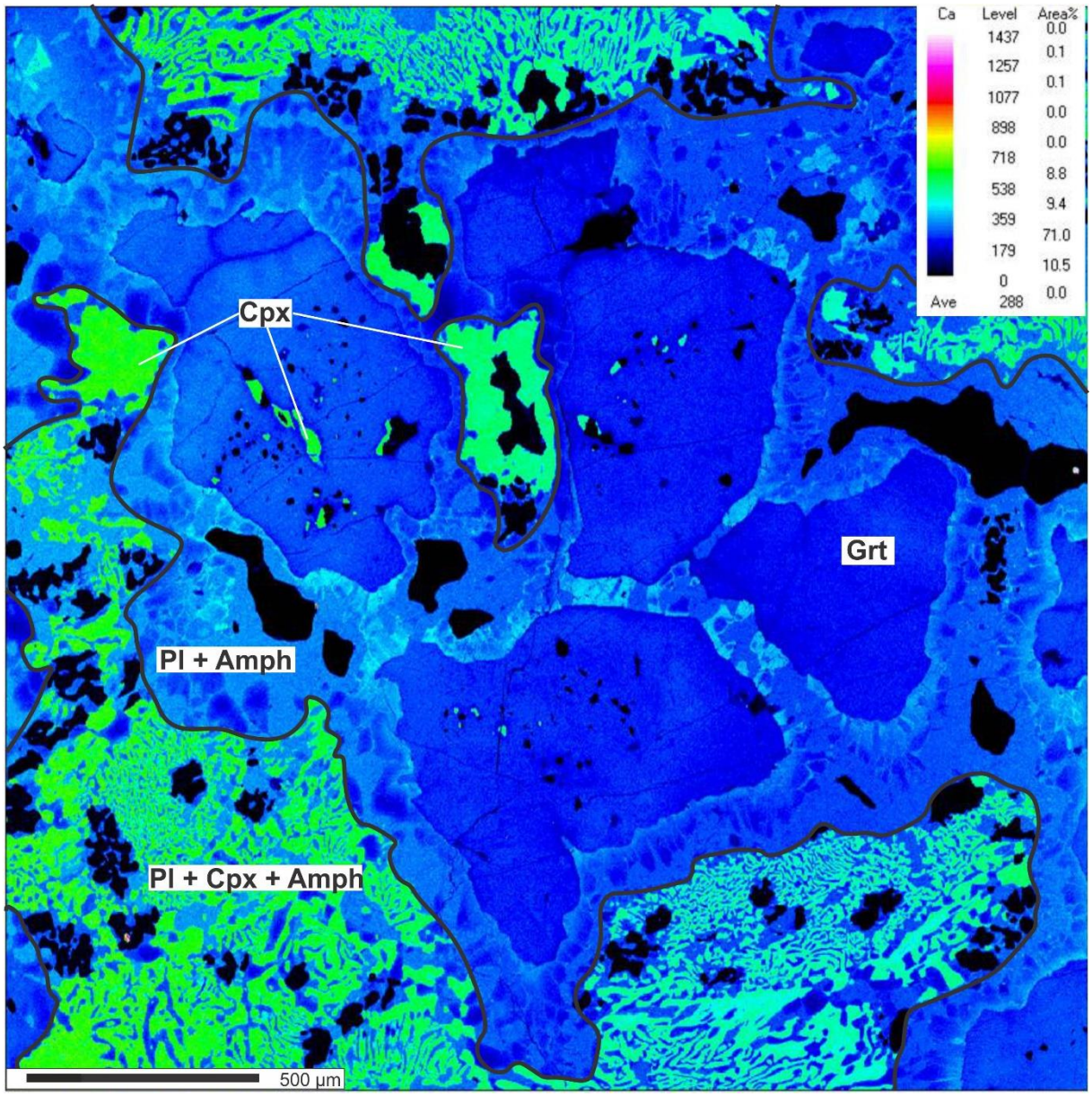

Figure 2.12. X-ray chemical mapping images of Campo Grande retro-eclogite, northeast Brazil. X-ray mapping of Ca. Clinopyroxene grains with higher Ca content (19.6 to 23.7 wt.% CaO). The slight decrease of Ca towards the Cpx-Pl-Amph symplectite rim is probably due to retrogression. The amphibole in symplectite has Ca content between 10 and 11 wt.% CaO. The garnet crystal presents low CaO (8 to 9 wt.%). Fe-amphibole and ilmenite are black in the Ca-map.

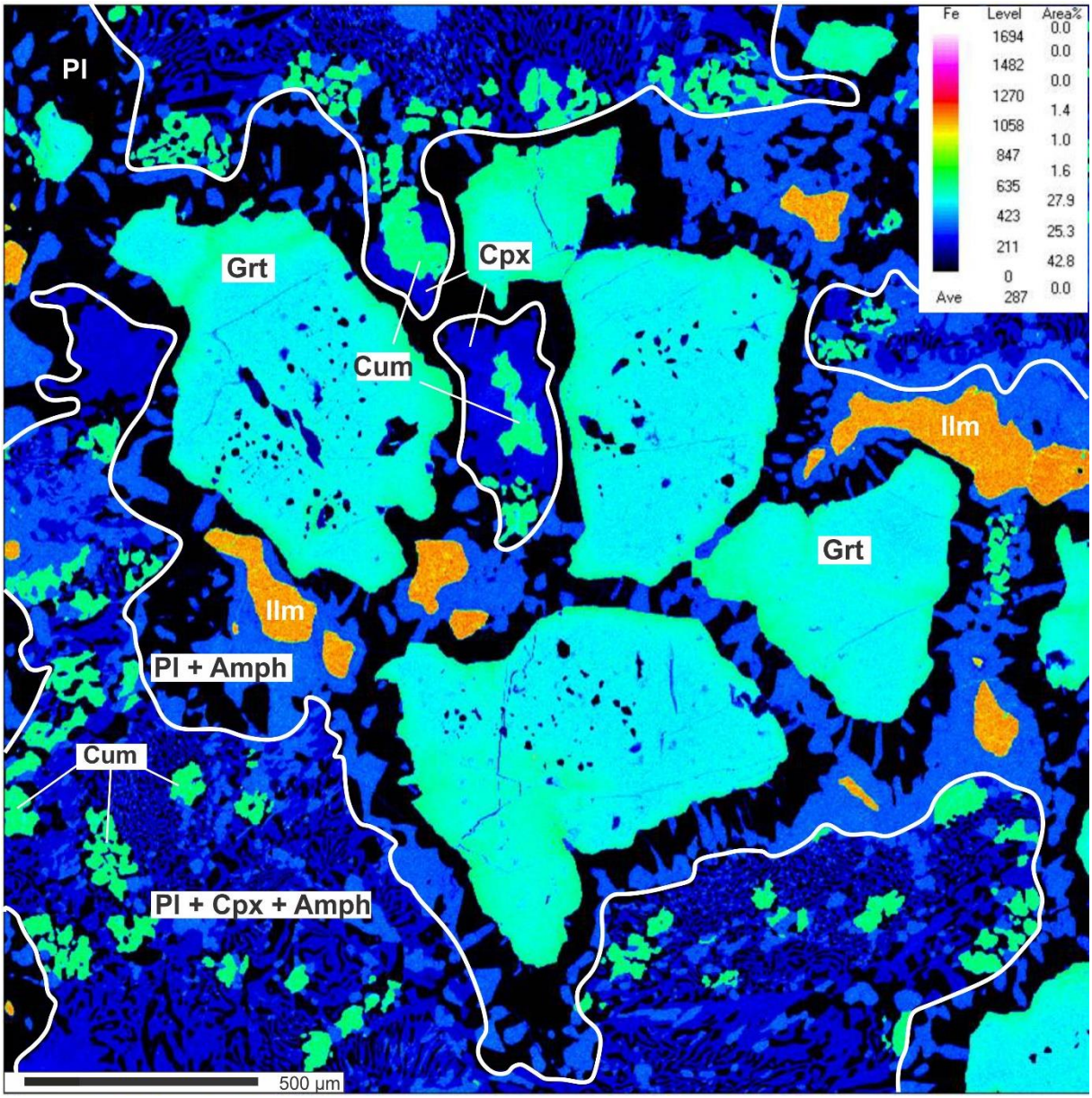

Figure 2.13. X-ray chemical mapping images of Campo Grande retro-eclogite, northeast Brazil. X-ray mapping of Fe. Ilmenite (43 to 44 wt.% FeO and 51 to 53 wt.%TiO_2; See Supplementary Table 2.5), Fe-amphibole (~34 wt.% FeO) and garnet rim (up to 31.3 wt.% FeO) appear highlighted in the Fe-map. The amphibole in symplectite has Fe content from 11.7 (Mg-hornblende) to 22.2 wt.% FeO (Fe-hornblende). Vermicular fine-grained clinopyroxene has low Fe content (7.5 to 13.8 wt.% FeO). Plagioclase appears black in the Fe-map.

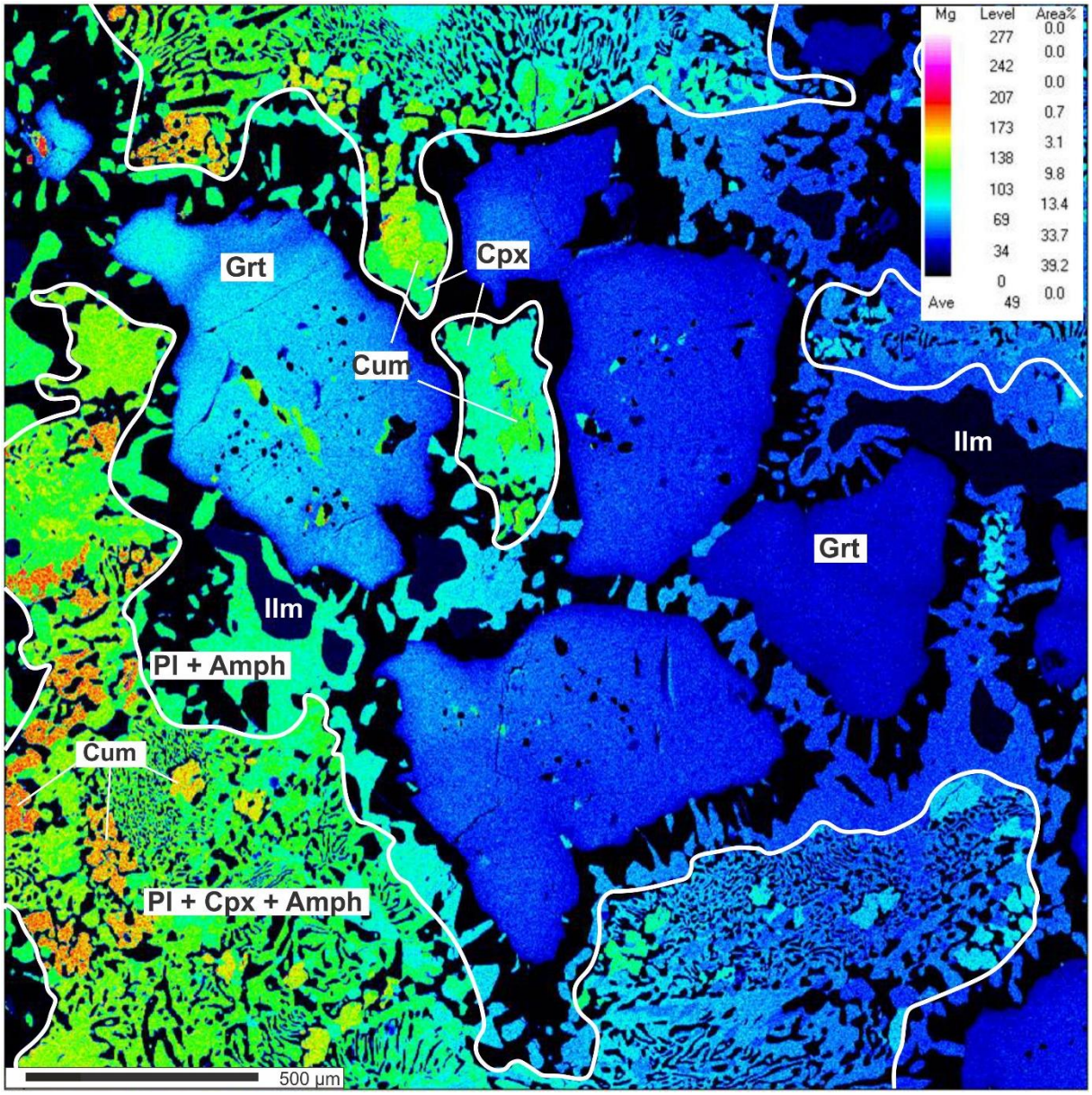

Figure 2.14. X-ray chemical mapping images of Campo Grande retro-eclogite, northeast Brazil. X-ray mapping of Mg. Fe-amphibole grains have higher Mg content (12.65 to 18.78 wt.% MgO). Clinopyroxene in symplectite has high Mg content from 10.1 to 16.5 wt.% MgO. Ca amphibole in symplectite has Mg content between 6.7 (Fe-hornblende) and 13.4 wt.% MgO (Mg-hornblende). Garnet shows strong decrease of Mg content from core (8.2 wt.% MgO) to rim (2.4 wt.% MgO) in some crystals. Plagioclase appears black in the Mg-map.

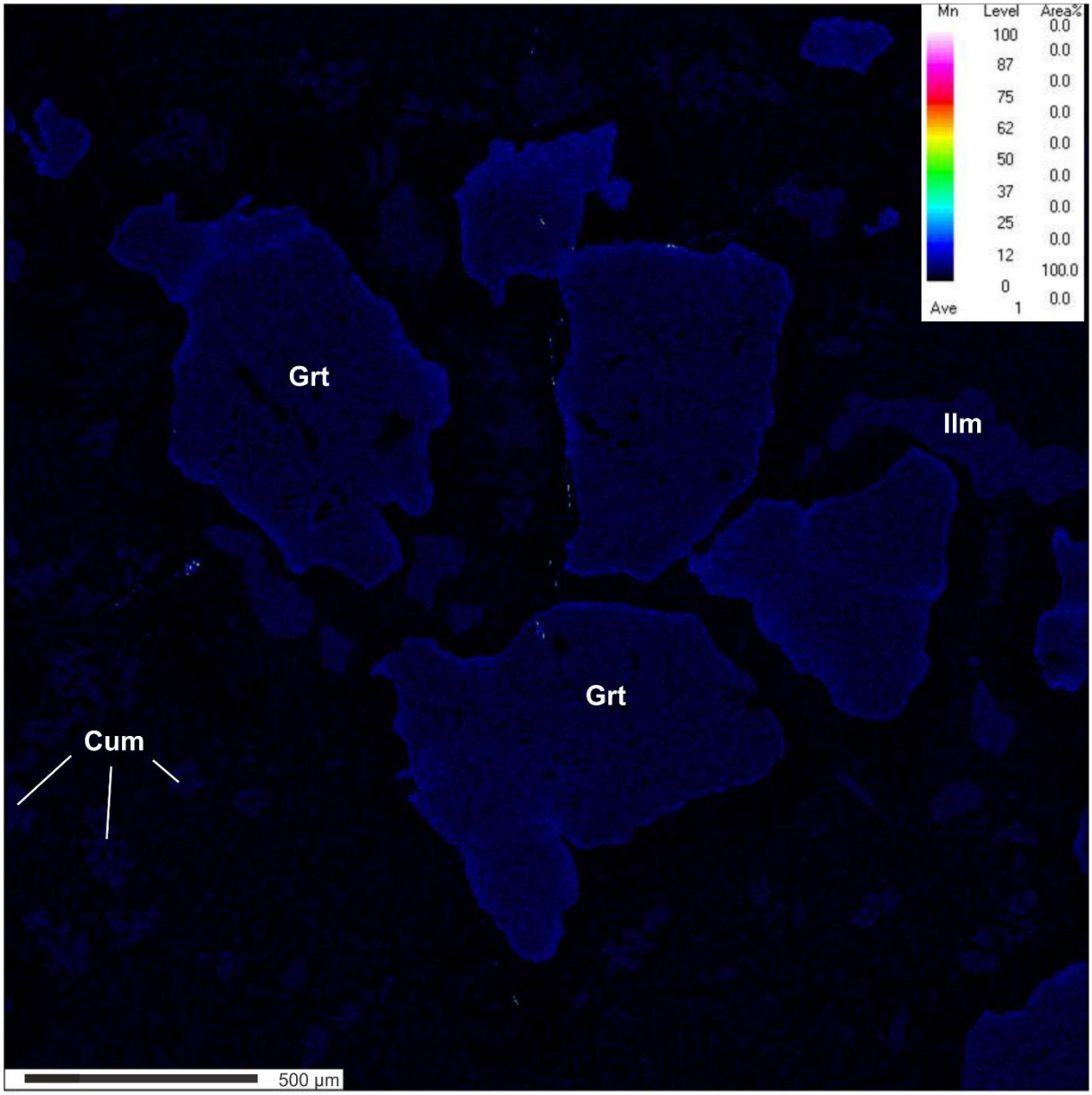

Figure 2.15. X-ray chemical mapping images of Campo Grande retro-eclogite, northeast Brazil. X-ray mapping of Mn. Garnet crystals show increase of Mg content from core (0.27 wt.% MgO) to rim (2.04 wt.% MgO). Ilmenite grains have high MnO between 0.37 and 0.58 wt.%. Fe-amphibole grains show 0.27 to 0.61 wt.% MnO (up to 0.8 wt.% MnO). Clinopyroxene symplectite has low Mn content (0.1 to 0.43 wt.% MnO). Plagioclase and Ca-amphibole symplectite appear black in the Mn-map.

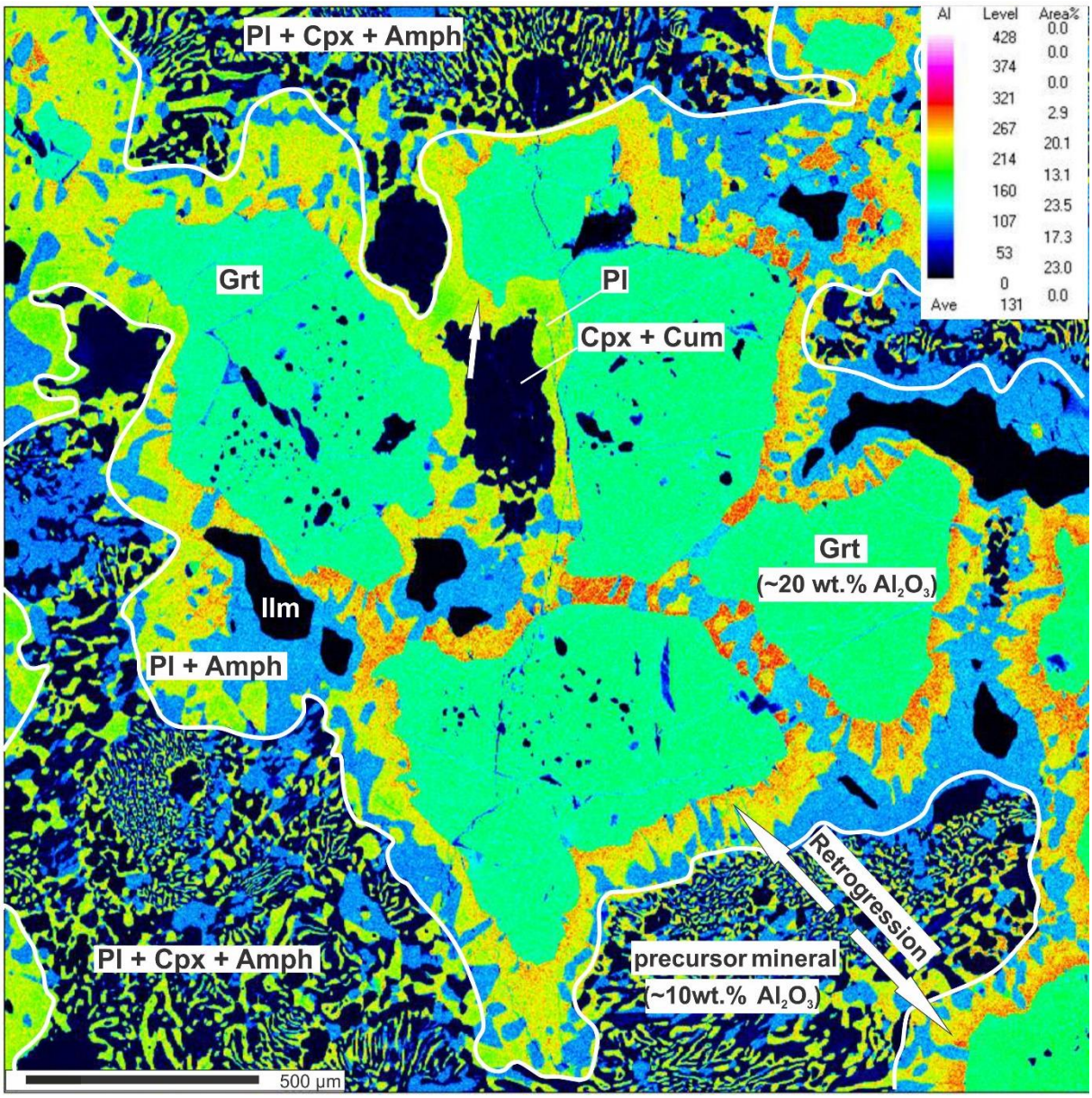

Figure 2.16. X-ray chemical mapping images of Campo Grande retro-eclogite, northeast Brazil. X-ray mapping of Al. Plagioclase symplectite is highlighted in the Al-map from 21.39 (when in the sympathetic growth with clinopyroxene) to 35.82 wt.% Al_2O_3 (when mantling garnet). Garnet crystals show Al content between 16.87 to 21.8 wt.% Al2O3 with slight decrease of Al towards the rims. Ca amphibole in symplectite exhibits Al content from 7.73 wt.% (Mg-hornblende) to 17.59 wt.% Al_2O_3 (pargasite). Cpx grains show low Al content (<2.14 wt.% Al_2O_3), a few have high values (3.35 to 5.14 wt.% Al_2O_3). Fe amphiboles grains have lower Al content (up to 1.08 wt.% Al_2O_3). Ilmenite grains appear black (0.01 to 0.04 wt. % Al_2O_3) in the Al-map.

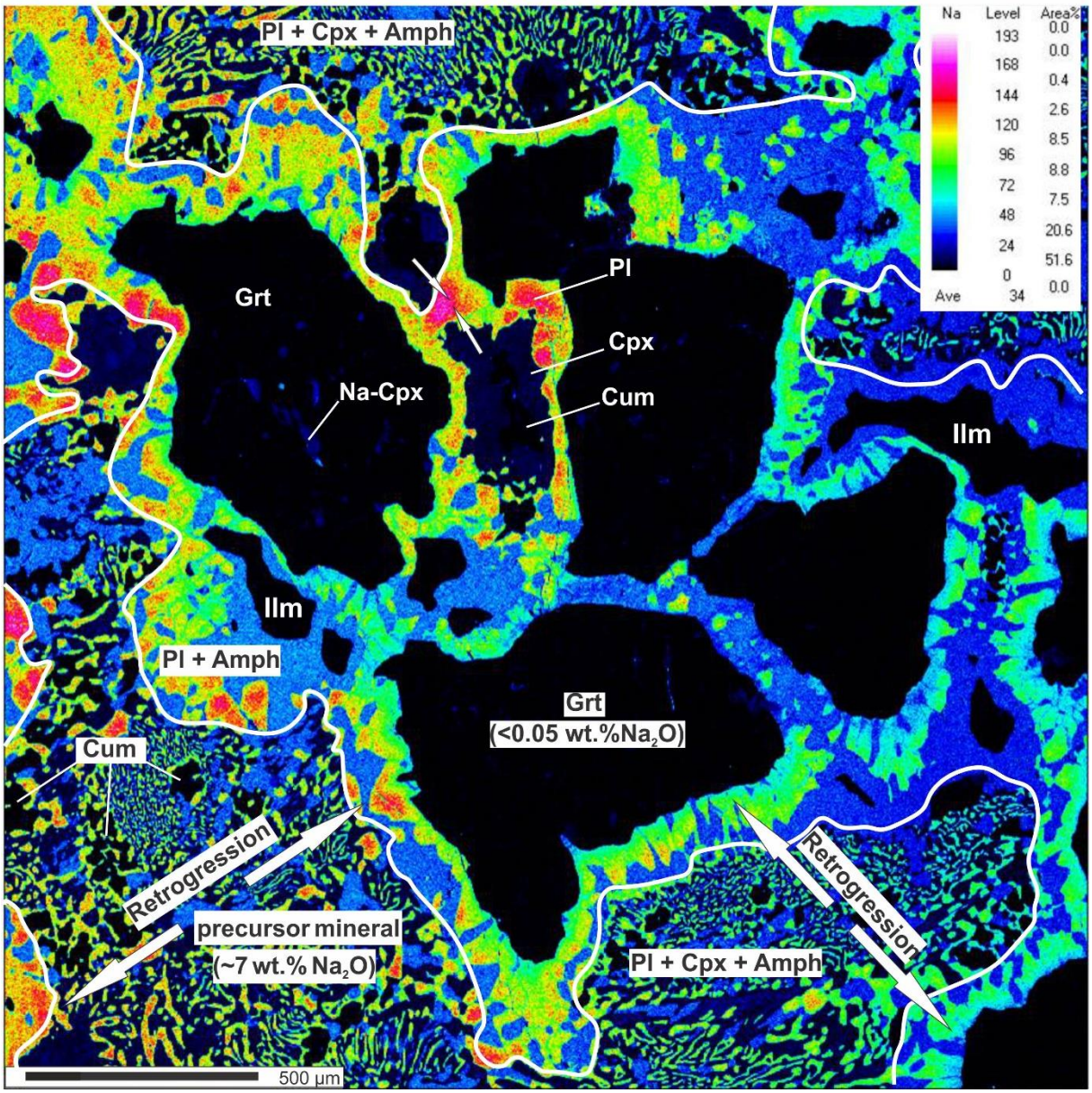

Figure 2.17. X-ray chemical mapping images of Campo Grande retro-eclogite, northeast Brazil. X-ray mapping of Na. Plagioclase grains show Na content from 0.5 wt.% Na_2O (when in garnet rim) to 9.62 wt.% Na_2O (when in the sympathetic growth with amphibole and minor clinopyroxene, highlighted in the Na-map). Ca amphiboles in symplectite exhibit Al content from 0.67 to 2.50 wt.% Na_2O (pargasite) at the garnet boundary. Clinopyroxene semplectites show low Na content, between 0.17 to 0.73 wt.% Na_2O. Ilmenite (<0.15 wt.% Na_2O), garnet (<0.1 wt.% Na_2O) and Fe amphibole (<0.06 wt.% Na_2O) grains appear black in the Na-map.

2.6 DISCUSSION

Decompression process obliterated the eclogitic mineral assemblages and formed retrogressive mineral phases mainly in disequilibrium textures as symplectites, coronae or reaction rims. These textures are incomplete mineral reactions, record path, from the original eclogite facies to retrogression assemblage. The various mineral compositions imply that there was a complex and continuous process of

element diffusion and migration between retrograded minerals after peak metamorphism of eclogite facies (Ota et al., 2004; Anderson and Moecher, 2007; O'Brien et al., 1990).

Eclogites consist of omphacite (Na-Al-rich clinopyroxene) and garnet (pyrope to Mg-rich almandine) formed under high-pressure conditions (>15 GPa). Eclogites never contain plagioclase. The presence of plagioclase, usually developing symplectitic texture with diopside, indicates the destabilization of omphacite during decompression (Carswell, 1990).

Microprobe analyses and X-ray Map showed the slight compositional variation from Mg-Ca-rich core to Fe-Mn-rich rim of the individual garnet crystals. The garnet cores often contain rutile needles and quartz inclusions that may be considered an indication of an HP eclogite precursor (Hellman and Green, 1979; Mposkos and Kostopoulos, 2001) and perhaps representing an older foliation. The highest Mg (8.27 wt.%) and Ca (10.82 wt.%) contents correspond to irregular inner core portions of the same retro-eclogite sample and can be interpreted as a remnant of growth under eclogite facies conditions. Increase in Fe and Mn content at the garnet rims, which reflects late resorption of garnet or cation exchange path (Brodie, 1995). Garnet breaks down to kelyphite of intergrown plagioclase, hornblende and/or aluminous pyroxenes suggesting resorption during corona and symplectite formation (Carlson and Johnson, 1991; White et al., 2008; Robyr et al., 2014; Lanari et al., 2017; Choudhuri and Silva, 2000). The results also suggest that Si and Al diffusion is the slowest (36-40.9 wt.% SiO_2 and 19.4-21.7 wt.% Al_2O_3) of the major constituent elements in pyrope-almandine garnet crystals and thus control rates of plastic deformation (Li et al., 2017).

The original HP omphacite was fully retrograded and forms symplectites composed of Na-poor pyroxene + Na-rich plagioclase, which is a typical texture in retro-eclogite (Boland and Roermund, 1983; Anderson and Moecher, 2007). The widespread development of these symplectites indicates that omphacite was abundant in the HP assemblage (Elvevold and Gilotti, 2000). Outworn omphacite can occur as minute inclusions in garnet grains (Fig. 2.12 and Fig. 3.17). The higher jadeite content clinopyroxenes occur in symplectite with distinct exsolution of Ca-rich plagioclase and minor amphibole, while low jadeite content analyses are recorded in symplectite with Na-rich plagioclase and major amphibole, indicating that they comprise a

retrogressive product of omphacite formed through the reaction omphacite + H2O → clinopyroxene + plagioclase + amphibole (Waters, 2003; Lanari et al., 2013; Tedeschi et l., 2017).

Amphibole is present as a retrograde phase formed by the breakdown of garnet and omphacite, being strongly zoned from Ca-Mg-rich to Fe-Na-Al-rich hornblende (Fig. 2.6, Fig. 2.7 and Fig. 2.12 to 2.17). Ca-Mg-rich amphibole is the main mineral phase that occurs in equilibrium with Ca-rich plagioclase (labradorite-bytownite) while Na-Al-rich amphibole occurs in equilibrium with intermediate plagioclase (oligoclase-andesine). Compositional profiles show high-Al amphibole near garnet and low-Al amphibole near symplectite, also indicating the transfer and lattice diffusion of Al through amphibole (Fig. 2.16, Al-map). Amphibole in the symplectite matrix is Mg-hornblende, tschermakite, hastingsite, pargasite and Fe-hornblende, whereas in the symplectite rim, it is cummingtonite and grunerite. Progressive decrease in Mg with coeval increase in Al, Fe and Na in amphibole studies reflect the continuous depletion of precursor minerals (omphacite and garnet) during metamorphic retrogression. Fe-sadanagaite and pargasite were reported as exsolutions in granoblastic garnet (Fig. 2.7A to F). Similar amphibole compositions are reported in NW Scotland and Colombian Andes retro-eclogite (Storey et al., 2005; Ríos-Reyes et al., 2017). Granoblastic to porphyroclastic amphiboles are recorded in more equilibrated retro-eclogite and are of Mg-Hornblende and pargasite composition (e.g., sample ADE-29). The mineral assemblage represented by amphibole inclusions reveals that the garnet path finished in the amphibolite facies after the eclogite facies.

Compositional profiles suggest that plagioclase in symplectic pyroxene is formed by omphacite breakdown reactions (Omph + SiO_2 = less Na-rich clinopyroxene + plagioclase) and diffusion of Na and Al from HP pyroxene towards plagioclase nucleation sites during decompression (Joanny et al., 1991; Elvevold and Gilotti, 2000). Higher Al-content in symplectite and mainly corona texture cannot be accounted for by the transport of Na and Al from pyroxene crystals, as an external Al-rich source as garnet (~20 wt.% Al_2O_3) is required. Plagioclase grains also occur at the contact between garnet and amphibole. In addition, it is observed as inclusions in garnet and can be considered a mineral phase from the post-eclogite facies. Retrograded symplectites are evidence of diffusion and migration of elements in strongly pressure dependent reactions along a nearly iso-thermal decompression

path. Thus, maintaining favorable reaction kinetics at nearly temperature peak conditions allowed nucleation of exsolution and diffusion controlled grain-coarsening.

Higher resolution images of Cpx-Pl-Amph and Pl-Amph symplectites show that quartz is not part of the symplectite mineral assemblages, suggesting a silica-poor precursor pyroxene or that quartz was consumed by the reactions Jd + Qtz = Ab and Ca-Tschermak's component + Qtz = An (Holland, 1983).

Plagioclase, clinopyroxene and hornblende lamellae within retrograded matrix are not controlled by the crystallographic orientation of the precursor mineral. The vermicular intergrowths are oriented perpendicularly to garnet rims, suggesting the catalytic effect of strain-induced recrystallization. The spatial arrangement of the symplectites follows the linear forms of the garnet, indicating some degree of structural control. Thus, microfractures in garnet crystals during the symplectitic stage may have constituted channels for fluid-assisted element transport (e.g., Straume and Austrheim, 1999), necessary for retrograde metamorphism (Fig. 2.16 and 2.17). Symplectites of amphibole and plagioclase require participation of H_2O (Elvevold and Gilotti, 2000) that may have preferentially percolated through these microfractures (Fig. 2.13, Fe-map, and Fig. 2.16, Al-map).

Diffusion-controlled chemical and mineral zoning in Cpx + Pl ± Amph symplectites are associated with rapid uplift rates and disequilibrium on a micron scale due to greater diffusion of Al and Na into symplectite during decompression, while Mg, and Ca tend to remain fixed.

We suggest based on our results that the tectonic development of the Campo Grande block includes eclogite facies formed by convergence and prograde metamorphism with increasing pressure, result of crustal thickening and shortening, at the maximum depth in the continental crust. Peak pressure followed by peak temperature is the most reasonable interpretation, since thermal relaxation is expected to follow crustal thickening. Exhumation occurs along a decompression path followed by cooling under amphibolite facies condicions along NNE-SSW and ENE-WSW trending shear zones. Then, this retrograded HP assemblage can mark paleosuture zones.

2.7 CONCLUSION

Peak eclogite facies is represented by the Ma-Ca-rich garnet porphyroblasts with preserved rutile and quartz inclusions + Na-rich pyroxene assemblage. Early stage of retrogressive metamorphism represented by Na-poor clinopyroxene + plagioclase ± amphibole symplectite assemblage formed by omphacite breakdown reaction (Omp + H_2O → Di-Aug + Na-rich Pl + Ca to Fe Amph), and Al-rich amphibole + Na-poor plagioclase inclusions in garnet cores coeval high-temperature post-eclogite phase and rapid tectonic exhumation with high overstepping. Late stage of retrogressive metamorphism of amphibolite facies represented by Al-rich plagioclase + Fe amphibole symplectite assemblage, Fe amphibole coronae and ilmenite exsolutions formed by garnet breakdown reactions. Diffusion-controlled chemical and mineral zoning in Cpx + Pl ± Amph symplectites and Pl + Fe-Amph coronae are associated with rapid uplift rates and disequilibrium on a micron scale due to higher diffusion of Fe, Al and Na while Mg and Ca tend to remain fixed.

At the beginning of Neoproterozoic orogenesis, the precursor rocks of this study were submitted to a subduction event, resulting in the production of high-grade metamorphism. During their post-orogenic exhumation, the eclogites underwent a retrograde metamorphism with corona-forming reactions in the amphibolite-facies conditions. Therefore, symplectic and corona textures correspond to a transitional stage of the eclogite-to-amphibolite transformation.

2.8 ACKNOWLEDGEMENTS

This study is part of the first author's PhD thesis in development at the Instituto de Geociências (Universidade de Brasília). The authors acknowledge the support of the INCT Estudos Tectônicos (CAPES/CNPq - 465613/2014-4 and FAPDF - 193.001.263/2017). ELD, TJSS, MT and RAF acknowledge CNPq research fellowships.

2.9 REFERENCES

Anderson, E.D. & Moecher, D.P., 2007. Omphacite breakdown reactions and relation to eclogite exhumation rates. Contributions to Mineralogy and Petrology, 154, 253–277. DOI 10.1007/s00410-007-0192-x.

Andrade, V., Vidal, O., Lewin, E., O'Brien, P., and Agard, P., 2006. Quantification of electron microprobe compositional maps of rock thin sections: An optimized method and examples. Journal of Metamorphic Geology 24, 655-668, doi:10.1111/j.1525-1314.2006.00660.

Arthaud, M.H., Caby, R., Fuck, R.A., Dantas, E.L., Parente, C.V., 2008. Geology of the northern Borborema Province, NE Brazil and its correlation with Nigeria, NW Africa. In: Pankhurst, R.J., Trouw, R.A.J., Brito Neves, B.B., de Wit, M.J. (Eds.), West Gondwana: Pre-Cenozoic Correlation Across the South Atlantic Region. Geological Society of London 294, pp. 49–67. doi.org/10.1144/SP294.4

Boland, J.N. and Van Roermund, H.L.M., 1983. Mechanisms of exsolution in omphacites from high temperature, type B, eclogites. Physics and Chemistry of Minerals, 9(1), pp. 30-37. DOI: 10.1007/BF00309467.

Brito Neves, B.B., Dos Santos, E.J., Van Schmus, W.R., 2000. Tectonic history of the Borborema Province, Northeastern Brazil, in: Cordani, U., Milani, E. J., Thomaz Filho, A., Campos, D. A., (Eds.), Tectonic evolution of South America, 31st International Geological Congress, Rio de Janeiro, Brazil, pp. 151–182.

Brodie, K. H., 1995. The development of oriented symplectites during deformation. Journal of Metamorphic Geology, 13, 499–508.

Bucher, K. and Frey, M., Petrogenesis of Metamorphic rocks: Complete revision of Winkler's textbook. Berlín: Springer-Verlag, 1994.

Carlson, W., D., Johnson, C., D., 1991. Coronal reaction textures in garnet amphibolites of the Llano Uplift. American Mineralogist 76, 756-772.

Carswell, D. A. (1990): Eclogite Facies Rocks. Blackie and Son Ltd., Glasgow, London.

Choudhuri, A. and Silva, D., 2000. A Clinopyroxene-Orthopyroxene-Plagioclase Symplectite Formed by Garnet Breakdown in Granulite Facies, Guaxupé, Minas Gerais, Brazil. Gondwana Research, V. 3, No. 4, pp. 445-452.

Dantas, E.L., Negrão, M.M., Buhn, B., 2008. 2.3 Ga continental crust generation in the Rio Grande do norte terrane, NE-Brazil, in: 6th South American Symposium on Isotope Geology, Abstract Volume, pp. 40.

Droop, G.T.R., 1987. A general equation for estimating Fe3+ concentrations in ferromagnesian silicates and oxides from microprobe analyses, using stoichiometric criteria. Mineralogical Magazine 51, 431-435.

Eskola, P., 1921. On the eclogites of Norway. Videnskapsselskapets Skrifter, I Mat Naturv Klasse 8:1–118.

Elvevold, S. and Gilotti, J.A., 2000. Pressure–temperature evolution of retrogressed kyanite eclogites, Weinschenk Island, North–East Greenland Caledonides. Lithos, 53, pp. 127-147. DOI: 10.1016/S0024-4937(00)00014-1.

Ernst, W.G., 1988. Tectonic history of subduction zones inferred from retrograde blueschist P-T paths. Geology, 16, pp. 1081-1085. DOI: 10.1029/94JB02421.

Faryad, S.W. and Kachlík, V., 2013. New evidence of blueschist facies rocks and their geotectonic implication for Variscan suture(s) in the Bohemian Massif. Journal of Metamorphic Geology, 31, pp. 63-82. DOI: 10.1111/jmg.12009.

Ganade de Araujo, C.E., Rubatto, D., Hermann, J., Cordani, U.G., Caby, R., Basei, M.A., 2014. Ediacaran 2,500-km-long synchronous deep continental subduction in the West Gondwana Orogen. Nat Commun 5, 5198. doi: 10.1038/ncomms6198.

Hawthorne, F. C., Oberti, R., Harlow, G. E., Maresch, W. V., Martin, R. F., Schumacher, J. C. and Welch, M. D., 2012. Nomenclature of the amphibole supergroup. American Mineralogist, 97, 2031-2048. doi.org/10.2138/am.2012.4276

Hellman, P. L., and Green, T. H. 1979. The role of sphene as an accessory phase in the high-pressure partial melting of hydrous mafic compositions. Earth Planet. Sci. Lett. 42:191–201.

Holland, T.J.B., 1983. The experimental determination of activities in disordered and short-range ordered jadeitic pyroxenes. Contrib Mineral Petrol 82: 214–220.

Hollanda, M.H.B.M., Archanjo, C.J., Souza, L.C., Dunyi, L., Armstrong, L., 2011. Long-lived Paleoproterozoic granitic magmatism in the Seridó-Jaguaribe domain, Borborema Province-NE Brazil. Journal of South American Earth Sciences 32, 287-300.

Hollanda, M.H.B.M., Archanjo, C.J., Bautista, J.R., Souza, L.C., 2015. Detrital zircon ages and Nd isotope compositions of the Seridó and Lavras da Mangabeira basins

(Borborema Province, NE Brazil): Evidence for exhumation and recycling associated with a major shift in sedimentary provenance. Precambrian Research 258, 186–207.

Joanny, V., Van Roermund, H. and Lardeaux, J.M., 1991. The clinopyroxene/plagioclase symplectite in retrograde eclogites: A potential geothermobarometer. Geologische Rundschau, 80 (2), pp. 303-320. DOI: 10.1007/BF01829368.

Johansson, L., Möller, C. and Söderlund, U., 2001. Geochronology of eclogite facies metamorphism in the Sveconorwegian Province of SW Sweden. Precambrian Research, 106(3-4), pp. 261-275. DOI: 10.1029/2005TC001844.

Lanari, P., Giuntoli, F., Loury, C., Burn, M., Engi, M., 2017. An inverse modelingapproach to obtain P-T conditions of metamorphic stages involving garnet growth and resorption. European Journal of Mineralogy 29, 181-199. DOI: 10.1127/ejm/2017/0029-2597.

Lanari, P., Riel, N., Guillot, S., Vidal, O., Schwartz, S., Pêcher, A., Hattori, K.H., 2013. Deciphering high-pressure metamorphism in collisional context using microprobe mapping methods: Application to the Stak eclogitic massif (northwest Himalaya). Geology 41(2), 111–114. doi:10.1130/g33523.1.

Li, B., Ge, J. & Zhang, B., 2017. Diffusion in garnet: a review. Acta Geochim 37: 19-31. https://doi.org/10.1007/s11631-017-0187-x

Morimoto, N., 1988. Nomenclature of Pyroxenes. Mineralogy and Petrology, Volume 39, Issue 1, pp 55–76.

Mposkos, E., and Kostopoulos, D., 2001. Diamond, former coesite and supersilicic garnet in metasedimentary rocks from the Greek Rhodope: a new ultrahighpressure metamorphic province established. Earth Planet. Sci. Lett. 192: 497–506.

Oliveira, R.G., Medeiros, W.E., 2018. Deep crustal framework of the Borborema Province, NE Brazil, derived from gravity and magnetic data. Precambrian Research, 315: 45-65.

O'Brien, P.J., 1997. Garnet zoning and reaction textures in overprinted eclogites, Bohemian Massif, European variscides: A record of their thermal history during exhumation. Lithos, 41, pp. 119-133. DOI: 10.1016/S0024-4937(97)82008-7.

O'Brien, P.J., Carswell, D.A., Gebauer, D., 1990. Eclogite formation and distribution in the European Variscides. In: Carswell DA (ed) Eclogite facies rocks. Chapman and Hall, New York, pp 204–224.

Ota, T., Terabayashi, M. and Katayama, I., 2004. Thermobaric structure and metamorphic evolution of the Iratsu eclogite body in the Sanbagawa belt, central Shikoku, Japan. Lithos, 73(1-2), pp. 95-126. DOI: 10.1016/j.lithos.2004.01.001.

Padilha, A.L., Vitorello, I., Padua, M.B., Bologna, M.S., 2014. Electromagnetic constraints for subduction zones beneath the northwest Borborema province: Evidence for Neoproterozoic island arc-continent collision in northeast Brazil. Geology 42, 91-94.

Padilha, A.L., Vitorello, Í., Pádua, M.B., Fuck, R.A., 2016. Deep magnetotelluric signatures of the early Neoproterozoic Cariris Velhos tectonic event within the Transversal sub-province of the Borborema Province, NE Brazil. Precambrian Research 275, 70-83.

Padilha, A.L., Vitorello, Í., Pádua, M.B., Fuck, R.A., 2017. Cryptic signatures of Neoproterozoic accretionary events in northeast Brazil imaged by magnetotellurics: Implications for the assembly of West Gondwana. Tectonophysics 699, 164-177.

Ríos-Reyes, C.A., Castellanos-Alarcón, O.M. and García-Ramírez, C.A., 2017. Petrogenetic significance of the eclogites from the Arquía Complex on southwestern Pijao, Central Cordillera (Colombia Andes), DYNA 84(200), pp. 291-301.

Robyr, M., Darbellay, B., Baumgartner, L.P., 2014. Matrix-dependent garnet growth in polymetamorphic rocks of the Sesia zone, Italian Alps. Journal of Metamorphic Geology 32(1), 3-24. doi:10.1111/jmg.12055.

Rubie, D. C., 1990. Role of kinetics in the formation and preservation of eclogites. In: Carswell DA (ed) Eclogite facies rocks. Chapman and Hall, New York, pp 111–140.

Santos, T.J.S., Fetter, A.H., Nogueira Neto, J.A., 2008. Comparisons between the northwestern Borborema Province, NE Brazil, and the southwestern Pharusian Dahomey Belt, SW Central Africa. In: Pankhurst, R.J., Trouw, R.A.J., Brito Neves, B.B., de Wit, M.J. (Eds.), West Gondwana: Pre-Cenozoic Correlation Across the South Atlantic Region. Geological Society, London, Special Publications 294, pp. 101–120. doi.org/10.1144/SP294.6

Santos, T.J.S., Garcia, M.G.M., Amaral, W.S., Caby, R., Wernick, E., Arthaud, M.H., Dantas, E.L., Santosh, M., 2009. Relics of eclogite facies assemblages in the Ceará Central Domain, NW Borborema Province, NE Brazil: implications for the assembly of West Gondwana. Gondwana Research 15, 454–470.

Shervais, J.W., Dennis, A.J., McGee, J.J., Secor, D., 2003. Deep in the Heart of Dixie: Pre-Alleghanian eclogite and HP granulite metamorphism in the Carolina terrane, South Carolina, USA. J Metamorph Geol 21:65–80.

Simakov, S.K., 2008. Garnet-clinopyroxene and clinopyroxene geothermobarometry of deep mantle and crust eclogites and peridotites. Lithos, 106, pp. 125-136,. DOI: 10.1016/j.lithos.2008.06.013.

Souza, Z.S., Martin, H., Peucat, J.J., Jardim de Sá, E. F., Macedo, M.H.F., 2007. Calc-Alkaline Magmatism at the Archean-Proterozoic Transition: The Caicó Complex Basement (Ne Brasil). Jounal of Petrology 48, 2149-2185.

Storey, C.D., Brewer, T.S. and Temperley, S., 2005. P-T conditions of Grenville-age eclogite facies metamorphism and amphibolite facies retrogression of the Glenelg–Attadale Inlier, NW Scotland. Geological Magazine, 142(5), pp. 1-11. DOI: 10.1017/S001675680500110X.

Straume, A. K. and Austrheim, H., 1999. Importance of fracturing during retro-metamorphism of eclogites. J. metamorphic Geol. 17, 637–652.

Tedeschi, M., Lanari, P., Rubatto, D., Pedrosa-Soares., A., Hermann, J., Dussin, I., Pinheiro, M. A. P., Bouvier, A. S., Baumgartner, L., 2017. Reconstruction of multiple P-T-t stages from retrogressed mafic rocks: subduction versus collision in the Southern Brasília orogen (SE Brazil). LITHOS 4431. doi: 10.1016/j.lithos.2017.09.025

Tubía, J. M., J. Cuevas, J. J. Esteban, and J. L. Gil Ibarguchi, 2009. Remnants of a Mesozoic rift in a subducted terrane of the Alpujarride Complex (Betic Cordilleras, southern Spain), Journal of Geology, 117, 71–87.

Van Schmus, W. R., Brito Neves, B.B., Williams, I. S., Hackspacher, P. C., Fetter, A. H., Dantas, E. L., Babinski, M., 2003. The Seridó Group of NE Brazil, a late Neoproterozoic pre- to syn-collisional basin in West Gondwana: insights form

SHRIMP U-Pb detrital zircon ages and Sm-Nd crustal residence (TDM) ages. Precambrian Research 127, 287-327.

Van Schmus, W.R., Oliveira, E.P, Silva Filho, A.F., Toteu, S.F., Penaye, J., Guimarães, I. P., 2008. Proterozoic links between the Borborema Province, NE Brazil, and the Central African Fold Belt. In: Pankhurst R.J., Trouw R.A.J., Brito Neves B.B and De Wit M.J. (eds.) West Gondwana: Pre-Cenozoic correlations across the South Atlantic region. Geological Society, London, Special Publication, v. 294, pp. 69-99.

Vogel, D.E., 1966. Nature and chemistry of the formation of clinopyroxene–plagioclase symplectite from omphacite. Neues Jahrb Mineral Monatsh 6:185–189.

Waters, D., 2003. P-T path from Cpx-Hbl-Pl symplectites, www.earth.ox.ac.uk/~davewa/index.html.

White, R.W., Powell, R., Baldwin, J.A., 2008. Calculated phase equilibria involving chemical potentials to investigate the textural evolution of metamorphic rocks. Journal of Metamorphic Geology 26, 181-198. doi.org/10.1111/j.1525-1314.2008.00764.x

Whitney, D.L., Evans, B.W., 2010. Abbreviations for names of rock-forming minerals. American Mineralogist 95, 185-187.

Xu, S., Yican, L., Wen, S., Rucheng, W., Laili, J., and Weiping, W., 2000. Discovery of the eclogite and its petrography in the Northern Dabie Mountain. Chinese Science Bulletin. 45. 273-278. 10.1007/BF02884690.

Zhao, G., Cawood, P. A., Wilde, S.A., Lu, L., 2001. High-pressure granulites (retrograded eclogites) from the Hengshan Complex, North China craton: petrology and tectonic implications. Journal of Petrology 42: 1141–1170.

Supplementary Table 2.1. Analyses of the garnets.

Sample	SiO2	TiO2	Al2O3	FeO	MnO	MgO	CaO	Na2O	K2O	F	Cl	Cr2O3	NiO	Total	Almandine	Pyrope	Grossular	Spessartine	Andradite	Uvarovite
ADE-09	38,41	0,08	21,04	22,92	0,65	6,70	9,80	0,00	0,00	0,00	0,00	0,00	0,00	99,61	45,20	26,01	23,26	1,44	4,08	0,00
ADE-09	37,75	0,01	20,29	22,57	0,56	6,53	9,55	0,02	0,01	0,00	0,00	0,03	0,03	97,36	45,62	25,90	22,62	1,27	4,48	0,11
ADE-09	38,37	0,10	20,90	22,25	0,40	6,77	9,61	0,00	0,00	0,00	0,00	0,04	0,05	98,48	45,63	26,47	23,95	0,89	2,94	0,11
ADE-09	38,09	0,00	20,76	22,43	0,62	6,51	9,55	0,03	0,00	0,00	0,00	0,11	0,00	98,10	46,16	25,53	23,49	1,39	3,10	0,35
ADE-09	37,54	0,00	20,57	22,07	0,55	6,48	9,35	0,00	0,01	0,00	0,01	0,00	0,00	96,59	46,24	25,78	23,78	1,25	2,95	0,00
ADE-09	38,07	0,00	20,86	23,21	0,58	6,71	9,05	0,00	0,01	0,00	0,00	0,00	0,07	98,56	46,95	26,29	21,69	1,29	3,78	0,00
ADE-09	38,35	0,31	20,89	22,70	0,47	6,26	9,36	0,04	0,02	0,00	0,00	0,00	0,06	98,46	47,56	24,77	24,62	1,05	2,00	0,00
ADE-09	36,80	0,19	20,21	23,82	0,47	5,51	9,17	0,00	0,01	0,00	0,00	0,01	0,02	96,21	49,88	22,34	23,02	1,07	3,65	0,04
ADE-09	38,24	0,05	20,72	24,01	0,60	5,86	9,00	0,01	0,02	0,00	0,01	0,00	0,01	98,51	49,88	23,20	22,79	1,34	2,79	0,00
ADE-09	38,27	0,00	20,83	24,22	0,66	5,69	9,02	0,00	0,00	0,05	0,02	0,02	0,01	98,79	50,55	22,41	22,93	1,48	2,55	0,07
ADE-09	37,99	0,00	20,69	25,69	0,71	5,05	8,98	0,02	0,01	0,00	0,00	0,06	0,00	99,20	53,21	19,84	21,81	1,59	3,37	0,18
ADE-09	36,84	0,14	20,35	25,59	1,01	4,40	9,11	0,03	0,00	0,00	0,00	0,09	0,00	97,57	53,37	17,80	22,57	2,32	3,64	0,29
ADE-09	37,36	0,15	20,99	26,62	1,14	4,50	8,70	0,03	0,00	0,00	0,02	0,10	0,00	99,60	54,52	17,94	21,43	2,59	3,23	0,30
ADE-09	38,50	0,00	20,64	26,79	1,02	4,68	8,67	0,00	0,01	0,00	0,01	0,00	0,00	100,31	54,80	18,39	20,85	2,28	3,68	0,00
ADE-09	37,95	0,00	21,05	27,38	1,34	4,37	7,71	0,00	0,00	0,00	0,00	0,00	0,00	99,81	58,06	17,17	19,62	3,00	2,16	0,00
ADE-09	38,07	0,18	20,39	27,14	1,37	3,53	8,31	0,01	0,00	0,00	0,00	0,00	0,03	99,03	58,33	14,30	22,29	3,17	1,92	0,00
ADE-9T	39,84	0,14	21,14	21,08	0,39	6,48	9,16	0,02	0,03	0,00	0,00	0,08	0,00	98,34	47,17	25,77	25,94	0,88	0,00	0,24
ADE-9T	38,93	0,21	20,60	23,27	0,45	5,76	7,98	0,04	0,00	0,00	0,00	0,11	0,04	97,38	52,10	23,47	23,03	1,05	0,00	0,36
ADE-9T	39,51	0,13	20,91	23,25	0,48	5,59	8,60	0,00	0,00	0,00	0,01	0,05	0,00	98,53	51,51	22,52	24,73	1,10	0,00	0,15
ADE-9T	39,61	0,00	21,43	21,40	0,38	6,52	8,58	0,00	0,00	0,00	0,00	0,07	0,05	98,03	49,03	25,76	24,14	0,86	0,00	0,21
ADE-9T	40,01	0,09	21,07	21,65	0,38	6,32	8,78	0,00	0,00	0,01	0,01	0,17	0,01	98,50	48,89	25,14	24,59	0,85	0,00	0,53
ADE-9T	39,75	0,00	21,28	22,46	0,49	6,21	8,51	0,00	0,02	0,00	0,00	0,00	0,02	98,73	50,09	24,59	24,22	1,10	0,00	0,00
ADE-9T	38,90	0,07	20,86	25,49	1,00	4,79	7,11	0,02	0,01	0,00	0,01	0,13	0,01	98,41	57,89	19,26	20,15	2,28	0,00	0,42
ADE-9T	39,19	0,00	20,96	21,26	0,34	6,43	8,71	0,00	0,00	0,00	0,01	0,00	0,00	96,90	48,17	25,85	25,19	0,79	0,00	0,00
ADE-9T	39,25	0,00	20,72	23,49	0,59	5,35	8,31	0,03	0,00	0,00	0,00	0,03	0,00	97,77	52,59	21,76	24,19	1,36	0,00	0,10
ADE-9T	38,58	0,00	20,91	23,22	0,58	5,31	8,10	0,00	0,00	0,00	0,02	0,00	0,04	96,76	53,78	21,41	23,48	1,33	0,00	0,00
ADE-9T	38,74	0,10	20,61	22,90	0,61	5,61	8,66	0,00	0,03	0,00	0,00	0,16	0,00	97,42	50,41	22,84	24,84	1,40	0,00	0,50
ADE-9T	37,95	0,20	20,52	23,85	0,71	5,29	7,91	0,03	0,00	0,04	0,00	0,08	0,01	96,59	53,34	21,68	23,07	1,66	0,00	0,25
ADE-9T	39,66	0,11	20,99	23,89	0,61	5,78	7,56	0,00	0,00	0,01	0,00	0,08	0,01	98,69	53,66	23,16	21,54	1,40	0,00	0,25

Sample	SiO2	TiO2	Al2O3	FeO	MnO	MgO	CaO	Na2O	K2O	F	Cl	Cr2O3	NiO	Total	Almandine	Pyrope	Grossular	Spessartine	Andradite	Uvarovite
ADE-9T	39,23	0,06	20,93	22,88	0,45	5,71	8,19	0,00	0,00	0,00	0,00	0,13	0,03	97,62	52,43	22,91	23,20	1,03	0,00	0,42
ADE-9T	39,64	0,18	21,12	23,20	0,57	5,73	7,97	0,04	0,00	0,00	0,00	0,09	0,05	98,59	53,07	22,82	22,54	1,29	0,00	0,28
ADE-16	37,49	0,04	20,14	25,58	0,58	4,36	9,30	0,00	0,00	0,00	0,00	0,00	0,00	97,48	53,99	17,63	23,70	1,34	3,34	0,00
ADE-16	38,29	0,02	20,41	27,00	0,89	3,91	9,22	0,01	0,00	0,00	0,00	0,02	0,00	99,77	55,96	15,60	22,92	2,02	3,44	0,07
ADE-16	37,95	0,03	20,80	27,56	0,94	3,96	9,00	0,01	0,02	0,00	0,00	0,09	0,03	100,38	56,93	15,56	21,68	2,09	3,47	0,28
ADE-16	38,82	0,00	20,39	26,72	1,22	3,53	8,45	0,06	0,02	0,05	0,02	0,00	0,00	99,30	57,79	14,48	23,94	2,85	0,95	0,00
ADE-16	37,45	0,00	19,83	27,86	1,03	3,34	8,71	0,03	0,00	0,00	0,00	0,04	0,04	98,33	58,57	13,60	21,10	2,38	4,22	0,14
ADE-16	37,33	0,01	20,36	28,61	1,32	3,47	8,17	0,05	0,01	0,00	0,00	0,00	0,00	99,32	59,71	13,86	19,36	2,99	4,08	0,00
ADE-16	37,35	0,01	19,93	28,35	1,06	3,36	8,16	0,02	0,00	0,00	0,01	0,00	0,08	98,33	60,09	13,63	19,85	2,45	3,98	0,00
ADE-16	36,72	0,00	20,09	28,01	1,47	3,08	8,21	0,01	0,02	0,00	0,00	0,00	0,08	97,68	60,17	12,49	20,34	3,39	3,61	0,00
ADE-16	36,14	0,02	19,41	28,95	1,70	2,53	7,34	0,07	0,06	0,00	0,00	0,06	0,01	96,28	63,42	10,54	17,97	4,03	3,86	0,18
ADE-20	37,54	0,00	20,69	22,97	0,67	5,34	9,93	0,03	0,00	0,00	0,00	0,10	0,00	97,27	48,95	21,20	25,80	1,51	2,23	0,32
ADE-20	38,35	0,02	20,77	23,94	1,05	4,84	9,35	0,02	0,00	0,00	0,00	0,05	0,00	98,38	51,32	19,38	25,54	2,38	1,23	0,15
ADE-20	36,72	0,00	20,06	27,19	1,39	3,72	8,14	0,00	0,03	0,00	0,03	0,01	0,01	97,29	57,95	15,09	19,95	3,20	3,77	0,04
ADE-20	38,10	0,00	19,78	26,23	1,79	3,43	7,61	0,03	0,00	0,00	0,01	0,14	0,01	97,13	58,23	14,45	21,85	4,29	0,71	0,47
ADE-24A	38,86	0,46	20,70	24,45	0,45	5,55	10,62	0,00	0,02	0,00	0,00	0,00	0,00	101,12	47,80	21,56	25,02	1,00	4,62	0,00
ADE-24A	39,56	0,06	20,43	23,73	0,61	4,54	10,01	0,01	0,00	0,01	0,00	0,01	0,00	98,96	50,45	18,62	28,91	1,41	0,56	0,04
ADE-24A	39,04	0,00	20,41	26,62	0,67	4,53	9,67	0,00	0,01	0,00	0,00	0,00	0,00	100,96	53,16	17,90	23,02	1,49	4,43	0,00
ADE-24A	40,97	0,03	16,87	28,56	2,04	3,80	6,71	0,07	0,07	0,00	0,33	0,12	0,00	99,57	55,15	17,43	13,81	5,31	7,87	0,43
ADE-24A	38,50	0,00	19,76	28,98	1,95	2,39	8,63	0,02	0,00	0,00	0,00	0,02	0,00	100,25	60,29	9,77	21,35	4,54	3,98	0,07
ADE-29	39,31	0,07	20,31	21,24	0,49	5,77	10,28	0,01	0,01	0,00	0,00	0,08	0,01	97,57	44,80	23,70	29,33	1,13	0,79	0,25
ADE-29	39,72	0,06	20,72	22,32	0,70	6,34	9,68	0,00	0,00	0,00	0,01	0,01	0,00	99,55	45,39	25,29	25,71	1,59	1,99	0,03
ADE-29	39,43	0,00	20,92	22,87	0,55	6,18	9,64	0,06	0,01	0,01	0,02	0,00	0,00	99,67	46,98	24,41	25,46	1,23	1,91	0,00
ADE-29	39,30	0,00	20,20	23,27	0,52	5,39	9,34	0,00	0,01	0,00	0,01	0,00	0,03	98,07	49,00	22,16	26,22	1,21	1,40	0,00
ADE-29	38,57	0,07	20,27	24,02	0,52	5,57	9,15	0,02	0,03	0,05	0,00	0,00	0,02	98,30	49,73	22,50	23,70	1,20	2,88	0,00
ADE-29	39,06	0,13	20,33	24,43	0,70	4,93	9,77	0,04	0,01	0,00	0,02	0,13	0,06	99,59	50,35	19,81	25,20	1,59	2,63	0,42
ADE-29	39,16	0,01	20,12	24,90	0,74	4,75	9,18	0,00	0,00	0,00	0,01	0,00	0,00	98,86	51,86	19,42	24,70	1,72	2,30	0,00
ADE-29	37,79	2,35	19,81	24,63	0,93	4,68	8,54	0,00	0,02	0,00	0,02	0,00	0,00	98,75	52,30	19,67	24,65	2,21	1,17	0,00
ADE-29	37,71	0,10	20,08	25,36	1,13	4,52	8,86	0,07	0,00	0,00	0,01	0,11	0,02	97,97	53,34	18,27	22,19	2,60	3,24	0,35
AP-14	40,18	0,00	21,35	21,27	0,46	8,09	9,92	0,00	0,03	0,00	0,00	0,05	0,00	101,35	41,01	30,84	23,62	0,99	3,38	0,16

Sample	SiO2	TiO2	Al2O3	FeO	MnO	MgO	CaO	Na2O	K2O	F	Cl	Cr2O3	NiO	Total	Almandine	Pyrope	Grossular	Spessartine	Andradite	Uvarovite
AP-14	39,12	0,22	20,82	19,95	0,39	7,65	9,31	0,03	0,01	0,00	0,00	0,04	0,08	97,62	41,73	30,60	25,58	0,89	1,06	0,14
AP-14	38,51	0,00	21,25	20,28	0,34	8,27	8,63	0,04	0,02	0,00	0,01	0,02	0,10	97,46	42,76	32,27	22,63	0,75	1,52	0,07
AP-14	39,41	0,00	21,44	21,82	0,51	7,59	9,41	0,00	0,00	0,00	0,00	0,08	0,01	100,27	43,97	29,04	23,22	1,11	2,44	0,23
AP-14	39,16	0,00	20,61	26,24	1,27	4,38	9,50	0,02	0,00	0,00	0,02	0,11	0,04	101,35	53,10	17,21	22,94	2,84	3,57	0,34
AP-14	38,41	0,00	20,50	26,73	1,24	5,31	7,14	0,02	0,00	0,00	0,01	0,03	0,00	99,39	55,60	21,15	17,27	2,80	3,07	0,10
AP-14	37,74	0,07	19,92	27,67	1,92	4,01	5,98	0,04	0,00	0,00	0,00	0,05	0,00	97,40	60,90	16,67	16,22	4,55	1,50	0,17
AP-14	37,40	0,00	19,74	29,50	0,79	3,46	8,02	0,03	0,02	0,00	0,01	0,00	0,00	98,97	60,91	13,99	17,88	1,82	5,41	0,00
AP-14	38,48	0,05	20,37	30,87	0,79	3,72	7,69	0,04	0,01	0,00	0,01	0,00	0,02	102,05	62,02	14,57	16,30	1,75	5,36	0,00
AP-14	38,50	0,00	20,27	31,37	0,83	3,60	7,31	0,07	0,01	0,00	0,00	0,00	0,00	101,95	63,29	14,19	15,35	1,85	5,33	0,00
AP-14	40,42	0,10	20,50	22,41	1,13	4,94	8,75	0,01	0,01	0,00	0,00	0,04	0,00	98,31	51,25	20,30	25,71	2,63	0,00	0,11
AP-14	41,84	0,04	21,51	20,18	0,34	6,08	10,04	0,00	0,02	0,00	0,00	0,00	0,00	100,04	47,12	23,84	28,28	0,76	0,00	0,00
AP-14	41,94	0,00	21,24	20,92	0,84	5,39	10,15	0,02	0,01	0,00	0,00	0,00	0,00	100,50	47,77	21,40	28,94	1,89	0,00	0,00
AP-14	41,78	0,11	21,75	19,54	0,53	6,27	10,32	0,04	0,00	0,00	0,01	0,00	0,00	100,34	45,54	24,40	28,89	1,17	0,00	0,00
AP-14	42,05	0,09	21,60	18,61	0,41	6,43	10,48	0,01	0,03	0,00	0,02	0,03	0,01	99,76	44,31	25,23	29,44	0,91	0,00	0,11
AP-14	42,13	0,19	21,50	19,40	0,29	6,70	10,14	0,05	0,01	0,00	0,00	0,00	0,00	100,41	44,48	26,29	28,58	0,66	0,00	0,00
AP-14	42,56	0,11	21,72	20,10	0,67	5,79	10,24	0,00	0,00	0,00	0,01	0,00	0,00	101,20	47,30	22,55	28,67	1,47	0,00	0,00
AP-14	42,39	0,26	21,73	18,80	0,57	6,45	10,72	0,02	0,00	0,00	0,00	0,00	0,00	100,94	43,82	25,01	29,90	1,26	0,00	0,00
AP-14	42,16	0,00	21,65	19,41	0,57	6,51	9,85	0,00	0,01	0,00	0,00	0,01	0,00	100,17	45,66	25,43	27,61	1,26	0,00	0,04
AP-14	40,67	0,09	20,91	22,68	1,05	4,35	9,33	0,00	0,00	0,00	0,01	0,07	0,00	99,15	53,11	17,50	26,77	2,41	0,00	0,21
AP-14	41,51	0,14	21,42	18,83	0,66	6,46	10,41	0,03	0,00	0,00	0,00	0,02	0,00	99,47	43,68	25,41	29,38	1,47	0,00	0,07
AP-14	38,96	0,16	21,30	24,09	0,74	4,59	9,14	0,03	0,02	0,06	0,03	0,00	0,00	99,11	54,18	18,15	26,01	1,66	0,00	0,00
AP-14	39,59	0,11	21,01	20,52	0,40	6,58	9,34	0,05	0,04	0,00	0,00	0,00	0,06	97,70	45,75	26,41	26,93	0,91	0,00	0,00
AP-14	39,24	0,12	21,23	20,72	0,45	6,44	9,18	0,01	0,04	0,00	0,00	0,02	0,00	97,44	47,22	25,57	26,13	1,01	0,00	0,07
AP-14	39,37	0,09	20,86	21,26	0,48	6,32	9,46	0,01	0,00	0,00	0,01	0,00	0,00	97,85	45,88	25,55	27,48	1,09	0,00	0,00
AP-14	40,18	0,00	21,43	20,43	0,31	6,67	9,38	0,03	0,02	0,00	0,01	0,09	0,00	98,56	46,67	26,16	26,19	0,70	0,00	0,28
AP-14	39,04	0,00	20,77	21,28	0,41	6,09	8,79	0,03	0,01	0,00	0,00	0,01	0,00	96,42	48,69	24,72	25,60	0,94	0,00	0,04
AP-14	38,50	0,11	21,14	24,10	0,88	4,65	8,77	0,03	0,00	0,02	0,00	0,00	0,02	98,22	54,32	18,53	25,15	2,00	0,00	0,00
AP-14	38,09	0,11	20,83	25,76	1,04	3,94	8,71	0,01	0,00	0,03	0,00	0,03	0,06	98,60	56,59	15,85	24,59	2,38	0,49	0,11
AP-14	39,57	0,17	21,31	20,59	0,42	6,68	9,70	0,00	0,02	0,00	0,00	0,00	0,00	98,45	45,04	26,44	27,59	0,94	0,00	0,00
AP-14	39,89	0,15	21,47	21,37	0,44	6,26	9,25	0,02	0,00	0,00	0,01	0,00	0,00	98,86	48,36	24,57	26,10	0,97	0,00	0,00

Sample	SiO2	TiO2	Al2O3	FeO	MnO	MgO	CaO	Na2O	K2O	F	Cl	Cr2O3	NiO	Total	Almandine	Pyrope	Grossular	Spessartine	Andradite	Uvarovite
AP-14	40,41	0,00	21,32	20,64	0,46	6,57	9,30	0,06	0,03	0,00	0,03	0,00	0,03	98,84	46,55	26,00	26,43	1,02	0,00	0,00
AP-14	40,04	0,00	21,51	21,86	0,59	6,79	8,33	0,00	0,02	0,01	0,00	0,10	0,01	99,26	48,76	26,52	23,11	1,30	0,00	0,31
AP-14	40,51	0,00	21,46	21,07	0,47	6,61	9,27	0,00	0,02	0,00	0,00	0,00	0,00	99,40	46,81	25,96	26,17	1,05	0,00	0,00
AP-14	39,90	0,01	21,26	20,48	0,46	7,11	9,18	0,08	0,01	0,03	0,00	0,00	0,04	98,56	44,59	28,19	26,17	1,04	0,00	0,00
AP-14	38,64	0,01	20,60	26,56	1,36	3,16	8,22	0,00	0,01	0,00	0,00	0,00	0,08	98,64	59,74	12,92	24,17	3,17	0,00	0,00
AP-14	39,88	0,14	21,46	21,43	0,57	6,41	9,09	0,02	0,02	0,00	0,03	0,10	0,06	99,19	48,04	25,11	25,27	1,27	0,00	0,31
AP-14	41,40	0,17	21,45	18,73	0,51	6,32	10,52	0,03	0,00	0,00	0,00	0,00	0,02	99,12	44,22	24,87	29,77	1,13	0,00	0,00
AP-14	41,79	0,00	21,68	18,66	0,41	6,01	10,50	0,10	0,09	0,01	0,04	0,00	0,00	99,29	45,38	23,81	29,89	0,92	0,00	0,00
AP-14	41,38	0,06	21,63	18,85	0,55	6,31	10,77	0,05	0,02	0,00	0,00	0,00	0,02	99,63	43,88	24,67	30,24	1,21	0,00	0,00
AP-14	41,90	0,17	21,74	19,38	0,56	6,42	10,36	0,01	0,02	0,00	0,03	0,05	0,00	100,65	44,95	24,92	28,74	1,23	0,00	0,16
AP-14	41,38	0,12	21,42	18,94	0,53	6,39	10,15	0,02	0,01	0,00	0,00	0,00	0,00	98,95	44,81	25,22	28,78	1,19	0,00	0,00
AP-14	42,23	0,00	21,80	18,94	0,44	6,61	10,26	0,00	0,01	0,00	0,01	0,00	0,00	100,29	44,59	25,72	28,70	0,98	0,00	0,00
AP-14	41,93	0,00	21,80	19,90	0,57	6,35	10,19	0,02	0,00	0,00	0,01	0,03	0,00	100,80	45,83	24,57	28,25	1,25	0,00	0,10
AT-09	38,22	0,09	20,64	20,34	0,49	7,28	10,50	0,02	0,02	0,00	0,00	0,15	0,03	97,76	40,85	28,50	25,44	1,08	3,67	0,46
AT-09	38,07	0,06	20,96	19,88	0,56	7,40	10,17	0,00	0,00	0,00	0,00	0,08	0,02	97,20	41,14	28,99	25,90	1,23	2,48	0,26
AT-09	37,80	0,45	20,42	20,17	0,39	7,80	9,36	0,05	0,00	0,00	0,02	0,09	0,00	96,55	41,17	31,10	23,40	0,88	3,15	0,29
AT-09	38,73	0,06	20,64	20,13	0,49	7,05	10,36	0,01	0,00	0,00	0,02	0,12	0,00	97,62	41,26	28,02	26,97	1,10	2,29	0,36
AT-09	37,16	0,14	20,52	20,27	0,30	7,44	9,71	0,01	0,02	0,00	0,01	0,00	0,03	95,60	41,46	29,83	24,56	0,69	3,46	0,00
AT-09	37,69	0,09	20,55	19,89	0,47	7,42	9,66	0,01	0,00	0,00	0,00	0,02	0,00	95,80	41,56	29,63	25,11	1,08	2,56	0,07
AT-09	38,66	0,22	20,64	20,43	0,45	7,20	10,04	0,00	0,01	0,00	0,00	0,10	0,09	97,83	41,79	28,55	25,77	1,01	2,55	0,32
AT-09	37,65	0,08	20,43	20,64	0,47	7,13	10,16	0,00	0,00	0,00	0,01	0,09	0,03	96,67	41,81	28,22	24,69	1,05	3,94	0,28
AT-09	38,06	0,00	20,71	20,08	0,55	6,83	10,45	0,01	0,00	0,03	0,01	0,08	0,02	96,82	41,90	27,10	27,19	1,23	2,33	0,26
AT-09	37,80	0,11	20,56	20,37	0,53	7,17	9,82	0,00	0,02	0,00	0,00	0,00	0,00	96,39	42,14	28,56	25,22	1,19	2,89	0,00
AT-09	38,07	0,12	20,79	20,37	0,43	7,42	9,68	0,05	0,00	0,00	0,00	0,00	0,06	96,98	42,25	29,30	24,92	0,96	2,57	0,00
AT-09	38,73	0,00	20,90	20,55	0,43	7,51	9,63	0,03	0,04	0,02	0,00	0,15	0,02	97,99	42,36	29,50	24,59	0,95	2,14	0,46
AT-09	37,82	0,03	20,47	20,39	0,48	7,21	9,61	0,01	0,00	0,00	0,00	0,00	0,00	96,02	42,37	28,86	24,89	1,10	2,78	0,00
AT-09	37,76	0,00	20,91	19,91	0,43	7,40	9,61	0,01	0,00	0,00	0,00	0,03	0,00	96,06	42,40	29,28	25,55	0,96	1,70	0,10
AT-09	38,02	0,10	20,72	20,57	0,33	7,38	9,73	0,00	0,00	0,03	0,01	0,04	0,00	96,93	42,46	29,18	24,75	0,74	2,77	0,11
AT-09	37,53	0,21	20,51	20,57	0,56	7,23	9,51	0,02	0,00	0,00	0,01	0,00	0,00	96,16	42,65	28,82	24,20	1,28	3,05	0,00
AT-09	38,23	0,00	20,79	20,42	0,37	7,09	9,98	0,00	0,01	0,00	0,02	0,09	0,00	96,98	42,71	28,07	26,07	0,82	2,04	0,29

Sample	SiO2	TiO2	Al2O3	FeO	MnO	MgO	CaO	Na2O	K2O	F	Cl	Cr2O3	NiO	Total	Almandine	Pyrope	Grossular	Spessartine	Andradite	Uvarovite
AT-09	38,32	0,00	20,70	20,29	0,39	7,02	9,77	0,03	0,03	0,00	0,00	0,01	0,00	96,54	42,83	28,15	26,52	0,88	1,58	0,03
AT-09	37,64	0,12	20,41	20,52	0,39	6,95	9,86	0,03	0,01	0,00	0,01	0,09	0,03	96,06	42,89	27,85	25,35	0,88	2,74	0,29
AT-09	38,09	0,04	20,48	20,72	0,37	7,11	9,68	0,02	0,02	0,00	0,01	0,06	0,00	96,59	42,90	28,43	24,97	0,83	2,69	0,18
AT-09	37,82	0,00	20,42	20,95	0,44	7,13	9,72	0,01	0,01	0,00	0,01	0,08	0,03	96,62	42,93	28,34	23,96	0,98	3,53	0,26
AT-09	37,30	0,09	20,46	20,99	0,53	6,92	9,78	0,00	0,00	0,00	0,04	0,01	0,00	96,12	43,04	27,66	24,45	1,21	3,59	0,04
AT-09	37,62	0,18	20,74	21,18	0,46	7,13	9,65	0,05	0,01	0,00	0,00	0,13	0,00	97,12	43,26	28,23	23,98	1,03	3,10	0,40
AT-09	37,90	0,05	20,96	20,43	0,44	7,31	9,32	0,00	0,00	0,00	0,02	0,02	0,06	96,51	43,61	28,90	24,84	0,98	1,60	0,07
AT-09	37,71	0,08	20,62	21,03	0,45	6,80	9,78	0,00	0,00	0,00	0,00	0,08	0,00	96,54	44,04	27,01	25,10	1,03	2,57	0,25
AT-09	37,73	0,18	20,79	21,01	0,50	6,42	9,84	0,02	0,02	0,00	0,00	0,00	0,04	96,56	45,02	25,62	26,67	1,13	1,57	0,00
AT-09	38,29	0,11	20,54	21,42	0,44	7,68	7,84	0,01	0,00	0,00	0,00	0,10	0,03	96,47	45,37	30,92	20,77	1,01	1,61	0,32
AT-09	37,42	0,00	20,78	21,88	0,51	6,18	9,61	0,00	0,00	0,00	0,02	0,01	0,02	96,43	46,71	24,62	25,41	1,16	2,06	0,04
AT-09	37,11	0,31	20,54	23,25	0,72	5,79	8,57	0,05	0,00	0,00	0,00	0,02	0,05	96,43	50,30	23,28	22,73	1,65	1,98	0,07
AT-09	37,63	0,00	20,38	25,42	1,10	4,95	8,46	0,06	0,00	0,00	0,01	0,07	0,05	98,12	53,45	19,78	20,79	2,49	3,27	0,22
AT-24	39,42	0,00	21,18	20,73	0,49	7,14	10,68	0,00	0,03	0,00	0,00	0,00	0,00	99,67	41,47	27,69	27,14	1,09	2,61	0,00
AT-24	38,63	0,00	21,31	21,07	0,33	7,21	10,57	0,00	0,01	0,00	0,00	0,00	0,07	99,20	42,14	27,81	26,13	0,73	3,19	0,00
AT-24	39,32	0,23	21,30	20,50	0,27	6,86	10,60	0,01	0,03	0,00	0,00	0,01	0,02	99,15	42,64	26,90	28,89	0,59	0,93	0,04
AT-24	38,97	0,23	21,20	21,27	0,31	6,93	10,80	0,02	0,01	0,01	0,00	0,05	0,00	99,79	42,66	26,73	26,94	0,67	2,87	0,14
AT-24	39,74	0,00	21,57	20,96	0,39	6,97	10,71	0,03	0,00	0,00	0,00	0,03	0,00	100,41	42,73	26,81	28,01	0,85	1,49	0,10
AT-24	39,24	0,13	21,52	20,90	0,45	6,95	10,54	0,02	0,00	0,00	0,02	0,05	0,01	99,81	43,05	26,77	27,54	0,99	1,48	0,17
AT-24	39,57	0,00	21,77	21,59	0,44	7,12	10,76	0,00	0,04	0,00	0,01	0,05	0,02	101,35	43,11	26,81	26,45	0,93	2,55	0,13
AT-24	38,91	0,00	21,14	21,74	0,31	6,42	10,82	0,04	0,00	0,00	0,03	0,02	0,00	99,43	44,20	24,92	27,51	0,68	2,62	0,07
AT-24	38,82	0,00	21,12	21,84	0,43	6,54	10,42	0,00	0,00	0,00	0,01	0,00	0,04	99,22	44,54	25,41	26,43	0,95	2,68	0,00
AT-24	38,77	0,04	20,85	22,63	0,51	6,34	10,30	0,03	0,02	0,00	0,00	0,05	0,00	99,53	45,35	24,70	25,14	1,12	3,56	0,14
AT-24	38,80	0,00	21,52	21,86	0,52	6,14	10,24	0,02	0,00	0,00	0,00	0,00	0,00	99,10	46,39	23,85	27,78	1,15	0,82	0,00
AT-24	39,33	0,00	21,40	23,01	0,57	5,72	10,57	0,02	0,01	0,00	0,00	0,04	0,00	100,66	47,32	22,09	27,44	1,24	1,78	0,14
AT-24	39,03	0,24	21,25	24,35	0,87	5,66	9,79	0,00	0,00	0,02	0,00	0,10	0,01	101,32	49,30	21,75	23,93	1,91	2,80	0,31
AT-24	38,48	0,06	21,09	24,15	0,53	5,02	10,54	0,02	0,00	0,00	0,01	0,00	0,01	99,92	49,82	19,54	26,76	1,18	2,70	0,00
AT-24	38,04	0,01	20,91	23,88	0,58	4,76	10,55	0,00	0,00	0,00	0,00	0,01	0,02	98,77	50,17	18,72	27,38	1,29	2,41	0,03
AT-24	38,19	0,08	20,72	24,55	0,69	5,08	9,75	0,00	0,01	0,00	0,00	0,00	0,00	99,06	50,79	20,03	24,57	1,55	3,07	0,00
AT-24	38,46	0,26	20,81	24,98	0,71	4,42	10,27	0,00	0,00	0,00	0,00	0,05	0,05	100,00	51,90	17,42	26,37	1,58	2,58	0,14

Sample	SiO2	TiO2	Al2O3	FeO	MnO	MgO	CaO	Na2O	K2O	F	Cl	Cr2O3	NiO	Total	Almandine	Pyrope	Grossular	Spessartine	Andradite	Uvarovite
AT-24	39,02	0,02	21,21	25,73	0,57	5,93	7,40	0,00	0,00	0,00	0,01	0,10	0,01	100,00	54,59	23,25	19,61	1,27	0,97	0,31
AT-24	37,87	0,18	20,55	25,92	0,90	3,69	10,01	0,01	0,01	0,00	0,02	0,07	0,04	99,26	54,62	14,71	25,67	2,04	2,74	0,22
AT-24	37,07	0,02	20,43	27,90	1,44	2,94	8,60	0,01	0,02	0,00	0,01	0,00	0,05	98,47	60,05	11,80	22,04	3,28	2,82	0,00

Supplementary Table 2.2. Analyses of the clinopyroxenes.

Sample	SiO2	TiO2	Al2O3	FeO	MnO	MgO	CaO	Na2O	Cr2O3	V2O3	NiO	Total	Si	Al	Ca	Mg	Fe2+	Na	Total	%Jd	XMg	Mineral
ADE-09	52,054	0,13	0,9	10,695	0,23	12,75	22,292	0,311	0	0,02	0,1	99,483	1,965	0,04	0,9	0,007	0,294	0,02	3,978	3,848	0,8	Diopside
ADE-09	51,23	0,13	0,82	10,05	0,16	12,93	22,24	0,25	0,00	0,00	0,03	97,83	1,96	0,04	0,91	0,74	0,27	0,02	3,95	3,55	0,78	Diopside
ADE-09	51,689	0,17	1,025	9,021	0,174	13,22	21,98	0,494	0,046	0,04	0,06	97,923	1,968	0,046	0,9	0,006	0,245	0,04	3,992	4,447	0,8	Diopside
ADE-09	50,636	0,045	1,311	7,655	0,197	14,1	22,185	0,244	0	0,04	0	96,412	1,946	0,059	0,9	0,006	0,183	0,02	3,954	5,527	0,8	Diopside
ADE-16	50,505	0,057	1,259	14,726	0,313	10,39	21,807	0,313	0	0,05	0,069	99,484	1,94	0,057	0,9	0,01	0,391	0,02	3,939	5,273	0,7	Diopsídio
ADE-16	53,23	0,17	1,43	13,92	0,21	10,17	21,48	0,21	0,00	0,11	0,01	100,93	2,02	0,06	0,87	0,57	0,44	0,02	4,00	6,32	0,62	Diopside
ADE-16	53,47	0,30	1,28	13,77	0,32	11,02	21,25	0,24	0,02	0,09	0,00	101,75	2,00	0,06	0,85	0,62	0,43	0,02	4,00	5,62	0,66	Augite
ADE-16	53,69	0,29	1,43	12,62	0,30	10,93	21,58	0,30	0,00	0,08	0,00	101,22	2,02	0,06	0,87	0,61	0,40	0,02	4,00	6,33	0,66	Diopside
ADE-16	53,78	0,00	1,40	13,46	0,27	11,03	21,96	0,25	0,07	0,08	0,08	102,38	2,00	0,06	0,87	0,61	0,42	0,02	4,00	6,05	0,66	Diopside
ADE-16	52,78	0,15	1,20	15,12	0,12	10,88	20,82	0,26	0,08	0,06	0,00	101,47	1,99	0,05	0,84	0,61	0,48	0,02	4,00	5,24	0,64	Augite
ADE-16	53,37	0,07	1,41	13,19	0,28	10,67	22,19	0,33	0,11	0,03	0,01	101,65	2,00	0,06	0,89	0,60	0,41	0,02	4,00	6,15	0,64	Diopside
ADE-16	53,95	0,16	0,98	12,29	0,26	11,49	22,21	0,36	0,00	0,05	0,00	101,74	2,01	0,04	0,89	0,64	0,38	0,03	4,00	4,30	0,67	Diopside
ADE-20	47,73	1,09	5,01	13,70	0,19	11,74	15,98	0,71	0,10	0,10	0,03	96,38	1,87	0,23	0,67	0,68	0,43	0,05	3,98	20,24	0,81	Augite
ADE-20	50,19	0,45	5,14	13,88	0,13	12,91	16,66	0,73	0,12	0,16	0,04	100,40	1,88	0,23	0,67	0,72	0,39	0,05	3,95	19,55	0,86	Augite
ADE-20	52,56	0,34	1,39	12,24	0,29	12,41	21,73	0,24	0,13	0,06	0,05	101,43	1,96	0,06	0,87	0,69	0,37	0,02	3,98	5,88	0,73	Augite
ADE-20	52,67	0,11	0,83	10,58	0,25	12,72	22,78	0,19	0,12	0,07	0,06	100,38	1,97	0,04	0,91	0,71	0,31	0,01	3,98	3,58	0,74	Diopside
ADE-20	52,20	0,05	1,02	11,19	0,27	11,76	22,29	0,18	0,07	0,03	0,00	99,06	1,99	0,05	0,91	0,67	0,36	0,01	4,00	4,51	0,70	Diopside
ADE-20	52,00	0,22	0,84	11,06	0,31	12,43	22,50	0,27	0,00	0,05	0,00	99,68	1,96	0,04	0,91	0,70	0,31	0,02	3,96	3,60	0,74	Diopside
ADE-20	50,20	0,80	4,29	13,65	0,15	11,86	17,75	0,72	0,00	0,12	0,00	99,54	1,90	0,19	0,72	0,67	0,42	0,05	3,99	17,28	0,77	Augite
ADE-24A	53,05	0,47	1,11	12,15	0,22	11,39	22,84	0,23	0,00	0,11	0,00	101,57	1,98	0,05	0,91	0,63	0,38	0,02	4,00	4,83	0,67	Diopside
ADE-24A	52,27	0,07	1,62	14,46	0,43	10,63	21,70	0,31	0,00	0,11	0,03	101,63	1,96	0,07	0,87	0,60	0,44	0,02	3,98	6,88	0,63	Diopside
ADE-24A	52,03	0,17	2,14	13,45	0,21	11,18	21,06	0,32	0,03	0,04	0,06	100,71	1,96	0,10	0,85	0,63	0,42	0,02	4,00	9,10	0,67	Augite
ADE-24A	52,12	0,34	2,08	13,35	0,28	11,88	20,48	0,41	0,00	0,21	0,05	101,20	1,95	0,09	0,82	0,66	0,41	0,03	3,98	8,75	0,71	Augite

Sample	SiO2	TiO2	Al2O3	FeO	MnO	MgO	CaO	Na2O	Cr2O3	V2O3	NiO	Total	Si	Al	Ca	Mg	Fe2+	Na	Total	%Jd	XMg	Mineral
ADE-24A	52,51	0,16	1,99	13,63	0,13	11,51	19,69	0,36	0,07	0,07	0,00	100,14	1,99	0,09	0,80	0,65	0,43	0,03	4,00	8,64	0,71	Augite
ADE-24A	52,46	0,29	1,25	14,17	0,21	11,25	20,82	0,25	0,06	0,04	0,00	100,79	1,98	0,06	0,84	0,63	0,45	0,02	4,00	5,48	0,67	Augite
ADE-24A	51,87	0,23	3,89	10,67	0,28	12,66	21,47	0,20	0,01	0,00	0,04	101,31	1,92	0,17	0,85	0,70	0,33	0,01	4,00	15,27	0,77	Diopside
ADE-24A	53,11	0,06	1,43	12,70	0,28	10,91	21,30	0,30	0,00	0,10	0,00	100,20	2,01	0,06	0,87	0,62	0,40	0,02	4,00	6,36	0,66	Diopside
ADE-24A	53,64	0,15	0,98	12,74	0,25	11,35	21,52	0,21	0,08	0,07	0,07	101,05	2,02	0,04	0,87	0,64	0,40	0,02	4,00	4,35	0,67	Diopside
ADE-24A	53,40	0,00	0,88	12,04	0,19	11,17	22,08	0,23	0,02	0,05	0,07	100,12	2,02	0,04	0,90	0,63	0,38	0,02	4,00	3,94	0,66	Diopside
ADE-24A	53,61	0,41	1,86	12,02	0,17	12,07	20,50	0,34	0,04	0,03	0,05	101,10	2,00	0,08	0,82	0,67	0,38	0,02	4,00	8,04	0,74	Augite
ADE-24A	53,52	0,16	1,49	12,77	0,21	11,67	21,86	0,39	0,02	0,10	0,02	102,20	1,98	0,06	0,87	0,64	0,40	0,03	4,00	6,36	0,68	Diopside
ADE-24A	53,39	0,41	1,34	11,74	0,23	11,71	21,97	0,29	0,00	0,05	0,00	101,13	2,00	0,06	0,88	0,65	0,37	0,02	4,00	5,84	0,70	Diopside
ADE-24A	53,72	0,07	1,13	11,90	0,24	11,51	21,74	0,27	0,00	0,06	0,00	100,63	2,02	0,05	0,88	0,65	0,37	0,02	4,00	5,03	0,68	Diopside
ADE-29	53,45	0,00	1,22	10,80	0,19	11,94	22,87	0,48	0,00	0,01	0,01	100,96	1,99	0,05	0,91	0,66	0,34	0,03	4,00	5,29	0,70	Diopside
ADE-29	53,27	0,30	1,73	10,87	0,24	12,70	22,11	0,36	0,07	0,05	0,00	101,70	1,97	0,08	0,88	0,70	0,34	0,03	4,00	7,31	0,74	Diopside
ADE-29	53,62	0,19	1,33	10,29	0,17	12,49	22,32	0,32	0,00	0,02	0,03	100,77	2,00	0,06	0,89	0,69	0,32	0,02	4,00	5,77	0,74	Diopside
ADE-29	52,80	0,32	1,31	10,32	0,20	12,55	22,29	0,32	0,04	0,07	0,02	100,21	1,98	0,06	0,90	0,70	0,32	0,02	4,00	5,67	0,74	Diopside
ADE-29	49,84	0,44	3,35	12,05	0,10	11,85	19,71	0,61	0,13	0,10	0,00	98,18	1,91	0,15	0,81	0,68	0,34	0,05	3,95	13,63	0,77	Augite
ADE-29	53,27	0,05	1,47	13,24	0,15	11,77	21,04	0,41	0,00	0,03	0,00	101,43	1,99	0,06	0,84	0,65	0,41	0,03	4,00	6,34	0,69	Augite
ADE-29	51,41	0,09	1,55	10,14	0,15	12,06	21,66	0,34	0,08	0,10	0,00	97,56	1,98	0,07	0,89	0,69	0,33	0,03	4,00	6,84	0,73	Diopside
ADE-29	51,94	0,04	2,09	10,80	0,26	12,83	21,92	0,39	0,11	0,07	0,01	100,47	1,94	0,09	0,88	0,71	0,28	0,03	3,95	8,50	0,78	Diopside
ADE-29	52,29	0,12	1,71	10,59	0,11	12,32	22,51	0,37	0,04	0,04	0,04	100,14	1,96	0,08	0,90	0,69	0,31	0,03	3,98	7,19	0,74	Diopside
AP-17	53,97	0,06	0,17	3,83	0,21	16,58	23,79	0,17	0,17	0,05	0,08	99,08	1,99	0,01	0,94	0,91	0,11	0,01	3,99	0,74	0,93	Diopside
AP-17	52,49	0,24	1,07	15,75	0,21	10,39	20,97	0,30	0,00	0,05	0,14	101,60	1,98	0,05	0,85	0,58	0,50	0,02	4,00	4,69	0,61	Augite

Supplementary Table 2.3. Analyses of the amphiboles.

Sample	SiO_2	TiO_2	Al_2O_3	FeO	MnO	MgO	CaO	Na_2O	K_2O	Cl	Cr_2O_3	V_2O_3	NiO	F	Total	XMg	Species
ADE-09	50,159	0	0,428	29,81	0,5	16,55	0,557	0	0	0	0,042	0	0	0	98,046	0,82535	Cummingtonite
ADE-09	41,55	1,061	12,472	15,935	0,204	10,385	11,413	1,993	0,673	0,246	0,046	0,027	0,043	0	95,988	0,589756	Pargasite
ADE-09	42,91	1,267	11,529	14,276	0,065	10,656	11,748	1,712	0,65	0,16	0,302	0,13	0,017	0	95,382	0,578998	Pargasite
ADE-09	43,925	0,97	10,549	15,297	0,154	11,442	11,41	1,57	0,512	0,158	0,161	0,094	0,009	0	96,211	0,628782	Mg-hornblende
ADE-09	50,01	0,01	0,714	29,809	0,431	16,946	0,446	0	0,02	0,01	0,01	0,028	0	0	98,434	0,851775	Cummingtonite
ADE-09	43,10	1,31	11,39	15,53	0,15	10,39	11,27	1,44	0,58	0,19	0,13	0,04	0,03	0,00	95,50	0,576225	Mg-hornblende
ADE-09	43,33	1,53	10,69	15,18	0,14	11,28	11,06	1,83	0,47	0,14	0,02	0,12	0,00	0,00	95,77	0,611258	Pargasite
ADE-16	48,16	0	0,63	34,55	0,803	12,65	0,664	0	0,01	0	0	0,06	0,043	0	97,57	0,66139	Grunerite
ADE-16	43,54	1,77	10,40	19,57	0,13	6,69	11,26	1,14	0,67	0,31	0,00	0,16	0,04	0,00	95,62	0,378491	Fe-hornblende
ADE-16	44,36	1,83	10,58	19,06	0,19	8,66	11,37	1,44	0,64	0,34	0,04	0,12	0,07	0,00	98,63	0,470015	Fe-hornblende
ADE-16	42,89	2,15	10,68	19,23	0,17	8,04	11,12	1,72	0,61	0,36	0,08	0,13	0,03	0,00	97,13	0,439692	Fe-hornblende
ADE-16	43,82	1,82	10,56	19,72	0,14	8,03	11,21	1,58	0,64	0,40	0,05	0,19	0,02	0,00	98,08	0,438912	Fe-hornblende
ADE-16	43,53	2,15	10,76	20,25	0,19	7,93	11,06	1,66	0,55	0,30	0,08	0,19	0,03	0,00	98,61	0,432078	Fe-hornblende
ADE-16	44,14	1,68	10,52	19,29	0,10	8,46	11,23	1,39	0,62	0,26	0,09	0,21	0,00	0,00	97,94	0,464934	Fe-hornblende
ADE-20	45,84	0,97	7,96	16,35	0,07	11,00	11,56	1,16	0,27	0,08	0,15	0,29	0,02	0,00	95,69	0,578099	Mg-hornblende
ADE-20	45,90	1,19	8,47	15,95	0,11	11,20	11,07	1,24	0,25	0,11	0,10	0,13	0,08	0,00	95,77	0,60371	Mg-hornblende
ADE-20	47,38	0,82	7,73	15,98	0,19	11,76	11,35	1,08	0,25	0,09	0,02	0,14	0,04	0,00	96,81	0,614093	Mg-hornblende
ADE-20	46,81	1,10	7,86	16,17	0,26	11,49	10,99	1,14	0,22	0,10	0,00	0,14	0,04	0,00	96,29	0,613019	Mg-hornblende
ADE-20	45,57	1,21	8,74	16,44	0,21	10,70	11,25	1,24	0,29	0,09	0,00	0,14	0,12	0,00	95,99	0,575641	Mg-hornblende
ADE-20	45,82	1,32	8,49	17,35	0,14	11,01	11,40	1,27	0,27	0,08	0,07	0,12	0,02	0,00	97,33	0,584391	Mg-ferri-hornblende
ADE-20	46,07	1,65	8,93	16,73	0,27	11,07	10,92	1,23	0,32	0,08	0,09	0,19	0,02	0,00	97,53	0,600394	Mg-ferri-hornblende
ADE-20	46,83	1,26	8,24	15,60	0,16	11,90	11,79	1,16	0,28	0,08	0,11	0,11	0,02	0,00	97,51	0,611644	Mg-hornblende
ADE-20	45,72	1,41	8,58	16,71	0,22	10,94	10,99	1,23	0,32	0,09	0,06	0,14	0,05	0,00	96,43	0,591372	Mg-hornblende
ADE-20	46,52	1,09	8,36	15,64	0,18	11,82	11,24	1,17	0,30	0,10	0,02	0,10	0,06	0,04	96,61	0,626948	Mg-hornblende
ADE-24A	45,49	1,22	9,29	19,69	0,18	9,86	10,72	1,39	0,41	0,02	0,04	0,20	0,03	0,03	98,56	0,542187	Mg-ferri-hornblende
ADE-24A	49,70	0,07	5,87	17,88	0,16	11,84	11,37	0,69	0,24	0,00	0,00	0,14	0,07	0,02	98,04	0,597457	Mg-ferri-hornblende
ADE-24A	43,94	1,68	10,68	19,88	0,16	8,84	11,07	1,42	0,54	0,02	0,10	0,32	0,05	0,00	98,69	0,482327	Fe-hornblende
ADE-24A	45,70	1,23	9,40	19,23	0,12	9,73	11,00	1,41	0,40	0,00	0,02	0,24	0,11	0,01	98,59	0,528483	Mg-hornblende

Sample	SiO_2	TiO_2	Al_2O_3	FeO	MnO	MgO	CaO	Na_2O	K_2O	Cl	Cr_2O_3	V_2O_3	NiO	F	Total	XMg	Species
ADE-24A	45,23	1,51	10,29	17,99	0,23	8,99	11,40	1,41	0,57	0,01	0,00	0,15	0,05	0,03	97,83	0,483684	Fe-hornblende
ADE-24A	44,17	1,64	10,28	17,94	0,28	9,04	10,85	1,49	0,55	0,03	0,06	0,13	0,09	0,00	96,53	0,50396	Mg-hornblende
ADE-24A	43,91	1,44	10,20	17,13	0,16	9,48	11,09	1,23	0,55	0,00	0,07	0,07	0,03	0,00	95,38	0,528863	Mg-hornblende
ADE-24A	45,10	1,57	10,00	18,16	0,09	9,06	11,45	1,36	0,58	0,00	0,00	0,16	0,03	0,01	97,54	0,484776	Fe-hornblende
ADE-24A	45,31	1,65	10,17	18,62	0,11	9,29	11,16	1,34	0,55	0,01	0,08	0,14	0,06	0,00	98,48	0,505671	Mg-hornblende
ADE-24A	44,50	1,34	10,77	18,03	0,07	8,98	11,26	1,40	0,56	0,01	0,02	0,13	0,04	0,00	97,10	0,494711	Fe-hornblende
ADE-29	41,30	1,84	11,78	17,96	0,05	9,45	11,22	2,05	0,84	0,06	0,20	0,14	0,00	0,03	96,87	0,517225	pargasite
ADE-29	42,81	1,94	11,55	16,92	0,08	10,28	11,45	1,98	0,69	0,05	0,03	0,12	0,00	0,00	97,87	0,549377	pargasite
ADE-29	42,50	1,65	11,77	16,44	0,19	9,59	11,64	1,89	0,82	0,06	0,09	0,16	0,00	0,10	96,84	0,517563	pargasite
ADE-29	41,55	1,93	11,80	17,25	0,11	9,42	11,17	1,90	0,82	0,06	0,17	0,20	0,02	0,04	96,41	0,521031	pargasite
ADE-29	42,57	1,67	11,25	17,38	0,12	9,56	11,16	1,95	0,69	0,10	0,16	0,11	0,05	0,00	96,73	0,520838	pargasite
ADE-29	42,38	1,73	11,65	15,44	0,15	10,01	11,17	1,78	0,68	0,08	0,10	0,16	0,00	0,06	95,35	0,555122	pargasite
ADE-29	42,23	2,19	11,47	17,02	0,16	10,14	11,19	1,91	0,66	0,05	0,04	0,10	0,05	0,00	97,20	0,551465	pargasite
ADE-29	42,39	1,87	11,61	16,78	0,15	10,04	11,33	1,99	0,70	0,06	0,10	0,05	0,00	0,00	97,06	0,543159	pargasite
ADE-29	43,50	1,60	11,52	16,63	0,13	9,77	11,67	1,82	0,83	0,09	0,01	0,09	0,00	0,03	97,66	0,52001	pargasite
ADE-29	43,14	1,25	10,58	16,97	0,07	10,12	11,44	1,59	0,73	0,04	0,08	0,10	0,03	0,03	96,15	0,544613	pargasite
ADE-29	43,41	1,82	11,08	16,16	0,08	9,92	11,62	1,65	0,78	0,06	0,34	0,25	0,05	0,03	97,22	0,533477	pargasite
AP-14	43,13	0,75	13,92	15,31	0,10	11,48	10,84	1,70	0,67	0,14	0,00	0,16	0,06	0,00	98,23	0,685282	Mg-hornblende
AP-14	43,84	0,83	12,74	13,14	0,09	11,71	11,25	1,35	0,57	0,07	0,15	0,09	0,03	0,00	95,82	0,674655	Mg-hornblende
AP-14	44,05	1,15	12,24	13,69	0,13	11,61	11,44	1,23	0,53	0,08	0,19	0,04	0,01	0,00	96,38	0,658023	Mg-hornblende
AP-14	43,52	1,54	12,65	15,29	0,15	11,49	11,15	1,28	0,57	0,09	0,03	0,04	0,00	0,01	97,78	0,670144	Mg-hornblende
AP-14	40,78	1,10	12,29	13,62	0,26	11,66	9,63	1,23	0,52	0,12	0,15	0,02	0,00	0,00	91,34	0,756878	ferri-tschermakite
AP-14	46,20	0,96	9,82	13,38	0,14	12,31	10,94	0,89	0,33	0,06	0,08	0,08	0,10	0,00	95,27	0,685894	Mg-hornblende
AP-14	46,79	0,91	9,12	13,22	0,24	12,76	11,27	0,96	0,36	0,05	0,11	0,12	0,04	0,00	95,94	0,688589	Mg-hornblende
AP-14	46,13	0,76	9,99	14,73	0,15	12,21	11,60	0,91	0,36	0,05	0,40	0,06	0,03	0,00	97,38	0,672819	Mg-hornblende
AP-14	46,31	1,14	10,11	14,33	0,19	12,03	11,29	0,97	0,40	0,06	0,18	0,11	0,07	0,00	97,16	0,660045	Mg-hornblende
AP-14	57,54	0,00	0,60	20,19	0,28	16,31	0,47	0,06	0,02	0,00	0,02	0,00	0,00	0,00	97,60	0,72237	cummingtonite
AP-14	46,07	0,46	13,14	12,25	0,13	10,03	11,13	1,11	0,42	0,07	0,02	0,12	0,00	0,00	96,98	0,593483	magnesio-hornblende
AP-14	49,23	0,80	9,68	12,57	0,11	10,88	11,15	0,83	0,33	0,07	0,07	0,07	0,01	0,00	97,85	0,606578	magnesio-

Sample	SiO_2	TiO_2	Al_2O_3	FeO	MnO	MgO	CaO	Na_2O	K_2O	Cl	Cr_2O_3	V_2O_3	NiO	F	Total	XMg	Species
																	hornblende
AP-14	57,54	0,00	10,55	13,60	0,23	13,09	3,67	0,67	0,14	0,02	0,04	0,00	0,05	0,00	101,76	0,756718	cummingtonite
AP-14	57,85	0,00	1,08	17,75	0,23	18,10	0,61	0,04	0,01	0,00	0,00	0,08	0,07	0,00	97,96	0,805625	cummingtonite
AP-14	45,62	0,94	11,35	14,13	0,16	12,48	10,98	1,23	0,49	0,11	0,11	0,08	0,00	0,00	97,65	0,702443	Mg-hornblende
AP-17	42,06	2,05	10,76	22,29	0,21	7,96	11,13	1,32	1,29	0,08	0,12	0,14	0,09	0,10	99,52	0,451916	hastingsite
AP-17	43,65	1,27	10,54	21,11	0,05	8,13	10,98	1,13	1,23	0,08	0,00	0,24	0,00	0,11	98,46	0,443529	Fe-hornblende
AP-17	42,95	1,71	10,63	21,46	0,00	8,07	11,04	1,29	1,17	0,08	0,12	0,18	0,02	0,00	98,71	0,449963	Fe-ferri-hornblende
AT-09	50,05	0,00	0,78	26,37	0,33	18,78	0,61	0,00	0,00	0,01	0,04	0,04	0,09	0,00	97,10	0,946605	Cummingtonite
AT-09	50,05	0,11	0,89	26,06	0,35	18,27	0,54	0,02	0,01	0,00	0,04	0,03	0,00	0,00	96,37	0,910485	Cummingtonite
AT-09	45,65	1,46	9,71	11,78	0,20	13,43	12,12	1,85	0,11	0,11	0,20	0,02	0,00	0,00	96,62	0,680655	Mg-hornblende
AT-09	41,57	1,77	12,03	12,85	0,17	11,78	10,96	2,50	0,11	0,10	0,01	0,11	0,00	0,01	93,94	0,655198	Pargasite
AT-24	37,06	0,50	17,64	18,03	0,05	7,60	11,37	2,42	0,69	1,56	0,05	0,09	0,00	0,00	96,70	0,499714	Fe-sadanagaite
AT-24	38,16	0,24	16,66	17,59	0,08	8,04	11,50	2,28	0,70	1,46	0,00	0,06	0,00	0,00	96,42	0,511086	pargasite
AT-24	50,83	0,02	0,75	33,21	0,40	14,46	0,63	0,01	0,00	0,00	0,00	0,11	0,00	0,00	100,41	0,708688	Cummingtonite
AT-24	50,74	0,16	0,74	32,40	0,30	14,90	0,57	0,00	0,02	0,01	0,00	0,09	0,00	0,00	99,92	0,728103	Cummingtonite
AT-24	50,73	0,00	0,72	34,96	0,56	13,82	0,57	0,00	0,01	0,00	0,00	0,04	0,00	0,00	101,39	0,68151	Grunerite
AT-24	50,53	0,00	0,68	33,32	0,42	14,68	0,57	0,01	0,00	0,00	0,10	0,06	0,00	0,06	100,41	0,727252	Cummingtonite
AT-24	50,86	0,06	0,63	33,09	0,27	14,53	0,49	0,00	0,00	0,00	0,05	0,08	0,00	0,00	100,06	0,709362	Grunerite
AT-24	49,87	0,00	0,62	34,99	0,60	13,66	0,58	0,02	0,01	0,00	0,10	0,02	0,00	0,00	100,46	0,688	Grunerite
AT-24	50,22	0,00	0,57	34,03	0,61	13,81	0,55	0,03	0,00	0,00	0,00	0,04	0,00	0,01	99,85	0,685984	Grunerite
AT-24	50,39	0,24	0,75	32,75	0,38	15,05	0,52	0,00	0,00	0,00	0,08	0,01	0,00	0,00	100,17	0,744739	Cummingtonite
AT-24	49,43	0,19	0,68	34,45	0,41	13,69	0,67	0,01	0,00	0,02	0,00	0,06	0,00	0,00	99,58	0,693203	Grunerite
AT-24	49,46	0,00	0,62	34,63	0,54	13,39	0,59	0,01	0,00	0,02	0,10	0,00	0,00	0,00	99,36	0,678872	Grunerite

Supplementary Table 2.4. Analyses of the plagioclases.

Sample	Na_2O	K2O	SiO_2	Al_2O_3	FeO	CaO	Total	Na	K	Si	Al	Fe2+	Ca	Total	% An
ADE-09	6,14	0,07	53,91	27,29	0,07	9,74	97,21	0,55	0,00	2,48	1,48	0,00	0,48	5,00	46,54
ADE-09	5,68	0,08	53,74	27,66	0,21	10,22	97,60	0,51	0,00	2,47	1,50	0,00	0,50	4,99	49,63
ADE-09	4,82	0,04	52,59	28,76	0,12	11,78	98,11	0,43	0,00	2,42	1,56	0,00	0,58	4,99	57,34
ADE-09	6,64	0,12	55,67	26,94	0,05	9,09	98,63	0,58	0,01	2,52	1,44	0,00	0,44	5,00	42,78
ADE-09	6,46	0,06	55,23	27,52	0,34	9,65	99,44	0,56	0,00	2,49	1,46	0,00	0,47	4,99	45,07
ADE-09	4,91	0,06	52,54	29,58	0,23	12,31	99,89	0,43	0,00	2,38	1,58	0,00	0,60	4,99	57,89
ADE-16	5,76	0,10	52,21	26,60	0,36	10,21	95,34	0,53	0,01	2,46	1,48	0,00	0,52	5,00	49,22
ADE-16	3,32	0,08	52,18	30,21	0,18	13,87	99,84	0,29	0,00	2,39	1,63	0,01	0,68	5,00	69,46
ADE-16	5,23	0,17	56,21	27,65	0,14	10,58	99,97	0,46	0,01	2,54	1,47	0,01	0,51	4,99	52,24
ADE-16	5,63	0,08	57,73	27,18	0,12	9,88	100,61	0,49	0,00	2,59	1,43	0,00	0,47	4,99	49,01
ADE-16	5,34	0,11	56,10	28,04	0,11	11,05	100,75	0,46	0,01	2,51	1,48	0,00	0,53	5,00	53,04
ADE-16	3,92	0,07	53,30	30,01	0,25	13,22	100,76	0,34	0,00	2,41	1,60	0,01	0,64	5,00	64,83
ADE-16	5,63	0,11	56,85	27,95	0,11	10,28	100,93	0,49	0,01	2,53	1,47	0,00	0,49	4,99	49,89
ADE-16	5,08	0,34	57,06	27,73	0,26	10,52	100,99	0,44	0,02	2,56	1,46	0,01	0,50	4,99	52,27
ADE-16	5,88	0,10	56,83	27,83	0,18	10,30	101,12	0,51	0,01	2,52	1,46	0,01	0,49	4,98	48,92
ADE-16	4,46	0,10	54,72	29,55	0,14	12,35	101,31	0,39	0,01	2,45	1,56	0,01	0,59	4,99	60,14
ADE-16	5,65	0,10	57,83	27,72	0,32	9,72	101,34	0,49	0,01	2,57	1,45	0,01	0,46	5,00	48,45
ADE-16	5,04	0,08	56,54	28,55	0,08	11,08	101,36	0,44	0,00	2,52	1,50	0,00	0,53	4,99	54,59
ADE-16	6,29	0,12	58,48	26,91	0,27	9,53	101,59	0,54	0,01	2,58	1,40	0,01	0,45	4,99	45,27
ADE-16	5,83	0,12	57,60	27,59	0,31	10,32	101,77	0,50	0,01	2,54	1,44	0,01	0,49	4,98	49,12
ADE-16	7,16	0,19	61,73	25,73	0,15	7,53	102,50	0,61	0,01	2,70	1,32	0,01	0,35	5,00	36,34
ADE-20	2,27	0,05	46,24	30,59	0,24	15,84	95,22	0,21	0,00	2,22	1,73	0,00	0,82	4,99	79,19
ADE-20	2,16	0,10	46,41	30,72	0,15	15,99	95,52	0,20	0,01	2,23	1,74	0,00	0,82	4,99	79,87
ADE-20	2,22	0,04	46,58	31,43	0,06	16,04	96,37	0,20	0,00	2,21	1,76	0,00	0,82	4,99	79,78
ADE-20	2,56	0,16	48,56	30,96	0,17	15,60	98,02	0,23	0,01	2,26	1,70	0,00	0,78	4,98	76,37
ADE-20	2,41	0,00	48,09	31,67	0,22	15,92	98,32	0,22	0,00	2,24	1,74	0,01	0,79	4,99	78,50
ADE-20	2,51	0,04	48,56	31,26	0,10	15,87	98,33	0,23	0,00	2,26	1,71	0,00	0,79	5,00	77,58
ADE-20	2,43	0,08	48,08	31,66	0,14	16,11	98,50	0,22	0,00	2,23	1,73	0,00	0,80	4,99	78,23
ADE-20	1,76	0,03	47,14	32,47	0,19	16,98	98,58	0,16	0,00	2,20	1,78	0,01	0,85	5,00	84,04

Sample	Na_2O	K2O	SiO_2	Al_2O_3	FeO	CaO	Total	Na	K	Si	Al	Fe2+	Ca	Total	% An
ADE-20	2,84	0,05	49,08	30,98	0,16	15,50	98,61	0,25	0,00	2,27	1,69	0,00	0,77	4,99	74,89
ADE-20	2,34	0,05	48,91	31,22	0,25	15,89	98,66	0,21	0,00	2,27	1,71	0,01	0,79	5,00	78,72
ADE-20	2,26	0,03	47,89	31,95	0,22	16,38	98,73	0,20	0,00	2,22	1,75	0,00	0,81	4,98	79,93
ADE-20	3,85	0,07	51,43	29,62	0,13	13,66	98,75	0,34	0,00	2,36	1,60	0,00	0,67	4,99	65,97
ADE-20	1,90	0,02	46,94	32,70	0,24	17,03	98,83	0,17	0,00	2,18	1,79	0,00	0,85	4,98	83,14
ADE-20	4,95	0,06	53,63	28,23	0,09	11,93	98,89	0,44	0,00	2,45	1,52	0,00	0,58	4,99	56,90
ADE-20	1,80	0,06	47,33	32,62	0,10	17,17	99,08	0,16	0,00	2,19	1,78	0,00	0,85	5,00	83,75
ADE-20	1,74	0,04	47,39	32,75	0,18	17,24	99,35	0,16	0,00	2,19	1,79	0,01	0,85	5,00	84,34
ADE-20	2,08	0,00	48,07	32,43	0,23	16,66	99,47	0,19	0,00	2,22	1,76	0,01	0,82	4,99	81,60
ADE-20	1,84	0,03	47,74	32,53	0,36	17,21	99,72	0,16	0,00	2,20	1,77	0,01	0,85	5,00	83,61
ADE-24A	5,35	0,18	56,68	25,45	0,30	8,62	96,57	0,49	0,01	2,65	1,40	0,01	0,43	4,99	46,54
ADE-24A	5,81	0,14	55,63	27,28	0,34	9,66	98,87	0,51	0,01	2,52	1,46	0,01	0,47	4,98	47,47
ADE-24A	6,95	0,18	59,02	25,66	0,05	7,45	99,30	0,61	0,01	2,66	1,36	0,00	0,36	5,00	36,81
ADE-24A	3,88	0,09	51,94	30,42	0,00	12,99	99,32	0,34	0,01	2,37	1,64	0,00	0,64	4,99	64,53
ADE-24A	6,05	0,17	56,59	26,79	0,25	9,51	99,36	0,53	0,01	2,56	1,43	0,01	0,46	5,00	46,05
ADE-24A	5,95	0,15	57,96	26,14	0,04	9,19	99,44	0,52	0,01	2,62	1,39	0,00	0,45	4,99	45,63
ADE-24A	7,37	0,23	59,94	24,77	0,04	7,12	99,46	0,64	0,01	2,69	1,31	0,00	0,34	5,00	34,37
ADE-24A	7,40	0,20	59,77	25,09	0,05	7,13	99,63	0,64	0,01	2,68	1,32	0,00	0,34	5,00	34,34
ADE-24A	6,28	0,12	57,66	26,72	0,13	8,79	99,70	0,55	0,01	2,59	1,42	0,01	0,42	4,99	43,28
ADE-24A	8,24	0,35	62,30	23,56	0,04	5,37	99,86	0,71	0,02	2,77	1,24	0,00	0,26	5,00	25,95
ADE-24A	6,36	0,19	59,30	25,68	0,09	8,30	99,92	0,55	0,01	2,67	1,36	0,00	0,40	5,00	41,43
ADE-24A	7,74	0,23	61,03	24,71	0,08	6,26	100,04	0,67	0,01	2,72	1,30	0,00	0,30	5,00	30,46
ADE-24A	6,07	0,17	57,52	26,80	0,09	9,42	100,07	0,53	0,01	2,58	1,42	0,00	0,45	4,99	45,69
ADE-24A	4,46	0,13	54,48	28,99	0,17	11,99	100,22	0,39	0,01	2,47	1,55	0,01	0,58	5,00	59,29
ADE-	7,09	0,15	60,71	25,34	0,09	7,39	100,77	0,61	0,01	2,69	1,33	0,00	0,35	4,99	36,23

Sample 24A	Na_2O	K2O	SiO_2	Al_2O_3	FeO	CaO	Total	Na	K	Si	Al	Fe2+	Ca	Total	% An
ADE-24A	2,84	0,07	51,16	31,84	0,12	14,92	100,94	0,25	0,00	2,32	1,70	0,00	0,72	5,00	74,12
ADE-29	6,89	0,19	57,37	24,80	0,26	8,45	97,97	0,61	0,01	2,62	1,33	0,00	0,41	4,98	39,98
ADE-29	7,46	0,24	62,74	22,55	0,17	5,11	98,26	0,66	0,01	2,86	1,21	0,01	0,25	4,99	27,07
ADE-29	5,69	0,10	55,87	26,78	0,13	10,10	98,67	0,50	0,01	2,55	1,44	0,00	0,49	4,99	49,24
ADE-29	6,14	0,14	57,03	25,85	0,09	9,55	98,80	0,54	0,01	2,59	1,39	0,00	0,47	5,00	45,88
ADE-29	8,63	0,18	61,96	22,73	0,06	5,32	98,88	0,75	0,01	2,78	1,20	0,00	0,26	4,99	25,15
ADE-29	7,49	0,17	59,37	24,51	0,15	7,20	98,89	0,65	0,01	2,68	1,30	0,00	0,35	4,99	34,37
ADE-29	9,35	0,30	64,07	21,39	0,06	3,78	98,95	0,81	0,02	2,86	1,13	0,00	0,18	4,99	17,95
ADE-29	9,38	0,36	64,60	21,50	0,10	3,65	99,58	0,81	0,02	2,87	1,13	0,00	0,17	5,00	17,32
ADE-29	8,26	0,31	61,14	23,57	0,16	6,15	99,58	0,71	0,02	2,73	1,24	0,00	0,29	4,99	28,65
ADE-29	9,06	0,20	62,56	22,88	0,09	4,90	99,69	0,78	0,01	2,77	1,20	0,00	0,23	4,99	22,76
ADE-29	6,99	0,12	59,26	25,08	0,27	8,06	99,77	0,61	0,01	2,66	1,33	0,01	0,39	5,00	38,67
ADE-29	9,62	0,27	64,88	21,74	0,05	3,60	100,16	0,82	0,02	2,86	1,13	0,00	0,17	5,00	16,87
ADE-29	6,46	0,12	57,48	26,59	0,16	9,66	100,48	0,56	0,01	2,57	1,40	0,00	0,46	4,99	44,94
ADE-29	9,34	0,27	64,24	23,22	0,22	5,00	102,29	0,78	0,01	2,78	1,18	0,00	0,23	4,99	22,51
AP-14	1,94	0,00	47,38	33,00	0,10	16,57	99,00	0,17	0,00	2,19	1,80	0,00	0,82	5,00	82,53
AP-14	1,48	0,03	46,48	33,78	0,27	17,10	99,15	0,13	0,00	2,15	1,84	0,01	0,85	4,99	86,26
AP-14	1,77	0,00	46,93	33,54	0,19	16,74	99,17	0,16	0,00	2,17	1,83	0,01	0,83	5,00	83,92
AP-14	2,03	0,01	47,71	33,07	0,26	16,19	99,27	0,18	0,00	2,20	1,80	0,01	0,80	4,99	81,43
AP-14	1,41	0,04	46,77	34,10	0,25	17,62	100,19	0,13	0,00	2,15	1,85	0,01	0,87	5,00	87,13
AP-14	1,74	0,00	47,69	33,58	0,37	17,09	100,47	0,15	0,00	2,18	1,81	0,01	0,84	4,99	84,41
AP-17	4,07	0,08	52,03	29,95	0,18	12,77	99,07	0,36	0,00	2,38	1,61	0,01	0,63	4,99	63,13
AP-17	3,84	0,05	51,85	30,27	0,58	13,48	100,05	0,34	0,00	2,35	1,62	0,02	0,66	4,99	65,81
AP-17	4,03	0,13	52,61	30,71	0,27	12,82	100,57	0,35	0,01	2,37	1,63	0,01	0,62	4,99	63,23
AT-09	8,32	0,02	57,91	23,60	0,12	6,17	96,19	0,74	0,00	2,67	1,28	0,00	0,30	5,00	29,06
AT-09	3,85	0,00	48,76	30,08	0,18	13,44	96,44	0,35	0,00	2,29	1,67	0,00	0,68	5,00	65,84
AT-09	5,82	0,00	53,32	27,20	0,15	10,05	96,86	0,52	0,00	2,47	1,49	0,00	0,50	4,99	48,80
AT-09	7,20	0,01	55,61	25,52	0,10	8,29	96,87	0,64	0,00	2,56	1,38	0,00	0,41	4,99	38,90
AT-09	5,93	0,03	53,27	27,65	0,16	10,27	97,35	0,53	0,00	2,45	1,50	0,00	0,51	5,00	48,81

Sample	Na_2O	K2O	SiO_2	Al_2O_3	FeO	CaO	Total	Na	K	Si	Al	Fe2+	Ca	Total	% An
AT-24	2,61	0,04	48,65	32,27	0,15	15,73	99,72	0,23	0,00	2,23	1,74	0,00	0,77	4,99	76,72
AT-24	0,65	0,01	44,17	35,79	0,43	18,73	99,78	0,06	0,00	2,04	1,95	0,00	0,93	5,00	94,11
AT-24	4,32	0,06	51,57	30,40	0,32	13,02	99,83	0,38	0,00	2,34	1,63	0,00	0,63	4,99	62,24
AT-24	2,89	0,01	48,29	32,76	0,22	15,43	99,87	0,26	0,00	2,21	1,76	0,00	0,76	4,99	74,63
AT-24	4,37	0,05	51,84	30,06	0,32	13,19	99,90	0,38	0,00	2,35	1,61	0,00	0,64	5,00	62,36
AT-24	2,14	0,03	47,57	33,43	0,32	16,49	99,98	0,19	0,00	2,18	1,81	0,00	0,81	5,00	80,87
AT-24	0,50	0,03	43,82	35,82	0,42	19,33	99,98	0,04	0,00	2,03	1,95	0,00	0,96	5,00	95,35
AT-24	2,02	0,03	47,40	33,66	0,58	16,53	100,25	0,18	0,00	2,17	1,82	0,00	0,81	5,00	81,74
AT-24	2,42	0,04	48,88	32,45	0,40	15,98	100,27	0,21	0,00	2,23	1,75	0,01	0,78	4,99	78,32
AT-24	2,05	0,04	47,18	33,43	0,34	17,09	100,32	0,18	0,00	2,16	1,80	0,00	0,84	4,99	81,93
AT-24	2,32	0,03	47,88	33,14	0,36	16,54	100,43	0,20	0,00	2,18	1,78	0,00	0,81	4,99	79,63
AT-24	2,07	0,03	47,46	33,91	0,35	17,02	100,88	0,18	0,00	2,16	1,82	0,00	0,83	5,00	81,82
AT-24	4,16	0,06	52,38	30,57	0,24	13,52	101,00	0,36	0,00	2,35	1,62	0,00	0,65	5,00	63,99
AT-24	4,33	0,04	52,96	30,50	0,32	12,91	101,07	0,38	0,00	2,38	1,61	0,00	0,62	5,00	62,05

Supplementary Table 2.5. Analyses of the oxide minerals.

Sample	SiO2	TiO2	Al2O3	FeO	MnO	MgO	CaO	Na2O	K2O	Cr2O3	V2O3	NiO	Total
ADE09_ilm 1	0,1130	51,7900	0,0470	43,7450	0,3780	0,7840	0,0610	0,1560	0,0450	0,1040	0,3410	0,0000	97,5640
ADE09_ilm 2	0,0000	53,1940	0,0150	44,7890	0,5870	0,8390	0,0260	0,0000	0,0000	0,0000	0,3720	0,0320	99,8540
ADE09_ilm 3	0,0000	52,7380	0,0200	44,4290	0,3850	0,8980	0,0000	0,0000	0,0060	0,0000	0,3680	0,0000	98,8440
ADE-16_ilm 1	0,0000	49,8960	0,0350	47,5960	0,5810	0,4990	0,0000	0,0740	0,0190	0,0000	0,5880	0,0000	99,2880
ADE-16_ilm 2	0,0520	51,5260	0,0210	46,7230	0,2720	0,5580	0,0020	0,0000	0,0300	0,0110	0,5260	0,0000	99,7210
ADE-16_ilm 3	0,0060	51,5950	0,0200	47,2060	0,3680	0,4450	0,0000	0,0000	0,0000	0,0000	0,4810	0,0530	100,1740
ADE-16_ilm 4	0,0380	51,6210	0,0530	46,3980	0,3850	0,4670	0,0260	0,0000	0,0200	0,0000	0,5380	0,0150	99,5610
ADE-16_ilm 5	0,0050	50,6460	0,0250	47,2790	0,7070	0,3890	0,0460	0,0740	0,0170	0,0750	0,5130	0,0000	99,7760
ADE-16_ilm 6	0,0680	50,1480	0,0230	46,8800	0,3840	0,6240	0,0000	0,0170	0,0000	0,0320	0,5300	0,0180	98,7240
ADE-16_ilm 7	0,0200	50,2050	0,0260	46,3470	0,4120	0,5420	0,0040	0,0000	0,0000	0,0300	0,5750	0,0000	98,1610
ADE-20_ilm 1	0,0790	49,7590	0,0000	45,6170	0,6370	0,6910	0,0270	0,0020	0,0120	0,0020	0,5500	0,0000	97,3760

Sample	SiO2	TiO2	Al2O3	FeO	MnO	MgO	CaO	Na2O	K2O	Cr2O3	V2O3	NiO	Total
ADE-20_ilm 2	0,0000	51,5890	0,0000	46,9850	0,4290	0,7540	0,0300	0,0140	0,0000	0,1400	0,4070	0,0180	100,3660
ADE-20_ilm 3	0,1600	51,2100	0,0160	45,6920	0,4730	0,6220	0,0360	0,0000	0,0030	0,0010	0,4250	0,0000	98,6380
ADE-20_ilm 4	0,0000	51,2030	0,0160	46,2040	0,5050	0,6810	0,0520	0,0000	0,0000	0,0750	0,5410	0,0080	99,2850
ADE-20_ilm 5	0,0560	48,9000	0,0060	47,1320	0,6030	0,7450	0,2030	0,0460	0,0000	0,1720	0,3710	0,0000	98,2340
ADE-20_ilm 6	0,0720	50,5840	0,0030	46,4460	0,5960	0,6840	0,0140	0,0890	0,0590	0,0630	0,5670	0,0000	99,1770
ADE-20_ilm 7	0,0610	51,8030	0,0110	46,7750	0,4990	0,6990	0,0190	0,0560	0,0070	0,0230	0,4830	0,0330	100,4690
ADE-20_ilm 8	0,3850	46,9960	0,1240	36,8340	0,4520	0,4160	0,0940	0,0490	0,0680	0,0770	0,3220	0,0180	85,8350
ADE-20_ilm 9	0,0960	52,2450	0,0000	45,7890	0,5550	0,5900	0,0140	0,0320	0,0440	0,0550	0,4980	0,0280	99,9460
ADE-29_ilm 1	0,0590	48,8380	0,0450	45,7700	0,4910	0,7350	0,0000	0,0470	0,0530	0,0230	0,4520	0,0200	96,5330
ADE-29_ilm 2	0,0620	52,2530	0,0000	47,0720	0,2540	0,7660	0,0120	0,0450	0,0000	0,0130	0,5400	0,0980	101,1150
ADE-29_ilm 3	0,0110	49,9790	0,0020	47,5540	0,4420	0,6350	0,0000	0,0000	0,0150	0,0430	0,4140	0,0000	99,0950
ADE-29_ilm 4	0,0050	50,7080	0,0140	46,2170	0,2800	0,6650	0,0450	0,0000	0,0080	0,0960	0,4540	0,0000	98,4920
ADE-29_ilm 5	0,0020	49,6900	0,0700	48,0260	0,3190	0,6770	0,0100	0,0240	0,0130	0,0740	0,4540	0,0200	99,3790
ADE-29_ilm 6	0,0850	49,9970	0,0980	46,9440	0,3420	0,8080	0,0880	0,1040	0,0120	0,0510	0,4030	0,0910	99,0230
ADE-29_ilm 7	0,0630	49,3520	0,0040	46,7210	0,4270	0,8190	0,0040	0,0560	0,0000	0,1090	0,5120	0,0000	98,0670
ADE-29_ilm 8	0,0000	49,6190	0,0380	47,1980	0,4020	0,7020	0,0000	0,0000	0,0000	0,0210	0,5010	0,0000	98,4810
ADE-29_ilm 9	0,0040	50,2400	0,0350	47,8610	0,3930	0,6900	0,0230	0,0140	0,0000	0,1170	0,4100	0,0000	99,7870

3. ARTIGO CIENTÍFICO 2: HIGH-PRESSURE METAMORPHIC ROCKS IN THE BORBOREMA PROVINCE, NORTHEAST BRAZIL: REWORKING OF ARCHEAN OCEANIC CRUST DURING PROTEROZOIC OROGENS

Alanielson da Câmara Dantas Ferreira[1], Elton Luiz Dantas[1], Ticiano José Saraiva dos Santos[2], Reinhardt A. Fuck[1], Mahyra Tedeschi[3]

[1]Instituto de Geociências, Universidade de Brasília (UnB), 70910-900 Brasília-DF, Brazil

[2]Instituto de Geociências, Universidade Estadual de Campinas (UNICAMP); Departamento de Geologia e Recursos Naturais, 13083-970 Campinas-SP, Brazil

[3]Instituto de Geociências, Universidade Federal de Minas Gerais (UFMG), 31270-901, Belo Horizonte- MG, Brazil

Corresponding author: Alanielson da Câmara Dantas Ferreira (ferreira.acd@gmail.com)

3.1 ABSTRACT

We present the first evidence of Archean oceanic crust formation submitted to Proterozoic high-pressure metamorphism in the South American Platform. Sm-Nd and Lu-Hf isotopic data combined with U-Pb geochronological data from the Campo Grande area, Rio Grande do Norte domain, in the Northern Borborema Province, reflect a complex Archean (2.9 and 2.6 Ga) and Paleoproterozoic (2.0 Ga) evolution, culminating in the Neoproterozoic Brasiliano/Pan-African orogeny (ca. 600 Ma). The more preserved mafic rocks contain massive poikiloblastic garnet and granoblastic amphibole with variable proportions of plagioclase + diopside in symplectitic texture, typical of high-pressure rocks. These clinopyroxene-garnet amphibolites and the more common garnet amphibolites from the Campo Grande area are exposed as rare lenses within an Archean migmatite complex. The amphibolite lenses represent

2.65 Ga juvenile tholeiitic magmatism derived from depleted mantle sources (positive $\varepsilon Hf_{(t)}$ values of +3.81 to +30.66) later enriched by mantle metassomatism (negative $\varepsilon Hf_{(t)}$ values of -7.97). Chondrite and Primitive Mantle-normalized REE and discriminant diagrams define two different oceanic affinities, with E-MORB and OIB signature. Negative Eu anomalies (Eu/Eu* = 0.75 to 0.95) indicate depletion of plagioclase in the source. Inherited zircon cores of 3.0 to 2.9 Ga in analyzed samples indicate that the Neoarchean tholeiitic magmatism was emplaced into 2923±14 Ma old Mesoarchean crust ($\varepsilon Nd_{(t)}$ = -2.58 and Nd T_{DM} = 3.2 Ga) of the Rio Grande do Norte domain. The age of retro-eclogite facies metamorphism is not yet completely understood. We suggest that two high-grade metamorphic events are recognized in the mafic rocks: the first at 2.0 Ga, recorded in few samples, and the second, at ca. 600 Ma, stronger and more pervasive and recorded in several of the mafic rock samples. The Neoproterozoic zircon grains are found in symplectite texture as inclusions in the garnet grains and thus represent the age of HP conditions in the area. These zircon grains show a younger cluster of concordant analyses between 623±3 Ma and 592±5 Ma with $\varepsilon Hf_{(t)}$ values of +0.74 to -65.88. The ca. 30 Ma interval is interpreted as the time between the formation of high-pressure rocks and the subsequent retrogression stage. The Campo Grande rock assemblage is composed of Archean units that were amalgamated to West Gondwana during Neoproterozoic Brasiliano orogeny continent-continent collision and crustal reworking.

Keywords: Archean oceanic crust, Proterozoic orogens, Borborema Province

3.2 INTRODUCTION

Subduction of oceanic crust similar to modern processes can be evidenced by eclogites, ultrahigh-pressure (UHP) and high-pressure (HP) rocks in Precambrian terranes (e.g. Rubatto and Hermann, 2001; Gordon et al., 2013; Zhang et al., 2019 and references therein). These relicts of oceanic crust mark suture zones between different blocks and terranes, and their study allows the recognition of different tectonic processes, as well as the identification of magmatic and metamorphic episodes and geodynamic scenarios that took place during crustal accretion (e.g. Brown, 2009; McClelland and Lapen, 2013). However, UHP and HP rocks are rare in Precambrian orogens, since tectonic processes tend to subduct mafic residues into the mantle (e.g. Weller and St-Onge, 2017; Zhang et al., 2019). Thus, only a few

remain preserved, and these are commonly retrogressed to lower grade conditions (e.g. Santos et al., 2009; 2015; Gilotti, 2013; Lanari et al., 2013). An additional reason for the uncommon occurrence of eclogites in Precambrian terranes (e.g. Mints et al., 2010; Li et al., 2015; Liu et al., 2017) is that during Archean and Paleoproterozoic times, the geothermal gradient was higher, favoring the occurrence of granulite-facies ultrahigh-temperature metamorphism (G-UHTM) (e.g. Brown, 2009). The opposite scenario occurs in the Phanerozoic orogenic systems, where the medium-temperature eclogite-high-pressure granulite metamorphism is mainly observed (E-HPGM) (e.g. Brown, 2014; Sizova et al., 2014). In addition, the absence of high-pressure and low-temperature metamorphism in the Archean record can also be attributed to the secular changes in oceanic crust composition, i.e., positive correlation between high geothermal gradients and MgO content throughout Earth history (e.g. Palin and White, 2016).

Almost all early mafic crusts were melted (and remelted) to form tonalite-trondhjemite-granodiorite (TTG) associations, which represent nearly 80% of the Archean continental crust (e.g. Rollinson, 2010). Trace elements, neodymium and hafnium isotope data from the scarce Neoarchean tholeiitic basalts suggest that the mantle had been depleted in incompatible elements by 2.5 Ga due to high Nb/Th, Nb/U, Sm/Nd and Lu/Hf ratios (e.g. Hawkesworth et al., 2010). Independent of plate tectonic and non-plate tectonic models, melting of basaltic crust under amphibolite or eclogite facies is required for the origin of these Archean TTGs (Polat et al., 2011; Polat, 2012). Therefore, the study of tholeiitic basalts (today amphibolites) allows the discussion of important questions like magma source and tectonic setting of the Archean oceanic crust.

Eclogites consist of Na-rich clinopyroxene and commonly Na-rich amphibole, and garnet formed under high-pressure conditions (>15 GPa) (e.g. Carswell, 1990). The presence of plagioclase, usually developing with diopside symplectitic texture, indicates the destabilization of omphacite during decompression (e.g. Carswell, 1990). This retrogression stage generates retro-eclogites (e.g., Powell and Holland, 2008; Lanari and Engi, 2017; Tedeschi et al., 2017). In the South American Platform (Fig. 3.1A), Neoproterozoic high-pressure rocks with typical retro-eclogite texture are reported from thrust-fold belts system in the southern Brasília orogen (Reno et al., 2012; Trouw et al., 2013; Tedeschi et al., 2017) and from the Ceará Central domain

(Santos et al., 2009, 2015), northwest portion of the Borborema Province. In both cases, the retro-eclogite occurrences are related to Brasiliano/Pan-African orogeny collision developed during west Gondwana amalgamation.

In this study, we present the first evidence of tholeiitic mafic crust remnants included in an Archean nucleus in the Borborema Province, NE Brazil. Our study is based on geological mapping, petrographic description, geochemical analyses, Sm-Nd and Lu-Hf isotopic data, and U-Pb geochronology.

3.3 GEOLOGICAL SETTING

The Borborema Province is formed of discontinuous remnants of Archean crust, Paleoproterozoic migmatite-gneiss complexes and Meso- and Neoproterozoic supracrustal rocks (e.g. Jardim de Sá, 1994; Brito Neves et al., 2000; Van Schmus et al., 2008). These units were amalgamated to West Gondwana during the complex and diachronic orogenic collage that took place in distinct pulses from ca. 800 to 500 Ma (e.g. Van Schmus et al., 2008; Arthaud et al., 2008; Brito Neves and Fuck, 2014; Padilha et al., 2017). The lithological and geochronological diversity, presence of Neoproterozoic zones of weakness and the position of these small crustal fragments in relation to the São Francisco, Amazonian and West Africa cratons generated high structural complexity, crustal reworking and pre- to post-tectonic granitogenesis in the Borborema Province (e.g. Dantas et al., 2004, Brito Neves, 2011; Archanjo et al., 2013).

The final configuration of the Borborema Province is characterized by the development of a continental-scale (>200,000 km^2) network of transcurrent shear zones that resulted from the convergence of the West African-São Luís and São Francisco-Congo cratons in Western Gondwana (Fig. 3.1A) (e.g. Arthaud et al., 2008; Padilha et al., 2017). These several shear zones represent local adjustments within each terrain, as well as divide the high-temperature, medium- to low-pressure metamorphic domains (e.g. Corsini et al., 1991, Arthaud et al., 2008; Oliveira and Medeiros, 2018). Moreover, this shear zone system is coeval with anatexis processes, and synkinematic magmatism, including crust- and mantle-derived magmas (e.g. Archanjo et al., 2013).

Several of these large shear zones extend into the Benin–Nigeria Province of NW Africa (e.g. Santos et al., 2008; Ganade de Araujo et al., 2014). Among these major tectonic lineaments, the Transbrasiliano-Kandi-4°50' Lineament is the most prominent mega-structure (Fig. 3.1A). It allows establishing a link between the Pharusian and Goiás Ocean, mainly by the correlation of the Neoproterozoic HP rocks in the Ceará Central domain (Santos et al., 2009) and in the Benin–Nigeria Province (Attoh and Nude, 2008) interpreted as a suture zone during final West Gondwana assembly (e.g. Ganade de Araujo et al., 2014; Santos et al., 2015).

The Rio Grande do Norte domain (RGDN) is located in the northeastern portion of the Borborema Province (Fig. 3.1B), and is limited by the NE-trending rectilinear Portalegre dextral strike-slip shear zone, correlated with the Ifewara-Zungeru fault in Africa, and the discontinuous Patos-Adamaoua EW-trending shear zones (e.g. Jardim de Sá, 1994; Brito Neves, 2011). It is suggested that this shear zone system developed within a heterogeneous continental crust to accommodate the deformation due to oblique collision (e.g. Jardim de Sá, 1994; Brito Neves et al., 2000). In the central portion (Fig. 3.1C), RGND includes banded gneiss, granitic to dioritic gneiss and migmatite underlying the Neoproterozoic Seridó Group (e.g. Van Schmus et al., 2008; Hollanda et al., 2015; Ferreira et al., 2019). Systematic U-Pb zircon geochronological studies indicate that Rhyacian (2.25 to 2.15 Ga) metamorphic high-K calc-alkaline magmatic rocks (e.g. Caicó Complex; Souza et al., 2007; Hollanda et al., 2011) and Siderian (2.3 Ga) supracrustal rocks (Dantas et al., 2008) form the basement of the Neoproterozoic Seridó Group.

The Campo Grande Archean nucleus is a basement inlier, limited to the west by the Portalegre Shear Zone, to the south by orthogneisses and granites of the Caicó Complex, to the east by the Seridó Group, and to the north it is covered by sedimentary deposits of the Cretaceous Potiguar Basin (Fig. 3.1C, 2). The area consists of a migmatitic gneiss complex with supracrustal lenses and intrusive Neoproterozoic granites (e.g. Galindo, 1993; Trindade et al., 1999). In this area (Fig. 3.2), we discovered amphibolite lenses with preserved textures that we interpret as evidence of the high-pressure mafic rocks in South America inside an Archean basement, a distinct setting from all retro-eclogites previously described within Neoproterozoic supracrustal sequences in West Gondwana.

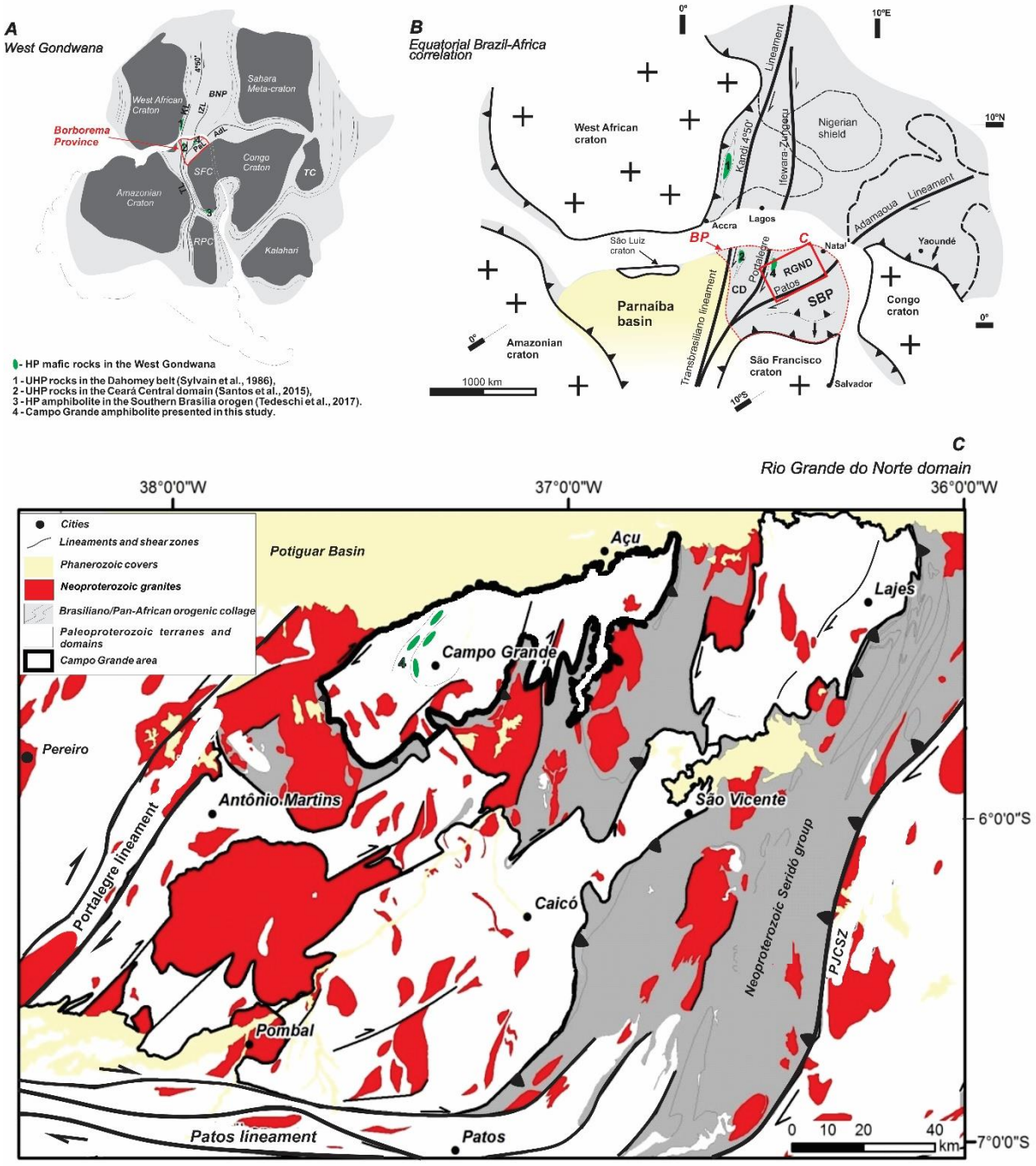

Figure 3.1. Regional geological setting. A) Localization map of the Borborema Province (BP) in West Gondwana. BNP - Benin-Nigeria Province, RPC - Rio de La Plata Craton, SFC - São Francisco Craton, TC - Tanzania Craton, TL - Transbrasiliano Lineament, KL- Kandi Lineament, IZL - Ifewara-Zungeru Lineament, PaL - Patos Lineament, ADL - Adamaoua Lineament. B) Equatorial Brazil-Africa correlation modified from Jardim de Sá (1994) and Van Schmus et al. (2008). CD - Ceará domain, RGND - Rio Grande do Norte domain, and SBP - Southern Borborema Province. C) Geological map of the Rio Grande do Norte domain from Jardim de Sá (1994). PJCSZ – Picuí-João Câmara shear zone.

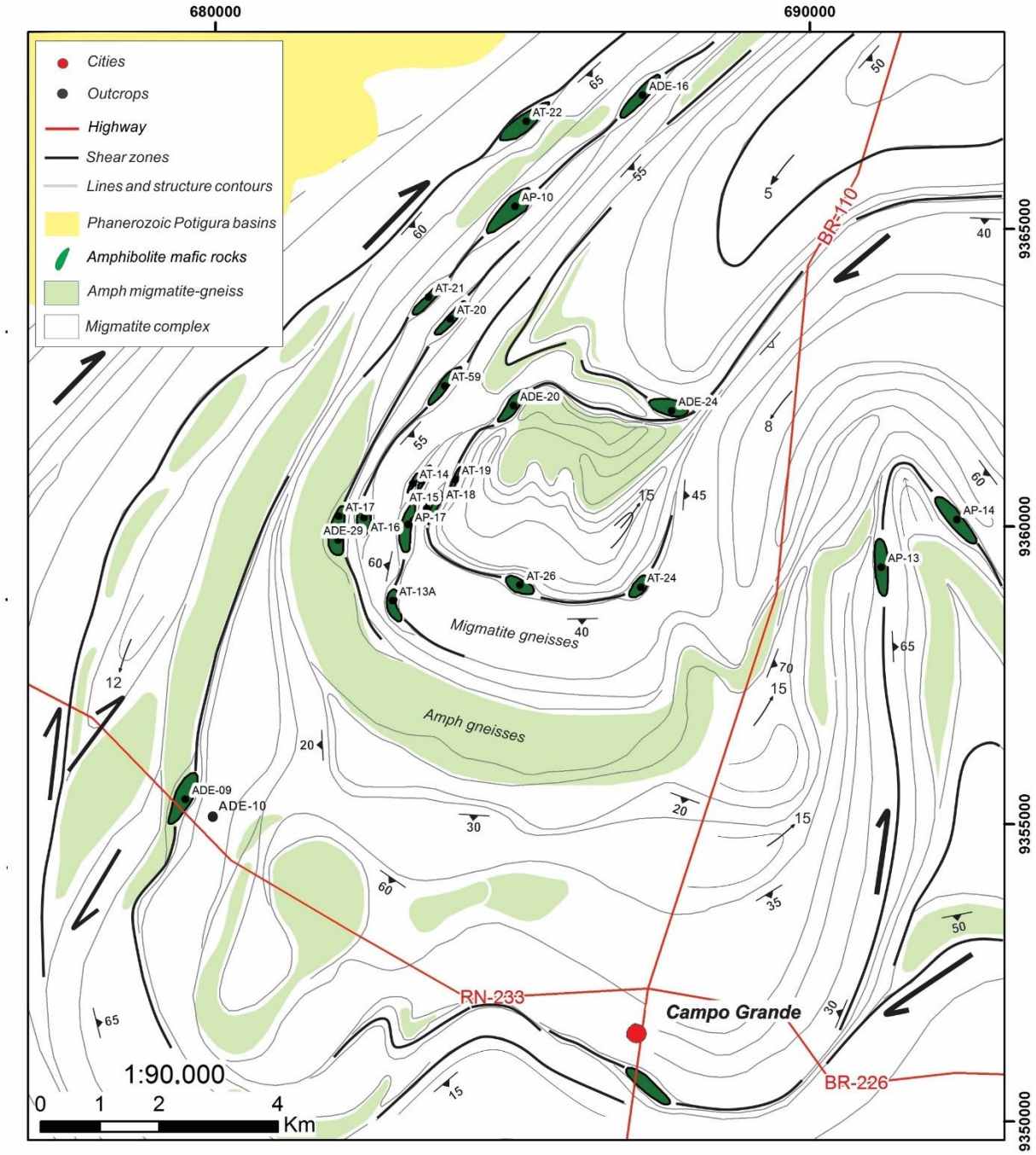

Figure 3.2. Simplified geological map of the Campo Grande area. The Campo Grande area represents an ellipsoidal gneissic-migmatitic block generated due to the combined stresses related to eastward push from the Neoproterozoic Portalegre shear zone and northward push from the Neoproterozoic Patos shear zone, which produced NW-SE shortening and amalgamation/accretion of allochthonous terranes, leading to an extensive network of dextral strike-slip shear zones.

3.4 MATERIALS AND METHODS

3.4.1 Geological Mapping and Petrography

Geological mapping in the Campo Grande area was carried out from 2016 to 2018 with the purpose of investigating the mafic bodies inserted in the gneiss-migmatite complex. Geological mapping was supported by geochemical, geophysical and petrographic surveys. Systematic thin sections cut relative to foliation were obtained from representative samples from fourteen outcrops of mafic lenses and host migmatite. Representative samples are from mafic lenses with a high modal concentration of pyroxene and garnet, since most mafic rock outcrops consist exclusively of amphibole, recording full retrogression of the HP mineral assemblage. The latter was done at the Microscopy Laboratory of the Institute of Geosciences of Universidade de Brasília (Brazil).

3.4.2 Geochemistry

Geochemical analyses were performed on 16 samples of the mapped mafic rocks. Analyses of major and trace elements were carried out by ACME Analytical Laboratories (Vancouver, Canada). Major and minor elements were obtained by X-ray fluorescence (XRF) after fusion of the sample with lithium tetraborate. Trace elements were determined from melting 0.2g of the sample with lithium metaborate/tetraborate, diluted nitric acid digestion and ICP-OES analysis. The loss on ignition (LOI) was given by weight difference after heating at 100°C. Precious metals and base metals were determined after 0.5 g of sample digestion with Acqua Regia with ICP-MS analysis.

3.4.3 U-Pb and Lu-Hf isotopes

Zircon grains from mafic lenses and host migmatite-gneiss were separated by conventional procedures and magnetic separator after concentration by hand panning. U-Pb and Lu-Hf isotopic analyses were performed on zircon grains using a Thermo-Fisher Neptune High Resolution Multicollector Inductively Coupled Plasma Mass Spectrometer (HR-MC-ICP-MS) coupled with a Nd:YAG UP213 New Wave laser ablation system at the Laboratory of Geochronology of Universidade de Brasília. U-Pb analyses on zircon grains were carried out by the standard-sample bracketing method (Albarède et al., 2004), using the GJ-1 standard zircon (Jackson et al., 2004) in order to quantify the amount of ICP-MS fractionation. The tuned masses were 238, 207, 206, 204 and 202. The integration time was 1 second and

the ablation time was 40 seconds. A 30 μm spot size was used and the laser setting was 10 Hz and 2-3 J/cm^2. Two to four unknown grains were analyzed between GJ-1 analyses. $^{206}Pb/^{207}Pb$ and $^{206}Pb/^{238}U$ ratios were time corrected. The raw data were processed off-line and reduced using an Excel worksheet (Bühn et al., 2009). During the analytical sessions, the zircon standard 91500 (Jackson et al., 2004) was also analyzed as an external standard.

Common ^{204}Pb was monitored using the ^{202}Hg and (^{204}Hg+^{204}Pb) masses. Common Pb corrections were not done due to very low signals of ^{204}Pb (< 30cps) and high $^{206}Pb/^{204}Pb$ ratios. Reported errors are propagated by quadratic addition [(2SD^2+2SE^2)1/2] (SD = standard deviation; SE = standard error) of external reproducibility and within-run precision. External reproducibility is represented by the standard deviation obtained from repeated analyses (~1.1 % for $^{207}Pb/^{206}Pb$ and up to ~2 % for $^{206}Pb/^{238}U$) of the GJ-1 zircon standard during the analytical sessions, and the within-run precision is the standard error calculated for each analysis. Concordia diagrams (2σ error ellipses), probability density plots and weighted average ages were calculated using the Isoplot-3/Ex software (Ludwig, 2008).

Zircon crystals previously analyzed for U-Pb isotopes and showing concordant to slightly discordant (<10%) data were selected for Lu-Hf analyses. Lu-Hf isotopic data were collected over 50 s of ablation time and using a 50 μm spot size. During the analytical sessions, replicate analyses of the GJ-1 standard zircon were performed, obtaining an average $^{176}Hf/^{177}Hf$ ratio of 0.282006 ± 16 (2σ), in good agreement with the reference value for the GJ standard zircon (Morel et al., 2008). Measurement spots were carefully positioned in the same growth area but not onto the same spot analyzed for U-Pb data. The signals of the interference-free isotopes ^{171}Yb, ^{173}Yb and ^{175}Lu were monitored during analysis in order to correct for isobaric interferences of ^{176}Yb and ^{176}Lu on the ^{176}Hf signal. The ^{176}Yb and ^{176}Lu contributions were calculated using the isotopic abundance of Lu and Hf (Chu et al., 2002). Contemporaneous measurements of ^{171}Yb and ^{173}Yb provide a method to correct for mass-bias of Yb using a $^{173}Yb/^{171}Yb$ normalization factor of 1.132685 (Chu et al., 2002). The Hf isotope ratios were normalized to $^{179}Hf/^{177}Hf$ of 0.7325 (Patchett, 1983). $\varepsilon_{Hf}(t)$ was calculated using the decay constant λ=1.865*10-11(Scherer et al., 2001) and the $^{176}Lu/^{177}Hf$ and $^{176}Hf/^{177}Hf$ CHUR values of 0.0332 and 0.282772 (Blichert-Toft and Albarède, 1997), respectively. Two-stage model ages (T_{DM}) were calculated from the initial Hf isotopic composition of zircon, using an average crustal Lu/Hf ratio (e.g.

Gerdes and Zeh, 2009). The values of $^{176}Lu/^{177}Hf$ = 0.0384 and $^{176}Hf/^{177}Hf$ = 0.28325 were used for depleted mantle (Chauvel and Blichert-Toft, 2001), and $^{176}Lu/^{177}Hf$ = 0.0113 for average crust (Wedepohl, 1995).

The Lu–Hf system is analogous to the Sm–Nd isotopic system (e.g. Vervoort and Blichert-Toft, 1999) and provides an unparalleled time series of changing magmatic and metamorphic conditions during crystal growth (e.g. Hawkesworth and Kemp, 2006). The zircon grains preserve the initial $^{176}Hf/^{177}Hf$ isotopic ratios inherited by the magma from which they crystallized. Since zircon is highly robust and has high Hf contents (1 to 3 %), Hf isotope ratios are largely impervious to deep weathering, deformation and alteration, all of which can disturb bulk rock isotope systems, including Sm–Nd (e.g. Hawkesworth and Kemp, 2006).

These analyzed zircon grains are rounded and unzoned (50 to 100 µm) to elongated (100 to 200 µm) with length/width ratio of 2:1 and 3:1, respectively. Images of the selected zircon grains in backscattered electrons (BSE) mode were obtained using a Scanning Electron Microprobe (SEM) in order to gather information on the internal structure of the studied grains. The BSE images also allowed to differentiate Hf-rich, bright and Hf-poor, from less bright portions of zircon grains. The studied grains from the amphibolite samples show unzoned Hf-poor cores rimmed by Hf-rich borders (Fig. 3.12B)

Hafnium depleted mantle model ages give a qualitative estimate of the time of separation of the source rocks (e.g. Hawkesworth and Kemp, 2006). Therefore, depleted mantle model ages do not necessarily provide any real age information. However, Hf T_{DM} with $\varepsilon Hf_{(t)}$ values are useful in identifying older crustal versus juvenile magmatic contributions (e.g. Nebel et al., 2007; Gerdes and Zeh, 2009).

3.4.4 Sm-Nd Isotopes

Sm–Nd isotopic analyses followed the method described by Gioia and Pimentel (2000) and were also carried out at the Geochronology Laboratory of Universidade de Brasília. Whole-rock powders (~ 50 mg) of 11 representative samples were mixed with ^{149}Sm–^{150}Nd spike solution and dissolved in Savillex Digestion Vessels. Sm and Nd extraction of whole-rock samples followed conventional cation exchange chromatography techniques, with Teflon columns containing LN-Spec resin (HDEHP

– diethylhexil phosphoric acid supported on PTFE powder). Sm and Nd fractions were loaded on Re evaporation filaments of double filament assemblies, and the isotopic measurements were carried out on a multicollector TRITON thermal ionization mass spectrometer in static mode. Uncertainties of Sm/Nd and $^{143}Nd/^{144}Nd$ ratios were better than ±0.1% (2 σ standard error) and ±0.0015% (1σ), respectively, according to repeated analyses of the international rock standard BHVO-1. $^{143}Nd/^{144}Nd$ ratios were normalized to $^{146}Nd/^{144}Nd=0.7219$, and the decay constant used was 6.54×10^{-12}. The T_{DM} values were calculated using the DePaolo (1981) model.

3.5 RESULTS

3.5.1 Field Relationships and Petrography

Field description was based on mafic rocks found in outcrops in the Campo Grande area, central portion of Rio Grande do Norte State, in northeastern Brazil. These rocks comprise clinopyroxene-garnet amphibolites that crop out as discontinuous lenticular bodies, forming boudins, with variable sizes (~30 cm to 120 m long) (Fig. 3.2). The amphibolite boudins are hosted in a migmatite-gneiss complex (Fig. 3.3A, 3.4A), which includes alkali biotite to amphibole-biotite migmatite-gneiss, clinopyroxenite and paragneiss. The amphibolite outcrops form a lenticular pattern of concordant mafic bodies parallel to foliation of the host migmatites. They also occur as isolated lenses within the north-northeast to east-west trending shear zone systems (Fig. 3.2) that underline the ellipsoid shape of the Campo Grande Block. Garnet-biotite paragneiss layers, calc-silicate rocks, and alkaline granite intrusion also occur in the study area.

The mafic lenses are isotropic in their central portions and foliated at their rims. In the core portions the mafic rocks are medium- to coarse-grained and contain garnet porphyroblasts (15–25 %) with 200 to 800µm, and granoblastic amphibole (25-45 %), with variable proportions of plagioclase + clinopyroxene + amphibole (35–45 %), forming a typical symplectitic texture (Fig. 3.3C-H) within the inner domains of the bodies. The symplectitic texture is a typical indication of a high-pressure metamorphic event (e.g. Santos et al., 2009; 2015; Tedeschi et al., 2017). Garnet with symplectitic overgrowth of plagioclase + clinopyroxene + amphibole represents

the retrograded HP mineral assemblage. However, most mafic rock outcrops consist mainly of granoblastic amphibole (ca. 60%) and plagioclase (ca. 40%) recording full retrogression of the former mineral assemblage. These rocks show medium- to fine-grained texture towards their rims, which are foliated due to deformation related to the development of shear zones (Fig. 3.4A).

Garnet crystals exhibit irregular shapes with lobate edges, and a composite corona texture is developed on their borders, composed of an inner plagioclase and an outer amphibole corona. The garnet porphyroblasts display inclusions of quartz, ilmenite, clinopyroxene and zircon (Fig. 3.3C). Garnet grains are irregular in shape due to breakdown reaction rims imposed by retrogression. The deformation is better observed in outcrop-scale mainly by the boudinage process along the Campo Grande shear zones systems, indicating that the emplacement of these mafic rocks was coeval or prior to the last deformation. Thus, zircon inclusions in the garnet may represent the time of the HP metamorphism or the previous phases recorded in the protolith sources or the host migmatite rock.

Clinopyroxene occurs as subhedral crystals in contact with amphibole or developing symplectitic texture with plagioclase and amphibole. Amphibole occurs by replacing both primary and secondary pyroxene and garnet crystals as vermicular fine-grained crystals in symplectite, inclusions in granoblastic garnet and developed corona texture (Fig. 3.3C-H). Plagioclase grains occur in the symplectite and corona texture. Rutile, ilmenite, apatite, zircon and titanite are accessory minerals (<3%). Quartz inclusions were examined by Raman spectroscopy, but high-pressure polymorphs (e.g. coesite) were not found. Some lenses are completely retrograded, marked by the increase in amphibole concentration. The amphibolite rims show the same tectonic foliation imprinted in the host gneiss complex. Sometimes, 3-5 m wide shear zones characterize the contact between mafic rocks and gneisses (Fig. 3.4A).

The country rocks comprise mainly of deformed tonalitic migmatitic gneiss (Fig. 3.4B) and garnet-biotite gneiss (Fig. 3.4C). Melanosome bands consist mainly of biotite and amphibole, with feldspar and quartz porphyroclasts surrounded by biotite and red garnet porphyroblasts. The leucosome bands are composed of microcline and plagioclase with quartz ribbons, forming augen textures and making up the major part of the felsic layers. Titanite, ilmenite, apatite and zircon are accessory phases. Garnet crystals from gneisses exhibit a pseudo-automorphic shape (Fig. 3.4D) with

some lobed edges and quartz inclusions, while pressure shadows host biotite growths. Sometimes the idiomorphic shape of the garnet crystals indicates deformation and resorption (Fig. 3.4E), with feldspar and biotite along the mylonitic zone.

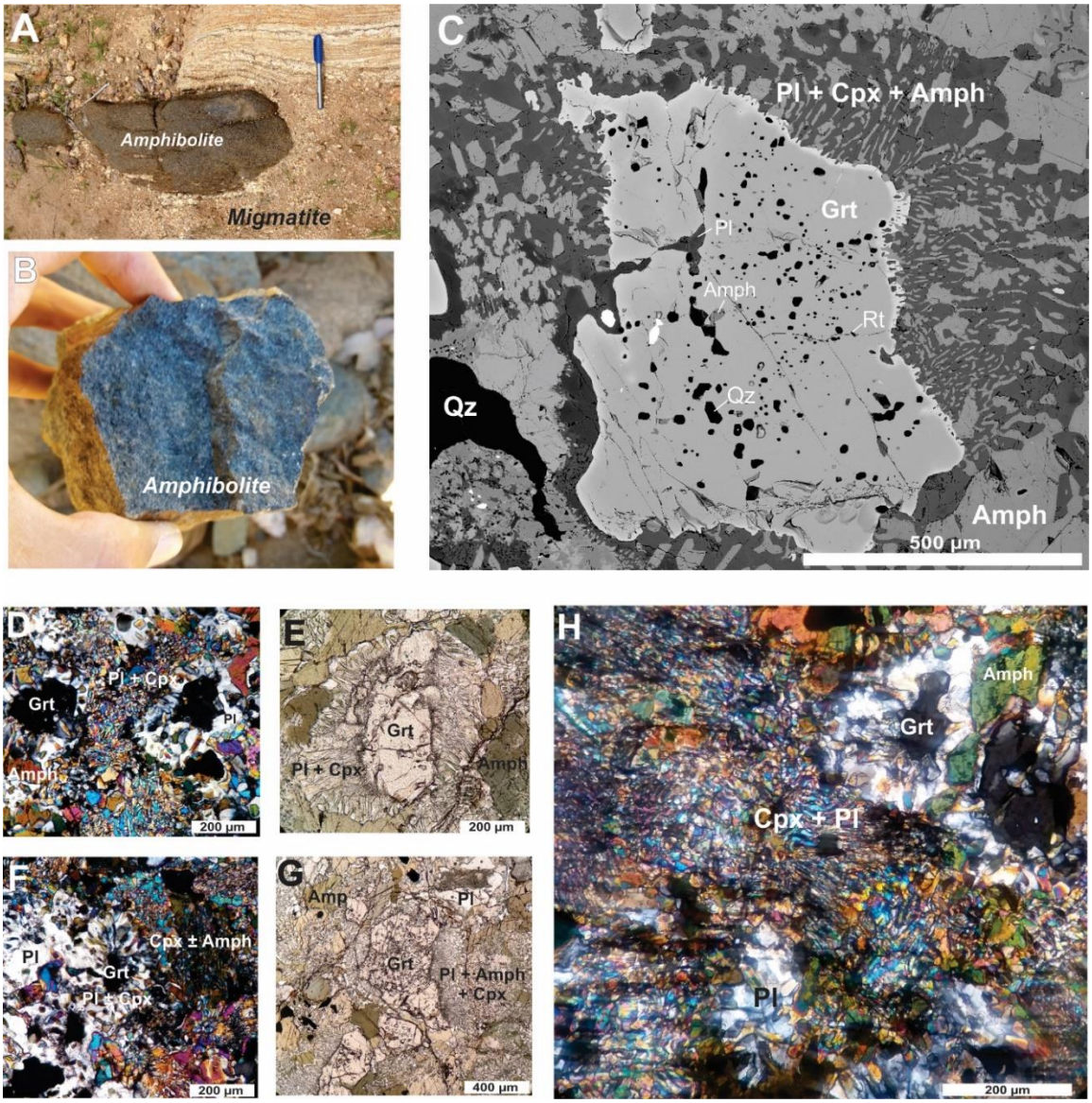

Figure 3.3. Petrographic features and symplectitic texture of the Campo Grande amphibolites. A) AP-10 mafic lens parallel to foliation of the host migmatite. B) Hand ADE-20 sample. C) Symplectitic texture in scanning electron microscope image of sample AP-14. Photomicrographs of D) Sample ADE-16, E) Sample ADE-24B, F) Sample ADE-20, G) Sample AP-17, H) Petrographic features and symplectitic texture of the ADE-29 sample. D, E, F, H crossed polarizers, G parallel polarizers. Mineral symbols follow Whitney and Evans (2010).

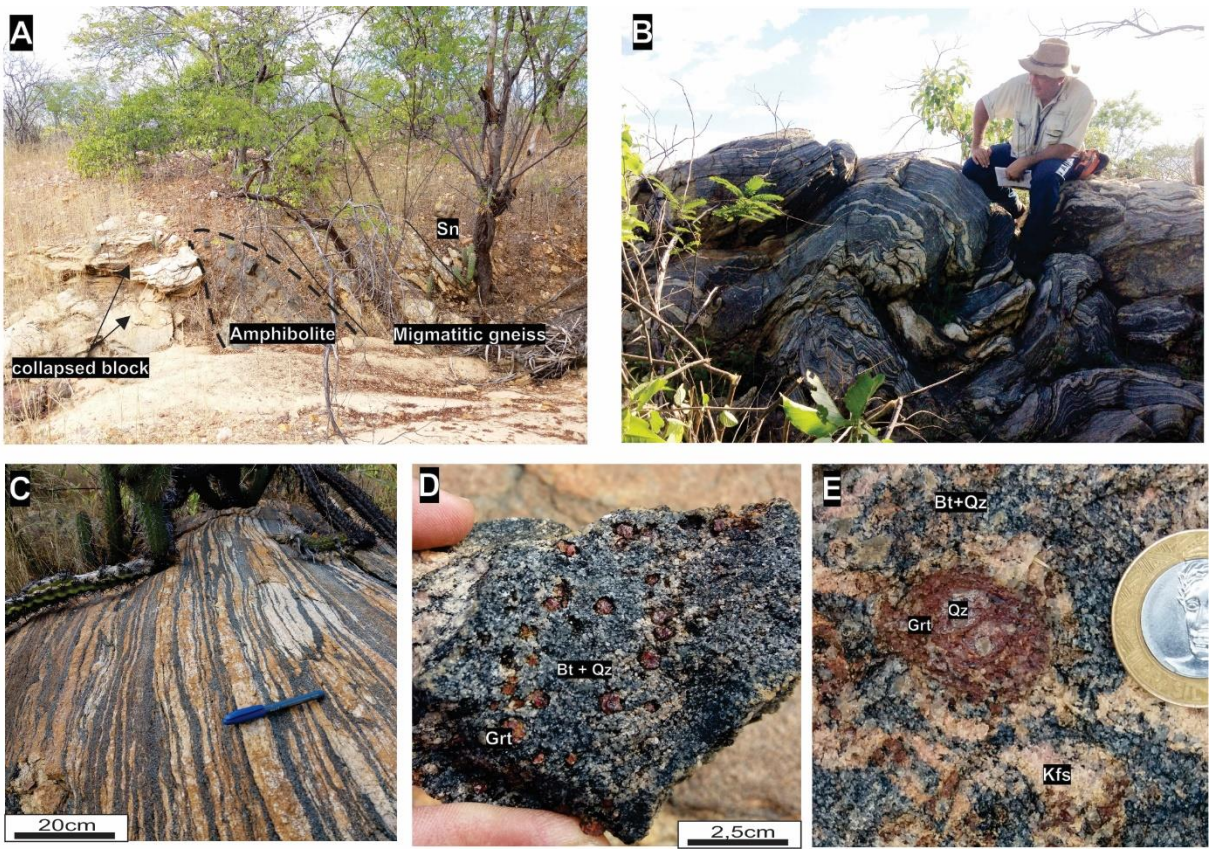

Figure 3.4. Field views of amphibolites and host gneiss. A) AT-26 mafic lens concordant and parallel to low-angle Sn foliation dipping 35º to the south. B) Strongly folded stromatic structure of tonalitic paleosome (sample ADE-10). C Strongly deformed garnet-biotite gneiss along a NE-SW-trending shear zone. D) Hand sample of garnet-biotite gneiss showing garnet crystals with pseudo-automorphic shape and some lobed edges. E) Syntectonic garnet porphyroblast with internal zonation (helicitic inclusion trails) that indicate top-to-the-SW rotation of more than 180°.

3.5.2 Geochemistry

Sixteen samples amphibolites were selected for geochemical analyses in the study area (see localization in Fig. 3.2 and Supplementary Table 3.1). The samples were collected mainly in the central portions of the mafic boudins, where features indicating retrogression of HP mineral assemblages are preserved. Whole-rock chemical compositions of representative samples of the investigated amphibolites are listed in Supplementary Table 3.2. The plot of major element oxides (Al_2O_3, Na_2O, CaO, Fe_2O_3, P_2O_3, TiO_2 and K_2O) against the Mg# (Mg / [Mg+Fe] x 100) (Fig. 3.5A-G) indicates that bulk compositions are mainly controlled by different amounts of amphibole, garnet, clinopyroxene and plagioclase in the mafic rock. Thus, samples rich in Na_2O% and CaO% have higher modal concentrations of clinopyroxene, while samples with high FeO% have higher Fe-amphibole content. In addition, lower K_2O

content corroborates the absence of K-bearing minerals. Mg# was used as an index of fractionation because it largely reflects the changes in the samples MgO content.

These bivariate diagrams (Fig. 3.5A-G) indicate that amphibolite protoliths crystallized from fractionated mafic magmas with Mg# between 40.9 and 54.56, higher Al_2O_3 (13.4 to 15.4 wt. %) and CaO (9.77 to 11.90 wt. %) and lower Fe_2O_3 (10.65 to 15.19 wt. %). A more fractionated sample group was observed, with lower Al_2O_3 (< 13.95 wt. %), CaO (< 5.67 wt. %) and Mg# ranging between 30.06 and 37.15, with higher Fe_2O_3 (14.55 to 20.70 wt. %), P_2O_3 (0.19 to 0.45 wt. %) and TiO_2 (1.78 to 3.21 wt. %). The group with lower Mg# has high Th (1.38 to 8.11 ppm), Ba (65.7 to 599 ppm) and Rb (4 to 47.6 ppm) when compared to the group with higher Mg# that shows low Th (0.3 to 3.24 ppm), Ba (20 to 310 ppm) and Rb (0.9 to 13.5 ppm). The high Mg# group has a higher concentration of garnet and pyroxene with well-developed symplectitic texture, whereas the lower Mg# group consists mainly of granoblastic amphiboles. The samples in both groups, more fractionated and more primitive, have relatively low percentages of K_2O (~0.1 wt. %) and low concentration of lithophile elements (Supplementary Table 3.2). These samples also have tholeiitic affinity (Fig. 3.6A) (Irvine and Baragar, 1971) and sub-alkaline basaltic composition, with low $Na_2O + K_2O$ (0.99 to 4.38 ppm wt. %), Si_2O (46.9 to 56.1 wt. %), Zr/Ti (0.007-0.02) and Nb/Y (0.1-0.8) ratios (Fig. 3.6B) (Pearce, 2008).

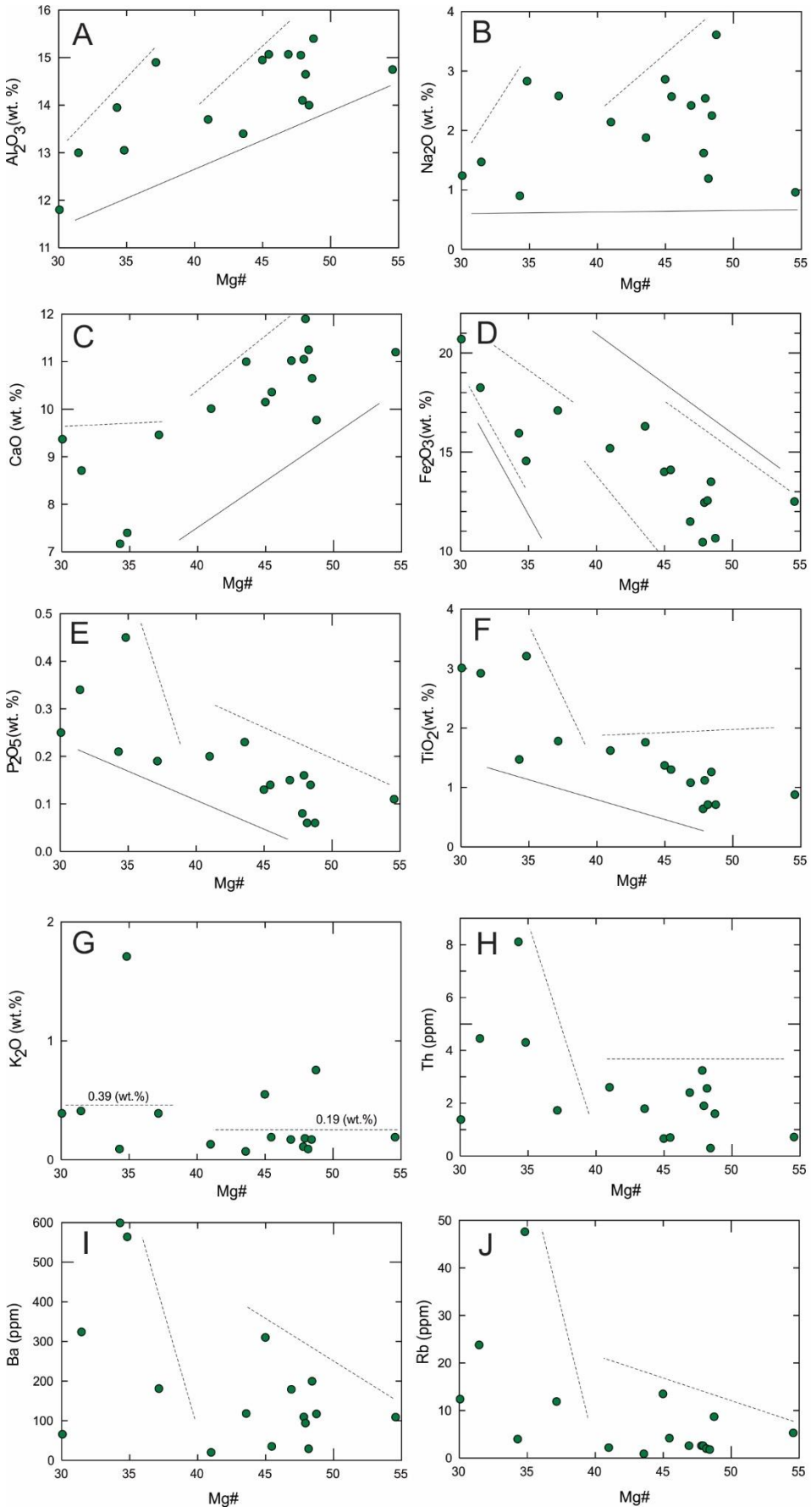

Figure 3.5. A-J) Mg# versus major and trace elements of Campo Grande amphibolites. Data from Supplementary Table 3.2.

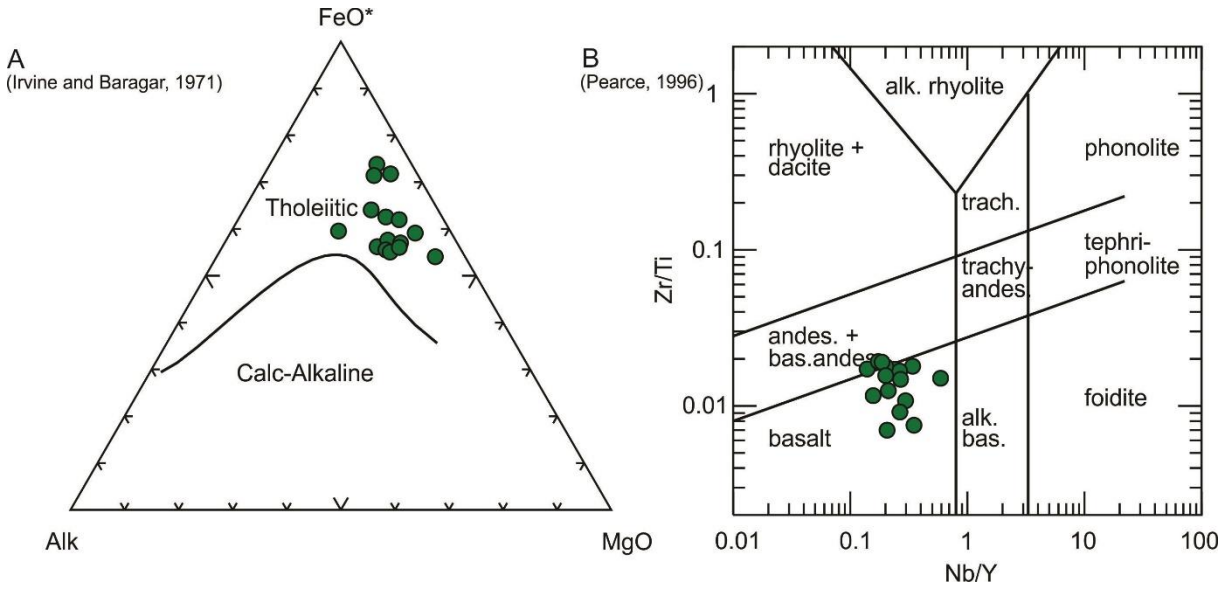

Figure 3.6. A) AFM diagram (Irvine and Baragar, 1971) and B) Zr/Ti versus Nb/ Y (Pearce, 1996) plot for Campo Grande amphibolite samples. Data from Supplementary Table 3.2.

Chondrite-normalized rare earth elements (REE) profiles show a similar pattern to fractionated E-MORB from Sun & McDonough (1989) for the higher Mg# samples (Fig. 3.7A). These REE profiles have distinctively positive slopes for light REE, $(La/Yb)_N$ = 1.62 to 3.10, and flat distribution of heavy REE, $(Tb/Yb)_N$ = 0.91 to to 1.27. The lower Mg# group shows a similar pattern to ocean island basalts (OIB) (Fig. 3.7A) with higher enrichment of LREE, $(La/Yb)_N$ = 1.92 to 8.34, and HREE, $(Tb/Yb)_N$ = 1.17 to 1.89. A negative Eu anomaly (Eu / Eu * = 0.75 to 1.06) indicates plagioclase depletion in both amphibolite groups sources.

Primitive mantle trace elements profiles exhibit slight enrichment of Cs, Ba, Th, U, La, Pb and LREE (as Dy, Yb and Lu), and depletion of Rb, Nb, K, Sr, and Ti in relation to the E-MORB pattern (Fig. 3.7B). The samples are enriched in Dy, Y, Yb and Lu in comparison to the OIB pattern, while the other elements are depleted. Pb shows the strongest fractionation in relation to the E-MORB and OIB patterns.

In the TiO_2 - K_2O - P_2O_3 diagram (Pearce, et al., 1975), amphibolite samples plot in the oceanic basalt field (Fig. 3.8A) with the exception of two samples (AT-02 and AP-14A) with high Ba (117 and 564 ppm) and Sr (152 and 551 ppm). The Hf/3-Nb/16-Th ternary discrimination diagram (Wood, 1980) shows that most samples plot in the D field of island arc tholeiite; progressive enrichment of Th shifts samples from E-MORB to arc-basalts (Fig. 3.8B). In the Nb*2-Zr/4–Y diagram (Meschede, 1986), amphibolite samples also plot in the N-MORB to volcanic arc basalts fields (Fig.

3.8C). Thus, discriminant diagrams corroborate an oceanic crust, with E-MORB and OIB signatures, as source of the studied mafic rocks.

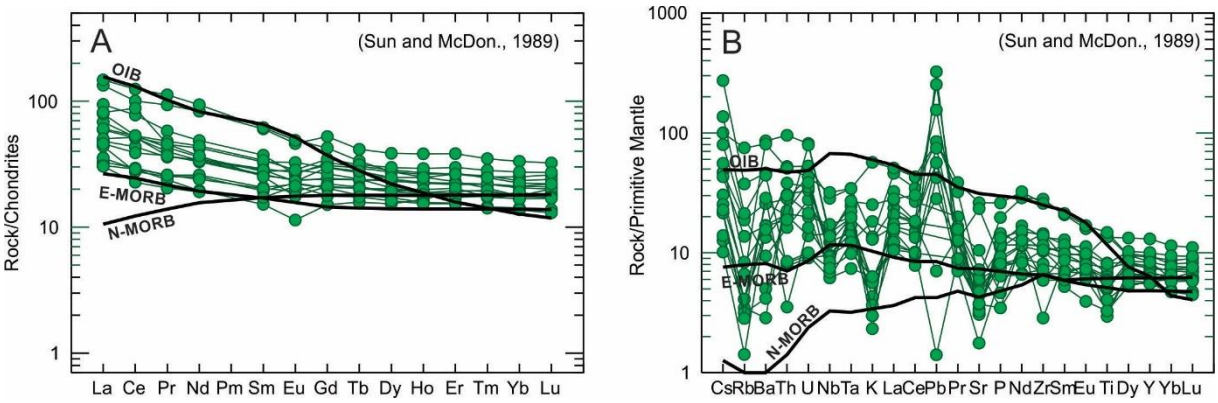

Figure 3.7. A-B) Chondrite normalized REE and primitive mantle (Sun and McDonough, 1989) normalized trace element pattern for the Campo Grande amphibolite samples (data from Supplementary Table 3.2). Samples with higher Mg# show a similar pattern to fractionated E-MORB, whereas amphibolites with lower Mg# have a similar pattern to ocean island basalts (OIB).

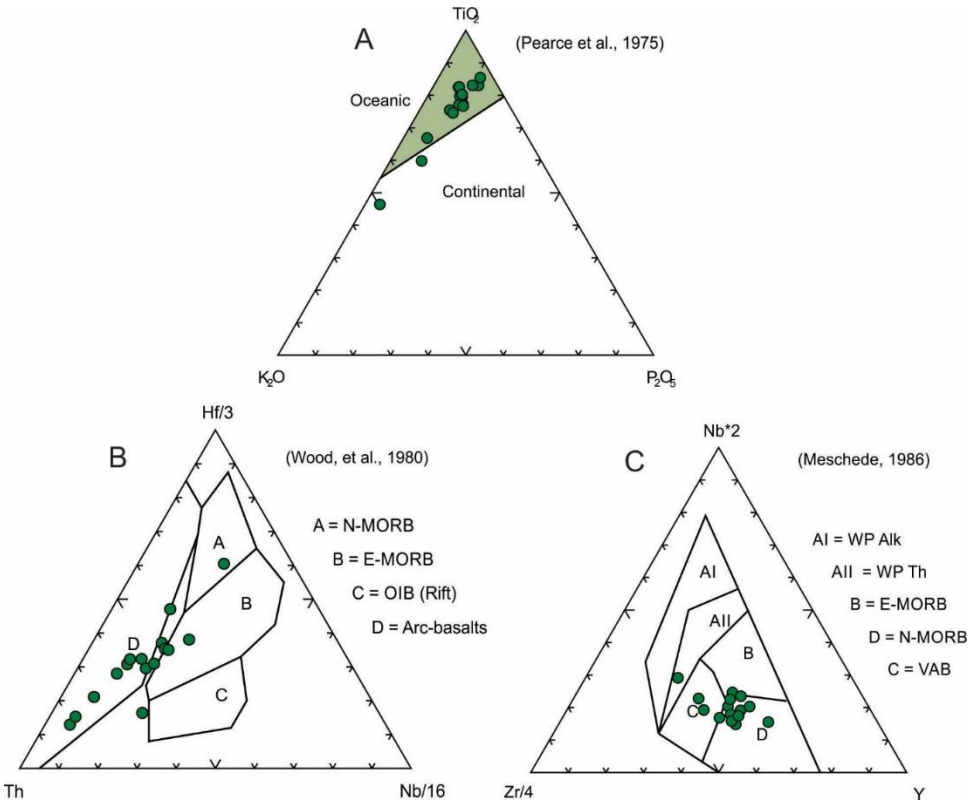

Figure 3.8. A) TiO2-K2O-P2O3 discriminant diagram (Pearce el al., 1975), B) Hf/3-Nb/16-Th ternary discrimination diagram (Wood, 1980) and C) Nb*2, Zr/4 and Y discriminant diagram (Meschede, 1986) for Campo Grande amphibolites. Legend of 7C: VAB – volcanic arc basalts, WPAlk – within-plate alkali basalts and WPTh – within-plate tholeiite.

3.5.3 U-Pb Geochronology

Six amphibolite samples and one host tonalitic paleosome gneiss sample were dated (Supplementary Table 3.3). The samples were selected based on the presence of the porphyroblastic garnet surrounded by symplectitic growth of plagioclase + clinopyroxene + amphibole that may represent the retrograded HP mineral assemblage, and the spatial distribution of the samples to map the geochronological extension of the high-pressure mafic rocks. These amphibolites contain two zircon populations, one represented by elongated (between 100 and 200 μm in length), euhedral to subhedral crystals, and the other by well-rounded grains (from 50 to 100 μm across) (Fig. 3.9A to I). Cathodoluminescence and backscattered electrons imaging reveals zoned cores that are surrounded by high luminescent rims (prismatic habit) and homogeneous crystals (rounded shapes) for amphibolite zircon crystals (Fig. 3.9A to I). On the other hand, the host migmatite rock only contains oscillatory-zoned prismatic grains (100 to 300 μm) (Fig. 3.9G).

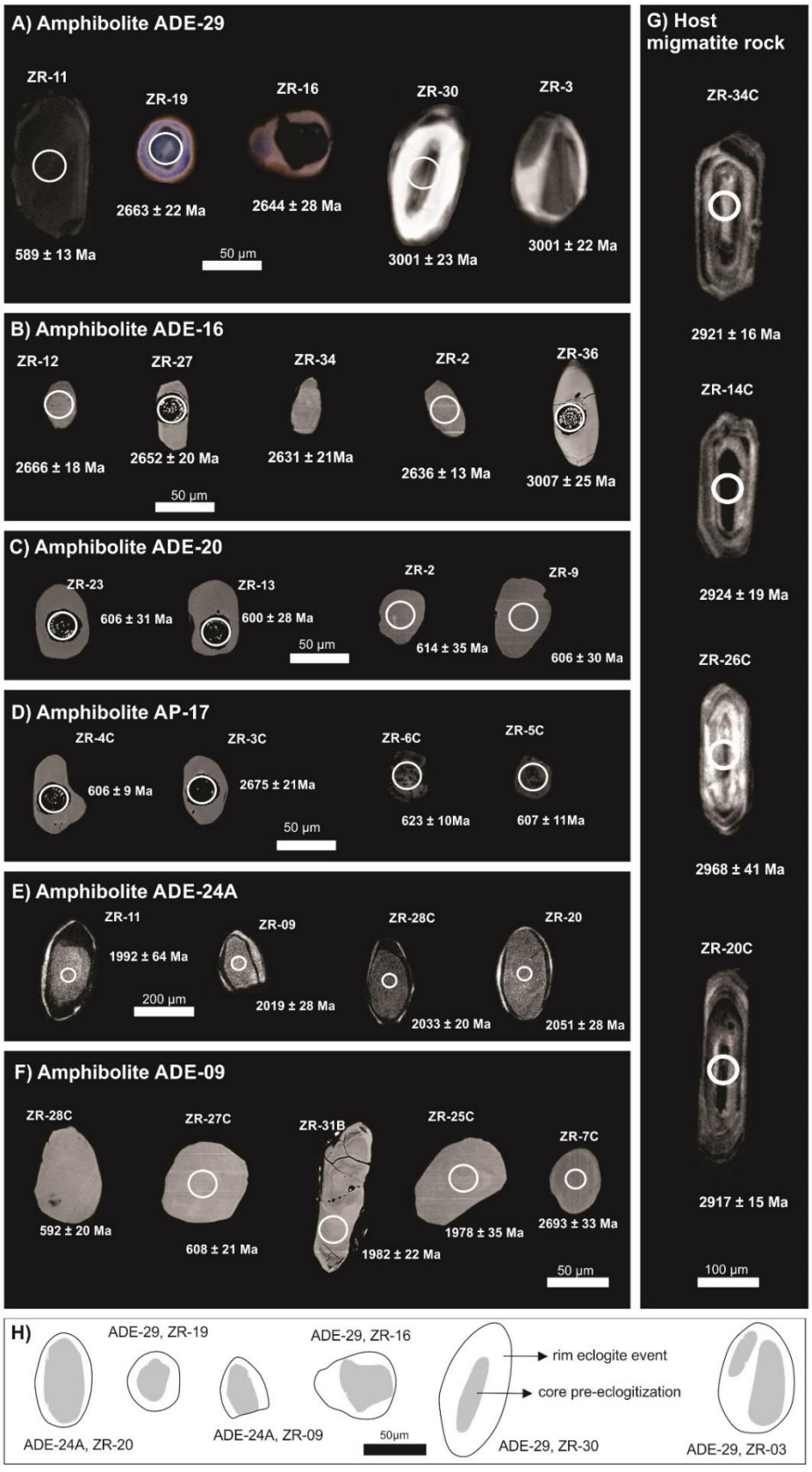

Figure 3.9. A to G) Representative CL (A, E and G) and BSE (B, C, D and F) images of zircon grains from amphibolite lenses and host migmatite from the Campo Grande area. The 207Pb/206Pb (>1.0 Ga) and 206Pb/238U (<1.0 Ga) ages are in Ma. H) Schematic model of different domains of zircon from center to rim show inherited core followed by CL-bright oscillatory zoned rim. Amphibolite zircon core followed by CL-dark inner rim with oscillatory banding with outermost thin CL-bright rim.

3.5.3.1 Amphibolite ADE-29

Collected at the southern limit of the mapped area, the amphibolite sample ADE-29 has well-rounded (40 to 50 μm) zircon grains surrounded by high luminescent rims with Th/U ratio ranging between 0.116 and 0.587. These zircon grains display a U-Pb discordia age of 2663±16 Ma (Fig. 3.10A), that we interpreted as the crystallization age of the mafic protolith. An inherited component is given by four prismatic (100 to 150 μm) zircon grains from this amphibolite, providing the age of 2992±17 Ma (MSDW = 1.14) (Fig. 3.10A). These Mesoarchean zircon grains show high luminescent rims (Fig. 3.9A) and Th/U ratios between 0.412 and 0.842. A metamorphic Neoproterozoic age (589±13 Ma; $^{206}Pb/^{238}U$ age), was obtained on a subhedral (~150 μm) zircon core with low Th/U ratio of 0.002.

3.5.3.2 Amphibolite ADE-16

The amphibolite sample ADE-16, located in the central portion of the area, displays a U–Pb discordia age of 2657±14 Ma (Fig. 3.10B). The zircon grains are subhedral (~50 μm) and have Th/U ratios of 0.121 to 0.326. One Mesoarchean inherited age of 3007±25 Ma ($^{207}Pb/^{206}Pb$ age) was obtained on a prismatic (~100 μm) zircon core with the highest Th/U ratio (0.461). This sample presents a similar evolution to that recorded in sample ADE-29, but without the registration of Neoproterozoic metamorphic zircon.

3.5.3.3 Amphibolite ADE-20

The amphibolite sample ADE-20 shows a single group of zircon grains (Fig. 3.9C), yielding a Neoproterozoic concordia age of 605±6 Ma (Fig. 3.10C) in well-rounded (~50 μm) zircon crystals that exhibit low Th/U ratios, ranging from 0.005 to 0.084.

3.5.3.4 Amphibolite AP-17

The amphibolite sample AP-17 displays an Archean age of 2675±21 Ma and concordant zircon grains at the lower intercept, near 600 Ma (Fig. 3.10D). The latter subpopulation yields two concordia ages of 606±3 Ma and 623±3 Ma (Fig. 3.10D) indicating progression of metamorphic ages with weighted mean concordia age of 614±10Ma (MSWD=0.72). All Neoproterozoic zircon grains are rounded, and do not show internal zonation (Fig. 3.9C, D), and have Th/U ratio from 0.009 to 0.050.

3.5.3.5 Amphibolite ADE-24A

The amphibolite sample ADE-24A, located at the central area, is unique in that it defines a Paleoproterozoic discordia age of 2023±30 Ma (Fig. 3.10E), with concordant analyses between 2019±28 Ma and 1961±31 Ma, and a concordia age at 2005±8 Ma (Fig. 3.10E). The zircon analyses show low Th/U ratio between 0.004 and 0.078. These Paleoproterozoic zircon crystals are well-rounded (100 to 200 μm) with unzoned cores followed by CL-dark inner rim and outermost CL-bright overgrowths (Fig. 3.9E) possibly due to a subsequent event. The narrowness of these zircon rims overgrowth prevented dating attempts. The Paleoproterozoic age obtained is taken as the record of a metamorphic event at ca. 2.0 Ga.

3.5.3.6 Amphibolite ADE-09

Sample ADE-09 relays a more complex history with three zircon populations displaying different discordia ages (Fig. 3.10F), reflecting polycyclic deformation in the area. The Neoarchean age of 2692±13 Ma is taken as the crystallization age of the amphibolite protolith. The Paleoproterozoic age of 1986±21 Ma and the Neoproterozoic concordia age of 592±5 Ma represent metamorphic events (Fig. 3.10F). Neoarchean zircon grains are well rounded (~50 μm) (Fig. 3.9F) with Th/U ratio between 0.147 and 0.323. The concordant Paleoproterozoic zircon is represented by rims of prismatic grains (~200 μm), and displays Th/U ratio between 0.011 and 0.162. Neoproterozoic zircon grains are rounded (~100 μm) and show the lowest Th/U ratios (0.001 to 0.003).

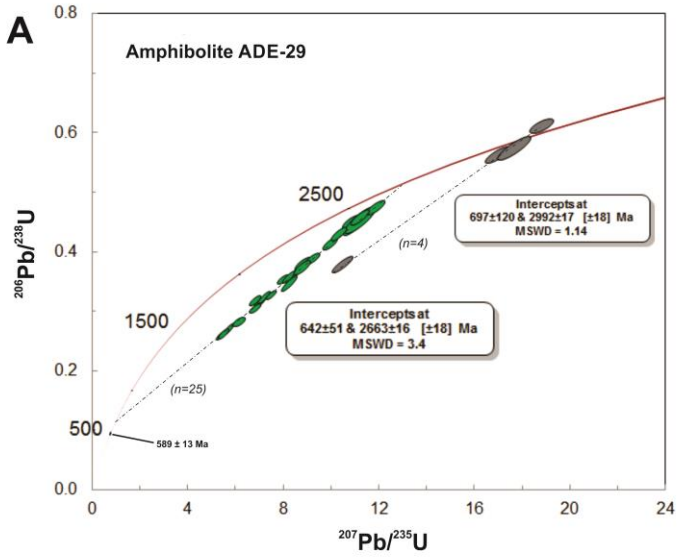
A
Amphibolite ADE-29
2500
1500
500
(n=4)
(n=25)
Intercepts at
697±120 & 2992±17 [±18] Ma
MSWD = 1.14
Intercepts at
642±51 & 2663±16 [±18] Ma
MSWD = 3.4
589 ± 13 Ma
206Pb/238U
207Pb/235U

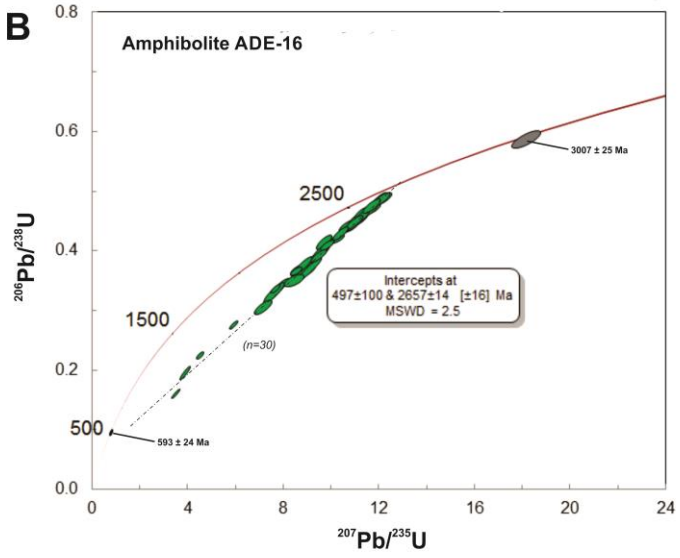
B
Amphibolite ADE-16
2500
1500
500
(n=30)
3007 ± 25 Ma
Intercepts at
497±100 & 2657±14 [±16] Ma
MSWD = 2.5
593 ± 24 Ma
206Pb/238U
207Pb/235U

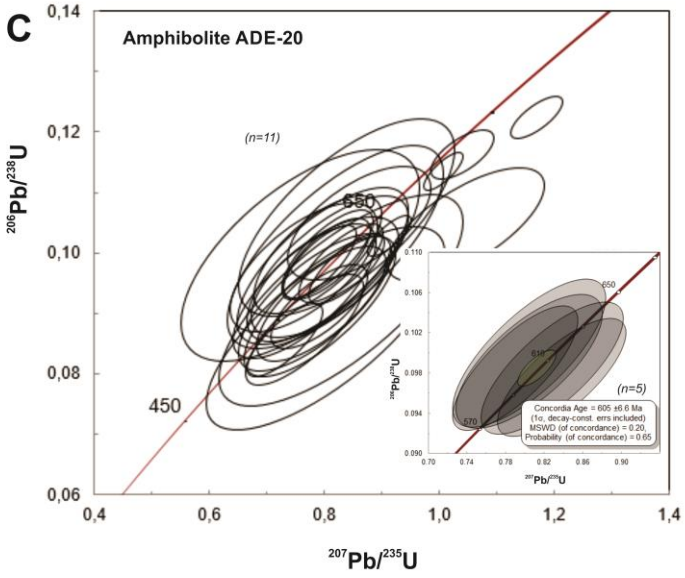
C
Amphibolite ADE-20
(n=11)
650
450
(n=5)
Concordia Age = 605 ±6.6 Ma
(1σ, decay-const. errs included)
MSWD (of concordance) = 0.20,
Probability (of concordance) = 0.65
206Pb/238U
207Pb/235U

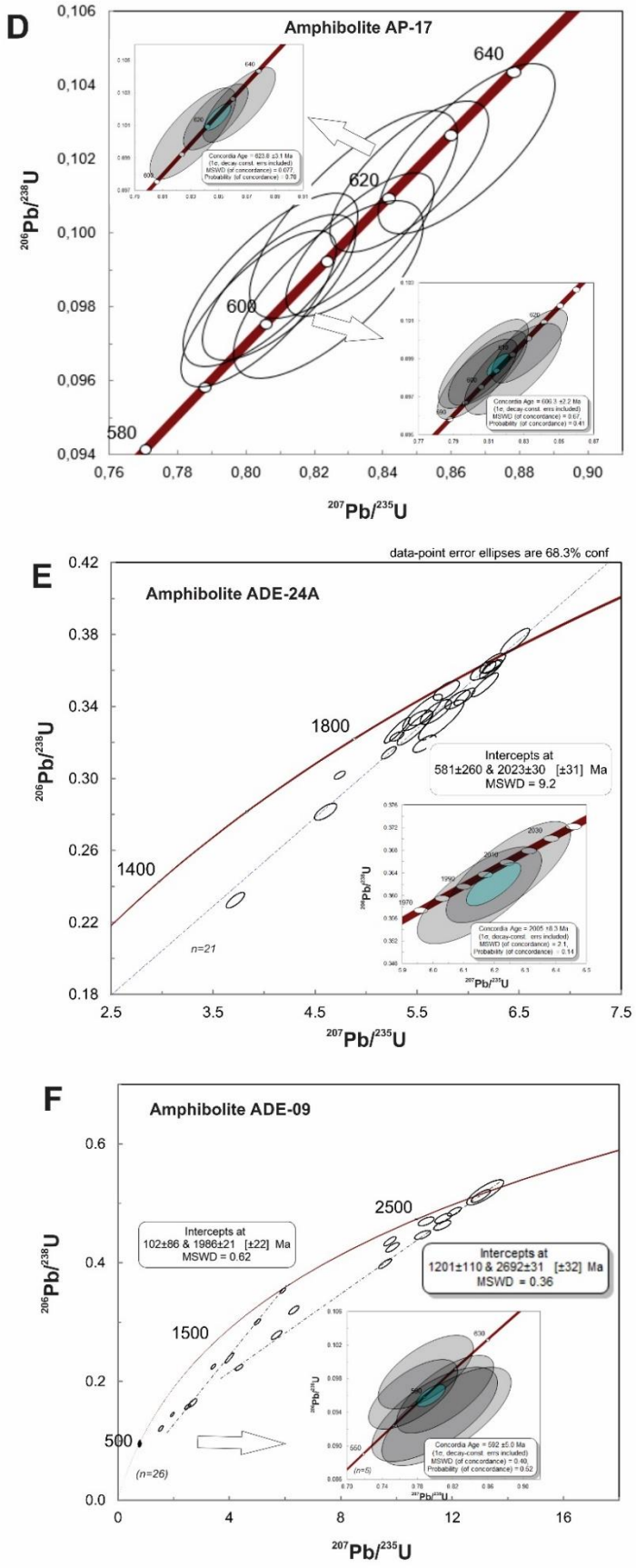

Figure 3.10. Concordia diagrams of U-Pb zircon data of amphibolite samples. Data from Supplementary Table 3.3.

3.5.3.7 Host migmatite ADE-10

The sample ADE-10 was collected from the tonalitic paleosome component of the host migmatite rocks. All zircon crystals are prismatic (100 to 300 μm), with Th/U ratios from 0.125 to 0.583 and internal zonation (Fig. 3.9G), typical magmatic crystal features (e.g. Corfu et al., 2003). Their analyses define a discordia age of 2923±14 Ma (Fig. 3.11) with a concordant age of 2921±16 Ma, interpreted as the crystallization age of the protolith.

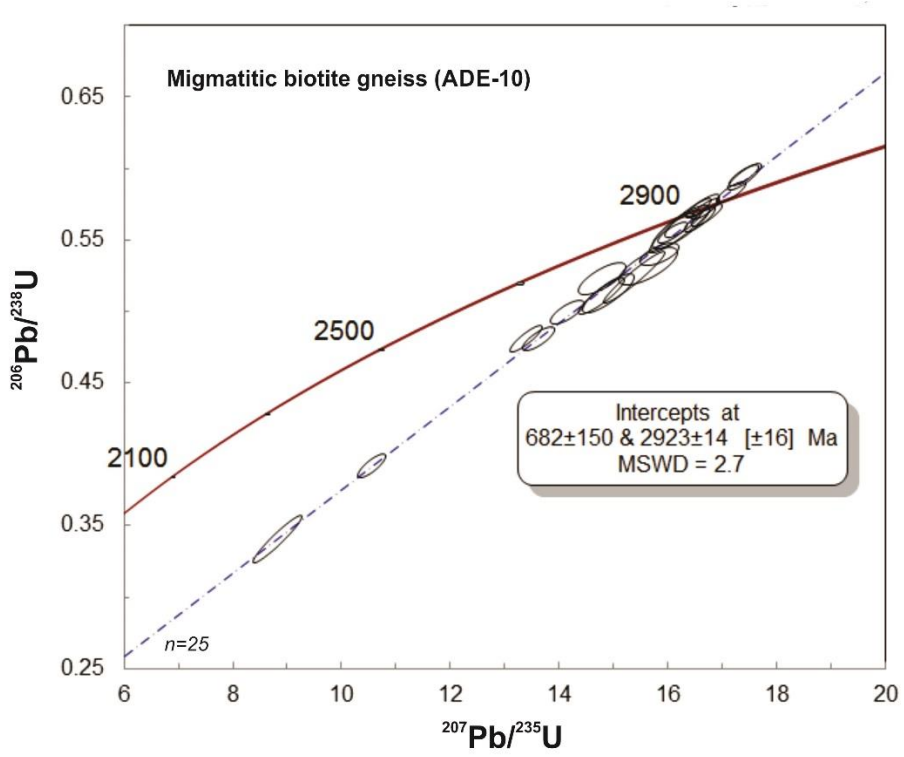

Figure 3.11. Concordia diagram of U-Pb zircon data from host migmatitic biotite gneiss. Data from Supplementary Table 3.3.

3.5.4 Lu-Hf Isotope

19 analyzed zircon grains from five amphibolite samples were chosen for Lu-Hf isotope analyses (Supplementary Table 3.4, Fig. 3.12A, B). The Mesoarchean zircon cores of ~3000 Ma yield low initial $^{176}Hf/^{177}Hf_{(t)}$ ratios of 0.280998 to 0.281280, and positive $\varepsilon_{Hf\ (t)}$ values of +5.4 to +15.3, with T_{DM} model ages of 2.65 to 3.02 Ga. On the other hand, Neoarchean zircon grains of 2693 to 2633 Ma show heterogeneous Hf composition with high $^{176}Hf/^{177}Hf$ ratios of 0.281199 to 0.281926, with positive $\varepsilon_{Hf\ (t)}$ values of +3.8 to +30.6, and T_{DM} values of 1.78 to 2.76 Ga. The T_{DM} ages are less than the U-Pb crystallization age due to $\varepsilon_{Hf(t)}$ plotted above the fractionated depleted

mantle. The Lu-Hf Isotope analyses show Pb loss, forming a horizontal distribution line, indicating that they are most likely derived from the $^{176}Hf/^{177}Hf$ isotopic system of 2.65 Ga (Fig. 3.12A). The Neoproterozoic zircon grains of 623 to 576 Ma yield initial $^{176}Hf/^{177}Hf_{(t)}$ ratios of 0.281586 to 0.282478 and $\varepsilon_{Hf(t)}$ values of +1.98 to -28.9 for the core and rim with younger T_{DM} Hf model ages of 1.1 to 2.2 Ga. There is an increase over time in the difference between the $^{176}Hf/^{177}Hf$ ratios of the 2.65 Ga igneous protolith and the Neoproterozoic metamorphism. The Neoproterozoic ZR-02 and ZR-06 zircon grains from sample AP-17 have lower $^{176}Hf/^{177}Hf_{(t)}$ ratios (0.280531-0.280583) and strong negative ε_{Hf} values (-64.6 and -65.8). However, these zircon crystals were affected by alteration and dissolution (Fig. 3.9D). In spite of metamict cores, they still preserve Neoproterozoic metamorphic age. Such T_{DM} model ages from the magmatic zircon grains indicate 1.8 to 2.7 Ga crustal residence time for the amphibolite lenses.

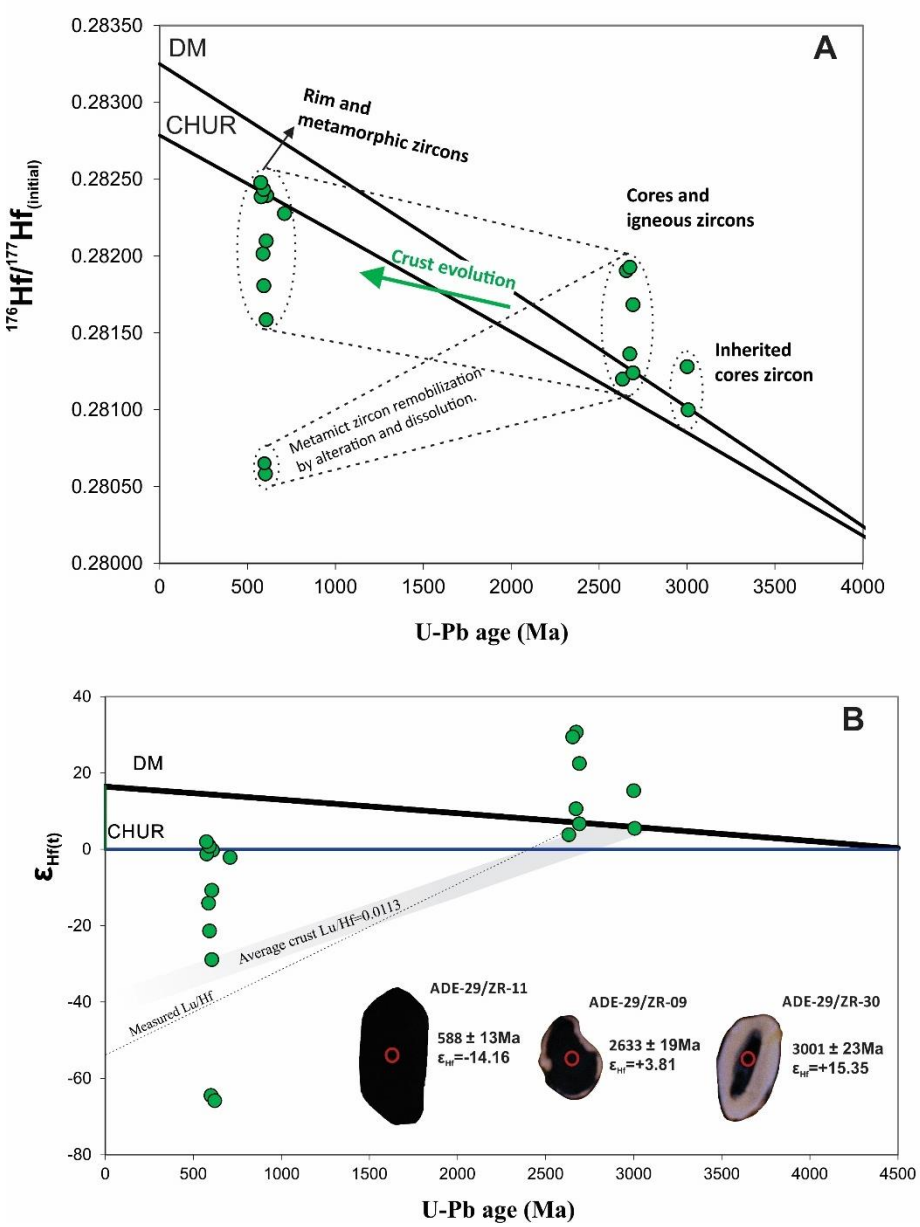

Figure 3.12. Integrated zircon Lu-Hf isotope diagrams from the amphibolites samples. Initial $^{176}Hf/^{177}Hf$ (t) value (A) and εHf(t) (B) versus age (t), including CL images of zircon grains with analyzed spots for $^{207}Pb/^{206}Pb$ age and $\varepsilon Hf_{(t)}$. Data from Supplementary Table 3.4.

3.5.5 Sm-Nd Isotope

T_{DM} model ages and $\varepsilon_{Nd\ (t)}$ for thirteen whole rock samples suggest a complex history for the amphibolites (Supplementary Table 3.5, Fig. 3.13). The amphibolites display two Nd isotopic groups (G1 and G2) based on T_{DM} model ages older and younger than 2.6 Ga, the crystallization age of the mafic protolith. In G1, four samples (ADE-24A, ADE-16, AT-14 and AT-16) have negative $\varepsilon_{Nd\ (2.65\ Ga)}$ values (−1.03 to −7.97) and older T_{DM} model ages between 3.7 and 3.3 Ga; in this group, sample AP-10 has a less negative $\varepsilon_{Nd\ (2.6)}$ value (-1.12) and a younger T_{DM} age of 3.19 Ga. The second

group, G2, shows positive $\varepsilon_{Nd\ (2.6\ Ga)}$ values (+1.97 to +8.17), with younger T_{DM} model ages of 1,95 to 2.65 Ga. Nd isotopic data obtained for the host tonalitic paleosome (sample ADE-10) shows T_{DM} model age of 3.2 Ga, with negative $\varepsilon_{Nd(2.9\ Ga)}$ = -2.58 (Supplementary Table 3.5, Fig. 3.13).

The $\varepsilon_{Nd(2.6\ Ga)}$ plotted against 1/Nd and $^{147}Sm/^{144}Nd$ shows the evolution and the distinction between amphibolites with different Nd isotopic signatures (Group 2) and preserved Nd Isotopic system (Group 1) (Fig. 3.14A-B). T_{DM} model age vs 1/Nd and $^{147}Sm/^{144}Nd$ diagrams also separate G1 and G2 amphibolite samples (Fig. 3.14C-D). The samples of the G2 group have higher Mg# and modal concentration of garnet and pyroxene with well-developed symplectitic texture, whereas the samples of the G1 group show lower Mg# and consist mainly of granoblastic amphiboles. Thus, we suggest that the more negative values of $\varepsilon_{Nd(2.65Ga)}$ and anomalously high T_{DM} for the G1 group (Fig. 3.13) are due to mantle enrichment processes.

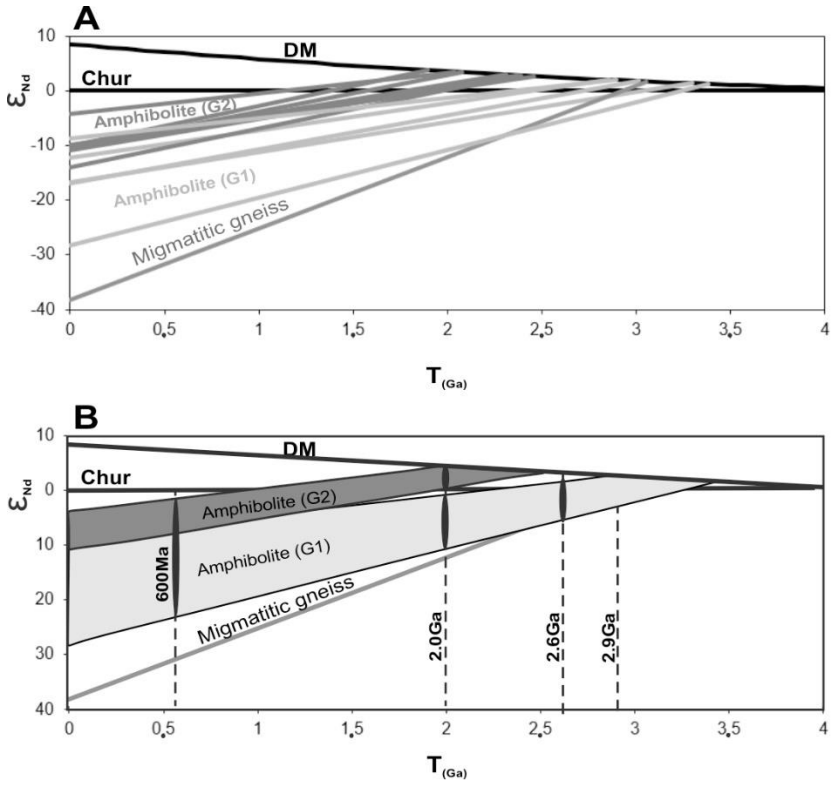

Figure 3.13. A-B) Nd isotope compositions of amphibolites and host migmatitic gneiss samples. Data from Supplementary Table 3.5.

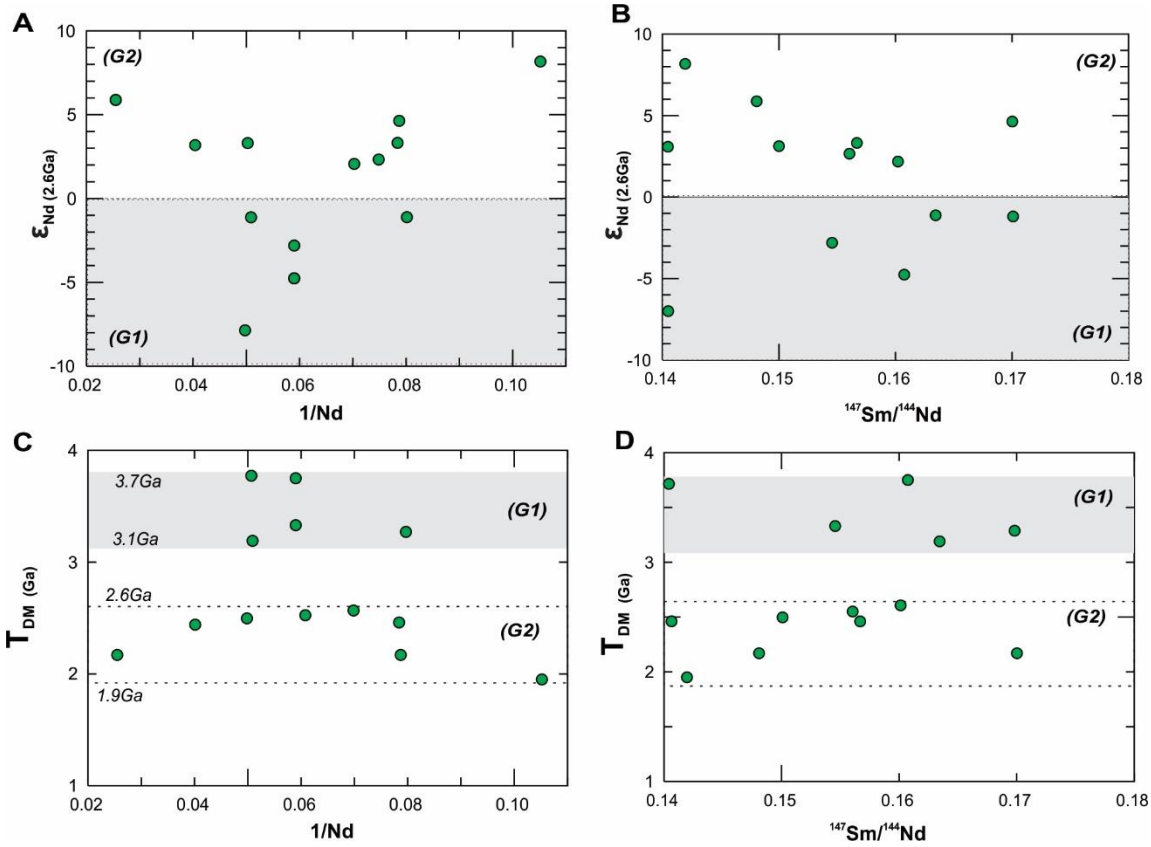

Figure 3.14. A-B) εNd(t) vs 1/Nd and 147Sm/144Nd ratios. C-D) TDM model age vs 1/Nd and 147Sm/144Nd rations for Campo Grande amphibolites.

3.6 DISCUSSION

3.6.1 Origin of Amphibolites

The studied amphibolites have basaltic composition, displaying subalkaline character and tholeiitic affinity (Fig. 3.6A-B), which is typical of basaltic melts in oceanic ridges or in supra-subduction zones (e.g. Pearce, 2008). However, the tholeiitic samples from the Campo Grande area display two different oceanic signatures, varying from E-MORB to OIB types in the Th/Yb vs Nb/Yb and TiO_2/Yb vs Nb/Yb discriminant diagrams (Fig. 3.15) (Pearce, 2008).

The Th–Nb proxy demonstrates volcanic arc array affinity and oceanic subduction setting (Fig. 3.15A). The amphibolite samples are displaced above the MORB–OIB trend, similar to basaltic melts in subduction zones, while all oceanic basalts lie within a diagonal MORB–OIB array (Pearce, 2008). The Ti–Yb proxy is used to indicate melting depth, mantle temperature and the thickness of the conductive lithosphere (Pearce, 2008). The TiO_2/Yb vs Nb/Yb diagram shows that the amphibolite samples with MORB signature were generated at shallow-melting setting, while samples with OIB signature indicate deep-melting setting (Fig. 3.15B). In the Hf/Ta vs Zr/Nb plot, mafic samples define an approximately linear distribution (Fig. 3.15C), as expected for oceanic basalts (Jochum et al., 1986), with similar evolution from primitive mantle to E-MORB. In this diagram, samples display a pattern of enrichment greater than reference values, supporting an enriched mantle source or continental assimilation of Zr and Hf. This latter hypothesis is evidenced by the presence of inherited zircon cores of 3.0–2.9 Ga, possibly from the host migmatite. Again, low Th/La ratios between 0.10 and 0.20 (Fig. 3.15D) are consistent with oceanic basalts (Plank, 2005) and a source similar to the primitive mantle (~0.11, Sun & McDonough, 1989). High Th/La ~0.2 indicates an enriched source due to the preferential partitioning of La over Th in mafic and accessory minerals within the mantle (e.g. Rudnick and Gao, 2003; Plank, 2005).

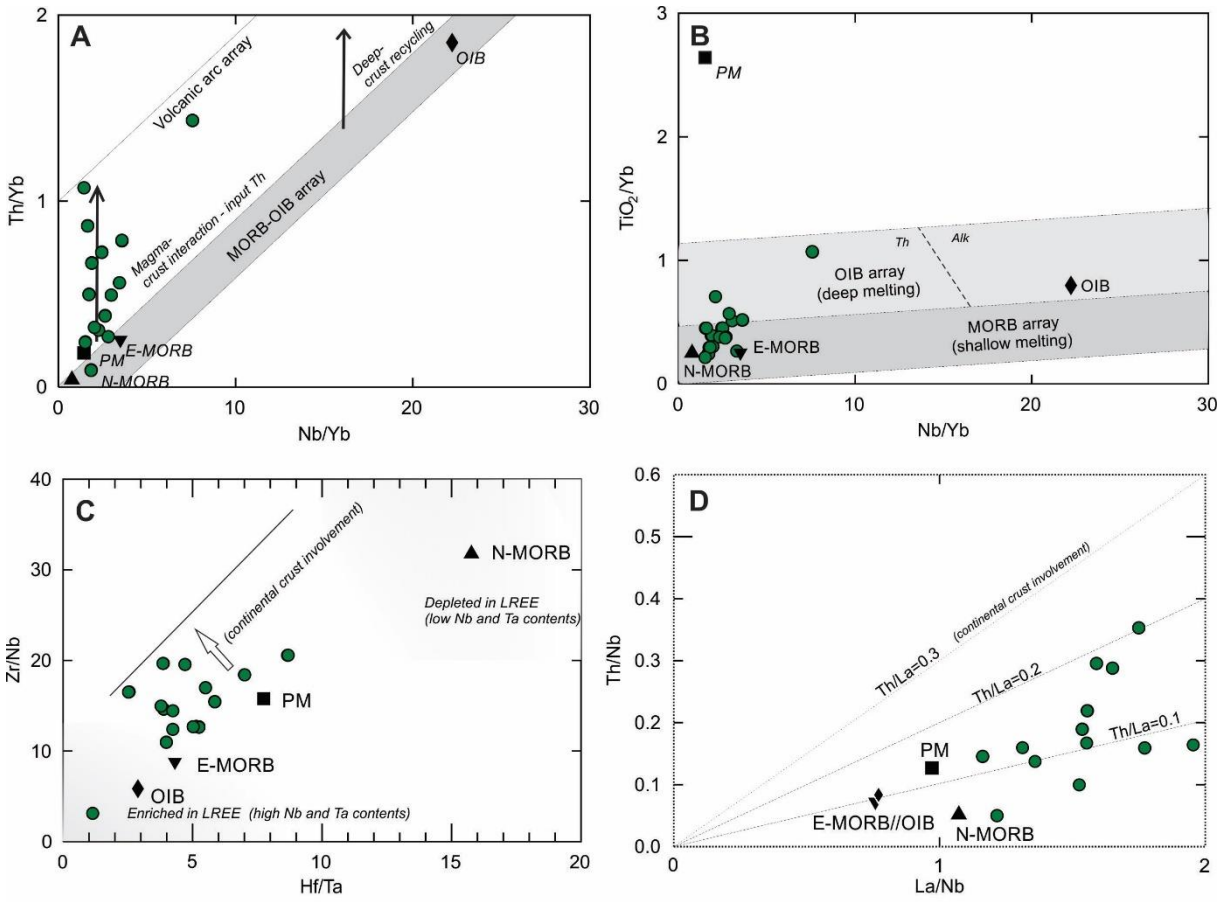

Figure 3.15. A) Th/Yb vs. Nb/Yb (Pearce, 2008) for discrimination of oceanic basaltic rocks and (B) TiO2 vs Nb/Yb (Pearce, 2008) discriminating between intra-oceanic settings of basaltic rocks formation. C) Zr/Nb vs Hf/Ta for source character identification (Jochum et al., 1986). D) Th/Nb vs La/Nb (Plank, 2005) for crustal contamination definition. Reference values for N-MORB, E-MORB, OIB and PM are from Sun & McDonough (1989).

Subsequent metasomatism in the amphibolite protoliths can be observed in Nb/Ta, La/Sm and Y/Ho ratios. These elements exhibit extremely coherent behavior during magmatic processes (e.g. Bau, 1996; Bau and Dulski, 1999). Therefore, disturbances in these ratios indicate hybridization processes and enriched component. Enrichment of Ta relative to Nb (Fig. 3.16A) and enrichment in HREE (Fig. 3.16B) reflects the partitioning process within the crust-mantle system (e.g. Green, 1995). Despite the uniform Y/Ho ratio, increase in the absolute concentration of Y is observed (from 25 to 45 ppm, Fig. 3.16C), while Y/Ho ratios show little variation (29 to 26), indicating non-CHARAC (CHArge-and-RAdius-Controlled) trace element behavior, possibly due to silicate melts or aqueous fluids (e.g. Bau, 1996). The amphibolite samples display decreasing Nb/Ta ratios from similar E-MORB compositions (~17.5) to more fractionated melts (~5), suggesting Ta enrichment in the oceanic protoliths, possibly during subduction.

The tectonic discriminant Ti-V diagram (Fig. 3.16D; Shervais, 1982) shows the typical subalkaline (tholeiitic) differentiation trend from arc-tholeiite to E-MORB. Strong Ti increase (0.4 to 1.8%) is due to the very low partition coefficient of this element, almost always <<1 (Shervais, 1982). Depletion of V relative to Ti is a function of fO_2 of the magma and its source, the degree of partial melting and subsequent fractional crystallization (Shervais, 1982). Again, two groups are described, based on vanadium concentration. The first group has values between 250 and 350 ppm (MORB signature samples) and the second group displays V around 450 ppm (OIB signature samples).

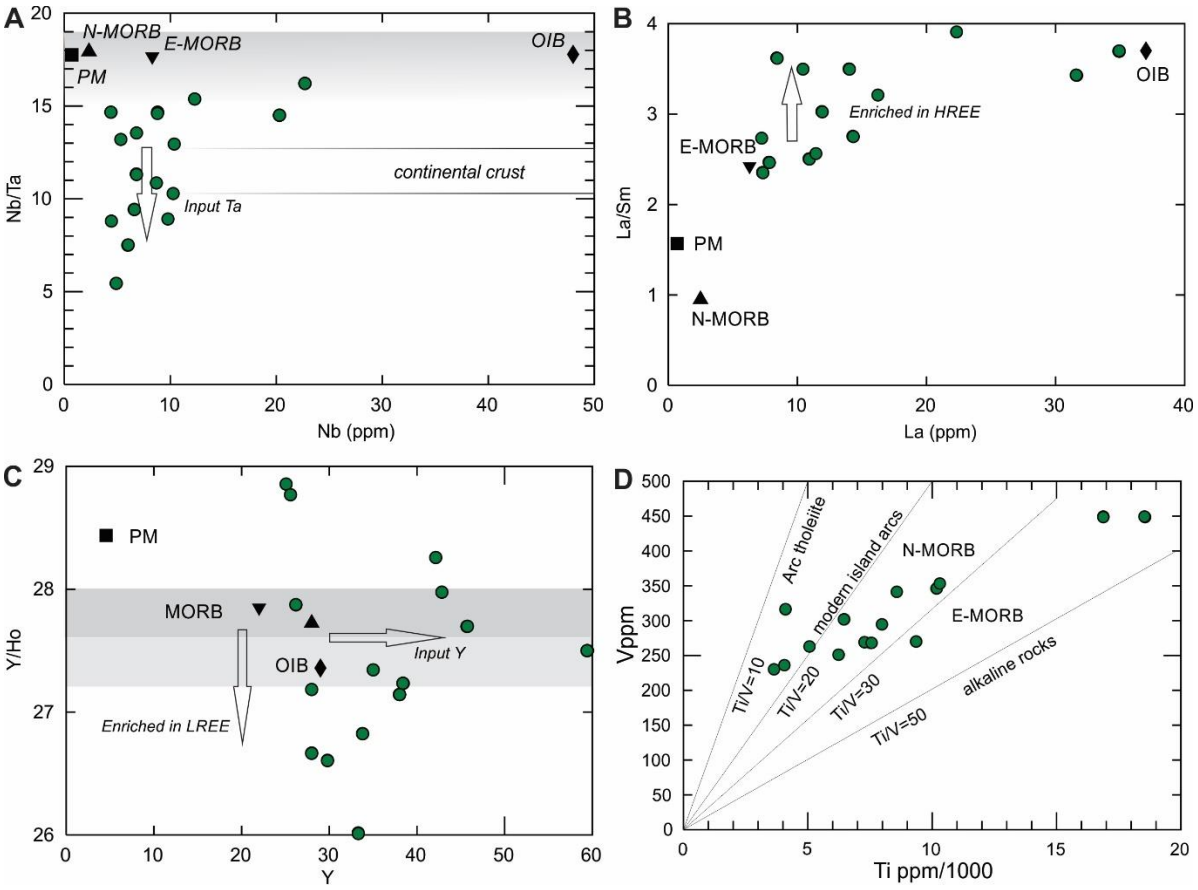

Figure 3.16. Plots of (A) Nb/Ta vs Nb, (B) La/Sm vs La and (C) Y/Ho vs Y for Campo Grande amphibolites. Compatible behavior during igneous processes increases from A to C. Reference values for N-MORB, E-MORB, OIB and PM are from Sun & McDonough (1989). (D) Vanadium vs Ti/1000 variation diagram (Shervais, 1982) for Campo Grande amphibolites.

The increase in incompatible elements, mainly Na, K, Ba, Ta, Ti, Th and LREE, can be attributed to the effect of mantle metasomatism, leading to a more plausible enriched source, previous to subduction (e.g. Willbold and Stracke, 2010; Huang et al., 2012; Kiseeva et al., 2016). Consequently, mafic to ultramafic oceanic crust enriched in incompatible elements implies that the mantle had already been strongly depleted at 2.65 Ga, as previously described in tholeiitic basalts enriched in Th and

LREEs associated to subducted oceanic crust processes in the Archean of SW Greenland (Hawkesworth et al., 2010; Polat el al., 2011). The erratic and enriched pattern of the distribution of Zr, Hf and mainly Pb (Fig. 3.7B) is attributed to the assimilation of Archean zircon grains of the host migmatite during protolith crystallization, while changes in Sr, Ba and Nd patterns can be attributed to high-grade metamorphic processes (See topic 5.2). In summary, the geochemical data allow us to propose that the enriched amphibolite protoliths were crystallized at ca. 2.65 Ga in an oceanic crust with E-MORB and OIB signature.

A similar inference can be drawn from Hf and Nd isotopes. Hafnium compositions provide greater resolution in identifying discrete crust–mantle differentiation and the $\varepsilon_{Hf(t)}$ values are useful for identifying older crustal versus juvenile mantle components (e.g. Chauvel and Blichert-Toft, 2001; Hawkesworth and Kemp, 2006; Zeh et al., 2007, Gerdes and Zeh, 2009).

The $^{76}Hf/^{177}Hf_{(t)}$ ratios, εHf(t) and T_{DM} obtained in our rocks indicate that the amphibolite protoliths crystallized at 2.65 Ga from juvenile magma derived from sources with positive $\varepsilon_{Hf(t)}$ values of +3.81 to +30.66. It is an evidence of a juvenile Archean oceanic crust formation in the Borborema Province. However, Nd isotopes data of these juvenile mafic rocks show negative $\varepsilon_{Nd(2.65\ Ga)}$ values (−1.03 to −7.976) and T_{DM} model ages of 3.7 and 3.3 Ga, suggesting a component of metasomatism in the subcontinental lithospheric mantle, causing enrichment in the Sm-Nd isotopic system during Archean times. The group of mafic rocks with T_{DM}=1.95 to 2.65 Ga could represent a new juvenile magmatic event at 2.0 Ga with $\varepsilon_{Nd(2.0\ Ga)}$ range from ? or ascent of asthenospheric mantle due to an extensional exhumation process in the region at this time. This hypothesis has to be better understood and proved yet. Until this moment, there is no relationship between the amphibolite groups (G1 and G2) with the source or the U-Pb age of crystallization, as high metamorphic grade altered both MORB and OIB signature of the rocks crystallized ca. 2.65Ga.

3.6.2 Age of Metamorphism and Isotopes Constraints

Several amphibolite lenses show the same age at around 2.65 Ga, interpreted as the age of crystallization of the protolith based on internal zonation, morphology and high Th/U ratio in zircon cores. The presence of inherited zircon cores of 3.0 to 2.9 Ga indicates that the amphibolites represent tholeiitic magma emplaced into the

Mesoarchean basement during extension. The Archean age at 2.9 Ga of the basement migmatite-gneiss suggests reworked Mesoarchean continental crust in this segment of the Rio Grande do Norte domain and shows the existence of an old block not recognized previously in the regional context of the Borborema Province.

The age of the metamorphic history of the region is still an open question. Zircon crystals are crucial to help interpret such dates in the context of the P-T history, despite of they being stable over a wide range of metamorphic conditions (e.g. Kohn et al., 2015). For new metamorphic zircon to form under high-grade metamorphism conditions, either the presence of a hydrous fluid or melt phase is required (e.g. Tichomirowa et al., 2005) or else via solid-state recrystallization (e.g. Rubatto et al. 2006). Several zircon grains analyzed in the amphibolite samples record evidence of a first metamorphic event of 2.0 Ga. These grains are rounded and unzoned, and generally have Th/U ratios < 0.1 (Fig. 3.17), characteristics that are attributed to metamorphic zircon (e.g. Rubatto and Gebauer, 2000). However, it is known that metamorphic zircon in some high-grade rocks (e.g. granulite facies) displays Th/U ratios > 0.1 (e.g. Korhonen et al. 2013). The higher Th/U ratios in zircon formed under granulite-eclogite facies conditions reflects both an increase in Th and a decrease in U contents (e.g. Yakymchuk and Brown, 2019). Thus, these ratios are controlled by other major or accessory mineral phases and their partitioning coefficient with zircon.

In addition, the internal textures from the Campo Grande amphibolite zircon grains are consistent with zircon in eclogites (e.g. Corfu et al., 2003). These zircon crystals occur both in the matrix (symplectic texture) and as inclusions in different places within garnet porphyroblasts. They are subrounded and somewhat irregular and show relatively homogeneous internal textures (Fig. 3.9H). Retro-eclogites may contain complex zircon types: older homogeneous or growth zoned cores pre-dating eclogitization and metamorphic rims. The interfaces between irregular cores and rims are well-defined, showing either very fine or very coarse bands (Fig. 3.9H), and indicating resorption and recrystallization (e.g. Corfu et al., 2003). We interpret that this is the case of analyzed zircon grains from Campo Grande mafic rocks.

The second metamorphic event at 600 Ma was more pervasive and is recorded in the majority of dated amphibolite lenses. the Neoproterozoic zircon grains, forming the youngest cluster of concordant analyses between 623±3 Ma and 592±5 Ma, are with low Th/U ratios (<0.1, Fig. 3.17). High-grade metamorphic event as indicated by

zircon rims in the mafic rocks from Campo Grande region, shows negative $\varepsilon_{Hf(t)}$ values up to -65.88.

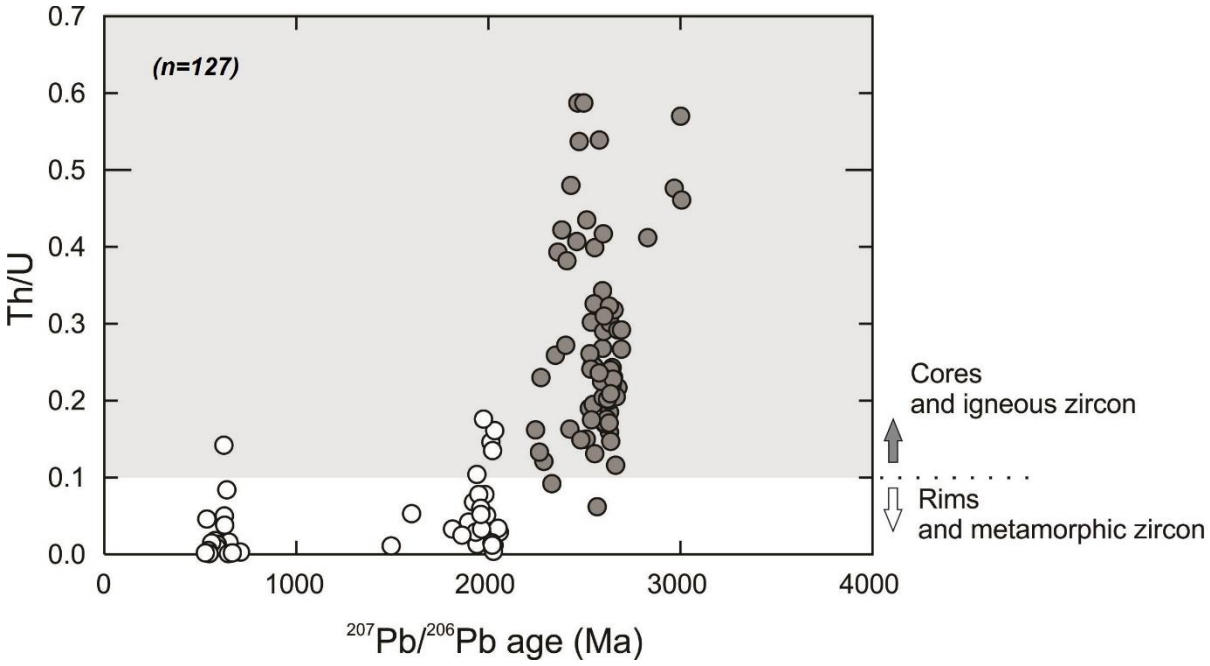

Figure 3.17. Th/U ratio vs 207Pb/206Pb ages from the Campo Grande amphibolite samples. Th/U ranges from 0.01–1.4 in magmatic cores and 0.01–0.1 in metamorphic rims and grains.

Theoretical models show that the time required to produce unzoned crystals of 2-3 mm size is in the order of 10-50 Ma (Caddick et al., 2010) for metamorphic temperatures around 690°C. Furthermore, zircon is likely to grow under retrograde conditions when garnet is dissolved (e.g. Kohn et al., 2015; Tedeschi et al., 2017). Hence, these amphibolites may have experienced HP conditions during around 30 Ma (623 to 592 Ma). Therefore, we do not have the mineral assemblage to prove that Th/U ratios <0.1 are an unfailing indicator of metamorphic recrystallization. Symplectite texture formed through the reaction omphacite + H_2O → clinopyroxene + plagioclase + amphibole ± quartz is observed in these rocks and are considered as related to retrogressed mafic eclogites (e.g. Waters, 2003; Lanari et al., 2013; Tedeschi et al., 2017). We found this texture developed as coronae around garnet porphyroblasts in the studied rocks. The shape of the garnet crystals, showing lobed edges, suggests resorption during the formation of the corona (e.g. White et al., 2008; Lanari et al., 2017). Similar reactions have been observed in retrogressed mafic eclogites (e.g. Waters, 2003; Lanari et al., 2013) and in HP rocks (Tedeschi et al., 2017), corresponding to the amphibolite-eclogite facies transition (ca. 650 to 700ºC at 13 to 15 kbar), followed by near isothermal decompression.

Therefore, based on morphology, internal zoning, Th/U composition and combined U-Pb and Lu-Hf in situ analyses on zircon, we propose that the Campo Grande Block was submitted to a complex polycyclic evolution (Fig. 3.18).

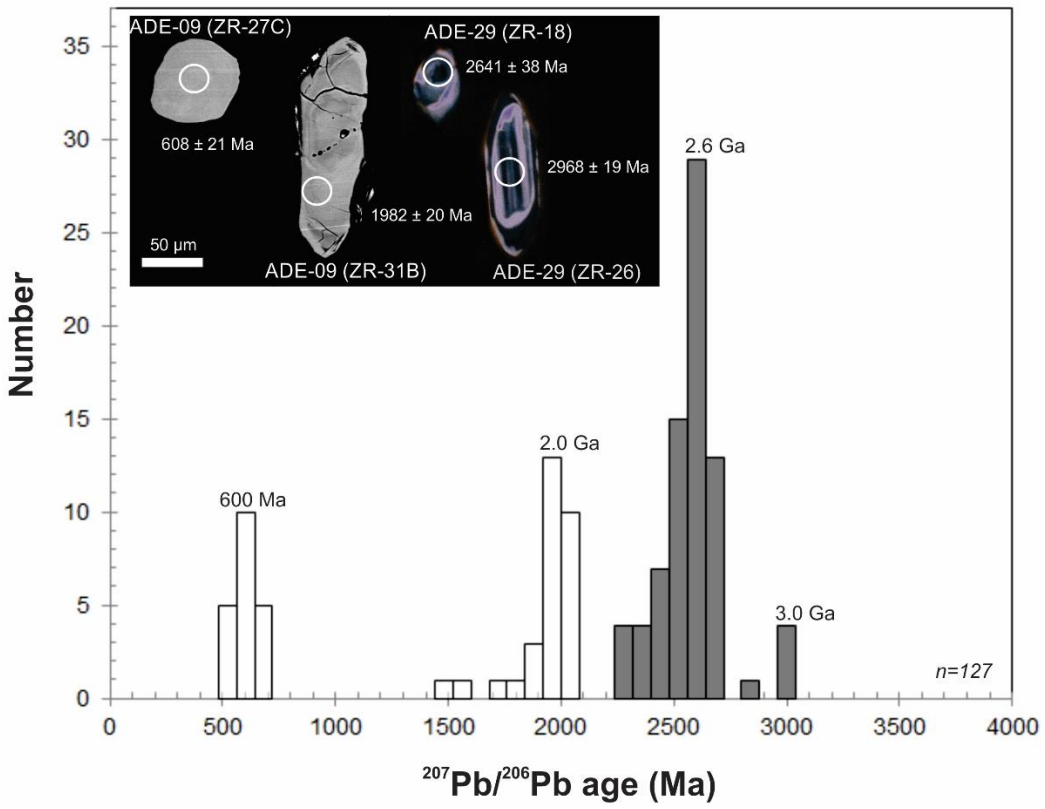

Figure 3.18. Histogram of 207Pb/206Pb ages of the Campo Grande mafic rocks, including CL and BSE images of zircon grains with analyzed spots for 207Pb/206Pb (>1.0 Ga) and 206Pb/238U (<1.0 Ga) age. Data from Supplementary Table 3.3.

3.6.3 Implications for West Gondwana

High-pressure amphibolites of the Campo Grande area present a clear evidence of oceanic crust generation during the Archean in the Borborema Province. We interpret this assemblage as retro-eclogites that represent a different context in terms of temporal and petrogenetic correlation with other occurrences described in the Borborema Province and in other Brazilian provinces

In the Southern Brasília orogen, a Neoproterozoic collisional belt, (U–Th)–Pb ages in the range 620–588 Ma from monazite grains and from matrix-hosted patchy monazite are recorded. These ages are interpreted to date exhumation of HP rocks, as recorded by close-to-isothermal decompression, and subsequent close-to-isobaric

cooling (Reno et al., 2012), which metamorphic peak was dated around 630 Ma and retrogression conditions at 603±7 Ma (Tedeschi et al., 2017).

In the Borborema Province, the Santa Quitéria Magmatic arc (Fetter et al., 2003; Ganade de Araújo et al., 2014) is associated to collisional and high-grade metamorphic event dated at 640–620 Ma (Santos et al., 2008; Arthaud et al., 2008; Amaral et al., 2017). The 614.9±7.9 Ma age of a metamafic rock, interpreted as retro-eclogite records the minimum age of the high-grade metamorphic conditions (upper amphibolite/granulite facies) (Santos et al., 2009; 2015, Ganade de Araujo et al., 2014).

HP mafic rocks from the Borborema and Mantiqueira provinces were generated between 640 and 590 Ma in West Gondwana (Santos et al., 2009, 2015; Ganade de Araujo et al., 2014; Tedeschi et al., 2017), therefore, recording an important link for the correlation between the Goiás and Pharusian oceans as suggested by Santos et al. (2008, 2009, 2015). Thus, all eclogite evidences described before in Brazil are related to tectonic events affecting piles of metasedimentary rocks inside Neoproterozoic fold-and-thrust belts. Although similar Neoproterozoic ages were found in the Campo Grande high-pressure mafic rocks, they are associated to a basement inlier within the Neoproterozoic supracrustal sequences in the Borborema Province. On the other hand, similar eclogite forming events at 2.0 Ga are recorded in migmatite domes in Africa (Loose and Schenk, 2018; François et al., 2018) and Russia (e.g. Imayama et al., 2017).

3.7 CONCLUSION

The main conclusions of this study are as follows:

I. Amphibolites of the Campo Grande area, Rio Grande do Norte domain, Borborema Province, Northeast Brazil, display typical textures found in amphibolite representing retro-eclogite, e.g. massive plagioclase-clinopyroxene symplectite between poikiloblastic garnet and granoblastic amphibole.

II. Chondrite-normalized REE and trace elements of amphibolite suggest an enriched mantle source with E-MORB and OIB signature for the amphibolite protolith.

III. Amphibolite samples have Archean crystallization age of 2.65 Ga and were metamorphosed at 2.0 Ga and 600 Ma. These samples contain inherited zircon grains of 2.9 Ga compatible with host migmatite-gneiss zircon of 2923±14 Ma.

IV. Petrographic and symplectite texture from the amphibolites suggest maximal conditions at the amphibolite/eclogite facies boundary, followed by near isothermal decompression related to orogenic collision stages between Archean and Paleoproterozoic terranes.

V. The Campo Grande rock assemblage is composed of Archean units that were amalgamated to West Gondwana during crustal reworking associated to the Neoproterozoic Brasiliano/Pan-African orogeny.

VI. Therefore, we propose that the Campo Grande Block comprising tonalite magmatism at ca. 2.9 Ga, juvenile tholeiitic magmatism at ca. 2.65 Ga, which formed the amphibolite protoliths, followed by high-grade metamorphic events at ca. 2.0 Ga and ca. 600 Ma.

3.8 ACKNOWLEDGMENTS

This study is part of the first author's PhD thesis in development at the Institute of Geosciences (Universidade de Brasília). The authors acknowledge the support of the INCT Estudos Tectônicos (CAPES/CNPq - 465613/2014-4 and FAPDF - 193.001.263/2017). ELD, TJSS, RAF and MT acknowledge CNPq research fellowships.

3.9 REFERENCES

Albarède, F., Telouk, P., Blichert-Toft, J., Boyet. M., Agranier, A., Nelson, B., 2004. Precise and accurate isotopic measurements using multiple-collector ICPMS. Geochimica et Cosmochimica Acta 68, 2725-2744. (doi.org/10.1016/j.gca.2003.11.024)

Amaral, W.S., Kraus, R.K., Dantas, E.L., Fuck, R.A., Pitombeira, J.P.A., 2017. Sinistral reactivation of the Transbrasiliano Lineament: Structural and geochronological evidences in the Cariré Granulite Zone, Borborema Province - NE Brazil. Journal of South American Earth Sciences 79, 409-420. (doi.org/10.1016/j.jsames.2017.08.022)

Archanjo, C.J., Viegas, L.G.F., Hollanda, M.H.B.M., Souza, L.C., Liu, D., 2013. Timing of the HT/LP transpression in the Neoproterozoic Seridó Belt (Borborema Province, Brazil): constraints from U\Pb (SHRIMP) geochronology and implications for the connections between NE Brazil and West Africa. Gondwana Research 23, 701– 714. (doi:10.1016/j.gr.2012.05.005)

Arthaud, M.H., Caby, R., Fuck, R.A., Dantas, E.L., Parente, C.V., 2008. Geology of the northern Borborema Province, NE Brazil and its correlation with Nigeria, NW Africa. In: Pankhurst, R.J., Trouw, R.A.J., Brito Neves, B.B., de Wit, M.J. (Eds.), West Gondwana: Pre-Cenozoic Correlation across the South Atlantic Region. Geological Society of London 294, 49–67. (doi.org/10.1144/SP294.4)

Attoh, K., Nude, P.M., 2008. Tectonic significance of carbonatite and ultrahigh-pressure rocks in the Pan-African Dahomeyide suture zone, southeastern Ghana. In: Ennih, N., Leiégeois, J.-P. (Eds.), the Boundaries of the West African Craton. Geological Society of London. Spec. Publ. 297, 217–231. (doi.10.1144/SP297.10)

Bau, M., 1996. Controls on the fractionation of isovalent trace elements in magmatic and aqueous systems: evidence from Y/Ho, Zr/Hf, and lanthanide tetrad effect. Contrib. Mineral Petrol. 123, 23–333. (doi.org/10.1007/s004100050)

Bau, M., Dulski, P., 1999. Comparing yttrium and rare earths in hydrothermal fluids from the Mid-Atlantic Ridge: implications for Y and REE behaviour during near-vent mixing and for the Y/Ho ratio of Proterozoic seawater. Chem. Geol. 155, 77-90. (doi.org/10.1016/S0009-2541(98)00142-9)

Blichert-Toft, J., Albarède, F., 1997. The Lu-Hf isotope geochemistry of chondrites and the evolution of the mantle-crust system. Earth Planet. Sci. Lett. 148, 243-258. (doi.org/10.1016/S0012-821X(97)00040-X)

Brito Neves, B.B., Dos Santos, E.J., Van Schmus, W.R., 2000. Tectonic history of the Borborema Province, Northeastern Brazil, in: Cordani, U., Milani, E. J., Thomaz Filho, A., Campos, D. A., (Eds.), Tectonic evolution of South America, 31st International Geological Congress, Rio de Janeiro, Brazil, pp. 151–182.

Brito Neves, B.B., 2011. The Paleoproterozoic in the South-American continent: Diversity in the geologic time. Journal of South American Earth Sciences 32, 270–286. (doi.10.1016/j.jsames.2011.02.004).

Brito Neves, B.B., Fuck, R. A., 2014. The basement of the South American platform: Half Laurentian (N-NW) + half Gondwanan (E-SE) domains. Precambrian Research, 244. 75-86. (doi: 10.1016/j.precamres.2013.09.020)

Brown, M., 2009. Metamorphic patterns in orogenic systems and the geological record. Geological Society, London, Special Publications 318, 37-74. (doi.10.1144/SP318.2)

Brown, M., 2014. The contribution of metamorphic petrology to understanding lithosphere evolution and geodynamics. Geoscience Frontiers 5, 553-569. (doi.org/10.1016/j.gsf.2014.02.005)

Bucher, K., Frey, M., 2002. Petrogenesis of metamorphic rocks, seventh ed. Springer, Berlim. (doi.10.1007/978-3-662-04914-3)

Bühn, B.M., Pimentel, M, M., Matteini, M., Dantas, E.L., 2009. High spatial resolution analyses of Pb and U isotopes for geochronology by laser ablation multi-collector inductively coupled plasma mass spectrometry LA-MC-ICP-MS. Anais da Academia Brasileira de Ciências 81, 1-16. (doi.org/10.1590/S0001-37652009000100011)

Burbank, D.W., 2002. Rates of erosion and their implications for exhumation. Mineralogical Magazine 66, 25-52. (doi.org/10.1180/00264610266100140)

Caddick, M.J., Konopasek, J., Thompson, A.B., 2010. Preservation of garnet growth zoning and the duration of prograde metamorphism. Journal of Petrology 51, 2327-2347. (doi.org/10.1093/petrology/egq059)

Carswell, D. A., 1990. Eclogite Facies Rocks. Blackie and Son Ltd., Glasgow, London.

Chauvel, C., Blichert-Toft, J., 2001. A hafnium isotope and trace element perspective on melting of the depleted mantle. Earth Planet. Sci. Lett. 190, 137– 151. (doi.org/10.1016/S0012-821X(01)00379-X)

Chu, N.C., Taylor, R.N., Chavagnac, V., Nesbitt, R.W., Boella, R.M., Milton, J.A., German, C.R., Bayon, G., Burton, K., 2002. Hf isotope ratio analysis using multicollector inductively coupled plasma mass spectrometry: an evaluation of isobaric interference corrections. J. Anal. Atom. Spectrom. 17, 1567-1574. (doi.10.1039/b206707b)

Corfu, F., Hanchar, J.M., Hoskin, P.O.W., Kinny, P., 2003. Atlas of zircon textures, in Zircon, Hanchar, J. M. and Hoskin, P.W.O. (Eds.), Reviews in Mineralogy & Geochemistry. Mineralogical Society of America and Geochemical Society 53, 469–500. (doi.org/10.2113/0530469)

Corsini, M., Vauchez, A., Archanjo, C., Jardim de Sá, E. F., 1991. Strain transfer at continental scale from a transcurrent shear zone to a transpressional fold belt: the Patos-Seridó system, northeastern Brazil. Geology 19, 586-589.

Dantas, E.L., Negrão, M.M., Buhn, B., 2008. 2.3 Ga continental crust generation in the Rio Grande do Norte terrane, NE-Brazil, in: 6th South American Symposium on Isotope Geology, Abstract Volume, 40.

Dantas, E. L., Van Schmus W.R., Hackspacher P. C., Fetter A. H., Neves B. B. B., Cordani U.G., Nutman A.P., Williams S., 2004. The 3.4-3.5 São José do Campestre Massif, NE Brazil: remnants of the oldest crust in South America. Precambrian Research 130, 113-137. (doi.10.1016/j.precamres.2003.11.002).

DePaolo, D. J., 1981. A neodymium and strontium isotopic study of the Mesozoic calc-alkaline granitic batholithys of the Sierra Nevada and Peninsular Ranges, California. Journal of Geophysical Research 86, 10470-10488. (doi.org/10.1029/JB086iB11p10470)

Ferreira, A.C.D., Ferreira Filho, C.F., Dantas, E.L., Souza, V.S., 2019. Paleoproterozoic Mafic-Ultramafic Magmatism in the Northern Borborema Province, NE Brazil: Tectonic Setting and Potential for Deposits. The Journal of Geology, 127. 483-504. (doi.10.1086/704256)

Fetter, A.H., Santos, T.J.S., Van Schmus, W.R., Hackspacher, P.C., Brito Neves, B.B., Arthaud, M.H., Nogueira Neto, J.A., Wernick, E., 2003. Evidence for Neoproterozoic continental arc magmatism in the Santa Quitéria Batholith of Ceará State, NW Borborema Province, NE Brazil: implications for the assembly of West Gondwana. Gondwana Research 6, 265–273. (doi.org/10.1016/S1342-937X(05)70975-8)

François, C., Debaille, V., Paquette, J-L., Baudet, D., Javaux, L.J., 2018. The earliest evidence for modern-style plate tectonics recorded by HP–LT metamorphism in the Paleoproterozoic of the Democratic Republic of the Congo. Scientific Reports 8, Article number: 15452. (doi.org/10.1038/s41598-018-33823-yDO)

Galindo, A. C. Petrologia dos granitoides brasilianos da região de Caraúbas e Umarizal, oeste do Rio Grande do Norte. Natal, 1993. 370p. Tese (Doutorado) - Centro de Geociências, Universidade Federal do Pará.

Ganade de Araújo, C. E., Rubatto, D., Hermann, J., Cordani, U. G., Caby, R., Basei, M. A., 2014. Ediacaran 2,500-km-long synchronous deep continental subduction in the West Gondwana Orogen. Nature Communications 5, 5198. (doi: 10.1038/ncomms6198).

Garcia, M.G.M., Santos, T.J.S., Amaral, W.S., 2014. Provenance and tectonic setting of Neoproterozoic supracrustal rocks from the Ceará Central Domain, Borborema Province (NE Brazil): constraints from geochemistry and detrital zircon ages. International Geology Review 56, 481–500. (doi.org/10.1080/00206814.2013.875489)

Gerdes, A., Zeh, A., 2009. Zircon formation versus zircon alteration - new insights from combined U-Pb and Lu-Hf in-situ LA-ICP-MS analyses, and consequences for the interpretation of Archean zircon from the Central Zone of the Limpopo Belt. Chem. Geol. 261, 230-243. (doi.org/10.1016/j.chemgeo.2008.03.005)

Gilotti, J. A., 2013. The realm of ultrahigh-pressure metamorphism. Elements 9, 255-260. (doi.10.2113/gselements.9.4.255

Gioia, S.M.C. L. and Pimentel, M.M., 2000. The Sm-Nd isotopic method in the Geochronology Laboratory of the University of Brasília. Anais Academia Brasileira de Ciências 72, 219-245. (doi.org/10.1590/S0001-37652000000200009)

Gordon, S.M., Whitney, D. L., Teyssier, C., Fossen, H., 2013. U–Pb dates and trace-element geochemistry of zircon from migmatite, Western Gneiss Region, Norway: Significance for history of partial melting in continental subduction. Lithos 170-171, 35-53. (doi.org/10.1016/j.lithos.2013.02.003)

Green, T. H., 1995. Significance of Nb/Ta as an indicator of geochemical processes in the crust-mantle system. Chemical Geology 20, 347-359. (doi.org/10.1016/0009-2541(94)00145-X)

Hawkesworth, C.J., and Kemp, A.I.S., 2006. Using hafnium and oxygen isotopes in zircons to unravel the record of crustal evolution. Chemical Geology 226, 144-162. (doi.org/10.1016/j.chemgeo.2005.09.018)

Hawkesworth, C.J., Dhuime, B. Pietranik., A.B. Cawood, P.A., Kemp A.I.S., Storey, C.D., 2010. The generation and evolution of the continental crust: Journal of the Geological Society 167, 229–248. (doi:10.1144/0016-76492009-072)

Hollanda, M.H.B.M., Archanjo, C.J., Souza, L.C., Dunyi, L., Armstrong, L., 2011. Long-lived Paleoproterozoic granitic magmatism in the Seridó-Jaguaribe domain, Borborema Province-NE Brazil. Journal of South American Earth Sciences 32, 287-300. (10.1016/j.jsames.2011.02.008)

Hollanda, M.H.B.M., Archanjo, C.J., Bautista, J.R., Souza, L.C., 2015. Detrital zircon ages and Nd isotope compositions of the Seridó and Lavras da Mangabeira basins (Borborema Province, NE Brazil): Evidence for exhumation and recycling associated with a major shift in sedimentary provenance. Precambrian Research 258, 186–207. (10.1016/j.precamres.2014.12.009)

Huang, J.X., Gréau, Y., Griffin, W.L., O'Reilly, S.Y., Pearson, N.J., 2012. Multi-stage origin of Roberts Victor eclogites: Progressive metasomatism and its isotopic effects. Lithos 142, 161-181. (doi.org/10.1016/j.lithos.2012.03.002)

Imayama, T., Oh, C-W., Baltybaev, S.K., Park, C-S., Yi, K., Jung, H., 2017. Paleoproterozoic high-pressure metamorphic history of the Salma eclogite on the Kola Peninsula, Russia. Lithosphere 2017, 855-873. (doi.org/10.1130/L657.1).

Irvine, T. N., Baragar, W. R. A., 1971. A guide to the chemical classification of the common volcanic rocks. Canadian Journal of Earth Sciences 8, 523-548. (doi.org/10.1139/e71-055)

Jackson, S.E., Pearson, N. J., Griffin, W.L., Belousova, E.A., 2004. The application of laser ablation-inductively coupled plasma-mass spectrometry to in situ U-Pb zircon geochronology. Chemical Geology 211, 47-69. (doi.org/10.1016/j.chemgeo.2004.06.017)

Jardim de Sá, E.F., 1994. A Faixa Seridó (Província Borborema, Ne Brasil) e o seu Significado Geodinâmico na Cadeia Brasiliana/Pan-Africana. Tese de Doutorado, Universidade De Brasília, 803pp.

Jochum, K.P., Seufert, H.M., Spettel, B., Palme, H., 1986. The solar system abundances of Nb, Ta and Y and the relative abundances of refractory lithophile

elements in differentiated planetary bodies. Geochim. Cosmochim. Acta 50, 1173-1184. (doi.org/10.1016/0016-7037(86)90400-X)

Kiseeva, E. S., Kamenetsky, V. S., Yaxley, G. M., Shee, S. R., 2016. Mantle melting versus mantle metasomatism – “the chicken or the egg” dilemma Chemical Geology 455, 220-130. (10.1016/j.chemgeo.2016.10.026)

Kohn, M., Corrie, S., Markley, C., 2015. The fall and rise of metamorphic zircon. American Mineralogist 100, 897–908. (doi.org/10.2138/am-2015-5064)

Lages, G.A., Dantas, E.L., 2016. Floresta and Bodocó Mafic–Ultramafic Complexes, western Borborema Province, Brazil: Geochemical and isotope constraints for evolution of a Neoproterozoic arc environment and retro-eclogitic hosted Ti-mineralization. Precambrian Research 280, 95-119. (doi.org/10.1016/j.precamres.2016.04.017)

Lanari, P., Engi, M., 2017. Local bulk composition effects on mineral assemblages, in: Kohn, M.J., Lanari, P., Engi, M. (Eds.) Petrochronology. Reviews in Mineralogy and Geochemistry 83, 55-102. (doi.org/10.2138/rmg.2017.83.3)

Lanari, P., Giuntoli, F., Loury, C., Burn, M., Engi, M., 2017. An inverse modeling approach to obtain P-T conditions of metamorphic stages involving garnet growth and resorption. European Journal of Mineralogy 29, 181-199. (doi.10.1127/ejm/2017/0029-2597)

Lanari, P., Riel, N., Guillot, S., Vidal, O., Schwartz, S., Pêcher, A., Hattori, K.H., 2013. Deciphering high-pressure metamorphism in collisional context using microprobe mapping methods: Application to the Stak eclogitic massif (northwest Himalaya). Geology 41, 111–114. (doi:10.1130/g33523.1)

Li, X., Zhang, L., Wei, C., Slabunov, A. I., 2015. Metamorphic PT path and zircon U–Pb dating of Archean eclogite association in Gridino complex, Belomorian province, Russia. Precambrian Research 268, 74-96. (doi.org/10.1016/j.precamres.2015.07.009)

Liu, F., Zhang, L., Li, X., Slabunov, A. I., Wei, C., Bader, T., 2017. The metamorphic evolution of Paleoproterozoic eclogites in Kuru-Vaara, northern Belomorian Province, Russia: Constraints from P-T pseudosections and zircon dating. Precambrian Research 298, 31-47. (doi.org/10.1016/j.precamres.2016.11.011)

Loose, D., Schenk, V., 2018. 2.09 Ga old eclogites in the Eburnian-Transamazonian orogen of southern Cameroon: Significance for Palaeoproterozoic plate tectonics. Precambrian Research, 304, 1-11. (doi.org/10.1016/j.precamres.2017.10.018)

Loury, C., Rolland, Y., Cenki-Tok, B., Lanari, P., Guillot, S., 2016. Late Paleozoic evolution of the South Tien Shan: Insights from P – T estimates and allanite geochronology on retrogressed eclogites (Chatkal range, Kyrgyzstan). Journal of Geodynamics 96, 62-80. (doi.org/10.1016/j.jog.2015.06.005)

Ludwig, K. R., 2008. User's Manual for Isoplot 3.0. A geochronological Toolkit for Microsoft Excel. Berkeley Geochronology Center, 4(4), 76.

Magini, C., Hackspacher, C., 2008. Geoquímica e ambiência tectônica do arco magmático de Pereiro, região NE da Província Borborema. Revista Brasileira de Geociências 38, 336-355.

Melo, O. O., Beurlen, H., 2004. Petrology of the Red Rod Fe-Ti Ore Body and its Metamafic Host rocks, Custódia-PE, Northeast Brazil. Revista Brasileira de Geociências 34, 521-530.

McClelland, W.C., Lapen, T.J., 2013. Linking Time to the Pressure–Temperature Path for Ultrahigh-Pressure Rocks. Elements 9, 273-279. (doi. 10.2113/gselements.9.4.273).

Meschede, M., 1986. A method of discrimination between different types of mid-ocean ridge basalts and continental tholeiites with the Nb-Zr-Y diagram, Chem. Geol. 56, 207-218. (doi.org/10.1016/0009-2541(86)90004-5)

Morel, M.L.A., Nebel, O., Nebel-Jacobsen, Y.L., Miller, J.S., Vroon, P.Z., 2008. Hafnium isotope characterization of the GJ-1 zircon reference material by solution and laser-ablation MC-ICPMS. Chem. Geol. 255, 231-235. (doi.org/10.1016/j.chemgeo.2008.06.040)

Mints, M.V., Konilov, A.N., Dokukina, K.A., Kaulina, T.V., Belousova, E.A., Natapov, L.M., 10 Griffin, W.L., O'Reilly, S.Y., 2010. The Belomorian eclogite province: Unique evidence of Meso-Neoarchaean subduction and collision. Doklady Earth Sciences 434, 1311-1316. (doi.10.1134/S1028334X10100053)

Nebel, O., Nebel-Jacobsen, Y., Mezger, K., Berndt, J., 2007. Initial Hf isotope compositions in magmatic zircon from early Proterozoic rocks from the Gawler

Craton, Australia: a test for zircon model ages. Chem. Geol. 241, 23-37. (doi.org/10.1016/j.chemgeo.2007.02.008)

Oliveira, R.G., Medeiros, W.E., 2018. Deep crustal framework of the Borborema Province, NE Brazil, derived from gravity and magnetic data. Precambrian Research 315, 45-65. (doi.org/10.1016/j.precamres.2018.07.004)

Padilha, A.L., Vitorello, Í., Pádua, M.B., Fuck, R.A., 2017. Cryptic signatures of Neoproterozoic accretionary events in northeast Brazil imaged by magnetotellurics: Implications for the assembly of West Gondwana. Tectonophysics 699, 164-177. (doi.org/10.1016/j.tecto.2017.01.022)

Palin, R.M., White, R.W., 2016. Emergence of blueschist on Earth linked to secular changes in oceanic crust composition. Nature Geoscience 9, 60–64. (doi.org/10.1038/ngeo2605)

Patchett, J.P., 1983. The importance of the Lu–Hf isotopic system in studies of planetary chronology and chemical evolution. Geochim. Cosmochim. Acta 47, 81–91. (doi.org/10.1016/0016-7037(83)90092-3)

Pearce, J.A., 2008. Geochemical fingerprinting of oceanic basalts with applications to ophiolite classification and the search for Archean oceanic crust. Lithos 100, 14-48. (doi.org/10.1016/j.lithos.2007.06.016).

Pearce, J. A., Gorman, B. E., Birkett, T. C. 1975. The TiO_2 - K_2O - P_2O_5 diagram: a method of discriminating between oceanic and non- oceanic basalts. Earth Planet. Sci. Lett. 24, 419 – 426. (doi.org/10.1016/0012-821X(75)90149-1)

Plank, T., 2005. Constraints from Thorium/Lanthanum on Sediment Recycling at Subduction Zones and the Evolution of the Continents. Journal of Petrology 46, 921–944. (doi.org/10.1093/petrology/egi005).

Polat, A., 2012. Growth of Archean continental crust in oceanic island arcs. Geology 40, 383-384. (doi.org/10.1130/focus042012.1)

Polat, A., Fryer, B., Samson, I.M., Weisener, C., Appel, P.W.U., Frei, R., Windley, B.F., 2011. Geochemistry of ultramafic rocks and hornblendite veins in the Fiskenæsset layered anorthosite complex, SW Greenland: Evidence for hydrous upper mantle in the Archean. Precambrian Research 214–215, 124-153. (doi: 10.1016/j.precamres.2011.11.013)

Powell, R., Holland, T.J.B., 2008. On thermobarometry. Journal of Metamorphic Geology 26, 155-179. (doi:10.1111/j.1525-1314.2007.00756.x)

Reno, B.L., Piccoli, P.M., Brown, M., Trouw, R.A.J., 2012. In situ monazite (U-Th)-Pb ages from the Southern Brasília Belt, Brazil: constraints on the high-temperature retrograde evolution of HP granulites. Journal of Metamorphic Geology 30, 81-112. (doi.org/10.1111/j.1525-1314.2011.00957.x)

Rollinson, H., 2010. Coupled evolution of Archean continental crust and subcontinental lithospheric mantle: Geology 38, 1083–1086. (doi:10.1130/G31159.1.)

Rubatto, D., Gebauer, D., 2000. Use of cathodoluminescence for U–Pb zircon dating by ion microprobe: some examples from the Western Alps. In: Pagel M, Barbin V, Blanc P, Ohnenstetter D (eds) Cathodoluminescence in geosciences. Springer, Berlin, Heidelberg, 373–400. (doi.org/10.1007/978-3-662-04086-7_15)

Rubatto, D., Hermann, J., Buick, I.S., 2006. Temperature and bulk composition control on the growth of monazite and zircon during low-pressure anatexis (Mount Stafford, central Australia). Journal of Petrology 47, 1973–1996. (doi.10.1093/petrology/egl033)

Rubatto, D., Hermann, J., 2001. Exhumation as fast as subduction? Geology 29(1), 3-6. (doi.10.1130/0091-7613(2001)029<0003:EAFAS>2.0.CO;2)

Rudnick, R.L., Gao, S., 2003. The composition of the continental crust. In: Treatise on Geochemistry - The Crust. Rudnick, R.L., Holland, H.D. and Turekian, K.K. (Editors), Elsevier, Oxford. 1-64. (doi:10.1016/B0-08-043751-6/03016-4)

Santos, T. J. S., Amaral, W. S., Ancelmi, M. F., Pitarello, M. Z, Fuck, R. A., Dantas, E. L., 2015. U–Pb age of the coesite-bearing eclogite from NW Borborema Province, NE Brazil: Implications for western Gondwana assembly. Gondwana Research 28, 1183-1196. (doi.org/10.1016/j.gr.2014.09.013)

Santos, T.J.S., Fetter, A.H., Nogueira Neto, J.A., 2008. Comparisons between the northwestern Borborema Province, NE Brazil, and the southwestern Pharusian Dahomey Belt, SW Central Africa. In: Pankhurst, R.J., Trouw, R.A.J., Brito Neves, B.B., de Wit, M.J. (Eds.), West Gondwana: Pre-Cenozoic Correlation Across the South Atlantic Region. Geological Society, London, Special Publications 294, 101–120. (doi.org/10.1144/SP294.6)

Santos, T.J.S., Garcia, M.G.M., Amaral, W.S., Caby, R., Wernick, E., Arthaud, M.H., Dantas, E.L., Santosh, M., 2009. Relics of eclogite facies assemblages in the Ceará Central Domain, NW Borborema Province, NE Brazil: implications for the assembly of West Gondwana. Gondwana Research 15, 454–470. (doi.org/10.1016/j.gr.2009.01.003)

Scherer, E. Münker, C., Mezger, K., 2001. Calibration of the lutetium-hafnium clock. Science 293, 683-687. (doi.10.1126/science.1061372)

Shervais, J.W., 1982. Ti-V plot and the petrogenesis of modern and ophilitic lavas. Earth and Planetary Science Letters 59, 101-118.

Sizova, E., Gerya, T., Brown, M., 2014. Contrasting styles of Phanerozoic and Precambrian continental collision. Gondwana Research 25, 522-545. (doi.org/10.1016/j.gr.2012.12.011)

Souza, Z.S., Martin, H., Peucat, J.J., Jardim de Sá, E. F., Macedo, M.H.F., 2007. Calc-Alkaline Magmatism at the Archean-Proterozoic Transition: The Caicó Complex Basement (Ne Brasil). Journal of Petrology 48, 2149-2185; (doi.10.1093/petrology/egm055)

Sun, S.S., McDonough, W.F., 1989. Chemical and isotopic systematics of oceanic basalts: implications for mantle composition and processes. Geological Society, London, Special Publications 42, 313-345. (doi.org/10.1144/GSL.SP.1989.042.01.19)

Tedeschi, M., Lanari, P., Rubatto, D., Pedrosa-Soares., A., Hermann, J., Dussin, I., Pinheiro, M. A. P., Bouvier, A. S., Baumgartner, L., 2017. Reconstruction of multiple P-T-t stages from retrogressed mafic rocks: subduction versus collision in the Southern Brasília orogen (SE Brazil). Lithos 294–295, 283–303. (doi.10.1016/j.lithos.2017.09.025)

Tichomirowa, M., Whitehouse, M.J., Nasdala, L., 2005. Resorption, growth, solid state recrystallisation, and annealing of granulite facies zircon—a case study from the Central Erzgebirge, Bohemian Massif. Lithos 82:25–50 (https://doi.org/10.1016/j.lithos.2004.12.005)

Trindade, R. I. F., Dantas, E. L., Babinski, M., & Van Schmus, W. R., 1999. Short-lived granitic magmatism along shear zones: evidence from U-Pb zircon and sphene ages of Caraúbas and Tourão granites. In Actas. Cordoba: SEGEMAR.

Trouw, R.A.J., Peternel, R., Ribeiro, A., Heilbron, M., Vinagre, R., Duffles, P., Trouw, C.C., Fontainha, M., Kussama, H.H., 2013. A new interpretation for the interference zone between the southern Brasília belt and the central Ribeira belt, SE Brazil. Journal of South American Earth Sciences 48, 43-57. (doi.org/10.1016/j.jsames.2013.07.012)

Van Schmus, W.R., Oliveira, E.P, Silva Filho, A.F., Toteu, S.F., Penaye, J., Guimarães, I. P., 2008. Proterozoic links between the Borborema Province, NE Brazil, and the Central African Fold Belt. Geological Society, London, Special Publication 294, 69-99. (doi.org/10.1144/SP294.5)

Vervoort, J.D., Blichert-Toft, J., 1999. Evolution of the depleted mantle: Hf isotope evidence from juvenile rocks through time. Geochim. Cosmochim. Ac 63, 533-556. (doi.org/10.1016/S0016-7037(98)00274-9)

Waters, D., 2003. P-T path from Cpx-Hbl-Pl symplectites, www.earth.ox.ac.uk/~davewa/index.html

Wedepohl, K.H., 1995. The compositions of the continental crust. Geochim. Cosmochim. Acta 59, 1217-1232. (doi.org/10.1016/0016-7037(95)00038-2)

Weller, O.M., St-Onge, M.R., 2017. Record of modern-style plate tectonics in the Palaeoproterozoic Trans-Hudson orogeny. Nature Geoscience 10, 305-311. (doi.10.1038/NGEO2904)

White, R.W., Powell, R., Baldwin, J.A., 2008. Calculated phase equilibria involving chemical potentials to investigate the textural evolution of metamorphic rocks. Journal of Metamorphic Geology 26, 181-198. (doi.org/10.1111/j.1525-1314.2008.00764.x)

Whitney, D.L. and Evans, B.W., 2010. Abbreviations for names of rock-forming minerals. American Mineralogist 95, 185-187. (doi.10.2138/am.2010.3371)

Willbold, M., Stracke, A., 2010. Formation of enriched mantle components by recycling of upper and lower continental crust. Chemical Geology 276, 188–197. (doi.org/10.1016/j.chemgeo.2010.06.005)

Wood, D. A., 1980. The Application of Th-Hf-Ta diagram in problems of tectonomagmatic classification and to establishing the nature of crustal

contamination of basaltic lavas of the British Tertiary volcanic province. Earth planet Sci. Lett. 50, 11-30. (doi.org/10.1016/0012-821X(80)90116-8)

Yakymchuk, C., Brown, M., 2019. Divergent behaviour of Th and U during anatexis: Implications for the thermal evolution of orogenic crust. J. Metamorph. Geol. 2019 (37), 899–916. (doi.10.1111/jmg.12469)

Zhang, L., Zhang, Z., Schertl, H. P., Wei. C., 2019. HP–UHP metamorphism and tectonic evolution of orogenic belts: introduction. Geological Society, London, Special Publications 474, 1-4. (doi.org/10.1144/SP474.15)

Zeh, A., Gerdes, A., Klemd, R. And Barton Jr. J. M., 2007. Archaean to Proterozoic Crustal Evolution in the Central Zone of the Limpopo Belt (South Africa-Botswana): Constraints from Combined U-Pb and Lu-Hf Isotope Analyses of Zircon. Journal of Petrology 48, 605-1639. (doi.10.1093/petrology/egm032)

Supplementary Table 3.1. Localization of the studied samples.

Sample	UTM X	UTM Y	Rock
ADE-09	679495	9355415	Amphibolite
ADE-16	687186	9367246	Amphibolite
ADE-20	685014	9362028	Amphibolite
ADE–24A	687678	9361941	Amphibolite
ADE-24B	687678	9361941	Amphibolite
ADE-29	682062	9359773	Amphibolite
At-10	694967	9361572	Amphibolite
At-14a	683321	9360722	Amphibolite
At-16	682499	9360150	Amphibolite
At-24	687154	9358978	Amphibolite
At-26	685121	9359016	Amphibolite
At-32	683195	9351556	Amphibolite
AP-10	689429	9365786	Amphibolite
AP-17	683241	9360032	Amphibolite
ADE-10	679434	9355088	Tonalite paleosome

Supplementary Table 3.2. Whole-rock analyses of representative samples from the Campo Grande amphibolite.

Sample	ADE-09	ADE-29	AT-20	AT-10	AT-16	ADE-16	AP-10	AT-26	ADE-24A	AT-24	ADE-24B	ADE-20	AT-02	AP-14B	AP-14A	AP-17
SiO2	48,80	49,20	46,90	56,10	47,90	50,83	48,20	50,60	52,05	55,60	50,70	54,00	53,60	48,90	49,80	51,10
Al2O3	14,00	15,07	11,80	13,95	14,90	13,70	13,40	14,95	15,07	15,05	14,10	14,65	15,40	14,75	13,05	13,00
Fe2O3	13,50	14,10	20,70	15,95	17,10	15,19	16,30	14,00	11,49	10,45	12,45	12,55	10,65	12,50	14,55	18,25
MnO	0,20	0,21	0,25	0,25	0,24	0,22	0,21	0,20	0,18	0,16	0,22	0,22	0,21	0,20	0,20	0,25
MgO	7,11	6,59	4,99	4,67	5,67	5,92	7,06	6,42	5,69	5,37	6,43	6,54	5,68	8,42	4,36	4,70
CaO	10,65	10,36	9,37	7,17	9,46	10,01	11,00	10,15	11,02	11,05	11,90	11,25	9,77	11,20	7,40	8,71
Na2O	2,25	2,57	1,24	0,90	2,58	2,14	1,88	2,86	2,42	1,62	2,54	1,19	3,61	0,96	2,83	1,47
K2O	0,17	0,19	0,39	0,09	0,39	0,13	0,07	0,55	0,17	0,11	0,18	0,09	0,76	0,19	1,71	0,41
P2O5	0,14	0,14	0,25	0,21	0,19	0,20	0,23	0,13	0,15	0,08	0,16	0,06	0,06	0,11	0,45	0,34
TiO2	1,26	1,30	3,01	1,47	1,78	1,62	1,76	1,37	1,08	0,64	1,12	0,71	0,71	0,88	3,21	2,92
Cr2O3	0,04	0,05	<0.01	0,01	0,01	0,03	0,04	0,03	0,01	0,04	0,02	0,03	0,06	0,05	0,01	0,01
LOI	0,45	0,00	0,26	0,12	0,30	0,20	0,11	0,57	0,40	0,14	0,61	-0,02	1,01	1,00	2,41	0,20
TOTAL	98,60	99,79	98,65	100,96	100,54	99,80	100,28	101,87	99,75	100,33	100,46	101,28	101,53	99,17	100,11	101,41
Mg#	48,42	45,45	30,06	34,29	37,15	40,99	43,57	44,98	46,89	47,81	47,93	48,16	48,74	54,56	34,82	31,46
Sc	39,00	35,00	45,00	38,00	37,00	37,00	40,00	36,00	33,00	38,00	36,00	44,00	31,00	35,00	27,00	37,00
V	269,00	268,00	726,00	341,00	353,00	270,00	346,00	294,00	251,00	229,00	302,00	316,00	235,00	262,00	449,00	449,00
Cr	280,00	<10	<10	60,00	80,00	<10	300,00	170,00	<10	240,00	130,00	220,00	420,00	360,00	70,00	80,00
Co	83,00	56,80	113,00	116,00	91,00	55,90	60,00	70,00	66,50	88,00	70,00	81,00	46,00	76,00	41,00	68,00
Ni	102,00	89,00	71,00	65,00	94,00	64,00	117,00	104,00	124,00	47,00	120,00	65,00	176,00	105,00	43,00	62,00
Cu	28,00	94,90	329,00	128,00	155,00	102,60	61,00	85,00	61,20	107,00	45,00	149,00	85,00	10,00	127,00	461,00
Zn	101,00	7,00	124,00	78,00	120,00	6,00	181,00	107,00	5,00	61,00	96,00	76,00	105,00	92,00	134,00	147,00
Ga	17,30	16,70	21,70	16,60	22,40	15,60	16,80	19,00	17,40	16,10	17,50	14,80	20,60	17,10	24,90	22,60
Rb	1,80	4,20	12,40	4,00	11,90	2,20	0,90	13,50	2,60	2,60	2,60	2,00	8,70	5,30	47,60	23,80

Sample	ADE-09	ADE-29	AT-20	AT-10	AT-16	ADE-16	AP-10	AT-26	ADE-24A	AT-24	ADE-24B	ADE-20	AT-02	AP-14B	AP-14A	AP-17
Sr	79,40	95,10	64,80	64,50	121,00	71,40	68,40	127,50	492,80	221,00	99,70	78,50	152,50	37,20	551,00	132,50
Y	29,80	28,00	42,10	42,80	35,00	33,30	45,70	25,60	33,80	31,50	38,00	26,20	28,00	25,10	38,40	59,40
Zr	118,00	90,50	126,00	151,00	115,00	162,10	156,00	75,00	115,60	66,00	129,00	81,00	32,00	66,00	289,00	314,00
Nb	6,00	4,40	8,70	10,30	10,40	8,80	12,30	6,80	6,80	4,40	6,60	4,90	9,80	5,30	22,70	20,30
Cs	0,18	0,20	0,63	0,24	0,37	0,10	0,08	1,08	<0.1	0,11	0,17	0,17	0,34	0,44	0,79	2,16
Ba	199,50	35,00	65,70	599,00	181,00	20,00	118,00	310,00	179,00	109,50	93,90	29,10	117,00	109,00	564,00	324,00
Hf	3,10	2,60	3,40	3,90	3,20	4,20	4,20	2,00	3,30	1,90	3,30	2,30	1,30	1,70	7,20	8,20
Ta	0,80	0,30	0,80	1,00	0,80	0,60	0,80	0,50	0,60	0,50	0,70	0,90	1,10	0,40	1,40	1,40
Pb	<	0,10	<	<	<	0,50	4,00	23,00	5,30	18,00	2,00	4,00	11,00	3,00	6,00	6,00
Th	0,30	0,70	1,38	8,11	1,73	2,60	1,79	0,66	2,40	3,24	1,90	2,56	1,60	0,72	4,30	4,45
U	0,34	0,20	0,58	1,71	0,29	0,70	0,42	0,19	0,90	0,74	0,81	0,45	1,66	0,21	0,90	1,11
La	7,30	7,80	11,40	22,30	16,20	14,00	14,30	10,40	11,90	18,80	10,90	8,40	19,30	7,20	34,90	31,60
Ce	17,70	18,00	26,60	47,50	31,70	31,30	32,50	16,90	31,60	32,60	23,80	17,60	53,70	13,90	76,20	61,30
Pr	2,46	2,46	3,41	5,51	4,30	3,78	4,56	2,40	3,51	4,07	3,50	2,26	4,33	1,94	10,65	8,87
Nd	11,20	12,10	16,10	22,70	19,80	15,80	20,60	11,70	15,40	16,80	15,70	9,10	17,20	8,90	43,70	38,80
Sm	3,10	3,16	4,44	5,70	5,04	4,00	5,19	2,97	3,93	4,23	4,35	2,32	3,85	2,63	9,44	9,21
Eu	1,12	1,27	1,57	1,53	1,89	1,36	1,65	1,30	1,38	1,65	1,34	0,66	1,02	1,23	2,83	2,67
Gd	4,52	4,25	6,36	6,64	6,08	5,00	7,12	4,19	4,93	5,45	6,13	3,10	4,33	3,64	8,74	10,75
Tb	0,78	0,76	1,10	1,14	1,01	0,89	1,17	0,67	0,89	0,90	1,04	0,59	0,76	0,65	1,25	1,55
Dy	4,89	5,10	6,95	7,21	6,11	6,07	7,56	4,35	5,89	5,20	6,28	3,89	4,87	4,11	7,00	9,79
Ho	1,12	1,05	1,49	1,53	1,28	1,28	1,65	0,89	1,26	1,06	1,40	0,94	1,03	0,87	1,41	2,16
Er	3,38	3,09	4,40	4,37	3,67	3,69	4,93	2,56	3,61	3,23	4,37	3,16	2,84	2,54	3,80	6,34
Tm	0,44	0,44	0,64	0,65	0,56	0,56	0,72	0,37	0,56	0,49	0,63	0,50	0,45	0,36	0,52	0,89
Yb	3,23	2,88	4,26	3,97	3,48	3,58	4,65	2,41	3,59	3,02	3,80	2,95	2,84	2,33	3,00	5,65
Lu	0,44	0,47	0,66	0,61	0,51	0,53	0,69	0,35	0,56	0,51	0,56	0,44	0,43	0,33	0,46	0,82

Sample	ADE-09	ADE-29	AT-20	AT-10	AT-16	ADE-16	AP-10	AT-26	ADE-24A	AT-24	ADE-24B	ADE-20	AT-02	AP-14B	AP-14A	AP-17
(La/Yb)N	1,62	1,94	1,92	4,03	3,34	2,81	2,21	3,10	2,38	4,47	2,06	2,04	4,87	2,22	8,34	4,01
(La/Sm)N	1,52	1,59	1,66	2,53	2,08	2,26	1,78	2,26	1,95	2,87	1,62	2,34	3,24	1,77	2,39	2,21
(Tb/Yb)N	1,10	1,20	1,17	1,31	1,32	1,13	1,14	1,26	1,13	1,35	1,24	0,91	1,22	1,27	1,89	1,25
Eu/Eu*	0,91	1,06	0,90	0,76	1,04	0,93	0,83	1,13	0,96	1,05	0,79	0,75	0,76	1,21	0,95	0,82

Supplementary Table 3.3. U-Pb zircon data from amphibolite samples and host migmatite rock.

Sample	Zircon	^{204}Pb cps	^{206}Pb mV[1]	Th/U	^{206}Pb/^{204}Pb	1s%	^{207}Pb/^{206}Pb	1s %	^{207}Pb/^{235}U	1s %	^{206}Pb/^{238}U	1s %	Rho	^{207}Pb/^{206}Pb	2s abs	^{206}Pb/^{238}U	2s abs	^{207}Pb/^{235}U	2s abs	% U-Pb disc[4]
ADE-29	006-ZR3	14	0,0153	0,570	419605	17,66	0,22280	0,69	18,809	1,12	0,6122	0,80	0,72	3001	22	3079	39	3032	22	-2,59
	036-ZR26	15	0,0092	0,476	220317	19,98	0,21823	0,60	16,966	1,21	0,5638	0,99	0,82	2968	19	2882	46	2933	23	2,88
	040-ZR30	23	0,0091	0,842	173700	48,93	0,22274	0,73	17,665	1,63	0,5751	1,41	0,86	3001	23	2929	66	2972	31	2,39
	039-ZR29	28	0,0118	0,412	146252	31,14	0,20045	0,74	10,482	1,73	0,3792	1,52	0,88	2830	24	2073	54	2478	32	26,76
	041-ZR31	11	0,0049	0,393	139083	17,13	0,15141	0,90	5,513	1,66	0,2640	1,34	0,81	2362	31	1511	36	1903	28	36,05
	038-ZR28	12	0,0060	0,159	193114	16,02	0,17762	0,66	11,231	1,42	0,4585	1,20	0,85	2631	22	2433	48	2542	26	7,51
	037-ZR27	11	0,0094	0,435	281967	16,53	0,16540	0,59	7,503	1,25	0,3290	1,04	0,83	2512	20	1833	33	2173	22	27,00
	035-ZR25	10	0,0068	0,343	244616	17,40	0,17386	0,63	10,346	1,29	0,4316	1,07	0,82	2595	21	2313	41	2466	24	10,88
	034-ZR24	43	0,0086	0,399	28642	28,20	0,16963	0,85	8,781	1,61	0,3754	1,32	0,82	2554	28	2055	46	2316	29	19,54
	030-ZR22	11	0,0087	0,480	313935	14,56	0,15755	1,17	6,161	1,64	0,2836	1,08	0,66	2430	40	1609	31	1999	28	33,76
	029-ZR21	10	0,0190	0,537	755972	16,19	0,16169	0,85	6,823	1,47	0,3060	1,14	0,78	2473	29	1721	34	2089	26	30,42
	028-ZR20	30	0,0107	0,539	117929	31,02	0,17204	0,69	9,234	1,28	0,3892	1,01	0,79	2578	23	2119	36	2361	23	17,78
	027-ZR19	11	0,0068	0,116	195554	17,97	0,18108	0,68	11,870	1,31	0,4754	1,06	0,81	2663	22	2507	44	2594	24	5,84
	026-ZR18	12	0,0060	0,233	299866	38,55	0,17872	1,16	11,199	2,36	0,4545	2,02	0,86	2641	38	2415	81	2540	44	8,56
	025-ZR17	30	0,0117	0,259	1713420	93,24	0,15025	0,73	5,377	1,40	0,2595	1,14	0,81	2349	25	1488	30	1881	24	36,67
	024-ZR16	12	0,0094	0,243	320129	16,86	0,17904	0,85	11,087	2,13	0,4491	1,92	0,90	2644	28	2391	77	2530	39	9,56

Sample	Zircon	^{204}Pb cps	^{206}Pb mV[1]	Th/U	^{206}Pb/^{204}Pb	1s%	^{207}Pb/^{206}Pb	1s %	^{207}Pb/^{235}U	1s %	^{206}Pb/^{238}U	1s %	Rho	^{207}Pb/^{206}Pb	2s abs	^{206}Pb/^{238}U	2s abs	^{207}Pb/^{235}U	2s abs	% U-Pb disc[4]
	019-ZR14	9	0,0080	0,170	301371	13,99	0,17490	0,99	10,894	1,52	0,4517	1,10	0,72	2605	33	2403	44	2514	28	7,76
	018-ZR13	12	0,0105	0,422	354686	16,89	0,15330	0,72	5,734	1,61	0,2712	1,39	0,87	2383	24	1547	38	1936	28	35,08
	017-ZR12	7	0,0084	0,190	333691	15,85	0,16684	0,58	8,271	1,40	0,3595	1,21	0,87	2526	20	1980	41	2261	25	21,62
	015-ZR10	30	0,0071	0,303	92127	31,60	0,17226	0,62	8,259	1,64	0,3477	1,48	0,90	2580	20	1924	49	2260	30	25,43
	014-ZR9	8	0,0069	0,233	310069	29,88	0,17785	0,59	11,158	1,30	0,4550	1,10	0,85	2633	19	2417	44	2536	24	8,19
	013-ZR8	19	0,0069	0,302	211690	43,77	0,16780	0,97	8,828	1,60	0,3815	1,22	0,76	2536	32	2083	43	2320	29	17,84
	010-ZR7	8	0,0152	0,417	526604	14,71	0,17421	0,72	9,960	1,29	0,4146	1,01	0,78	2599	24	2236	38	2431	24	13,95
	009-ZR6	15	0,0096	0,382	218719	21,99	0,15570	0,74	6,842	1,40	0,3187	1,13	0,81	2409	25	1783	35	2091	25	25,99
	008-ZR5	10	0,0123	0,195	447680	12,99	0,16884	0,58	8,536	1,34	0,3667	1,15	0,86	2546	19	2014	40	2290	24	20,91
	007-ZR4	18	0,0139	0,587	348591	22,29	0,16100	0,58	7,192	1,54	0,3240	1,37	0,89	2466	20	1809	43	2136	27	26,65
	005-ZR2	11	0,0092	0,407	351330	16,28	0,16045	0,80	7,019	1,34	0,3172	1,01	0,75	2460	27	1776	31	2114	24	27,81
	004-ZR1	12	0,0146	0,587	405253	19,61	0,16400	0,70	8,013	1,22	0,3543	0,93	0,76	2497	24	1955	31	2232	22	21,71
	016-ZR11	9	0,0022	0,460	91016	16,52	0,05960	0,94	0,784	1,54	0,0955	1,17	0,76	589	40	588	13	588	14	0,22
AP-17	016-ZR11	9	0,0024	0,017	73006	16,30	0,05998	0,90	0,831	1,50	0,1005	1,14	0,76	603	39	617	13	614	14	-2,44
	015-ZR10	15	0,0109	0,387	201178	23,68	0,10430	0,56	3,986	1,17	0,2772	0,95	0,82	1702	21	1577	27	1631	19	7,34
	014-ZR9	17	0,0034	0,050	94726	18,89	0,06060	0,59	0,833	1,06	0,0997	0,79	0,75	625	25	613	9	615	10	1,99
	013-ZR8	16	0,0043	0,016	124898	17,51	0,06127	0,72	0,864	1,23	0,1023	0,92	0,75	649	31	628	11	632	12	3,20
	010-ZR7	23	0,0039	0,038	103104	33,03	0,06066	0,87	0,824	1,37	0,0985	0,99	0,72	627	37	606	11	610	13	3,46
	009-ZR6	18	0,0059	0,142	133371	23,49	0,06053	0,67	0,848	1,12	0,1016	0,82	0,73	623	29	623	10	623	10	-0,15
	008-ZR5	9	0,0024	0,018	106593	19,48	0,05925	0,77	0,807	1,30	0,0988	0,97	0,75	576	33	607	11	601	12	-5,35
	007-ZR4	8	0,0030	0,013	101356	14,06	0,05957	0,69	0,809	1,13	0,0985	0,82	0,72	588	30	606	9	602	10	-3,05
	006-ZR3	9	0,0027	0,217	101213	20,38	0,18246	0,62	12,004	1,14	0,4771	0,88	0,77	2675	21	2515	37	2605	21	6,00
	005-ZR2	10	0,0031	0,009	96965	18,34	0,05947	0,65	0,803	1,16	0,0980	0,88	0,76	584	28	602	10	599	10	-3,08
ADE-20	034-ZR24	15	0,0017	0,816	41462	23,55	0,06427	1,00	0,913	1,71	0,1031	1,34	0,78	750	42	632	16	659	17	15,72
	033-ZR23	13	0,0006	0,084	17413	17,24	0,06095	2,38	0,828	3,64	0,0985	2,73	0,75	638	101	606	31	613	33	4,99

Sample	Zircon	^{204}Pb cps	^{206}Pb mV[1]	Th/U	^{206}Pb/^{204}Pb	1s%	^{207}Pb/^{206}Pb	1s %	^{207}Pb/^{235}U	1s %	^{206}Pb/^{238}U	1s %	Rho	^{207}Pb/^{206}Pb	2s abs	^{206}Pb/^{238}U	2s abs	^{207}Pb/^{235}U	2s abs	% U-Pb disc[4]
	030-ZR22	13	0,0026	0,314	152204	57,79	0,06919	0,98	1,169	1,56	0,1226	1,16	0,74	904	40	745	16	786	17	17,58
	026-ZR18	15	0,0006	0,133	16920	23,60	0,06481	1,56	1,040	2,16	0,1164	1,44	0,67	768	65	710	19	724	22	7,62
	017-ZR13	10	0,0005	0,215	17741	15,33	0,06226	2,09	0,838	3,25	0,0976	2,46	0,76	683	88	600	28	618	30	12,10
	014-ZR9	15	0,0005	0,046	13967	20,10	0,05812	2,11	0,790	3,35	0,0985	2,57	0,77	534	91	606	30	591	30	-13,41
	010-ZR7	9	0,0003	0,008	13120	14,31	0,06278	3,03	0,791	4,35	0,0913	3,10	0,71	701	126	564	33	592	39	19,59
	009-ZR6	9	0,0006	0,031	23929	22,78	0,06182	2,31	0,731	3,72	0,0858	2,90	0,78	668	97	530	29	557	32	20,57
	006-ZR3	12	0,0004	0,015	15561	14,57	0,05879	2,68	0,804	3,85	0,0992	2,74	0,71	559	115	610	32	599	35	-9,04
	005-ZR2	13	0,0004	0,005	17373	25,00	0,05832	2,66	0,804	4,03	0,1000	3,00	0,75	542	114	614	35	599	36	-13,39
	004-ZR1	24	0,0024	0,070	15194	24,72	0,06423	0,77	1,007	1,40	0,1137	1,10	0,79	749	32	694	15	707	14	7,37
ADE-16	049-ZR36	16	0,0049	0,461	118344	20,19	0,22362	0,79	18,142	1,35	0,5884	1,04	0,76	3007	25	2983	49	2997	26	0,80
	048-ZR35	19	0,0052	0,171	91234	23,65	0,17521	0,68	9,496	1,35	0,3931	1,11	0,82	2608	23	2137	40	2387	25	18,06
	047-ZR34	17	0,0066	0,185	126434	21,30	0,17766	0,63	11,674	1,30	0,4765	1,07	0,82	2631	21	2512	44	2579	24	4,53
	046-ZR33	94	0,0074	0,163	27521	44,06	0,15707	0,64	3,495	2,09	0,1614	1,95	0,94	2424	22	964	35	1526	33	60,22
	045-ZR32	14	0,0078	0,230	252276	19,43	0,17568	0,60	10,407	1,28	0,4296	1,07	0,83	2612	20	2304	41	2472	24	11,81
	044-ZR31	13	0,0066	0,268	220465	16,95	0,17384	0,66	9,833	1,19	0,4102	0,92	0,77	2595	22	2216	34	2419	22	14,61
	040-ZR30	43	0,0095	0,290	25745	24,35	0,17434	1,43	8,458	1,91	0,3518	1,21	0,63	2600	47	1943	41	2281	34	25,25
	038-ZR28	13	0,0068	0,200	216673	16,63	0,17742	0,58	10,966	1,33	0,4482	1,14	0,86	2629	19	2387	45	2520	25	9,18
	037-ZR27	13	0,0048	0,230	156080	15,88	0,17993	0,59	12,095	1,18	0,4875	0,96	0,81	2652	20	2560	40	2612	22	3,48
	036-ZR26	27	0,0079	0,301	138840	23,85	0,17796	0,69	9,075	2,38	0,3698	2,25	0,94	2634	23	2029	78	2346	43	22,98
	035-ZR25	17	0,0073	0,240	183123	17,10	0,17816	0,53	10,885	0,99	0,4431	0,76	0,76	2636	17	2364	30	2513	18	10,30
	034-ZR24	16	0,0038	0,226	147758	28,42	0,17834	0,59	11,285	1,11	0,4589	0,87	0,78	2638	20	2435	35	2547	21	7,69
	033-ZR23	9	0,0083	0,228	303263	16,36	0,17615	0,65	11,282	1,15	0,4645	0,87	0,76	2617	22	2459	36	2547	21	6,02
	030-ZR22	11	0,0056	0,176	217145	14,59	0,17619	0,74	10,248	1,16	0,4218	0,81	0,70	2617	25	2269	31	2457	21	13,32
	029-ZR21	9	0,0062	0,213	205779	15,32	0,17904	0,68	11,600	1,19	0,4699	0,90	0,76	2644	22	2483	37	2573	22	6,09
	028-ZR20	13	0,0066	0,247	170920	21,35	0,16840	0,69	8,531	1,13	0,3674	0,81	0,72	2542	23	2017	28	2289	20	20,64

Sample	Zircon	^{204}Pb cps	^{206}Pb mV[1]	Th/U	^{206}Pb/^{204}Pb	1s%	^{207}Pb/^{206}Pb	1s %	^{207}Pb/^{235}U	1s %	^{206}Pb/^{238}U	1s %	Rho	^{207}Pb/^{206}Pb	2s abs	^{206}Pb/^{238}U	2s abs	^{207}Pb/^{235}U	2s abs	% U-Pb disc[4]
	027-ZR19	12	0,0072	0,226	237843	17,66	0,17753	0,94	11,102	1,45	0,4535	1,04	0,72	2630	31	2411	42	2532	27	8,32
	026-ZR18	10	0,0028	0,204	98345	15,58	0,17400	0,84	9,571	1,58	0,3989	1,29	0,82	2597	28	2164	47	2394	29	16,66
	025-ZR17	17	0,0063	0,150	141345	21,15	0,16520	0,52	7,679	1,08	0,3371	0,87	0,81	2510	17	1873	28	2194	19	25,37
	024-ZR16	19	0,0079	0,326	158057	19,58	0,16929	1,25	7,138	2,09	0,3058	1,64	0,78	2551	42	1720	49	2129	37	32,57
	020-ZR15	15	0,0042	0,131	90129	21,36	0,16961	0,74	9,718	1,39	0,4155	1,12	0,81	2554	25	2240	42	2408	25	12,29
	019-ZR14	11	0,0082	0,171	253890	15,54	0,17742	0,69	11,115	1,21	0,4544	0,93	0,77	2629	23	2415	37	2533	22	8,15
	018-ZR13	16	0,0059	0,244	159208	17,79	0,16947	0,69	8,834	1,68	0,3780	1,49	0,88	2552	23	2067	52	2321	30	19,02
	017-ZR12	18	0,0107	0,205	199382	21,64	0,18148	0,55	12,233	1,06	0,4889	0,83	0,78	2666	18	2566	35	2622	20	3,77
	016-ZR11	16	0,0084	0,223	270726	18,02	0,17938	0,58	11,241	1,14	0,4545	0,91	0,80	2647	19	2415	37	2543	21	8,77
	015-ZR10	9	0,0067	0,225	226244	14,71	0,17325	2,02	8,810	2,42	0,3688	1,27	0,53	2589	67	2024	44	2318	44	21,85
	014-ZR9	13	0,0069	0,261	497473	56,80	0,16715	1,01	7,621	2,35	0,3307	2,09	0,89	2529	34	1842	67	2187	42	27,19
	013-ZR8	11	0,0091	0,241	278638	14,00	0,16766	0,77	7,973	1,54	0,3448	1,28	0,83	2534	26	1910	42	2228	28	24,64
	010-ZR7	18	0,0075	0,202	146549	19,96	0,17644	1,07	10,750	1,53	0,4419	1,03	0,67	2620	35	2359	41	2502	28	9,95
	009-ZR6	16	0,0078	0,228	176781	21,29	0,17967	0,82	11,693	1,23	0,4720	0,84	0,68	2650	27	2492	35	2580	23	5,95
	008-ZR5	59	0,0072	0,230	37658	38,55	0,14385	0,81	3,886	2,43	0,1959	2,26	0,93	2274	28	1153	48	1611	39	49,28
	007-ZR4	21	0,0091	0,236	177168	22,00	0,17196	0,57	9,096	1,44	0,3836	1,27	0,88	2577	19	2093	45	2348	26	18,77
	006-ZR3	26	0,0083	0,121	122527	29,61	0,14507	0,80	4,504	1,39	0,2252	1,08	0,77	2289	28	1309	26	1732	23	42,80
	005-ZR2	17	0,0110	0,209	274098	22,98	0,17820	0,38	12,009	1,01	0,4887	0,86	0,85	2636	13	2565	36	2605	19	2,70
	004-ZR1	47	0,0070	0,272	22082	28,24	0,15512	0,48	5,930	1,21	0,2773	1,05	0,86	2403	16	1578	29	1966	21	34,35
ADE-09	048-ZR33C	19	0,0034	0,033	77960	19,47	0,11080	0,95	3,446	1,59	0,2255	1,22	0,77	1813	34	1311	29	1515	25	27,68
	045-ZR31B	69	0,0188	0,078	69397	46,60	0,12173	0,61	5,932	1,11	0,3534	0,85	0,77	1982	22	1951	29	1966	19	1,56
	040-ZR30C	10	0,0027	0,147	100904	14,63	0,17830	1,20	11,687	1,71	0,4753	1,15	0,67	2637	40	2507	48	2580	32	4,94
	039-ZR29C	9	0,0054	0,318	187983	14,11	0,18023	0,82	12,089	1,34	0,4864	1,00	0,74	2655	27	2555	42	2611	25	3,75
	038-ZR28C	13	0,0007	0,001	21140	17,23	0,05842	1,96	0,775	2,66	0,0962	1,76	0,66	546	85	592	20	583	23	-8,54
	037-ZR27C	10	0,0009	0,002	43314	25,47	0,05790	2,10	0,789	2,79	0,0988	1,81	0,65	526	91	608	21	591	25	-15,49

Sample	Zircon	^{204}Pb cps	^{206}Pb mV[1]	Th/U	^{206}Pb/^{204}Pb	1s%	^{207}Pb/^{206}Pb	1s %	^{207}Pb/^{235}U	1s %	^{206}Pb/^{238}U	1s %	Rho	^{207}Pb/^{206}Pb	2s abs	^{206}Pb/^{238}U	2s abs	^{207}Pb/^{235}U	2s abs	% U-Pb disc[4]
	035-ZR25C	6	0,0029	0,050	118219	12,28	0,12150	1,00	4,019	2,62	0,2399	2,40	0,91	1978	35	1386	60	1638	42	29,94
	034-ZR24C	15	0,0049	0,149	109520	19,07	0,16250	0,81	9,780	1,48	0,4365	1,18	0,80	2482	27	2335	46	2414	27	5,92
	030-ZR22C	10	0,0011	0,053	44865	14,73	0,09871	1,31	1,972	2,16	0,1449	1,68	0,78	1600	49	872	27	1106	29	45,47
	029-ZR21C	10	0,0037	0,133	109790	15,07	0,14317	1,17	6,330	1,91	0,3206	1,46	0,77	2266	40	1793	46	2023	33	20,88
	028-ZR20C	22	0,0019	0,162	32803	20,48	0,14149	1,34	4,369	2,04	0,2240	1,50	0,73	2246	46	1303	35	1707	34	41,98
	027-ZR19C	8	0,0030	0,323	128845	12,99	0,17757	1,23	10,947	1,70	0,4471	1,12	0,66	2630	41	2382	44	2519	31	9,43
	025-ZR17C	19	0,0011	0,032	25681	20,85	0,11581	1,86	2,523	2,71	0,1580	1,94	0,72	1892	66	945	34	1279	39	50,04
	024-ZR16C	12	0,0028	0,175	86330	15,66	0,16788	0,93	9,869	1,59	0,4263	1,24	0,78	2537	31	2289	48	2423	29	9,75
	020-ZR15C	14	0,0005	0,003	17868	15,55	0,06302	2,65	0,813	3,70	0,0935	2,56	0,69	709	111	576	28	604	33	18,67
	019-ZR14C	21	0,0017	0,292	54730	14,31	0,18234	1,24	11,655	1,74	0,4635	1,16	0,67	2674	41	2455	47	2577	32	8,20
	017-ZR12C	12	0,0007	0,001	22338	15,99	0,06118	1,95	0,811	2,80	0,0962	1,97	0,71	646	83	592	22	603	25	8,30
	016-ZR11C	12	0,0007	0,011	20221	16,29	0,09332	2,34	1,560	3,51	0,1212	2,60	0,74	1494	87	738	36	955	43	50,63
	015-ZR10C	11	0,0006	0,002	16956	16,99	0,06178	2,67	0,799	3,64	0,0938	2,45	0,67	667	112	578	27	596	33	13,27
	014-ZR9C	10	0,0025	0,310	135152	33,18	0,17468	0,80	9,606	1,62	0,3988	1,35	0,84	2603	27	2164	50	2398	30	16,88
	013-ZR8C	15	0,0031	0,023	113642	23,13	0,12098	0,81	5,021	1,42	0,3010	1,10	0,78	1971	29	1696	33	1823	24	13,93
	010-ZR7C	12	0,0021	0,292	65296	16,30	0,18438	1,00	13,038	1,75	0,5128	1,39	0,79	2693	33	2669	61	2682	33	0,89
	009-ZR6C	9	0,0057	0,062	192438	15,40	0,17092	1,26	11,078	1,68	0,4700	1,04	0,62	2567	42	2484	43	2530	31	3,23
	008-ZR5C	11	0,0007	0,013	25918	18,02	0,11900	2,42	2,700	3,67	0,1646	2,73	0,74	1941	85	982	50	1329	54	49,41
	006-ZR3C	5	0,0019	0,092	88590	11,05	0,14867	1,34	5,713	2,24	0,2787	1,75	0,78	2331	46	1585	49	1933	38	32,01
	005-ZR2C	18	0,0020	0,267	77931	12,57	0,18437	1,88	13,192	3,32	0,5189	2,71	0,82	2693	61	2695	119	2693	62	-0,07
ADE-24A	048-ZR35C	11	0,0019	0,042	56992	15,89	0,11612	0,94	3,722	1,60	0,2324	1,23	0,77	1897	34	1347	30	1576	25	28,99
	047-ZR34C	13	0,0027	0,012	99474	20,81	0,12510	0,56	6,226	1,17	0,3610	0,97	0,82	2030	20	1987	33	2008	20	2,14
	045-ZR32C	13	0,0014	0,029	34551	17,82	0,11860	1,05	4,606	1,56	0,2816	1,10	0,70	1935	37	1600	31	1750	26	17,34
	040-ZR30C	14	0,0010	0,022	27783	16,31	0,12516	1,22	5,741	2,57	0,3326	2,23	0,87	2031	43	1851	71	1938	44	8,86
	039-ZR29C	16	0,0054	0,146	180638	27,87	0,12387	0,85	6,150	1,34	0,3601	0,97	0,72	2013	30	1983	33	1997	23	1,49

Sample	Zircon	^{204}Pb cps	^{206}Pb mV[1]	Th/U	^{206}Pb/^{204}Pb	1s%	^{207}Pb/^{206}Pb	1s %	^{207}Pb/^{235}U	1s %	^{206}Pb/^{238}U	1s %	Rho	^{207}Pb/^{206}Pb	2s abs	^{206}Pb/^{238}U	2s abs	^{207}Pb/^{235}U	2s abs	% U-Pb disc[4]
	038-ZR28C	15	0,0041	0,161	120463	21,47	0,12527	0,55	5,969	1,13	0,3456	0,92	0,81	2033	20	1913	30	1971	20	5,86
	033-ZR23C	24	0,0045	0,029	89672	23,20	0,12701	0,56	6,168	1,41	0,3522	1,25	0,88	2057	20	1945	42	2000	25	5,45
	029-ZR21C	95	0,0519	0,068	62318	19,77	0,11776	0,51	5,308	1,57	0,3269	1,44	0,92	1923	18	1823	46	1870	27	5,16
	028-ZR20C	19	0,0032	0,034	120130	12,80	0,12657	0,81	5,575	1,34	0,3195	1,00	0,74	2051	28	1787	31	1912	23	12,86
	019-ZR14C	15	0,0024	0,078	72239	28,70	0,11959	1,14	5,556	2,31	0,3369	1,97	0,85	1950	41	1872	64	1909	39	4,01
	018-ZR13C	10	0,0060	0,135	150117	19,89	0,12454	0,65	6,463	1,46	0,3764	1,26	0,86	2022	23	2059	44	2041	26	-1,83
	014-ZR9C	11	0,0018	0,015	231734	57,25	0,12435	0,78	6,244	1,32	0,3642	1,00	0,76	2019	28	2002	34	2011	23	0,87
	010-ZR7C	22	0,0019	0,051	48613	20,00	0,12235	1,09	5,688	1,77	0,3371	1,35	0,76	1991	39	1873	44	1930	30	5,92
	009-ZR6C	50	0,0286	0,033	76288	31,27	0,12056	0,44	5,227	0,92	0,3144	0,72	0,78	1964	16	1763	22	1857	16	10,28
	008-ZR5C	103	0,1327	0,025	101461	12,90	0,11396	0,44	4,745	0,76	0,3020	0,50	0,66	1863	16	1701	15	1775	13	8,71
	007-ZR4C	14	0,0039	0,176	85487	19,80	0,12125	0,88	5,485	2,12	0,3280	1,89	0,89	1975	31	1829	60	1898	36	7,38
	006-ZR3C	106	0,0439	0,104	27987	4,62	0,11892	0,55	5,304	0,86	0,3235	0,54	0,63	1940	20	1807	17	1870	15	6,87
	004-ZR1C	71	0,0245	0,060	92294	58,40	0,12027	1,06	5,537	1,41	0,3338	0,85	0,60	1960	38	1857	27	1906	24	5,27
	011-ZR6C	13	0,0016	0,052	53188	16,02	0,12033	0,96	5,792	1,46	0,3491	1,03	0,71	1961	34	1930	34	1945	25	1,58
	006-ZR3C	6	0,0031	0,004	138851	9,54	0,12490	0,57	6,237	0,94	0,3621	0,65	0,69	2027	20	1992	22	2010	16	1,73
	005-ZR2C	16	0,0022	0,012	61171	19,14	0,12439	0,85	5,899	1,37	0,3439	1,01	0,74	2020	30	1905	33	1961	24	5,68
ADE-10 (host migmatite gneiss)	048-ZR35	44	0,0264	0,224	692032	60,60	0,21261	1,51	15,619	2,26	0,5328	1,64	0,72	2926	49	2753	73	2854	43	5,89
	047-ZR34	37	0,0094	0,540	289747	18,72	0,21204	0,51	17,400	1,18	0,5951	1,00	0,85	2921	16	3010	48	2957	23	-3,04
	046-ZR33	19	0,0212	0,578	501395	21,91	0,21295	0,44	17,150	1,00	0,5841	0,82	0,82	2928	14	2965	39	2943	19	-1,27
	045-ZR32	16	0,0108	0,583	336071	17,69	0,21339	0,46	16,715	1,11	0,5681	0,94	0,85	2931	15	2900	44	2919	21	1,08
	044-ZR31	134	0,0439	0,125	157120	47,26	0,20965	0,53	16,073	1,13	0,5560	0,92	0,82	2903	17	2850	42	2881	21	1,82
	043-ZR30	89	0,0109	0,258	77210	36,81	0,19035	0,79	10,841	1,86	0,4130	1,64	0,88	2745	26	2229	62	2510	34	18,81
	042-ZR29	149	0,0232	0,415	56331	31,00	0,20984	0,68	16,270	1,37	0,5623	1,14	0,83	2904	22	2876	53	2893	26	0,97
	039-ZR28	88	0,0418	0,303	79718	46,65	0,21023	1,08	16,230	2,10	0,5599	1,76	0,84	2907	35	2866	81	2890	40	1,41
	038-ZR27	12	0,0124	0,238	456441	15,09	0,20944	0,74	14,764	1,85	0,5112	1,66	0,89	2901	24	2662	72	2800	35	8,25
	037-ZR26	56	0,0364	0,174	122112	53,18	0,21831	1,28	16,445	2,14	0,5463	1,67	0,78	2968	41	2810	76	2903	40	5,34

Sample	Zircon	^{204}Pb cps	^{206}Pb mV[1]	Th/U	^{206}Pb/^{204}Pb	1s%	^{207}Pb/^{206}Pb	1s %	^{207}Pb/^{235}U	1s %	^{206}Pb/^{238}U	1s %	Rho	^{207}Pb/^{206}Pb	2s abs	^{206}Pb/^{238}U	2s abs	^{207}Pb/^{235}U	2s abs	% U-Pb disc[4]
	036-ZR25	82	0,0253	0,306	152044	41,54	0,21025	1,09	14,888	2,10	0,5135	1,75	0,84	2908	35	2672	77	2808	40	8,11
	035-ZR24	68	0,0441	0,172	196193	55,07	0,20127	0,57	13,374	1,44	0,4819	1,27	0,88	2837	19	2536	53	2706	27	10,61
	034-ZR23	255	0,0549	0,322	18639	14,93	0,20515	0,91	14,142	1,47	0,4999	1,10	0,75	2868	29	2614	47	2759	28	8,86
	031-ZR22	14	0,0078	0,394	316641	15,72	0,20519	0,81	13,617	1,44	0,4813	1,13	0,79	2868	26	2533	47	2723	27	11,68
	028-ZR20	14	0,0125	0,557	409625	15,84	0,21154	0,46	17,377	1,02	0,5957	0,83	0,81	2917	15	3013	40	2956	20	-3,27
	026-ZR18	173	0,0390	0,182	16561	6,91	0,19486	0,88	10,548	1,66	0,3926	1,35	0,82	2784	29	2135	49	2484	30	23,31
	025-ZR17	165	0,0221	0,228	9198	9,11	0,18758	0,96	8,824	3,35	0,3411	3,19	0,95	2721	31	1892	104	2320	60	30,46
	023-ZR15	92	0,0617	0,151	390068	65,19	0,21264	0,49	16,573	1,16	0,5652	0,98	0,85	2926	16	2888	46	2910	22	1,29
	022-ZR14	58	0,0286	0,337	44218	14,37	0,21246	0,57	15,376	2,40	0,5248	2,30	0,96	2924	19	2720	102	2839	45	7,00
	019-ZR13	178	0,0089	0,515	369945	51,99	0,21232	1,06	15,835	1,47	0,5409	0,94	0,64	2923	34	2787	43	2867	28	4,66
	018-ZR12	541	0,0369	0,307	69758	73,55	0,21023	0,91	16,300	2,57	0,5623	2,38	0,92	2907	29	2876	110	2895	49	1,08
	016-ZR10	8	0,0167	0,360	658708	14,80	0,21120	0,40	16,680	0,98	0,5727	0,82	0,83	2915	13	2919	38	2917	19	-0,15
	015-ZR9	227	0,0476	0,343	61045	75,09	0,20462	1,24	14,781	1,95	0,5239	1,45	0,75	2863	40	2715	64	2801	37	5,17
	014-ZR8	24	0,0222	0,283	678856	37,25	0,20929	0,32	16,549	0,93	0,5734	0,79	0,85	2900	10	2922	37	2909	18	-0,76
	013-ZR7	159	0,0238	0,243	53197	69,31	0,20323	1,28	10,886	2,78	0,3885	2,44	0,88	2852	41	2116	88	2513	51	25,83

Data report template (with modifications) from http://www.plasmage.org/recommendations

[1] Convertion factor from mV to CPS is 62500000

[2] concentration uncertainty c.20%

[3] data not corrected for common-Pb

[4] not corrected for common-Pb

[5] Discordance calculated as (1-(^{206}Pb/^{238}U age/^{207}Pb/^{206}Pb age))*100

Decay constants of Jaffey et al 1971 used

Supplementary Table 3.4. LA-MC-ICPMS Lu-Hf isotopes from the Campo Grande amphibolite.

			CHUR	DM	Sample (present-day ratios)				Sample (initial ratios)			Crust Model Ages (Ga)		TDM (Hf)
Sample	**Zircon**	**U-Pb age (Ma)**	**176Hf/177Hf (t)**	**176Hf/177Hf(t)**	**176Hf/177Hf**	**±2SE**	**176Lu/177Hf**	**±2SE**	**176Hf/177Hf(t)**	**eHf (t)**	**±2SE**	**Mafic**	**Felsic**	**(Ga)**
ADE-16	ZR29	593	0,282411	0,282818	0,281814	0,000025	0,000763	0,000026	0,281806	-21,43	1,61	3,73	2,44	1,98
	ZR36	3007	0,280845	0,281009	0,281057	0,000029	0,001014	0,000005	0,280998	5,47	0,07	3,04	3,03	3,02
ADE-29	ZR9	2633	0,281092	0,281295	0,281221	0,000344	0,000433	0,000019	0,281199	3,81	0,20	2,94	2,81	2,76
	ZR11	588	0,282414	0,282822	0,282023	0,000030	0,000742	0,000020	0,282014	-14,16	0,70	3,10	2,07	1,70
	ZR30	3001	0,280849	0,281014	0,281310	0,000029	0,000523	0,000040	0,281280	15,35	1,29	2,15	2,50	2,65
ADE-20	ZR3	610	0,282400	0,282806	0,282393	0,001102	0,000012	0,000002	0,282392	-0,27	0,07	1,91	1,37	1,17
	ZR9	606	0,282403	0,282809	0,282098	0,000105	0,000006	0,000001	0,282098	-10,78	1,82	2,82	1,91	1,57
	ZR18	710	0,282337	0,282732	0,282277	0,000088	0,000021	0,000002	0,282277	-2,12	0,21	2,14	1,55	1,33
ADE-09	ZR2C	2693	0,281052	0,281249	0,281263	0,000077	0,000447	0,000014	0,281240	6,67	0,37	2,72	2,71	2,71
	ZR7C	2693	0,281052	0,281249	0,281708	0,000151	0,000466	0,000014	0,281684	22,47	0,97	1,29	1,88	2,11
	ZR29C	2655	0,281078	0,281278	0,281922	0,000224	0,000339	0,000005	0,281905	29,44	0,72	0,62	1,48	1,82
	ZR10C	578	0,282420	0,282829	0,282385	0,000022	0,000018	0,000000	0,282385	-1,25	0,08	1,97	1,40	1,18
	ZR12C	592	0,282412	0,282819	0,282433	0,000110	0,000025	0,000001	0,282433	0,74	0,07	1,81	1,31	1,12
	ZR14C	2674	0,281065	0,281264	0,281389	0,000059	0,000523	0,000021	0,281362	10,58	0,60	2,36	2,49	2,54
	ZR15C	576	0,282422	0,282830	0,282478	0,000043	0,000016	0,000001	0,282478	1,98	0,27	1,69	1,23	1,06
AP-17	ZR2	602	0,282405	0,282811	0,280583	0,001610	0,000053	0,000006	0,280583	-64,54	9,42	7,27	4,59	3,56
	ZR3	2675	0,281064	0,281263	0,281960	0,000484	0,000652	0,000023	0,281926	30,67	1,39	0,52	1,43	1,78
	ZR4	606	0,282403	0,282809	0,281586	0,000241	0,000042	0,000002	0,281586	-28,93	1,66	4,37	2,83	2,25
	ZR6	623	0,282392	0,282796	0,280534	0,000969	0,000182	0,000009	0,280531	-65,88	4,61	7,40	4,68	3,64

Supplementary Table 3.5. Sm-Nd isotopic data for the Campo Grande amphibolite and host migmatite gneiss.

Sample	Rock	Sm (ppm)	Nd (ppm)	147Sm/144Nd	143Nd/144Nd ± 2SE	εNd (0)	εNd (t)	TDM (Ga)
ADE-29	Amph (G2)	3.57	12.7	0.17	0.512416+/-13	-4.32	4.63	2.17
ADE-09		3.30	12.74	0.1566	0.512121+/-3	-10.09	3.32	2.46
ADE-20		2.23	9.5	0.1419	0.512116+/-5	-10.18	8.17	1.95
ADE-24B		4.24	16.43	0.156	0.512077+/-2	-10.95	2.66	2.55
AT-16		5.33	20.7	0.1558	0.512099+/-12	-10.51	3.17	2.48
AT-10		5.9	24.52	0.1454	0.511922+/-19	-13.97	3.18	2.5
AT-32		3.98	14.95	0.1609	0.512125+/-15	-10,00	1.97	2.65
AP-17		9.59	39.15	0.148	0.512104+/-3	-10.42	5.88	2.17
AP-10	Amph (G1)	5.31	19.65	0.1634	0.512011+/-4	-12.23	-1.12	3.19
AT-26		3.59	12.53	0.1734	0.512187+/-12	-8.8	-1.03	3.34
AT-14		4.44	19.77	0.1358	0.511189+/-4	-28.27	-7.97	3.69
ADE-16		4.33	16.94	0.1545	0.511773+/-8	-16.87	-2.81	3.33
ADE–24A		4.5	16.93	0.1607	0.511780+/-20	-16.74	-4.76	3.75
ADE-10	Host	5.55	33.2	0.1011	0.510677+/-8	-38.25	-2.58	3.22

4. ARTIGO CIENTÍFICO 3: MULTIPLE MIGMATITE GENERATION AND MAGMA DIFFERENTIATION AS A CRUCIAL FACTOR OF ARCHEAN TO PROTEROZOIC CONTINENTAL EVOLUTION IN THE BORBOREMA PROVINCE, NORTHEAST BRAZIL

Alanielson da Câmara Dantas Ferreira, Elton Luiz Dantas, Reinhardt A. Fuck, Ingrid Moerschberger Nedel, Wolf Uwe Reimold

Instituto de Geociências, Universidade de Brasília (UnB), 70910-900 Brasília-DF, Brazil

4.1 Abstract

Multiple partial melting events are documented in Archean to Neoproterozoic migmatites in granitoids of the Borborema Province of NE Brazil. These events preserved the isotopic and geochemical signature of the protolith despite intense crustal reworking documented by a progressive increase of LILE elements in the younger phases related to differentiation and growth of continental crust in this region. The Campo Grande migmatites underwent complex history. The 2.9 Ga tonalite and 2.65 Ga granodiorite paleosomes are enriched in restite minerals in relation to the more fertile bands of 1.95 Ga concordant granitic leucosomes. Biotite-enriched layers and biotite schlieren are observed as small irregular leucosome patches and characterize the melanosome phase. The ca. 568 Ma injected alkali-feldspar granitic leucosomes are less voluminous than the other migmatite components and occur as alkaline granite and pegmatite. Fractional crystallization of sodic-plagioclase, K-feldspar, and accessory minerals (zircon, apatite and titanite) played a significant role as seen in the geochemical patterns for leucosomes that are consistent with melts having been produced in a continental magmatic arc environment. Primary biotite from the tonalite paleosome follows a magnesium-enrichment trend with orogenic calc-alkaline signature, whereas biotite in the granitic leucosome shows an iron-enrichment trend with peraluminous signature. Pb-Hf-Nd isotopes reveal 2.9 Ga and 2.65 Ga juvenile and reworked calc-alkaline magmatic protolith sources for this migmatite. These precursors were emplaced into a Paleoarchean continental crust formed at

ca. 3.25 Ga. The 1.95 Ga zircon rims and grains from the concordant granitic leucosomes yield a wide range of negative and positive $\varepsilon Hf_{(t)}$ values, with $T_{DM(Hf)}$ between 1.7 and 2.91 Ga, and negative $\varepsilon Nd_{(t)}$ with $T_{DM(Nd)}$ between 2.41 and 2.59 Ga. Neoproterozoic zircon from the injected alkaline leucosomes has negative $\varepsilon Hf_{(t)}$ values with younger $T_{DM(Hf)}$ between 1.41 and 2.56 Ga, and negative $\varepsilon Nd_{(t)}$ plot with comparatively younger $T_{DM(Nd)}$ of 2.1 and 2.3 Ga. This suggests increasing of crustal reworking and recycling in the Borborema Province during the Late Archean to Early Proterozoic. Our results support that anatexis involved melting aided by water fluxing of intermediate to felsic rocks, through the breakdown of biotite (630º-680ºC) at relatively low pressures (4-6 kbar) in the mid-crust. These partial melting processes could have been the result of magmatic heating and release of H_2O-rich fluid due to Paleo- and Neoproterozoic post-collisional magmatism. Multiple stages of generation of migmatite in continental crust related to an Archean to Neoproterozoic magmatic arc attests anatexis to have been a crucial factor in the complex evolution of migmatite terranes.

Keywords: Archean protolith; Paleo- and Neoproterozoic anatexis; continental crust differentiation; Borborema Province.

4.2 Introduction

The formation and evolution of Archean continental crust in high-grade metamorphic terranes are significant scientific issues in geological research. Migmatites are the products of an integral process of deformation-driven melt segregation in deep levels of the continental crust during partial melting of mafic to intermediate protoliths (e.g., Sawyer, 2008; Sawyer et al., 2011). Melt extraction or segregation in migmatites depends on the fertile bulk-rock composition, pressure, and importantly temperature when the heat exceeds the wet solidus (e.g., Clemens, 2006; Brown, 2014). The formation of migmatites in orogenic belts or magmatic arcs affects rheological behavior, chemical differentiation, architecture, and density of the continental crust (Vanderhaeghe, 2009; Brown et al., 2011; Reichardt and Weinberg, 2012). The geochemical features of migmatite are controlled by precursor composition and structure, and reactions of partial melting that result in chemical disequilibrium between the melt,

neosome representing the fertile rock components, and residual paleosome representing the infertile components (Sawyer, 2008; Gao et al., 2016). Boudin necks, veins, dykes, and shear bands are evidence for melt extraction in migmatite complexes, observed mainly at hand specimen and outcrop scales. Thus, the study of migmatites is prerequisite for understanding the evolution and differentiation of continental crust.

Zircon U-Pb and Lu-Hf isotopic systematics may reveal crust/mantle interactions, evolution of the continental crust, and may reflect the character of precursor lithologies (e.g., Harrison et al., 2005; Liu et al., 2017). The architecture of continental crust is important to understand the relationship between anatexis, melt segregation, and geochemical characteristics, such as depleted REE abundances and positive Eu anomalies of arc-related leucosomes of migmatites in magmatic arcs (e.g. Bhadra et al., 2007; Zeng et al., 2011). Most neosomes of migmatites are generated from fertile metapelite or metagreywacke sources, whereby less fertile and infertile precursors have been less studied (e.g. Carvalho el al., 2017). However, the presence of these less fertile rocks plays a major role in the distribution and segregation of melt within the more fertile layers of precursors during coaxial deformation and positively influences the development of migmatites (e.g. Ganzhorn et al., 2016; Carvalho et al., 2017). Granites generated during partial melting of the lower and mid-continental crust (Clemens et al., 2010) show high FeO + MgO contents, which indicate that the restite (garnet, cordierite, pyroxene and biotite) and melt fractions mix to some degree at the site of melting ("restite unmixing" model of White & Chappell, 1977; Sawyer, 2014).

Bounded by the Portalegre and Patos shear zones, the Campo Grande migmatite complex (Fig. 4.1) represents an important tectonic unit of the Mesoarchean to Neoproterozoic Rio Grande do Norte domain of the Borborema Province, NE Brazil. The migmatites represent a basement complex and are spatially associated with garnet-bearing amphibolite bodies of ~10 cm to 60 m extent. The high-grade metamorphic terranes in the Campo Grande domain offer an opportunity to investigate partial melting processes in mid- to lower continental crust. Numerous late Neoproterozoic granitoid plutons were emplaced in the Borborema Province (Jardim de Sá, 1994; Van Schmus et al., 2011; Archanjo et

al., 2013; Nascimento et al., 2015; Souza et al., 2016), but their petrogenesis and protolith sources are still under debate.

In this study, we present field observations, petrography, mineral chemistry, whole-rock geochemistry, and zircon U–Pb geochronology with Hf isotope and rare-earth element analyses of zircon from the multiple generations of migmatite in the Campo Grande Block. Our aims are (1) to identify the petrological and geochemical patterns of the Campo Grande migmatite phases; (2) to determine the zircon Pb-Hf and whole-rock Nd isotopic behavior during multiple migmatite generation; (3) to gain insight into the thermodynamic conditions under which partial melting processes occurred; and (4) to make a contribution to the understanding of the evolution of crustal differentiation in this terrane.

4.3 Geologic setting

The Borborema Province is a Precambrian shield within the north-northeastern part of the South American continent (Almeida et al., 1981). It consists of Paleo- to Neoarchean blocks and terrains reworked during the Paleo- to Neoproterozoic collisional orogeny (Dantas et al., 2004; 2008; 2013). This province includes a complex system of crustal-scale high-temperature shear zones that separate domains of variably strained massifs, terrains consisting of metasupracrustal sequences and Neoproterozoic granite intrusions (Caby et al., 1991; Jardim de Sá, 1994). The final configuration of the Borborema Province (Fig. 4.1A) resulted from the convergence of the West African-São Luís and São Francisco-Congo cratons during the assembly of Western Gondwana (Arthaud et al., 2008; Van Schmus et al., 2008; Padilha et al., 2017).

The Rio Grande do Norte domain (RGND) is located in the northeastern portion of the Borborema Province. It is limited to the west by the Portalegre shear zone, correlated with the Ifewara-Zungeru fault in Africa, and to the south by the Patos-Adamaoua Lineament (Jardim de Sá, 1994; Brito Neves et al., 2011). The RGND includes Archean rocks of the São José do Campestre Massif composed of medium- to high-grade orthogneisses that have recorded a series of intrusion events between 3.41 and 2.66 Ga and subordinate metasupracrustal rocks (Dantas et al., 2004; 2013). Paleoproterozoic orthogneisses (ca. 2.2 - 2.15 Ga)

surround the Archean core of the domain and are correlated with the Caicó Complex basement in the RGND (Souza et al., 2007).

The Rio Piranhas-Seridó terrane, the central portion of the RGND (Fig. 4.1B), includes calc-alkaline banded gneiss, granitic to dioritic gneiss, and migmatite underlying the Neoproterozoic Seridó Group (Van Schmus et al., 2003). Systematic U-Pb zircon geochronological studies have indicated that Rhyacian (2.25 to 2.15 Ga) metamorphosed high-K calc-alkaline magmatic rocks (e.g., Caicó Complex; Souza et al., 2007; Hollanda et al., 2011), Siderian (2.3 Ga) supracrustal rocks (Dantas et al., 2008), and 2.19 Ga tholeiitic magmatic rocks (Ferreira et al., 2019a) form the basement of the Neoproterozoic Seridó Group (Hollanda et al., 2015). Archean to Paleoproterozoic basement and Neoproterozoic metasupracrustal sequences have been subsequently intruded by large Neoproterozoic granite complexes, at ca. 575 Ma (Archanjo et al., 2013; Nascimento et al., 2015; Souza et al., 2016). Paleoproterozoic events have been recognized in all parts of the Borborema Province and represent a significant period of crustal growth within the South American continent (Brito Neves, 2011; Brito Neves and Fuck, 2014).

The Campo Grande Block is a poorly studied basement inlier in the Rio Piranhas-Seridó terrane that is characterized by strong migmatization. These migmatites occur within the granite-gneiss complex in the northwestern portion of the Rio Grande do Norte domain. The Campo Grande migmatite complex represents multiple phases of migmatization and allows a systematic study of their different components and textures.

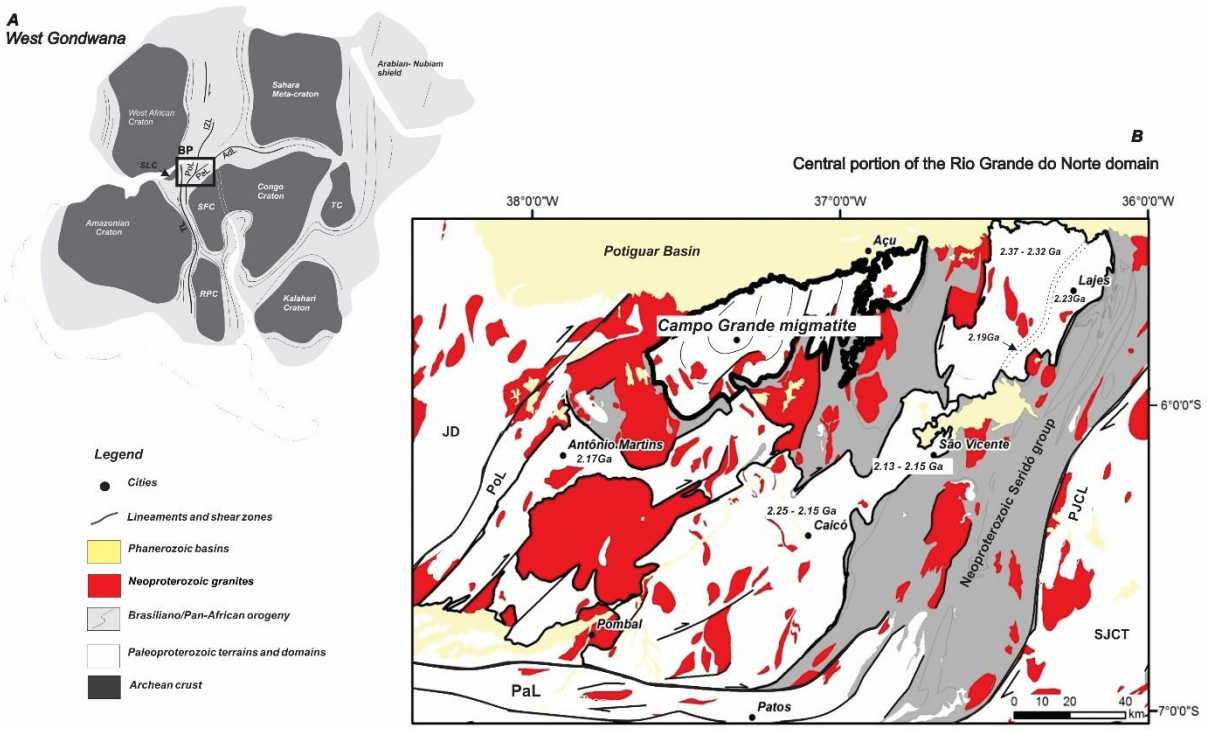

Figure 4.1. Regional geological setting. A) Localization map of the Borborema Province in West Gondwana. B) Geological map of the central portion of the Rio Grande do Norte domain. Legend: RPC - Rio de La Plata Craton, SFC - São Francisco Craton, SLC – São Luiz Craton, and TC - Tanzania Craton. IZL - Ifewara-Zungeru Lineament, PoL - Portalegre Lineament, PJCL – Picuí-João Câmara Lineament, PaL - Patos Lineament, ADL - Adamaoua Lineament. JD – Jaguaribe domain and SJCT - São José do Campestre terrain. U-Pb ages for the Paleoproterozoic terrains from Souza et al. (2007), Dantas et al. (2008), Hollanda et al., 2011 (2011) and Ferreira et al. (2019a).

4.4 Analytical methods and procedures

4.4.1 Mineral Chemistry

Mineral analyses from the Campo Grande migmatite were performed on polished thin sections using a JEOL JXA-8230 SuperProbe with 5 wavelength-dispersive (WDS) spectrometers at the Electron Microprobe Laboratory of the Universidade de Brasília (Brazil). Systematic WDS analyses were obtained for garnet, clinopyroxene, plagioclase and amphibole. Operating conditions were 15 kV accelerating voltage, a beam current of 10 nA, and a beam diameter of 3 μm for all minerals, except for plagioclase (5 μm). Counting times on peak and on background were 10 s and 5 s, respectively. Both synthetic and natural mineral standards were used. The Fe^{3+} contents presented below were estimated using site and charge balance calculations on cation-normalized analyses (Droop, 1987).

4.4.2 Geochemistry

Geochemical analyses were performed on 14 representative samples of the Campo Grande migmatite rocks. Analyses of major, minor and trace elements were carried out by ALS Global Analytical Laboratories Ltd (Belo Horizonte, Brazil). Major and minor elements were obtained by X-ray fluorescence (XRF) after fusion with lithium tetraborate. Trace elements were determined from melting of 0.2 g sample with lithium metaborate/tetraborate, diluted nitric acid digestion, and ICP-OES analysis. The loss on ignition (LOI) was given by weight difference after heating at 100°C. Precious metal and base metal abundances were determined after 0.5 g of sample digestion with Acqua Regia by ICP-MS analysis.

4.4.3 U-Pb and Lu-Hf isotopes

U-Pb and Lu-Hf isotopic analyses were performed on zircon grains using a Thermo-Fisher Neptune HR-MC-ICP-MS coupled with a Nd:YAG UP213 New Wave laser ablation system at the Laboratory of Geochronology of the Universidade de Brasília. U-Pb analyses on zircon grains were carried out by the standard-sample bracketing method (Albarède et al., 2004), using the GJ-1 standard zircon (Jackson et al., 2004) in order to quantify the amount of ICP-MS fractionation. The tuned masses were 238, 207, 206, 204 and 202. The integration time was 1 second and the ablation time was 40 seconds. A 30 µm spot size was used and the laser setting was 10 Hz and 2-3 J/cm^2. Two to four unknown grains were analyzed between GJ-1 analyses. $^{206}Pb/^{207}Pb$ and $^{206}Pb/^{238}U$ ratios were time corrected. The raw data were processed off-line and reduced using an Excel worksheet (Bühn et al., 2009). During the analytical sessions the zircon standard 91500 (Jackson et al., 2004) was also analyzed as an external standard.

Common ^{204}Pb was monitored using the ^{202}Hg and (^{204}Hg+^{204}Pb) masses. Common Pb corrections were not done due to very low signals for ^{204}Pb (< 30cps) and high $^{206}Pb/^{204}Pb$ ratios. Reported errors are propagated by quadratic addition [(2SD^2+2SE^2)1/2] (SD = standard deviation; SE = standard error) of external reproducibility and within-run precision. External reproducibility is represented by the standard deviation obtained from repeated analyses (~1.1 % for $^{207}Pb/^{206}Pb$ and up to ~2 % for $^{206}Pb/^{238}U$) of the GJ-1 zircon standard during the analytical

sessions, and the within-run precision is the standard error calculated for each analysis. Concordia diagrams (2σ error ellipses), probability density plots and weighted average ages were calculated using the Isoplot-3/Ex software (Ludwig, 2008).

Zircon crystals previously analyzed for U-Pb isotopes and showing concordant to slightly discordant data were selected for Lu-Hf analyses. Lu-Hf isotopic data were collected over 50 s of ablation time and using a 50 μm spot size. During the analytical sessions, replicate analyses of the GJ-1 standard zircon were performed, obtaining an average $^{176}Hf/^{177}Hf$ ratio of 0.282006 ± 16 (2σ), in good agreement with the reference value for the GJ standard zircon (Morel et al., 2008). Measurement spots were carefully positioned in the same growth area but not onto the same spot analyzed for U-Pb data. The signals of the interference-free isotopes ^{171}Yb, ^{173}Yb and ^{175}Lu were monitored during analysis in order to correct for isobaric interferences of ^{176}Yb and ^{176}Lu on the ^{176}Hf signal. The ^{176}Yb and ^{176}Lu contributions were calculated using the isotopic abundance of Lu and Hf (Chu et al., 2002). Contemporaneous measurements of ^{171}Yb and ^{173}Yb provide a method to correct for mass-bias of Yb using a $^{173}Yb/^{171}Yb$ normalization factor of 1.132685 (Chu et al., 2002). The Hf isotope ratios were normalized to $^{179}Hf/^{177}Hf$ of 0.7325 (Patchett, 1983). $\varepsilon_{Hf}(t)$ was calculated using the decay constant λ=1.865*10-11(Scherer et al., 2001) and the $^{176}Lu/^{177}Hf$ and $^{176}Hf/^{177}Hf$ CHUR values of 0.0332 and 0.282772 (Blichert-Toft and Albarède, 1997), respectively. Two-stage model ages (T_{DM}) were calculated from the initial Hf isotopic composition of zircon, using an average crustal Lu/Hf ratio (e.g. Gerdes and Zeh, 2009). The values of $^{176}Lu/^{177}Hf$ = 0.0384 and $^{176}Hf/^{177}Hf$ = 0.28325 were used for depleted mantle (Chauvel and Blichert-Toft, 2001), and $^{176}Lu/^{177}Hf$ = 0.0113 for average crust (Wedepohl, 1995).

4.4.4 Sm-Nd Isotopes

Sm–Nd isotopic analyses followed the method described by Gioia and Pimentel (2000) and were also carried out at the Geochronology Laboratory of Universidade de Brasília. Whole-rock powders (~ 50 mg) of 11 representative samples were mixed with ^{149}Sm–^{150}Nd spike solution and dissolved in Savillex beakers. Sm and Nd extraction of whole-rock samples followed conventional

cation exchange chromatography techniques, with Teflon columns containing LN-Spec resin (HDEHP – diethylhexil phosphoric acid supported on PTFE powder). Sm and Nd fractions were loaded on Re evaporation filaments of double filament assemblies, and the isotopic measurements were carried out on a multicollector TRITON thermal ionization mass spectrometer in static mode. Uncertainties of Sm/Nd and $^{143}Nd/^{144}Nd$ ratios were better than ±0.1% (2 σ standard error) and ±0.0015% (1σ), respectively, according to repeated analyses of the international rock standard BHVO-1. $^{143}Nd/^{144}Nd$ ratios were normalized to $^{146}Nd/^{144}Nd$ = 0.7219, and the decay constant used was (σ) 6.54 x 10^{-12}. The T_{DM} values were calculated using the DePaolo (1981) model.

4.5 Results

4.5.1 Migmatite Morphology and Petrography

In the field, it was possible to distinguish paleosome, melanosome, as well as concordant and injected leucosome components in the migmatites. The first component is represented by paleosome of tonalite to granodiorite composition, depending on the modal variation of plagioclase, biotite, quartz and minor K-feldspar. The second phase is characterized by leucosome with granite composition involving plagioclase, quartz, K-feldspar, and minor biotite. Granodioritic to tonalitic paleosome and granitic leucosome layers are concordant and folded. K-feldspar-rich alkaline pegmatite veins that cut through the two older migmatite phases mark the third phase. In this study, migmatite samples including paleosome, melanosome and leucosome have been collected from diatexite and metatexite, according to the nomenclature of Sawyer (2008). Representative illustrations are given in Figures 4.2 and 4.3.

Metatexites are easily recognized because the pre-existing structures of the paleosome are partially overprinted by a steeper syn-anatectic foliation and magmatic flow-banding representing the leucosome component that forms a strongly folded stromatic structure (Fig. 4.2E, F). The stromatic structure indicates that partial melting was synchronous with folding development (Fig. 4.2B, C). Progressive increase of partial melting led to transition from metatexites to diatexites. The diatexites (Fig. 4.2A, B, C) are coarse-grained and heterogeneous,

characterized by variably plagioclase- or biotite-rich paleosome portions that are separated by quartz-feldspathic leucosome and biotite-rich melanosome. The melanosome and leucosome components in the diatexites form schlieren and nebulitic structures (Fig. 4.2B). These structures are defined mainly by biotite trails that were developed during migration of leucosome melt. As folding proceeded, biotite schlieren thickness increased in the axial plane of the folded diatexites. The biotite melanosome schlieren are truncated by coarse-grained leucosome layers along the axial plane of tight asymmetric folds (Fig. 4.2C), evidencing coeval deformation and melting (e.g., Brown et al., 2011).

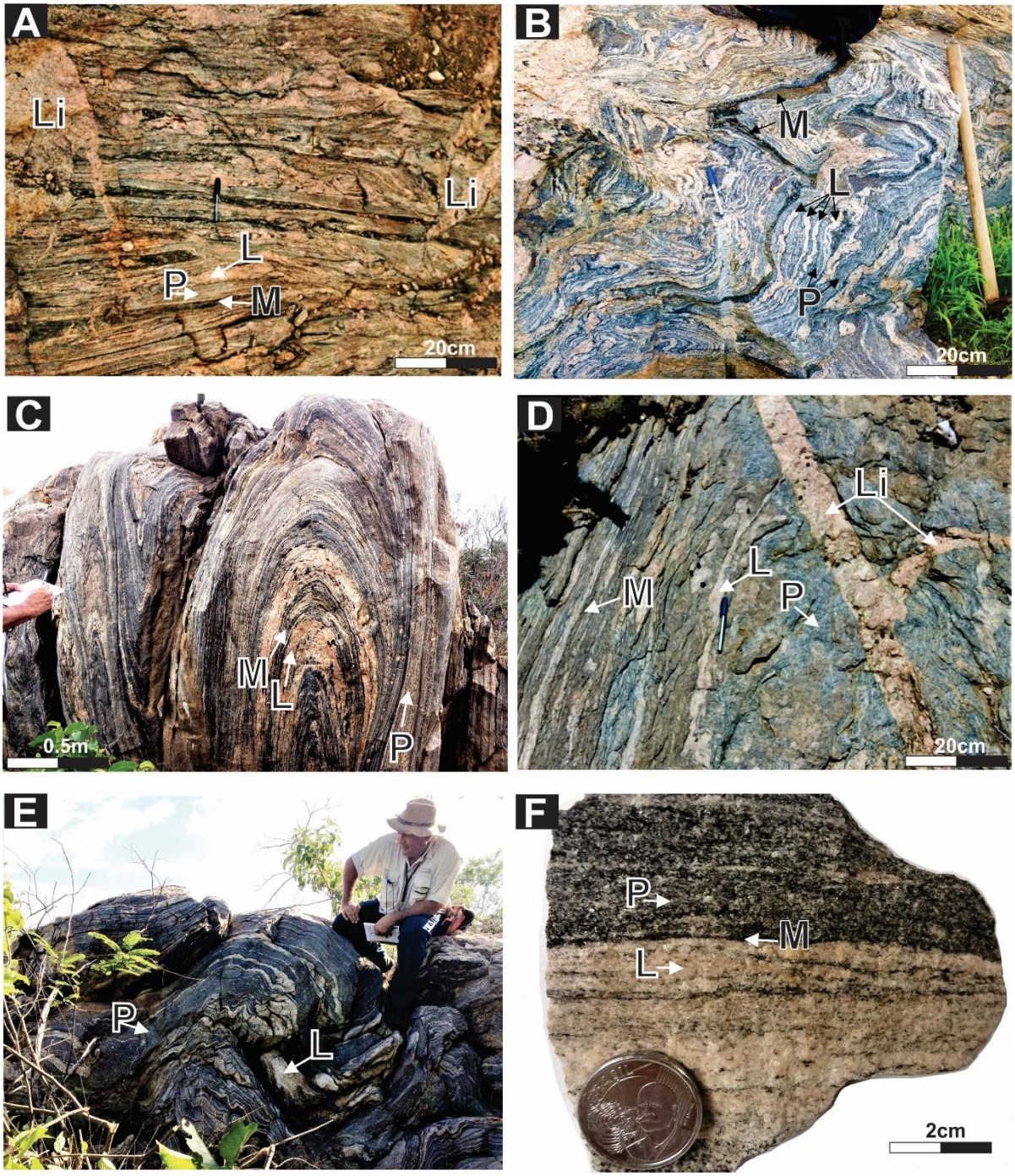

Figure 4.2. Macroscopic features of the Campo Grande migmatites exhibiting typically heterogeneous aspect and spatial relationship of quartzo-feldspathic neosome, both for in-situ (L) and injected granitic leucosome (Li), melanosome (M) rich in biotite, and paleosome (P). A and B) Diatexites with schlieren and nebulitic structures. C) Folded diatexite. D to F) Stromatic metatexite with discrete leucosome, melanosome and paleosome components with vein-structured leucosome (Li).

In addition, euhedral K-feldspar and plagioclase crystals are imbricated in a tile-like microstructure (Fig. 4.3A), also indicating recrystallization and crystal flow in the fold hinge during deformation. Portions of paleosome occur as boudins at the layer scale. These restite components underwent boudinage in response to layer-parallel extension of granitic leucosome.

The paleosome layers have tonalite to granodiorite compositions (Fig. 4.3B, C, D), with primary plagioclase crystals (40-50%) plus quartz (20-30%), and are enriched in the restite components - mainly euhedral biotite (20-30%) - in relation to the more fertile layers that generated granite to alkaline pegmatite leucosomes. Plagioclase crystals in the paleosome display straight boundaries with biotite and quartz (Fig. 4.3B, C, D), indicating that this mineral assemblage grew from a former melt phase (e.g. Holness et al., 2011). Feldspar grains show melt-filled triple junctions at their corners (Fig. 4.3B, C, D). These melt-filled triple junctions are not interconnected. They represent trapped melt pockets of K-feldspar and minor Na-rich plagioclase. Leucosome was mobilized when the melt-filled triple junctions became interconnected to form canaliculi that allowed melt extraction. The leucocratic veins of crystallized melt consist of different modal proportions of quartz (30-50%), plagioclase (20-30%), K-feldspar (10-20%), and biotite (5-10%). Leucosomes are approximately 1 to 10 cm wide, and are medium-grained, light-colored quartz-feldspathic mineral assemblages within layers of alkali-granite composition. This concordant leucosome (L) is located at the original site of partial melting (in-situ or in-source), and can be recognized by the adjacent presence of melanosome (M). Patchy biotite accumulation (Fig. 4.2A, F) is regarded a result of melt extraction from the concordant leucosomes, and interpreted as peritectic products of incongruent melting reactions. Thin albite rims also occur along plagioclase and K-feldspar boundaries. The melanosome samples display medium-grained lepidoblastic texture and are composed of biotite (50-60%), quartz (20-30%), and plagioclase (10-20%). Variably biotite-enriched layers or schlieren characterize melanosome components (Fig. 4.2B, C). The main fabric is more strongly developed in melanosome, due to high biotite content, that is concordant with in-situ or in-source leucosomes (Fig. 4.2F). Cuspate fine- to medium-grained quartz occurs at grain junctions in the melanosome (Fig. 4.3A). Therefore, melanosome layers or patches represent the residual mixture of restite minerals and retained peritectic minerals after the

extraction of anatectic melt (Sawyer, 2008). Injected leucosomes are less common than the other migmatite components and occur as vein-structured alkali pegmatite (5 to 15 cm wide, Fig. 4.2D) and granitic intrusions. They are discordant, with well-defined boundaries and generally no adjacent melanosome, and can no longer be traced back to their source. The injected alkali leucosomes contain up to 60-80% K-feldspar, quartz (10-20%), plagioclase (5-10%), and biotite (1-5%), and display coarse-grained phaneritic texture (Fig. 4.3E, F). Coarse-grained, euhedral, poikilitic K-feldspar crystals have inclusions of quartz, plagioclase and biotite. Medium-grained, corroded and dispersed biotite occurs in the quartz-feldspar matrix of injected leucosome (Fig. 4.3F).

Migmatite morphology and petrography have allowed to recognize at least two phases of partial melting and consequent generation of migmatite. The older phase is represented by Pl + Bt + Qz paleosome parallel to the main foliation, along which in-source Qz + Pl + Bt ± Kfs stromatic leucosome developed coeval with biotite-rich schlieren and stromatic melanosome. These earlier migmatite phases were folded and intruded by Kfs + Qz ± Pl pegmatites that represent the younger leucosome generation. Representative samples of these multiple migmatite phases were selected for mineral chemistry, geochemistry, and isotopic analysis.

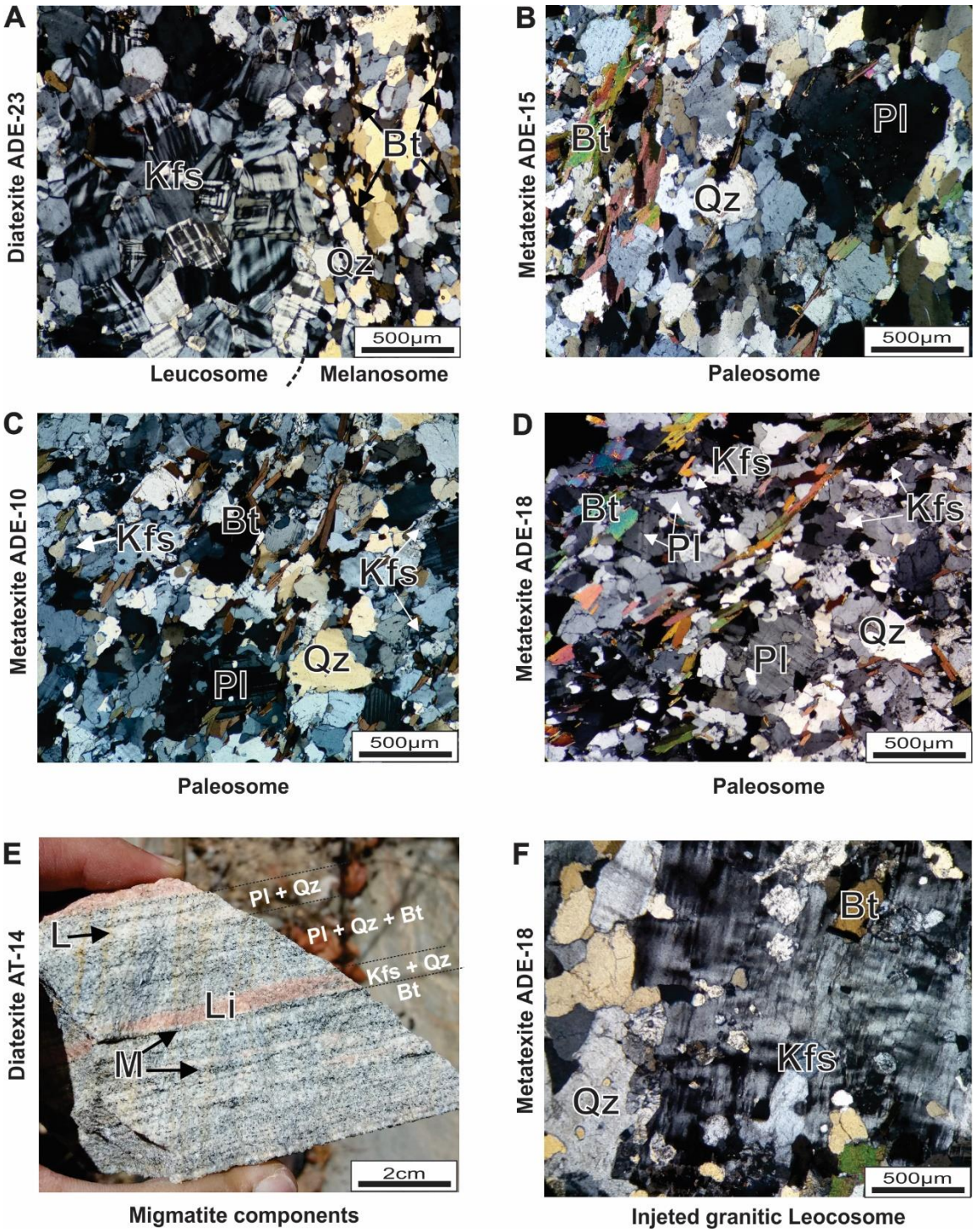

Figure 4.3. Petrographic features of the paleosome, melanosome and leucosome from the Campo Grande migmatite complex. A) Medium-grained lepidoblastic texture of the quartz-feldspathic leucosome with tile microstructure, and the biotite-quartz dominated melanosome. B to D) Euhedral, primary biotite and plagioclase crystals, and K-feldspar and quartz grains from the paleosome components. E and F) coarse-grained phaneritic texture in injected leucosome. Mineral symbols follow Whitney and Evans (2010). Bt – biotite, Kfs – K-feldspar, Pl – plagioclase and Qz – quartz.

4.5.2 Mineral Chemistry

Field observations and petrographic data suggest that anatexis of the migmatite protolith was the result of water-aided melting via reactions such as Pl + Bt + Qz + H_2O = melt. Therefore, we used mineral chemical data on biotite (Supplementary Table 4.1) to try to recognize different sources for the paleosome and concordant leucosome. We selected samples (paleosome: ADE-10P and ADE-15P, and concordant leucosome: ADE-12L and ADE-23L) in which the relations between paleosome and leucosome were more evident, because some samples show a transitional or progressive limit.

Textural features indicate that biotite is clearly primary, with only rare evidence of secondary transformation and/or alteration, such as chloritization, muscovite formation, or oxidation (Fig. 4.3A to F). Biotite occurs as greenish lamellar/bladed crystals of dominantly hypidiomorphic shape. Inclusions of magnetite and small hypidiomorphic crystals of epidote, allanite, and zircon are common. Biotite analyses from the paleosome are more Mg-rich end-members (phlogopite) with Mg/(Mg + Fe) values ranging from 0.4 to 0.5, whereas biotite from concordant leucosome is more Fe-rich (annite) with Mg/(Mg + Fe) values ranging from 0.2 to 0.3 (Fig. 4.4A). Note that the ADE-12L concordant leucosome records the presence of biotite and muscovite (Fig. 4.4A), comprising two-mica granite composition. In the discriminant diagram for primary magmatic biotites, reequilibrated, and neoformed biotite grains (after Nachit et al., 2005), our analyses plot into the field of primary biotite (Fig. 4.4B), as already indicated by the microtextural features. MgO content decreases in biotite with increasing temperature at constant pressure (e.g., Gardien et al., 2000), which may suggest a lower temperature paleosome. However, reequilibrated Mg-richer biotite grains with can be reported for the ADE-15P paleosome.

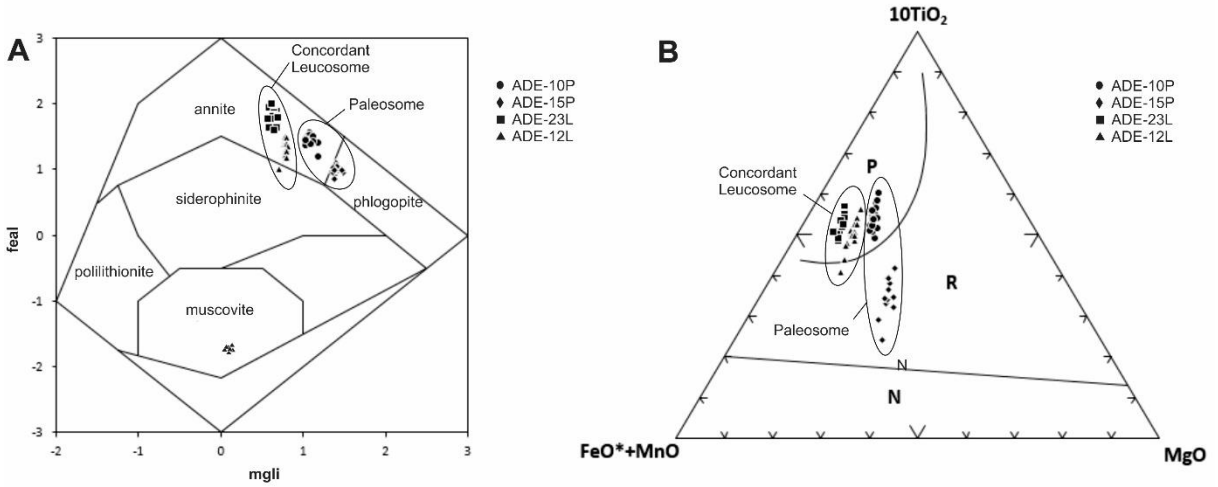

Figure 4.4. A) A simplified classification diagram Mg minus Li (= mgli) vs. VIFet+Mn+Ti minus VIAl (= feal) of micas (Tischendorf et al., 1997). B) Discrimination between primary magmatic biotite, reequilibrated, and neoformed biotite grains (after Nachit et al., 2005). Atoms per formula unit were calculated using 22 oxygens.

Plagioclase is the major constituent of migmatites and occurs as hypidiomorphic to anhedral crystals of 200 to 500 µm size (Fig. 4.3A to F). Some crystals have corroded shapes and exhibit sharply defined polysynthetic twinning. In addition, a few crystals present alteration in their central portion in the form of fine-grained epidote and white mica. Plagioclase also occurs as exsolution lamellae (<100 m) in perthite texture within twinned K-feldspar. The plagioclase crystals exhibit compositional zoning and a few grains show deformation twinning due to dislocation along the S_n foliation. This indicates that exsolution intergrowth of plagioclase was produced during anatexis.

Plagioclase analyses show a narrow range of oligoclase compositions (Supplementary Table 4.2 and Fig. 4.5A), which are a function of the textural relationships with distinct phases during migmatisation processes. Plagioclase crystals from paleosome have higher Ca (5.09 to 6.48 wt.% CaO) with An_{24-30}, and Al (23.1 to 24.6 wt.% Al_2O_3) contents (Fig. 4.5B). In contrast, the plagioclase analyses from concordant leucosome components contain higher Na (8.8 to 9.7 wt.% Na_2O) and lower Ca (2.4 to 5.3 wt.% CaO) with An_{17-23}, and lower Al (21.8 to 23.5 wt.% Al_2O_3) contents (Fig. 4.5B).

Migmatite K-feldspar crystals are light reddish, euhedral to subhedral coarse phaneritic (200 µm to 3 mm), and display plagioclase, quartz and apatite inclusions (5 to 30 µm). The K-feldspar analyses show 13.6 to 14.9 wt.% K_2O (Or_{88-93}), with 0.45 to 1.25 wt.% Na_2O (Ab_{4-12}), and are classified as K-sanidine and orthoclase (Supplementary Table 4.2 and Fig. 4.5A). Melting experiments

have shown that with rising temperature the Ab content increases, as a result of increasing solid solution of the albite component in K-feldspar, and Ab content tends to decrease with increasing pressure (e.g., Gardien et al., 2000). Therefore, the increase of the melt fraction diluted the K_2O content of the melt. It is not possible to discriminate the paleosome and concordant leucosome by alkali feldspar composition (Fig. 4.5C), in contrast to the plagioclase results. K-feldspar grains occur as euhedral to subhedral phaneritic in the leucosome, whereas in the paleosome they occur as rare interstitial films along the junctions between corroded plagioclase and biotite crystals. These alkaline interstitial films may be interpreted as incipient melt of the leucosome.

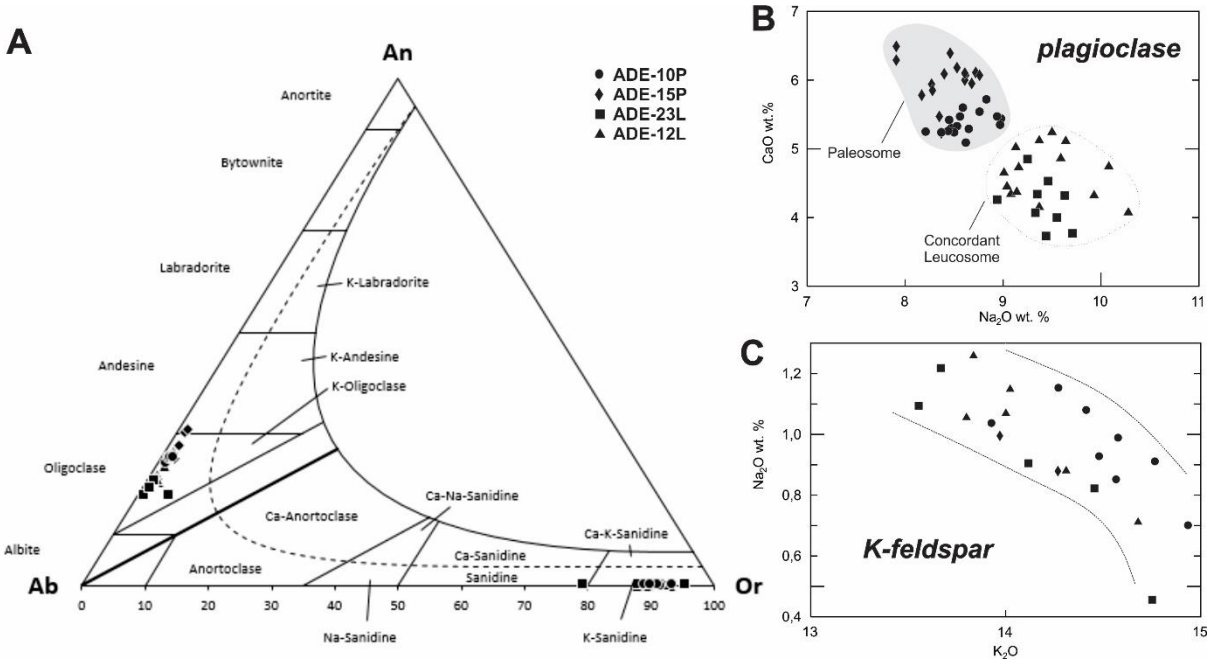

Figure 4.5. A) Ab-Na-Or diagram (after Barker, 1979) with the plagioclase compositions of the studied migmatites. B) CaO wt.% vs Na_2O wt.% plot of the plagioclase analyses separated by samples. C) K_2O wt.% vs Na_2O wt.% plot of the K-feldspar analyses separated by samples. Atoms per formula unit were calculated using 8 oxygens.

4.5.3 Whole-rock Geochemistry

Major and trace element compositions of fourteen samples of paleosome, and concordant and injected leucosome components from the Campo Grande migmatite are given in Supplementary Table 4.3.

The migmatite samples plot into the calc-alkaline field on the AFM diagram (Irvine and Baragar, 1971), displaying progressive increase of alkali contents from paleosome to injected leucosome (Fig. 4.6A). The paleosomes plot into the

tonalite and granodiorite fields, while most leucosomes plot in the granite field on the normative An–Ab–Or diagram (Barker, 1979), also showing an increase of K-feldspar content from paleosome to leucosome components (Fig. 4.6B). All migmatite components are peraluminous with A/CNK values ranging from 1.0 to 1.2 (Fig. 4.6C).

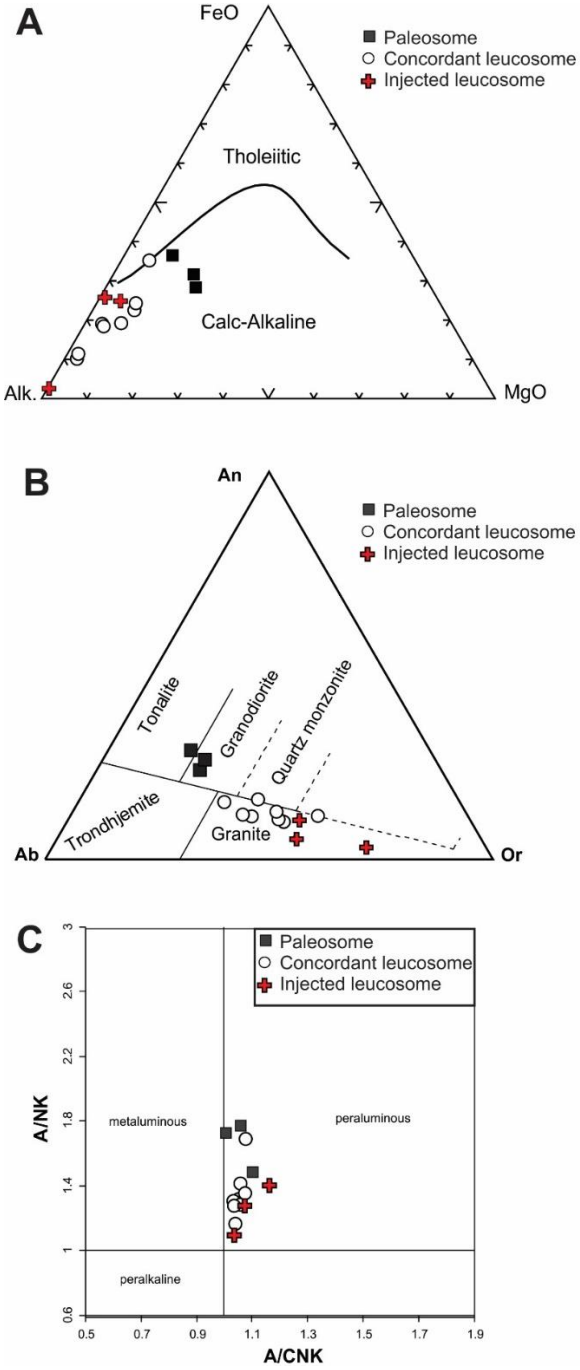

Figure 4.6. A) AFM diagram (after Irvine and Baragar, 1971) and B) An–Ab–Or classification diagram (Barker, 1979) showing the compositions of paleosome and concordant and injected leucosome of the Campo Grande migmatite. C) A/CNK-A/NK diagram (Shand, 1943).

The multiple migmatite phases have different geochemical composition. Some major element variations are shown in Fig. 4.7. They define a linear trend in most of the major elements negatively correlated with increase of SiO_2 from paleosome (66.8 wt.%) to injected leucosome (76.2 wt.%) samples (Fig. 4.7A to H). The concordant and injected leucosomes are significantly depleted in MgO, CaO, Na_2O, FeO_t, P_2O_2 and TiO_2 in comparison to the paleosomes. The tonalitic paleosome has high CaO + Na_2O and low K_2O compared to the granitic leucosomes. These tonalite remnants of protoliths are higher in Na_2O (3.59-4.02 wt.%) than K_2O (2.03–2.32 wt.%) contents (~2:1 ratios).

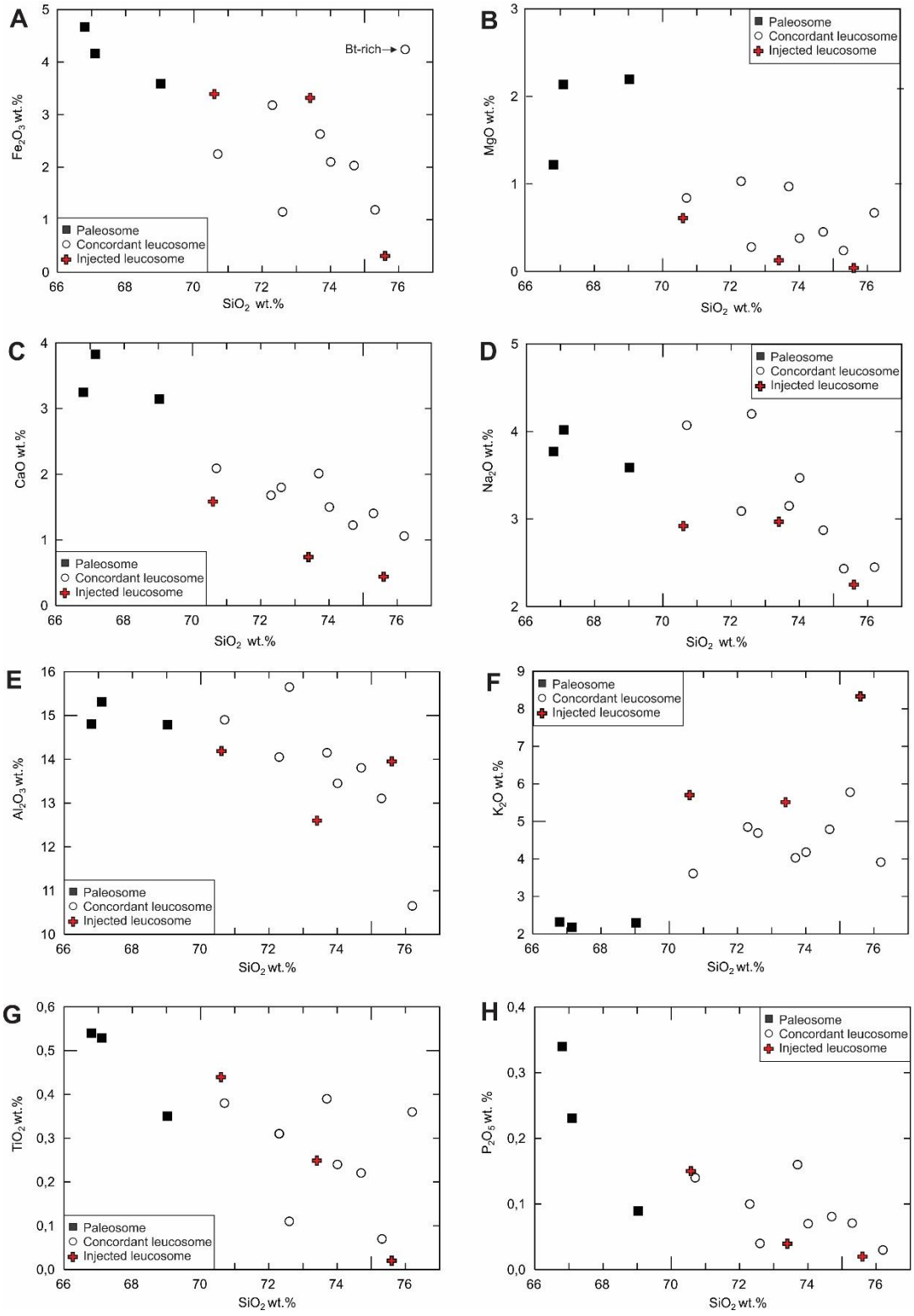

Figure 4.7. A to H) Harker variation diagrams showing the major element compositions of paleosome, concordant and injected leucosome.

In the paleosome samples, Al_2O_3 shows positive correlation with CaO and Na_2O, confirming that plagioclase played a major role in determining the tonalitic paleosome composition. K_2O contents in the granitic leucosomes are positively correlated with Rb/Sr ratios (Fig. 4.8A), indicating variation in the feldspar assemblage during partial melting. The granitic leucosomes have higher K_2O (3.9–8.3 wt.%) than Na_2O (2.4-4.2 wt.%) contents (up to > 3:1 ratios) due to higher K-feldspar (40 to 60 % modal percentage) - mainly in the pegmatite and granite intrusions. The concordant and injected leucosomes are enriched in trace elements such as Rb, Ba, Y and Nb (Fig. 4.8A to D) that can be accommodated in feldspars. This geochemical behavior is consistent with the plagioclase and K-feldspar cumulate structure in the tonalitic paleosomes and granitic leucosomes. Therefore, fractional crystallization of feldspar was crucial during migmatite generation. The migmatites show a positive correlation of Hf with Zr (Fig. 4.8E), Th vs. Sum of REE (Fig. 4.8F), P_2O_5 vs. Sum of REE (Fig. 4.8G) and V vs. TiO_2 (Fig. 4.8H) contents, which indicates that accessory minerals also exerted a significant control on the trace element contents.

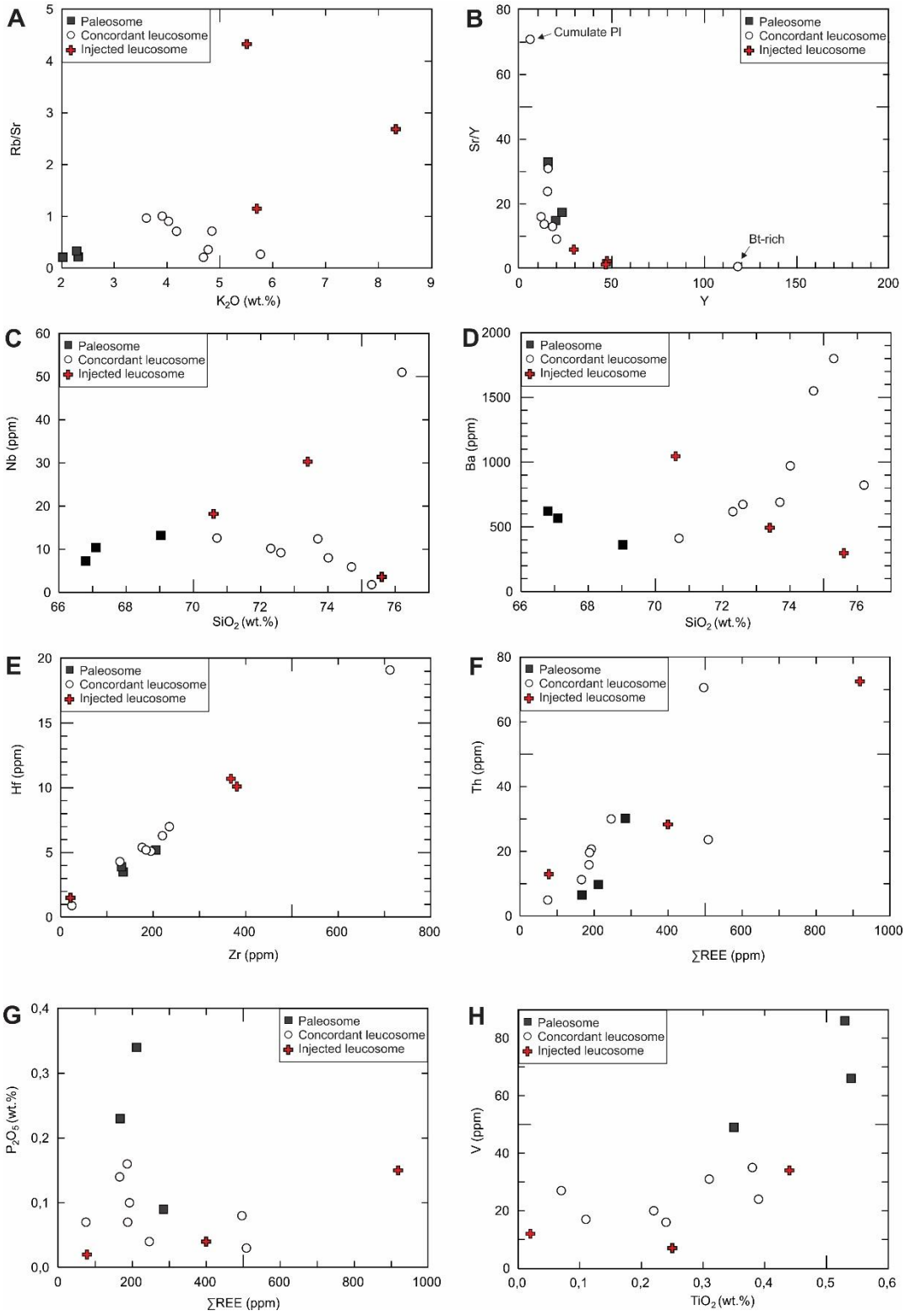

Figure 4.8. Harker variation diagrams showing some major and trace element compositions for paleosome, concordant and injected leucosome migmatite components. A) K2O vs. Rb/Sr ratio. B) Y vs. Sr/Y ratio. C) SiO2 vs. Nb content. D) SiO2 vs. Ba content. E) Hf vs. Zr content. F) Th vs. sum REE content. G) P2O5 vs. REE content, and H) V vs. TiO2 content. Oxides are plotted as weight percent. Trace element concentrations are plotted as parts per million (ppm).

In the normative Qz-(Ab+Or)-An diagram (after Johannes and Holtz, 1996), the concordant and injected leucosomes plot towards the cotectic reaction line of the system Qz-(Ab+Or)-An, with low quartz contents compared to experimental melts generated at 5 kbar and < 750ºC (Fig. 4.9). Melt extraction and mineral segregation related to leucosome formation may not have involved pure melts. The comparatively higher abundance of biotite in paleosome explains its position off the cotectic curve (Fig. 4.9). Another hypothesis could be that the paleosomes were crystallized at a relatively higher pressure.

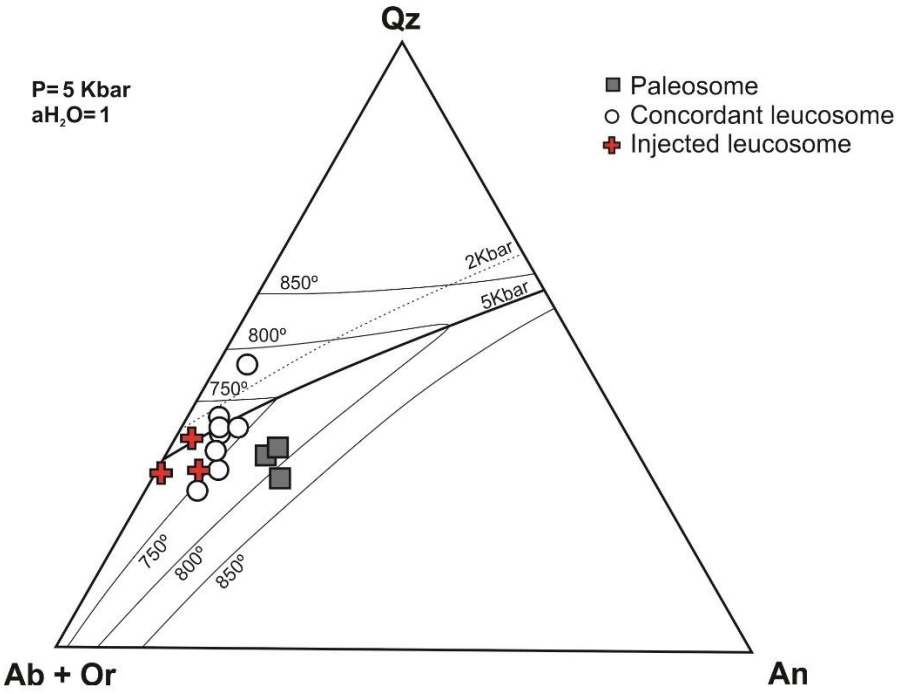

Figure 4.9. Isobaric equilibrium diagram for the system Qz-(Ab+Or)-An-H20 (after Johannes and Holtz, 1996). The thick black line represents the compositions of the cotectic reaction. Thin continuous lines represent determined and the thin dashed line an estimated isotherm on the quartz and alkali feldspar liquidus surfaces.

The REE contents of paleosomes show $(La/Yb)_N$ values ranging from 13.4 to 35.5 that define a gentle to strong sloping trend with Eu anomaly between negligible (0.99) and mainly negative (0.46) (Fig. 4.10A). The concordant leucosomes are characterized by a more fractionated REE pattern with $(La/Yb)_N$ values of 5.6 to 73.6, and strong negative Eu anomalies ranging from 0.36 to 0.73, with a unique positive Eu anomaly of 1.84 (Fig. 4.10C and D). The latter is due to abundance of cumulate plagioclase in the ADE-18L leucosome sample. The granitic leucosome with lower $(La/Yb)_N$ of 5.6 but higher REE content (508.5 ppm) of the ADE-23L leucosome sample may reflect the higher modal concentration of biotite in this

sample or, more likely, entrainment of zircon (mainly elevated HREE content) that would be consistent with the highest Zr content (712 ppm) of this sample amongst the leucosome samples. The injected granitic leucosomes show less-fractionated REE patterns, $(La/Yb)_N$ = 1.7 in ADE-18Li pegmatite sample, to more-fractionated patterns, $(La/Yb)_N$ = 110.77 in AT-23Li granite sample, both with strong negative Eu anomalies (0.23 to 0.39) (Fig. 4.10E). These negative Eu values are due to the abundance of cumulate feldspar in the injected leucosome sources. Trace element compositions of migmatite samples are characterized by depletion in high field strength elements (such as Nb, Ta, and Ti) relative to large ion lithophile elements (Pb, K, Ba, and Rb) (Fig. 4.10B, D, F). Feldspar and REE-rich accessory mineral accumulation during melt segregation and extraction may explain the variable total REE, mainly Eu, and trace element contents among tonalitic paleosomes and granitic leucosomes (e.g. Sawyer, 2008).

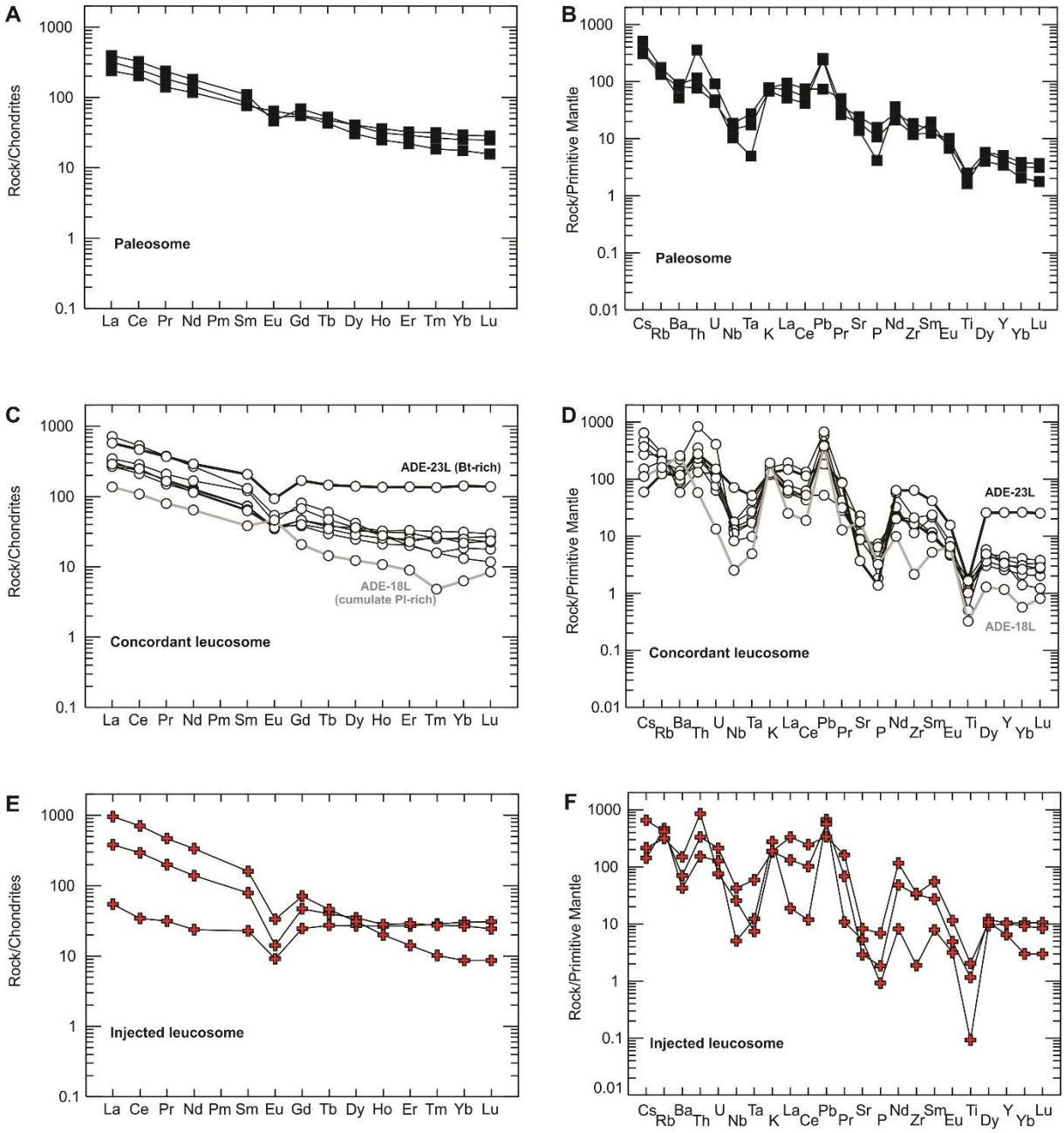

Figure 4.10. Chondrite-normalized REE diagrams (A, C, E and G) and Primitive mantle-normalized incompatible element diagrams (B, D, F and H) for the Campo Grande migmatite components (normalization values from Sun and McDonough, 1989).

4.5.4 U-Pb and Lu-Hf isotopes

Five migmatite samples were chosen for zircon U-Pb and Lu-Hf isotope analyses (Supplementary Tables 4.4 and 4.5). The studied zircon grains were separated from paleosome, concordant and injected leucosome samples.

4.5.4.1 Paleosome

Zircon grains from the ADE-18P sample are prismatic with lengths of 100-300 µm, length/width ratios of 2:1 to 4:1, and show typical oscillatory zoning in CL images (Fig. 4.11C). Twenty-seven zircon cores and rims yielded a discordant upper intercept age of 2979±12 Ma (MSWD=3.5, Fig. 4.11A) and Th/U ratios between 0.16 and 1.13 (Supplementary Table 4.4). Eight zircon grains yielded a concordia age of 2983±4 Ma (MSWD=0.77, Fig. 4.11B), interpreted as the paleosome crystallization age. Other analyses with $^{207}Pb/^{206}Pb$ ages ranging from 2974 to 2895 Ma plot below the concordia curve, indicating Pb loss. The Mesoarchean zircon grains have $^{176}Hf/^{177}Hf$ ratios of 0.280862 to 0.281049, with mainly positive $\varepsilon_{Hf(t)}$ values between -0.03 to +6.49, and display T_{DM} ages between 2.95 and 3.21Ga (Supplementary Table 4.5, Fig. 4.11D, E).

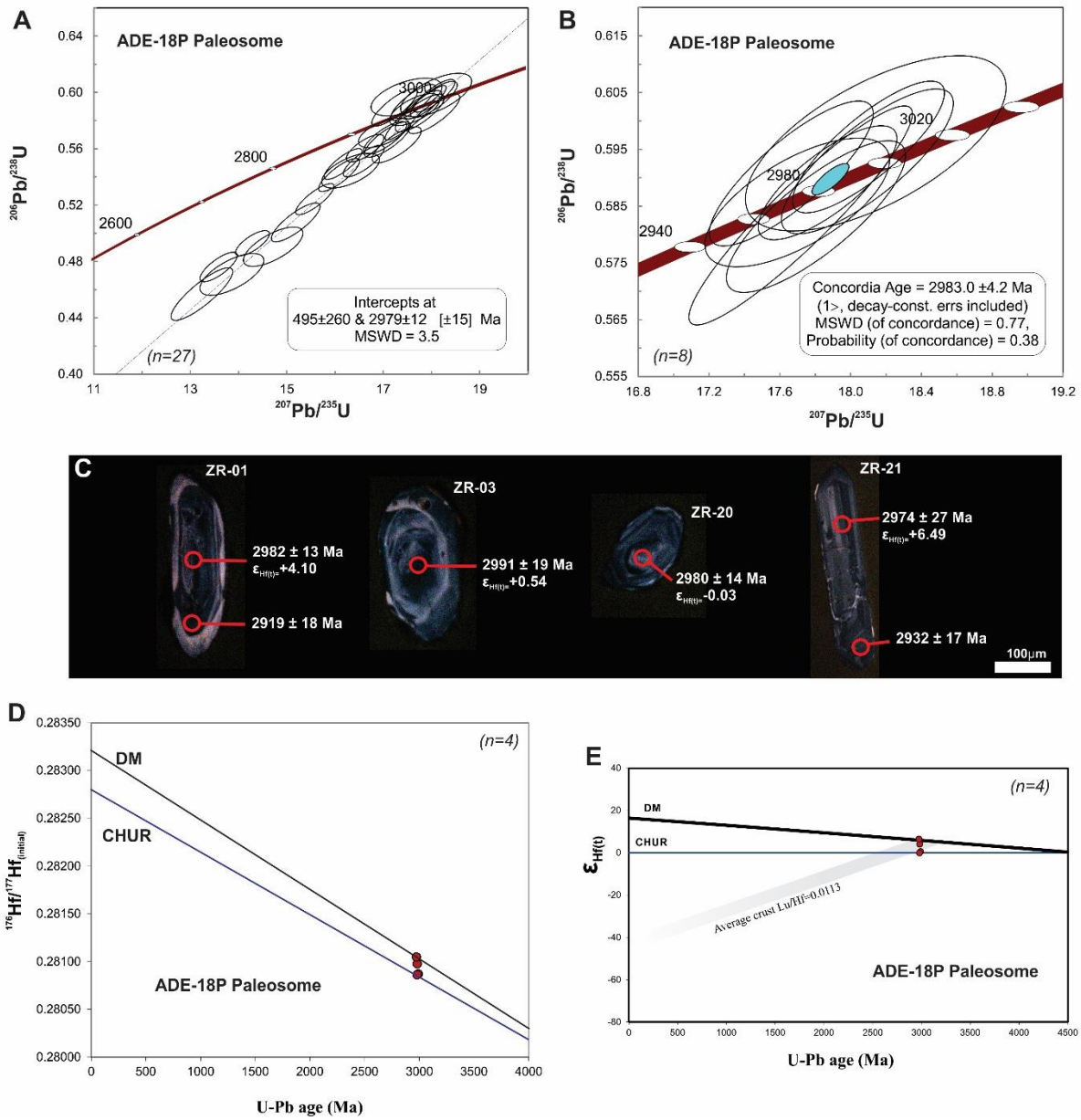

Figure 4.11. Discordia and B) concordia diagram for U-Pb zircon data, and C) representative CL images of zircon grains with their ages from the ADE-18P paleosome. D) Initial 176Hf/177Hf(t) value versus age (t), and E) the εHf (t) value versus age (t) from the ADE-18P paleosome. Data from Supplementary tables 4.4 and 4.5.

Similar ages were obtained for the zircon grains from the ADE-10P paleosome. The zircon crystals are prismatic in shape, with lengths of 100-200 μm and length/width ratio of 2:1 (Fig. 4.12C). Twenty-three analyses were performed on zircon cores. These analyses yield a discordant upper intercept age of 2923±12 Ma (MSWD=1.9, Fig. 4.12A). The zircon grains exhibit oscillatory and banded zonation patterns in CL images, and yield Th/U ratios of 0.125-0.583 (Supplementary Table 4.4). Ten $^{207}Pb/^{206}Pb$ ages plot onto the concordia curve

and yield a concordia age of 2911±12 Ma (MSWD=1.05) (Fig. 4.12B). This concordia age is interpreted as the magmatic crystallization age of the paleosome. Four Lu-Hf isotopic analyses were performed on representative dated zircon grains of this paleosome. These analyses gave $^{176}Hf/^{177}Hf$ ratios of 0.280920 to 0.281100, with $\varepsilon_{Hf(t)}$ values between -1.66 and +4.23, and Mesoarchean T_{DM} ages ranging from 3.00 to 3.21 Ga (Supplementary Table 4.5, Fig. 4.12D and E).

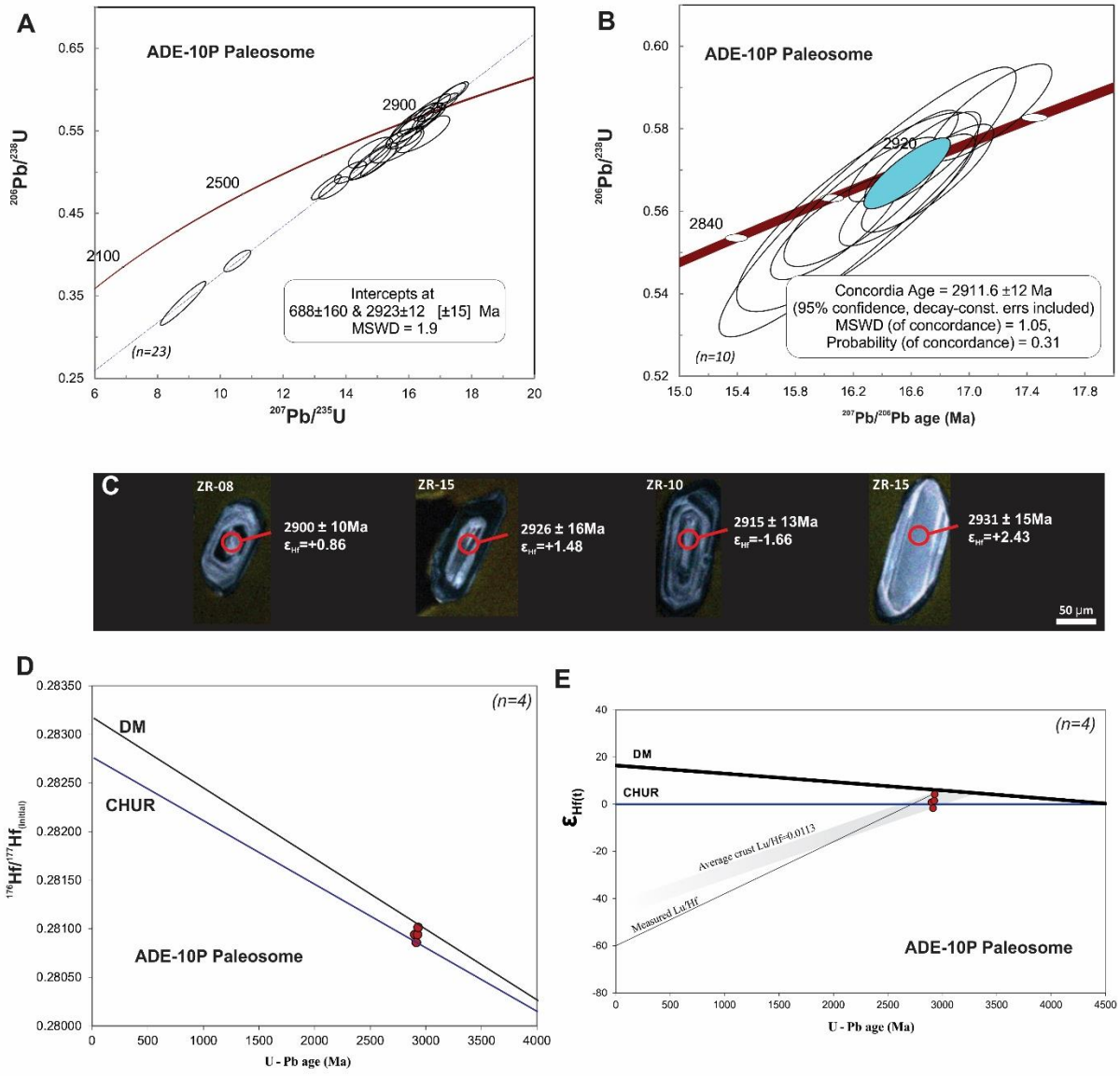

Figure 4.12. A) Discordia and B) concordia diagram for U-Pb zircon data, and C) representative CL images of zircon grains with their ages from the ADE-10P paleosome. D) Initial 176Hf/177Hf(t) value versus age (t), and E) the εHf(t) value versus age (t) from the ADE-10P paleosome. Data from Supplementary tables 4.4 and 4.5.

A more complex history is revealed by the 65 U-Pb isotopic analyses performed on cores and rims of oscillatory zoned zircon grains from the ADE-15 migmatite

sample. Zircon U-Pb-Lu-Hf isotope systematics and Th/U ratios combined with CL imagery allowed the recognition of four discordant age trends for this sample (Supplementary Table 4.4 and Fig. 4.13A). Six zircon cores display a comparatively older discordia age of 3311±52 Ma, reflecting an inherited component. The largest number of analyses, from 30 zircon cores, yield a discordia age of 2896±20 Ma, suggesting that this may be the crystallization age of this rock. These cores have Th/U ratios of 0.12 to 0.47 (Fig. 4.13D) and have very thin, light-colored rims (Fig. 4.13E) that suggest enrichment of Hf in the melt extraction rim. Eighteen zircon cores and rims reveal a discordia age of 1971±11 Ma (Fig. 4.13.A), and a concordia age of 1987.6 ± 3.7 Ma (n=8), with low Th/U ratios between 0.021 and 0.068 (Fig. 4.12D), which is interpreted as a metamorphic age. A metamorphic event is also indicated by the data for six zircon rims and grains that result in a Neoproterozoic discordia age of 594±12 Ma (MSWD=0.55) (Fig. 4.13B). These grains have lower Th/U ratios from 0.006 to 0.046 (Fig. 4.13D).

For the ADE-15 migmatite sample, 12 zircon grains were chosen for Lu-Hf isotope analysis (Supplementary Table 4.5, Fig. 4.13F, G). These Hf analyses exhibit a wide range of initial $^{176}Hf/^{177}Hf_{(t)}$ and $\varepsilon_{Hf(t)}$ values, which can be divided into four groups. The first, for inherited zircon cores of 3256 and 3155 Ma age have $^{176}Hf/^{177}Hf_{(t)}$ ratios of 0.280599-0.280794 and $\varepsilon_{Hf(t)}$ values of -2.87 to +1.69, with T_{DM} values of 3294 to 3558 Ma. The second, magmatic zircon with core ages of 3009 to 2913 Ma yields initial $^{176}Hf/^{177}Hf_{(t)}$ ratios of 0.280715-0.281147 with variable $\varepsilon_{Hf(t)}$ values of -6.85 to +9.85 and T_{DM} values of 2822 to 3410 Ma. The third group of metamorphic zircon core and rim age of ca. 1971 Ma display high $^{176}Hf/^{177}Hf_{(t)}$ ratios of 0.281097 to 0.281272 and negative $\varepsilon_{Hf(t)}$ of -8.5 to -15.3, with T_{DM} ages between 2680 and 2913 Ma. The last group of Neoproterozoic metamorphic zircon grains show higher $^{176}Hf/^{177}Hf_{(t)}$ ratios (0.281318 to 0.282237), more negative $\varepsilon_{Hf(t)}$ (-5.7 to -35.65), and younger T_{DM} ages (1412 to 2558 Ma).

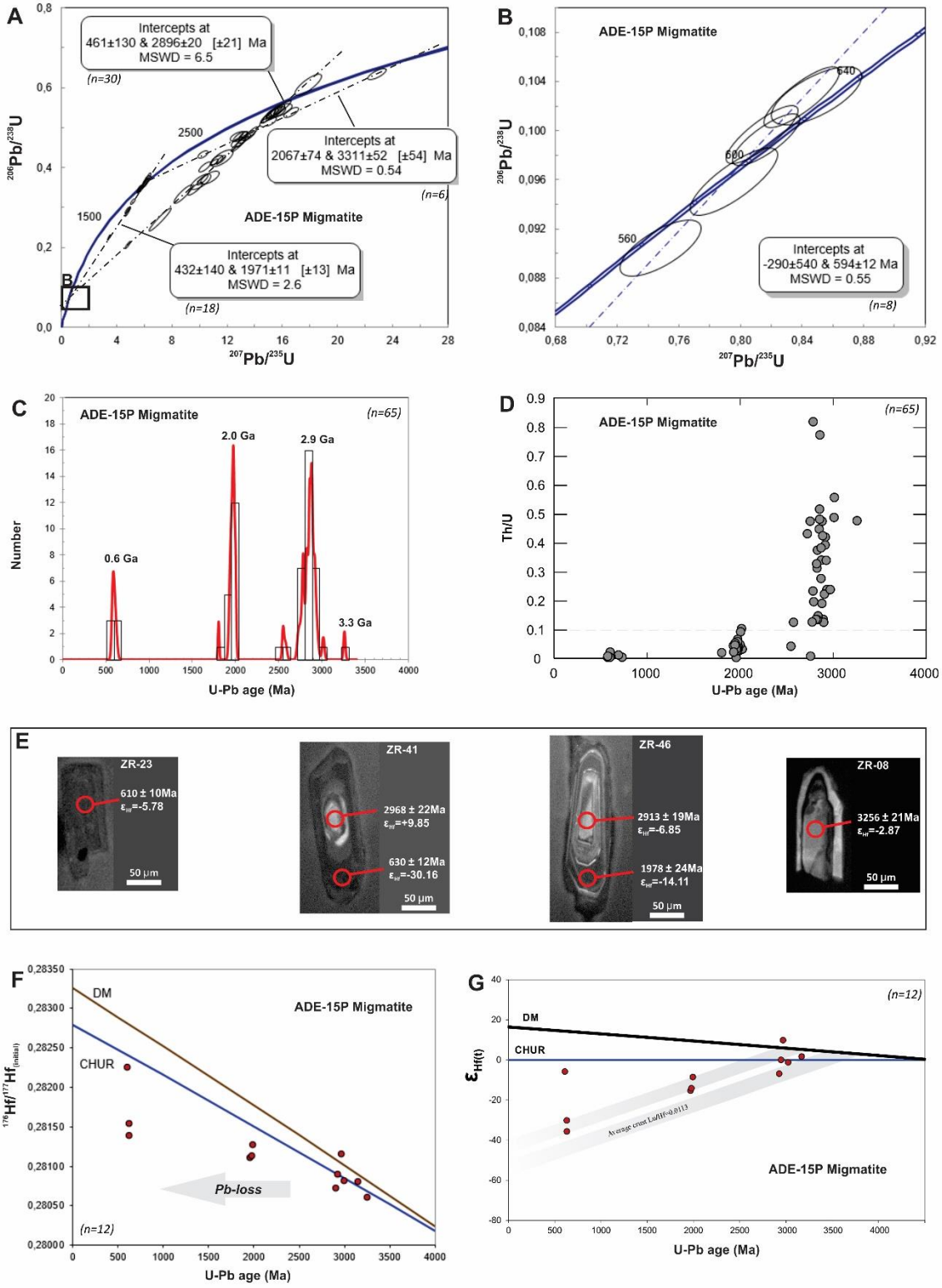

Figure 4.13. A and B) Discordia diagrams for U-Pb zircon data from the ADE-15P paleosome. C) Histogram of $^{207}Pb/^{206}Pb$ ages, D) and Th/U ratio vs $^{207}Pb/^{206}Pb$ ages from ADE-15 migmatite. E) Representative CL images of zircon grains with their ages from the ADE-15 migmatite. D) Initial $^{176}Hf/^{177}Hf(t)$ value versus age (t), and E) the $\varepsilon Hf_{(t)}$ value versus age (t) from the ADE-15 migmatite. Data from Supplementary tables 4.4 and 4.5.

The ADE-23 paleosome sample is from a strongly migmatized igneous protolith with thick felsic veins (Fig. 4.2C), from the central portion of the Campo Grande study area (Fig. 4.1B). The 56 U-Pb isotopic analyses were performed on cores and rims of oscillatory zoned zircon grains. Pb and Hf isotope systematics and Th/U ratios combined with CL imagery allow the recognition of three discordant age trends (Supplementary Table 4.4, Fig. 4.14A). Forty-four zircon crystals yield a Neoarchean discordia age of 2651±19 Ma with high MSWD (7.7) due to concordant zircon analyses between 2682±25 Ma and 2536±30 Ma (Fig. 4.14A, B). The other zircon analyses have a wide $^{207}Pb/^{206}Pb$ age range from 2708 to 2358 Ma and plot below the concordia indicating significant Pb-loss. Data for six zircon cores and rims yield discordant ages at 2525±17 Ma (MSDW=0.79, Fig. 4.14A and B). These Archean zircon grains are rounded (~100 µm) to prismatic (100–200 µm), with length/width ratio of 2:1, show oscillatory banding (Fig. 4.14D), and have Th/U ratios of 0.1 to 0.496 (Fig. 4.14C). Zircon grains dated at 2.65 Ga age can be interpreted as magmatic crystals, representing a protolith crystallization age, whereas zircon grains of 2.52 Ga could represent the first phase of anatexis or a new magmatic pulse (e.g., the grains with Th/U > 0.1). Zircon rims yield discordant ages of 1939±19 Ma (MSDW=1.9, Fig. 4.13A). These Paleoproterozoic U-Pb ages are from zircon rims with lower Th/U ratios (0.013 to 0.048; Fig. 4.14C) and are, thus, interpreted as indicating a metamorphic phase. Like the 2.9 Ga zircon cores of the other paleosomes, most of the 2.65 Ga zircon cores in this paleosome have 1.95 Ga old, very thin, light-colored rims (Fig. 4.14D) that suggest high Hf isotope content as expected for a system that was closed during melt extraction (e.g., Yakymchuk et al., 2015; Li et al., 2018). A single prismatic zircon grain dated at 2133 ± 35 Ma was recorded and can be interpreted to be of an intrusive igneous inheritance.

The $^{176}Hf/^{177}Hf$ initial ratios exhibit a very wide range from 0.281082 to 0.281512. These analyses show Pb loss, forming a horizontal trend indicating that they are most likely derived from the $^{176}Hf/^{177}Hf$ isotopic system of 2.65 Ga (Supplementary Table 4.5, Fig. 4.14E). These Neoarchean zircon analyses have $\varepsilon_{Hf(t)}$ values of -2.17 to +13.49 and T_{DM} values of 2.32 to 2.93 Ga (Fig. 4.14E). Paleoproterozoic zircon rims have $^{176}Hf/^{177}Hf_{(t)}$ from 0.28093 to 0.281607 with variable $\varepsilon_{Hf(t)}$ values between -14.38 and + 5.04, and T_{DM} values of 2.24 to 3.18

Ga (Supplementary Table 4.5, Fig. 4.14E, F). This indicates juvenile sources and reworking during 1.95 Ga anatexis.

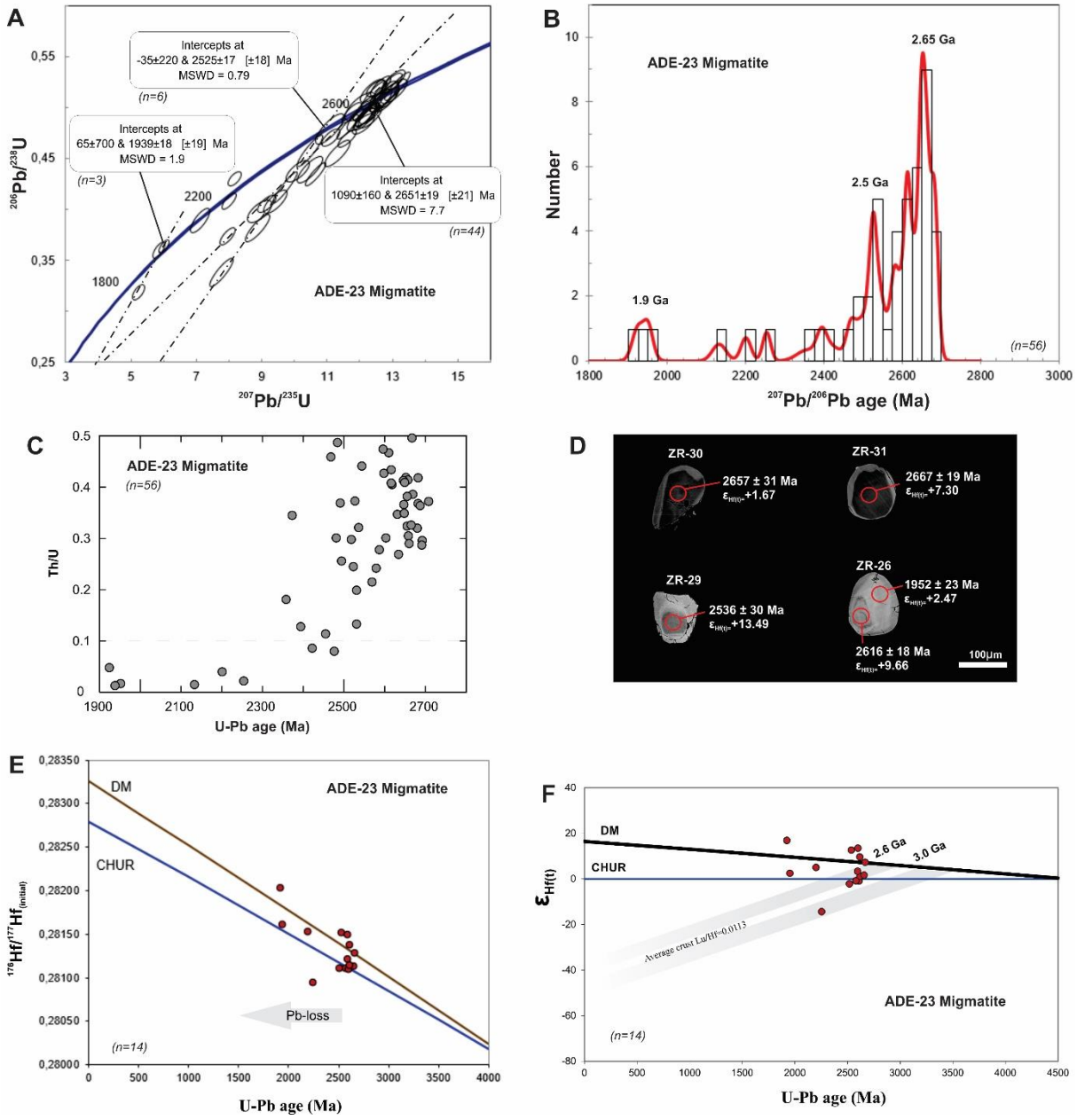

Figure 4.14. A and B) Discordia diagrams for U-Pb zircon data and Histogram of $^{207}Pb/^{206}Pb$ ages from the ADE-23 migmatite. C) Th/U ratio vs $^{207}Pb/^{206}Pb$ ages and D) Representative CL images of zircon grains with their ages from the ADE-23 migmatite. E) Initial $^{176}Hf/^{177}Hf(t)$ value versus age (t), and F) the $\varepsilon Hf_{(t)}$ value versus age (t) from the ADE-23 migmatite. Data from Supplementary tables 4.4 and 4.5.

4.5.4.2 Concordant Leucosome

Zircon grains from the ADE-12L concordant granitic leucosome are prismatic, with lengths of 100-300 µm and length/width ratios of 2:1 to 3:1, and show oscillatory zonation in CL images (Fig.4.15C). Fifteen zircon cores yielded a discordant

upper intercept age of 1950±14 Ma (MSWD=1.9, Fig. 4.15A). These grains have Th/U ratios between 0.02 and 0.85 (Supplementary Table 4.4). The Paleoproterozoic zircon grains have $^{176}Hf/^{177}Hf$ ratios of 0.281177 to 0.281372 with negative $\varepsilon_{Hf(t)}$ values between -3.10 and -8.84 and T_{DM} age from 2.55 to 2.79 Ga (Supplementary Table 4.5, Fig. 4.15B and D). This suggests reworking of Archean crust.

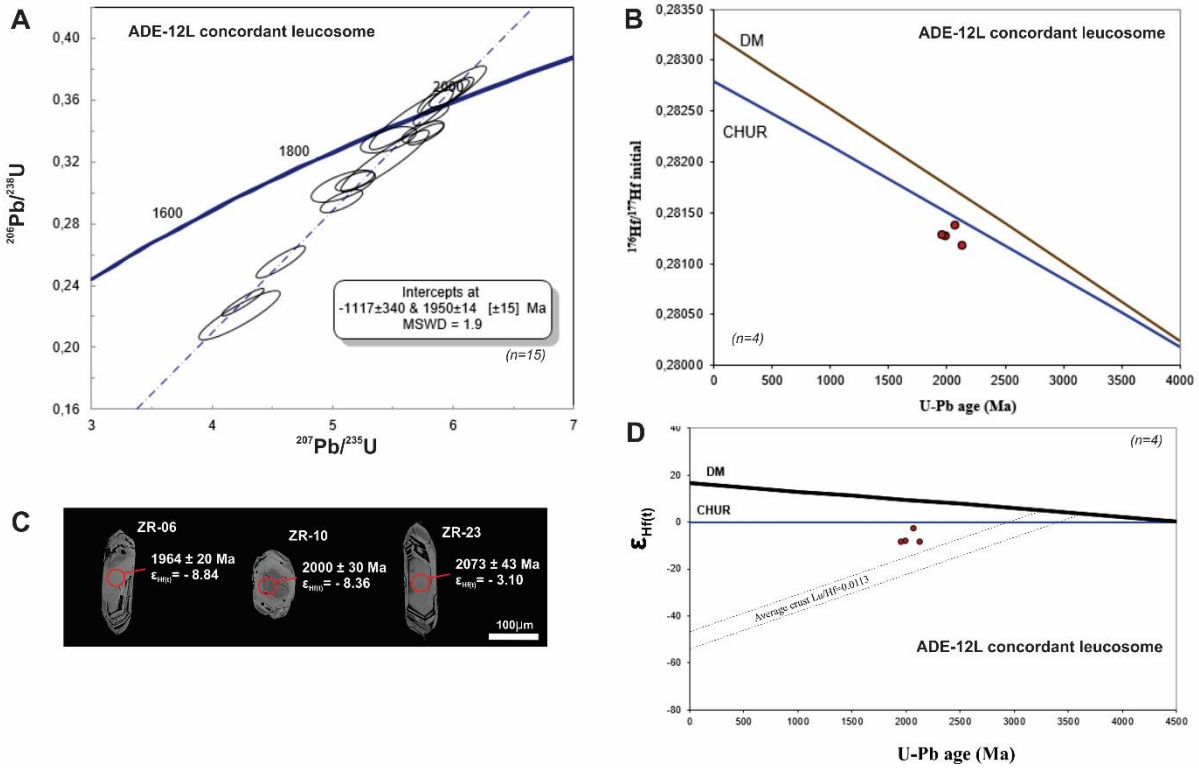

Figure 4.15. A) Discordia diagram for U-Pb zircon data from the ADE-12L concordant leucosome. B) Initial $^{176}Hf/^{177}Hf(t)$ value versus age (t), and D) the εHf(t) value versus age (t) from the ADE-12L concordant leucosome. C) Representative CL images of zircon grains with their ages from the ADE-12L concordant leucosome. Data from Supplementary tables 4.4 and 4.5.

4.5.4.3 Injected Leucosome

Twenty-seven zircon grains from the ADE-18Li injected pegmatite leucosome were subjected to U-Pb isotope analysis (Supplementary Table 4.4, Fig. 4.16). Four zircon rims and one zircon core gave data that align for a discordia age of 571 Ma, with a concordia age of 568±11 Ma (Fig. 4.16B). These Neoproterozoic zircon grains have Th/U ratios from 0.049 to 0.183 (Fig. 4.16D) and are of high brightness (Hf-rich) in CL images (Fig. 4.16E). They are interpreted to have been formed during late anatexis. Fifteen zircon grains combine to yield a discordia age of 2911±27 Ma (MSWD=3.7, Fig. 4.16A), with $^{207}Pb/^{206}Pb$ ages ranging from 2927 to 2628 Ma, and there is one concordant zircon grain of 2901±13 Ma that is

considered an inheritance from a Neoarchean source. Similar behavior was recorded for three Paleoproterozoic zircon cores: two cores yielded a discordia age of 2246±46 Ma and another showed a $^{207}Pb/^{206}Pb$ age of 2238 Ma. This sample supports that the main source for Neoproterozoic partial melting is Archean.

Four dated zircon grains from the injected leucosome were chosen for Lu-Hf isotope analysis (Supplementary Table 4.5, Fig. 4.16F, G). The Neoarchean zircon cores and rims form a group of low $^{176}Hf/^{177}Hf$ ratios of 0.280891 to 0.280985 with Archean T_{DM} ages of 3.04 to 3.17 Ga. They yield $\varepsilon_{Hf(t)}$ values ranging from -2.35 to +2.16. Zircon 17 has a $^{207}Pb/^{206}Pb$ age of 2238 Ma with a $^{176}Hf/^{177}Hf$ ratio of 0.281798, positive $\varepsilon_{Hf(t)}$ value of +15.88, and T_{DM} age of 1.95 Ga, for its core, whereas its rim has a $^{206}Pb/^{238}U$ age of 572 Ma with a $^{176}Hf/^{177}Hf$ ratio of 0.281768, negative $\varepsilon_{Hf(t)}$ of -23.14, and T_{DM} age of 2.11 Ga. Neoproterozoic zircon 15 also has a high $^{176}Hf/^{177}Hf$ ratio of 0.282097 with negative $\varepsilon_{Hf(t)}$ of -12.02 and a T_{DM} age of 1.71 Ga.

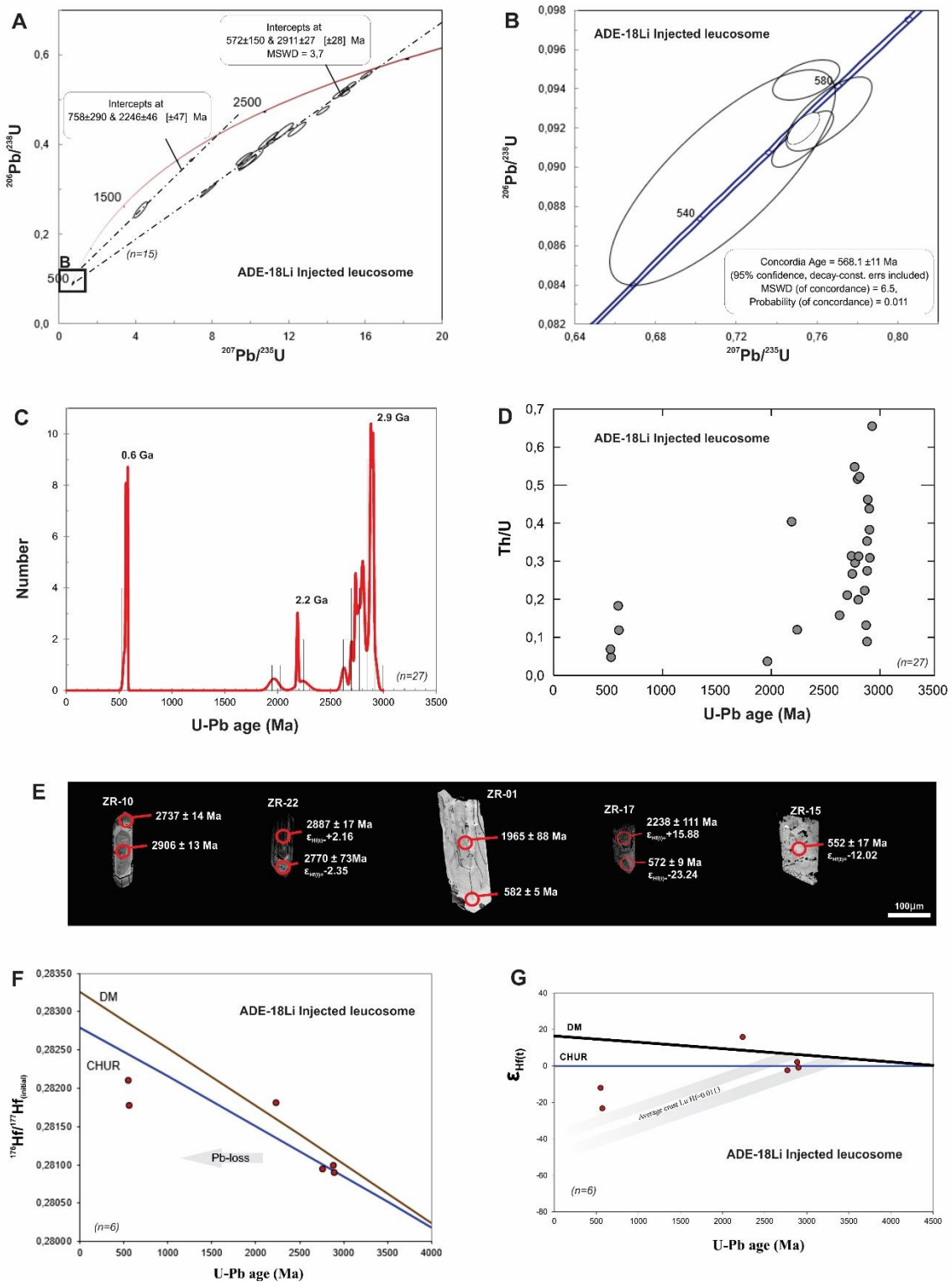

Figure 4.16. A) Discordia and B) concordia diagrams for U-Pb zircon data from the ADE-18Li injected leucosome. C) Histogram of $^{207}Pb/^{206}Pb$ ages, D) and Th/U ratio vs $^{207}Pb/^{206}Pb$ ages from ADE-18Li migmatite sample. E) Representative CL images of zircon grains with their ages from the ADE-Li injected leucosome. D) Initial $^{176}Hf/^{177}Hf(t)$ value versus age (t), and E) the $\varepsilon Hf_{(t)}$ value versus age (t) from the ADE-12Li pegmatite. Data from Supplementary tables 4.4 and 4.5.

4.5.5 Rare Earth Elements in Zircon

The chondrite-normalized REE patterns of zircon cores and rims from migmatite show clearly significant HREE enrichment relative to LREE (Supplementary Table 4.6, and Fig. 4.17). All zircon analyses display this similar REE fractionation behavior. Both Archean magmatic cores and metamorphic cores and rims have negative Eu and positive Ce anomalies with different concentrations of HREE and LREE. These anomalies indicate magmatic source(s) (e.g., Erdmann et al., 2013). Concentrations of REE in the inherited Archean cores are relatively higher than in Paleoproterozoic cores and Neoproterozoic zircon rims. The 1.95 Ga and 0.6 Ga ages can be interpreted to record the timing of metamorphism and migmatite generation. Therefore, zircon trace element patterns may support that anatexis processes occurred in a relatively closed-system fractional crystallization.

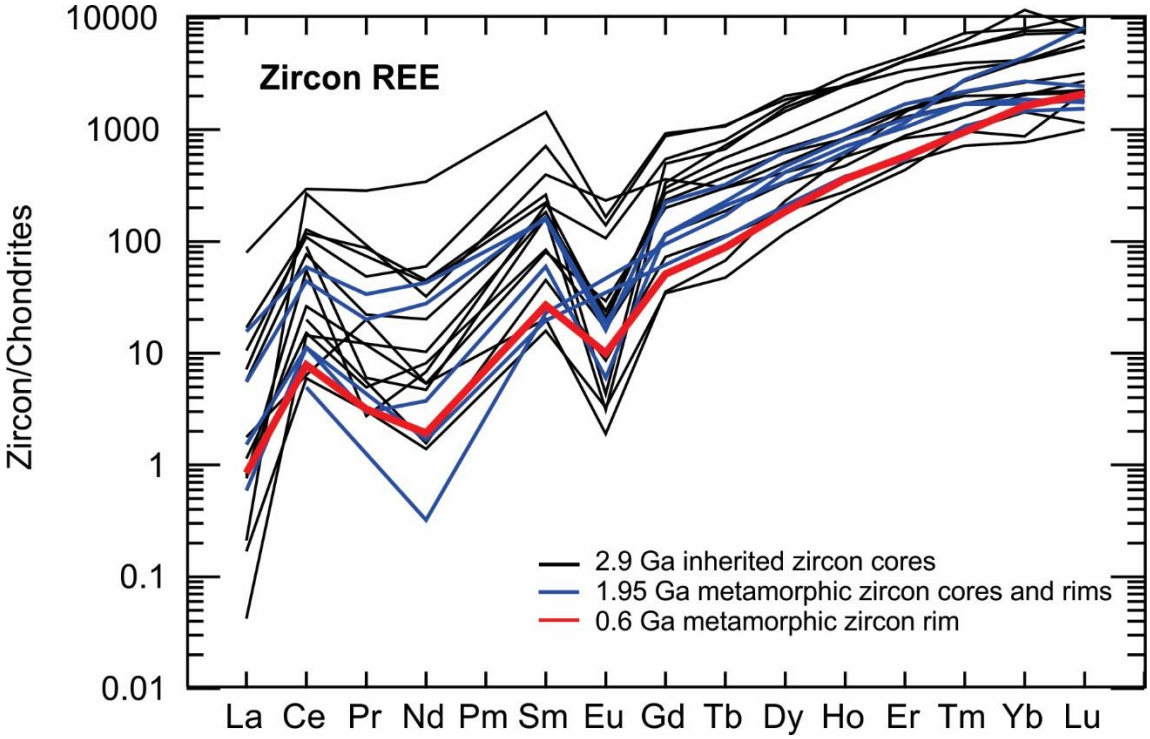

Figure 4.17. Chondrite-normalized REE patterns for zircon from the Campo Grande migmatite (data from Supplementary Table 4.6). Chondrite values are from Sun and McDonough (1989).

4.5.6 Sm-Nd isotopes

T_{DM} model ages and $\varepsilon_{Nd(t)}$ for eleven migmatite samples also suggest a complex history for the studied migmatites (Supplementary Table 4.7, and Fig. 4.18). The paleosome samples have positive and negative $\varepsilon_{Nd(t)}$ values of -3.9 to +4.8, both

with T_{DM} model ages between 2.59 and 3.31 Ga. The concordant leucosome components have negative $\varepsilon_{Nd(t)}$ values (-5.47 to -2.74) and T_{DM} ages between 2.41 and 2.59 Ga. The injected leucosome analyses present strongly negative $\varepsilon_{Nd(t)}$ values (-20.57 and -14.25) with relatively younger T_{DM} model ages of 2.10 and 2.39 Ga. Therefore, whole-rock Nd isotope results also indicate that the isotope systems remained relatively closed despite multiple, protracted phases of migmatite generation.

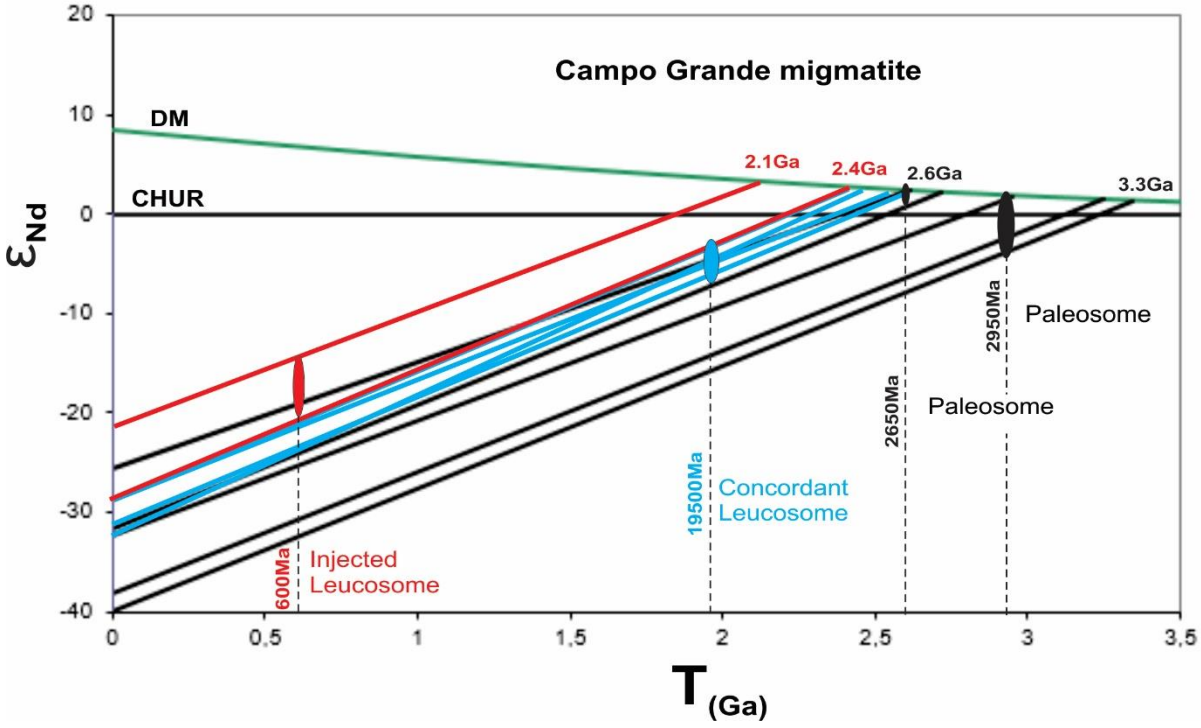

Figure 4.18. Nd isotope compositions of the Campo Grande migmatite phases. Nd evolution diagram for calculated crystallization and migmatisation ages for each sample (data from Supplementary Table 4.7).

4.6 Discussion

4.6.1 Protolith of the Migmatites

U-Pb and Lu-Hf isotope data for zircon from the Campo Grande migmatite were used to constrain the formation ages of the protolith source(s) and the timing of multiple stages of partial melting (Fig. 4.19A to F). The 2.9 Ga and 2.65 Ga inherited zircon grains have enriched HREE and negative Eu and positive Ce anomalies, which supports a magmatic origin for the CL-dark zircon cores. This provides evidence that the migmatites in the Campo Grande area have Archean

precursors. Hafnium isotopic analysis on zircon cores from Archean tonalitic paleosomes yield εHf(t) values of −6.8 to +9.8 and T_{DM} ages of 2.8 - 3.4 Ga (Fig. 4.19D, F). High Th/U ratios (>0.1) in 2.9 Ga and 2.65 Ga zircon (Fig. 4.19E) could reflect inheritance from their magmatic protoliths (e.g. Yakymchuk et al., 2015). The magmatic precursors were emplaced into a Paleoarchean continental crust formed at or > ca. 3.25 Ga, as indicated by inherited zircon cores with negative εHf(t) and T_{DM}(Hf) modal ages of 3.6 Ga (Fig. 4.19F). These Hf results suggest that the protoliths were derived from reworking of Paleo- to Mesoarchean crust generated from juvenile mantle-derived magmatism. In addition, these protoliths may also represent remnants of Archean arc magmatism. The 2.2 Ga inherited zircon crystals may be sourced from the underlying magmatic or supracrustal (e.g., quartz-rich) host during partial melting. Considering that the ADE-23 leucosome sample is the only neosome that contains two such inherited Rhyacian zircon crystals, we exclude this age from further discussion of the protolith(s) of the migmatites. However, we do not rule out the possibility of a minor contribution of partial melting of 2.2 Ga sources to the granitic leucosomes. The tonalitic paleosomes have positive and negative εNd(t) values of -3.9 to +4.8, with Nd T_{DM} model ages of 2.6 to 3.3 Ga. These whole-rock Nd isotope data again support mixing of Archean juvenile and reworked precursors (Fig. 4.18, 4.19F).

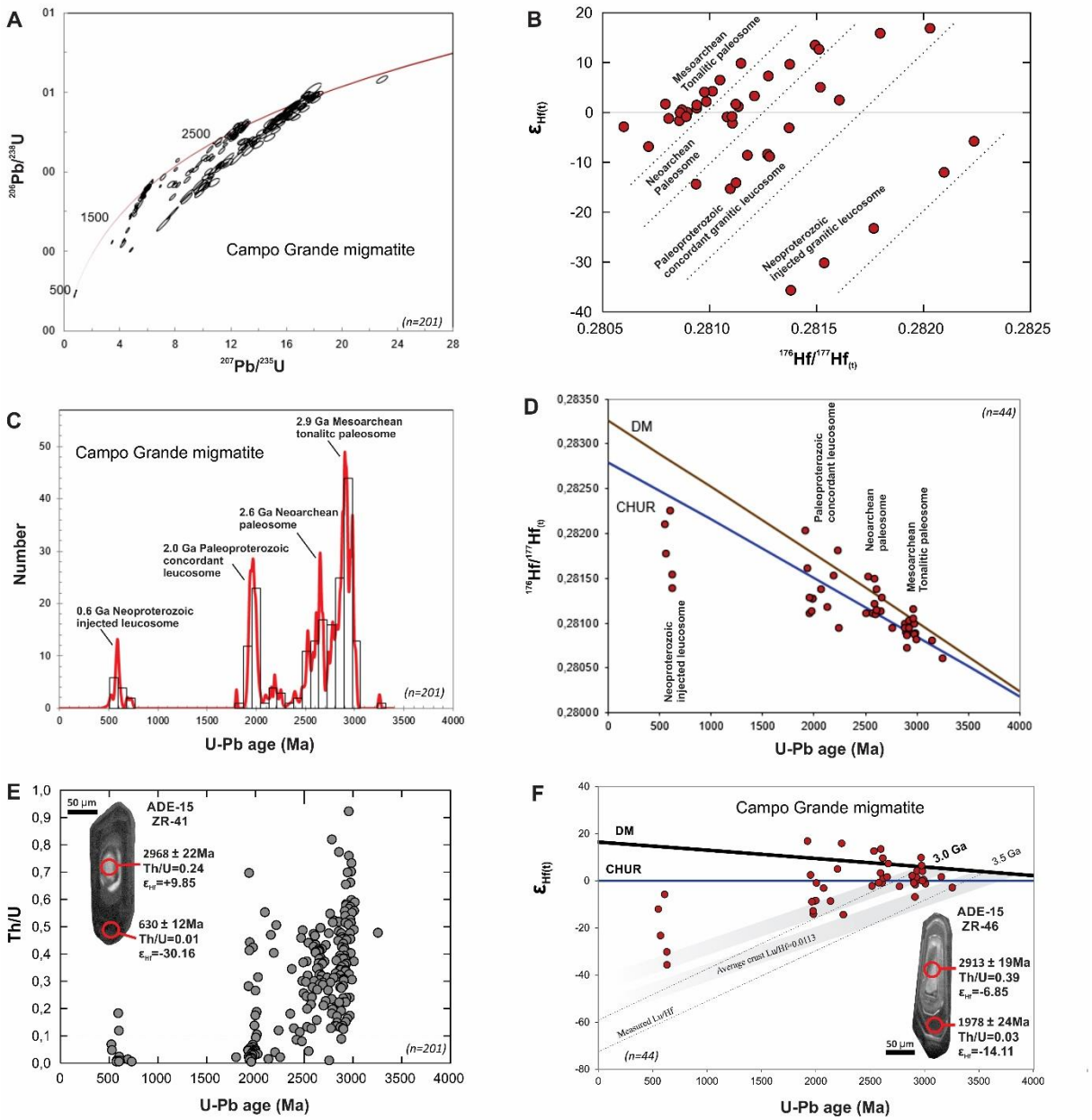

Figure 4.19. A) Discordia diagrams for U-Pb zircon data, B) εHf(t) versus initial $^{176}Hf/^{177}Hf(t)$, C) histogram of U-Pb ages, D) initial $^{176}Hf/^{177}Hf(t)$ value versus age (t), E) Th/U ratio versus $^{207}Pb/^{206}Pb$ and $^{207}Pb/^{235}U$ ages, and F) $\varepsilon Hf_{(t)}$ value versus age (t) from the Campo Grande migmatite components.

Each new migmatite generation developed progressive growth of metamorphic zircon rims on the igneous or older metamorphic cores, and the Nd isotope system was reset by each new leucosome generation (e.g. Gaeta et al., 2018). However, even with the intense crustal reworking with different degrees of partial melting, the isotopic signature of the precursor source remained preserved in the magmatic zircon cores and in the Nd isotope systematics of the paleosome samples. Therefore, U-Pb zircon geochronology, Nd isotopic data, REE and Hf

isotopes in zircon support the presence of an Archean crust as the protolith of the Campo Grande migmatite.

4.6.2 Petrogenesis and Timing of Migmatites

Zircon crystals extracted from migmatite components preserved evidence for solid-state recrystallization (Fig. 4.17, 4.19E). Zircon grains from granitic leucosomes exhibit similar chondrite-normalized REE patterns with negative Eu and positive Ce anomalies, implying that crustal anatexis occurred in the presence of plagioclase and not in equilibrium with garnet (e.g., Rubatto et al., 2009), as supported by the petrographic observations.

Hf isotope compositions of zircon in migmatites are used to characterize the origin of their source rocks and evaluate whether isotopic systems remained closed or opened during partial melting (e.g., Flowerdew et al., 2006; Gerdes and Zeh, 2009; Li et al., 2018). We observed that the initial $^{176}Hf/^{177}Hf$ ratios and εHf(t) values are lower for the 2.9 Ga and 2.65 magmatic zircon crystals than for the 1.95 Ga and 0.6 Ga metamorphic cores and rims. These data suggest that zircon from anatectic melt has more pronounced Hf isotopic heterogeneity than zircon from protolith. The minor variations in initial $^{176}Hf/^{177}Hf$ ratios from inherited zircon cores suggest that Hf isotopes were rather homogenized in the Archean magmatic protolith (e.g., Flowerdew et al., 2006). Initial $^{176}Hf/^{177}Hf$ ratios and εHf(t) ratios of metamorphic rims of zircon grains in the concordant leucosomes are less fractionated than those of zircon cores and rims from injected leucosomes with higher $^{176}Hf/^{177}Hf$ ratios and strong negative εHf(t). This confirms the isotopic disequilibrium during the growth of anatectic zircon grains and rims for the 1.95 Ga concordant and 0.6 Ga injected leucosome. It was possible to recognize metamorphic zircon grains and rims formed during at least two partial melting stages.

The first one is denoted by 1.95 Ga Paleoproterozoic zircon rims and grains with a a wide range of εHf(t) values, between -15.31 and +16.87, with T_{DM}(Hf) model ages between 1.62 and 2.91 Ga (Fig. 4.19D to F). The second anatexis stage is recorded in the pegmatite and granite intrusions that represent the injected leucosomes. These leucosomes have Neoproterozoic (ca. 568 Ma) zircon rims and grains with strong negative εHf(t) of -5.7 to -35.6, and younger T_{DM}(Hf) model

ages ranging from 1.41 to 2.56 Ga (Fig. 4.19D to F). The timing of metamorphism and partial melting in the Campo Grande migmatite is coeval with the crystallization of ca. 1.95 Ga felsic intrusions and ca. 575 Ma syn-transcurrent granitoids in the Borborema Province (Ganade de Araujo et al., 2013; Santos and Santos, 2019).

Zircon crystals from different Archean paleosomes display similar initial $^{176}Hf/^{177}Hf$ ratios and εHf(t) values. These overlapping Hf isotope systematics suggest that they were all derived from analogous protolith sources. On the other hand, the Hf isotope compositions from the Paleo- and Neoproterozoic granitic leucosomes show Hf isotope heterogeneity, which may be related to contributions of externally derived melt or unidentified protoliths. Zircon dissolution tends to release Hf to the melt during anatexis and this Hf will be incorporated into growing zircon rims or grains formed during melt crystallization. Therefore, in a closed Hf isotope system, newly crystallized zircon rims or grains are expected to have similar Hf isotope ratios as their precursor (e.g., Yakymchuk et al., 2015; Li et al., 2018). Most metamorphic zircon rims yield initial $^{176}Hf/^{177}Hf$ ratios and εHf(t) values compatible with those of their inherited cores, supporting that partial melting occurred mainly in a relatively closed isotopic system. Some dissolution textures from zircon crystals in the Campo Grande migmatite also demonstrate that preexisting grains were partially dissolved during anatexis. All this evidence supports that most Paleo- and Neoproterozoic zircon rims and grains are derived from the breakdown of Archean igneous zircon crystals during partial melting in a closed isotopic system.

In the ADE-23 paleosome six zircon grains yield a discordia age of 2.52 Ga that could represent a first migmatitzation phase, but due to the absence of systematic isotopic analyses on these zircon crystals, we have no way to further investigate this possibility. However, despite the Th/U ratio > 0.1 (valid for recognizing the other metamorphic zircon grains of the Campo Grande migmatite), we cannot rule out the possibility of a minor ca. 2.5 Ga anatectic melting event, as already reported for Neoarchean arc-related migmatites in the western Gyeonggi Massif (Lee and Cho, 2013).

4.6.3 Leucosome Composition and Modification

Granitic leucosomes in migmatites are the product of partial melting, but during melt migration, segregation, ascent, and emplacement occurs significant change from initial melt compositions (e.g. Morfin et al., 2014; Carvalho et al., 2017; Li et al., 2018). Therefore, compositional variations of leucosomes reflect the fractional crystallization sequence of evolving partial melting. The variation of granitic leucosome REE patterns with negative and positive Eu anomalies may reflect the process of fractional crystallization of feldspar (e.g. Sawyer, 2008). Concentrations of Al_2O_3, Na_2O, K_2O, Rb, Sr and Ba are negatively correlated with increasing SiO_2, which also suggests that the evolving compositions of granitic leucosomes are controlled by the fractional crystallization of sodic plagioclase, K-feldspar and quartz (e.g., Morfin et al., 2014; Carvalho et al., 2017). Some biotite crystals have irregular and corroded rims. Such crystals occur in leucosomes in variable proportion, which suggests that the entrainment of residual biotite contributed to compositional evolution of anatectic melts (Fig. 4.10C, D). The entrainment of peritectic biotite can lead to an increase of the concentrations of Y, resulting in relatively low Sr/Y ratios in leucosome samples (Fig. 4.8A).

The ADE-18L concordant granitic leucosome formed at 1.95 Ga is interpreted to represent an early-formed feldspar cumulate. This leucosome has a higher Sr/Y ratio (Fig. 4.8B) and a positive Eu anomaly reflecting the high proportion of cumulate plagioclase (Fig. 4.10C). The ADE-18Li injected pegmatite leucosome, formed at 568 ± 11 Ma, has a negative Eu anomaly that indicates feldspar at its source. This pegmatite has similar HREE patterns to the ADE-18L concordant leucosome and strong enrichment in LREE, which indicates a low melting rate, as expected for pegmatite formation (Yu et al., 2019).

Covariations between Zr and Hf (Fig. 4.8E), as well as Sum of REE and Th (Fig. 4.8F) suggest that zircon and monazite are the main controls on the compositions of these elements in granitic leucosomes. The REE are negatively correlated with P_2O_5 (Fig. 4.8G), which suggests that apatite was an important control on REE element content - mainly in the injected leucosome, but invariably in the paleosomes. Covariation between TiO_2 and SiO_2 (Fig. 4.8H) and depletion of Nb, Ta and Ti on a primitive-mantle normalized diagram (Fig. 4.10B, D, F) could reflect the entrainment of peritectic or residual titanite (e.g., Storkey et al., 2005; Li

et al., 2018) in the absence of rutile. Concentrations of V are positively correlated with increasing TiO_2 (Fig. 4.8H) and this element is most enriched in paleosome, which suggests that ilmenite was also involved in partial melting. Covariation among FeO + MgO, HREE and SiO_2 in the migmatite samples may be explained by the segregation of biotite from anatectic melt in the absence of garnet and amphibole. Therefore, fractional crystallization of feldspar and biotite, together with the behavior of zircon, apatite and titanite, all affected the geochemical patterns of the Campo Grande migmatite.

4.6.4 Migmatite Temperature Estimates

Temperatures of the Campo Grande migmatite were calculated from whole-rock compositions (Supplementary Table 4.8) based on zircon saturation temperature (T_{zicsat}; e.g. Milord et al., 2001). In addition, the liquidus temperature of the melt (T_{melt}) was also calculated from Ti in biotite concentrations in paleosome and leucosome (Supplementary Table 4.9). The Watson and Harrison (1983) model, $T_{Zircsat}$ (°C) = (12900/ln(497600 / Zr (ppm)) + 3.8 + 0.85 (M-1))−273, was revised by Boehnke et al. (2013) to $T_{Zircsat}$ (°C) = (10108/ln(497600 / Zr (ppm)) + 1.48 + 1.16 (M-1)) − 273, which is commonly used to calculate $T_{Zircsat}$. These models use the cationic ratio M [(Na+K+2Ca)/(Al.Si)}], and Zr contents are used to find $T_{zircsat}$. The M parameter ranges from 1.2 to 1.5 (see Supplementary Table 4.3) in the migmatite components. These values are within the calibration range (0.9–1.9), allowing the calculation of $T_{Zircsat}$. The more recent models of Gervasoni et al. (2016), $T_{Zircsat}$ (°C) = lnZr (ppm) − 4.29 + 1.35(lnG)/0.0056, include G as the molar ratio $(3Al_2O_3+SiO_2)/(Na_2O+K_2O+CaO+MgO+FeO)$ and Zr (ppm) as the concentration of Zr measured in whole-rock compositions. “Temperature of zircon saturation” geothermometers are interpreted to give maximum melting temperatures because of the common presence of inherited zircon cores.

By using the geothermometer of Watson and Harrison (1983), $T_{Zircsat}$ from paleosomes shows a range from 764°C to 830°C. Concordant leucosome values range from 649°C to 953°C, and $T_{Zircsat}$ for injected leucosomes yields temperatures between 640°C and 872°C. The Boehnke et al. (2013) temperature equation yields ranges for lower values from 540° to 591°C for paleosome, 449° to 688°C for concordant leucosome, and 442° to 624°C for injected leucosome.

The Gervasoni et al. (2016) model yields intermediate temperature ranges for paleosome (538° - 717°C), concordant leucosome (381° - 937°C), and injected leucosome (379° - 830°C). Therefore, a large variation in temperature is observed due to the application of different geothermometers (Fig. 4.20A). Furthermore, the $T_{Zircsat}$ increases with increasing SiO_2 contents from paleosome to leucosome, but T_{melt} decreases with increasing silica values (Siégel et al., 2017). Thus, the $T_{Zircsat}$ may not reflect the T_{melt}, mainly for the leucosome. Charlier et al. (2005) also showed that for higher silica values (SiO_2 > 72 wt.%), $T_{Zircsat}$ will be higher than T_{melt} due to the fact that melts can be zircon-oversaturated (Watson and Harrison, 1983). To overcome this problem, T_{melt} should be estimated by the Ti geothermometers for zircon (e.g., Ferry and Watson, 2007) and for biotite (e.g., Wu and Chen, 2015). By using the model of Wu and Chen (2015), biotite crystallization temperatures can be determined by calculating T from the equation: $\ln[T(°C)]= 6.313+0.224\ln(X_{Ti}) – 0.288\ln(X_{Fe}) – 0.449\ln(X_{Mg}) + 0.15\ P(GPa)$, with Xj=j/(Fe+Mg+AlVI+Ti). This geothermometer can be applied within the calibration range from (50 – 840 ºC, for 0.1 – 1.9 GPa, and X_{Ti} = 0.02–0.14 in biotite. This then provides a minimum temperature of crystallization.

The Wu and Chen (2015) geothermometer shows that biotite crystallized around ~ 512º and ~ 634ºC in the 2.9 Ga paleosome samples, whereas biotite crystals from 1.95 Ga concordant leucosomes were crystallized at ~ 689º and ~741°C (Supplementary Table 4.9). These temperatures are slightly lower than those obtained by the conventional $T_{zircsat}$ method of Watson and Harrison (1983), but they are consistent with the Boehnke et al. (2013) and Gervasoni et al. (2016) geothermometer results (Fig. 4.20B). The variable temperatures may possibly be the result of different growth stages of biotite, and/or variable degrees of modification due to from re-equilibration during partial melting. Biotite crystals in the 1.95 Ga concordant leucosome define higher and heterogeneous temperatures (598 to 793ºC), suggesting that the calculated temperatures may represent different conditions of crystallization. These partial melting temperatures are consistent with a melt-producing reaction related to the breakdown of muscovite (Ms + Pl + Qtz + H_2O = melt) that would have produced more sodic melt with no production of peritectic minerals at temperatures of 650º ± 50°C and pressures of 5 ± 1 kbar (e.g., Patiño Douce and Harris, 1998). Absence of garnet and cordierite indicates that the biotite dehydration melting

reaction (biotite + Al_2SiO_5 = garnet + K-feldspar + cordierite + melt) was not attained. In addition, biotite is not required as a reactant as evidenced by absence of ferromagnesian peritectic phases. On the other hand, the lower temperatures obtained from biotite grains of 2.9 Ga paleosomes could be related to re-equilibration of their primary composition (e.g., 432º - 546ºC; ADE-15 sample).

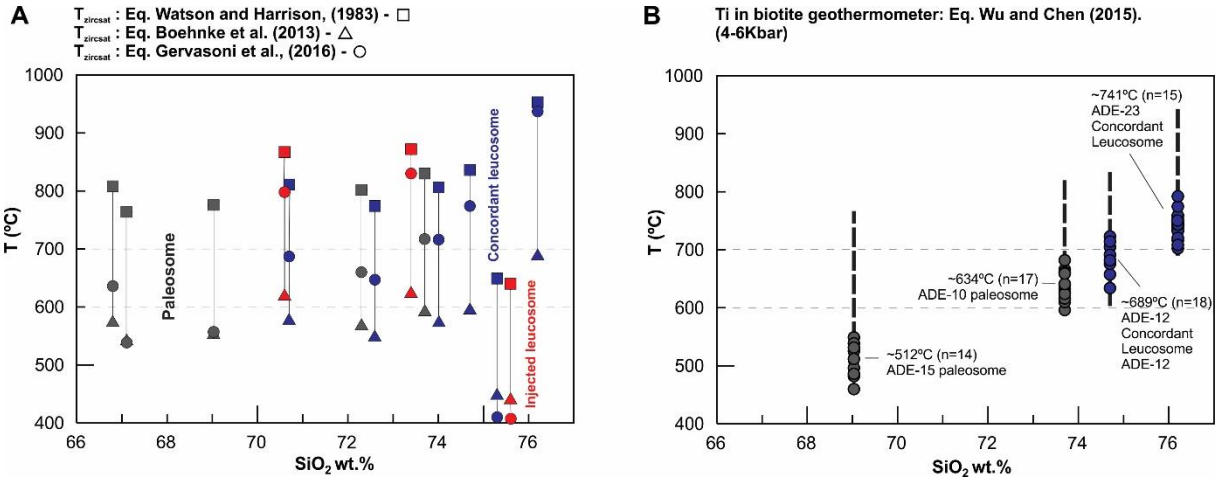

Figure 4.20. Temperatures calculated for Campo Grande migmatite phases. A) Zircon saturation temperatures (Tzircsat) according the Watson and Harrison (1983), Boehnke et al. (2013), and Gervasoni et al. (2016) geothermometers plotted versus SiO2 contents. Black symbols represent the analyses of paleosomes, blue - concordant leucosomes and red – injected leucosomes. B) Ti-in-biotite geothermometer after Wu and Chen (2015) versus SiO_2 contents. Black dashed lines show the Tzircsat range.

4.6.5 Campo Grande Anatexis Reactions

Partial melting represents the main process in the generation of granite melts, mainly by the breakdown of hydrous minerals, such as muscovite, biotite or amphibole, due to externally derived water-aided melting (e.g., Weinberg and Hasalová, 2015). Therefore, anatexis is a crucial process in the evolution of many high-grade metamorphic terranes (Reichardt and Weinberg, 2012; Weinberg and Hasalová, 2015; Li at al., 2018). The presence of an H_2O-bearing fluid decreases the melting temperature of biotite-bearing Archean metatonalite, so that in the presence of a hydrous fluid at 6 kbar, melting begins at temperatures of about 680°C (Watkins et al., 2007). Coarse-grained amphibole with inclusions of resorbed reactant minerals, such as biotite, plagioclase and quartz, is interpreted as evidence of this reaction (Reichardt and Weinberg, 2012). Following these studies, it is reasonable to propose that the absence of amphibole in the Campo

Grande leucogranites again indicates that anatexis occurred at a temperature below 680ºC.

The main evidence that supports fluid-aided melting in the Campo Grande migmatite is the fact that there are no anhydrous peritectic minerals (e.g., garnet) that could be interpreted as products of incongruent fluid-absent melting reactions (e.g., Clemens, 2006). The metamorphic zircon rims are enriched in the HREE. This enrichment would not have been possible if the zircon rims and grains had been crystallized in equilibrium with garnet (e.g., Rubatto, 2009). The amount of in-situ and in-source leucosome (20 to 40 vol%) would hardly be generated from fluid-absent melting (e.g., Palin et al., 2016). Therefore, petrological and mineral chemistry data support that anatexis can be represented by the following melting reaction involving fluid: Mg-rich Bt + Ca-rich Pl + Qz + H_2O-rich fluid = Fe-rich Bt + Na-rich Pl + (Kfs + Na-rich Pl + H_2O + Qz) melt, at a minimum temperature of 634ºC (Ti in biotite from granitic leucosome – see Migmatite Temperature Estimates above) and 4-6 kbar pressure.

The abundance of granitic leucosome in the Campo Grande migmatite requires influx of externally sourced H_2O-rich fluids during partial melting, due to the rheological properties of the mid– to lower crust (Weinberg and Hasalová, 2015). Source(s) of water may be granitic melts that release a large amount of H_2O into the host rock during emplacement (e.g., Morfin et al., 2014). Shear zones have a prominent control on water-fluxed melting of granite and orthogneiss and supply the major pathway for migration of aqueous fluid (e.g. Genier et al., 2008). Deep structure reactivation such as the Portalegre shear zone during Paleo- and Neoproterozoic orogeny may have functioned as permeable transport conduit for H_2O-rich fluids to support the melting reactions. Therefore, the Campo Grande Block likely experienced pervasive ductile deformation during partial melting and developed many high-strain zones. These structures could have facilitated the migration of aqueous fluids (see also Sawyer, 2010). The isotopic signature and nature of the aqueous fluid source that percolated through these ductile shear zones will require specific alteration of isotope systematics due to large-scale influx of such fluids.

4.6.5.1 Biotite Composition Variation

Biotite is the most common ferromagnesian mineral phase in igneous and metamorphic rocks in the continental crust, and as such a powerful indicator of the genesis and evolution of continental crust (e.g., Nachit et al., 2005; Acosta-Vigil et al., 2010; 2012). In the Al_2O_3 vs. FeO and MgO vs FeO diagrams (Abdel-Rahman, 1994), the analyzed migmatites define two distinct groups: biotite analyses from the tonalite paleosomes have calc-alkaline orogenic suite signature (Fig. 4.21A, B, C), and represent the pre-migmatisation phase. The composition of preserved protolith source, little or unaffected by melting and melt extraction, is represented by tonalite ADE-18P paleosome (FeO + MgO = 5 – 6%). On the other hand, biotite crystals from the concordant granitic leucosomes have a signature consistent with peraluminous magmatism (Fig. 4.21A, B, C), and represent primary biotite formed during migmatite generation. The Rb vs. (Y + Nb) discrimination diagram (Pearce, 1996) for whole-rock analyses also supports the post-collisional character of the Campo Grande migmatisation (Fig. 4.21D).

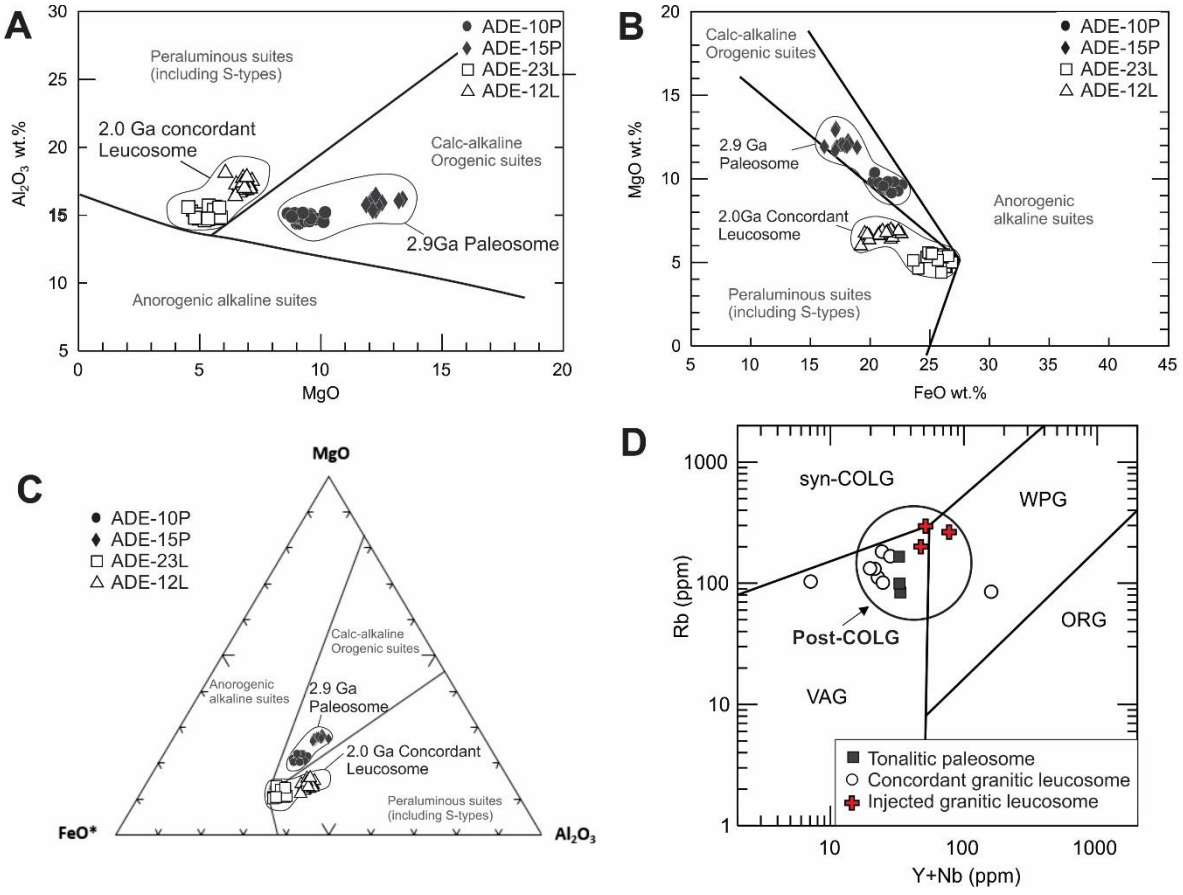

Figure 4.21. A, B and C) Biotite versus “magmatic suites" diagrams (Abdel-Rahman, 1994) for biotite from the Campo Grande migmatite constituents. The $A_{l2}O_3$ - FeO - MgO diagram confirms that biotite in the paleosome component has calc-alkaline signatures, while biotite grains obtained in concordant

leucosome have peraluminous signature. Atoms per formula unit were calculated using 22 oxygens for biotite. D) Rb vs. (Y + Nb) discrimination diagram (after Pearce, 1996) supporting the post-collisional character of the Campo Grande migmatisation.

Concordant leucosomes consist of a mineral assemblage fully formed during partial melting. These leucosomes also have low FeO and MgO contents (FeO + MgO = 1-2 %), indicating minor dissolution of biotite and minor influence of residue contamination (Patiño Douce and Harris, 1998). However, leucosome layers contain a proportion of biotite residues (e.g., ADE-23L sample; FeO + MgO = 4%) mainly at the interface with the paleosome layers. Therefore, some elements (e.g., Fe, Ti, Fe, Mg and Nb) are strongly concentrated into the restite layers that constitute the melanosome migmatite component (e.g. Sola et al., 2013). The biotite composition depends on the conditions during cooling (Nachit et al., 2005), and magmatic biotite from paleosomes follows a more Mg-rich trend with low temperature (~512º and ~634ºC), whereas biotite from partial melting shows a Fe-rich trend with high temperature (~689º and 741ºC). Therefore, biotite remained stable and was used as a tracer for the solid fraction during melt segregation (e.g. Milord et al., 2001) to distinguish the 2.9 Ga Mg-rich biotite orogenic precursors and 1.95 Ga Fe-rich biotite from peraluminous anatexis (Fig. 4.22A to C).

4.6.5.2 Plagioclase Composition Variation

The REE patterns with Eu anomalies support that plagioclase fractionation was crucial for migmatite differentiation. Plagioclase analyses show the difference between tonalitic paleosome and granitic leucosome. Oligoclase analyses from the 2.9 Ga protolith have higher Ca content with An_{24-30}, whereas plagioclase crystals from the 1.95 Ga anatectic melt have lower Ca content with An_{17-23} (Fig. 4.22D). These mineral chemistry variations occur because during melting of plagioclase, Na should preferentially fractionate into the neosome (e.g., leucosome and melanosome), leaving an anorthite-enriched plagioclase in the paleosome residue (e.g. Gardien et al., 2000; Marchildon and Brown, 2001).

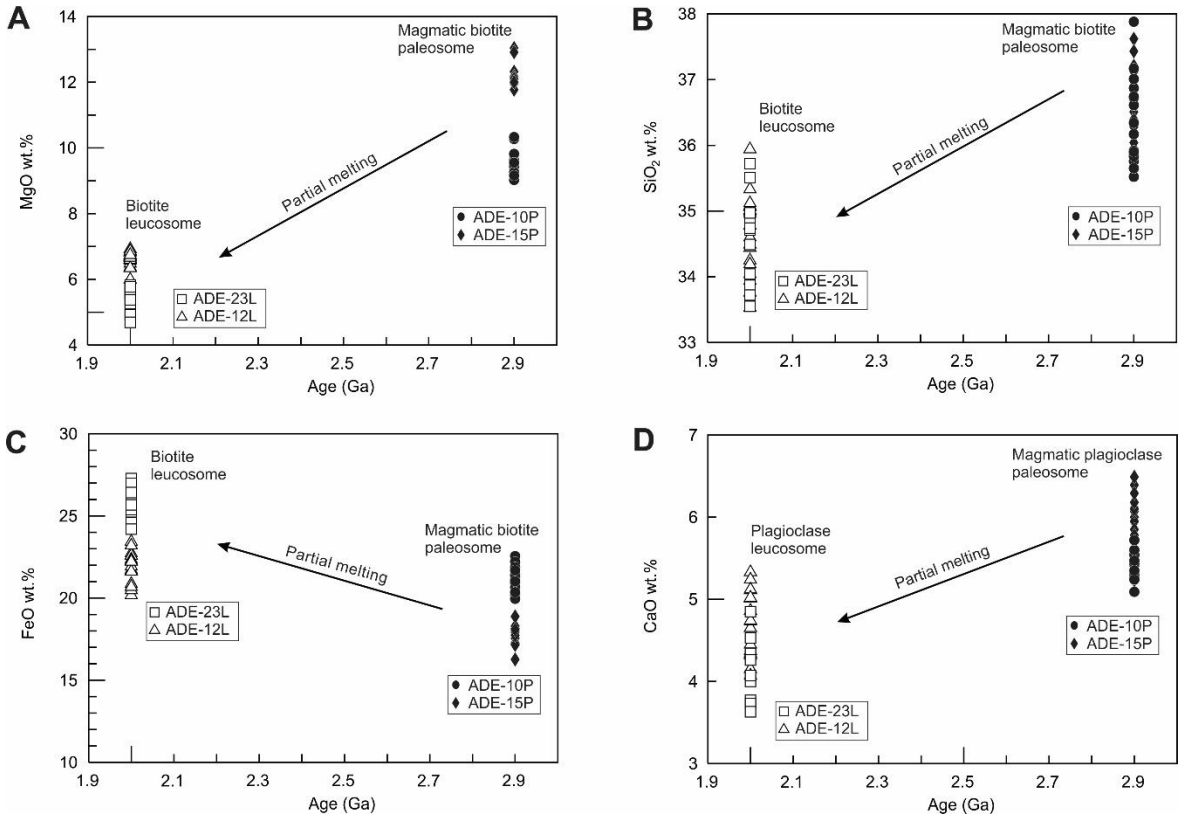

Figure 4.22. A to C) Harker type diagrams showing the biotite element compositions the -Pb ages of paleosome (ADE-15P and ADE-10P) and concordant leucosome (ADE-12L and ADE-23L) from the Campo Grande migmatite. Mg-rich biotite in the 2.9 Ga tonalitic protolith is of lower temperature than Fe-rich biotite from the 1.95 Ga granitic leucosome. D) Harker diagram showing the plagioclase CaO compositions versus U-Pb ages of paleosomes and leucosomes from the Campo Grande migmatite.

4.6.6 Tectonic Implications

The evolution of orogenic systems includes crustal thickening followed by orogenic collapse, thinning and exhumation with extensive post-orogenic anatexis (e.g., Wang et al., 2011). Granites and migmatite generated in these systems have a wide range of zircon ages due to extensive continuum or intermittent melting (e.g., Yu et al., 2019). Partial melting requires high regional heat influx into the crust, mainly by fluids that could have been channeled along regional shear zones or by advection of regional metamorphic fluids (Brown et al., 2011; Weinberg and Hasalová, 2015). Therefore, all data support that multiple migmatite generations in the Campo Grande Block were formed at mid-crustal conditions (4-6 kbar and 561º- 682ºC). A 1.95 Ga melt crystallized within the source, giving rise to feldspar-enriched in-situ or in-source leucosome, whereas ca. 568 Ma melt was extracted and intruded into the previous migmatitic phases at upper-crustal level.

The Campo Grande migmatite phases are a consequence of melt evolution involving fractional crystallization and melt extraction at mid-crustal conditions, likely assisted by regional deformation. Field and geochronological relationships constrain the evolution of migmatite generation, supported by the ~1.4 Ga age gap between the crystallization of the 1.95 Ga granitic concordant leucosome and the 568 Ma intrusive pegmatite leucosome. Therefore, we interpret that Rhyacian and Neoproterozoic orogens generated crustal thickening accompanied by progressive crustal anatexis, with formation of extensive low-T migmatites linked to the influx of fluids and extra heat from post-collision processes.

4.6.7 Geodynamic Significance of the Campo Grande migmatite

The Rio Grande do Norte domain records a complex and long history of accretionary processes from the Paleoarchean to Neoproterozoic (Dantas et al., 2004; 2013). High-pressure metamorphic rocks reflect continental collision after the subduction of oceanic crust in the Campo Grande Block, which is characterized by retrogression eclogite-facies conditions (Ferreira et al., 2019b). The protoliths of eclogites are Archean (ca. 2.65 Ga) mafic igneous rocks with tholeiitic composition interpreted as oceanic crust, that also records 1.95 Ga and 0.6 Ga metamorphic events (Ferreira et al., 2019b). Therefore, the Campo Grande metamorphic complex records multiple igneous and metamorphic events. The anatexis processes corroborate the Paleo- and Neoproterozoic tectonic-thermal evolution history recognized in the Campo Grande Block and Rio Grande do Norte domain.

The Campo Grande anatexis products are compatible with hydrate-breakdown melting at relatively low pressures in the mid-crust. High-K calc-alkaline magmatism in a continental arc setting and partial melting of HP amphibolite-facies rocks occurred between 2.2 and 2.0 G Ma in the Rio Grande do Norte domain (e.g., Souza et al., 2007). The Nd isotopic characteristics of negative $\varepsilon Nd(t)$ and $T_{DM}(Nd)$ between 2.41 and 2.59 Ga for the concordant leucosomes are consistent with Rhyacian high-K calc-alkaline magmatism recorded elsewhere within the Rio Grande do Norte domain (e.g., Souza et al., 2007; Hollanda et al., 2011; Ferreira el al., 2019a). These events are older than the timing of 1.95 Ga concordant granitic leucosomes in the Campo Grande Block. Moreover,

Neoproterozoic injected leucosomes are also younger than the oceanic subduction event (620 – 590 Ma) (Ferreira et al., 2019b), but it is coeval with continental arc magmatism (ca. 575 Ma) in the Rio Grande do Norte domain (e.g., Archanjo et al., 2013; Ganade de Araujo et al., 2013). The Nd isotopic compositions from the injected leucosomes, pegmatite and granite intrusions, show negative εNd(t) and T_{DM}(Nd) model ages between 2.1 and 2.3 Ga, and overlap with the compositions of the Neoproterozoic igneous rocks of the Rio Grande do Norte domain (Souza et al., 2016). Therefore, we propose that the most likely hypothesis is that partial melting processes resulted from heat advected by continental arc magmatism (e.g., Slagstad et al., 2005; Li et al., 2018).

The Campo Grande Block is bounded by the Jaguaribe terrane to the west and is part of the Rio Piranhas-Seridó terrane. The Lajes region also has a tectonic evolution evidenced in the Rio Piranhas-Seridó basement with Archean records and Proterozoic tectono-thermal events (Ferreira el al., 2019b). The Campo Grande Block is a smaller-scale microcontinent fragment that was accreted to the margin of the Jaguaribe terrain, whereby the Portalegre shear zone was developed during the Brasiliano-Pan African orogeny.

The Campo Grande migmatite complex is located in the northeastern part of the Borborema Province. These migmatites had a Meso- and Neoarchean protolith source(s) and were subject to high-temperature (630-680°C) and low-pressure (4-6 kbar) crustal anatexis at 1.95 Ga and ca. 568 Ma. We propose that these partial melting processes resulted from magmatic heating and H_2O-rich fluid released by coeval post-collisional magmatism caused by continental crustal differentiation.

4.7 Conclusion

In the field paleosome, melanosome, concordant and injected leucosomes were distinguished as components of the Campo Grande migmatite complex. Petrography, mineral chemistry, whole-rock geochemistry, zircon U–Pb geochronology with Hf isotope and rare-earth element analyses of zircon from the various migmatite phases allowed us to recognize the petrogenetic evolution of the Campo Grande migmatite, i.e., to describe the differentiation of continental crust in this portion of the Borborema Province.

The main findings of this work are:

1. Hf isotope and REE compositions support that anatectic zircon rims grew in a relatively closed isotopic system by dissolution-reprecipitation of pre-existing magmatic zircon cores. Nd isotope patterns also advocate the hypothesis of a closed isotope system during the multiple stages of migmatite generation.

2. Migmatites were formed by water-aided melting of intermediate to felsic rocks through the breakdown of biotite (630º-680ºC) at relatively low pressures in the mid-crust (4-6 kbar). Fractional crystallization of sodic-plagioclase, K-feldspar and accessory minerals growth and dissolution had a significant influence role on the geochemical patterns of the granitic leucosomes.

3. Partial melting likely took place at 1.95 Ga and 568 Ma in a post-collisional tectonic setting, reworking Archean continental basement.

4. The protoliths of the migmatites were tonalites magmas with continental arc signature that represent a Mesoarchean (2.9 Ga) calc-alkaline crust.

4.8 Acknowledgments

This study is part of the first author's PhD thesis in development at the Institute of Geosciences, Universidade de Brasília. The authors acknowledge support from INCT Estudos Tectônicos (CAPES/CNPq - 465613/2014-4 and FAPDF - 193.001.263/2017). ELD, RAF, IMN and WUR acknowledge CNPq research fellowships.

4.9 Reference

Abdel-Rahman, A.M. 1994. Nature of biotites from alkaline, calc-alkaline, and peraluminous magmas. Journal of Petrology 35, 525-541.

Acosta-Vigil, A. Buick, I. Cesare, B. London, D. Morgan, VI, G.B., 2012. The extent of equilibration between melt and residuum during regional anatexis and its implications for differentiation of the continental crust: A study of partially melted metapelitic enclaves. Journal of Petrology 53, 1319–1356.

Albarède, F., Telouk, P., Blichert-Toft, J., Boyet. M., Agranier, A., Nelson, B., 2004. Precise and accurate isotopic measurements using multiple-collector ICPMS. Geochimica et Cosmochimica Acta 68, 2725-2744.

Almeida, F.F.M., Brito Neves, B.B., Fuck, R., 1981. Brazilian structural provinces: an introduction. Earth Science Reviews 17, 1–29.

Archanjo, C.J., Viegas, L.G.F., Hollanda, M.H.B.M., Souza, L.C. and Liu, D., 2013. Timing of the HT/LP transpression in the Neoproterozoic Seridó Belt (Borborema Province, Brazil): constraints from U\Pb (SHRIMP) geochronology and implications for the connections between NE Brazil and West Africa. Gondwana Research 23, 701– 714.

Arthaud, M.H., Caby, R., Fuck, R.A., Dantas, E.L., Parente, C.V., 2008. Geology of the northern Borborema Province, NE Brazil and its correlation with Nigeria, NW Africa. In: Pankhurst, R.J., Trouw, R.A.J., Brito Neves, B.B., de Wit, M.J. (Eds.), West Gondwana: Pre-Cenozoic Correlation Across the South Atlantic Region. Geological Society of London 294, 49–67. doi.org/10.1144/SP294.

Barker, F., 1979. Trondhjemite: definition, environment and hypotheses of origin, in: Barker, F. (ed.), Trondhjemites, Dacites and Related Rocks, Elsevier Amsterdam, 1-12.

Bhadra, S., Das, S., Bhattacharya, A., 2007. Shear zone-hosted migmatites (Eastern India): the role of dynamic melting in the generation of REE-depleted felsic melts, and implications for disequilibrium melting. Journal of Petrology 48, 435–457.

Blichert-Toft, J. and Albarède, F., 1997. The Lu-Hf isotope geochemistry of chondrites and the evolution of the mantle-crust system. Earth Planet. Sci. Lett. 148, 243-258.

Boehnke, P., Watson, E.B., Trail, D., Harrison, T.M., Schmitt, A.K., 2013. Zircon saturation re-revisited. Chem. Geol. 351, 324–334.

Brito Neves, B.B., 2011. The Paleoproterozoic in the South-American continent: Diversity in the geologic time. Journal of South American Earth Sciences 32, 270–286.

Brito Neves, B.B., and Fuck, R. A., 2014. Basement of the South american platform: Half Laurentian (N-NW) + Half Gondwanan. Precambrian Research, 244:75-86.

Brown, M., Korhnen, F.J., Siddoway, C.S., 2011. Organizing melt flow through the crust. Elements 7, 261–266.

Brown, M., 2014. The contribution of metamorphic petrology to understanding lithosphere evolution and geodynamics. Geoscience Frontiers 5, 553-569.

Bühn, B.M., Pimentel, M,M., Matteini, M., Dantas, E.L., 2009. High spatial resolution analyses of Pb and U isotopes for geochronology by laser ablation multi-collector inductively coupled plasma mass spectrometry LA-MC-ICP-MS. Anais da Academia Brasileira de Ciências 81, 1-16.

Caby, R., Sial, A.N., Arthaud, M.H., Vauchez, A., 1991. Crustal evolution and the Brasiliano orogeny in northeast Brazil. In: Dallmeyer, R.D., Lécorché, J.P. (Eds.), The West African Orogens and Circum-Pacific-Atlantic Correlatives. Springer-Verlag, Berlin,373–397.

Carvalho, B. B., Sawyer, E. W. and Janasi, V. A., 2017. Enhancing Maficity of Granitic Magma during Anatexis: Entrainment of Infertile Mafic Lithologies. Journal of Petrology 58, 1333–1362.

Charlier, B.L.A., Wilson, C.J.N., Lowenstern, J.B., Blake, S., Van Calsteren, P.W., Davidson, J.P., 2005. Magma generation at a large, hyperactive silicic volcano (Taupo, New Zealand) revealed by U/Th and U/Pb systematics in zircons. Journal of Petrology 46, 3-32.

Chauvel, C. and Blichert-Toft, J., 2001. A hafnium isotope and trace element perspective on melting of the depleted mantle. Earth Planet. Sci. Lett. 190, 137-151.

Chu, N.C., Taylor, R.N., Chavagnac, V., Nesbitt, R.W., Boella, R.M., Milton, J.A., German, C.R., Bayon, G., Burton, K., 2002. Hf isotope ratio analysis using multicollector inductively coupled plasma mass spectrometry: an evaluation of isobaric interference corrections. J. Anal. Atom. Spectrom. 17, 1567-1574.

Clemens, J. D., 2006. Melting of the continental crust: fluid regimes, melting reactions, and source-rock fertility. In: Brown, M. & Rushmer, T. (eds) Evolution and Differentiation of the Continental Crust. Cambridge University Press, 297–331.

Clemens, J. D., Helps, P. A. & Stevens, G., 2010. Chemical structure in granitic magmas—a signal from the source? Earth and Environmental Science Transactions of the Royal Society of Edinburgh 100, 159–172.

Dantas, E.L., Negrão, M.M., Buhn, B., 2008. 2.3 Ga continental crust generation in the Rio Grande do norte terrane, NE-Brazil, in: 6th South American Symposium on Isotope Geology, Abstract Volume, 40.

Dantas, E. L., Souza, Z. S., Wernick, E., Hackspacher, P. C., Martin, H., Xiaodong, D., & Li, J. W., 2013. Crustal growth in the 3.4-2.7 Ga São José de Campestre

Massif, Borborema Province, NE Brazil. Precambrian Research, 227, 120–156.

Dantas, E.L., Van Schmus W.R., Hackspacher P.C., Fetter A.H., Neves B.B.B., Cordani U.G., Nutman A.P., Williams S., 2004. The 3.4-3.5 São José do Campestre Massif, NE Brazil: remnants of the oldest crust in South America. Precambrian Research 130, 113-137.

DePaolo, D. J., 1981. A neodymium and strontium isotopic study of the Mesozoic calc-alkaline granitic batholithys of the Sierra Nevada and Peninsular Ranges, California. Journal of Geophysical Research 86, 10470-10488.

Droop, G.T.R., 1987. A general equation for estimating Fe3+ concentrations in ferromagnesian silicates and oxides from microprobe analyses, using stoichiometric criteria. Mineralogical Magazine 51, 431-435.

Erdmann, S., Wodicka, N., Jackson, S.E., Corrigan, D., 2013. Zircon textures and composition: refractory recorders of magmatic volatile evolution? Contrib. Mineral. Petrol. 165 (1), 45–71.

Ferreira, A.C.D., Ferreira Filho, C.F., Dantas, E.L., Souza, V.S., 2019a. Paleoproterozoic Mafic-Ultramafic Magmatism in the Northern Borborema Province, NE Brazil: Tectonic Setting and Potential for Deposits. The Journal of Geology, 127. https://doi.org/10.1086/704256

Ferreira, A.C.D., Dantas, E.L., Santos, T.J. S., Fuck, R.A, Tedeschi, M., 2019b. High-pressure metamorphic rocks in the Borborema Province, Northeast Brazil: reworking of Archean oceanic crust during Neoproterozoic orogeny. Geoscience Frontiers, GSF-D-19-00183.

Ferry, J., Watson, E., 2007. New thermodynamic models and revised calibrations for the Ti-in-zircon and Zr-in rutile thermometers. Contrib. Mineral. Petrol. 154 (4), 429–437.

Flowerdew, M.J., Millar, I.L., Vaughan, A.P.M., Horstwood, M.S.A., Fanning, C.M., 2006. The source of granitic gneisses and migmatites in the Antarctic Peninsula: a combined U–Pb SHRIMP and laser ablation Hf isotope study of complex zircons. Contributions to Mineralogy and Petrology 151, 751–768.

Gaeta, M., Giuliani, A., Di Rocco, T., Tecchiato, V., Perinelli, V., Kamenetsky. V.S., 2018. Isotopic disequilibrium in migmatitic hornfels of the gennargentu igneous complex (Sardinia, Italy) records the formation of low 87Sr/86Sr melts from a mica-rich source. J. Petrol., 59, 1309-1328.

Ganade de Araujo, C. E., Weinberg, R. F. and Cordani, U. G., 2013. Extruding the Borborema Province (NE-Brazil): a two-stage Neoproterozoic collision process. Terra Nova 26 (2), 157–168.

Ganzhorn, A. C., Trap, P., Arbaret, L., Champallier, R., Fauconnier, J., Labrousse, L. and Prouteau, G., 2016. Impact of gneissic layering and localized incipient melting upon melt flow during experimental deformation of migmatites. Journal of Structural Geology 85, 68–84.

Gardien, V., Thompson, A.B., Ulmer, P., 2000. Melting of biotite + plagioclase + quartz gneisses: the role of H2O in the stability of amphibole. Journal of Petrology 41, 651–666.

Gao, L.E., Zeng, L., Asimow, P.D., 2016. Contrasting geochemical signatures of fluid-absent versus fluid-fluxed melting of muscovite in metasedimentary sources: the Himalayan leucogranites. Geology 45, 39–42.

Genier, F., Bussy, F., Epard, J.L., Baumgartner, L., 2008. Water-assisted migmatization of metagraywackes in a Variscan shear zone, Aiguilles-Rouges massif, western Alps. Lithos 102, 575–59.

Gerdes, A. and Zeh, A., 2009. Zircon formation versus zircon alteration - new insights from combined UePb and LueHf in-situ LA-ICP-MS analyses, and consequences for the interpretation of Archean zircon from the Central Zone of the Limpopo Belt. Chem. Geol. 261, 230-243.

Gervasoni, F., Klemme, S., Rocha-Júnior, E.R.V., Berndt, J., 2016. Zircon saturation in silicate melts: a new and improved model for aluminous and alkaline melts. Contrib. Mineral. Petrol. 171 (3), 1–12.

Gioia, S.M.C. L. and Pimentel, M.M., 2000. The Sm-Nd isotopic method in the Geochronology Laboratory of the University of Brasília. Anais Academia Brasileira de Ciências 72, 219-245.

Harrison, T.M., Blichert-Toft, J., Müller, W., Albarede, F., Holden, P., Mojzsis, S.J., 2005. Heterogeneous Hadean Hafnium: Evidence of Continental Crust at 4.4 to 4.5 Ga. Science 310, 1947–1950.

Hollanda, M.H.B.M., Archanjo, C.J., Souza, L.C., Dunyi, L., Armstrong, L., 2011. Long-lived Paleoproterozoic granitic magmatism in the Seridó-Jaguaribe domain, Borborema Province-NE Brazil. Journal of South American Earth Sciences 32, 287-300.

Hollanda, M.H.B.M., Archanjo, C.J., Bautista, J.R., Souza, L.C., 2015. Detrital zircon ages and Nd isotope compositions of the Seridó and Lavras da Mangabeira basins (Borborema Province, NE Brazil): Evidence for exhumation and recycling associated with a major shift in sedimentary provenance. Precambrian Research 258, 186–207.

Holness, M.B., Cesare, B., Sawyer, E.W., 2011. Melted rocks under the microscope: microstructures and their interpretation. Elements 7, 247–252.

Jackson, S.E., Pearson, N. J., Griffin, W.L., Belousova, E.A., 2004. The application of laser ablation-inductively coupled plasma-mass spectrometry to in situ U-Pb zircon geochronology. Chemical Geology 211, 47-69.

Jardim de Sá, E.F., 1994. A Faixa Seridó (Província Borborema, Ne Brasil) e o seu Significado Geodinâmico na Cadeia Brasiliana/Pan-Africana. Tese de Doutorado, Universidade De Brasília, 803pp.

Johannes, W., Holtz, F., 1996. Petrogenesis and Experimental Petrology of Granitic Rocks, vol. 335. Springer, Berlin.

Lee, Y. and Cho, M., 2013. Fluid-present disequilibrium melting in Neoarchean arc-related migmatites of Daeijak Island, western Gyeonggi Massif, Korea. Lithos 179, 249-262.

Li, X., Niua, M., Yakymchuk, C., Yanc, Z., Fu. C., Zhaoa, Q., 2018. Anatexis of former arcmagmatic rocks during oceanic subduction: A case study from the NorthWulan gneiss complex. Gondwana Research 61, 128–149.

Liu, S.W., Wang, M.J., Wan, Y.S., Guo, R.R., Wang, W., Wang, K., Guo, B.R., Fu, J.H., Hu., F.Y., 2017. A reworked ~3.45 Ga continental microblock of the North China Craton: constraints from zircon U-Pb-Lu-Hf isotopic systematics of the Archean Beitai-Waitoushan migmatite-syenogranite complex. Precambr. Research 303, 332-354

Ludwig, K. R. 2008. User's Manual for Isoplot 3.0. A geochronological Toolkit for Microsoft Excel. Berkeley Geochronology Center, 4, 76.

Marchildon, N., and Brown, M., 2001. Melt segregation in late syn-tectonic anatectic migmatites: an example from the Onawa Contact Aureole, Maine, USA. Phys. Chem. Earth (Part A: Solid Earth Geodesy) 26, 225–229.

Milord, I., Sawyer, E.W, and Brown, M., 2001. Formation of Diatexite Migmatite and Granite Magma during Anatexis of Semi-pelitic Metasedimentary Rocks: an Example from St. Malo, France, Journal of Petrology 42 (3), 487–505.

Morfin, S., Sawyer, E.W., Bandyayera, D., 2014. The geochemical signature of a felsic injection complex in the continental crust: Opinaca Subprovince, Quebec. Lithos 196, 339–355.

Morel, M.L.A., Nebel, O., Nebel-Jacobsen, Y.L., Miller, J.S., Vroon, P.Z., 2008. Hafnium isotope characterization of the GJ-1 zircon reference material by solution and laser-ablation MC-ICPMS. Chem. Geol. 255, 231-235.

Nascimento, M.A.L., Galindo, A.C., Medeiros, V.C., 2015. Ediacaran to Cambrian magmatic suites in the Rio Grande do Norte domain, extreme Northeastern Borborema Province (NE of Brazil): Current knowledge. Journal of South American Earth Sciences 58, 281-299.

Nachit, H.; Ibhi, A.; Abia, E.H.;Ohoud, M.B. 2005. Discrimination between primary magmatic biotites, reequilibrated and neoformed biotites. C.R. Geoscience 337, 1415-1420.

Padilha, A.L., Vitorello, Í., Pádua, M.B., Fuck, R.A., 2017. Cryptic signatures of Neoproterozoic accretionary events in northeast Brazil imaged by magnetotellurics: Implications for the assembly of West Gondwana. Tectonophysics 699, 164-177.

Palin, R.M.,White, R.W., Green, E.C.R., Diener, J.F.A., Powell, R., Holland, T.J.B., 2016. High-grade metamorphism and partial melting of basic and intermediate rocks. Journal of Metamorphic Geology 34, 871–892.

Patchett, J.P., 1983. The importance of the Lu–Hf isotopic system in studies of planetary chronology and chemical evolution. Geochim. Cosmochim. Acta 47, 81–91.

Patiño Douce, A.E., Harris, N., 1998. Experimental constraints on Himalayan anatexis. Journal of Petrology 39, 689–710.

Pearce, J. A., 1996. Sources and settings of granitic rocks. Episodes 19(4), 120-125.

Reichardt, H., Weinberg, R.F., 2012. Hornblende chemistry and meta- and diatexites and its retention in the source of leucogranites: an example from the Karakoram shear zone, NW India. Journal of Petrology 53, 1287–1318.

Rubatto, D., Hermann, J., Berger, A., Engi, M., 2009. Protracted fluid-induced melting during Barrovian metamorphism in the Central Alps. Contributions to Mineralogy and Petrology 158, 703–722.

Santos, E., and Santos, L. C. M. L, 2019. Reappraisal of the Sumé Complex: geochemistry and geochronology of metaigneous rocks and implications for

Paleoproteorozoic subduction-accretion events in the Borborema Province, NE Brazil. Braz. J. Geol. vol.49, n.1. n.1, e20180083. Epub Apr 08, 2019. ISSN 2317-4889. http://dx.doi.org/10.1590/2317-4889201920180083.

Sawyer, E. W., 2008. Atlas of Migmatites. Canadian Mineralogist, Special Publication 9, 371pp.

Sawyer, E.W., 2010. Migmatites formed by water-fluxed partial melting of a leucogranodiorite protolith: microstructures in the residual rocks and source of the fluid. Lithos 116, 273–286

Sawyer, E.W., 2014. The inception and growth of leucosomes: Microstructure at the start of melt segregation in migmatites. Journal of Metamorphic Geology 32, 695–712.

Sawyer, E. W., Cesare, B. & Brown, M., 2011. When the continental crust melts. Elements 7, 229–234.

Scherer, E. Münker, C., and Mezger, K., 2001. Calibration of the lutetium-hafnium clock. Science 293, 683-687.

Siégel, C., Bryan, S.E., Allen, C.M., Gust, D.A., 2017. Use and abuse of zircon-based thermometers: a critical review and a recommended approach to identify antecrystic zircons. Earth Sci. Rev. 176, 87–116. http://dx.doi.org/10.1016/j.earscirev.2017.08.011.

Shand, S. J., 1943. Eruptive Rocks. Their Genesis, Composition, Classification, and Their Relation to Ore-Deposits with a Chapter on Meteorite New York: John Wiley & Sons.

Slagstad, T., Jamieson, R.A., Culshaw, N.G., 2005. Formation, crystallization, and migration of melt in the mid-orogenic crust: Muskoka domain migmatites, Grenville Province, Ontario. Journal of Petrology 46, 893–919.

Sola, A.M., Becchio, R.A., Pimentel, M.M., 2013. Petrogenesis of migmatites and leucogranites from Sierra de Molinos, Salta, Northwest Argentina: a petrologic and geochemical study. Lithos 177, 470–491

Souza, Z. S., Kalsbeek, F., Deng X. D., Frei, R., Kokfelt, T. F., Dantas, E. L., Li, J.W., Pimentel, M., Galindo, A. C., 2016. Generation of continental crust in the northern part of the Borborema Province, northeastern Brazil, from Archean to Neoproterozoic. Journal of South American Earth Sciences 68, 68-96.

Souza, Z.S., Martin, H., Peucat, J.J., Jardim de Sá, E. F., Macedo, M.H.F., 2007. Calc-Alkaline Magmatism at the Archea Souza, Z.S., Martin, H., Peucat, J.J.,

Jardim de Sá, E. F., Macedo, M.H.F., 2007. Calc-Alkaline Magmatism at the Archean-Proterozoic Transition: The Caicó Complex Basement (Ne Brasil). Jounal of Petrology 48, 2149-2185.n-Proterozoic Transition: The Caicó Complex Basement (Ne Brasil). Jounal of Petrology 48, 2149-2185.

Storkey, A.C., Hermann, J., Hand, M., Buick, I.S., 2005. Using in situ trace-element determinations to monitor partial-melting processes in metabasites. Journal of Petrology 46, 1283–1308.

Tischendorf, G., Gottesmann, B., Förster, H. J., and Trumbull, R. B., 1997. On Li-bearing micas: estimating Li from electron microprobe analyses and improved diagram for graphical representation: Mineralogical Magazine, v. 61, 809 – 834.

Vanderhaeghe, O., 2009. Migmatites, granites and orogeny: flow modes of partially molten rocks and magmas associated with melt/solid segregation in orogenic belts. Tectonophysics 477, 119–134.

Van Schmus, W. R., Brito Neves, B.B., Williams, I. S., Hackspacher, P. C., Fetter, A. H., Dantas, E. L., Babinski, M., 2003. The Seridó Group of NE Brazil, a late Neoproterozoic pre- to syn-collisional basin in West Gondwana: insights form SHRIMP U-Pb detrital zircon ages and Sm-Nd crustal residence (TDM) ages. Precambrian Research 127, 287-327.

Van Schmus, W.R., Kozuch, M., Brito Neves, B.B., 2011. Precambrian history of the Zona Transversal of the Borborema Province, NE Brazil: insights from Sm–Nd and U–Pb geochronology. Journal of South American Earth Sciences 31, 227-252.

Van Schmus, W.R., Oliveira, E.P, Silva Filho, A.F., Toteu, S.F., Penaye, J., Guimarães, I. P., 2008. Proterozoic links between the Borborema Province, NE Brazil, and the Central African Fold Belt. In: Pankhurst R.J., Trouw R.A.J., Brito Neves B.B and De Wit M.J. (eds.) West Gondwana: Pre-Cenozoic correlations across the South Atlantic region. Geological Society, London, Special Publication 294, 69-99.

Wang, Y.J., Zhang, A.M., Fan, W.M., Zhao, G.C., Zhang, G.W., Zhang, Y.Z., Zhang, F.F., Li, S.Z., 2011. Kwangsian crustal anatexis within the eastern South China Block: geochemical, zircon U–Pb geochronological and Hf isotopic fingerprints from the gneissoid granites of Wugong and Wuyi-Yunkai domains. Lithos 127, 239–260.

Watkins, J.M., Clemens, J.D., Treloar, P.J., 2007. Archaean TTGs as sources of younger granitic magmas: melting of sodic metatonalites at 0.6–1.2 GPa. Contributions to Mineralogy and Petrology 154, 91–110.

Watson, E.B., Harrison, T.M., 1983. Zircon saturation revisited: temperature and composition effects in a variety of crustal magma types. Earth Planet. Sci. Lett. 64 (2), 295–304.

Weinberg, R.F., Hasalová, P., 2015. Water-fluxed melting of the continental crust: a review. Lithos 212, 158–188.

Wedepohl, K.H., 1995. The compositions of the continental crust. Geochim. Cosmochim. Acta 59, 1217-1232.

White, A. J. & Chappell, B. W., 1977. Ultrametamorphism and granitoid genesis. Tectonophysics 43, 7–22.

Whitney, D.L. and Evans, B.W., 2010. Abbreviations for names of rock-forming minerals. American Mineralogist 95, 185-187.

Wu, C.M., and Chen, H. X., 2015. Revised Ti-in-biotite geothermometer for ilmenite or rutile-bearing crustal metapelites. Sci. Bull. 60, 116–121. DOI 10.1007/s11434-014-0674-y

Yakymchuk, C., Brown, C.R., Brown, M., Siddoway, C.S., Fanning, C.M., Korhonen, F.J., 2015. Paleozoic evolution of western Marie Byrd Land, Antarctica. Geological Society of America Bulletin 127, 1464–1484.

Yu, P.P., Zhang, Y.Z., Zhou, Y.Z., Weinberg, R.F., Zheng, Y., Yang, W.B., 2019. Melt evolution of crustal anatexis recorded by the Early Paleozoic Baiyunshan migmatite-granite suite in South China. Lithos 332–333:83–98.

Supplementary Table 4.1. Analyses of micas from the Campo Grande migmatite.

Sample	SiO2	TiO2	Al2O3	FeO	MnO	MgO	CaO	Na2O	K2O	F	Cl	Cr2O3	V2O3	NiO	Total	Mg/(Mg+Fe)
ADE-12 Bt 1	33,53	2,71	17,02	22,57	0,39	6,37	0,07	0,12	9,76	0,00	0,11	0,00	0,08	0,01	92,75	0,33
ADE-12 Bt 2	34,25	3,10	16,99	23,21	0,48	6,68	0,02	0,05	9,62	0,00	0,09	0,02	0,00	0,04	94,55	0,34
ADE-12 Bt 3	33,94	2,67	16,51	22,72	0,36	6,48	0,10	0,09	8,34	0,00	0,09	0,00	0,03	0,00	91,34	0,34
ADE-12 Bt 4	35,94	2,68	17,74	20,17	0,32	5,99	0,14	0,13	8,40	0,00	0,12	0,03	0,05	0,01	91,72	0,35
ADE-12 Bt 5	35,01	2,60	17,02	20,48	0,32	6,72	0,15	0,10	8,79	0,00	0,14	0,01	0,03	0,00	91,37	0,37
ADE-12 Bt 6	35,08	3,17	16,95	21,71	0,42	6,73	0,06	0,05	9,39	0,00	0,11	0,00	0,02	0,03	93,72	0,36
ADE-12 Bt 7	34,44	2,84	17,42	21,64	0,38	6,61	0,03	0,11	9,39	0,00	0,13	0,00	0,00	0,01	92,98	0,35
ADE-12 Bt 8	34,04	3,19	16,97	23,42	0,49	6,69	0,00	0,12	9,82	0,00	0,10	0,02	0,00	0,00	94,87	0,34
ADE-12 Bt 9	34,99	3,85	17,24	22,58	0,31	6,92	0,00	0,16	9,85	0,00	0,07	0,00	0,09	0,01	96,06	0,35
ADE-12 Bt 10	34,49	3,37	16,92	23,19	0,42	6,85	0,03	0,11	9,59	0,00	0,10	0,00	0,09	0,02	95,19	0,35
ADE-12 Bt 11	35,06	2,96	16,97	22,34	0,24	6,82	0,04	0,10	8,86	0,36	0,08	0,00	0,00	0,01	93,83	0,35
ADE-12 Bt 12	34,78	3,47	16,67	22,25	0,41	6,73	0,07	0,08	8,43	0,24	0,09	0,06	0,07	0,03	93,38	0,35
ADE-12 Bt 13	34,19	3,01	16,76	21,91	0,39	6,85	0,02	0,09	8,92	0,18	0,08	0,07	0,03	0,03	92,52	0,36
ADE-12 Bt 14	34,60	3,06	16,84	20,85	0,26	6,57	0,02	0,08	8,86	0,24	0,08	0,09	0,08	0,00	91,62	0,36
ADE-12 Bt 15	33,76	2,83	17,14	21,60	0,32	6,60	0,03	0,09	8,40	0,27	0,11	0,02	0,03	0,02	91,20	0,35
ADE-12 Bt 17	35,33	2,76	16,80	20,68	0,39	6,66	0,10	0,14	8,07	0,23	0,12	0,00	0,01	0,00	91,28	0,36
ADE-12 Bt 18	35,12	2,01	17,47	22,21	0,29	6,74	0,07	0,09	8,13	0,26	0,12	0,00	0,04	0,04	92,57	0,35
ADE-12 Ms 1	46,44	0,95	31,63	1,77	0,05	0,92	0,00	0,37	9,16	0,00	0,01	0,06	0,05	0,00	91,39	
ADE-12 Ms 2	46,26	0,74	32,14	1,71	0,05	0,81	0,00	0,45	8,92	0,00	0,02	0,08	0,00	0,00	91,16	
ADE-12 Ms 3	46,25	1,15	31,99	1,53	0,00	0,84	0,01	0,41	8,83	0,00	0,00	0,05	0,04	0,07	91,18	
ADE-12 Ms 4	45,59	0,98	32,28	1,45	0,02	0,63	0,02	0,37	9,55	0,00	0,01	0,00	0,06	0,03	91,00	
ADE-12 Ms 5	45,47	1,04	31,69	1,37	0,00	0,65	0,01	0,35	8,78	0,00	0,01	0,05	0,02	0,00	89,43	
ADE-12 Ms 6	44,85	1,01	30,85	1,43	0,00	0,71	0,03	0,53	8,43	0,00	0,04	0,00	0,00	0,00	87,86	
ADE-12 Ms 7	45,60	0,94	31,15	1,70	0,05	0,90	0,03	0,38	8,67	0,00	0,02	0,01	0,00	0,00	89,45	
ADE-12 Ms 8	45,92	0,64	31,41	1,56	0,00	0,75	0,03	0,39	8,80	0,00	0,02	0,05	0,03	0,00	89,61	
ADE-15 Bt 1	35,92	2,03	15,28	16,26	0,23	11,98	0,04	0,13	9,53	0,00	0,16	0,12	0,04	0,03	91,75	0,57
ADE-15 Bt 2	36,51	1,44	16,00	17,19	0,22	13,04	0,01	0,11	9,33	0,00	0,18	0,18	0,10	0,00	94,32	0,57
ADE-15 Bt 3	36,40	1,80	15,88	17,20	0,18	11,96	0,02	0,05	9,59	0,00	0,18	0,01	0,11	0,02	93,39	0,55
ADE-15 Bt 4	36,04	1,99	15,30	18,05	0,24	12,10	0,00	0,07	9,61	0,00	0,21	0,00	0,03	0,04	93,68	0,54
ADE-15 Bt 5	36,64	1,72	15,98	17,56	0,17	12,09	0,01	0,11	9,73	0,17	0,14	0,13	0,04	0,05	94,53	0,55
ADE-15 Bt 6	36,33	1,94	15,51	17,92	0,23	12,02	0,02	0,08	9,95	0,00	0,13	0,08	0,08	0,01	94,30	0,54
ADE-15 Bt 7	36,39	1,52	15,76	18,16	0,28	12,32	0,02	0,07	9,47	0,00	0,21	0,14	0,05	0,00	94,39	0,55
ADE-15 Bt 8	36,28	1,62	15,89	17,14	0,30	12,91	0,03	0,06	9,55	0,00	0,18	0,29	0,07	0,00	94,30	0,57
ADE-15 Bt 9	36,58	1,61	15,60	18,29	0,27	12,17	0,02	0,13	8,77	0,30	0,20	0,03	0,03	0,03	94,01	0,54

Sample	SiO2	TiO2	Al2O3	FeO	MnO	MgO	CaO	Na2O	K2O	F	Cl	Cr2O3	V2O3	NiO	Total	Mg/(Mg+Fe)
ADE-15 Bt 10	37,12	1,28	15,89	18,88	0,28	11,94	0,05	0,11	9,24	0,25	0,20	0,00	0,04	0,07	95,33	0,53
ADE-15 Bt 11	37,21	1,52	15,82	17,26	0,26	11,96	0,02	0,09	9,13	0,23	0,19	0,01	0,08	0,00	93,79	0,55
ADE-15 Bt 12	36,91	1,89	15,63	17,15	0,30	11,77	0,00	0,04	8,94	0,22	0,19	0,11	0,04	0,01	93,20	0,55
ADE-15 Bt 13	37,62	0,95	16,24	17,74	0,20	12,10	0,04	0,06	8,97	0,24	0,15	0,07	0,07	0,00	94,44	0,55
ADE-15 Bt 14	37,43	1,59	15,28	18,07	0,18	12,00	0,08	0,13	8,79	0,26	0,21	0,10	0,04	0,00	94,15	0,54
ADE-23 Bt 1	33,63	3,16	14,65	26,61	0,26	5,72	0,00	0,13	9,95	0,26	0,15	0,07	0,00	0,00	94,57	0,28
ADE-23 Bt 2	33,87	3,24	14,75	25,66	0,30	5,63	0,09	0,14	9,49	0,00	0,25	0,00	0,00	0,00	93,41	0,28
ADE-23 Bt 3	33,83	4,16	14,89	26,74	0,20	5,01	0,00	0,05	9,58	0,00	0,19	0,00	0,01	0,02	94,67	0,25
ADE-23 Bt 4	34,04	4,02	14,51	27,27	0,25	5,26	0,00	0,09	9,61	0,00	0,20	0,01	0,01	0,00	95,27	0,26
ADE-23 Bt 5	34,90	3,93	14,84	26,53	0,21	5,56	0,03	0,13	9,88	0,10	0,19	0,00	0,09	0,00	96,38	0,27
ADE-23 Bt 6	34,85	3,17	15,29	26,36	0,24	5,60	0,03	0,02	9,84	0,00	0,20	0,03	0,05	0,00	95,68	0,27
ADE-23 Bt 7	34,71	3,31	15,37	26,97	0,25	5,63	0,00	0,02	9,94	0,00	0,29	0,00	0,01	0,00	96,51	0,27
ADE-23 Bt 8	34,49	3,85	15,44	26,14	0,26	5,40	0,01	0,06	9,79	0,00	0,19	0,00	0,03	0,00	95,65	0,27
ADE-23 Bt 9	33,87	3,64	15,16	25,25	0,31	5,58	0,03	0,11	9,53	0,00	0,23	0,04	0,04	0,03	93,83	0,28
ADE-23 Bt 10	33,72	3,36	15,07	25,50	0,20	5,77	0,02	0,12	9,67	0,00	0,26	0,01	0,04	0,03	93,75	0,29
ADE-23 Bt 11	35,51	2,94	14,70	25,39	0,22	5,83	0,03	0,06	8,65	0,80	0,23	0,00	0,10	0,04	94,48	0,29
ADE-23 Bt 12	35,72	3,01	15,31	25,67	0,23	5,77	0,00	0,11	8,65	0,77	0,23	0,00	0,04	0,00	95,51	0,29
ADE-23 Bt 13	34,74	3,38	14,67	24,58	0,15	4,92	0,00	0,08	8,94	0,67	0,24	0,00	0,01	0,00	92,37	0,26
ADE-23 Bt 14	34,97	3,25	14,62	24,19	0,21	5,38	0,00	0,09	8,97	0,70	0,22	0,06	0,07	0,00	92,71	0,28
ADE-23 Bt 15	33,55	3,17	15,33	26,42	0,10	4,69	0,08	0,11	7,40	0,51	0,20	0,00	0,04	0,00	91,59	0,24
ADE-10 Bt 1	35,65	4,16	14,47	21,14	0,41	9,34	0,00	0,07	9,96	0,00	0,12	0,10	0,04	0,02	95,47	0,44
ADE-10 Bt 2	35,52	2,96	14,70	20,32	0,34	10,26	0,03	0,08	9,70	0,00	0,12	0,09	0,10	0,08	94,29	0,47
ADE-10 Bt 3	35,86	4,29	14,85	20,96	0,34	9,43	0,00	0,09	9,80	0,00	0,11	0,12	0,13	0,00	95,96	0,45
ADE-10 Bt 4	35,76	3,70	14,48	20,90	0,34	9,43	0,00	0,08	9,79	0,00	0,15	0,08	0,06	0,02	94,77	0,45
ADE-10 Bt 5	35,83	3,67	14,83	21,32	0,32	9,37	0,02	0,06	10,08	0,00	0,09	0,05	0,00	0,08	95,72	0,44
ADE-10 Bt 6	36,72	3,57	14,85	21,36	0,34	9,42	0,00	0,03	9,97	0,00	0,13	0,03	0,06	0,00	96,49	0,44
ADE-10 Bt 7	35,65	3,52	15,05	20,19	0,37	9,82	0,00	0,05	9,87	0,00	0,12	0,06	0,07	0,03	94,80	0,46
ADE-10 Bt 8	36,34	3,12	14,98	20,65	0,32	9,76	0,00	0,10	9,84	0,00	0,11	0,03	0,06	0,08	95,38	0,46
ADE-10 Bt 9	35,92	3,27	14,57	20,31	0,34	10,27	0,02	0,07	9,85	0,38	0,12	0,08	0,07	0,03	95,29	0,47
ADE-10 Bt 10	35,90	3,77	15,10	19,95	0,30	9,02	0,00	0,10	9,85	0,00	0,08	0,26	0,00	0,10	94,45	0,45
ADE-10 Bt 11	36,87	4,65	14,94	21,42	0,27	9,44	0,00	0,03	9,12	0,52	0,11	0,00	0,06	0,01	97,45	0,44
ADE-10 Bt 12	37,17	3,50	14,62	22,55	0,25	9,63	0,02	0,09	9,26	0,53	0,12	0,12	0,02	0,00	97,89	0,43
ADE-10 Bt 13	37,88	3,99	15,11	22,20	0,37	9,26	0,00	0,06	9,18	0,61	0,12	0,08	0,12	0,08	99,05	0,43
ADE-10 Bt 14	36,17	3,28	14,62	21,88	0,31	9,79	0,00	0,13	8,97	0,62	0,11	0,00	0,09	0,01	95,97	0,44
ADE-10 Bt 15	36,61	3,38	14,78	21,39	0,20	9,82	0,06	0,07	8,99	0,72	0,11	0,00	0,07	0,00	96,20	0,45
ADE-10 Bt 16	36,74	3,58	15,13	21,02	0,40	9,55	0,00	0,05	8,89	0,69	0,13	0,14	0,05	0,04	96,39	0,45

Sample	SiO2	TiO2	Al2O3	FeO	MnO	MgO	CaO	Na2O	K2O	F	Cl	Cr2O3	V2O3	NiO	Total	Mg/(Mg+Fe)
ADE-10 Bt 17	37,01	3,88	14,90	21,69	0,18	9,16	0,00	0,06	9,11	0,49	0,10	0,01	0,09	0,00	96,66	0,43
ADE-10 Bt 18	37,17	1,88	15,17	20,35	0,35	10,33	0,00	0,10	9,14	0,66	0,11	0,08	0,01	0,05	95,41	0,48

Supplementary Table 4.2. Analyses of feldspar group from the Campo Grande migmatite.

Sample	SiO2	TiO2	Al2O3	FeO	MnO	MgO	CaO	Na2O	K2O	Cr2O3	V2O3	NiO	Total	% An	% Ab	% Or	Mineral
ADE-12 Kfs 1	64,46	0,00	18,03	0,02	0,07	0,03	0,05	1,15	14,02	0,00	0,01	0,04	97,88	0,25	11,04	88,71	Sanidine
ADE-12 Kfs 2	63,88	0,00	17,92	0,00	0,04	0,02	0,00	0,71	14,68	0,00	0,05	0,00	97,30	0,00	6,86	93,14	Sanidine
ADE-12 Kfs 3	63,21	0,00	17,89	0,08	0,05	0,01	0,01	0,88	14,31	0,02	0,00	0,00	96,46	0,03	8,54	91,43	Sanidine
ADE-12 Kfs 5	63,46	0,01	18,00	0,02	0,01	0,00	0,00	1,06	13,80	0,00	0,06	0,00	96,41	0,00	10,41	89,59	Sanidine
ADE-12 Kfs 6	65,17	0,04	18,01	0,09	0,01	0,03	0,00	1,26	13,84	0,00	0,01	0,00	98,46	0,00	12,14	87,86	Sanidine
ADE-12 Kfs 7	64,43	0,00	17,83	0,01	0,02	0,00	0,00	1,07	14,00	0,00	0,01	0,01	97,38	0,00	10,40	89,60	Sanidine
ADE-12 Pl 1	62,51	0,02	22,99	0,05	0,00	0,01	4,65	9,01	0,18	0,00	0,04	0,00	99,47	21,97	77,04	0,99	Oligoclase
ADE-12 Pl 2	63,08	0,05	22,75	0,07	0,01	0,02	4,34	9,08	0,32	0,00	0,05	0,04	99,79	20,54	77,68	1,78	Oligoclase
ADE-12 Pl 3	63,26	0,13	22,76	0,01	0,09	0,00	4,37	9,14	0,16	0,00	0,01	0,03	99,96	20,71	78,41	0,88	Oligoclase
ADE-12 Pl 4	63,23	0,00	22,46	0,01	0,06	0,00	4,15	9,37	0,18	0,00	0,00	0,04	99,50	19,47	79,55	0,98	Oligoclase
ADE-12 Pl 5	61,80	0,00	23,51	0,00	0,02	0,02	5,01	8,80	0,20	0,00	0,04	0,01	99,39	23,65	75,22	1,13	Oligoclase
ADE-12 Pl 6	61,75	0,05	22,80	0,06	0,01	0,02	4,73	9,16	0,18	0,05	0,00	0,03	98,84	21,98	77,00	1,01	Oligoclase
ADE-12 Pl 7	62,39	0,04	22,48	0,03	0,04	0,02	4,32	9,93	0,12	0,01	0,00	0,04	99,42	19,26	80,10	0,64	Oligoclase
ADE-12 Pl 8	61,26	0,00	23,25	0,01	0,00	0,00	5,33	8,78	0,15	0,03	0,00	0,09	98,89	24,89	74,29	0,81	Oligoclase
ADE-12 Pl 9	62,00	0,01	23,01	0,00	0,03	0,00	5,11	9,64	0,19	0,02	0,00	0,00	100,01	22,42	76,60	0,98	Oligoclase
ADE-12 Pl 10	62,06	0,00	22,88	0,00	0,00	0,00	4,74	10,08	0,12	0,00	0,00	0,02	99,90	20,52	78,86	0,62	Oligoclase
ADE-12 Pl 11	61,46	0,00	23,00	0,00	0,00	0,01	5,24	9,50	0,18	0,02	0,01	0,00	99,43	23,13	75,91	0,96	Oligoclase
ADE-12 Pl 12	61,12	0,00	22,98	0,00	0,03	0,00	4,86	9,59	0,27	0,00	0,06	0,00	98,91	21,57	77,00	1,43	Oligoclase
ADE-12 Pl 13	61,23	0,00	22,98	0,02	0,00	0,00	5,12	9,37	0,26	0,00	0,00	0,05	99,01	22,86	75,78	1,36	Oligoclase
ADE-12 Pl 14	60,57	0,00	22,56	0,01	0,03	0,00	5,02	9,13	0,14	0,05	0,00	0,01	97,53	23,13	76,13	0,75	Oligoclase
ADE-12 Pl 15	63,47	0,02	22,65	0,00	0,03	0,01	4,07	10,28	0,11	0,02	0,04	0,07	100,76	17,85	81,55	0,60	Oligoclase
ADE-12 Pl 16	62,60	0,10	22,77	0,04	0,00	0,02	4,45	9,04	0,24	0,00	0,00	0,05	99,29	21,09	77,57	1,34	Oligoclase
ADE-15 Kfs 1	64,65	0,01	18,12	0,03	0,01	0,00	0,00	1,00	13,97	0,00	0,01	0,02	97,82	0,02	9,77	90,22	Sanidine
ADE-15 Kfs 2	64,06	0,17	17,92	0,04	0,00	0,01	0,01	0,88	14,27	0,00	0,08	0,00	97,43	0,06	8,56	91,38	Sanidine
ADE-15 Pl 1	60,23	0,00	24,04	0,05	0,00	0,01	6,09	8,40	0,30	0,01	0,02	0,05	99,20	28,12	70,22	1,67	Oligoclase
ADE-15 Pl 2	59,78	0,00	23,87	0,02	0,00	0,00	6,11	8,72	0,29	0,00	0,00	0,00	98,79	27,50	70,96	1,54	Oligoclase
ADE-15 Pl 3	60,15	0,01	24,49	0,03	0,02	0,00	6,39	8,46	0,17	0,02	0,00	0,00	99,73	29,17	69,90	0,92	Oligoclase
ADE-15 Pl 4	60,02	0,05	23,79	0,03	0,02	0,02	6,07	8,62	0,25	0,00	0,02	0,04	98,93	27,64	71,02	1,34	Oligoclase
ADE-15 Pl 5	60,30	0,01	23,97	0,00	0,00	0,01	5,94	8,27	0,18	0,03	0,00	0,03	98,75	28,11	70,87	1,02	Oligoclase

Sample	SiO2	TiO2	Al2O3	FeO	MnO	MgO	CaO	Na2O	K2O	Cr2O3	V2O3	NiO	Total	% An	% Ab	% Or	Mineral
ADE-15 Pl 6	60,52	0,02	24,11	0,06	0,05	0,02	6,00	8,61	0,20	0,01	0,00	0,00	99,59	27,48	71,43	1,09	Oligoclase
ADE-15 Pl 7	60,46	0,00	23,84	0,00	0,00	0,00	5,95	8,68	0,21	0,02	0,01	0,06	99,24	27,14	71,71	1,16	Oligoclase
ADE-15 Pl 8	60,68	0,00	24,19	0,00	0,00	0,01	6,07	8,76	0,26	0,00	0,01	0,02	100,00	27,29	71,32	1,40	Oligoclase
ADE-15 Pl 9	60,43	0,01	23,60	0,05	0,01	0,00	6,10	8,61	0,28	0,02	0,01	0,00	99,10	27,73	70,76	1,51	Oligoclase
ADE-15 Pl 10	60,54	0,01	23,99	0,03	0,00	0,00	6,18	8,53	0,34	0,02	0,00	0,00	99,62	28,06	70,11	1,82	Oligoclase
ADE-15 Pl 11	61,33	0,08	24,24	0,09	0,00	0,00	5,85	8,28	0,29	0,00	0,00	0,00	100,16	27,62	70,74	1,64	Oligoclase
ADE-15 Pl 12	61,48	0,05	23,70	0,02	0,00	0,00	5,78	8,17	0,26	0,01	0,03	0,00	99,51	27,70	70,83	1,47	Oligoclase
ADE-15 Pl 13	61,24	0,00	23,46	0,06	0,00	0,00	5,47	8,35	0,24	0,00	0,00	0,00	98,80	26,20	72,43	1,37	Oligoclase
ADE-15 Pl 14	62,06	0,00	23,12	0,01	0,10	0,00	5,23	8,37	0,35	0,05	0,00	0,00	99,29	25,16	72,85	1,99	Oligoclase
ADE-15 Pl 15	61,02	0,00	24,66	0,14	0,05	0,00	6,29	7,91	0,23	0,07	0,04	0,04	100,46	30,11	68,56	1,33	Andesine
ADE-15 Pl 16	60,55	0,01	24,65	0,00	0,04	0,00	6,49	7,91	0,22	0,00	0,08	0,09	100,03	30,82	67,93	1,25	Andesine
ADE-23 Kfs 1	63,55	0,01	17,51	0,03	0,00	0,01	0,06	1,14	13,73	0,00	0,01	0,04	96,07	0,31	11,18	88,51	Sanidine
ADE-23 Kfs 2	64,55	0,15	17,62	0,00	0,00	0,00	0,04	1,09	13,55	0,00	0,09	0,05	97,15	0,20	10,90	88,89	Sanidine
ADE-23 Kfs 3	62,55	0,03	17,11	0,00	0,01	0,00	0,03	1,06	13,22	0,03	0,01	0,01	94,06	0,16	10,81	89,02	Sanidine
ADE-23 Kfs 4	62,22	0,00	17,75	0,04	0,00	0,00	0,05	2,20	12,77	0,04	0,05	0,00	95,12	0,27	20,66	79,08	Sanidine
ADE-23 Kfs 5	64,82	0,08	17,86	0,03	0,00	0,00	0,01	0,91	14,12	0,05	0,04	0,01	97,93	0,04	8,87	91,09	Sanidine
ADE-23 Kfs 6	64,95	0,04	17,70	0,01	0,00	0,00	0,00	0,82	14,46	0,00	0,02	0,00	98,00	0,00	7,95	92,05	Sanidine
ADE-23 Kfs 7	64,77	0,06	17,68	0,00	0,07	0,00	0,02	1,22	13,67	0,00	0,00	0,00	97,49	0,09	11,92	87,99	Sanidine
ADE-23 Kfs 8	65,01	0,04	17,57	0,00	0,00	0,01	0,02	0,46	14,75	0,00	0,02	0,00	97,88	0,12	4,48	95,39	Ortoclase
ADE-23 Pl 1	62,18	0,05	22,43	0,01	0,04	0,01	4,85	9,25	0,19	0,00	0,00	0,01	99,00	22,22	76,75	1,02	Oligoclase
ADE-23 Pl 2	61,46	0,01	22,01	0,06	0,00	0,03	4,32	9,63	0,22	0,01	0,03	0,06	97,85	19,64	79,18	1,18	Oligoclase
ADE-23 Pl 3	62,85	0,00	21,99	0,08	0,07	0,00	4,00	9,55	0,15	0,01	0,04	0,02	98,74	18,65	80,52	0,83	Oligoclase
ADE-23 Pl 4	62,36	0,00	22,70	0,04	0,00	0,00	4,53	9,46	0,27	0,00	0,01	0,03	99,40	20,63	77,93	1,44	Oligoclase
ADE-23 Pl 5	62,64	0,00	20,04	0,03	0,00	0,01	2,43	5,86	6,26	0,04	0,00	0,00	97,31	11,86	51,76	36,38	Ca-Anorthoclase
ADE-23 Pl 6	62,83	0,02	20,21	0,04	0,03	0,01	2,44	6,20	5,89	0,03	0,00	0,03	97,72	11,79	54,30	33,91	Ca-Anorthoclase
ADE-23 Pl 7	62,51	0,00	22,04	0,04	0,00	0,02	4,34	9,35	0,31	0,01	0,02	0,00	98,63	20,06	78,25	1,70	Oligoclase
ADE-23 Pl 9	64,09	0,00	22,08	0,08	0,00	0,02	3,77	9,71	0,19	0,00	0,04	0,01	99,98	17,50	81,45	1,05	Oligoclase
ADE-23 Pl 10	62,23	0,11	22,52	0,09	0,05	0,00	4,26	8,94	0,18	0,10	0,00	0,00	98,48	20,60	78,34	1,06	Oligoclase
ADE-23 Pl 11	63,56	0,00	21,87	0,04	0,02	0,00	3,73	9,44	0,17	0,00	0,00	0,00	98,82	17,74	81,28	0,99	Oligoclase
ADE-23 Pl 12	62,58	0,06	22,36	0,01	0,04	0,00	4,07	9,33	0,20	0,03	0,00	0,00	98,66	19,21	79,68	1,11	Oligoclase
ADE-23 Pl 13	60,66	0,00	22,83	0,09	0,00	0,04	3,63	8,75	0,86	0,01	0,00	0,00	96,86	17,74	77,27	4,98	Oligoclase
ADE-10 Kfs 1	65,72	0,09	17,92	0,00	0,00	0,01	0,03	0,85	14,57	0,00	0,00	0,00	99,19	0,14	8,15	91,71	Sanidine
ADE-10 Kfs 2	65,76	0,08	18,32	0,02	0,00	0,02	0,06	1,08	14,41	0,01	0,04	0,00	99,81	0,29	10,19	89,52	Sanidine
ADE-10 Kfs 3	65,39	0,00	17,99	0,12	0,01	0,00	0,03	0,99	14,58	0,06	0,01	0,00	99,17	0,15	9,33	90,52	Sanidine
ADE-10 Kfs 4	65,53	0,00	18,02	0,08	0,00	0,02	0,03	1,15	14,27	0,00	0,00	0,00	99,10	0,14	10,92	88,94	Sanidine
ADE-10 Kfs 5	65,39	0,18	18,33	0,05	0,02	0,00	0,00	0,91	14,77	0,00	0,00	0,00	99,64	0,00	8,57	91,43	Sanidine

Sample	SiO2	TiO2	Al2O3	FeO	MnO	MgO	CaO	Na2O	K2O	Cr2O3	V2O3	NiO	Total	% An	% Ab	% Or	Mineral
ADE-10 Kfs 6	65,58	0,07	18,00	0,03	0,01	0,00	0,02	0,70	14,94	0,00	0,00	0,04	99,37	0,08	6,65	93,27	Sanidine
ADE-10 Kfs 7	64,08	0,00	17,54	0,03	0,00	0,01	0,06	0,93	14,48	0,00	0,00	0,13	97,28	0,33	8,85	90,83	Sanidine
ADE-10 Kfs 8	65,40	0,00	18,16	0,02	0,00	0,00	0,02	1,04	13,93	0,00	0,00	0,02	98,58	0,08	10,16	89,76	Sanidine
ADE-10 Pl 1	62,17	0,00	23,81	0,00	0,07	0,00	5,30	8,47	0,23	0,00	0,03	0,04	100,13	25,35	73,34	1,32	Oligoclase
ADE-10 Pl 2	62,52	0,05	23,76	0,11	0,00	0,00	5,09	8,62	0,22	0,04	0,07	0,03	100,51	24,29	74,47	1,23	Oligoclase
ADE-10 Pl 3	62,53	0,05	23,81	0,04	0,00	0,00	5,25	8,21	0,29	0,06	0,02	0,00	100,26	25,68	72,66	1,66	Oligoclase
ADE-10 Pl 4	62,77	0,00	24,00	0,06	0,00	0,00	5,33	8,53	0,21	0,00	0,00	0,03	100,92	25,36	73,48	1,16	Oligoclase
ADE-10 Pl 5	62,28	0,00	23,64	0,02	0,04	0,00	5,24	8,50	0,24	0,05	0,01	0,00	100,01	25,07	73,55	1,38	Oligoclase
ADE-10 Pl 6	63,34	0,06	23,79	0,06	0,01	0,04	5,29	8,65	0,22	0,00	0,06	0,00	101,52	24,94	73,84	1,22	Oligoclase
ADE-10 Pl 7	62,82	0,04	23,63	0,04	0,00	0,00	5,26	8,44	0,24	0,00	0,10	0,00	100,58	25,25	73,36	1,39	Oligoclase
ADE-10 Pl 8	60,65	0,14	23,11	0,01	0,00	0,03	5,24	8,37	0,29	0,00	0,03	0,01	97,87	25,28	73,03	1,68	Oligoclase
ADE-10 Pl 9	61,01	0,00	23,50	0,01	0,02	0,00	5,54	8,76	0,22	0,01	0,03	0,00	99,09	25,61	73,21	1,19	Oligoclase
ADE-10 Pl 10	59,72	0,02	22,85	0,06	0,00	0,00	5,42	8,45	0,24	0,00	0,02	0,00	96,77	25,82	72,83	1,35	Oligoclase
ADE-10 Pl 11	60,84	0,00	23,34	0,07	0,01	0,00	5,60	8,59	0,25	0,01	0,02	0,00	98,75	26,13	72,47	1,40	Oligoclase
ADE-10 Pl 12	60,75	0,00	23,60	0,04	0,00	0,00	5,47	8,56	0,26	0,04	0,02	0,03	98,76	25,71	72,82	1,47	Oligoclase
ADE-10 Pl 13	61,99	0,02	23,54	0,05	0,04	0,03	5,44	8,98	0,22	0,00	0,00	0,00	100,28	24,78	74,05	1,18	Oligoclase
ADE-10 Pl 14	60,98	0,06	23,68	0,02	0,01	0,00	5,35	8,97	0,24	0,02	0,06	0,02	99,40	24,48	74,24	1,29	Oligoclase
ADE-10 Pl 15	60,68	0,00	23,75	0,03	0,04	0,02	5,72	8,83	0,22	0,00	0,02	0,00	99,29	26,06	72,76	1,17	Oligoclase
ADE-10 Pl 16	61,26	0,03	23,49	0,03	0,02	0,01	5,47	8,94	0,22	0,00	0,00	0,00	99,46	24,94	73,86	1,20	Oligoclase

Supplementary Table 4.3. Whole-rock analyses from the Campo Grande migmatite.

Sample	ADE-14P	ADE-15P	ADE-18P	ADE-19L	ADE-10L	ADE-23L	ADE-04L	ADE-12L	ADE-18L	AT-13L	AT-28L	ADE-13Li	ADE-18Li	AT-23Li
Migmatite Components	Tonalitic paleosome			Concordant granitic leucosome								Injected leucosome Alk. granite - Pegmatite - Granite		
SiO2	66.8	69.03	67.1	72.3	73.7	76.2	74.01	74.7	75.3	72.6	70.7	73.4	75.6	70.6
Al2O3	14.8	14.79	15.3	14.05	14.15	10.65	13.45	13.8	13.1	15.65	14.9	12.6	13.95	14.2
Fe2O3	4.67	3.59	4.16	3.18	2.63	4.24	2.1	2.02	1.18	1.15	2.25	3.32	0.31	3.39
MnO	0.05	0.05	0.06	0.06	0.04	0.03	0.04	0.04	0.01	0.01	0.05	0.06	0.01	0.03
MgO	1.22	2.2	2.13	1.03	0.97	0.67	0.38	0.45	0.24	0.28	0.84	0.13	0.04	0.61
CaO	3.25	3.15	3.85	1.68	2.01	1.06	1.5	1.22	1.41	1.8	2.09	0.74	0.44	1.58
Na2O	3.77	3.59	4.02	3.09	3.15	2.45	3.47	2.87	2.43	4.2	4.07	2.97	2.25	2.92

Sample	ADE-14P	ADE-15P	ADE-18P	ADE-19L	ADE-10L	ADE-23L	ADE-04L	ADE-12L	ADE-18L	AT-13L	AT-28L	ADE-13Li	ADE-18Li	AT-23Li
K2O	2.32	2.29	2.03	4.85	4.03	3.91	4.18	4.78	5.77	4.69	3.61	5.51	8.33	5.7
P2O5	0.34	0.09	0.23	0.1	0.16	0.03	0.07	0.08	0.07	0.04	0.14	0.04	0.02	0.15
TiO2	0.54	0.35	0.53	0.31	0.39	0.36	0.24	0.22	0.07	0.11	0.38	0.25	0.02	0.44
Cr2O3	0.04	0.041	0.06	0.02	0.01	0.02	0.01	0.02	0.08	bd	0.01	0.01	0.02	0.02
LOI	0.41	0.6	0.64	0.49	0.57	0.65	0.4	0.62	0.34	0.58	0.67	0.48	0.31	0.54
TOTAL	98.3	99.8	100.2	101.2	101.9	100.3	99.9	101,0	100.2	101.2	99.7	99.6	101.3	100.3
Mg#	31.7	52.2	47.7	36.6	39.6	21.9	24.4	28.4	26.6	30.2	39.9	6.5	18.6	24.2
Sc	7	9	8	5	5	6	4	5	1	2	5	6	1	4
V	66	49	86	31	24	bd	16	20	27	17	35	7	12	34
Cr	310	bd	460	90	90	130	bd	100	580	bd	30	90	140	130
Co	9	13	16	5	6	2	1.8	3	5	86	84	1	3	6
Ni	13	45	42	12	22	3	2	4	18	3	12	2	4	11
Cu	20	22.9	18	6	5	5	5.5	6	5	1	5	2	3	4
Zn	59	51	66	51	55	52	36	32	9	23	51	91	3	49
Ga	20.4	20.7	20.4	16.9	19.4	22.5	17	15.5	14.8	20.5	23	23.1	18.9	21.3
Rb	112	97	84	167	166	78	131	131	102	101	182	264	298	200
Sr	507	291	400	233	183	78	184	363	377	480	188	61	111	174
Y	15	20	23	18	20	118	13	15	5	16	12	47	47	29
Zr	206	131	135	176	220	712	185	235	24	128	195	368	21	381
Nb	7.3	13.2	10.4	10.2	12.4	51	8	5.9	1.8	9.2	12.6	30.3	3.6	18.2
Cs	4.02	2.6	2.43	2.14	3.73	0.47	1.2	2.93	0.88	0.89	5.12	5.18	1.13	1.7
Ba	621	361	567	618	690	822	971	1550	1800	673	411	493	297	1045
Hf	5.2	3.9	3.5	5.4	6.3	19.1	5.2	7	0.9	4.3	5.1	10.7	1.5	10.1
Ta	0.2	1.1	0.7	0.8	1.1	2.1	0.7	0.4	0.2	0.7	1.7	2.4	0.5	0.3
Pb	18	5	17	27	29	13	4	48	27	41	25	40	48	24
Th	10	30	7	21	16	24	20	71	5	30	11	28.3	12.95	72.5
U	1,00	1,90	0,90	2,60	1,33	3,15	2,20	8,59	0,28	1,62	2,60	4,47	2,68	1,59

Sample	ADE-14P	ADE-15P	ADE-18P	ADE-19L	ADE-10L	ADE-23L	ADE-04L	ADE-12L	ADE-18L	AT-13L	AT-28L	ADE-13Li	ADE-18Li	AT-23Li
La	50	65	35	48	39.7	101.5	43.4	133	17	54.1	39.4	90	13	227
Ce	96	132	74	85.1	88.1	202	92.9	236	33	110.5	76.4	180	21	434
Pr	10.15	13.77	7.24	9.26	9.16	23.6	8.72	24	3.55	11.6	7.77	18.9	2.98	44
Nd	37	49	29	31.8	29.9	86.1	27	78	13	44	28.3	65	11.1	157
Sm	6.23	8.61	5.48	5.16	5.12	18.55	4.26	10.5	2.32	9.58	4.43	12.1	3.49	24.5
Eu	1.3	1.13	1.69	0.78	0.83	2.63	0.82	1.34	1.11	1.01	0.89	0.82	0.53	1.93
Gd	4.91	6.53	5.01	3.94	3.9	19.4	3.28	6.24	1.47	7.84	3.11	9.66	5.05	14.6
Tb	0.66	0.85	0.76	0.59	0.55	2.95	0.5	0.73	0.17	0.99	0.41	1.49	1.02	1.72
Dy	2.95	4.15	4.22	3.18	3.64	19,00	2.68	3.59	0.95	4.28	2.24	8.89	6.84	7.86
Ho	0.51	0.68	0.81	0.67	0.7	4.08	0.52	0.58	0.18	0.58	0.41	1.59	1.5	1.13
Er	1.29	1.82	2.07	1.89	2.09	12.1	1.47	1.32	0.42	1.13	1.16	4.8	4.44	2.34
Tm	0.16	0.25	0.31	0.23	0.31	1.82	0.23	0.25	0.03	0.13	0.13	0.7	0.73	0.26
Yb	1,00	1.56	1.87	1.59	2,00	12.95	1.51	1.29	0.28	0.69	1.05	4.54	5.16	1.47
Lu	0.13	0.23	0.27	0.25	0.28	1.87	0.2	0.21	0.06	0.09	0.15	0.62	0.78	0.22
∑REE	211.7	284.28	167.03	192.44	186.28	508.55	187.79	496.35	74.64	246.12	165.85	399.51	77.52	918.43
(La/Yb)N	35.5	29.65	13.38	21.65	14.23	5.62	20.61	73.67	44.31	56.24	26.91	14.28	1.79	110.76
(Ce/Yb)N	26.5	23.43	10.94	14.86	12.23	4.3	17.08	50.81	33.13	44.48	20.21	11.01	1.13	82.01
(La/Eu)N	9.3	13.96	5.05	15.06	11.7	9.4	12.95	24.19	3.81	13.1	10.83	26.97	5.95	28.78
(La/Sm)N	5.1	4.83	4.11	6,00	5,00	3.53	6.57	8.14	4.81	3.64	5.74	4.82	2.38	5.98
(Gd/Lu)N	4.6	3.5	2.29	1.94	1.72	1.28	2.02	3.67	3.02	10.77	2.56	1.92	0.8	8.2
(Tb/Yb)N	3,00	2.47	1.84	1.68	1.25	1.03	1.5	2.57	2.75	6.52	1.77	1.49	0.89	5.31
(La/Lu)N	40.8	30.05	13.85	20.57	15.19	5.81	23.25	67.62	30.9	64.42	28.15	15.62	1.77	110.58
Eu/Eu*	0.71	0.46	0.98	0.52	0.56	0.42	0.67	0.5	1.83	0.35	0.73	0.23	0.38	0.31
M	1.4	1.3	1.5	1.3	1.2	1.2	1.3	1.2	1.3	1.3	1.3	1.3	1.3	1.4
G	6.48	6.52	5.89	8.04	8.64	9,00	9.82	10.43	11.07	9.67	8.35	9.42	12.1	8.04

bd = below detection limit

Supplementary Table 4.4. U-Pb zircon data from Campo Grande migmatite.

ADE-18P	^{204}Pb cps	^{206}Pb mV[1]	Th/U	^{206}Pb/^{204}Pb	1σ%	^{207}Pb/^{206}Pb	1σ %	^{207}Pb/^{235}U	1σ %	^{206}Pb/^{238}U	1σ %	Rho	^{207}Pb/^{206}Pb	2σ abs	^{206}Pb/^{238}U	2σ abs	^{207}Pb/^{235}U	2σ abs	% U-Pb disc[4]
050-ZR27C	14	0,0368	0,451	808497	19,11	0,21378	1,40	17,528	1,71	0,5946	0,92	0,54	2934	45	3008	44	2964	33	-2,51
049-ZR26C	97	0,0105	0,476	69755	33,83	0,21847	0,67	15,232	1,35	0,5056	1,11	0,82	2969	22	2638	48	2830	26	11,16
048-ZR25B	12	0,0083	0,306	233735	17,70	0,22132	0,54	18,095	1,10	0,5929	0,88	0,80	2990	17	3001	42	2995	21	-0,37
047-ZR25C	118	0,0056	0,590	3191	5,50	0,22525	0,57	18,101	1,20	0,5828	0,99	0,82	3019	18	2960	47	2995	23	1,94
046-ZR24B	21	0,0160	0,326	437644	21,96	0,21726	0,93	17,052	1,25	0,5692	0,75	0,60	2960	30	2905	35	2938	24	1,89
045-ZR24C	19	0,0090	0,598	182681	25,54	0,22045	0,41	18,101	0,97	0,5955	0,80	0,82	2984	13	3012	38	2995	19	-0,92
044-ZR23C	38	0,0096	0,760	159013	23,43	0,21693	0,48	16,131	1,08	0,5393	0,89	0,83	2958	15	2780	40	2885	20	6,00
039-ZR21B	10	0,0295	0,365	964978	16,11	0,21341	0,51	17,279	1,11	0,5872	0,92	0,82	2932	17	2978	44	2950	21	-1,58
038-ZR21C	11	0,0123	0,662	416302	14,81	0,21915	0,83	17,698	1,20	0,5857	0,79	0,66	2974	27	2972	38	2973	23	0,09
037-ZR20C	11	0,0088	0,514	286851	14,64	0,21996	0,43	17,869	0,90	0,5892	0,70	0,78	2980	14	2986	33	2983	17	-0,19
036-ZR19C	23	0,0130	0,733	208892	27,84	0,22072	1,22	18,142	1,66	0,5961	1,06	0,64	2986	39	3014	51	2997	32	-0,94
034-ZR17B	18	0,0077	0,455	212010	21,43	0,21906	0,55	17,085	1,07	0,5656	0,83	0,78	2974	18	2890	39	2940	20	2,83
033-ZR17C	9	0,0069	0,573	256529	15,44	0,21889	1,11	16,370	1,49	0,5423	0,93	0,62	2973	35	2793	42	2899	28	6,03
028-ZR14C	49	0,0053	0,455	40698	39,56	0,20864	0,62	13,634	1,16	0,4739	0,90	0,78	2895	20	2501	37	2725	22	13,62
027-ZR13B	27	0,0084	0,508	114241	26,03	0,21656	0,51	16,670	0,96	0,5583	0,72	0,75	2955	17	2859	33	2916	18	3,24
020-ZR11C	27	0,0115	0,699	158620	24,31	0,21521	1,40	13,909	1,94	0,4687	1,29	0,66	2945	45	2478	53	2743	36	15,87
019-ZR10C	9	0,0052	0,373	203528	18,33	0,22410	0,66	17,325	1,20	0,5606	0,93	0,78	3010	21	2869	43	2953	23	4,69
018-ZR9B	19	0,0075	0,403	195903	18,49	0,21976	0,50	16,641	1,04	0,5491	0,84	0,80	2979	16	2822	38	2914	20	5,28
017-ZR9C	15	0,0116	0,566	324817	19,71	0,21708	0,46	15,629	1,04	0,5221	0,86	0,83	2959	15	2708	38	2854	20	8,48
015-ZR7C	13	0,0112	1,134	354027	16,05	0,22011	0,58	17,131	1,14	0,5645	0,91	0,80	2981	19	2885	42	2942	22	3,24
014-ZR6C	7	0,0216	0,163	943566	14,68	0,21492	0,41	16,213	0,99	0,5471	0,82	0,83	2943	13	2813	37	2889	19	4,41
013-ZR5C	11	0,0174	0,923	626750	15,25	0,21683	0,48	17,664	1,07	0,5908	0,88	0,82	2957	15	2993	42	2972	20	-1,19
010-ZR4C	52	0,0053	0,526	121984	28,67	0,21927	1,19	14,765	1,71	0,4883	1,17	0,69	2975	38	2564	49	2800	32	13,84
009-ZR3B	76	0,0060	0,457	80509	39,12	0,21192	0,96	13,289	1,96	0,4548	1,68	0,85	2920	31	2416	67	2700	37	17,25
008-ZR3C	13	0,0179	0,551	490232	17,72	0,22140	0,58	17,804	1,16	0,5832	0,94	0,81	2991	19	2962	44	2979	22	0,98

ADE-18P	^{204}Pb cps	^{206}Pb mV[1]	Th/U	^{206}Pb/^{204}Pb	1σ%	^{207}Pb/^{206}Pb	1σ %	^{207}Pb/^{235}U	1σ %	^{206}Pb/^{238}U	1σ %	Rho	^{207}Pb/^{206}Pb	2σ abs	^{206}Pb/^{238}U	2σ abs	^{207}Pb/^{235}U	2σ abs	% U-Pb disc[4]
005-ZR1B	99	0,0090	0,384	10435	17,87	0,21182	0,55	14,336	1,00	0,4908	0,75	0,75	2919	18	2574	32	2772	19	11,82
004-ZR1C	76	0,0199	0,702	27353	18,38	0,22024	0,40	17,718	1,46	0,5834	1,35	0,93	2982	13	2963	64	2975	28	0,67
ADE-10P	**^{204}Pb cps**	**^{206}Pb mV[1]**	**Th/U**	**^{206}Pb/^{204}Pb**	**1σ%**	**^{207}Pb/^{206}Pb**	**1σ %**	**^{207}Pb/^{235}U**	**1σ %**	**^{206}Pb/^{238}U**	**1σ %**	**Rho**	**^{207}Pb/^{206}Pb**	**2σ abs**	**^{206}Pb/^{238}U**	**2σ abs**	**^{207}Pb/^{235}U**	**2σ abs**	**% U-Pb disc[4]**
048-ZR35	44	0,0264	0,224	692032	60,60	0,21261	1,51	15,619	2,26	0,5328	1,64	0,72	2926	49	2753	73	2854	43	5,89
047-ZR34	37	0,0094	0,540	289747	18,72	0,21204	0,51	17,400	1,18	0,5951	1,00	0,85	2921	16	3010	48	2957	23	-3,04
046-ZR33	19	0,0212	0,578	501395	21,91	0,21295	0,44	17,150	1,00	0,5841	0,82	0,82	2928	14	2965	39	2943	19	-1,27
045-ZR32	16	0,0108	0,583	336071	17,69	0,21339	0,46	16,715	1,11	0,5681	0,94	0,85	2931	15	2900	44	2919	21	1,08
044-ZR31	134	0,0439	0,125	157120	47,26	0,20965	0,53	16,073	1,13	0,5560	0,92	0,82	2903	17	2850	42	2881	21	1,82
042-ZR29	149	0,0232	0,415	56331	31,00	0,20984	0,68	16,270	1,37	0,5623	1,14	0,83	2904	22	2876	53	2893	26	0,97
039-ZR28	88	0,0418	0,303	79718	46,65	0,21023	1,08	16,230	2,10	0,5599	1,76	0,84	2907	35	2866	81	2890	40	1,41
038-ZR27	12	0,0124	0,238	456441	15,09	0,20944	0,74	14,764	1,85	0,5112	1,66	0,89	2901	24	2662	72	2800	35	8,25
037-ZR26	56	0,0364	0,174	122112	53,18	0,21831	1,28	16,445	2,14	0,5463	1,67	0,78	2968	41	2810	76	2903	40	5,34
036-ZR25	82	0,0253	0,306	152044	41,54	0,21025	1,09	14,888	2,10	0,5135	1,75	0,84	2908	35	2672	77	2808	40	8,11
031-ZR22	14	0,0078	0,394	316641	15,72	0,20519	0,81	13,617	1,44	0,4813	1,13	0,79	2868	26	2533	47	2723	27	11,68
028-ZR20	14	0,0125	0,557	409625	15,84	0,21154	0,46	17,377	1,02	0,5957	0,83	0,81	2917	15	3013	40	2956	20	-3,27
023-ZR15	92	0,0617	0,151	390068	65,19	0,21264	0,49	16,573	1,16	0,5652	0,98	0,85	2926	16	2888	46	2910	22	1,29
022-ZR14	58	0,0286	0,337	44218	14,37	0,21246	0,57	15,376	2,40	0,5248	2,30	0,96	2924	19	2720	102	2839	45	7,00
019-ZR13	178	0,0089	0,515	369945	51,99	0,21232	1,06	15,835	1,47	0,5409	0,94	0,64	2923	34	2787	43	2867	28	4,66
018-ZR12	541	0,0369	0,307	69758	73,55	0,21023	0,91	16,300	2,57	0,5623	2,38	0,92	2907	29	2876	110	2895	49	1,08
016-ZR10	8	0,0167	0,360	658708	14,80	0,21120	0,40	16,680	0,98	0,5727	0,82	0,83	2915	13	2919	38	2917	19	-0,15
015-ZR9	227	0,0476	0,343	61045	75,09	0,20462	1,24	14,781	1,95	0,5239	1,45	0,75	2863	40	2715	64	2801	37	5,17
014-ZR8	24	0,0222	0,283	678856	37,25	0,20929	0,32	16,549	0,93	0,5734	0,79	0,85	2900	10	2922	37	2909	18	-0,76
035-ZR24	68	0,0441	0,172	196193	55,07	0,20127	0,57	13,374	1,44	0,4819	1,27	0,88	2837	19	2536	53	2706	27	10,61
034-ZR23	255	0,0549	0,322	18639	14,93	0,20515	0,91	14,142	1,47	0,4999	1,10	0,75	2868	29	2614	47	2759	28	8,86
026-ZR18	173	0,0390	0,182	16561	6,91	0,19486	0,88	10,548	1,66	0,3926	1,35	0,82	2784	29	2135	49	2484	30	23,31
025-ZR17	165	0,0221	0,228	9198	9,11	0,18758	0,96	8,824	3,35	0,3411	3,19	0,95	2721	31	1892	104	2320	60	30,46
ADE-15	**^{204}Pb cps**	**^{206}Pb mV[1]**	**Th/U**	**^{206}Pb/^{204}Pb**	**1σ%**	**^{207}Pb/^{206}Pb**	**1σ %**	**^{207}Pb/^{235}U**	**1σ %**	**^{206}Pb/^{238}U**	**1σ %**	**Rho**	**^{207}Pb/^{206}Pb**	**2σ abs**	**^{206}Pb/^{238}U**	**2σ abs**	**^{207}Pb/^{235}U**	**2σ abs**	**% U-Pb disc[4]**

ADE-18P	^{204}Pb cps	^{206}Pb mV[1]	Th/U	^{206}Pb/^{204}Pb	1σ%	^{207}Pb/^{206}Pb	1σ %	^{207}Pb/^{235}U	1σ %	^{206}Pb/^{238}U	1σ %	Rho	^{207}Pb/^{206}Pb	2σ abs	^{206}Pb/^{238}U	2σ abs	^{207}Pb/^{235}U	2σ abs	% U-Pb disc[4]
017-ZR8C	11	0,0058	0,478	159816	15,46	0,26148	0,68	22,874	1,18	0,6344	0,89	0,75	3256	21	3167	44	3222	23	2,72
033-ZR16C	264	0,0261	0,127	6248	2,97	0,17156	1,03	10,259	1,41	0,4337	0,89	0,63	2573	34	2322	35	2458	26	9,74
076-ZR44C	31	0,0090	0,558	113258	24,08	0,22427	0,84	16,641	1,32	0,5381	0,94	0,71	3012	27	2776	42	2914	25	7,84
018-ZR9C	33	0,0086	0,421	105096	29,53	0,21126	1,26	14,999	1,63	0,5149	0,96	0,59	2915	41	2677	42	2815	31	8,16
029-ZR15C	22	0,0211	0,198	390100	21,21	0,19570	1,67	12,875	2,01	0,4771	1,06	0,53	2791	54	2515	44	2671	38	9,89
035-ZR25	50	0,0138	0,137	311045	55,25	0,20836	1,88	10,770	2,58	0,3749	1,73	0,67	2893	60	2052	61	2504	47	29,06
010-ZR7	364	0,0336	0,449	6417	4,68	0,20286	1,10	9,712	2,22	0,3472	1,90	0,85	2849	36	1921	63	2408	41	32,57
009-ZR6	126	0,0131	0,476	7325	6,65	0,19113	1,40	8,798	3,12	0,3339	2,76	0,89	2752	46	1857	89	2317	56	32,52
024-ZR16	10	0,0117	0,127	481170	17,24	0,20902	0,81	15,530	1,74	0,5388	1,50	0,86	2898	26	2779	67	2848	33	4,12
029-ZR21	32	0,0299	0,240	348922	30,88	0,21340	1,27	17,878	2,24	0,6076	1,81	0,81	2932	41	3060	88	2983	43	-4,39
014-ZR9	18	0,0179	0,376	340675	21,21	0,20052	1,19	12,842	1,65	0,4644	1,07	0,65	2830	39	2459	44	2668	31	13,12
008-ZR5	26	0,0194	0,224	552568	22,50	0,20989	1,35	15,553	1,79	0,5374	1,12	0,63	2905	43	2772	50	2850	34	4,55
039-ZR29	22	0,0074	0,314	164897	21,37	0,19995	0,60	11,585	1,21	0,4202	0,98	0,81	2826	20	2261	37	2571	22	19,97
036-ZR26	14	0,0210	0,342	629270	18,48	0,20594	0,58	14,977	1,44	0,5274	1,27	0,88	2874	19	2731	56	2814	27	4,99
026-ZR13C	17	0,0057	0,489	256868	46,53	0,22389	0,67	18,284	1,30	0,5923	1,05	0,81	3009	21	2999	50	3005	25	0,34
070-ZR41C	34	0,0137	0,240	177514	40,36	0,21825	0,69	17,144	1,27	0,5697	1,00	0,79	2968	22	2906	47	2943	24	2,07
067-ZR38C	905	0,0232	0,341	2307	21,51	0,21258	1,44	15,940	1,94	0,5438	1,24	0,64	2925	46	2799	56	2873	37	4,31
078-ZR46C	46	0,0099	0,394	72595	31,53	0,21093	0,60	16,020	1,60	0,5508	1,43	0,90	2913	19	2828	65	2878	30	2,89
010-ZR5C	37	0,0168	0,426	101629	30,46	0,20756	0,72	15,476	1,23	0,5407	0,93	0,75	2887	23	2787	42	2845	23	3,47
069-ZR40C	50	0,0224	0,476	98781	54,88	0,20690	0,64	15,259	1,96	0,5349	1,81	0,93	2881	21	2762	81	2832	37	4,15
048-ZR25C	17	0,0097	0,192	273498	17,45	0,20654	0,55	15,260	1,13	0,5358	0,91	0,81	2879	18	2766	41	2832	21	3,91
014-ZR6C	50	0,0128	0,384	73434	39,41	0,20542	0,56	13,804	1,33	0,4873	1,15	0,86	2870	18	2559	49	2736	25	10,82
056-ZR30C	26	0,0066	0,278	104520	24,43	0,20537	0,79	13,580	1,39	0,4796	1,08	0,78	2869	26	2525	45	2721	26	11,99
009-ZR4C	18	0,0215	0,774	464233	21,50	0,20381	0,67	13,274	1,31	0,4723	1,06	0,81	2857	22	2494	44	2699	25	12,71
055-ZR29C	22	0,0128	0,483	241611	27,67	0,20341	0,54	12,817	1,66	0,4570	1,52	0,92	2854	17	2426	61	2666	31	14,98
007-ZR3C	486	0,0422	0,518	6953	12,22	0,20328	0,44	12,975	1,14	0,4629	0,98	0,86	2853	14	2452	40	2678	21	14,04
050-ZR27C	270	0,0120	0,149	2718	3,71	0,20134	0,77	10,232	1,69	0,3686	1,46	0,86	2837	25	2023	51	2456	31	28,71

ADE-18P	^{204}Pb cps	^{206}Pb mV[1]	Th/U	^{206}Pb/^{204}Pb	1σ%	^{207}Pb/^{206}Pb	1σ %	^{207}Pb/^{235}U	1σ %	^{206}Pb/^{238}U	1σ %	Rho	^{207}Pb/^{206}Pb	2σ abs	^{206}Pb/^{238}U	2σ abs	^{207}Pb/^{235}U	2σ abs	% U-Pb disc[4]
027-ZR14C	25	0,0035	0,136	83393	51,76	0,20057	2,01	10,088	2,95	0,3647	2,12	0,72	2831	65	2005	73	2443	54	29,19
054-ZR28C	118	0,0331	0,329	103227	58,24	0,19954	2,02	11,637	2,89	0,4229	2,03	0,70	2822	65	2274	78	2576	53	19,44
045-ZR22C	683	0,0297	0,137	3740	16,52	0,19862	0,50	13,150	1,07	0,4801	0,87	0,81	2815	16	2528	36	2690	20	10,20
020-ZR11C	84	0,0269	0,820	24701	15,40	0,19485	1,11	11,252	1,57	0,4188	1,04	0,66	2784	36	2255	39	2544	29	18,99
015-ZR6B	224	0,0282	0,235	8232	3,25	0,19478	0,53	12,782	1,17	0,4759	0,98	0,83	2783	17	2509	40	2664	22	9,83
038-ZR19B	295	0,0124	0,128	2891	4,69	0,19369	0,57	11,054	1,06	0,4139	0,82	0,77	2774	19	2233	31	2528	20	19,51
057-ZR31C	1	0,0060	0,010	374437	25,01	0,19163	1,23	7,145	4,60	0,2704	4,41	0,96	2756	40	1543	121	2130	80	44,02
058-ZR32C	44	0,0307	0,433	205289	33,99	0,18767	0,95	10,389	1,68	0,4015	1,33	0,79	2722	31	2176	49	2470	31	20,06
006-ZR2C	368	0,0301	0,044	5861	5,65	0,16880	0,64	4,801	1,89	0,2063	1,74	0,92	2546	21	1209	38	1785	32	52,51
030-ZR22	66	0,0371	0,030	98231	42,89	0,12247	0,69	6,143	1,18	0,3637	0,88	0,75	1993	25	2000	30	1996	21	-0,37
027-ZR19	60	0,0445	0,046	489542	32,80	0,12253	0,53	6,073	1,00	0,3594	0,76	0,76	1993	19	1980	26	1986	17	0,70
026-ZR18	75	0,0923	0,021	339987	46,74	0,11918	0,54	5,711	1,02	0,3475	0,77	0,76	1944	19	1923	26	1933	17	1,09
028-ZR20	39	0,0269	0,034	270687	29,47	0,12458	2,12	6,212	2,69	0,3616	1,62	0,60	2023	74	1990	55	2006	47	1,63
020-ZR15	172	0,0253	0,105	29947	28,16	0,12405	2,16	6,019	2,64	0,3519	1,49	0,56	2015	76	1944	50	1979	46	3,55
016-ZR11	17	0,0250	0,046	31621608	98,94	0,11806	0,69	5,599	1,09	0,3439	0,76	0,70	1927	25	1905	25	1916	19	1,13
015-ZR10	16	0,0343	0,050	973409	20,25	0,12289	0,43	6,162	1,05	0,3637	0,88	0,84	1999	15	1999	30	1999	18	-0,04
037-ZR27	113	0,0501	0,043	43957	15,43	0,12156	0,46	6,019	1,47	0,3591	1,35	0,92	1979	16	1978	46	1979	25	0,07
006-ZR3	203	0,0495	0,005	16056	4,37	0,12007	0,46	4,792	1,62	0,2895	1,51	0,93	1957	16	1639	44	1784	27	16,27
004-ZR1	10	0,0208	0,022	1088104	30,43	0,11013	0,44	3,428	1,36	0,2257	1,23	0,91	1802	16	1312	29	1511	21	27,18
036-ZR18C	21	0,0106	0,094	211588	19,79	0,12325	2,03	2,480	2,95	0,1460	2,11	0,71	2004	71	878	35	1266	42	56,17
079-ZR46B	97	0,0365	0,034	29184	8,78	0,12149	0,67	5,955	1,46	0,3555	1,24	0,85	1978	24	1961	42	1969	25	0,89
060-ZR34C	18	0,0351	0,068	502453	24,07	0,12111	1,02	6,251	1,29	0,3743	0,70	0,54	1973	36	2050	24	2012	22	-3,91
074-ZR42C	32	0,0183	0,060	215184	26,40	0,12108	0,51	6,041	1,11	0,3618	0,92	0,82	1972	18	1991	31	1982	19	-0,94
005-ZR1B	34	0,0562	0,038	309811	39,94	0,12096	0,42	6,329	0,85	0,3795	0,64	0,75	1970	15	2074	23	2022	15	-5,24
066-ZR37C	25	0,0373	0,029	622342	23,34	0,12080	0,87	6,093	1,18	0,3658	0,70	0,59	1968	31	2010	24	1989	20	-2,11
068-ZR39C	94	0,0316	0,039	101627	52,07	0,12078	0,79	6,035	1,26	0,3624	0,91	0,72	1968	28	1993	31	1981	22	-1,30
040-ZR20B	17	0,0226	0,034	549421	19,38	0,12029	0,65	5,745	1,11	0,3464	0,82	0,74	1960	23	1917	27	1938	19	2,20

ADE-18P	^{204}Pb cps	^{206}Pb mV[1]	Th/U	^{206}Pb/^{204}Pb	1σ%	^{207}Pb/^{206}Pb	1σ %	^{207}Pb/^{235}U	1σ %	^{206}Pb/^{238}U	1σ %	Rho	^{207}Pb/^{206}Pb	2σ abs	^{206}Pb/^{238}U	2σ abs	^{207}Pb/^{235}U	2σ abs	% U-Pb disc[4]
025-ZR12C	89	0,0281	0,055	23227	9,84	0,11922	0,61	5,167	1,15	0,3143	0,90	0,78	1945	22	1762	28	1847	19	9,39
049-ZR26C	20	0,0232	0,048	469433	22,08	0,11918	1,01	5,683	1,57	0,3458	1,15	0,73	1944	36	1914	38	1929	27	1,52
053-ZR27B	109	0,0531	0,024	135279	51,93	0,11832	0,60	4,783	1,34	0,2931	1,15	0,85	1931	21	1657	33	1782	22	14,19
034-ZR24	463	0,0277	0,006	4288	4,36	0,06366	0,73	0,797	1,25	0,0908	0,95	0,76	731	31	561	10	595	11	23,27
028-ZR14B	40	0,0047	0,014	43831	30,63	0,06252	0,66	0,861	1,16	0,0999	0,88	0,76	692	28	614	10	631	11	11,32
025-ZR17	16	0,0184	0,010	482176	20,69	0,06018	0,78	0,796	1,46	0,0959	1,17	0,80	610	34	590	13	594	13	3,26
075-ZR43C	28	0,0133	0,006	173053	29,35	0,05923	0,54	0,814	1,17	0,0997	0,97	0,83	575	23	612	11	605	11	-6,41
033-ZR23	64	0,0307	0,007	195405	34,15	0,05966	0,54	0,817	1,09	0,0993	0,87	0,80	591	23	610	10	606	10	-3,23
059-ZR33C	43	0,0185	0,024	82740	43,14	0,05997	0,96	0,748	1,45	0,0904	1,02	0,71	603	41	558	11	567	13	7,39
034-ZR16B	20	0,0133	0,006	317236	20,88	0,05991	0,98	0,850	1,41	0,1028	0,95	0,67	600	42	631	11	624	13	-5,11
073-ZR41B	52	0,0249	0,010	74184	39,26	0,05928	0,56	0,840	1,20	0,1027	0,99	0,83	577	24	630	12	619	11	-9,22
ADE-23	**^{204}Pb cps**	**^{206}Pb mV[1]**	**Th/U**	**^{206}Pb/^{204}Pb**	**1σ%**	**^{207}Pb/^{206}Pb**	**1σ %**	**^{207}Pb/^{235}U**	**1σ %**	**^{206}Pb/^{238}U**	**1σ %**	**Rho**	**^{207}Pb/^{206}Pb**	**2σ abs**	**^{206}Pb/^{238}U**	**2σ abs**	**^{207}Pb/^{235}U**	**2σ abs**	**% U-Pb disc[4]**
040-ZR30	10	0,0108	0,368	388044	16,86	0,18323	0,75	13,038	1,28	0,5160	0,96	0,75	2682	25	2682	42	2682	24	0,00
038-ZR28	10	0,0124	0,366	416473	15,22	0,17932	0,49	11,610	0,99	0,4695	0,78	0,78	2647	16	2482	32	2573	18	6,23
035-ZR25	9	0,0111	0,347	377506	17,84	0,17762	0,41	10,649	1,22	0,4348	1,09	0,89	2631	13	2327	42	2493	22	11,53
027-ZR19	274	0,0135	0,199	201729	40,61	0,16733	0,94	9,414	1,53	0,4080	1,15	0,75	2531	31	2206	43	2379	28	12,85
026-ZR18B	12	0,0236	0,405	868227	14,13	0,17629	0,46	12,125	1,15	0,4988	0,98	0,86	2618	15	2609	42	2614	21	0,37
025-ZR17	15	0,0232	0,459	827172	23,06	0,16113	0,66	8,209	1,35	0,3695	1,12	0,83	2468	22	2027	39	2254	24	17,86
024-ZR16	6	0,0107	0,364	764391	35,93	0,18378	0,41	12,865	1,10	0,5077	0,95	0,86	2687	13	2647	41	2670	21	1,51
020-ZR15	12	0,0126	0,419	829567	56,75	0,17988	0,61	12,239	1,22	0,4935	0,99	0,81	2652	20	2586	42	2623	23	2,49
017-ZR12B	9	0,0114	0,320	753478	42,19	0,18296	0,37	13,145	1,20	0,5210	1,08	0,90	2680	12	2703	48	2690	23	-0,88
013-ZR8	13	0,0377	0,467	1163089	16,47	0,17543	0,38	11,629	1,16	0,4807	1,03	0,89	2610	12	2530	43	2575	21	3,05
058-ZR41	8	0,0031	0,269	138325	12,27	0,17800	0,82	12,064	1,48	0,4915	1,17	0,79	2634	27	2577	50	2609	28	2,17
056-ZR39	9	0,0059	0,305	178722	16,11	0,18059	0,63	12,624	1,12	0,5069	0,85	0,76	2658	21	2644	37	2652	21	0,56
055-ZR38	13	0,0054	0,278	189053	17,61	0,17302	0,81	10,482	1,51	0,4394	1,21	0,81	2587	27	2348	48	2478	28	9,25
054-ZR37C	10	0,0037	0,324	135685	13,51	0,18022	0,71	11,309	1,40	0,4551	1,15	0,82	2655	23	2418	46	2549	26	8,93
053-ZR36	11	0,0055	0,256	220553	17,53	0,16370	0,76	9,154	1,19	0,4055	0,84	0,71	2494	25	2194	31	2353	22	12,02

ADE-18P	^{204}Pb cps	^{206}Pb mV[1]	Th/U	^{206}Pb/^{204}Pb	1σ%	^{207}Pb/^{206}Pb	1σ %	^{207}Pb/^{235}U	1σ %	^{206}Pb/^{238}U	1σ %	Rho	^{207}Pb/^{206}Pb	2σ abs	^{206}Pb/^{238}U	2σ abs	^{207}Pb/^{235}U	2σ abs	% U-Pb disc[4]
050-ZR35	10	0,0212	0,474	796624	15,70	0,17399	1,05	12,024	1,58	0,5012	1,13	0,71	2596	35	2619	48	2606	29	-0,86
048-ZR33	12	0,0039	0,290	134781	18,18	0,18078	0,64	12,308	1,09	0,4937	0,80	0,74	2660	21	2587	34	2628	20	2,75
046-ZR31	10	0,0098	0,496	490951	27,30	0,18149	0,57	12,744	1,36	0,5092	1,18	0,87	2667	19	2653	51	2661	26	0,49
045-ZR30	13	0,0104	0,414	316069	16,09	0,18046	0,93	12,742	1,46	0,5121	1,07	0,73	2657	31	2665	46	2661	27	-0,32
044-ZR29	18	0,0336	0,427	1627654	63,56	0,17417	0,73	12,402	1,22	0,5164	0,91	0,74	2598	24	2684	40	2635	23	-3,30
037-ZR26C	14	0,0207	0,408	544929	17,42	0,17608	0,54	12,429	1,27	0,5119	1,09	0,86	2616	18	2665	48	2637	24	-1,85
036-ZR25	10	0,0028	0,296	103496	14,38	0,18436	0,68	12,660	1,17	0,4980	0,88	0,75	2692	22	2605	38	2655	22	3,24
035-ZR24	15	0,0140	0,413	404663	19,09	0,17921	0,43	12,163	1,06	0,4922	0,90	0,85	2646	14	2580	38	2617	20	2,47
034-ZR23	10	0,0027	0,326	90433	16,92	0,18135	0,70	12,107	1,16	0,4842	0,84	0,73	2665	23	2545	35	2613	22	4,50
033-ZR22	12	0,0201	0,434	1005132	25,07	0,17602	0,50	12,642	0,98	0,5209	0,76	0,78	2616	17	2703	34	2653	18	-3,33
029-ZR20	13	0,0063	0,386	201334	15,18	0,18180	0,71	12,309	1,19	0,4910	0,88	0,74	2669	24	2575	37	2628	22	3,53
028-ZR19	6	0,0046	0,418	191721	14,10	0,18322	0,58	12,868	1,08	0,5094	0,84	0,77	2682	19	2654	36	2670	20	1,06
024-ZR15	12	0,0044	0,181	121175	19,17	0,15103	1,60	7,705	2,11	0,3700	1,33	0,63	2358	54	2029	46	2197	38	13,93
019-ZR13B	12	0,0025	0,372	445018	85,40	0,18609	1,29	12,045	1,79	0,4694	1,17	0,66	2708	42	2481	48	2608	33	8,38
018-ZR13C	13	0,0054	0,128	426854	65,75	0,15428	0,75	7,949	1,25	0,3737	0,93	0,74	2394	25	2047	32	2225	22	14,51
016-ZR11	19	0,0431	0,242	862579	23,41	0,17223	0,49	11,749	1,03	0,4947	0,82	0,80	2579	16	2591	35	2585	19	-0,45
015-ZR10	9	0,0124	0,086	539967	14,41	0,15685	1,31	7,966	1,68	0,3683	0,98	0,59	2422	44	2022	34	2227	30	16,53
014-ZR9	14	0,0068	0,349	172807	23,53	0,17952	0,62	13,026	1,11	0,5262	0,84	0,76	2648	21	2726	37	2682	21	-2,91
013-ZR8	18	0,0320	0,301	805400	21,86	0,17465	0,66	12,496	1,00	0,5189	0,66	0,66	2603	22	2694	29	2642	19	-3,52
010-ZR7	15	0,0328	0,215	753028	20,53	0,17118	0,65	11,108	1,04	0,4706	0,73	0,70	2569	22	2486	30	2532	19	3,23
008-ZR5	13	0,0232	0,487	660430	19,94	0,16273	1,18	8,938	1,65	0,3983	1,10	0,66	2484	39	2161	40	2332	30	13,00
007-ZR4	14	0,0108	0,409	349442	15,86	0,17958	0,50	12,977	0,97	0,5241	0,75	0,77	2649	17	2716	33	2678	18	-2,54
006-ZR3	13	0,0302	0,133	783760	17,86	0,16736	0,93	10,100	1,41	0,4377	1,00	0,71	2531	31	2340	39	2444	26	7,56
005-ZR2	9	0,0091	0,382	311129	15,06	0,18024	0,55	12,195	1,21	0,4907	1,01	0,84	2655	18	2574	43	2620	23	3,07
004-ZR1	6	0,0046	0,287	186334	13,77	0,18417	1,41	12,527	1,74	0,4933	0,96	0,55	2691	46	2585	41	2645	32	3,93
047-ZR32	9	0,0366	0,345	1221664	15,69	0,15241	0,73	8,186	1,28	0,3895	0,99	0,77	2373	25	2121	36	2252	23	10,64
026-ZR17	16	0,0268	0,080	745848	18,74	0,16193	0,53	9,713	1,00	0,4350	0,75	0,76	2476	18	2328	29	2408	18	5,96

ADE-18P	^{204}Pb cps	^{206}Pb mV[1]	Th/U	^{206}Pb/^{204}Pb	1σ%	^{207}Pb/^{206}Pb	1σ %	^{207}Pb/^{235}U	1σ %	^{206}Pb/^{238}U	1σ %	Rho	^{207}Pb/^{206}Pb	2σ abs	^{206}Pb/^{238}U	2σ abs	^{207}Pb/^{235}U	2σ abs	% U-Pb disc[4]
009-ZR6	12	0,0404	0,114	1392995	17,10	0,15993	0,56	9,244	1,03	0,4192	0,78	0,76	2455	19	2257	30	2362	19	8,08
049-ZR34	11	0,0263	0,369	24603455	96,49	0,16337	0,69	10,060	1,32	0,4466	1,07	0,81	2491	23	2380	42	2440	24	4,45
020-ZR14	22	0,0196	0,301	337389	22,52	0,16246	0,85	10,195	1,33	0,4551	0,96	0,72	2481	29	2418	39	2453	25	2,55
039-ZR29B	12	0,0084	0,321	417726	20,95	0,16780	0,90	11,085	1,62	0,4791	1,30	0,80	2536	30	2523	54	2530	30	0,49
019-ZR14	8	0,0117	0,441	554167	25,35	0,16863	0,80	8,865	1,70	0,3813	1,45	0,85	2544	27	2082	51	2324	31	18,16
008-ZR5B	30	0,0578	0,298	1179726	25,20	0,16600	0,51	10,471	1,50	0,4574	1,36	0,91	2518	17	2428	55	2477	28	3,55
005-ZR2	13	0,0099	0,373	329473	15,59	0,16689	0,40	9,704	1,59	0,4217	1,49	0,94	2527	14	2268	57	2407	29	10,24
004-ZR1	112	0,0512	0,245	427724	24,05	0,16650	0,84	7,766	1,94	0,3383	1,71	0,88	2523	28	1878	56	2204	35	25,54
016-ZR11B	45	0,0931	0,040	323623	47,01	0,13787	0,74	8,172	1,08	0,4298	0,69	0,64	2201	26	2305	27	2250	19	-4,74
018-ZR13B	11	0,0327	0,022	1036766	17,01	0,14216	0,60	7,999	1,09	0,4081	0,83	0,76	2254	21	2206	31	2231	20	2,11
017-ZR12	5	0,0210	0,015	902285	12,63	0,13259	1,02	7,116	1,69	0,3892	1,30	0,77	2133	35	2119	47	2126	30	0,63
038-ZR26B	12	0,0271	0,017	883570	15,92	0,11971	0,65	6,003	1,07	0,3637	0,77	0,71	1952	23	2000	26	1976	19	-2,44
025-ZR16	23	0,0086	0,013	210003	23,19	0,11877	1,12	5,227	1,52	0,3192	0,97	0,63	1938	40	1786	30	1857	26	7,86
027-ZR18	10	0,0140	0,048	558429	14,05	0,11784	0,75	5,851	1,21	0,3601	0,87	0,72	1924	27	1983	30	1954	21	-3,06
ADE-12L	**^{204}Pb cps**	**^{206}Pb mV[1]**	**Th/U**	**^{206}Pb/^{204}Pb**	**1σ%**	**^{207}Pb/^{206}Pb**	**1σ %**	**^{207}Pb/^{235}U**	**1σ %**	**^{206}Pb/^{238}U**	**1σ %**	**Rho**	**^{207}Pb/^{206}Pb**	**2σ abs**	**^{206}Pb/^{238}U**	**2σ abs**	**^{207}Pb/^{235}U**	**2σ abs**	**% U-Pb disc[4]**
012-ZR34B	2755	0,0332	0,506	884	6,26	0,13893	1,43	4,228	3,26	0,2207	2,90	0,89	2214	49	1286	67	1679	53	41,93
028-ZR42C	1733	0,0212	0,470	854	3,52	0,13459	0,50	4,253	1,68	0,2291	1,56	0,93	2159	17	1330	37	1684	27	38,39
019-ZR38	1485	0,0306	0,553	1497	5,13	0,12995	0,77	4,572	1,83	0,2552	1,62	0,88	2097	27	1465	42	1744	30	30,14
018-ZR13	1604	0,0299	0,315	1184	7,22	0,12484	0,92	5,073	1,45	0,2947	1,05	0,73	2027	32	1665	31	1832	24	17,85
013-ZR8	153	0,0306	0,188	13525	4,84	0,12379	0,57	5,772	1,08	0,3381	0,84	0,78	2012	20	1878	27	1942	19	6,66
015-ZR10	72	0,0200	0,266	22822	12,33	0,12298	0,84	5,751	1,24	0,3391	0,84	0,68	2000	30	1883	27	1939	21	5,87
010-ZR7	229	0,0311	0,175	25689	44,21	0,12291	0,98	5,430	2,75	0,3204	2,55	0,93	1999	35	1792	79	1890	47	10,36
039-ZR29B	248	0,0185	0,138	5736	9,70	0,12228	0,84	5,181	1,26	0,3073	0,85	0,68	1990	30	1727	26	1849	21	13,19
006-ZR32C	758	0,0494	0,424	4561	4,29	0,12124	1,59	5,086	2,16	0,3042	1,42	0,66	1975	56	1712	43	1834	36	13,28
009-ZR6	52	0,0367	0,020	121702	50,22	0,12052	0,58	5,818	1,04	0,3501	0,78	0,75	1964	20	1935	26	1949	18	1,48
036-ZR45C	141	0,0179	0,443	8167	16,10	0,11902	0,57	5,986	1,27	0,3647	1,07	0,85	1942	20	2005	37	1974	22	-3,24
027-ZR41B	343	0,0445	0,413	10733	12,39	0,11881	0,48	5,931	1,38	0,3620	1,23	0,90	1938	17	1992	42	1966	24	-2,75

ADE-18P	^{204}Pb cps	^{206}Pb mV[1]	Th/U	^{206}Pb/^{204}Pb	1σ%	^{207}Pb/^{206}Pb	1σ %	^{207}Pb/^{235}U	1σ %	^{206}Pb/^{238}U	1σ %	Rho	^{207}Pb/^{206}Pb	2σ abs	^{206}Pb/^{238}U	2σ abs	^{207}Pb/^{235}U	2σ abs	% U-Pb disc[4]
023-ZR39B	550	0,0428	0,697	4998	5,89	0,11861	1,37	5,462	1,76	0,3340	1,03	0,59	1935	49	1858	33	1895	30	4,02
016-ZR36B	289	0,0189	0,282	4870	7,93	0,11810	0,97	5,654	2,51	0,3472	2,29	0,91	1928	35	1921	76	1924	43	0,35
014-ZR9	41	0,0065	0,342	262509	47,11	0,13284	0,74	7,000	1,15	0,3821	0,81	0,70	2136	26	2086	29	2111	20	2,32
033-ZR23	601	0,0266	0,857	6109	19,43	0,12813	1,23	7,183	2,07	0,4066	1,63	0,79	2073	43	2199	61	2134	37	-6,11
025-ZR40B	1515	0,0192	0,342	781	4,22	0,12558	0,59	3,917	2,49	0,2262	2,39	0,96	2037	21	1315	57	1617	40	35,46
016-ZR11	1061	0,0159	0,201	1586	10,53	0,14490	0,63	1,800	3,88	0,0901	3,81	0,98	2287	22	556	41	1046	50	75,68
018-ZR37B	1893	0,0156	0,290	536	5,62	0,12723	1,90	3,357	3,05	0,1914	2,35	0,77	2060	66	1129	49	1495	47	45,20
019-ZR14	702	0,0128	0,332	4985	24,64	0,12661	1,96	5,524	2,39	0,3164	1,33	0,56	2051	68	1772	41	1904	41	13,62
024-ZR16	328	0,0277	0,509	6022	5,12	0,12674	0,43	5,606	1,60	0,3208	1,49	0,93	2053	15	1794	47	1917	27	12,65
027-ZR19	1470	0,0174	0,432	1005	17,13	0,12752	1,30	5,829	1,64	0,3315	0,92	0,56	2064	46	1846	29	1951	28	10,58
ADE-18Li	**^{204}Pb cps**	**^{206}Pb mV[1]**	**Th/U**	**^{206}Pb/^{204}Pb**	**1s%**	**^{207}Pb/^{206}Pb**	**1s %**	**^{207}Pb/^{235}U**	**1s %**	**^{206}Pb/^{238}U**	**1s %**	**Rho**	**^{207}Pb/^{206}Pb**	**2s abs**	**^{206}Pb/^{238}U**	**2s abs**	**^{207}Pb/^{235}U**	**2s abs**	**% U-Pb disc[4]**
049-ZR22B	363	0,1019	0,296	93944	81,06	0,19329	2,24	10,361	2,67	0,3887	1,39	0,52	2770	73	2117	50	2468	49	23,59
048-ZR22C	725	0,0672	0,462	10077	16,05	0,20756	0,52	15,251	1,13	0,5329	0,93	0,82	2887	17	2753	42	2831	21	4,61
046-ZR21C	99	0,0964	0,223	243099	60,86	0,20410	1,53	14,006	1,66	0,4977	0,52	0,71	2859	49	2604	22	2750	31	8,94
047-ZR21B	22	0,0671	0,275	1446018	19,48	0,20692	0,39	14,927	0,81	0,5232	0,61	0,75	2882	13	2713	27	2811	15	5,86
040-ZR18C	175	0,0877	0,132	210659	45,47	0,20570	1,69	14,023	3,81	0,4944	3,40	0,89	2872	54	2590	144	2751	71	9,83
037-ZR16C	1167	0,0787	0,516	35152	83,40	0,19606	1,95	9,976	4,32	0,3690	3,83	0,89	2794	63	2025	132	2433	78	27,52
030-ZR13C	162	0,0622	0,089	26388	5,26	0,20685	0,89	12,409	2,54	0,4351	2,35	0,93	2881	29	2328	91	2636	47	19,18
029-ZR12C	21	0,0369	0,383	915919	19,24	0,20966	0,55	13,768	1,57	0,4762	1,42	0,91	2903	18	2511	59	2734	29	13,51
028-ZR11B	1400	0,0803	0,158	3641	3,45	0,17729	1,38	7,280	2,61	0,2978	2,18	0,84	2628	46	1680	64	2146	46	36,05
026-ZR10B	2311	0,0796	0,314	2636	7,30	0,18937	0,43	7,803	3,63	0,2988	3,59	0,99	2737	14	1686	106	2209	64	38,41
025-ZR10C	25	0,0562	0,309	1122563	22,75	0,21005	0,41	14,950	0,99	0,5162	0,82	0,83	2906	13	2683	36	2812	19	7,67
024-ZR9B	98	0,0248	0,313	15877	9,76	0,19717	1,08	11,685	3,03	0,4298	2,80	0,93	2803	35	2305	108	2580	56	17,77
020-ZR9C	889	0,0951	0,267	7782	5,12	0,19029	1,09	9,662	2,75	0,3682	2,49	0,91	2745	36	2021	86	2403	50	26,37
018-ZR8C	167	0,0570	0,211	27281	7,96	0,18511	0,70	9,913	1,21	0,3883	0,91	0,76	2699	23	2115	33	2427	22	21,64
016-ZR7C	289	0,0862	0,548	24598	10,18	0,19276	0,80	10,908	3,12	0,4104	2,99	0,96	2766	26	2217	112	2515	57	19,86
015-ZR6B	311	0,0448	0,199	11476	24,37	0,19680	0,85	11,053	1,43	0,4073	1,09	0,76	2800	28	2203	41	2528	27	21,33

ADE-18P	^{204}Pb cps	^{206}Pb mV[1]	Th/U	^{206}Pb/^{204}Pb	1σ%	^{207}Pb/^{206}Pb	1σ %	^{207}Pb/^{235}U	1σ %	^{206}Pb/^{238}U	1σ %	Rho	^{207}Pb/^{206}Pb	2σ abs	^{206}Pb/^{238}U	2σ abs	^{207}Pb/^{235}U	2σ abs	% U-Pb disc[4]
014-ZR6C	401	0,0498	0,353	11392	10,65	0,20689	0,58	14,612	1,45	0,5122	1,28	0,88	2881	19	2666	56	2790	27	7,47
010-ZR5C	1220	0,0642	0,655	5581	11,53	0,21277	1,16	10,523	2,70	0,3587	2,41	0,89	2927	37	1976	82	2482	50	32,49
009-ZR4C	280	0,0333	0,522	8044	5,27	0,19815	0,78	9,854	3,21	0,3606	3,09	0,96	2811	25	1985	105	2421	58	29,38
007-ZR2C	405	0,0643	0,438	19439	17,52	0,20942	0,41	16,053	1,27	0,5559	1,15	0,90	2901	13	2850	53	2880	24	1,77
008-ZR3C	21	0,0307	0,404	760206	19,33	0,13688	0,42	6,899	0,82	0,3655	0,60	0,73	2188	15	2008	21	2098	15	8,22
004-ZR1C	237	0,0971	0,037	596854	27,26	0,12061	2,50	4,241	5,37	0,2550	4,73	0,88	1965	88	1464	123	1682	86	25,49
038-ZR17C	1322	0,0382	0,120	2469	5,42	0,14089	3,26	3,816	3,64	0,1964	1,58	0,43	2238	111	1156	33	1596	58	48,34
006-ZR1BB	578	0,0972	0,048	240307	84,68	0,05794	0,68	0,755	0,90	0,0945	0,44	0,49	528	30	582	5	571	8	-10,26
039-ZR17B	66	0,0204	0,119	111250	56,15	0,05990	0,69	0,766	1,14	0,0927	0,83	0,73	600	30	572	9	577	10	4,73
005-ZR1B	98	0,0575	0,183	39839	5,40	0,05971	0,38	0,753	0,83	0,0914	0,64	0,77	593	16	564	7	570	7	4,87
036-ZR15C	4926	0,1175	0,069	334390	20,32	0,05781	1,97	0,713	3,21	0,0895	2,51	0,78	523	85	552	27	547	27	-5,69

Data report template (with modifications) from http://www.plasmage.org/recommendations

[1] Convertion factor from mV to CPS is 62500000

[2] Concentration uncertainty c.20%

[3] Data not corrected for common-Pb

[4] Not corrected for common-Pb

[5] Discordance calculated as (1-(^{206}Pb/^{238}U age/^{207}Pb/^{206}Pb age))*100

Decay constants of Jaffey et al. (1971) used

Supplementary Table 4.5. Lu-Hf isotopes from the Campo Grande migmatite.

		CHUR	DM	Sample (present-day ratios)				Sample (initial ratios)			Crust Model Ages (Ga)		TDM (Hf)
Migmatite/Zircon	U-Pb age (Ma)	^{176}Hf/^{177}Hf (t)	^{176}Hf/^{177}Hf(t)	^{176}Hf/^{177}Hf	±2σ	^{176}Lu/^{177}Hf	±2σ	^{176}Hf/^{177}Hf(t)	epsilon Hf (t)	±2σ	Mafic	Felsic	(Ga)
ADE-15-ZR41R	630	0,282387	0,282791	0,281558	0,000034	0,001855	0,000111	0,281536	-30,16	2,39	4,49	2,91	2,40
ADE-15-ZR16R	631	0,282387	0,282790	0,281389	0,000029	0,000774	0,000013	0,281380	-35,65	1,24	4,95	3,19	2,56
ADE-15-ZR23	610	0,282400	0,282806	0,282255	0,000079	0,001574	0,000048	0,282237	-5,78	0,39	2,39	1,66	1,41
ADE-15-ZR19	1993	0,281511	0,281779	0,281308	0,000020	0,000966	0,000010	0,281272	-8,51	0,19	3,59	2,93	2,68
ADE-15-ZR46R	1978	0,281521	0,281790	0,281180	0,000026	0,001488	0,000041	0,281124	-14,11	0,56	4,06	3,20	2,89

		CHUR	DM	Sample (present-day ratios)				Sample (initial ratios)			Crust Model Ages (Ga)		TDM (Hf)
Migmatite/Zircon	U-Pb age (Ma)	$^{176}Hf/^{177}Hf$ (t)	$^{176}Hf/^{177}Hf$(t)	$^{176}Hf/^{177}Hf$	±2σ	$^{176}Lu/^{177}Hf$	±2σ	$^{176}Hf/^{177}Hf$(t)	epsilon Hf (t)	±2σ	Mafic	Felsic	(Ga)
ADE-15-ZR39C	1968	0,281528	0,281798	0,281129	0,000021	0,000854	0,000004	0,281097	-15,31	0,28	4,16	3,26	2,91
ADE-15-ZR41C	2968	0,280871	0,281039	0,281215	0,000029	0,001181	0,000016	0,281147	9,85	0,21	2,62	2,77	2,82
ADE-15-ZR46C	2913	0,280907	0,281082	0,280766	0,000048	0,000915	0,000034	0,280715	-6,85	0,30	4,07	3,59	3,40
ADE-15-ZR21	2932	0,280894	0,281067	0,281013	0,000075	0,002078	0,000076	0,280896	0,04	0,00	3,48	3,25	3,17
ADE-15-ZR13C	3009	0,280843	0,281008	0,280840	0,000030	0,000533	0,000010	0,280809	-1,21	0,03	3,64	3,38	3,27
ADE-15-ZR30	3155	0,280746	0,280896	0,280901	0,000032	0,001767	0,000064	0,280794	1,69	0,07	3,48	3,34	3,29
ADE-15-ZR8C	3256	0,280679	0,280818	0,280743	0,000044	0,002303	0,000040	0,280599	-2,87	0,07	3,95	3,66	3,56
ADE-23-ZR29R	2598	0,281115	0,281322	0,281609	0,000025	0,002301	0,000068	0,281494	13,49	0,52	2,04	2,28	2,36
ADE-23-ZR12R	2610	0,281107	0,281312	0,281181	0,000038	0,001999	0,000042	0,281082	-0,91	0,02	3,34	3,04	2,93
ADE-23-ZR18R	2618	0,281102	0,281306	0,281310	0,000065	0,003496	0,000059	0,281135	1,19	0,03	3,16	2,94	2,86
ADE-23-ZR5R	2518	0,281168	0,281383	0,281346	0,000048	0,004978	0,000135	0,281107	-2,17	0,07	3,39	3,03	2,93
ADE-23-ZR11	2579	0,281128	0,281336	0,281279	0,000029	0,003520	0,000034	0,281105	-0,81	0,01	3,31	3,01	2,91
ADE-23-ZR35	2596	0,281116	0,281323	0,281426	0,000033	0,004354	0,000045	0,281210	3,32	0,06	2,96	2,81	2,76
ADE-23-ZR31	2667	0,281070	0,281269	0,281509	0,000041	0,004596	0,000081	0,281275	7,30	0,19	2,65	2,66	2,66
ADE-23-ZR30	2657	0,281076	0,281277	0,281221	0,000093	0,001923	0,000083	0,281123	1,67	0,09	3,14	2,94	2,87
ADE-23-ZR29	2536	0,281156	0,281369	0,281759	0,000049	0,005096	0,000064	0,281512	12,66	0,27	2,08	2,27	2,32
ADE-23-ZR26C	2616	0,281103	0,281308	0,281583	0,000047	0,004164	0,000135	0,281375	9,66	0,40	2,40	2,49	2,52
ADE-23-ZR11R	2201	0,281376	0,281623	0,281658	0,000053	0,003352	0,000065	0,281518	5,04	0,16	2,53	2,40	2,35
ADE-23-ZR13R	2254	0,281341	0,281583	0,281085	0,000038	0,003462	0,000076	0,280937	-14,38	0,45	4,27	3,44	3,18
ADE-23-ZR26R	1952	0,281538	0,281810	0,281718	0,000041	0,002974	0,000036	0,281607	2,47	0,06	2,59	2,33	2,24
ADE-23-ZR18	1924	0,281556	0,281831	0,282183	0,000085	0,004154	0,000111	0,282031	16,87	0,65	1,28	1,55	1,62
ADE-10-ZR8	2900	0,280916	0,281091	0,281002	0,000037	0,001119	0,000035	0,280940	0,86	0,03	3,38	3,18	3,10
ADE-10-ZR10	2915	0,280906	0,281080	0,280920	0,000039	0,001084	0,000009	0,280859	-1,66	0,03	3,61	3,32	3,21
ADE-10-ZR15	2926	0,280898	0,281071	0,281077	0,000042	0,002440	0,000117	0,280940	1,48	0,08	3,34	3,17	3,11
ADE-10-ZR32	2931	0,280895	0,281068	0,281100	0,000040	0,001528	0,000012	0,281014	4,23	0,07	3,10	3,03	3,00
ADE-18-ZR1C	2982	0,280861	0,281029	0,281083	0,000031	0,001857	0,000024	0,280976	4,10	0,08	3,15	3,08	3,05

		CHUR	DM	Sample (present-day ratios)				Sample (initial ratios)			Crust Model Ages (Ga)		TDM (Hf)
Migmatite/Zircon	**U-Pb age (Ma)**	**$^{176}Hf/^{177}Hf$ (t)**	**$^{176}Hf/^{177}Hf$(t)**	**$^{176}Hf/^{177}Hf$**	**±2σ**	**$^{176}Lu/^{177}Hf$**	**±2σ**	**$^{176}Hf/^{177}Hf$(t)**	**epsilon Hf (t)**	**±2σ**	**Mafic**	**Felsic**	**(Ga)**
ADE-18-ZR3C	2991	0,280855	0,281022	0,280934	0,000028	0,001112	0,000012	0,280871	0,54	0,01	3,47	3,27	3,19
ADE-18-ZR20	2980	0,280863	0,281030	0,280931	0,000031	0,001213	0,000022	0,280862	-0,03	0,00	3,51	3,29	3,21
ADE-18-ZR21C	2974	0,280867	0,281035	0,281213	0,000053	0,002878	0,000131	0,281049	6,49	0,34	2,93	2,95	2,95
ADE-18Li-ZR2	2901	0,280915	0,281091	0,280957	0,000028	0,001186	0,000031	0,280891	-0,84	0,03	3,53	3,27	3,17
ADE-18Li-ZR15C	552	0,282437	0,282848	0,282147	0,000025	0,004806	0,000056	0,282097	-12,02	0,62	2,89	1,93	1,71
ADE-18Li-ZR17C	2238	0,281351	0,281594	0,281920	0,000076	0,002858	0,000118	0,281798	15,88	0,82	1,58	1,86	1,95
ADE-18Li-ZR17R	572	0,282424	0,282833	0,281795	0,000088	0,002497	0,000108	0,281768	-23,24	1,91	3,87	2,52	2,11
ADE-18Li-ZR22C	2887	0,280924	0,281101	0,281063	0,000032	0,001416	0,000061	0,280985	2,16	0,11	3,26	3,10	3,04
ADE-18Li-ZR22R	2770	0,281002	0,281191	0,281023	0,000033	0,001638	0,000023	0,280936	-2,35	0,05	3,58	3,24	3,12
ADE-12-ZR9	2136	0,281418	0,281672	0,281178	0,000029	0,000036	0,000005	0,281177	-8,58	1,28	3,69	3,05	2,79
ADE-12-ZR10	2000	0,281507	0,281774	0,281294	0,000031	0,000602	0,000016	0,281271	-8,36	0,34	3,58	2,93	2,67
ADE-12-ZR6	1964	0,281530	0,281801	0,281323	0,000028	0,001126	0,000025	0,281281	-8,84	0,29	3,60	2,92	2,67
ADE-12-ZR23	2073	0,281459	0,281719	0,281416	0,000041	0,001119	0,000050	0,281372	-3,10	0,20	3,17	2,71	2,55

Supplementary Table 4.6. Rare-earth elements in zircon from the Campo Grande migmatite.

Migmatite Sample	Zircon Crystal	Age (Ma)	Hf	La	Ce	Pr	Nd	Sm	Eu	Gd	Tb	Dy	Y	Ho	Er	Tm	Yb	Lu
											(ppm)							
ADE-10	ZR-32	2931	8230	0,01	8,80	<LD	4,80	25,5	1,38	48,0	14,1	158	1380	47,1	214	43,7	357	57,5
ADE-10	ZR29	2904	7800	1,70	78,0	<LD	20,0	34,0	1,21	55,4	17,0	172	1690	56,0	251	54,7	450	81,0
ADE-10	ZR-10	2915	9810	<LD	12,2	<LD	0,73	6,90	0,50	14,90	4,20	47,3	491	15,8	84,0	18,3	131	25,5
ADE-15	ZR-4	2898	8600	0,27	9,30	0,47	3,80	12,9	0,96	24,0	7,00	85,0	890	26,8	146	33,0	350	54,0
ADE-15	ZR-5	2905	9100	2,50	67,0	4,60	27,9	109	8,10	180	41,0	470	3300	139	560	101	710	141
ADE-15	ZR-19	1993	7100	0,36	6,90	0,28	1,75	9,10	0,35	23,8	8,50	119	1510	46,5	206	43,2	290	46,8
ADE-15	ZR-17	610	8400	0,20	4,80	0,30	0,90	4,10	0,58	10,5	3,30	47,0	740	20,5	95,0	24,4	277	53,0
ADE-15	ZR-16	2898	10020	0,19	33,80	0,26	3,17	32,5	6,20	112	30,2	430	4960	171	750	187	1370	263
ADE-15	ZR-10	1999	7370	<LD	3,03	<LD	0,15	3,51	<LD	19,5	6,40	106	1384	40,2	173	43,5	316	44,6
ADE-15	ZR-11	1927	8700	3,70	36,0	3,20	20,0	24,0	0,93	46,0	12,0	162	1870	56,0	280	56,0	460	62,0
ADE-15	ZR-25	2893	7750	0,49	4,59	1,49	1,26	<LD	0,37	5,80	1,90	23,9	200	6,9	29,0	4,9	40,0	4,30
ADE-15	ZR-27	1979	7700	0,14	6,90	<LD	0,78	3,00	<LD	12,7	4,10	53,0	800	21,6	88,0	27,4	250	39,1
ADE-15	ZR-29C	2826	6630	0,05	164	<LD	15,00	60,50	13,50	74,0	11,3	105	1000	32,4	139	24,8	244	29,1
ADE-15	ZR-26	2874	6610	0,18	16,1	<LD	2,50	12,30	1,70	41,0	11,3	129	1460	48,0	244	51,2	347	69,0
ADE-23	ZR-18	1924	8580	1,31	27,0	1,90	13,0	25,0	1,10	23,2	7,80	87,0	1200	35,7	190	71,3	757	209
ADE-23	ZR-11	2579	10100	18,8	180	27,0	160	220	9,60	190	40,0	510	5100	140	690	140	1300	200
ADE-23	ZR-35	2596	5000	1,35	47,0	2,10	9,40	28,0	1,12	62,0	21,0	230	3000	87,0	440	89,0	690	140
ADE-23	ZR-31	2667	6000	4,00	72,0	8,30	21,0	40,0	0,25	102	25,0	400	4500	144	680	140	1210	190
ADE-23	ZR-30	2657	6400	0,04	3,65	0,29	0,65	2,43	0,19	7,06	1,77	30,2	452	14,0	72,0	24,6	148	56,0
ADE-23	ZR-29	2536	6800	<LD	55,0	0,57	2,20	25,0	0,18	69,0	27,0	370	4700	140	680	160	2000	200
ADE-23	ZR-26	2616	7560	0,42	3,90	1,90	2,50	3,10	0,11	7,30	2,52	58,6	1159	32,7	237	69,2	<LD	160

Supplementary Table 4.7. Sm-Nd isotopic data for the Campo Grande migmatite.

Sample	Component migmatite	Sm (ppm)	Nd (ppm)	$^{147}Sm/^{144}Nd$	$^{143}Nd/^{144}Nd \pm 2SE$	$\varepsilon Nd_{(0)}$	$\varepsilon Nd_{(t)}$	T_{DM}(Ga)
AT-28P	Paleosome	3.16	19.13	0.1000	0.510589+/-19	-39.97	-3.92	3.3
ADE-15P	Paleosome	9.08	55.32	0.0993	0.511019+/-1	-31.57	4.8	2.69
ADE-18P	Paleosome	4.86	27.77	0.1058	0.510976+/-8	-32.41	2.56	2.93
ADE-10P	Paleosome	5.55	33.2	0.1011	0.510677+/-8	-38.25	-2.6	3.22
ADE-23P	Paleosome	17.42	93.43	0.1127	0.511325+/-4	-25.6	3.01	2.59
ADE-14L	Concordant Leucosome	5.05	32.01	0.0954	0.511166+/-4	-28.71	-2.74	2.41
ADE-03L	Concordant Leucosome	6.09	36.56	0.1006	0.511149+/-9	-29.05	-4.42	2.55
ADE-04L	Concordant Leucosome	5.01	31.61	0.0958	0.511032+/-17	-31.32	-5.46	2.59
ADE-12L	Concordant Leucosome	3.52	24.35	0.0873	0.510997+/-11	-32.01	-3.96	2.46
AT-23Li	Injected Leucosome	26.93	169.75	0.0959	0.511189+/-13	-28.27	-20.57	2.39
ADE-13Li	Injected Leucosome	12.48	70.89	0.1064	0.511554+/-9	-21.14	-14.25	2.1

Supplementary Table 4.8. Zircon saturation temperature related to Watson and Harrison (1983), Boehnke et al. (2013) and Gervasoni et al. (2016) geothermometer, and Ti-in-biotite.

Sample	Rock	Migmatite component	Watson and Harrison (1983)	Boehnke et al. (2013)	Gervasoni et al. (2016)	Wu and Chen (2015) (biotite at 4kbar)	Wu and Chen (2015) (biotite at 6kbar)
ADE-10P	Granodiorite	Paleosome	830ºC	591ºC	717ºC	561 - 643ºC	596 - 682ºC
ADE-14P	Granodiorite		808ºC	574ºC	635ºC		
ADE-15P	Tonalite		776ºC	549ºC	557ºC	432 - 514ºC	459 - 546ºC
ADE-18P	Tonalite		764ºC	539ºC	537ºC		
ADE-23L	Alkali granite	Concordant leucosome	953ºC	687ºC	936ºC	661 - 747ºC	702 - 793ºC
ADE-12L	Granite		836ºC	596ºC	774ºC	598 - 692ºC	634 - 724ºC
AT-28L	Granite		811ºC	576ºC	687ºC		
ADE-04L	Granite		806ºC	572ºC	716ºC		
ADE-19L	Granite		801ºC	569ºC	659ºC		
ADE-18L	Granite		648ºC	449ºC	381ºC		
ADE-13Li	Granite	Injected leucosome	872ºC	624ºC	829ºC		
AT-23Li	Granite		867ºC	620ºC	797ºC		
ADE-18Li	Pegmatite		640ºC	442ºC	378ºC		

Supplementary Table 4.9. Biotite formation temperatures from the Campo Grande migmatite based on Wu and Chen (2015) geothermometer.

Sample	SiO2	TiO2	Al2O3	FeO(tot)	MnO	MgO	CaO	Na2O	K2O	Cr2O3	NiO	Sum	AlVI	X(Fe)	X(Mg)	X(Ti)	ln[T(ºC)]	T (ºC)
ADE-12 Bt 1	33,53	2,71	17,02	22,57	0,39	6,37	0,07	0,12	9,76	0,00	0,01	92,56	0,32	0,52	0,29	0,06	6,52	680
ADE-12 Bt 2	34,25	3,10	16,99	23,21	0,48	6,68	0,02	0,05	9,62	0,02	0,04	94,46	0,29	0,52	0,30	0,07	6,54	690
ADE-12 Bt 3	33,94	2,67	16,51	22,72	0,36	6,48	0,10	0,09	8,34	0,00	0,00	91,21	0,33	0,52	0,30	0,06	6,52	675
ADE-12 Bt 4	35,94	2,68	17,74	20,17	0,32	5,99	0,14	0,13	8,40	0,03	0,01	91,55	0,50	0,46	0,28	0,06	6,58	720
ADE-12 Bt 5	35,01	2,60	17,02	20,48	0,32	6,72	0,15	0,10	8,79	0,01	0,00	91,21	0,41	0,47	0,31	0,06	6,52	677
ADE-12 Bt 6	35,08	3,17	16,95	21,71	0,42	6,73	0,06	0,05	9,39	0,00	0,03	93,58	0,34	0,49	0,31	0,07	6,55	701
ADE-12 Bt 7	34,44	2,84	17,42	21,64	0,38	6,61	0,03	0,11	9,39	0,00	0,01	92,85	0,37	0,49	0,30	0,07	6,54	689
ADE-12 Bt 8	34,04	3,19	16,97	23,42	0,49	6,69	0,00	0,12	9,82	0,02	0,00	94,77	0,27	0,52	0,30	0,07	6,54	692
ADE-12 Bt 9	34,99	3,85	17,24	22,58	0,31	6,92	0,00	0,16	9,85	0,00	0,01	95,90	0,28	0,50	0,31	0,09	6,58	724
ADE-12 Bt 10	34,49	3,37	16,92	23,19	0,42	6,85	0,03	0,11	9,59	0,00	0,02	95,00	0,27	0,51	0,31	0,08	6,55	698
ADE-12 Bt 11	35,06	2,96	16,97	22,34	0,24	6,82	0,04	0,10	8,86	0,00	0,01	93,39	0,34	0,50	0,31	0,07	6,53	686
ADE-12 Bt 12	34,78	3,47	16,67	22,25	0,41	6,73	0,07	0,08	8,43	0,06	0,03	92,98	0,31	0,50	0,30	0,08	6,57	714
ADE-12 Bt 13	34,19	3,01	16,76	21,91	0,39	6,85	0,02	0,09	8,92	0,07	0,03	92,22	0,32	0,50	0,31	0,07	6,53	685
ADE-12 Bt 14	34,60	3,06	16,84	20,85	0,26	6,57	0,02	0,08	8,86	0,09	0,00	91,22	0,38	0,48	0,30	0,07	6,56	705
ADE-12 Bt 15	33,76	2,83	17,14	21,60	0,32	6,60	0,03	0,09	8,40	0,02	0,02	90,80	0,37	0,49	0,30	0,07	6,53	688
ADE-12 Bt 17	35,33	2,76	16,80	20,68	0,39	6,66	0,10	0,14	8,07	0,00	0,00	90,93	0,41	0,47	0,31	0,06	6,54	689
ADE-12 Bt 18	35,12	2,01	17,47	22,21	0,29	6,74	0,07	0,09	8,13	0,00	0,04	92,15	0,43	0,49	0,30	0,05	6,45	634
ADE-15 Bt 1	35,92	2,03	15,28	16,26	0,23	11,98	0,04	0,13	9,53	0,12	0,03	91,55	0,24	0,35	0,52	0,04	6,30	546
ADE-15 Bt 2	36,51	1,44	16,00	17,19	0,22	13,04	0,01	0,11	9,33	0,18	0,00	94,04	0,24	0,35	0,54	0,03	6,20	492
ADE-15 Bt 3	36,40	1,80	15,88	17,20	0,18	11,96	0,02	0,05	9,59	0,01	0,02	93,10	0,26	0,36	0,50	0,04	6,27	530
ADE-15 Bt 4	36,04	1,99	15,30	18,05	0,24	12,10	0,00	0,07	9,61	0,00	0,04	93,45	0,20	0,38	0,51	0,04	6,28	533
ADE-15 Bt 5	36,64	1,72	15,98	17,56	0,17	12,09	0,01	0,11	9,73	0,13	0,05	94,19	0,25	0,36	0,51	0,04	6,26	521
ADE-15 Bt 6	36,33	1,94	15,51	17,92	0,23	12,02	0,02	0,08	9,95	0,08	0,01	94,09	0,21	0,37	0,51	0,04	6,28	532
ADE-15 Bt 7	36,39	1,52	15,76	18,16	0,28	12,32	0,02	0,07	9,47	0,14	0,00	94,13	0,23	0,37	0,51	0,03	6,21	500
ADE-15 Bt 8	36,28	1,62	15,89	17,14	0,30	12,91	0,03	0,06	9,55	0,29	0,00	94,05	0,22	0,35	0,53	0,03	6,23	506

Sample	SiO2	TiO2	Al2O3	FeO(tot)	MnO	MgO	CaO	Na2O	K2O	Cr2O3	NiO	Sum	AlVI	X(Fe)	X(Mg)	X(Ti)	ln[T(ºC)]	T (ºC)
ADE-15 Bt 9	36,58	1,61	15,60	18,29	0,27	12,17	0,02	0,13	8,77	0,03	0,03	93,49	0,24	0,38	0,50	0,03	6,23	509
ADE-15 Bt 10	37,12	1,28	15,89	18,88	0,28	11,94	0,05	0,11	9,24	0,00	0,07	94,86	0,26	0,39	0,49	0,03	6,18	484
ADE-15 Bt 11	37,21	1,52	15,82	17,26	0,26	11,96	0,02	0,09	9,13	0,01	0,00	93,29	0,29	0,36	0,50	0,03	6,24	512
ADE-15 Bt 12	36,91	1,89	15,63	17,15	0,30	11,77	0,00	0,04	8,94	0,11	0,01	92,75	0,28	0,36	0,50	0,04	6,29	539
ADE-15 Bt 13	37,62	0,95	16,24	17,74	0,20	12,10	0,04	0,06	8,97	0,07	0,00	93,99	0,33	0,36	0,50	0,02	6,13	459
ADE-15 Bt 14	37,43	1,59	15,28	18,07	0,18	12,00	0,08	0,13	8,79	0,10	0,00	93,64	0,25	0,37	0,50	0,03	6,24	511
ADE-23 Bt 1	33,63	3,16	14,65	26,61	0,26	5,72	0,00	0,13	9,95	0,07	0,00	94,16	0,13	0,61	0,26	0,07	6,56	705
ADE-23 Bt 2	33,87	3,24	14,75	25,66	0,30	5,63	0,09	0,14	9,49	0,00	0,00	93,17	0,17	0,59	0,26	0,08	6,58	718
ADE-23 Bt 3	33,83	4,16	14,89	26,74	0,20	5,01	0,00	0,05	9,58	0,00	0,02	94,48	0,14	0,62	0,23	0,10	6,68	793
ADE-23 Bt 4	34,04	4,02	14,51	27,27	0,25	5,26	0,00	0,09	9,61	0,01	0,00	95,06	0,11	0,62	0,24	0,09	6,65	769
ADE-23 Bt 5	34,90	3,93	14,84	26,53	0,21	5,56	0,03	0,13	9,88	0,00	0,00	96,01	0,14	0,60	0,25	0,09	6,63	755
ADE-23 Bt 6	34,85	3,17	15,29	26,36	0,24	5,60	0,03	0,02	9,84	0,03	0,00	95,43	0,20	0,60	0,25	0,07	6,58	720
ADE-23 Bt 7	34,71	3,31	15,37	26,97	0,25	5,63	0,00	0,02	9,94	0,00	0,00	96,21	0,18	0,60	0,25	0,08	6,59	724
ADE-23 Bt 8	34,49	3,85	15,44	26,14	0,26	5,40	0,01	0,06	9,79	0,00	0,00	95,43	0,18	0,59	0,25	0,09	6,64	764
ADE-23 Bt 9	33,87	3,64	15,16	25,25	0,31	5,58	0,03	0,11	9,53	0,04	0,03	93,56	0,18	0,58	0,26	0,09	6,61	745
ADE-23 Bt 10	33,72	3,36	15,07	25,50	0,20	5,77	0,02	0,12	9,67	0,01	0,03	93,45	0,18	0,59	0,27	0,08	6,58	720
ADE-23 Bt 11	35,51	2,94	14,70	25,39	0,22	5,83	0,03	0,06	8,65	0,00	0,04	93,35	0,24	0,58	0,27	0,07	6,55	702
ADE-23 Bt 12	35,72	3,01	15,31	25,67	0,23	5,77	0,00	0,11	8,65	0,00	0,00	94,46	0,26	0,57	0,26	0,07	6,57	712
ADE-23 Bt 13	34,74	3,38	14,67	24,58	0,15	4,92	0,00	0,08	8,94	0,00	0,00	91,45	0,26	0,58	0,23	0,08	6,65	771
ADE-23 Bt 14	34,97	3,25	14,62	24,19	0,21	5,38	0,00	0,09	8,97	0,06	0,00	91,73	0,25	0,57	0,25	0,08	6,61	741
ADE-23 Bt 15	33,55	3,17	15,33	26,42	0,10	4,69	0,08	0,11	7,40	0,00	0,00	90,84	0,27	0,61	0,22	0,07	6,65	772
ADE-10 Bt 1	35,65	4,16	14,47	21,14	0,41	9,34	0,00	0,07	9,96	0,10	0,02	95,31	0,09	0,46	0,41	0,09	6,49	659
ADE-10 Bt 2	35,52	2,96	14,70	20,32	0,34	10,26	0,03	0,08	9,70	0,09	0,08	94,08	0,14	0,44	0,45	0,06	6,39	596
ADE-10 Bt 3	35,86	4,29	14,85	20,96	0,34	9,43	0,00	0,09	9,80	0,12	0,00	95,72	0,11	0,45	0,41	0,09	6,50	666
ADE-10 Bt 4	35,76	3,70	14,48	20,90	0,34	9,43	0,00	0,08	9,79	0,08	0,02	94,56	0,12	0,46	0,42	0,08	6,46	641
ADE-10 Bt 5	35,83	3,67	14,83	21,32	0,32	9,37	0,02	0,06	10,08	0,05	0,08	95,63	0,13	0,46	0,41	0,08	6,46	641
ADE-10 Bt 6	36,72	3,57	14,85	21,36	0,34	9,42	0,00	0,03	9,97	0,03	0,00	96,31	0,15	0,46	0,41	0,08	6,46	639

Sample	SiO2	TiO2	Al2O3	FeO(tot)	MnO	MgO	CaO	Na2O	K2O	Cr2O3	NiO	Sum	AlVI	X(Fe)	X(Mg)	X(Ti)	ln[T(ºC)]	T (ºC)
ADE-10 Bt 7	35,65	3,52	15,05	20,19	0,37	9,82	0,00	0,05	9,87	0,06	0,03	94,61	0,15	0,44	0,43	0,08	6,45	632
ADE-10 Bt 8	36,34	3,12	14,98	20,65	0,32	9,76	0,00	0,10	9,84	0,03	0,08	95,21	0,17	0,44	0,42	0,07	6,42	615
ADE-10 Bt 9	35,92	3,27	14,57	20,31	0,34	10,27	0,02	0,07	9,85	0,08	0,03	94,72	0,12	0,44	0,45	0,07	6,41	610
ADE-10 Bt 10	35,90	3,77	15,10	19,95	0,30	9,02	0,00	0,10	9,85	0,26	0,10	94,37	0,18	0,44	0,40	0,09	6,49	661
ADE-10 Bt 11	36,87	4,65	14,94	21,42	0,27	9,44	0,00	0,03	9,12	0,00	0,01	96,76	0,13	0,45	0,40	0,10	6,53	682
ADE-10 Bt 12	37,17	3,50	14,62	22,55	0,25	9,63	0,02	0,09	9,26	0,12	0,00	97,22	0,13	0,47	0,41	0,07	6,44	627
ADE-10 Bt 13	37,88	3,99	15,11	22,20	0,37	9,26	0,00	0,06	9,18	0,08	0,08	98,20	0,16	0,46	0,39	0,08	6,49	661
ADE-10 Bt 14	36,17	3,28	14,62	21,88	0,31	9,79	0,00	0,13	8,97	0,00	0,01	95,16	0,13	0,46	0,42	0,07	6,42	616
ADE-10 Bt 15	36,61	3,38	14,78	21,39	0,20	9,82	0,06	0,07	8,99	0,00	0,00	95,30	0,16	0,45	0,42	0,07	6,44	624
ADE-10 Bt 16	36,74	3,58	15,13	21,02	0,40	9,55	0,00	0,05	8,89	0,14	0,04	95,53	0,18	0,45	0,41	0,08	6,46	641
ADE-10 Bt 17	37,01	3,88	14,90	21,69	0,18	9,16	0,00	0,06	9,11	0,01	0,00	95,99	0,17	0,46	0,39	0,08	6,49	659

5. ARTIGO CIENTÍFICO 4: THE PREVIOUSLY MISSING 2.9 GA CONTINENTAL CRUST IN WEST GONDWANA REVEALED IN NORTHEAST BRAZIL

Alanielson da C. D. Ferreira, Elton L. Dantas, Reinhardt A. Fuck

Instituto de Geociências, Universidade de Brasília (UnB), 70910-900 Brasília-DF, Brazil

5.1 ABSTRACT

The Campo Grande Archean basement is a small continental block reworked during the Rhyacian and Brasiliano-Pan African orogens. It is exposed within the Borborema Province, Northeast Brazil, and records a main crustal growth event at 2.9 Ga, an uncommon age episode in Archean evolution worldwide. Despite the several collisional events from the Archean to Neoproterozoic times, relicts of magmatic arc systems were preserved in Northeast Brazil as the main process for the growth and differentiation of the continental crust from 2.9 Ga onwards. The transition between Meso- and Neoarchean is characterized by the compositional change from 2.9 Ga calcium-rich (tonalite) to 2.7 Ga potassium-rich (sanukitoid) magmatism. In addition, a minor volume of 2.65 Ga tholeiitic magmatism also is recorded. The 2.9-2.7 Ga calc-alkaline and tholeiitic crust fragments were intensely reworked during Rhyacian (2.25-1.95 Ga) and Neoproterozoic (627-566 Ma) orogenic events. Rhyacian high-K_2O igneous activity is the most pervasive evidence of a strong reworking process that took place in a post-collisional tectonic setting. Similar Archean crust formation at 2.9 Ga and recycling during Paleo- and Neoproterozoic tectonic events is described in the West Africa counterpart of the Borborema Province. Two others 2.9 Ga old crust fragments are recorded in the South American continent, namely in the Amazonian and São Francisco cratons, more than 2000 km apart from the studied area in northeastern Brazil.

Keywords: 2.9 Ga Archean crust; continental reworking, Borborema Province, West Gondwana

5.2 INTRODUCTION

The evolution of the Archean continental crust and its accretion and collision boundaries are important as they record changes in crustal chemistry between sodic (tonalite–trondhjemite–granodiorite) and potassic granitic series from 3.2 to 2.7 Ga, associated with Phanerozoic-style subduction (e.g. Ernst, 2009; Tappe et al., 2011; Condie and Kroner, 2013; Nebel-Jacobsen et al., 2018). The Archean crust underwent several younger magmatic intrusions, as well as deformation and prograde and retrograde metamorphism (e.g. Rollinson, 2010; Moyen and Martin, 2012; Johnson et al., 2017; Holder et al., 2019). However, 2.9 Ga is interpreted as a period of tectonic quiescence, in which continental platforms were developed, with restricted igneous activity (e.g. Alexander et al., 2008; Liou et al., 2017), or it may reflect the secular change of tectono-magmatism at ca. 2.8-2.7 Ga (e.g. Sawada et al., 2018).

The first major crustal reworking is marked by 2.7 Ga more potassic ($K_2O = 2*Na_2O$) and higher compatible elements contents magmatism (e.g. Moyen and Martin, 2012), referenced as “archaic sanukitoid” (Shirey and Hanson, 1984), in relation to older sodic magmatism composition (tonalite-trondhjemite-granodiorite, TTG; Jahn et al., 1981), which was richer in Na_2O (4–5 wt.%), with lower heavy rare earth elements content (∑1.5–4 ppm). This transitional differentiation from Na- to K-rich magmatism composition supports source enrichment and transition to modern-style subduction (e.g. Nebel et al., 2018). Some studies suggest long time scales (3.2 to 2.5 Ga) for a profound change in average crustal chemistry (e.g. Nebel et al., 2018).

The 2.6 Ga Neoarchean to 2.3 Ga Paleoproterozoic transition suggests a pause of relative tectonic stability (e.g Brown, 2008; Reddy and Evans, 2009; Moyen and Martin, 2012), which is followed by the Rhyacian period, characterized by intense older crust reworking and minor juvenile magmatism related to magmatic arc environments (e.g. Reddy and Evans, 2009; Wei et al., 2014; Terentiev et al., 2016; Roverato et al., 2019). Reworking of 3.6-2.7 Ga Archean crust notwithstanding, Rhyacian orogenic events where responsible for the most significant crustal growth in South America (e.g. Brito Neves, 2011, Dantas et al., 2013; Brito Neves and Fuck, 2014) and Africa (e.g. Parra-Avilla et al., 2016; Eglinger et al., 2017). In this scenario, it is noted that 2.9 Ga continental crust is scarce in both continents (Fig. 5.1) (e.g. West Africa Craton; Rollinson, 2016; 2018; Amazonian and São Francisco cratons;

Albert et al., 2016; Roverato et al., 2019; Oliveira et al., 2019; Milhomem Neto and Lafon, 2019).

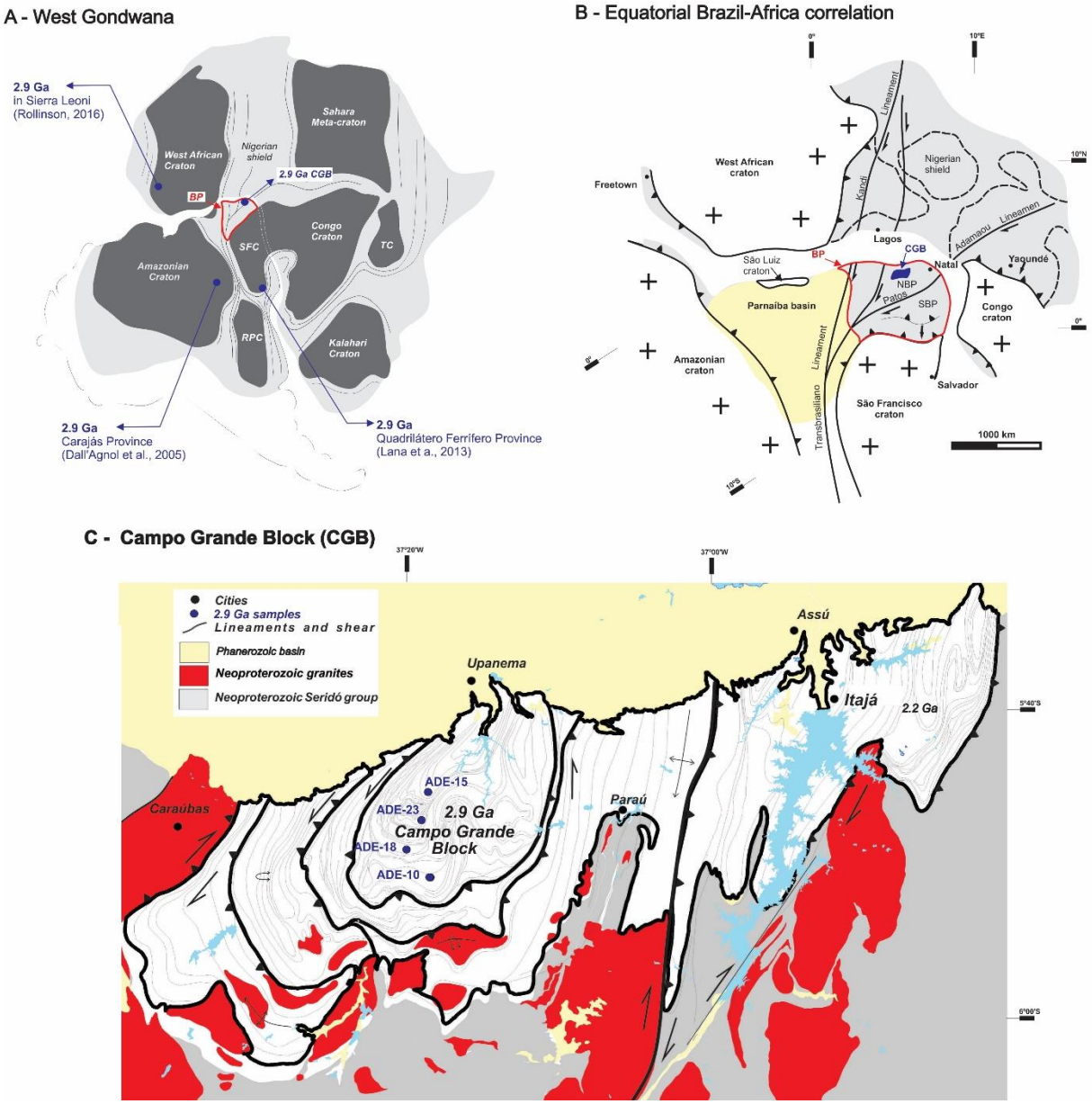

Figure 5.1. Regional geological setting. A) Localization map of the 2.9 Ga crust recorded in West Gondwana. RPC - Rio de La Plata Craton, SFC - São Francisco Craton, BP - Borborema Province, CGB - Campo Grande Block, and TC - Tanzania Craton. B) Equatorial Brazil-Africa correlation modified from Van Schmus et al. (2008). BP - Borborema Province, NBP - Northern Borborema Province, SBP - Southern Borborema Province and CGB - Campo Grande Block. C) Simplified geological map of the Campo Grande area. The Campo Grande Block represents an ellipsoidal gneissic-migmatitic block.

5.3 REGIONAL GEOLOGY

The Borborema Province is part of the Precambrian Brazilian shield in the northeastern South American continent (Almeida et al., 1981). It consists of 3.5 Ga Paleo- to 2.7 Ga Neoarchean blocks and terrains reworked during Paleo- to Neoproterozoic collisional orogenies (e.g.; Brito Neves et al., 2000; Van Schmus et al., 2008; Dantas et al., 2004, 2013). The final configuration of the Borborema Province resulted from the diachronic convergence of the West African, Amazonian and São Francisco-Congo cratons during the assembly of West Gondwana (Fig. 5.1A, B) (e.g. Arthaud et al., 2008; Ganade de Araujo et al., 2014; Padilha et al., 2017; Santos et al., 2018). The Archean crustal fragments can be considered as small Archean cores surrounded by Paleoproterozoic terrains (e.g. Brito Neves et al., 2000; Brito Neves and Fuck, 2014). These terrains comprise the majority of the 2.2-2.0 Ga gneiss-migmatite basement in the Borborema Province (e.g. Dantas et al., 2004; 2013). Despite of many studies in more than half a century, 2.9 Ga old magmatism had not yet been documented in the Borborema Province.

5.4 RESULT

5.4.1 Archean Campo Grande Block

The Campo Grande Block (CGB) is located in the northeastern portion of the Borborema Province (Fig. 5.1B), Rio Grande do Norte domain (Brito Neves et al., 2000). The combined stresses related to eastward push from the Portalegre Lineament and northward push from the Patos Lineament produced NW-SE shortening and amalgamation/accretion of allochthonous terranes, leading to an extensive network of strike-slip shear zones. The CGB consists mainly of a migmatite complex with multiple partial melting phases and ultramafic tholeiitic associations.

The Campo Grande block assembly was built in at least four thermal-tectonic events (Fig. 5.2 and 5.3; Supplementary Table 5.1 and 5.2). The main magmatic events are recorded (1) in tonalitic magmatism (2.98 to 2.91 Ga old paleosome migmatite component), (2) tholeiitic magmatism with basalt composition (2.69 to 2.65 Ga clinopyroxenite and amphibolite), and (3) high-K calc-alkaline magmatism (2.23 to 2.18 Ga orthogneiss). Furthermore, (4) inherited zircon crystals from 2.46 to 2.44 Ga

recorded in samples of migmatites and pyroxenites suggest Siderian age magmatic input. The 2.23 to 2.18 Ga high-K calc-alkaline magmatism is recorded in the eastern portion, but it is less pervasive in the central area of the CGB. In this central area, two high-grade metamorphic events affect the Archean protoliths. The first generates ca. 2.0 Ga clinopyroxene-garnet amphibolite followed by ca. 1.95 Ga concordant granitic leucosome generation, and a second cycle formed 614-593 Ma Cpx-Grt amphibolite and injected 575-566 Ma granitic leucosome into the migmatite complex.

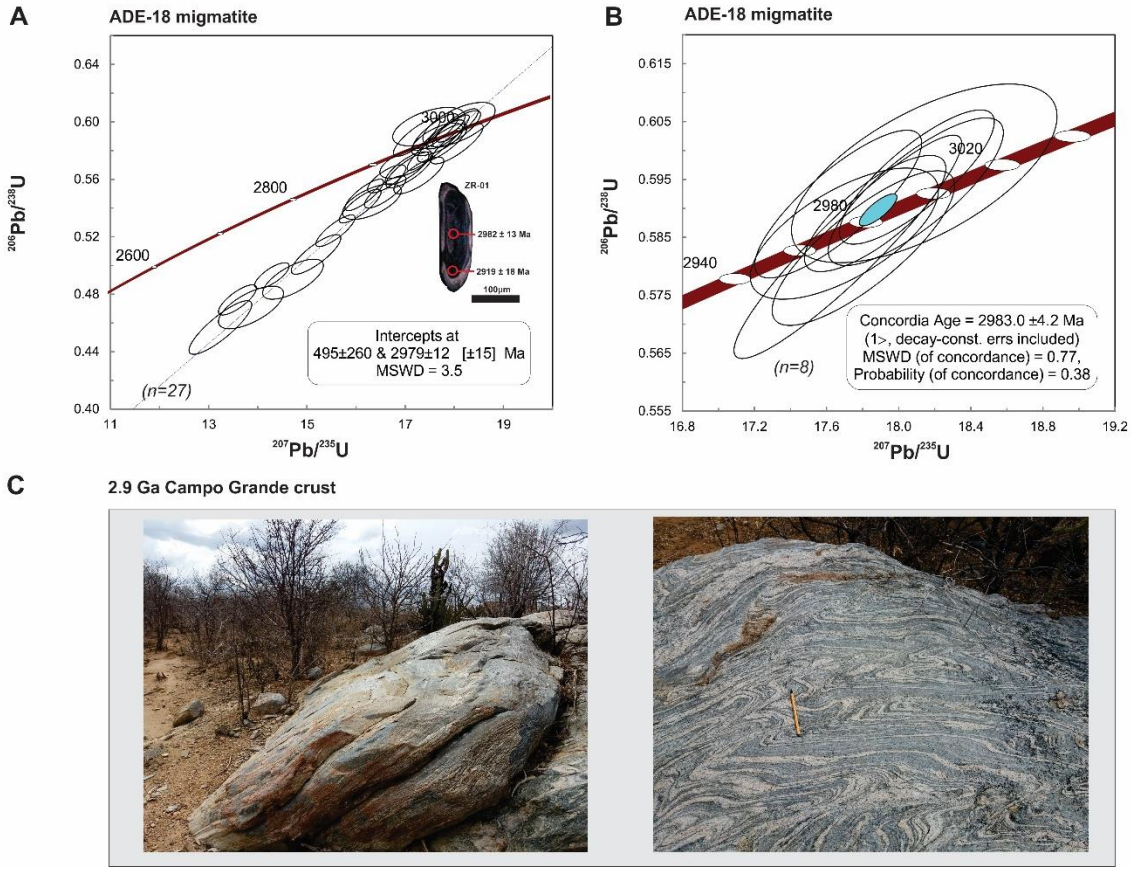

Figure 5.2. (A) Concordia diagram and (B) concordia age for the ADE-18 migmatite sample from the Campo Grande Block (Data from supplementary Table 5.2). C) Field photos of the 2.9 Ga Campo Grande migmatite.

U-Pb geochronology and Nd isotopic data suggest that Campo Grande migmatites represent a new discovered fragment of 1,500 km^2 of juvenile continental crust generation in this part of the Borborema Province. Several samples yield 2.9 Ga igneous crystallization ages of the main calc-alkaline magmatism present in this area. T_{DM} model ages between 2.6 and 3.2 Ga and positive and close to zero ε_{Nd} values attest to the Archean crust growth event in northeastern Brazil.

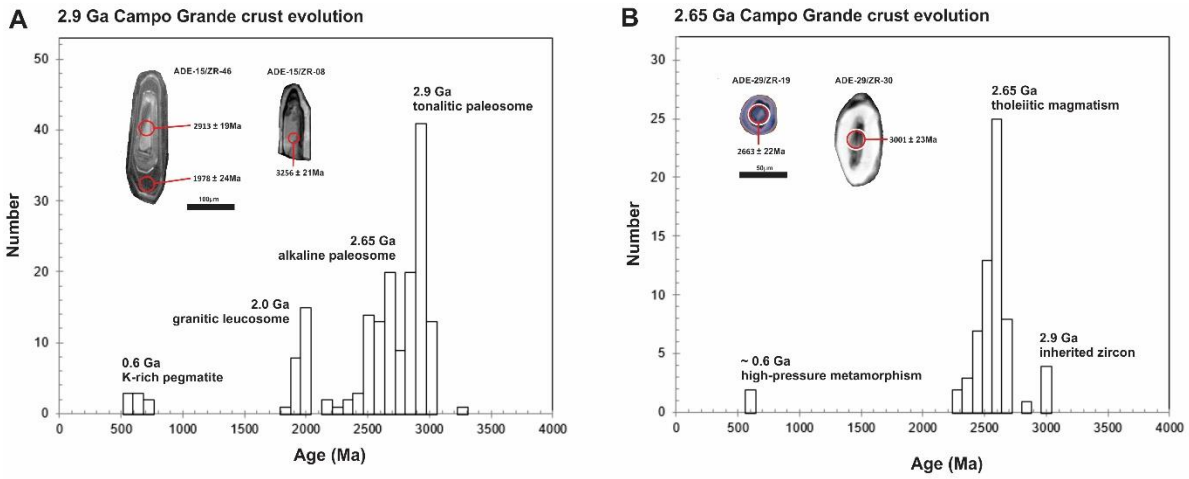

Figure 5.3. Histogram of U-Pb zircon age for the Campo Grande Block. (A) 2.9 Ga calc-alkaline and (B) 2.65 Ga tholeiitic magmatism evolution with cathodoluminescence images (Data from supplementary Table 5.2).

The main unit present in the Campo Grande block is a migmatite complex composed of tonalitic paleosome, granitic leucosome and K-rich pegmatite dykes. These migmatite components are formed of quartz + plagioclase + K-feldspar ± biotite leucosomes, biotite + plagioclase + quartz ± amphibole paleosome, and schlieren to layered biotite-rich melanosome. Also, there is evidence of ocean crust generation during Archean times, which was subducted at 2.65 Ga, recorded in ultramafic tholeiitic rocks. Exposed as small lenses (<500 m) in the central portion of the Campo Grande block, they consist of massive pyroxenites with cumulate texture, reequilibrated to cummingtonite-grunerite-rich rocks, with varying proportions of chlorite, serpentine and magnetite. These mafic boudins are typical high-pressure rocks, as indicated by the massive poikiloblastic garnet and granoblastic amphibole mineralogy, with variable proportions of plagioclase + diopside in symplectitic texture), interpreted as retro-eclogites. Vestiges of Archean supracrustal rocks present in the Campo Grande Block include garnet-bearing biotite schist, calc-silicate rocks and banded iron formations. The rocks present in this core were subject to several events of migmatite generation, with multiple periods of partial melting in the Archean, Paleoproterozoic and Neoproterozoic.

The high-K nature of the Rhyacian (2.25-1.95 Ga) magmatism from the Campo Grande margins can be the product of the reworked Mesoarchean tonalite crust. Archean and Paleoproterozoic crustal sources were reworked and recycled again during the Neoproterozoic Brasiliano-Pan African orogeny marked by 620-590 Ma high-grade metamorphism and widespread ca. 580-560 Ma syn- to late-tectonic

granitic magmatism, preferentially emplaced along large-scale shear zones or inherited crustal weaknesses.

5.5 DISCUSSION

5.5.1 2.9 Ga Connection in West Gondwana

Continental crust formation at 2.9 Ga is described in different Archean fragments and terranes worldwide (e.g. Moyen and Martin, 2012; Palin et al., 2016; Johnson et al., 2017; Rollinson, 2018). One of these was recently discovered in the West African Craton, with generation of 2.96-2.85 Ga felsic migmatite-gneiss representing an evidence of crustal growth in the end of Mesoarchean times in this continent (Rollinson, 2016; 2018). It comprises a huge volume of melting and calc-alkaline magmatism in an arc accretionary system associated to continent growth (Fig. 5.3). In the Limpopo belt and other Archean African high-grade terranes, granulites and migmatites are associated with collisional orogenic processes, which amalgamated several blocks into a major supercontinent mass (e.g. Barton et al., 2006; Khoza et al., 2013). The Archean fragments were deformed during the Eburnian orogenic collage (2.25-1.98 Ga), enclosed and surrounded by the Palaeoproterozoic volcanic, sedimentary and plutonic rocks (e.g. Eglinger et al., 2017). Similar to West Africa, 2.9 Ga calc-alkaline continental crust recorded in Northeast Brazil represents the main protolith source for the crustal reworking and recycling processes throughout the Neoarchean to Neoproterozoic crust growth and differentiation. The 2.9 Ga old tonalitic magmatism in the Campo Grande block was possibly derived from a mafic source with Nd T_{DM} between 3.1 and 3.7 Ga (Supplementary Table 5.1). In the São Francisco Craton, 2000 km southward from the Campo Grande study area, small exposures of 2.9 Ga old magmatic rocks are recorded, suggesting Mesoarchean crust formation at this time (Lana et al., 2013; Oliveira et al., 2019). Besides the Mesoarchean crust, the main period of crustal growth in the São Francisco Craton is represented by the large volume of 2.7 Ga K_20-rich magmatism, suggesting strong reworking of an ancestral sodic source (e.g. Lana et al., 2013; Farina et al., 2015; Albert et al., 2016). Furthermore, Paleoproterozoic São Francisco Craton evolution includes 2.19-2.07 Ga syn- to late tectonic K_2O-rich granitic magmatism and 2.08–2.04 Ga high-grade granulite to migmatite-gneiss formation, also suggesting strong

reworking of the Archean protolith sources (e.g. Zincone et al., 2017). Furthermore, in the Southeastern Amazonian Craton, 3000 km westward of the study area, there is also evidence of 2.96 Ga tonalitic and 2.86 Ga sanukitoid magmatism (e.g. Althoff et al., 2000; Dall'Agnol et al., 2005; Milhomem Neto and Lafon, 2019). The Archean units of the Amazonian Craton were reworked in a late-/post-orogenic (~2.0 Ga) to extensional regime (~1.88 Ga A-type granite) (e.g. Dall'Agnol et al., 2005; Roverato et al., 2019).

We argue that, in the Brazilian shield, the main 2.9 Ga magmatism event is Ca-rich, and was progressively changed in composition to K-rich rocks, formed at 2.7 Ga. This fact suggests strong modification in the chemistry of the deep source of crust generation in subduction related Meso- to Neoarchean magmatism. Furthermore, the 2.65 Ga juvenile tholeiitic magmatism recorded in the Campo Grande Block appears to support the installation of a new Archean tectonic regime in the Borborema Province, which preserved the Neoarchean oceanic crust after 2.65 Ga, similar to Greenland eclogites (e.g. Tappe et al., 2011). We suggest that continental crust growth in the Borborema Province was produced by accreted oceanic arcs and oceanic plateaus, during Paleo- until Neoarchean global events (e.g. Ernst, 2009; Condie and Kroner, 2013; Nebel-Jacobsen et al., 2018; Holder et al., 2019).

At the end of the Archean in the South American and African continents, there was a gap of crust production, with restricted magmatic-metamorphic activity between 2.6 Ga and 2.3 Ga (e.g. Rollinson, 2016; Albert et al., 2016; Roverato et al., 2019) in craton evolution paths. The tectonic quiescence persisted until ca. 2.25 Ga, when the Rhyacian crust growth cycles started in both continents (e.g. Brito Neves, 2011; Eglinger et al., 2017). The Paleoproterozoic is characterized by crustal reworking of the old Archean crust during several different orogenic cycles (.e.g. Reddy and Evans, 2009; Terentiev et al., 2016; Albert et al., 2016; Roverato et al., 2019).

5.6 CONCLUSIONS

1. The 2.9 Ga and 2.65 Ga Archaean Campo Grande core was reworked and recycled during 2.25-1.95 Ga Rhyacian and 630-560 Ma Brasiliano-Pan African orogenic cycles, which challenges the 3.0-2.9 Ga Archean crust mapping in northeastern Brazil.

2. Preservation of 2.9 Ga tonalitic calc-alkaline magmatism may indicate a correlation to the West African Craton. 2.65 Ga alkaline leucosome and clinopyroxene-garnet amphibolites can be correlated and contribute to the understanding of the evolution of other Mesoarchean crustal fragments with subsequent crustal reworking.

3. Our results support crustal recycling processes related to magmatic arcs as crucial mechanisms for continental crust growth and differentiation. However, the continental evolution is complex and includes several components of different scale, composition and any model that requires a single process to produce continental crust is unrealistic.

5.7 ACKNOWLEDGMENTS

This study is part of the first author's PhD thesis in development at the Institute of Geosciences, Universidade de Brasília. The authors acknowledge support from INCT Estudos Tectônicos (CAPES/CNPq - 465613/2014-4 and FAPDF - 193.001.263/2017). ELD and RAF acknowledge CNPq research fellowships.

5.8 REFERENCE

Albert, C., Farina, F., Lana, C., Stevens, G., Storey, C., Gerdes, A., Dopico, C.M., 2016. Archean crustal evolution in the Southern São Francisco craton, Brazil: constraints from U–Pb, Lu–Hf and O isotope analyses. Lithos 266, 64-86. (doi.org/10.1016/j.lithos.2016.09.029)

Alexander, B., Bau, M., Andersson, P., Dulski, P., 2008. Continentally-derived solutes in shallow Archean seawater: rare earth element and Nd isotope evidence in iron formation from the 2.9Ga Pongola Supergroup, South Africa. Geochim. Cosmochim. Acta 72, 378-394. (/doi.org/10.1016/j.gca.2007.10.028)

Almeida, F.F.M., Brito Neves, B.B., Fuck, R., 1981. Brazilian structural provinces: an introduction. Earth Science Reviews 17, 1–29. (doi:10.1016/0012-8252(81)90003-9)

Althoff, F., Barbey. P., Boullier, A.M., 2000. 2.8-3.0 Ga plutonism and deformation in the SE Amazonian craton: the Archaean granitoids of Marajoara (Carajás

Mineral Province, Brazil). Precambrian Research 104, 187-206. (doi.org/10.1016/S0301-9268(00)00103-0)

Arthaud, M.H., Caby, R., Fuck, R.A., Dantas, E.L., Parente, C.V., 2008. Geology of the northern Borborema Province, NE Brazil and its correlation with Nigeria, NW Africa. In: Pankhurst, R.J., Trouw, R.A.J., Brito Neves, B.B., de Wit, M.J. (Eds.), West Gondwana: Pre-Cenozoic Correlation Across the South Atlantic Region. Geological Society of London 294, 49–67. (doi:10.1144/SP294)

Barton, J.M., Klemd, R., Zeh, A., 2006. The Limpopo Belt: A result of Archean to Proterozoic, Turkic-type orogenesis? Special Paper of the Geological Society of America 405, 315-332. (doi.org/10.1130/2006.2405(16))

Brito Neves, B. B., Santos, E. J., & Schmus W. R. Q., 2000. Tectonic history of the Borborema Province, in: Umberto Cordani, Edson José Milani, Antonio Thomaz Filho, and Diogenes de Almeida Campos (org.), Tectonic Evolution of South America. Rio de Janeiro: 31st International Geological Congress, pp. 151-182, Special Publication.

Brito Neves, B.B., 2011. The Paleoproterozoic in the South-American continent: Diversity in the geologic time. Journal of South American Earth Sciences 32, 270–286. (doi:10.1016/j.jsames.2011.02.004)

Brito Neves, B.B., Fuck, R. A., 2014. The basement of the South American platform: Half Laurentian (N-NW) + half Gondwanan (E-SE) domains. Precambrian Research, 244. 75-86. (doi: 10.1016/j.precamres.2013.09.020)

Brown, M., 2008. Characteristic thermal regimes of plate tectonics and their metamorphic imprint throughout Earth history: When did Earth first adopt a plate tectonics mode of behavio. When Did Plate Tectonics Begin on Planet Earth?, Kent C. Condie, Victoria Pease(doi:10.1130/2008.2440(05))

Condie, K., and Kröner, A., 2013. The building blocks of continental crust: Evidence for a major change in the tectonic setting of continental growth at the end of the Archean. Gondwana Research 23, 394-402. (doi:10.1016/j.gr.2011.09.011)

Dall'Agnol, R., Teixeira, N.P., Ramö, O.T., Moura, C.AV., Macambira, M.J.B., Oliveira, D.C., 2005. Petrogenesis of the Paleoproterozoic rapakivi A-type granites of the Archean Carajás metallogenic province, Brazil. Lithos 80, 101-129. (doi.org/10.1016/j.lithos.2004.03.058)

Dantas, E. L., Van Schmus W.R., Hackspacher P. C., Fetter A. H., Neves B. B. B., Cordani U.G., Nutman A.P., Williams S., 2004. The 3.4-3.5 São José do Campestre Massif, NE Brazil: remnants of the oldest crust in South America. Precambrian Research 130, 113-137. (doi.10.1016/j.precamres.2003.11.002).

Dantas, E. L., Souza, Z. S., Wernick, E., Hackspacher, P. C., Martin, H., Xiaodong, D., & Li, J. W., 2013. Crustal growth in the 3.4-2.7 Ga São José de Campestre Massif, Borborema Province, NE Brazil. Precambrian Research, 227, 120–156. (doi:10.1016/j.precamres.2012.08.006)

Eglinger, A., Thebaud, N., Zeh, A., Davis, J., Miller, J., Parra-Avila, L.A., Loucks, R., McCuaig, C., Belousova, E., 2017. New insights into the crustal growth of the Paleoproterozoic margin of the Archean Kenema-Man domain, West African craton (Guinea): implications for gold mineral system. Precambrian Res. 292, 258-289. (doi.org/10.1016/j.precamres.2016.11.012)

Ernst, W.G., 2009. Archean plate tectonics, rise of Proterozoic supercontinentality and onset of regional, episodic stagnant-lid behavior. Gondwana Res. 15, 243–253. (doi:10.1016/j.gr.2008.06.010)

Farina, F., Albert, C., Lana, C., 2015. The Neoarchean transition between medium- and high-K granitoids: clues from the Southern São Francisco Craton (Brazil). Precambrian Research 266, 375-394. (doi.org/10.1016/j.precamres.2015.05.038)

Ferreira, A.C.D., 2019. Retroeclogitos e Migmatitos do Bloco Arqueano Campo Grande, Nordeste do Brasília. Universidade de Brasília. Tese de Doutorado. (http://repositorio.unb.br/)

Holder, R.M., Viete, D.R., Brown, M. Johnson, T.E., 2019. Metamorphism and the evolution of plate tectonics. Nature 572, 378–381. (doi:10.1038/s41586-019-1462-2)

Johnson, T.E., Brown, M., Gardiner, N.J., Kirkland, C.L., Smithies, H.R., 2017. Earth's first stable continents did not form by subduction. Nature Geosci. (doi.org/10.1038/nature21383)

Khoza, D., Jones, A.G., Muller, M.R., Evans, R.L., Webb, S.J. & Miensopust, M., 2013. Tectonic model of the Limpopo belt: constraints from magnetotelluric data. PrecambrianResearch 226 , 143–156. (doi.org/10.1016/j.precamres.2012.11.016)

Ibanez-Mejia, M., Pullen, A., Arenstein, J., Gehrels, G.E., Valley, J., Ducea, M, N., Mora, R.A., Pecha, M., Ruiz, J., 2015. Unraveling crustal growth and reworking processes in complex zircons from orogenic lower-crust: The Proterozoic Putumayo Orogen of Amazonia. Precambrian Research 267, 285–310. (doi.org/10.1016/j.precamres.2015.06.014)

Lana, C., Alkmim, F.F., Armonstrong, R., Scholz, R., Romano, R., Nalini Jr. H.R., 2013. The ancestry and magmatic evolution of Archaean TTG rocks of the Quadrilátero Ferrífero province, Southeast Brazil. Precambrian Research 231, 157-173. (doi.org/10.1016/j.precamres.2013.03.008)

Laurent, O., Martin, H., Moyen, J.F., Doucelance, R., 2014. The diversity and evolution of late-Archean granitoids: evidence for the onset of ‘modern-style’ plate tectonics between 3.0 and 2.5 Ga. Lithosphere 205, 208–235. (doi:10.1016/j.lithos.2014.06.012)

Liou, P., Guo, J.H., Huang, G., Fan, W.B., 2017. 2.9 Ga magmatism in Eastern Hebei, North China Craton. Precambrian Research 326, 6-23. (doi.10.1016/j.precamres.2017.11.002)

Milhomem Neto, J.M.M. Lafon, J.M., 2019. Zircon U-Pb and Lu-Hf isotope constraints on Archean crustal evolution in Southeastern Guyana Shield. Geoscience Frontiers 10, 1477-1506. (doi.org/10.1016/j.gsf.2018.09.012)

Moyen, J.F., Martin, H., 2012. Forty years of TTG research. Lithos 148, 312-336. (doi: 10.1016/j.lithos.2012.06.010)

Nebel, O., Capitanio, F. A., Moyen, J. F., Weinberg, R. F., Clos, F., Nebel-Jacobsen, Y.J., Cawood, P.A., 2018. When crust comes of age: on the chemical evolution of Archaean, felsic continental crust by crustal drip tectonics. Phil. Trans. R. Soc. A 376, 20180103. (doi:10.1098/rsta.2018.0103)

Nebel-Jacobsen, Y.J., Nebel, O., Wille, M., Cawood, P.A., 2018. A non-zircon Hf isotope record in Archean black shales from the Pilbara craton confirms changing crustal dynamics ca. 3 Ga ago. Scientfic Reports 8, 922. (doi:10.1038/s41598-018-19397-9)

Oliveira, E. P., Talavera, C., Windley, B.F., Zhao, L., Semprich, J.J., McNaughton, N.J., Amaral, W.S., Sombini, G., Navarro, M., Silva, 2019. Mesoarchaean (2820 Ma) high-pressure mafic granulite at Uauá, São Francisco Craton, Brazil, and its potential significance for the assembly of Archaean supercratons. Precambrian Research 331, 105366. (doi.org/10.1016/j.precamres.2019.105366)

Padilha, A.L., Vitorello, Í., Pádua, M.B., Fuck, R.A., 2017. Cryptic signatures of Neoproterozoic accretionary events in northeast Brazil imaged by magnetotellurics: Implications for the assembly of West Gondwana. Tectonophysics 699, 164-177. (doi:10.1016/j.tecto.2017.01.022)

Palin, R.M., White, R.W., Green, E.C.R., 2016. Partial melting of metabasic rocks and the generation of tonalitic-trondhjemitic-granodioritic (TTG) crust in the Archaean: constraints from phase equilibrium modelling. Precambrian Res. 287, 73-90. (doi.org/10.1016/j.precamres.2016.11.001)

Parra-Avilla, L.A., Belousova, E., Fiorentini, M.L., Baratoux, L., Davies, J., Miller, J., McCuig, T.C., 2016. Crustal evolution of the Palaeoproterozoic Birimian terranes of the Baoyle-Mossi domain, southern west African Craton: U-Pb and Hf isotope studies of detrital zircons. Precambrian Res. 274, 25-60.

Reddy, S. M., Evans, D.A.D., 2009. Palaeoproterozoic supercontinents and global evolution: correlations from core to atmosphere. Geological Society, London, Special Publications 323, 1-26. (doi.org/10.1144/SP323.1)

Rollinson, H., 2010. Coupled evolution of Archean continental crust and subcontinental lithospheric mantle: Geology, v. 38, p. 1083–1086, (doi:10.1130/G31159.1).

Rollinson, H., 2016. Archaean crustal evolution in West Africa: a new synthesis of the Archaean geology of Sierra Leone, Liberia, Guinea and ivory Coast. Precambrian Research 281, 1-12. (doi.org/10.1016/j.precamres.2016.05.005)

Rollinson, H., 2018. The geochemical evolution of Archaean felsic gneisses in the West African Craton in Sierra Leone. Journal of African Earth Sciences 143, 28-39. (doi.org/10.1016/j.jafrearsci.2018.03.018)

Roverato, M., Giordano, D., Giovanardi, T., Juliani, C., Polo, L., 2019. The 2.0–1.88 Ga Paleoproterozoic evolution of the southern Amazonian Craton (Brazil): an interpretation inferred by lithofaciological, geochemical and geochronological data. Gondwana Research 70, 1-24. (doi.org/10.1016/j.gr.2018.12.005).

Sawada, H., Isozaki, Y., Sakata, S., Hirata, T., Maruyama, S., 2018. Secular change in lifetime of granitic crust and the continental growth: a new view from detrital zircon ages of sandstones. Geoscience Frontiers 9, 1099-1115. (doi.10.1016/j.gsf. 2016.11.010)

Tappe, S., Smart, K. A., Pearson, D. G, Steenfelt, A., Simonetti, A., 2011. Craton formation in Late Archean subduction zones revealed by first Greenland eclogites. Geology; 39 (12): 1103–1106. (doi:10.1130/G32348.1)

Terentiev, R. A., Skryabin, V. Y., Santosh, M., 2016. U–Pb zircon geochronology and geochemistry of Paleoproterozoic magmatic suite from East Sarmatian Orogen: Tectonic implications on Columbia supercontinent. Precambrian Research 273, 165–184. (doi:10.1016/j.precamres.2015.12.009)

Van Schmus, W.R., Oliveira, E.P, Silva Filho, A.F., Toteu, S.F., Penaye, J., Guimarães, I. P., 2008. Proterozoic links between the Borborema Province, NE Brazil, and the Central African Fold Belt. Geological Society, London, Special Publication 294, 69-99. (doi.org/10.1144/SP294.5)

Wei, C., Qiana, J., Zhou, X., 2014. Paleoproterozoic crustal evolution of the Hengshan–Wutai–Fuping region, North China Craton. Geoscience Frontiers 5, 485–497. (doi:10.1016/j.gsf.2014.02.008)

Zincone, S.A., Oliveira, E.P., 2017. Field and geochronological evidence for origin of the Contendas-Mirante supracrustal Belt, São Francisco Craton, Brazil, as a Paleoproterozoic foreland basin. Precambrian Research 299, 117–131. (doi.org/10.1016/j.precamres.2017.07.031)

5.9 Supplementary Methods

5.9.1 Geological Mapping and Petrography

Geological mapping in the Campo Grande area was carried out from 2016 to 2018 with the purpose of investigating the mafic bodies inserted in the gneiss-migmatite complex. Geological mapping was supported by geochemical, geophysical and petrographic surveys. Systematic thin sections cut relative to foliation were obtained from representative samples from fourteen outcrops of mafic lenses and host migmatite. Representative samples are from mafic lenses with a high modal concentration of pyroxene and garnet, since most mafic rock outcrops consist exclusively of amphibole, recording full retrogression of the HP mineral assemblage. The latter was done at the Microscopy Laboratory of the Institute of Geosciences of Universidade de Brasília (Brazil).

5.9.2 U-Pb isotopes

Zircon grains from mafic lenses and host migmatite-gneiss were separated by conventional procedures and magnetic separator after concentration by hand panning. U-Pb and Lu-Hf isotopic analyses were performed on zircon grains using a Thermo-Fisher Neptune High Resolution Multicollector Inductively Coupled Plasma

Mass Spectrometer (HR-MC-ICP-MS) coupled with a Nd:YAG UP213 New Wave laser ablation system at the Laboratory of Geochronology of Universidade de Brasília. U-Pb analyses on zircon grains were carried out by the standard-sample bracketing method (Albarède et al., 2004), using the GJ-1 standard zircon (Jackson et al., 2004) in order to quantify the amount of ICP-MS fractionation. The tuned masses were 238, 207, 206, 204 and 202. The integration time was 1 second and the ablation time was 40 seconds. A 30 µm spot size was used and the laser setting was 10 Hz and 2-3 J/cm^2. Two to four unknown grains were analyzed between GJ-1 analyses. $^{206}Pb/^{207}Pb$ and $^{206}Pb/^{238}U$ ratios were time corrected. The raw data were processed off-line and reduced using an Excel worksheet (Bühn et al., 2009). During the analytical sessions, the zircon standard 91500 (Wiedenbeck et al., 2004) was also analyzed as an external standard.

Common ^{204}Pb was monitored using the ^{202}Hg and (^{204}Hg+^{204}Pb) masses. Common Pb corrections were not done due to very low signals of ^{204}Pb (< 30cps) and high $^{206}Pb/^{204}Pb$ ratios. Reported errors are propagated by quadratic addition [(2SD^2+2SE^2)1/2] (SD = standard deviation; SE = standard error) of external reproducibility and within-run precision. External reproducibility is represented by the standard deviation obtained from repeated analyses (~1.1 % for $^{207}Pb/^{206}Pb$ and up to ~2 % for $^{206}Pb/^{238}U$) of the GJ-1 zircon standard during the analytical sessions, and the within-run precision is the standard error calculated for each analysis. Concordia diagrams (2σ error ellipses), probability density plots and weighted average ages were calculated using the Isoplot-3/Ex software (Ludwig, 2008).

5.9.3 Reference

Bühn, B.M., Pimentel, M,M., Matteini, M., Dantas, E.L., 2009. High spatial resolution analyses of Pb and U isotopes for geochronology by laser ablation multi-collector

inductively coupled plasma mass spectrometry LA-MC-ICP-MS. Anais da Academia Brasileira de Ciências 81, 1-16. (doi.org/10.1590/S0001-37652009000100011)

Jackson, S.E., Pearson, N. J., Griffin, W.L., Belousova, E.A., 2004. The application of laser ablation-inductively coupled plasma-mass spectrometry to in situ U-Pb zircon geochronology. Chemical Geology 211, 47-69. (doi.org/10.1016/j.chemgeo.2004.06.017)

Ludwig, K. R., 2008. User's Manual for Isoplot 3.0. A geochronological Toolkit for Microsoft Excel. Berkeley Geochronology Center, 4(4), 76.

Wiedenbeck, M., Hanchar, J.M., Peck, W.H., Sylvester, P., Valley, J., Whitehouse, M., Kronz, A., Morishita, Y., Nasdala, L., Fiebig, J., Franchi, I., Girard, J.P., Greenwood, R.C., Hinton, R., Kita, N., Mason, P.R.D., Norman, M., Ogasawara, M., Piccoli, P.M., Rhede, D., Satoh, H., Schulz-Dobrick, B., Skår, O., Spicuzza, M.J., Terada, K., Tindle, A., Togashi, S., Vennemann, T., Xie, Q., Zheng, Y.F., 2004. Further characterisation of the 91500 zircon crystal. Geostandards and Geoanalytical Research 28, 9-39. (https://doi.org/10.1111/j.1751-908X.2004.tb01041.x)

Supplementary Table 5.1. Nd isotope analyses for the Campo Grande Block.

Sample	Protolith	Rock	Sm (ppm)	Nd (ppm)	147Sm/144Nd	143Nd/144Nd ± 2SE	εNd (0)	εNd(t)	TDM(Ga)
AT-28P	2.9 GA Calc-alkaline magmatism	Tonalitic Paleosome	3.16	19.13	0.1000	0.510589+/-19	-39.97	-3.92	3.3
ADE-15P		Tonalitic Paleosome	9.08	55.32	0.0993	0.511019+/-1	-31.57	4.8	2.69
ADE-18P		Tonalitic Paleosome	4.86	27.77	0.1058	0.510976+/-8	-32.41	2.56	2.93
ADE-10P		Tonalitic Paleosome	5.55	33.2	0.1011	0.510677+/-8	-38.25	-2.6	3.22
ADE-23P		Alkaline Paleosome	17.42	93.43	0.1127	0.511325+/-4	-25.6	3.01	2.59
ADE-14L		Granitic Leucosome	5.05	32.01	0.0954	0.511166+/-4	-28.71	-2.74	2.41
ADE-03L		Granitic Leucosome	6.09	36.56	0.1006	0.511149+/-9	-29.05	-4.42	2.55
ADE-04L		Granitic Leucosome	5.01	31.61	0.0958	0.511032+/-17	-31.32	-5.46	2.59
ADE-12L		Granitic Leucosome	3.52	24.35	0.0873	0.510997+/-11	-32.01	-3.96	2.46
AT-23Li		Alkaline Leucosome	26.93	169.75	0.0959	0.511189+/-13	-28.27	-20.57	2.39
ADE-13Li		Alkaline Leucosome	12.48	70.89	0.1064	0.511554+/-9	-21.14	-14.25	2.1
ADE-29	2.65 Ga tholeiitic magmatism	Cpx-Grt-amphibolite	3.57	12.7	0.17	0.512416+/-13	-4.32	4.63	2.17
ADE-09		Cpx-Grt-amphibolite	3.30	12.74	0.1566	0.512121+/-3	-10.09	3.32	2.46
ADE-20		Cpx-Grt-amphibolite	2.23	9.5	0.1419	0.512116+/-5	-10.18	8.17	1.95
ADE-24B		Cpx-Grt-amphibolite	4.24	16.43	0.156	0.512077+/-2	-10.95	2.66	2.55
AT-16		Cpx-Grt-amphibolite	5.33	20.7	0.1558	0.512099+/-12	-10.51	3.17	2.48
AT-10		Cpx-Grt-amphibolite	5.9	24.52	0.1454	0.511922+/-19	-13.97	3.18	2.5
AT-32		Cpx-Grt-amphibolite	3.98	14.95	0.1609	0.512125+/-15	-10,00	1.97	2.65
AP-17		Cpx-Grt-amphibolite	9.59	39.15	0.148	0.512104+/-3	-10.42	5.88	2.17
AP-10		Cpx-Grt-amphibolite	5.31	19.65	0.1634	0.512011+/-4	-12.23	-1.12	3.19
AT-26		Cpx-Grt-amphibolite	3.59	12.53	0.1734	0.512187+/-12	-8.8	-1.03	3.34
AT-14		Cpx-Grt-amphibolite	4.44	19.77	0.1358	0.511189+/-4	-28.27	-7.97	3.69
ADE-16		Cpx-Grt-amphibolite	4.33	16.94	0.1545	0.511773+/-8	-16.87	-2.81	3.33
ADE–24A		Cpx-Grt-amphibolite	4.5	16.93	0.1607	0.511780+/-20	-16.74	-4.76	3.75

Supplementary Table 5.2. U-Pb zircon data for the 2.9 Ga Campo Grande block.

ADE-18	Rock	^{206}Pb mV[1]	Th/U	$^{206}Pb/^{204}Pb$	1s%	$^{207}Pb/^{206}Pb$	1s %	$^{207}Pb/^{235}U$	1s %	$^{206}Pb/^{238}U$	1s %	Rho	$^{207}Pb/^{206}Pb$	2s abs	$^{206}Pb/^{238}U$	2s abs	$^{207}Pb/^{235}U$	2s abs	% U-Pb disc[4]
050-ZR27C		0,0368	0,451	808497	19,11	0,21378	1,40	17,528	1,71	0,5946	0,92	0,54	2934	45	3008	44	2964	33	-2,51
049-ZR26C		0,0105	0,476	69755	33,83	0,21847	0,67	15,232	1,35	0,5056	1,11	0,82	2969	22	2638	48	2830	26	11,16
048-ZR25B		0,0083	0,306	233735	17,70	0,22132	0,54	18,095	1,10	0,5929	0,88	0,80	2990	17	3001	42	2995	21	-0,37
047-ZR25C		0,0056	0,590	3191	5,50	0,22525	0,57	18,101	1,20	0,5828	0,99	0,82	3019	18	2960	47	2995	23	1,94
046-ZR24B		0,0160	0,326	437644	21,96	0,21726	0,93	17,052	1,25	0,5692	0,75	0,60	2960	30	2905	35	2938	24	1,89
045-ZR24C		0,0090	0,598	182681	25,54	0,22045	0,41	18,101	0,97	0,5955	0,80	0,82	2984	13	3012	38	2995	19	-0,92
044-ZR23C		0,0096	0,760	159013	23,43	0,21693	0,48	16,131	1,08	0,5393	0,89	0,83	2958	15	2780	40	2885	20	6,00
039-ZR21B		0,0295	0,365	964978	16,11	0,21341	0,51	17,279	1,11	0,5872	0,92	0,82	2932	17	2978	44	2950	21	-1,58
038-ZR21C		0,0123	0,662	416302	14,81	0,21915	0,83	17,698	1,20	0,5857	0,79	0,66	2974	27	2972	38	2973	23	0,09
037-ZR20C		0,0088	0,514	286851	14,64	0,21996	0,43	17,869	0,90	0,5892	0,70	0,78	2980	14	2986	33	2983	17	-0,19
036-ZR19C		0,0130	0,733	208892	27,84	0,22072	1,22	18,142	1,66	0,5961	1,06	0,64	2986	39	3014	51	2997	32	-0,94
034-ZR17B		0,0077	0,455	212010	21,43	0,21906	0,55	17,085	1,07	0,5656	0,83	0,78	2974	18	2890	39	2940	20	2,83
033-ZR17C	Migmatite	0,0069	0,573	256529	15,44	0,21889	1,11	16,370	1,49	0,5423	0,93	0,62	2973	35	2793	42	2899	28	6,03
028-ZR14C		0,0053	0,455	40698	39,56	0,20864	0,62	13,634	1,16	0,4739	0,90	0,78	2895	20	2501	37	2725	22	13,62
027-ZR13B		0,0084	0,508	114241	26,03	0,21656	0,51	16,670	0,96	0,5583	0,72	0,75	2955	17	2859	33	2916	18	3,24
020-ZR11C		0,0115	0,699	158620	24,31	0,21521	1,40	13,909	1,94	0,4687	1,29	0,66	2945	45	2478	53	2743	36	15,87
019-ZR10C		0,0052	0,373	203528	18,33	0,22410	0,66	17,325	1,20	0,5606	0,93	0,78	3010	21	2869	43	2953	23	4,69
018-ZR9B		0,0075	0,403	195903	18,49	0,21976	0,50	16,641	1,04	0,5491	0,84	0,80	2979	16	2822	38	2914	20	5,28
017-ZR9C		0,0116	0,566	324817	19,71	0,21708	0,46	15,629	1,04	0,5221	0,86	0,83	2959	15	2708	38	2854	20	8,48
015-ZR7C		0,0112	1,134	354027	16,05	0,22011	0,58	17,131	1,14	0,5645	0,91	0,80	2981	19	2885	42	2942	22	3,24
014-ZR6C		0,0216	0,163	943566	14,68	0,21492	0,41	16,213	0,99	0,5471	0,82	0,83	2943	13	2813	37	2889	19	4,41
013-ZR5C		0,0174	0,923	626750	15,25	0,21683	0,48	17,664	1,07	0,5908	0,88	0,82	2957	15	2993	42	2972	20	-1,19
010-ZR4C		0,0053	0,526	121984	28,67	0,21927	1,19	14,765	1,71	0,4883	1,17	0,69	2975	38	2564	49	2800	32	13,84
009-ZR3B		0,0060	0,457	80509	39,12	0,21192	0,96	13,289	1,96	0,4548	1,68	0,85	2920	31	2416	67	2700	37	17,25
008-ZR3C		0,0179	0,551	490232	17,72	0,22140	0,58	17,804	1,16	0,5832	0,94	0,81	2991	19	2962	44	2979	22	0,98

ADE-18	Rock	^{206}Pb mV[1]	Th/U	^{206}Pb/^{204}Pb	1s%	^{207}Pb/^{206}Pb	1s %	^{207}Pb/^{235}U	1s %	^{206}Pb/^{238}U	1s %	Rho	^{207}Pb/^{206}Pb	2s abs	^{206}Pb/^{238}U	2s abs	^{207}Pb/^{235}U	2s abs	% U-Pb disc[4]
005-ZR1B		0,0090	0,384	10435	17,87	0,21182	0,55	14,336	1,00	0,4908	0,75	0,75	2919	18	2574	32	2772	19	11,82
004-ZR1C		0,0199	0,702	27353	18,38	0,22024	0,40	17,718	1,46	0,5834	1,35	0,93	2982	13	2963	64	2975	28	0,67
ADE-10P	**Rock**	**^{206}Pb mV[1]**	**Th/U**	**^{206}Pb/^{204}Pb**	**1s%**	**^{207}Pb/^{206}Pb**	**1s %**	**^{207}Pb/^{235}U**	**1s %**	**^{206}Pb/^{238}U**	**1s %**	**Rho**	**^{207}Pb/^{206}Pb**	**2s abs**	**^{206}Pb/^{238}U**	**2s abs**	**^{207}Pb/^{235}U**	**2s abs**	**% U-Pb disc[4]**
048-ZR35		0,0264	0,224	692032	60,60	0,21261	1,51	15,619	2,26	0,5328	1,64	0,72	2926	49	2753	73	2854	43	5,89
047-ZR34		0,0094	0,540	289747	18,72	0,21204	0,51	17,400	1,18	0,5951	1,00	0,85	2921	16	3010	48	2957	23	-3,04
046-ZR33		0,0212	0,578	501395	21,91	0,21295	0,44	17,150	1,00	0,5841	0,82	0,82	2928	14	2965	39	2943	19	-1,27
045-ZR32		0,0108	0,583	336071	17,69	0,21339	0,46	16,715	1,11	0,5681	0,94	0,85	2931	15	2900	44	2919	21	1,08
044-ZR31		0,0439	0,125	157120	47,26	0,20965	0,53	16,073	1,13	0,5560	0,92	0,82	2903	17	2850	42	2881	21	1,82
042-ZR29		0,0232	0,415	56331	31,00	0,20984	0,68	16,270	1,37	0,5623	1,14	0,83	2904	22	2876	53	2893	26	0,97
039-ZR28		0,0418	0,303	79718	46,65	0,21023	1,08	16,230	2,10	0,5599	1,76	0,84	2907	35	2866	81	2890	40	1,41
038-ZR27		0,0124	0,238	456441	15,09	0,20944	0,74	14,764	1,85	0,5112	1,66	0,89	2901	24	2662	72	2800	35	8,25
037-ZR26		0,0364	0,174	122112	53,18	0,21831	1,28	16,445	2,14	0,5463	1,67	0,78	2968	41	2810	76	2903	40	5,34
036-ZR25		0,0253	0,306	152044	41,54	0,21025	1,09	14,888	2,10	0,5135	1,75	0,84	2908	35	2672	77	2808	40	8,11
031-ZR22		0,0078	0,394	316641	15,72	0,20519	0,81	13,617	1,44	0,4813	1,13	0,79	2868	26	2533	47	2723	27	11,68
028-ZR20	Migmatite	0,0125	0,557	409625	15,84	0,21154	0,46	17,377	1,02	0,5957	0,83	0,81	2917	15	3013	40	2956	20	-3,27
023-ZR15		0,0617	0,151	390068	65,19	0,21264	0,49	16,573	1,16	0,5652	0,98	0,85	2926	16	2888	46	2910	22	1,29
022-ZR14		0,0286	0,337	44218	14,37	0,21246	0,57	15,376	2,40	0,5248	2,30	0,96	2924	19	2720	102	2839	45	7,00
019-ZR13		0,0089	0,515	369945	51,99	0,21232	1,06	15,835	1,47	0,5409	0,94	0,64	2923	34	2787	43	2867	28	4,66
018-ZR12		0,0369	0,307	69758	73,55	0,21023	0,91	16,300	2,57	0,5623	2,38	0,92	2907	29	2876	110	2895	49	1,08
016-ZR10		0,0167	0,360	658708	14,80	0,21120	0,40	16,680	0,98	0,5727	0,82	0,83	2915	13	2919	38	2917	19	-0,15
015-ZR9		0,0476	0,343	61045	75,09	0,20462	1,24	14,781	1,95	0,5239	1,45	0,75	2863	40	2715	64	2801	37	5,17
014-ZR8		0,0222	0,283	678856	37,25	0,20929	0,32	16,549	0,93	0,5734	0,79	0,85	2900	10	2922	37	2909	18	-0,76
035-ZR24		0,0441	0,172	196193	55,07	0,20127	0,57	13,374	1,44	0,4819	1,27	0,88	2837	19	2536	53	2706	27	10,61
034-ZR23		0,0549	0,322	18639	14,93	0,20515	0,91	14,142	1,47	0,4999	1,10	0,75	2868	29	2614	47	2759	28	8,86
026-ZR18		0,0390	0,182	16561	6,91	0,19486	0,88	10,548	1,66	0,3926	1,35	0,82	2784	29	2135	49	2484	30	23,31
025-ZR17		0,0221	0,228	9198	9,11	0,18758	0,96	8,824	3,35	0,3411	3,19	0,95	2721	31	1892	104	2320	60	30,46
ADE-15	**Rock**	**^{206}Pb mV[1]**	**Th/U**	**^{206}Pb/^{204}Pb**	**1s%**	**^{207}Pb/^{206}Pb**	**1s %**	**^{207}Pb/^{235}U**	**1s %**	**^{206}Pb/^{238}U**	**1s %**	**Rho**	**^{207}Pb/^{206}Pb**	**2s abs**	**^{206}Pb/^{238}U**	**2s abs**	**^{207}Pb/^{235}U**	**2s abs**	**% U-Pb disc[4]**

ADE-18	Rock	^{206}Pb mV[1]	Th/U	$^{206}Pb/^{204}Pb$	1s%	$^{207}Pb/^{206}Pb$	1s %	$^{207}Pb/^{235}U$	1s %	$^{206}Pb/^{238}U$	1s %	Rho	$^{207}Pb/^{206}Pb$	2s abs	$^{206}Pb/^{238}U$	2s abs	$^{207}Pb/^{235}U$	2s abs	% U-Pb disc[4]
017-ZR8C		0,0058	0,478	159816	15,46	0,26148	0,68	22,874	1,18	0,6344	0,89	0,75	3256	21	3167	44	3222	23	2,72
033-ZR16C		0,0261	0,127	6248	2,97	0,17156	1,03	10,259	1,41	0,4337	0,89	0,63	2573	34	2322	35	2458	26	9,74
076-ZR44C		0,0090	0,558	113258	24,08	0,22427	0,84	16,641	1,32	0,5381	0,94	0,71	3012	27	2776	42	2914	25	7,84
018-ZR9C		0,0086	0,421	105096	29,53	0,21126	1,26	14,999	1,63	0,5149	0,96	0,59	2915	41	2677	42	2815	31	8,16
029-ZR15C		0,0211	0,198	390100	21,21	0,19570	1,67	12,875	2,01	0,4771	1,06	0,53	2791	54	2515	44	2671	38	9,89
035-ZR25		0,0138	0,137	311045	55,25	0,20836	1,88	10,770	2,58	0,3749	1,73	0,67	2893	60	2052	61	2504	47	29,06
010-ZR7		0,0336	0,449	6417	4,68	0,20286	1,10	9,712	2,22	0,3472	1,90	0,85	2849	36	1921	63	2408	41	32,57
009-ZR6		0,0131	0,476	7325	6,65	0,19113	1,40	8,798	3,12	0,3339	2,76	0,89	2752	46	1857	89	2317	56	32,52
024-ZR16		0,0117	0,127	481170	17,24	0,20902	0,81	15,530	1,74	0,5388	1,50	0,86	2898	26	2779	67	2848	33	4,12
029-ZR21		0,0299	0,240	348922	30,88	0,21340	1,27	17,878	2,24	0,6076	1,81	0,81	2932	41	3060	88	2983	43	-4,39
014-ZR9		0,0179	0,376	340675	21,21	0,20052	1,19	12,842	1,65	0,4644	1,07	0,65	2830	39	2459	44	2668	31	13,12
008-ZR5		0,0194	0,224	552568	22,50	0,20989	1,35	15,553	1,79	0,5374	1,12	0,63	2905	43	2772	50	2850	34	4,55
039-ZR29		0,0074	0,314	164897	21,37	0,19995	0,60	11,585	1,21	0,4202	0,98	0,81	2826	20	2261	37	2571	22	19,97
036-ZR26	Migmatite	0,0210	0,342	629270	18,48	0,20594	0,58	14,977	1,44	0,5274	1,27	0,88	2874	19	2731	56	2814	27	4,99
026-ZR13C		0,0057	0,489	256868	46,53	0,22389	0,67	18,284	1,30	0,5923	1,05	0,81	3009	21	2999	50	3005	25	0,34
070-ZR41C		0,0137	0,240	177514	40,36	0,21825	0,69	17,144	1,27	0,5697	1,00	0,79	2968	22	2906	47	2943	24	2,07
067-ZR38C		0,0232	0,341	2307	21,51	0,21258	1,44	15,940	1,94	0,5438	1,24	0,64	2925	46	2799	56	2873	37	4,31
078-ZR46C		0,0099	0,394	72595	31,53	0,21093	0,60	16,020	1,60	0,5508	1,43	0,90	2913	19	2828	65	2878	30	2,89
010-ZR5C		0,0168	0,426	101629	30,46	0,20756	0,72	15,476	1,23	0,5407	0,93	0,75	2887	23	2787	42	2845	23	3,47
069-ZR40C		0,0224	0,476	98781	54,88	0,20690	0,64	15,259	1,96	0,5349	1,81	0,93	2881	21	2762	81	2832	37	4,15
048-ZR25C		0,0097	0,192	273498	17,45	0,20654	0,55	15,260	1,13	0,5358	0,91	0,81	2879	18	2766	41	2832	21	3,91
014-ZR6C		0,0128	0,384	73434	39,41	0,20542	0,56	13,804	1,33	0,4873	1,15	0,86	2870	18	2559	49	2736	25	10,82
056-ZR30C		0,0066	0,278	104520	24,43	0,20537	0,79	13,580	1,39	0,4796	1,08	0,78	2869	26	2525	45	2721	26	11,99
009-ZR4C		0,0215	0,774	464233	21,50	0,20381	0,67	13,274	1,31	0,4723	1,06	0,81	2857	22	2494	44	2699	25	12,71
055-ZR29C		0,0128	0,483	241611	27,67	0,20341	0,54	12,817	1,66	0,4570	1,52	0,92	2854	17	2426	61	2666	31	14,98
007-ZR3C		0,0422	0,518	6953	12,22	0,20328	0,44	12,975	1,14	0,4629	0,98	0,86	2853	14	2452	40	2678	21	14,04
050-ZR27C		0,0120	0,149	2718	3,71	0,20134	0,77	10,232	1,69	0,3686	1,46	0,86	2837	25	2023	51	2456	31	28,71

ADE-18	Rock	^{206}Pb mV[1]	Th/U	^{206}Pb/^{204}Pb	1s%	^{207}Pb/^{206}Pb	1s %	^{207}Pb/^{235}U	1s %	^{206}Pb/^{238}U	1s %	Rho	^{207}Pb/^{206}Pb	2s abs	^{206}Pb/^{238}U	2s abs	^{207}Pb/^{235}U	2s abs	% U-Pb disc[4]
027-ZR14C		0,0035	0,136	83393	51,76	0,20057	2,01	10,088	2,95	0,3647	2,12	0,72	2831	65	2005	73	2443	54	29,19
054-ZR28C		0,0331	0,329	103227	58,24	0,19954	2,02	11,637	2,89	0,4229	2,03	0,70	2822	65	2274	78	2576	53	19,44
045-ZR22C		0,0297	0,137	3740	16,52	0,19862	0,50	13,150	1,07	0,4801	0,87	0,81	2815	16	2528	36	2690	20	10,20
020-ZR11C		0,0269	0,820	24701	15,40	0,19485	1,11	11,252	1,57	0,4188	1,04	0,66	2784	36	2255	39	2544	29	18,99
015-ZR6B		0,0282	0,235	8232	3,25	0,19478	0,53	12,782	1,17	0,4759	0,98	0,83	2783	17	2509	40	2664	22	9,83
038-ZR19B		0,0124	0,128	2891	4,69	0,19369	0,57	11,054	1,06	0,4139	0,82	0,77	2774	19	2233	31	2528	20	19,51
057-ZR31C		0,0060	0,010	374437	25,01	0,19163	1,23	7,145	4,60	0,2704	4,41	0,96	2756	40	1543	121	2130	80	44,02
058-ZR32C		0,0307	0,433	205289	33,99	0,18767	0,95	10,389	1,68	0,4015	1,33	0,79	2722	31	2176	49	2470	31	20,06
006-ZR2C		0,0301	0,044	5861	5,65	0,16880	0,64	4,801	1,89	0,2063	1,74	0,92	2546	21	1209	38	1785	32	52,51
030-ZR22		0,0371	0,030	98231	42,89	0,12247	0,69	6,143	1,18	0,3637	0,88	0,75	1993	25	2000	30	1996	21	-0,37
027-ZR19		0,0445	0,046	489542	32,80	0,12253	0,53	6,073	1,00	0,3594	0,76	0,76	1993	19	1980	26	1986	17	0,70
026-ZR18		0,0923	0,021	339987	46,74	0,11918	0,54	5,711	1,02	0,3475	0,77	0,76	1944	19	1923	26	1933	17	1,09
028-ZR20		0,0269	0,034	270687	29,47	0,12458	2,12	6,212	2,69	0,3616	1,62	0,60	2023	74	1990	55	2006	47	1,63
020-ZR15		0,0253	0,105	29947	28,16	0,12405	2,16	6,019	2,64	0,3519	1,49	0,56	2015	76	1944	50	1979	46	3,55
016-ZR11		0,0250	0,046	31621608	98,94	0,11806	0,69	5,599	1,09	0,3439	0,76	0,70	1927	25	1905	25	1916	19	1,13
015-ZR10		0,0343	0,050	973409	20,25	0,12289	0,43	6,162	1,05	0,3637	0,88	0,84	1999	15	1999	30	1999	18	-0,04
037-ZR27		0,0501	0,043	43957	15,43	0,12156	0,46	6,019	1,47	0,3591	1,35	0,92	1979	16	1978	46	1979	25	0,07
006-ZR3		0,0495	0,005	16056	4,37	0,12007	0,46	4,792	1,62	0,2895	1,51	0,93	1957	16	1639	44	1784	27	16,27
004-ZR1		0,0208	0,022	1088104	30,43	0,11013	0,44	3,428	1,36	0,2257	1,23	0,91	1802	16	1312	29	1511	21	27,18
036-ZR18C		0,0106	0,094	211588	19,79	0,12325	2,03	2,480	2,95	0,1460	2,11	0,71	2004	71	878	35	1266	42	56,17
079-ZR46B		0,0365	0,034	29184	8,78	0,12149	0,67	5,955	1,46	0,3555	1,24	0,85	1978	24	1961	42	1969	25	0,89
060-ZR34C		0,0351	0,068	502453	24,07	0,12111	1,02	6,251	1,29	0,3743	0,70	0,54	1973	36	2050	24	2012	22	-3,91
074-ZR42C		0,0183	0,060	215184	26,40	0,12108	0,51	6,041	1,11	0,3618	0,92	0,82	1972	18	1991	31	1982	19	-0,94
005-ZR1B		0,0562	0,038	309811	39,94	0,12096	0,42	6,329	0,85	0,3795	0,64	0,75	1970	15	2074	23	2022	15	-5,24
066-ZR37C		0,0373	0,029	622342	23,34	0,12080	0,87	6,093	1,18	0,3658	0,70	0,59	1968	31	2010	24	1989	20	-2,11
068-ZR39C		0,0316	0,039	101627	52,07	0,12078	0,79	6,035	1,26	0,3624	0,91	0,72	1968	28	1993	31	1981	22	-1,30
040-ZR20B		0,0226	0,034	549421	19,38	0,12029	0,65	5,745	1,11	0,3464	0,82	0,74	1960	23	1917	27	1938	19	2,20

ADE-18	Rock	^{206}Pb mV[1]	Th/U	^{206}Pb/^{204}Pb	1s%	^{207}Pb/^{206}Pb	1s %	^{207}Pb/^{235}U	1s %	^{206}Pb/^{238}U	1s %	Rho	^{207}Pb/^{206}Pb	2s abs	^{206}Pb/^{238}U	2s abs	^{207}Pb/^{235}U	2s abs	% U-Pb disc[4]
025-ZR12C		0,0281	0,055	23227	9,84	0,11922	0,61	5,167	1,15	0,3143	0,90	0,78	1945	22	1762	28	1847	19	9,39
049-ZR26C		0,0232	0,048	469433	22,08	0,11918	1,01	5,683	1,57	0,3458	1,15	0,73	1944	36	1914	38	1929	27	1,52
053-ZR27B		0,0531	0,024	135279	51,93	0,11832	0,60	4,783	1,34	0,2931	1,15	0,85	1931	21	1657	33	1782	22	14,19
034-ZR24		0,0277	0,006	4288	4,36	0,06366	0,73	0,797	1,25	0,0908	0,95	0,76	731	31	561	10	595	11	23,27
028-ZR14B		0,0047	0,014	43831	30,63	0,06252	0,66	0,861	1,16	0,0999	0,88	0,76	692	28	614	10	631	11	11,32
025-ZR17		0,0184	0,010	482176	20,69	0,06018	0,78	0,796	1,46	0,0959	1,17	0,80	610	34	590	13	594	13	3,26
075-ZR43C		0,0133	0,006	173053	29,35	0,05923	0,54	0,814	1,17	0,0997	0,97	0,83	575	23	612	11	605	11	-6,41
033-ZR23		0,0307	0,007	195405	34,15	0,05966	0,54	0,817	1,09	0,0993	0,87	0,80	591	23	610	10	606	10	-3,23
059-ZR33C		0,0185	0,024	82740	43,14	0,05997	0,96	0,748	1,45	0,0904	1,02	0,71	603	41	558	11	567	13	7,39
034-ZR16B		0,0133	0,006	317236	20,88	0,05991	0,98	0,850	1,41	0,1028	0,95	0,67	600	42	631	11	624	13	-5,11
073-ZR41B		0,0249	0,010	74184	39,26	0,05928	0,56	0,840	1,20	0,1027	0,99	0,83	577	24	630	12	619	11	-9,22
ADE-23	**Rock**	**^{206}Pb mV[1]**	**Th/U**	**^{206}Pb/^{204}Pb**	**1s%**	**^{207}Pb/^{206}Pb**	**1s %**	**^{207}Pb/^{235}U**	**1s %**	**^{206}Pb/^{238}U**	**1s %**	**Rho**	**^{207}Pb/^{206}Pb**	**2s abs**	**^{206}Pb/^{238}U**	**2s abs**	**^{207}Pb/^{235}U**	**2s abs**	**% U-Pb disc[4]**
040-ZR30		0,0108	0,368	388044	16,86	0,18323	0,75	13,038	1,28	0,5160	0,96	0,75	2682	25	2682	42	2682	24	0,00
038-ZR28		0,0124	0,366	416473	15,22	0,17932	0,49	11,610	0,99	0,4695	0,78	0,78	2647	16	2482	32	2573	18	6,23
035-ZR25		0,0111	0,347	377506	17,84	0,17762	0,41	10,649	1,22	0,4348	1,09	0,89	2631	13	2327	42	2493	22	11,53
027-ZR19		0,0135	0,199	201729	40,61	0,16733	0,94	9,414	1,53	0,4080	1,15	0,75	2531	31	2206	43	2379	28	12,85
026-ZR18B		0,0236	0,405	868227	14,13	0,17629	0,46	12,125	1,15	0,4988	0,98	0,86	2618	15	2609	42	2614	21	0,37
025-ZR17		0,0232	0,459	827172	23,06	0,16113	0,66	8,209	1,35	0,3695	1,12	0,83	2468	22	2027	39	2254	24	17,86
024-ZR16		0,0107	0,364	764391	35,93	0,18378	0,41	12,865	1,10	0,5077	0,95	0,86	2687	13	2647	41	2670	21	1,51
020-ZR15	Migmatite	0,0126	0,419	829567	56,75	0,17988	0,61	12,239	1,22	0,4935	0,99	0,81	2652	20	2586	42	2623	23	2,49
017-ZR12B		0,0114	0,320	753478	42,19	0,18296	0,37	13,145	1,20	0,5210	1,08	0,90	2680	12	2703	48	2690	23	-0,88
013-ZR8		0,0377	0,467	1163089	16,47	0,17543	0,38	11,629	1,16	0,4807	1,03	0,89	2610	12	2530	43	2575	21	3,05
058-ZR41		0,0031	0,269	138325	12,27	0,17800	0,82	12,064	1,48	0,4915	1,17	0,79	2634	27	2577	50	2609	28	2,17
056-ZR39		0,0059	0,305	178722	16,11	0,18059	0,63	12,624	1,12	0,5069	0,85	0,76	2658	21	2644	37	2652	21	0,56
055-ZR38		0,0054	0,278	189053	17,61	0,17302	0,81	10,482	1,51	0,4394	1,21	0,81	2587	27	2348	48	2478	28	9,25
054-ZR37C		0,0037	0,324	135685	13,51	0,18022	0,71	11,309	1,40	0,4551	1,15	0,82	2655	23	2418	46	2549	26	8,93
053-ZR36		0,0055	0,256	220553	17,53	0,16370	0,76	9,154	1,19	0,4055	0,84	0,71	2494	25	2194	31	2353	22	12,02

ADE-18	Rock	^{206}Pb mV[1]	Th/U	^{206}Pb/^{204}Pb	1s%	^{207}Pb/^{206}Pb	1s %	^{207}Pb/^{235}U	1s %	^{206}Pb/^{238}U	1s %	Rho	^{207}Pb/^{206}Pb	2s abs	^{206}Pb/^{238}U	2s abs	^{207}Pb/^{235}U	2s abs	% U-Pb disc[4]
050-ZR35		0,0212	0,474	796624	15,70	0,17399	1,05	12,024	1,58	0,5012	1,13	0,71	2596	35	2619	48	2606	29	-0,86
048-ZR33		0,0039	0,290	134781	18,18	0,18078	0,64	12,308	1,09	0,4937	0,80	0,74	2660	21	2587	34	2628	20	2,75
046-ZR31		0,0098	0,496	490951	27,30	0,18149	0,57	12,744	1,36	0,5092	1,18	0,87	2667	19	2653	51	2661	26	0,49
045-ZR30		0,0104	0,414	316069	16,09	0,18046	0,93	12,742	1,46	0,5121	1,07	0,73	2657	31	2665	46	2661	27	-0,32
044-ZR29		0,0336	0,427	1627654	63,56	0,17417	0,73	12,402	1,22	0,5164	0,91	0,74	2598	24	2684	40	2635	23	-3,30
037-ZR26C		0,0207	0,408	544929	17,42	0,17608	0,54	12,429	1,27	0,5119	1,09	0,86	2616	18	2665	48	2637	24	-1,85
036-ZR25		0,0028	0,296	103496	14,38	0,18436	0,68	12,660	1,17	0,4980	0,88	0,75	2692	22	2605	38	2655	22	3,24
035-ZR24		0,0140	0,413	404663	19,09	0,17921	0,43	12,163	1,06	0,4922	0,90	0,85	2646	14	2580	38	2617	20	2,47
034-ZR23		0,0027	0,326	90433	16,92	0,18135	0,70	12,107	1,16	0,4842	0,84	0,73	2665	23	2545	35	2613	22	4,50
033-ZR22		0,0201	0,434	1005132	25,07	0,17602	0,50	12,642	0,98	0,5209	0,76	0,78	2616	17	2703	34	2653	18	-3,33
029-ZR20		0,0063	0,386	201334	15,18	0,18180	0,71	12,309	1,19	0,4910	0,88	0,74	2669	24	2575	37	2628	22	3,53
028-ZR19		0,0046	0,418	191721	14,10	0,18322	0,58	12,868	1,08	0,5094	0,84	0,77	2682	19	2654	36	2670	20	1,06
024-ZR15		0,0044	0,181	121175	19,17	0,15103	1,60	7,705	2,11	0,3700	1,33	0,63	2358	54	2029	46	2197	38	13,93
019-ZR13B		0,0025	0,372	445018	85,40	0,18609	1,29	12,045	1,79	0,4694	1,17	0,66	2708	42	2481	48	2608	33	8,38
018-ZR13C		0,0054	0,128	426854	65,75	0,15428	0,75	7,949	1,25	0,3737	0,93	0,74	2394	25	2047	32	2225	22	14,51
016-ZR11		0,0431	0,242	862579	23,41	0,17223	0,49	11,749	1,03	0,4947	0,82	0,80	2579	16	2591	35	2585	19	-0,45
015-ZR10		0,0124	0,086	539967	14,41	0,15685	1,31	7,966	1,68	0,3683	0,98	0,59	2422	44	2022	34	2227	30	16,53
014-ZR9		0,0068	0,349	172807	23,53	0,17952	0,62	13,026	1,11	0,5262	0,84	0,76	2648	21	2726	37	2682	21	-2,91
013-ZR8		0,0320	0,301	805400	21,86	0,17465	0,66	12,496	1,00	0,5189	0,66	0,66	2603	22	2694	29	2642	19	-3,52
010-ZR7		0,0328	0,215	753028	20,53	0,17118	0,65	11,108	1,04	0,4706	0,73	0,70	2569	22	2486	30	2532	19	3,23
008-ZR5		0,0232	0,487	660430	19,94	0,16273	1,18	8,938	1,65	0,3983	1,10	0,66	2484	39	2161	40	2332	30	13,00
007-ZR4		0,0108	0,409	349442	15,86	0,17958	0,50	12,977	0,97	0,5241	0,75	0,77	2649	17	2716	33	2678	18	-2,54
006-ZR3		0,0302	0,133	783760	17,86	0,16736	0,93	10,100	1,41	0,4377	1,00	0,71	2531	31	2340	39	2444	26	7,56
005-ZR2		0,0091	0,382	311129	15,06	0,18024	0,55	12,195	1,21	0,4907	1,01	0,84	2655	18	2574	43	2620	23	3,07
004-ZR1		0,0046	0,287	186334	13,77	0,18417	1,41	12,527	1,74	0,4933	0,96	0,55	2691	46	2585	41	2645	32	3,93
047-ZR32		0,0366	0,345	1221664	15,69	0,15241	0,73	8,186	1,28	0,3895	0,99	0,77	2373	25	2121	36	2252	23	10,64
026-ZR17		0,0268	0,080	745848	18,74	0,16193	0,53	9,713	1,00	0,4350	0,75	0,76	2476	18	2328	29	2408	18	5,96

ADE-18	Rock	^{206}Pb mV[1]	Th/U	^{206}Pb/^{204}Pb	1s%	^{207}Pb/^{206}Pb	1s %	^{207}Pb/^{235}U	1s %	^{206}Pb/^{238}U	1s %	Rho	^{207}Pb/^{206}Pb	2s abs	^{206}Pb/^{238}U	2s abs	^{207}Pb/^{235}U	2s abs	% U-Pb disc[4]
009-ZR6		0,0404	0,114	1392995	17,10	0,15993	0,56	9,244	1,03	0,4192	0,78	0,76	2455	19	2257	30	2362	19	8,08
049-ZR34		0,0263	0,369	24603455	96,49	0,16337	0,69	10,060	1,32	0,4466	1,07	0,81	2491	23	2380	42	2440	24	4,45
020-ZR14		0,0196	0,301	337389	22,52	0,16246	0,85	10,195	1,33	0,4551	0,96	0,72	2481	29	2418	39	2453	25	2,55
039-ZR29B		0,0084	0,321	417726	20,95	0,16780	0,90	11,085	1,62	0,4791	1,30	0,80	2536	30	2523	54	2530	30	0,49
019-ZR14		0,0117	0,441	554167	25,35	0,16863	0,80	8,865	1,70	0,3813	1,45	0,85	2544	27	2082	51	2324	31	18,16
008-ZR5B		0,0578	0,298	1179726	25,20	0,16600	0,51	10,471	1,50	0,4574	1,36	0,91	2518	17	2428	55	2477	28	3,55
005-ZR2		0,0099	0,373	329473	15,59	0,16689	0,40	9,704	1,59	0,4217	1,49	0,94	2527	14	2268	57	2407	29	10,24
004-ZR1		0,0512	0,245	427724	24,05	0,16650	0,84	7,766	1,94	0,3383	1,71	0,88	2523	28	1878	56	2204	35	25,54
016-ZR11B		0,0931	0,040	323623	47,01	0,13787	0,74	8,172	1,08	0,4298	0,69	0,64	2201	26	2305	27	2250	19	-4,74
018-ZR13B		0,0327	0,022	1036766	17,01	0,14216	0,60	7,999	1,09	0,4081	0,83	0,76	2254	21	2206	31	2231	20	2,11
017-ZR12		0,0210	0,015	902285	12,63	0,13259	1,02	7,116	1,69	0,3892	1,30	0,77	2133	35	2119	47	2126	30	0,63
038-ZR26B		0,0271	0,017	883570	15,92	0,11971	0,65	6,003	1,07	0,3637	0,77	0,71	1952	23	2000	26	1976	19	-2,44
025-ZR16		0,0086	0,013	210003	23,19	0,11877	1,12	5,227	1,52	0,3192	0,97	0,63	1938	40	1786	30	1857	26	7,86
027-ZR18		0,0140	0,048	558429	14,05	0,11784	0,75	5,851	1,21	0,3601	0,87	0,72	1924	27	1983	30	1954	21	-3,06
ADE-29	**Rock**	**^{206}Pb mV[1]**	**Th/U**	**^{206}Pb/^{204}Pb**	**1s%**	**^{207}Pb/^{206}Pb**	**1s %**	**^{207}Pb/^{235}U**	**1s %**	**^{206}Pb/^{238}U**	**1s %**	**Rho**	**^{207}Pb/^{206}Pb**	**2s abs**	**^{206}Pb/^{238}U**	**2s abs**	**^{207}Pb/^{235}U**	**2s abs**	**% U-Pb disc[4]**
006-ZR3		0,0153	0,570	419605	17,66	0,22280	0,69	18,809	1,12	0,6122	0,80	0,72	3001	22	3079	39	3032	22	-2,59
036-ZR26		0,0092	0,476	220317	19,98	0,21823	0,60	16,966	1,21	0,5638	0,99	0,82	2968	19	2882	46	2933	23	2,88
040-ZR30		0,0091	0,842	173700	48,93	0,22274	0,73	17,665	1,63	0,5751	1,41	0,86	3001	23	2929	66	2972	31	2,39
039-ZR29		0,0118	0,412	146252	31,14	0,20045	0,74	10,482	1,73	0,3792	1,52	0,88	2830	24	2073	54	2478	32	26,76
041-ZR31		0,0049	0,393	139083	17,13	0,15141	0,90	5,513	1,66	0,2640	1,34	0,81	2362	31	1511	36	1903	28	36,05
038-ZR28	Ultramafic	0,0060	0,159	193114	16,02	0,17762	0,66	11,231	1,42	0,4585	1,20	0,85	2631	22	2433	48	2542	26	7,51
037-ZR27		0,0094	0,435	281967	16,53	0,16540	0,59	7,503	1,25	0,3290	1,04	0,83	2512	20	1833	33	2173	22	27,00
035-ZR25		0,0068	0,343	244616	17,40	0,17386	0,63	10,346	1,29	0,4316	1,07	0,82	2595	21	2313	41	2466	24	10,88
034-ZR24		0,0086	0,399	28642	28,20	0,16963	0,85	8,781	1,61	0,3754	1,32	0,82	2554	28	2055	46	2316	29	19,54
030-ZR22		0,0087	0,480	313935	14,56	0,15755	1,17	6,161	1,64	0,2836	1,08	0,66	2430	40	1609	31	1999	28	33,76
029-ZR21		0,0190	0,537	755972	16,19	0,16169	0,85	6,823	1,47	0,3060	1,14	0,78	2473	29	1721	34	2089	26	30,42

ADE-18	Rock	^{206}Pb mV[1]	Th/U	$^{206}Pb/^{204}Pb$	1s%	$^{207}Pb/^{206}Pb$	1s %	$^{207}Pb/^{235}U$	1s %	$^{206}Pb/^{238}U$	1s %	Rho	$^{207}Pb/^{206}Pb$	2s abs	$^{206}Pb/^{238}U$	2s abs	$^{207}Pb/^{235}U$	2s abs	% U-Pb disc[4]
028-ZR20		0,0107	0,539	117929	31,02	0,17204	0,69	9,234	1,28	0,3892	1,01	0,79	2578	23	2119	36	2361	23	17,78
027-ZR19		0,0068	0,116	195554	17,97	0,18108	0,68	11,870	1,31	0,4754	1,06	0,81	2663	22	2507	44	2594	24	5,84
026-ZR18		0,0060	0,233	299866	38,55	0,17872	1,16	11,199	2,36	0,4545	2,02	0,86	2641	38	2415	81	2540	44	8,56
025-ZR17		0,0117	0,259	1713420	93,24	0,15025	0,73	5,377	1,40	0,2595	1,14	0,81	2349	25	1488	30	1881	24	36,67
024-ZR16		0,0094	0,243	320129	16,86	0,17904	0,85	11,087	2,13	0,4491	1,92	0,90	2644	28	2391	77	2530	39	9,56
019-ZR14		0,0080	0,170	301371	13,99	0,17490	0,99	10,894	1,52	0,4517	1,10	0,72	2605	33	2403	44	2514	28	7,76
018-ZR13		0,0105	0,422	354686	16,89	0,15330	0,72	5,734	1,61	0,2712	1,39	0,87	2383	24	1547	38	1936	28	35,08
017-ZR12		0,0084	0,190	333691	15,85	0,16684	0,58	8,271	1,40	0,3595	1,21	0,87	2526	20	1980	41	2261	25	21,62
015-ZR10		0,0071	0,303	92127	31,60	0,17226	0,62	8,259	1,64	0,3477	1,48	0,90	2580	20	1924	49	2260	30	25,43
014-ZR9		0,0069	0,233	310069	29,88	0,17785	0,59	11,158	1,30	0,4550	1,10	0,85	2633	19	2417	44	2536	24	8,19
013-ZR8		0,0069	0,302	211690	43,77	0,16780	0,97	8,828	1,60	0,3815	1,22	0,76	2536	32	2083	43	2320	29	17,84
010-ZR7		0,0152	0,417	526604	14,71	0,17421	0,72	9,960	1,29	0,4146	1,01	0,78	2599	24	2236	38	2431	24	13,95
009-ZR6		0,0096	0,382	218719	21,99	0,15570	0,74	6,842	1,40	0,3187	1,13	0,81	2409	25	1783	35	2091	25	25,99
008-ZR5		0,0123	0,195	447680	12,99	0,16884	0,58	8,536	1,34	0,3667	1,15	0,86	2546	19	2014	40	2290	24	20,91
007-ZR4		0,0139	0,587	348591	22,29	0,16100	0,58	7,192	1,54	0,3240	1,37	0,89	2466	20	1809	43	2136	27	26,65
005-ZR2		0,0092	0,407	351330	16,28	0,16045	0,80	7,019	1,34	0,3172	1,01	0,75	2460	27	1776	31	2114	24	27,81
004-ZR1		0,0146	0,587	405253	19,61	0,16400	0,70	8,013	1,22	0,3543	0,93	0,76	2497	24	1955	31	2232	22	21,71
016-ZR11		0,0022	0,460	91016	16,52	0,05960	0,94	0,784	1,54	0,0955	1,17	0,76	589	40	588	13	588	14	0,22
ADE-16	**Rock**	**206Pb mV1**	**Th/U**	**206Pb/204Pb**	**1s%**	**207Pb/206Pb**	**1s %**	**207Pb/235U**	**1s %**	**206Pb/238U**	**1s %**	**Rho**	**207Pb/206Pb**	**2s abs**	**206Pb/238U**	**2s abs**	**207Pb/235U**	**2s abs**	**% U-Pb disc4**
049-ZR36		0,0049	0,461	118344	20,19	0,22362	0,79	18,142	1,35	0,5884	1,04	0,76	3007	25	2983	49	2997	26	0,80
048-ZR35		0,0052	0,171	91234	23,65	0,17521	0,68	9,496	1,35	0,3931	1,11	0,82	2608	23	2137	40	2387	25	18,06
047-ZR34		0,0066	0,185	126434	21,30	0,17766	0,63	11,674	1,30	0,4765	1,07	0,82	2631	21	2512	44	2579	24	4,53
046-ZR33	Ultramafic	0,0074	0,163	27521	44,06	0,15707	0,64	3,495	2,09	0,1614	1,95	0,94	2424	22	964	35	1526	33	60,22
045-ZR32		0,0078	0,230	252276	19,43	0,17568	0,60	10,407	1,28	0,4296	1,07	0,83	2612	20	2304	41	2472	24	11,81
044-ZR31		0,0066	0,268	220465	16,95	0,17384	0,66	9,833	1,19	0,4102	0,92	0,77	2595	22	2216	34	2419	22	14,61
040-ZR30		0,0095	0,290	25745	24,35	0,17434	1,43	8,458	1,91	0,3518	1,21	0,63	2600	47	1943	41	2281	34	25,25
039-ZR29		0,0008	0,616	26698	19,82	0,06070	2,23	0,806	3,10	0,0963	2,11	0,68	629	95	593	24	600	28	5,67

ADE-18	Rock	^{206}Pb mV[1]	Th/U	$^{206}Pb/^{204}Pb$	1s%	$^{207}Pb/^{206}Pb$	1s %	$^{207}Pb/^{235}U$	1s %	$^{206}Pb/^{238}U$	1s %	Rho	$^{207}Pb/^{206}Pb$	2s abs	$^{206}Pb/^{238}U$	2s abs	$^{207}Pb/^{235}U$	2s abs	% U-Pb disc[4]
038-ZR28		0,0068	0,200	216673	16,63	0,17742	0,58	10,966	1,33	0,4482	1,14	0,86	2629	19	2387	45	2520	25	9,18
037-ZR27		0,0048	0,230	156080	15,88	0,17993	0,59	12,095	1,18	0,4875	0,96	0,81	2652	20	2560	40	2612	22	3,48
036-ZR26		0,0079	0,301	138840	23,85	0,17796	0,69	9,075	2,38	0,3698	2,25	0,94	2634	23	2029	78	2346	43	22,98
035-ZR25		0,0073	0,240	183123	17,10	0,17816	0,53	10,885	0,99	0,4431	0,76	0,76	2636	17	2364	30	2513	18	10,30
034-ZR24		0,0038	0,226	147758	28,42	0,17834	0,59	11,285	1,11	0,4589	0,87	0,78	2638	20	2435	35	2547	21	7,69
033-ZR23		0,0083	0,228	303263	16,36	0,17615	0,65	11,282	1,15	0,4645	0,87	0,76	2617	22	2459	36	2547	21	6,02
030-ZR22		0,0056	0,176	217145	14,59	0,17619	0,74	10,248	1,16	0,4218	0,81	0,70	2617	25	2269	31	2457	21	13,32
029-ZR21		0,0062	0,213	205779	15,32	0,17904	0,68	11,600	1,19	0,4699	0,90	0,76	2644	22	2483	37	2573	22	6,09
028-ZR20		0,0066	0,247	170920	21,35	0,16840	0,69	8,531	1,13	0,3674	0,81	0,72	2542	23	2017	28	2289	20	20,64
027-ZR19		0,0072	0,226	237843	17,66	0,17753	0,94	11,102	1,45	0,4535	1,04	0,72	2630	31	2411	42	2532	27	8,32
026-ZR18		0,0028	0,204	98345	15,58	0,17400	0,84	9,571	1,58	0,3989	1,29	0,82	2597	28	2164	47	2394	29	16,66
025-ZR17		0,0063	0,150	141345	21,15	0,16520	0,52	7,679	1,08	0,3371	0,87	0,81	2510	17	1873	28	2194	19	25,37
024-ZR16		0,0079	0,326	158057	19,58	0,16929	1,25	7,138	2,09	0,3058	1,64	0,78	2551	42	1720	49	2129	37	32,57
020-ZR15		0,0042	0,131	90129	21,36	0,16961	0,74	9,718	1,39	0,4155	1,12	0,81	2554	25	2240	42	2408	25	12,29
019-ZR14		0,0082	0,171	253890	15,54	0,17742	0,69	11,115	1,21	0,4544	0,93	0,77	2629	23	2415	37	2533	22	8,15
018-ZR13		0,0059	0,244	159208	17,79	0,16947	0,69	8,834	1,68	0,3780	1,49	0,88	2552	23	2067	52	2321	30	19,02
017-ZR12		0,0107	0,205	199382	21,64	0,18148	0,55	12,233	1,06	0,4889	0,83	0,78	2666	18	2566	35	2622	20	3,77
016-ZR11		0,0084	0,223	270726	18,02	0,17938	0,58	11,241	1,14	0,4545	0,91	0,80	2647	19	2415	37	2543	21	8,77
015-ZR10		0,0067	0,225	226244	14,71	0,17325	2,02	8,810	2,42	0,3688	1,27	0,53	2589	67	2024	44	2318	44	21,85
014-ZR9		0,0069	0,261	497473	56,80	0,16715	1,01	7,621	2,35	0,3307	2,09	0,89	2529	34	1842	67	2187	42	27,19
013-ZR8		0,0091	0,241	278638	14,00	0,16766	0,77	7,973	1,54	0,3448	1,28	0,83	2534	26	1910	42	2228	28	24,64
010-ZR7		0,0075	0,202	146549	19,96	0,17644	1,07	10,750	1,53	0,4419	1,03	0,67	2620	35	2359	41	2502	28	9,95
009-ZR6		0,0078	0,228	176781	21,29	0,17967	0,82	11,693	1,23	0,4720	0,84	0,68	2650	27	2492	35	2580	23	5,95
008-ZR5		0,0072	0,230	37658	38,55	0,14385	0,81	3,886	2,43	0,1959	2,26	0,93	2274	28	1153	48	1611	39	49,28
007-ZR4		0,0091	0,236	177168	22,00	0,17196	0,57	9,096	1,44	0,3836	1,27	0,88	2577	19	2093	45	2348	26	18,77
006-ZR3		0,0083	0,121	122527	29,61	0,14507	0,80	4,504	1,39	0,2252	1,08	0,77	2289	28	1309	26	1732	23	42,80

ADE-18	Rock	^{206}Pb mV[1]	Th/U	$^{206}Pb/^{204}Pb$	1s%	$^{207}Pb/^{206}Pb$	1s %	$^{207}Pb/^{235}U$	1s %	$^{206}Pb/^{238}U$	1s %	Rho	$^{207}Pb/^{206}Pb$	2s abs	$^{206}Pb/^{238}U$	2s abs	$^{207}Pb/^{235}U$	2s abs	% U-Pb disc[4]
005-ZR2		0,0110	0,209	274098	22,98	0,17820	0,38	12,009	1,01	0,4887	0,86	0,85	2636	13	2565	36	2605	19	2,70
004-ZR1		0,0070	0,272	22082	28,24	0,15512	0,48	5,930	1,21	0,2773	1,05	0,86	2403	16	1578	29	1966	21	34,35

6. ARTIGO CIENTÍFICO 5: ARCHEAN TO NEOPROTEROZOIC ARC DOCKING AND CRUSTAL REWORKING IN NORTHEAST BRAZIL

Alanielson da C. D. Ferreira, Elton L. Dantas, Reinhardt A. Fuck

Instituto de Geociências, Universidade de Brasília (UnB), 70910-900 Brasília-DF, Brazil

6.1 ABSTRACT

Systematic Nd isotope and U-Pb geochronology data were applied to the Precambrian rocks of northeastern Brazil to produce a crustal-age distribution map for a small fragment (1,500 Km^2) of a basement inlier in the Neoproterozoic supracrustal belt related to the Brasiliano orogeny. The results support episodic crustal growth with five short crustal formation periods at ca. 2.9 Ga, 2.65 Ga, 2.25 Ga, 2.0 Ga and 0.6 Ga. About 60% of the crust was formed in the Archean, between 2.9 Ga and 2.65 Ga; the remaining 40% of accretionary crustal generation was added in the 2.0 to 2.0 Ga Rhyacian period. Crustal recycling of the Archean and Proterozoic protolith sources require chelogenic processes, which represent successive arc accretions surrounding an older core, becoming younger toward the margin, to explain the age zonation pattern displayed in the Archean core evolution. A similar process is observed only in large continental areas, more than 1.000,000 km^2 in size, as in the North American continent basement and in the Amazonian Craton. However, it had never been describe in the minor crustal block scale, as in the Campo Grande complex in Northeast Brazil.

Keywords: Archean crust; crustal reworking, arc docking, West Gondwana

6.2 INTRODUCTION

Understanding the evolution of the continental crust is a challenge due to the diversity of geological environments where lithosphere is formed and recycled, as well as its growth and differentiation processes, throughout geological time. In this perspective, chelogenic cycles (e.g. Sutton, 1963), terrane docking (e.g. Twiss and Moores, 1992), or continental accretion are the key processes that allow the preservation of the archives of crustal evolution (e.g. Nance et al., 2014; Hawkesworth et al., 2017; 2019). Terrane docking is one of the main

processes for lateral continental growth through Earth's history (e.g. Stern and Scholl, 2010; Tetreault and Buiter, 2014; Moresi et al., 2014).

Archean continental crust was produced by accreted oceanic arcs and oceanic plateaus, mainly through ultrahigh-temperature processes. Change to primarily continental arcs took place during the Proterozoic (e.g. Brown, 2008; Cawood et al., 2013; Holder et al., 2019) due to oceanic lithosphere becoming prone to subduction, allowing for ultrahigh-pressure processes. At the center of this debate is the physical crustal flow and subsidence behavior during the Archean and their lifetime, and how the transition to continental arcs and Phanerozoic-style subduction took place (e.g. Brown, 2008; Rollinson, 2010; Holder et al., 2019). Some studies suggest long time scales (3.2 to 2.5 Ga) for a profound change in average crustal chemistry (e.g. Nebel et al., 2018). Gradual decline in the rate of crustal generation may be explained by the secular cooling of the mantle (e.g. Korenaga, 2018), and decline in crustal recycling may be explained by the "cratonization" of continental crust (e.g., Hawkesworth et al., 2017).

Compositional diversity and complex evolution of the accretionary orogens are generated due to lateral migration parallel to the plate boundary, and orthogonal accretion of juvenile magmatism and reworked continental crust segments (e.g. Moresi et al., 2014). In this context, samarium–neodymium isotopes may provide a means of determining the (1) crustal residence time, i.e., the time the rock precursor was removed from the convecting mantle (e.g. DePaolo, 1981; DePaolo et al., 1991), (2) crustal recycling processes (e.g. Rosas and Korenaga, 2018), and (3) mantle mixing (e.g. Caro et al., 2017). Therefore, Nd isotopes allow to characterize reworking and juvenile protolith sources and to describe the geometry of continental crust growth (e.g. DePaolo et al., 1991; McLennan and Hemming, 1992).

The Campo Grande area represents a Precambrian basement dome wherein petrographic mapping and the spatial distribution of coupled U-Pb zircon ages and Sm-Nd isotopic data revealed successive crustal accretion events. It supports crustal recycling throughout the Archean and Proterozoic eons as the main process of continental growth from at least 2.9 Ga onwards in Northeast Brazil.

6.3 REGIONAL GEOLOGY

The Borborema Province (BP) contributes to the understanding of crustal growth processes (e.g. Brito Neves et al., 2000; Dantas et al., 2004; 2013; Souza et al., 2007; Van Schmus et al., 2008; Arthaud et al., 2008; Ganade de Araujo et al., 2014; Brito Neves and Fuck, 2014; Santos et al., 2018). The BP is a Precambrian shield within the north-northeastern part of the South American continent (Fig. 6.1A) (Almeida et al., 1981). It is formed of discontinuous

remnants of Archean crust, Paleoproterozoic migmatite-gneiss complexes and Meso- and Neoproterozoic supracrustal rocks (e.g. Jardim de Sá, 1994; Brito Neves et al., 2000; Van Schmus et al., 2008; Dantas et al., 2013).

The Rio Grande do Norte domain (RGND), northeast portion of the Borborema Province, consists of Archean crustal fragments and Paleoproterozoic migmatite terrains (Dantas et al., 2004; 2013; Souza et al., 2007). The Paleoproterozoic terrains comprise the 2.2-2.0 Ga gneiss-migmatite basement of Neoproterozoic supracrustal sequences and granite intrusions (e.g. Van Schmus et al., 2008; Archanjo et al., 2013; Hollanda et al., 2015). The central portion of the RGND can be divided into four distinct blocks (Fig. 6.1D). These high-grade terrains and anatectic domes may be related to the Eburnian orogenic collage in Africa (2.25-1.98 Ga; e.g. Dantas et al., 2004; 2013; Eglinger et al., 2017). The final configuration of the Borborema Province resulted from the diachronic convergence of the West African, Amazonian and São Francisco-Congo cratons during the Neoproterozoic Brasiliano/Pan-African orogeny (Fig. 6.1A) (e.g. Arthaud et al., 2008; Ganade de Araujo et al., 2014; Padilha et al., 2017; Santos et al., 2018).

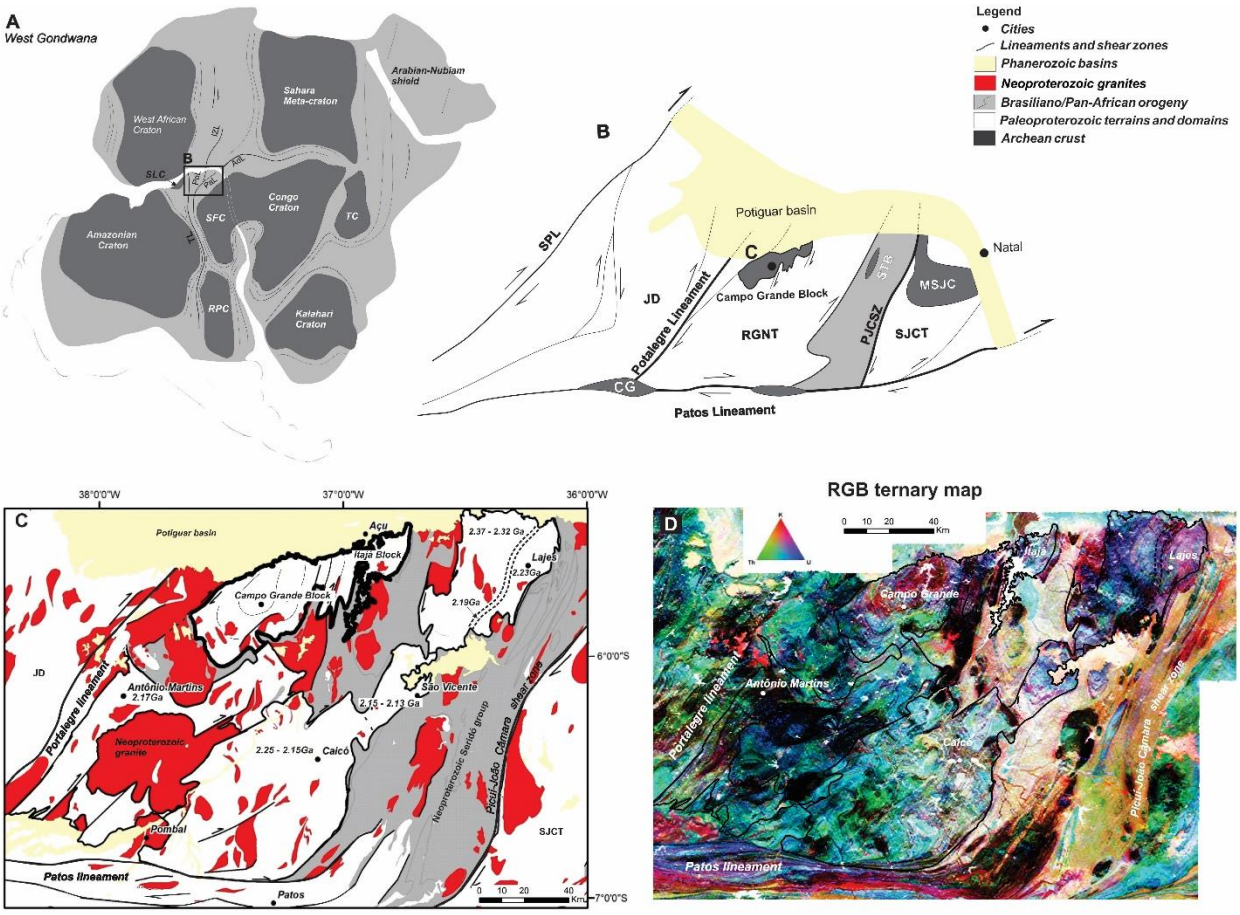

Figure 6.1. Regional geological setting. A) Localization map of the Borborema Province in West Gondwana. B) Geological map of the central portion of the Rio Grande do Norte domain. C) U-Pb zircon age distribution and D) ternary gamma-spectrometric map of the Caicó-São Vicente, Lajes, Antônio Martins and Campo Grande-Itajá regions in which the Rio Grande do Norte basement is

exposed. Legend: RPC - Rio de La Plata Craton, SFC - São Francisco Craton, SLC – São Luiz Craton, TC - Tanzania Craton. IZL - Ifewara-Zungeru Lineament, PoL - Portalegre Lineament, PJCSZ – Picuí-João Câmara shear zone, PaL - Patos Lineament, ADL - Adamaoua Lineament. JD - Jaguaribe domain, SJCT - São José do Campestre terrane. U-Pb ages for the Paleoproterozoic terrains from Souza et al. (2007), Hollanda et al. (2011) and Ferreira et al. (2019).

6.4 RESULTS

6.4.1 Geology

The Campo Grande block (CGB) is a small crustal fragment, 1,500 km^2 in size, with dome to ellipsoidal geometry, SSW-NNE axis, exposed in the central portion of the Rio Grande do Norte domain, around Campo Grande town (Fig. 6.1B, 6.2A). The CGB consists of an Archean tonalitic to granitic migmatite complex and cumulate ultramafic rocks in the core, rimmed by Paleoproterozoic alkaline orthogneisses, surrounded in turn by an outer rim of Neoproterozoic high-K granite intrusions (e.g. Caraúbas granite). The block shows strong deformation, with coaxial refolding, pervasive foliation, and north-northeast trending shear zone systems. The migmatites in the central area display higher Th and K concentrations, followed by an abrupt reduction of these elements in the inner rim orthogneiss, and again high contents in the outer rim granite, reflecting distinct geological compartments from west to east (Fig. 6.1D, 6.2B).

Integrated analysis of structural, petrological and geochronological data suggests that shear zone systems define major terrain boundaries. The Portalegre Lineament corresponds to a 20-40 km wide shear zone that separates the Rio Grande do Norte and Jaguaribe domains (Fig. 6.1C). The Paraú Lineament separates the west part of the Rio Grande do Norte domain into the distinct eastern Itajá and western Campo Grande blocks (Fig. 6.2A to D).

The Campo Grande migmatite complex displays multiple phases of migmatization and consists of gneissic-migmatitic associations. These Archean migmatites comprise tonalitic paleosomes, granitic leucosomes and alkaline dykes. Ultramafic rocks occur as lenticular boudins formed of pyroxenites with cumulate texture, reequilibrated to cummingtonite-grunerite-rich rocks, with varying proportions of chlorite, serpentine and magnetite. Amphibolite lenses comprise massive poikiloblastic garnet and granoblastic amphibole with variable proportions of plagioclase + diopside in symplectitic texture, typical of retrograded high-pressure rocks interpreted as retro-eclogites. The Itajá Block is composed of Paleoprotezoic K-feldspar-rich orthogneiss and wehrlite intrusions that occur as elongated boudins (<100 m) in the host orthogneiss (Fig. 6.2A to D); minor amphibolite and supracrustal rocks also are recorded. Neoproterozoic pegmatite and alkaline granite intrusions make up almost 20-30% of both blocks.

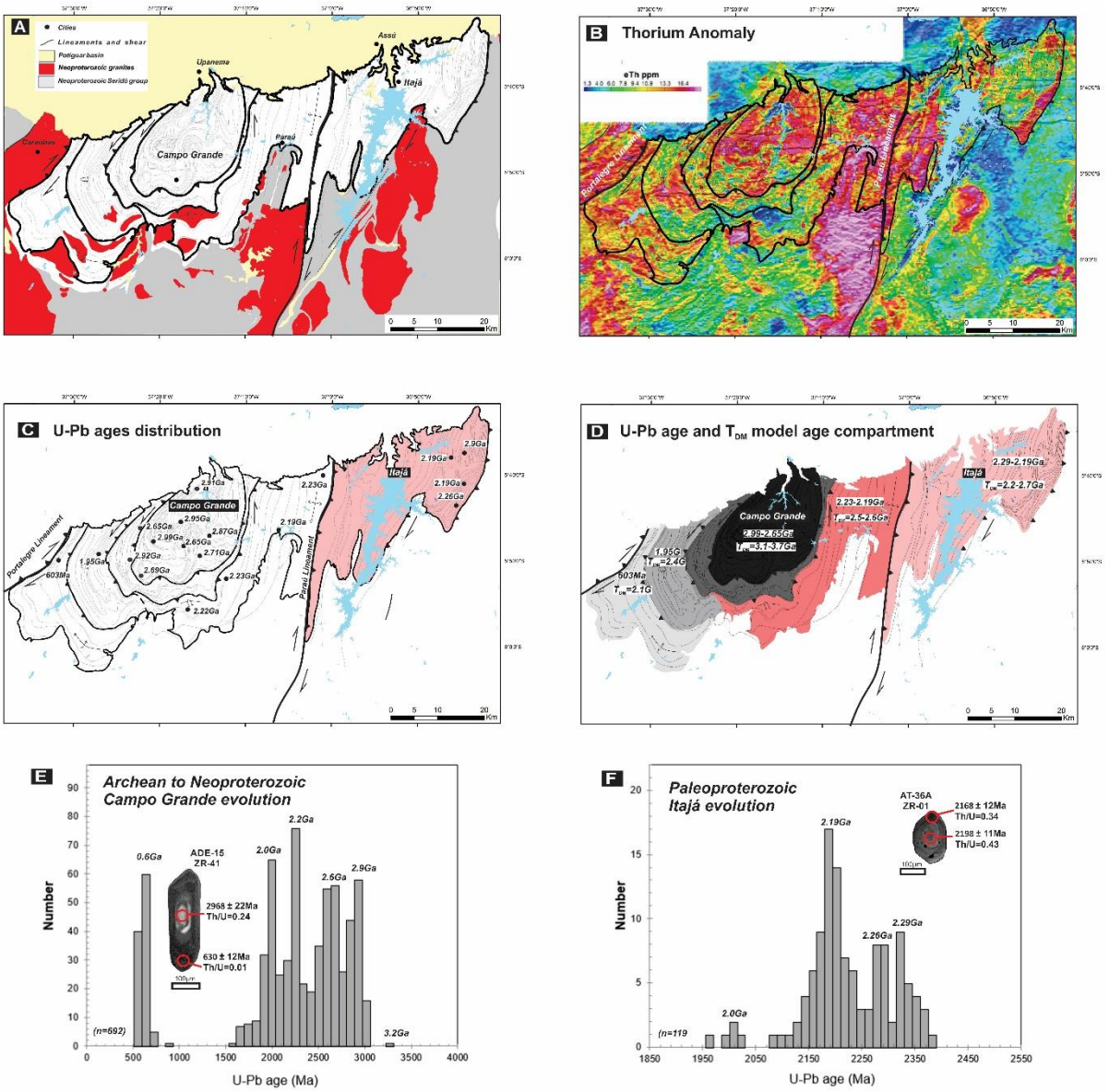

Figure 6.2. A) Simplified geological and B) Thorium anomaly map of the Campo Grande and Itajá blocks and adjacent areas. C) U-Pb zircon age distribution of the Campo Grande and Itajá blocks. D) TDM model age and U-Pb ages compartment of the Campo Grande and Itajá blocks (Data from Supplementary Table 6.1). U-Pb age data histograms of the (E) Campo Grande and (F) Itajá areas with cathodoluminescence (CL) images of representative zircon grains (Data from Supplementary Table 6.1 and 6.2).

6.4.2 Spatial Pattern of Ages based on the Nd Evidence for Diachronous Crustal Accretion

The Campo Grande block assembly was built due to at least seven thermal-tectonic events (Supplementary Table 6.3, Fig. 6.2E, 6.3). The first magmatic event is recorded in 2.98 to 2.91 Ga tonalitic paleosome, which constitutes the central core of the block. 2.69-2.65 Ga clinopyroxenite and garnet amphibolite lenses, representing tholeiitic magmatism, occur as m-sized boudins concordant with the main foliation in the migmatite core. The third magmatic

event is represented by 2.65 Ga concordant alkaline leucosome also in the Archean core. Archean rocks display positive and negative $\varepsilon_{Nd(t)}$ values of -3.9 to +4.8 and older T_{DM} model ages, between 2.7 and 3.3 Ga, suggesting juvenile sources and crustal reworking already at 2.9 Ga continental crust. All these Archean rocks are concentrated in the core of the structural dome shape of the Campo Grande Block. The 2.65 Ga clinopyroxene-garnet-amphibolite samples display also negative to positive $\varepsilon_{Nd(t)}$ values (−7.97 to +8.17) and variable T_{DM} between 2.1 and 3.7 Ga, supporting a juvenile tholeiitic oceanic crust generation at 2.65 Ga.

Siderian magmatism is represented by a few 2.46 to 2.44 Ga zircon ages, around the Archean nucleus. However, 2.23-2.18 Ga Rhyacian K_2O-rich alkaline magmatism generate a large volume (ca. 40%) of magmatic rock mainly in the eastern portions of the study area. These Rhyacian K-feldspar-rich orthogneisses display a Nd isotopic signature characterized by negative (-8.0) to positive (+5.0) $\varepsilon_{Nd(t)}$ values and T_{DM} between 2.3 and 3.1 Ga, indicating a new Rhyacian crustal reworking associated with juvenile sources. In contrast, inside the Archean core rocks, Paleoproterozoic events are record only in the 1.95 Ga concordant granitic leucosome generation and 2.0 Ga metamorphic overgrowth zircon rims in Neoarchean zircon core from the ultramafic protolith rocks, suggesting a Rhyacian high-grade metamorphic event. The ca. 2.0 Ga concordant granitic leucosomes recorded in the Archean core and western portion area have negative $\varepsilon_{Nd(t)}$ values (-5.47 to -2.74) and T_{DM} between 2.41 and 2.59 Ga. Thus, orthogneisses from the eastern portion and concordant granitic leucosome from the central and western block portions have similar T_{DM} model ages and $\varepsilon_{Nd(t)}$, meaning that both alkaline magmatism and crustal anatexis have similar Archean protolith sources. Nevertheless, crustal recycling was higher intense in the eastern block area, practically obliterating the Archean protolith record. A second high-grade metamorphic event - the seventh recorded event -, can indicated by 614-593 Ma zircon grains and rims around the Archean zircon cores from the amphibolite samples. Moreover, 575 Ma old K-feldspar-rich granitic intrusions and 566 Ma pegmatite injections support a more restricted Neoproterozoic partial melting when compared to the large volume of Rhyacian neosome generated. The Neoproterozoic granite intrusions and alkaline leucosome injections samples have strongly negative $\varepsilon_{Nd(t)}$ values (-20.57 and -14.25) and relatively younger T_{DM} ages of 2.10 and 2.39 Ga. These results suggest that Paleoproterozoic crust is the main protolith sources for the Neoproterozoic alkaline magmatism. That is, on the outermost overgrowths of the Archean dome the recycling process is dominant.

On the other hand, the Itajá block only records two events of magma generation (Supplementary Table 6.2). Mafic-ultramafic intrusions crystallized at 2.19 Ga (Fig. 6.2F, 6.3G) with positive $\varepsilon_{Nd(t)}$ values (Fig. 6.4H), while host orthogneisses were formed at 2.23 Ga

(Fig. 6.2F, 3G) and have negative to weak positive $\varepsilon_{Nd(t)}$ values with T_{DM} between 2.2 and 2.7 Ga (Fig. 6.4F,H). Therefore, calc-alkaline and tholeiitic magmatism took place in a short time interval of ~40 Ma, similar to the reported events in the Lajes Block (Ferreira et al., 2019), which is exposed 40 km eastwards of the Itajá area. The Itajá and Lajes blocks are separated by the Neoproterozoic Seridó intracontinental rift (Fig.6.1C). Inherited zircon grains of Siderian age (ca. 2.32 Ga) are recorded in the host orthogneiss from the Itajá area. The intense Rhyacian reworking obliterated the possible older sources in the Itajá area. Thus, a genetic correlation with the Campo Grande Archean core is debilitated. Nevertheless is undisputable that the protolith sources are predominant Neoarchean, as suggested for the Lajes block (Ferreira et al., 2019).

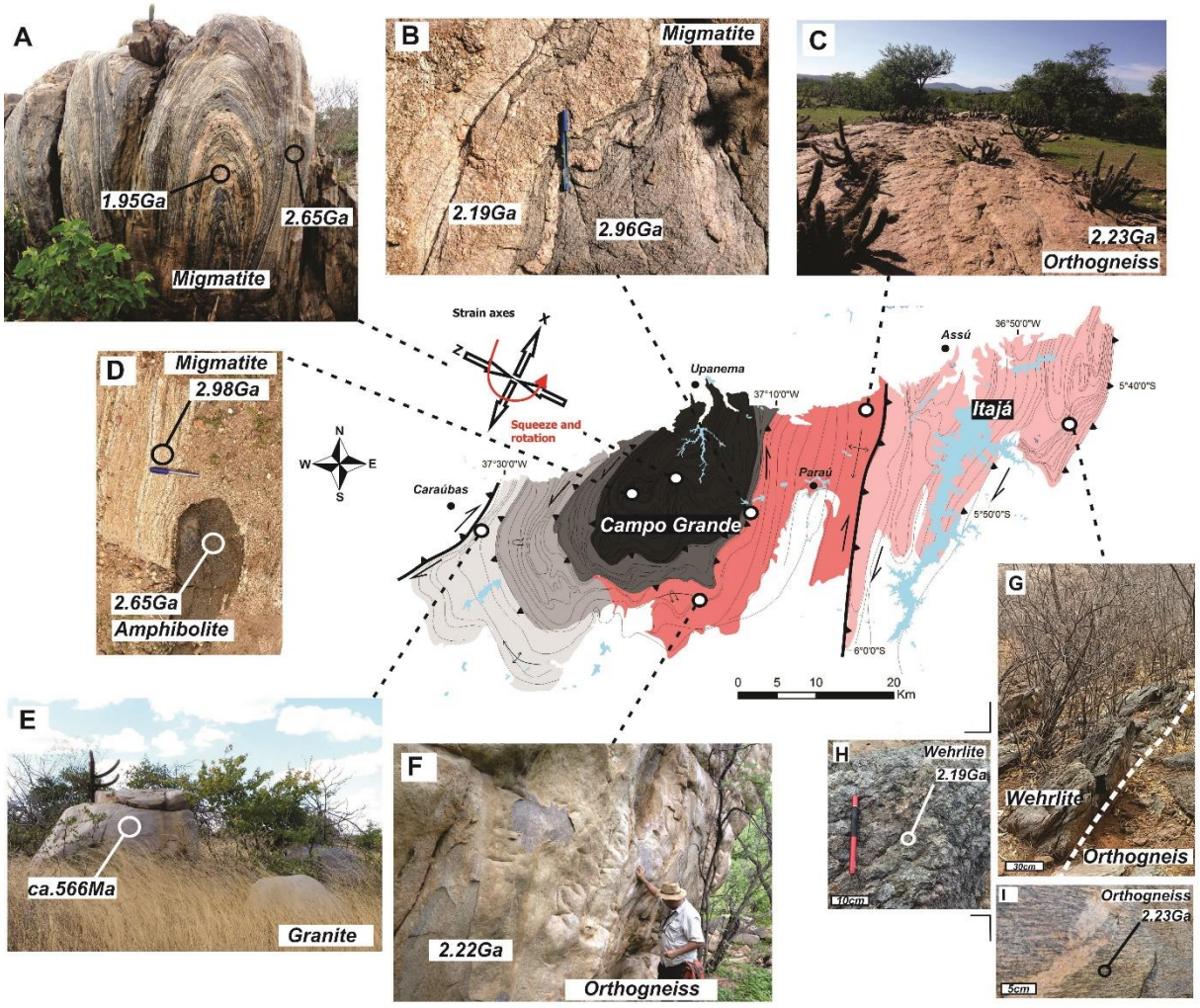

Figure 6.3. Representative field exposures of major rock types and schematic amalgamation with U-Pb zircon age of Campo Grande and Itajá blocks (Data from Supplementary Table 6.1 and 6.2), Northeast Brazil.

T_{DM} model ages and $\varepsilon_{Nd(t)}$ suggest a complex history for the Campo Grande and Itajá blocks (Supplementary Table 6.3, Fig. 6.4A to H). Therefore, whole-rock Nd isotope results indicate that the isotope system preserved the protolith source signature despite of crustal reworking

and high-grade metamorphic events in the Archean core. Moreover, they also support the docking process for the continental growth by lateral accretion of ever-younger terrains (Fig. 6.2D and 6.3). Thus, neodymium isotope evolution reflects the crustal growth from the Archean core protolith, following extensive Paleoprotezoic juvenile accretion and reworking, as well as Neoproterozoic crustal magmatism at the outer rim.

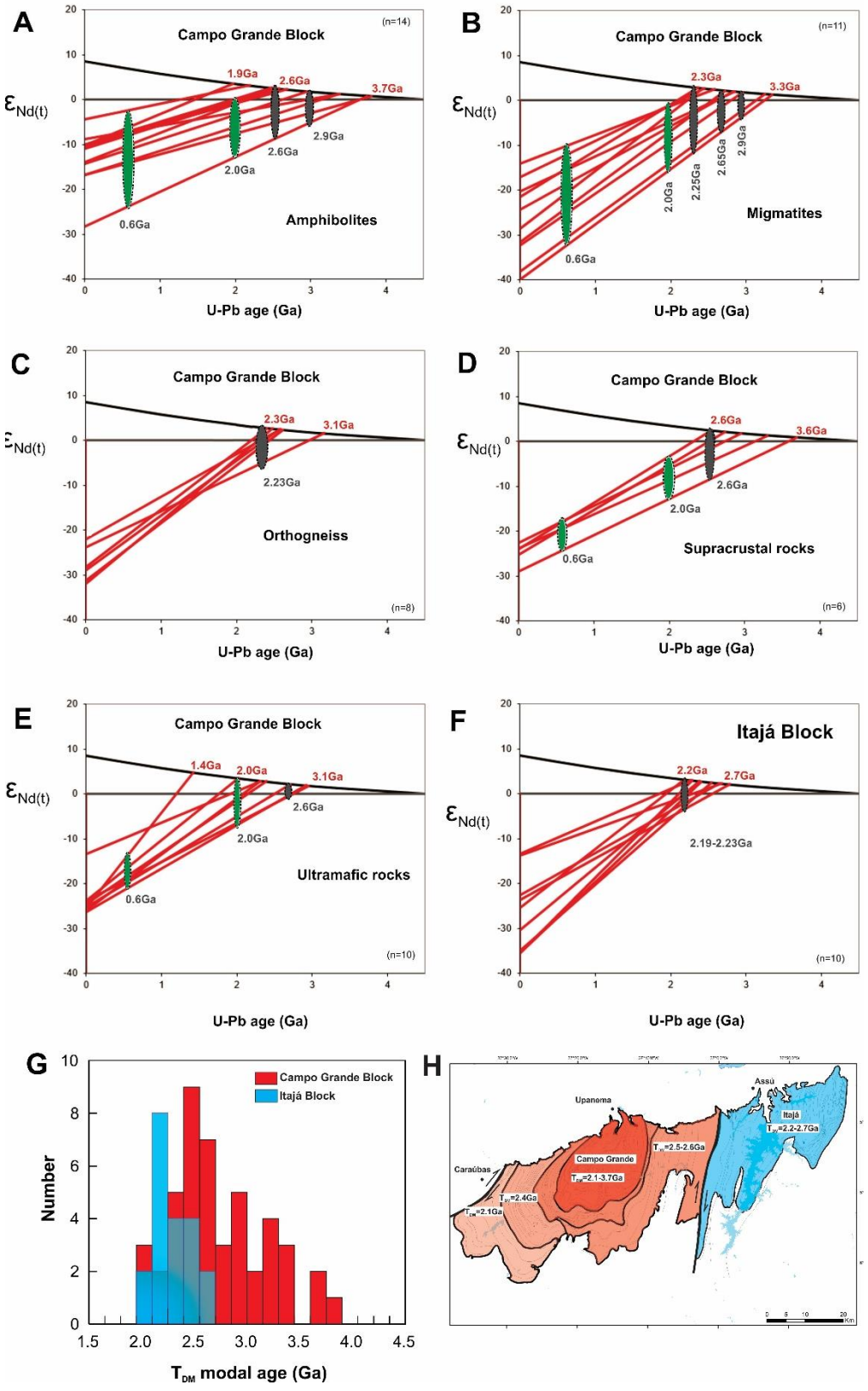

Figure 6.4. A to F) $\varepsilon Nd_{(t)}$ versus U-Pb zircon age from the major rock-types for the Campo Grande and Itajá blocks (Data from Supplementary Table 6.3), Northeast Brazil. Gray ellipse - magmatic age, green ellipse - metamorphic age. G) Histogram of T_{DM} model age for the Campo Grande and Itajá blocks. H) Schematic model of continental accretion for the Campo Grande and Itajá blocks.

6.4.3 Terrain Docking and Crustal Reworking

The integration of all isotopic geochemistry and geochronological data allowed the establishment of limits and genetic correlations between the crustal fragments that form the Campo Grande and Itajá blocks (Fig. 6.2 and 6.3). Our results support that 2.9 Ga and 2.6 Ga Archean crustal reworking and minor 2.2 Ga Paleoproterozoic juvenile protolith were main sources for the continental growth through docking mechanisms (e.g. Rollinson, 2010; Condie et al., 2015; Rosas and Korenaga, 2018; Hawkesworth et al., 2019). That is, the continental evolution is complex and includes several components of different scale, composition and age (e.g. Brown, 2008; Condie and Kröner, 2013; Nebel et al., 2018). In addition, U-Pb zircon age and Nd isotopic data suggest that at least ~60–70% of the Campo Grande continental crust were already formed at 2.9 Ga (Fig. 6.2 and 6.3). After 3.0 Ga, there was a decrease in the rate of continental crust growth, probably due to the subduction processes at convergent plate margins (e.g. Cawood et al., 2013), as evidenced by the 2.9 Ga calc-alkaline magmatism. Therefore, this result suggests that modern-style plate tectonics started around 2.9 Ga ago. However, any model that calls upon fractionation of a single magmatic event or process to produce continental crust is unrealistic (e.g. Moyen and Martin, 2012).

Although tectonic models for the Archean crust generation and its evolution are controversial (e.g Cawood et al., 2013), it appears that some crustal recycling mechanism has been active throughout Earth history (e.g. Armstrong, 1981). Accretion of allochthonous microcontinents and orogenic basins generated the lateral continental growth, while anatexis allowed crustal differentiation (e.g. Cawood et al., 2009). Therefore, the accretionary orogenic collage generates a complex diversity of protolith sources (Coney et al., 1980), as described in this study (Fig. 6.3 and 6.4).

Thermal and composition contrasts between continental and oceanic lithosphere leads to subsidence process by drip or plate tectonics regime (e.g. Nebel-Jacobsen et al., 2018). The subsidence allowed the efficient mechanical coupling of the microcontinents and remnant magmatic arcs in the orogenic wedge (e.g. Karig and Sherman, 1975). In this scenario, magmatic arc formation is probably the most important mechanism to maintain the continental crust reservoir (e.g. Reymer and Schubert, 1984). Thus, Paleoproterozoic 2.25-2.18 Ga high-K calc-alkaline magmatism may be interpreted as a thermal weakening zone that allowed the reworking as well as juvenile magmatism due to the materials extracted from the oceanic crust consumption (e.g. Cawood et al., 2009). In the Borborema Province, Paleoproterozoic arc magmatism generation represent a significant period of crustal growth within the South American continent (e.g. Brito Neves and Fuck, 2014). Terrain docking and

partial melting mainly in the root of the magmatic arc setting promote the differentiation and growth of the continental crustal (e.g. Brown et al., 2008; Moyen and Martin, 2012; Hawkesworth et al., 2019).

6.5 CONCLUSIONS

Nd isotopes data and U-Pb geochronology of crosscutting relationships within the distinct terrains provide constraints for the succession of magmatic and metamorphic phases that resulted in continental accretion of heterogeneous rocks from 2.9 Ga to ca. 566 Ma ago that led to the basement assembly of the Rio Grande do Norte domain. The Campo Grande region represents high-grade metamorphic terrains with multiple migmatite generation, meta-ultramafic and metamafic lenses that record polyphase metamorphism, significant partial melting, magmatism and intense shearing. Our data bear evidence that the distribution and nature of the continental crust reflects the secondary processes of recycling and reworking. These assemblies were diachronous and occurred in several discrete collisional and accretionary orogens. The age succession associated with the geochemical patterns of the Precambrian evolution of the Campo Grande area highlights the importance of the docking dynamics for the continental growth. The docking process is cyclic and repeated in space and time, allowing for continental growth starting with the older core, getting progressively larger as new accretions take place. In its turn, the crustal reworking process allows for crust differentiation and can be preserved in the isotopic signature of the protolith source. When the events ended at the Neoproterozoic (ca. 560 Ma), the Archean to Paleoproterozoic Campo Grande and Rhyacian Itajá complexes were amalgamated in the center of West Gondwana.

6.6 ACKNOWLEDGMENTS

This study is part of the first author's PhD thesis in development at the Institute of Geosciences, Universidade de Brasília. The authors acknowledge support from INCT Estudos Tectônicos (CAPES/CNPq - 465613/2014-4 and FAPDF - 193.001.263/2017). ELD, RAF acknowledge CNPq research fellowships.

6.7 REFERENCE

Almeida, F.F.M., Brito Neves, B.B., Fuck, R., 1981. Brazilian structural provinces: an introduction. Earth Science Reviews 17, 1–29. (doi.org/10.1016/0012-8252(81)90003-9)

Archanjo, C.J., Viegas, L.G.F., Hollanda, M.H.B.M., Souza, L.C., Liu, D., 2013. Timing of the HT/LP transpression in the Neoproterozoic Seridó Belt (Borborema Province, Brazil): constraints from U\Pb (SHRIMP) geochronology and implications for the connections between NE Brazil and West Africa. Gondwana Research 23, 701– 714. (doi:10.1016/j.gr.2012.05.005)

Armstrong, R.L., 1981. Radiogenic isotopes: The case for crustal recycling on a steady-state no-continental growth Earth: Philosophical Transactions of the Royal Society of London, ser. A, Mathematical and Physical Sciences 301, 443–472. (doi:10.1098/rsta.1981.0122)

Arthaud, M.H., Caby, R., Fuck, R.A., Dantas, E.L., Parente, C.V., 2008. Geology of the northern Borborema Province, NE Brazil and its correlation with Nigeria, NW Africa. In: Pankhurst, R.J., Trouw, R.A.J., Brito Neves, B.B., de Wit, M.J. (Eds.), West Gondwana: Pre-Cenozoic Correlation across the South Atlantic Region. Geological Society of London 294, 49–67. (doi.org/10.1144/SP294.4)

Brown, M., 2008. Characteristic thermal regimes of plate tectonics and their metamorphic imprint throughout Earth history: When did Earth first adopt a plate tectonics mode of behavior. When Did Plate Tectonics Begin on Planet Earth?, Kent C. Condie, Victoria Pease. (doi:10.1130/2008.2440(05)

Brito Neves, B. B., Santos, E. J., Schmus W. R. Q., 2000. Tectonic history of the Borborema Province, in: Umberto Cordani, Edson José Milani, Antonio Thomaz Filho, and Diogenes de Almeida Campos (org.), Tectonic Evolution of South America. Rio de Janeiro: 31st International Geological Congress, pp. 151-182, Special Publication.

Brito Neves, B.B., Fuck, R. A., 2014. The basement of the South American platform: Half Laurentian (N-NW) + half Gondwanan (E-SE) domains. Precambrian Research, 244. 75-86. (doi: 10.1016/j.precamres.2013.09.020)

Caro, G., Morino, P., Mojzsis, S.J., Cates, N.L., Bleeker, W., 2017. Sluggish Hadean geodynamics: evidence from coupled ^{146,147}Sm-^{142,143}Nd systematics in Eoarchean supracrustal rocks of the Inukjuak domain (Québec). Earth Planet. Sci. Lett. 457, 23–37. (doi.org/10.1016/j.epsl.2016.09.051)

Cawood, P.A., Hawkesworth, C.J., Dhuime, B., 2013. The continental record and the generation of continental crust. Geological Society of America Bulletin 125, 14-32. (doi:10.1130/B30722.1)

Cawood, P.A., Kröner, A., Collins, W.J., Kusky, T.M., Mooney, W.D., Windley, B.F., 2009. Accretionary orogens through Earth history. Geol. Soc. Lond. Spec. Publ. 318, 1–36. (doi.10.1144/SP318.1)

Condie, K., Kröner, A., 2013. The building blocks of continental crust: Evidence for a major change in the tectonic setting of continental growth at the end of the Archean. Gondwana Research 23, 394-402. (doi:10.1016/j.gr.2011.09.011)

Condie, K., Pisarevsky, S., Korenaga, J., Gardoll, S., 2015. Is the rate of supercontinent assembly changing with time? Precambrian Res.259, 278–289. (doi.org/10.1016/j.precamres.2014.07.015)

Coney, P. J., Jones, D. L., Monger, J. W. H., 1980. Cordilleran suspect terranes. Nature 288, 329–333. (doi.org/10.1038/288329a0)

Dantas, E. L., Van Schmus W.R., Hackspacher P. C., Fetter A. H., Neves B. B. B., Cordani U.G., Nutman A.P., Williams S., 2004. The 3.4-3.5 São José do Campestre Massif, NE Brazil: remnants of the oldest crust in South America. Precambrian Research 130, 113-137. (doi.10.1016/j.precamres.2003.11.002).

Dantas, E. L., Souza, Z. S., Wernick, E., Hackspacher, P. C., Martin, H., Xiaodong, D., & Li, J. W., 2013. Crustal growth in the 3.4-2.7 Ga São José de Campestre Massif, Borborema Province, NE Brazil. Precambrian Research, 227, 120–156. (doi:10.1016/j.precamres.2012.08.006)

DePaolo, D. J., 1981. A neodymium and strontium isotopic study of the Mesozoic calc-alkaline granitic batholithys of the Sierra Nevada and Peninsular Ranges, California. Journal of Geophysical Research 86, 10470-10488. (doi.org/10.1029/JB086iB11p10470)

DePaolo, D.J., Linn, A.M., Schubert, G., 1991. The continental crustal age distribution: Methods of determining mantle separation ages from Sm-Nd isotopic data and application to the southwestern United States. Journal of Geophysical Research 96, 2071-2088. (doi.10.1029/90jb02219)

Eglinger, A., Thebaud, N., Zeh, A., Davis, J., Miller, J., Parra-Avila, L.A., Loucks, R., McCuaig, C., Belousova, E., 2017. New insights into the crustal growth of the Paleoproterozoic margin of the Archean Kenema-Man domain, West African craton (Guinea): implications for gold mineral system. Precambrian Res. 292, 258-289.

Ferreira, A.C.D., Ferreira Filho, C.F., Dantas, E.L., Souza, V.S., 2019. Paleoproterozoic Mafic-Ultramafic Magmatism in the Northern Borborema Province, NE Brazil: Tectonic Setting and Potential for Deposits. The Journal of Geology, 127. 483-504. (doi.10.1086/704256)

Ganade de Araújo, C. E., Rubatto, D., Hermann, J., Cordani, U. G., Caby, R., Basei, M. A., 2014. Ediacaran 2,500-km-long synchronous deep continental subduction in the West Gondwana Orogen. Nature Communications 5, 5198. (doi: 10.1038/ncomms6198).

Hawkesworth, C.J., Cawood, P.A., Dhuime, B., Kemp, A.I.S., 2017. Earth's continental lithosphere through time. Annu. Rev. Earth. Sci.45, 169–198. (doi.org/10.1146/annurev-earth-063016-020525)

Hawkesworth, C., Cawood, P.A., Dhuime, B., 2019. Rates of generation and growth of the continental crust. Geoscience Frontiers 10, 165-173. (doi.org/10.1016/j.gsf.2018.02.004).

Holder, R.M., Viete, D.R., Brown, M. Johnson, T.E., 2019. Metamorphism and the evolution of plate tectonics. Nature 572, 378–381. (doi:10.1038/s41586-019-1462-2)

Hollanda, M.H.B.M., Archanjo, C.J., Bautista, J.R., Souza, L.C., 2015. Detrital zircon ages and Nd isotope compositions of the Seridó and Lavras da Mangabeira basins (Borborema Province, NE Brazil): Evidence for exhumation and recycling associated with a major shift in sedimentary provenance. Precambrian Research 258, 186–207. (10.1016/j.precamres.2014.12.009)

Jardim de Sá, E.F., 1994. A Faixa Seridó (Província Borborema, Ne Brasil) e o seu Significado Geodinâmico na Cadeia Brasiliana/Pan-Africana. Tese de Doutorado, Universidade De Brasília, 803pp.

Karig, D.E., Sherman III, G.F., 1975. Subduction and accretion in trenches. Geol. Soc. Am. Bull. 86, 377–389. (doi.org/10.1130/0016-7606(1975)86<377:SAAIT>2.0.CO;2)

Korenaga, J., 2018. Estimating the formation age distribution of continental crust by unmixing zircon age data. Earth Planet. Sci. Lett.482, 388–395. (doi.org/10.1016/j.epsl.2017.11.039)

McLennan, S.M., Hemming, S., 1992. Samarium/neodymium elemental and isotopic systematics in sedimentary rocks Geochimica et Cosmochimica Acta 56, 887-898. (doi.org/10.1016/0016-7037(92)90034-G)

Moresi, L., Betts, P. G., Miller, M. S., Cayley, R. A., 2014. Dynamics of continental accretion. Nature 508, 245–248. (doi.10.1038/nature13033)

Moyen, J.F., and Martin, H., 2012. Forty years of TTG research. Lithos 148, 312-336. (doi: 10.1016/j.lithos.2012.06.010)

Nance, R.D., Murphy, J.B., Santosh, M., 2014. The supercontinent cycle: A retrospective essay. Gondwana Research 25, 4-29. (doi.org/10.1016/j.gr.2012.12.026)

Nebel-Jacobsen, Y.J., Nebel, O., Wille, M., Cawood, P.A., 2018. A non-zircon Hf isotope record in Archean black shales from the Pilbara craton confirms changing crustal dynamics ca. 3 Ga ago. Scientfic Reports 8, 922. (doi:10.1038/s41598-018-19397-9)

Nebel, O., Capitanio, F. A., Moyen, J. F., Weinberg, R. F., Clos, F., Nebel-Jacobsen, Y.J., Cawood, P.A., 2018. When crust comes of age: on the chemical evolution of Archaean, felsic continental crust by crustal drip tectonics. Phil. Trans. R. Soc. A 376, 20180103. (doi:10.1098/rsta.2018.0103)

Reymer, A., Schubert, G., 1984. Phanerozoic addition rates to the continental crust and crustal growth. Tectonics 3, 63–77. (https://doi.org/10.1029/TC003i001p00063)

Rollinson, H., 2010. Coupled evolution of Archean continental crust and subcontinental lithospheric mantle: Geology, v. 38, p. 1083–1086, doi:10.1130/G31159.1.

Rosas, J.C., Korenaga, J., 2018. Rapid crustal growth and efficient crustal recycling in the early Earth: Implications for Hadean and Archean geodynamics. Earth and Planetary Science Letters 494, 42–49. (doi.org/10.1016/j.epsl.2018.04.051)

Santos, L.C.M.L., Dantas, EL., Cawood, P., Lages, G.A., Lima, H.L., Santos, E.J., 2018. Accretion Tectonics in Western Gondwana Deduced From Sm-Nd Isotope Mapping of Terranes in the Borborema Province, NE Brazil. Tectonics 37, 2727-2743. (doi.10.1029/2018TC005130)

Souza, Z.S., Martin, H., Peucat, J.J., Jardim de Sá, E. F., Macedo, M.H.F., 2007. Calc-Alkaline Magmatism at the Archean-Proterozoic Transition: The Caicó Complex Basement (Ne Brasil). Journal of Petrology 48, 2149-2185; (doi.10.1093/petrology/egm055)

Stern, R. J., Scholl, D. W., 2010. Yin and yang of continental crust creation and destruction by plate tectonic processes. International Geology Review 52, 1–31. (doi.10.1080/00206810903332322)

Sutton, J., 1963. Long-term cycles in the evolution of the continents. Nature 198, 731-735. (doi.10.1038/198731b0)

Tetreault, J.L., Buiter, J.H., 2014. Future accreted terranes: a compilation of island arcs, oceanic plateaus, submarine ridges, seamounts, and continental fragments. Solid Earth 5, 1243–1275. (doi:10.5194/se-5-1243-2014)

Twiss, R.J., Moores, E.M., 1992. Structural Geology. Freeman & Co, New York. Cloos, M., Shreve, R.L., 1988. Subduction channel model of prism accretion, mélange formation, sediment subduction, and subduction erosion at convergent plate margins: Implications and discussion. Paleophysics 128, 501–545. (doi.org/10.1007/BF00874548)

Van Schmus, W.R., Oliveira, E.P, Silva Filho, A.F., Toteu, S.F., Penaye, J., Guimarães, I. P., 2008. Proterozoic links between the Borborema Province, NE Brazil, and the Central African Fold Belt. Geological Society, London, Special Publication 294, 69-99. (doi.org/10.1144/SP294.5)

Supplementary Table 6.1. Campo Grande U-Pb zircon data.

ADE-18P	Th/U	$^{206}Pb/^{204}Pb$	1s%	$^{207}Pb/^{206}Pb$	1s %	$^{207}Pb/^{235}U$	1s %	$^{206}Pb/^{238}U$	1s %	Rho	$^{207}Pb/^{206}Pb$	2s abs	$^{206}Pb/^{238}U$	2s abs	$^{207}Pb/^{235}U$	2s abs	% U-Pb disc[4]
050-ZR27C	0,451	808497	19,11	0,21378	1,40	17,528	1,71	0,5946	0,92	0,54	2934	45	3008	44	2964	33	-2,51
049-ZR26C	0,476	69755	33,83	0,21847	0,67	15,232	1,35	0,5056	1,11	0,82	2969	22	2638	48	2830	26	11,16
048-ZR25B	0,306	233735	17,70	0,22132	0,54	18,095	1,10	0,5929	0,88	0,80	2990	17	3001	42	2995	21	-0,37
047-ZR25C	0,590	3191	5,50	0,22525	0,57	18,101	1,20	0,5828	0,99	0,82	3019	18	2960	47	2995	23	1,94
046-ZR24B	0,326	437644	21,96	0,21726	0,93	17,052	1,25	0,5692	0,75	0,60	2960	30	2905	35	2938	24	1,89
045-ZR24C	0,598	182681	25,54	0,22045	0,41	18,101	0,97	0,5955	0,80	0,82	2984	13	3012	38	2995	19	-0,92
044-ZR23C	0,760	159013	23,43	0,21693	0,48	16,131	1,08	0,5393	0,89	0,83	2958	15	2780	40	2885	20	6,00
039-ZR21B	0,365	964978	16,11	0,21341	0,51	17,279	1,11	0,5872	0,92	0,82	2932	17	2978	44	2950	21	-1,58
038-ZR21C	0,662	416302	14,81	0,21915	0,83	17,698	1,20	0,5857	0,79	0,66	2974	27	2972	38	2973	23	0,09
037-ZR20C	0,514	286851	14,64	0,21996	0,43	17,869	0,90	0,5892	0,70	0,78	2980	14	2986	33	2983	17	-0,19
036-ZR19C	0,733	208892	27,84	0,22072	1,22	18,142	1,66	0,5961	1,06	0,64	2986	39	3014	51	2997	32	-0,94
034-ZR17B	0,455	212010	21,43	0,21906	0,55	17,085	1,07	0,5656	0,83	0,78	2974	18	2890	39	2940	20	2,83
033-ZR17C	0,573	256529	15,44	0,21889	1,11	16,370	1,49	0,5423	0,93	0,62	2973	35	2793	42	2899	28	6,03
028-ZR14C	0,455	40698	39,56	0,20864	0,62	13,634	1,16	0,4739	0,90	0,78	2895	20	2501	37	2725	22	13,62
027-ZR13B	0,508	114241	26,03	0,21656	0,51	16,670	0,96	0,5583	0,72	0,75	2955	17	2859	33	2916	18	3,24
020-ZR11C	0,699	158620	24,31	0,21521	1,40	13,909	1,94	0,4687	1,29	0,66	2945	45	2478	53	2743	36	15,87
019-ZR10C	0,373	203528	18,33	0,22410	0,66	17,325	1,20	0,5606	0,93	0,78	3010	21	2869	43	2953	23	4,69
018-ZR9B	0,403	195903	18,49	0,21976	0,50	16,641	1,04	0,5491	0,84	0,80	2979	16	2822	38	2914	20	5,28
017-ZR9C	0,566	324817	19,71	0,21708	0,46	15,629	1,04	0,5221	0,86	0,83	2959	15	2708	38	2854	20	8,48
015-ZR7C	1,134	354027	16,05	0,22011	0,58	17,131	1,14	0,5645	0,91	0,80	2981	19	2885	42	2942	22	3,24
014-ZR6C	0,163	943566	14,68	0,21492	0,41	16,213	0,99	0,5471	0,82	0,83	2943	13	2813	37	2889	19	4,41
013-ZR5C	0,923	626750	15,25	0,21683	0,48	17,664	1,07	0,5908	0,88	0,82	2957	15	2993	42	2972	20	-1,19
010-ZR4C	0,526	121984	28,67	0,21927	1,19	14,765	1,71	0,4883	1,17	0,69	2975	38	2564	49	2800	32	13,84
009-ZR3B	0,457	80509	39,12	0,21192	0,96	13,289	1,96	0,4548	1,68	0,85	2920	31	2416	67	2700	37	17,25
008-ZR3C	0,551	490232	17,72	0,22140	0,58	17,804	1,16	0,5832	0,94	0,81	2991	19	2962	44	2979	22	0,98

ADE-18P	Th/U	$^{206}Pb/^{204}Pb$	1s%	$^{207}Pb/^{206}Pb$	1s %	$^{207}Pb/^{235}U$	1s %	$^{206}Pb/^{238}U$	1s %	Rho	$^{207}Pb/^{206}Pb$	2s abs	$^{206}Pb/^{238}U$	2s abs	$^{207}Pb/^{235}U$	2s abs	% U-Pb disc[4]
005-ZR1B	0,384	10435	17,87	0,21182	0,55	14,336	1,00	0,4908	0,75	0,75	2919	18	2574	32	2772	19	11,82
004-ZR1C	0,702	27353	18,38	0,22024	0,40	17,718	1,46	0,5834	1,35	0,93	2982	13	2963	64	2975	28	0,67
ADE-10P	**Th/U**	$^{206}Pb/^{204}Pb$	**1s%**	$^{207}Pb/^{206}Pb$	**1s %**	$^{207}Pb/^{235}U$	**1s %**	$^{206}Pb/^{238}U$	**1s %**	**Rho**	$^{207}Pb/^{206}Pb$	**2s abs**	$^{206}Pb/^{238}U$	**2s abs**	$^{207}Pb/^{235}U$	**2s abs**	**% U-Pb disc[4]**
048-ZR35	0,224	692032	60,60	0,21261	1,51	15,619	2,26	0,5328	1,64	0,72	2926	49	2753	73	2854	43	5,89
047-ZR34	0,540	289747	18,72	0,21204	0,51	17,400	1,18	0,5951	1,00	0,85	2921	16	3010	48	2957	23	-3,04
046-ZR33	0,578	501395	21,91	0,21295	0,44	17,150	1,00	0,5841	0,82	0,82	2928	14	2965	39	2943	19	-1,27
045-ZR32	0,583	336071	17,69	0,21339	0,46	16,715	1,11	0,5681	0,94	0,85	2931	15	2900	44	2919	21	1,08
044-ZR31	0,125	157120	47,26	0,20965	0,53	16,073	1,13	0,5560	0,92	0,82	2903	17	2850	42	2881	21	1,82
042-ZR29	0,415	56331	31,00	0,20984	0,68	16,270	1,37	0,5623	1,14	0,83	2904	22	2876	53	2893	26	0,97
039-ZR28	0,303	79718	46,65	0,21023	1,08	16,230	2,10	0,5599	1,76	0,84	2907	35	2866	81	2890	40	1,41
038-ZR27	0,238	456441	15,09	0,20944	0,74	14,764	1,85	0,5112	1,66	0,89	2901	24	2662	72	2800	35	8,25
037-ZR26	0,174	122112	53,18	0,21831	1,28	16,445	2,14	0,5463	1,67	0,78	2968	41	2810	76	2903	40	5,34
036-ZR25	0,306	152044	41,54	0,21025	1,09	14,888	2,10	0,5135	1,75	0,84	2908	35	2672	77	2808	40	8,11
031-ZR22	0,394	316641	15,72	0,20519	0,81	13,617	1,44	0,4813	1,13	0,79	2868	26	2533	47	2723	27	11,68
028-ZR20	0,557	409625	15,84	0,21154	0,46	17,377	1,02	0,5957	0,83	0,81	2917	15	3013	40	2956	20	-3,27
023-ZR15	0,151	390068	65,19	0,21264	0,49	16,573	1,16	0,5652	0,98	0,85	2926	16	2888	46	2910	22	1,29
022-ZR14	0,337	44218	14,37	0,21246	0,57	15,376	2,40	0,5248	2,30	0,96	2924	19	2720	102	2839	45	7,00
019-ZR13	0,515	369945	51,99	0,21232	1,06	15,835	1,47	0,5409	0,94	0,64	2923	34	2787	43	2867	28	4,66
018-ZR12	0,307	69758	73,55	0,21023	0,91	16,300	2,57	0,5623	2,38	0,92	2907	29	2876	110	2895	49	1,08
016-ZR10	0,360	658708	14,80	0,21120	0,40	16,680	0,98	0,5727	0,82	0,83	2915	13	2919	38	2917	19	-0,15
015-ZR9	0,343	61045	75,09	0,20462	1,24	14,781	1,95	0,5239	1,45	0,75	2863	40	2715	64	2801	37	5,17
014-ZR8	0,283	678856	37,25	0,20929	0,32	16,549	0,93	0,5734	0,79	0,85	2900	10	2922	37	2909	18	-0,76
035-ZR24	0,172	196193	55,07	0,20127	0,57	13,374	1,44	0,4819	1,27	0,88	2837	19	2536	53	2706	27	10,61
034-ZR23	0,322	18639	14,93	0,20515	0,91	14,142	1,47	0,4999	1,10	0,75	2868	29	2614	47	2759	28	8,86
026-ZR18	0,182	16561	6,91	0,19486	0,88	10,548	1,66	0,3926	1,35	0,82	2784	29	2135	49	2484	30	23,31
025-ZR17	0,228	9198	9,11	0,18758	0,96	8,824	3,35	0,3411	3,19	0,95	2721	31	1892	104	2320	60	30,46
ADE-15	**Th/U**	$^{206}Pb/^{204}Pb$	**1s%**	$^{207}Pb/^{206}Pb$	**1s %**	$^{207}Pb/^{235}U$	**1s %**	$^{206}Pb/^{238}U$	**1s %**	**Rho**	$^{207}Pb/^{206}Pb$	**2s abs**	$^{206}Pb/^{238}U$	**2s abs**	$^{207}Pb/^{235}U$	**2s abs**	**% U-Pb disc[4]**

ADE-18P	Th/U	$^{206}Pb/^{204}Pb$	1s%	$^{207}Pb/^{206}Pb$	1s %	$^{207}Pb/^{235}U$	1s %	$^{206}Pb/^{238}U$	1s %	Rho	$^{207}Pb/^{206}Pb$	2s abs	$^{206}Pb/^{238}U$	2s abs	$^{207}Pb/^{235}U$	2s abs	% U-Pb disc[4]
017-ZR8C	0,478	159816	15,46	0,26148	0,68	22,874	1,18	0,6344	0,89	0,75	3256	21	3167	44	3222	23	2,72
033-ZR16C	0,127	6248	2,97	0,17156	1,03	10,259	1,41	0,4337	0,89	0,63	2573	34	2322	35	2458	26	9,74
076-ZR44C	0,558	113258	24,08	0,22427	0,84	16,641	1,32	0,5381	0,94	0,71	3012	27	2776	42	2914	25	7,84
018-ZR9C	0,421	105096	29,53	0,21126	1,26	14,999	1,63	0,5149	0,96	0,59	2915	41	2677	42	2815	31	8,16
029-ZR15C	0,198	390100	21,21	0,19570	1,67	12,875	2,01	0,4771	1,06	0,53	2791	54	2515	44	2671	38	9,89
035-ZR25	0,137	311045	55,25	0,20836	1,88	10,770	2,58	0,3749	1,73	0,67	2893	60	2052	61	2504	47	29,06
010-ZR7	0,449	6417	4,68	0,20286	1,10	9,712	2,22	0,3472	1,90	0,85	2849	36	1921	63	2408	41	32,57
009-ZR6	0,476	7325	6,65	0,19113	1,40	8,798	3,12	0,3339	2,76	0,89	2752	46	1857	89	2317	56	32,52
024-ZR16	0,127	481170	17,24	0,20902	0,81	15,530	1,74	0,5388	1,50	0,86	2898	26	2779	67	2848	33	4,12
029-ZR21	0,240	348922	30,88	0,21340	1,27	17,878	2,24	0,6076	1,81	0,81	2932	41	3060	88	2983	43	-4,39
014-ZR9	0,376	340675	21,21	0,20052	1,19	12,842	1,65	0,4644	1,07	0,65	2830	39	2459	44	2668	31	13,12
008-ZR5	0,224	552568	22,50	0,20989	1,35	15,553	1,79	0,5374	1,12	0,63	2905	43	2772	50	2850	34	4,55
039-ZR29	0,314	164897	21,37	0,19995	0,60	11,585	1,21	0,4202	0,98	0,81	2826	20	2261	37	2571	22	19,97
036-ZR26	0,342	629270	18,48	0,20594	0,58	14,977	1,44	0,5274	1,27	0,88	2874	19	2731	56	2814	27	4,99
026-ZR13C	0,489	256868	46,53	0,22389	0,67	18,284	1,30	0,5923	1,05	0,81	3009	21	2999	50	3005	25	0,34
070-ZR41C	0,240	177514	40,36	0,21825	0,69	17,144	1,27	0,5697	1,00	0,79	2968	22	2906	47	2943	24	2,07
067-ZR38C	0,341	2307	21,51	0,21258	1,44	15,940	1,94	0,5438	1,24	0,64	2925	46	2799	56	2873	37	4,31
078-ZR46C	0,394	72595	31,53	0,21093	0,60	16,020	1,60	0,5508	1,43	0,90	2913	19	2828	65	2878	30	2,89
010-ZR5C	0,426	101629	30,46	0,20756	0,72	15,476	1,23	0,5407	0,93	0,75	2887	23	2787	42	2845	23	3,47
069-ZR40C	0,476	98781	54,88	0,20690	0,64	15,259	1,96	0,5349	1,81	0,93	2881	21	2762	81	2832	37	4,15
048-ZR25C	0,192	273498	17,45	0,20654	0,55	15,260	1,13	0,5358	0,91	0,81	2879	18	2766	41	2832	21	3,91
014-ZR6C	0,384	73434	39,41	0,20542	0,56	13,804	1,33	0,4873	1,15	0,86	2870	18	2559	49	2736	25	10,82
056-ZR30C	0,278	104520	24,43	0,20537	0,79	13,580	1,39	0,4796	1,08	0,78	2869	26	2525	45	2721	26	11,99
009-ZR4C	0,774	464233	21,50	0,20381	0,67	13,274	1,31	0,4723	1,06	0,81	2857	22	2494	44	2699	25	12,71
055-ZR29C	0,483	241611	27,67	0,20341	0,54	12,817	1,66	0,4570	1,52	0,92	2854	17	2426	61	2666	31	14,98
007-ZR3C	0,518	6953	12,22	0,20328	0,44	12,975	1,14	0,4629	0,98	0,86	2853	14	2452	40	2678	21	14,04
050-ZR27C	0,149	2718	3,71	0,20134	0,77	10,232	1,69	0,3686	1,46	0,86	2837	25	2023	51	2456	31	28,71

ADE-18P	Th/U	$^{206}Pb/^{204}Pb$	1s%	$^{207}Pb/^{206}Pb$	1s %	$^{207}Pb/^{235}U$	1s %	$^{206}Pb/^{238}U$	1s %	Rho	$^{207}Pb/^{206}Pb$	2s abs	$^{206}Pb/^{238}U$	2s abs	$^{207}Pb/^{235}U$	2s abs	% U-Pb disc[4]
027-ZR14C	0,136	83393	51,76	0,20057	2,01	10,088	2,95	0,3647	2,12	0,72	2831	65	2005	73	2443	54	29,19
054-ZR28C	0,329	103227	58,24	0,19954	2,02	11,637	2,89	0,4229	2,03	0,70	2822	65	2274	78	2576	53	19,44
045-ZR22C	0,137	3740	16,52	0,19862	0,50	13,150	1,07	0,4801	0,87	0,81	2815	16	2528	36	2690	20	10,20
020-ZR11C	0,820	24701	15,40	0,19485	1,11	11,252	1,57	0,4188	1,04	0,66	2784	36	2255	39	2544	29	18,99
015-ZR6B	0,235	8232	3,25	0,19478	0,53	12,782	1,17	0,4759	0,98	0,83	2783	17	2509	40	2664	22	9,83
038-ZR19B	0,128	2891	4,69	0,19369	0,57	11,054	1,06	0,4139	0,82	0,77	2774	19	2233	31	2528	20	19,51
057-ZR31C	0,010	374437	25,01	0,19163	1,23	7,145	4,60	0,2704	4,41	0,96	2756	40	1543	121	2130	80	44,02
058-ZR32C	0,433	205289	33,99	0,18767	0,95	10,389	1,68	0,4015	1,33	0,79	2722	31	2176	49	2470	31	20,06
006-ZR2C	0,044	5861	5,65	0,16880	0,64	4,801	1,89	0,2063	1,74	0,92	2546	21	1209	38	1785	32	52,51
030-ZR22	0,030	98231	42,89	0,12247	0,69	6,143	1,18	0,3637	0,88	0,75	1993	25	2000	30	1996	21	-0,37
027-ZR19	0,046	489542	32,80	0,12253	0,53	6,073	1,00	0,3594	0,76	0,76	1993	19	1980	26	1986	17	0,70
026-ZR18	0,021	339987	46,74	0,11918	0,54	5,711	1,02	0,3475	0,77	0,76	1944	19	1923	26	1933	17	1,09
028-ZR20	0,034	270687	29,47	0,12458	2,12	6,212	2,69	0,3616	1,62	0,60	2023	74	1990	55	2006	47	1,63
020-ZR15	0,105	29947	28,16	0,12405	2,16	6,019	2,64	0,3519	1,49	0,56	2015	76	1944	50	1979	46	3,55
016-ZR11	0,046	31621608	98,94	0,11806	0,69	5,599	1,09	0,3439	0,76	0,70	1927	25	1905	25	1916	19	1,13
015-ZR10	0,050	973409	20,25	0,12289	0,43	6,162	1,05	0,3637	0,88	0,84	1999	15	1999	30	1999	18	-0,04
037-ZR27	0,043	43957	15,43	0,12156	0,46	6,019	1,47	0,3591	1,35	0,92	1979	16	1978	46	1979	25	0,07
006-ZR3	0,005	16056	4,37	0,12007	0,46	4,792	1,62	0,2895	1,51	0,93	1957	16	1639	44	1784	27	16,27
004-ZR1	0,022	1088104	30,43	0,11013	0,44	3,428	1,36	0,2257	1,23	0,91	1802	16	1312	29	1511	21	27,18
036-ZR18C	0,094	211588	19,79	0,12325	2,03	2,480	2,95	0,1460	2,11	0,71	2004	71	878	35	1266	42	56,17
079-ZR46B	0,034	29184	8,78	0,12149	0,67	5,955	1,46	0,3555	1,24	0,85	1978	24	1961	42	1969	25	0,89
060-ZR34C	0,068	502453	24,07	0,12111	1,02	6,251	1,29	0,3743	0,70	0,54	1973	36	2050	24	2012	22	-3,91
074-ZR42C	0,060	215184	26,40	0,12108	0,51	6,041	1,11	0,3618	0,92	0,82	1972	18	1991	31	1982	19	-0,94
005-ZR1B	0,038	309811	39,94	0,12096	0,42	6,329	0,85	0,3795	0,64	0,75	1970	15	2074	23	2022	15	-5,24
066-ZR37C	0,029	622342	23,34	0,12080	0,87	6,093	1,18	0,3658	0,70	0,59	1968	31	2010	24	1989	20	-2,11
068-ZR39C	0,039	101627	52,07	0,12078	0,79	6,035	1,26	0,3624	0,91	0,72	1968	28	1993	31	1981	22	-1,30
040-ZR20B	0,034	549421	19,38	0,12029	0,65	5,745	1,11	0,3464	0,82	0,74	1960	23	1917	27	1938	19	2,20

ADE-18P	Th/U	$^{206}Pb/^{204}Pb$	1s%	$^{207}Pb/^{206}Pb$	1s %	$^{207}Pb/^{235}U$	1s %	$^{206}Pb/^{238}U$	1s %	Rho	$^{207}Pb/^{206}Pb$	2s abs	$^{206}Pb/^{238}U$	2s abs	$^{207}Pb/^{235}U$	2s abs	% U-Pb disc[4]
025-ZR12C	0,055	23227	9,84	0,11922	0,61	5,167	1,15	0,3143	0,90	0,78	1945	22	1762	28	1847	19	9,39
049-ZR26C	0,048	469433	22,08	0,11918	1,01	5,683	1,57	0,3458	1,15	0,73	1944	36	1914	38	1929	27	1,52
053-ZR27B	0,024	135279	51,93	0,11832	0,60	4,783	1,34	0,2931	1,15	0,85	1931	21	1657	33	1782	22	14,19
034-ZR24	0,006	4288	4,36	0,06366	0,73	0,797	1,25	0,0908	0,95	0,76	731	31	561	10	595	11	23,27
028-ZR14B	0,014	43831	30,63	0,06252	0,66	0,861	1,16	0,0999	0,88	0,76	692	28	614	10	631	11	11,32
025-ZR17	0,010	482176	20,69	0,06018	0,78	0,796	1,46	0,0959	1,17	0,80	610	34	590	13	594	13	3,26
075-ZR43C	0,006	173053	29,35	0,05923	0,54	0,814	1,17	0,0997	0,97	0,83	575	23	612	11	605	11	-6,41
033-ZR23	0,007	195405	34,15	0,05966	0,54	0,817	1,09	0,0993	0,87	0,80	591	23	610	10	606	10	-3,23
059-ZR33C	0,024	82740	43,14	0,05997	0,96	0,748	1,45	0,0904	1,02	0,71	603	41	558	11	567	13	7,39
034-ZR16B	0,006	317236	20,88	0,05991	0,98	0,850	1,41	0,1028	0,95	0,67	600	42	631	11	624	13	-5,11
073-ZR41B	0,010	74184	39,26	0,05928	0,56	0,840	1,20	0,1027	0,99	0,83	577	24	630	12	619	11	-9,22
ADE-23	**Th/U**	**$^{206}Pb/^{204}Pb$**	**1s%**	**$^{207}Pb/^{206}Pb$**	**1s %**	**$^{207}Pb/^{235}U$**	**1s %**	**$^{206}Pb/^{238}U$**	**1s %**	**Rho**	**$^{207}Pb/^{206}Pb$**	**2s abs**	**$^{206}Pb/^{238}U$**	**2s abs**	**$^{207}Pb/^{235}U$**	**2s abs**	**% U-Pb disc[4]**
040-ZR30	0,368	388044	16,86	0,18323	0,75	13,038	1,28	0,5160	0,96	0,75	2682	25	2682	42	2682	24	0,00
038-ZR28	0,366	416473	15,22	0,17932	0,49	11,610	0,99	0,4695	0,78	0,78	2647	16	2482	32	2573	18	6,23
035-ZR25	0,347	377506	17,84	0,17762	0,41	10,649	1,22	0,4348	1,09	0,89	2631	13	2327	42	2493	22	11,53
027-ZR19	0,199	201729	40,61	0,16733	0,94	9,414	1,53	0,4080	1,15	0,75	2531	31	2206	43	2379	28	12,85
026-ZR18B	0,405	868227	14,13	0,17629	0,46	12,125	1,15	0,4988	0,98	0,86	2618	15	2609	42	2614	21	0,37
025-ZR17	0,459	827172	23,06	0,16113	0,66	8,209	1,35	0,3695	1,12	0,83	2468	22	2027	39	2254	24	17,86
024-ZR16	0,364	764391	35,93	0,18378	0,41	12,865	1,10	0,5077	0,95	0,86	2687	13	2647	41	2670	21	1,51
020-ZR15	0,419	829567	56,75	0,17988	0,61	12,239	1,22	0,4935	0,99	0,81	2652	20	2586	42	2623	23	2,49
017-ZR12B	0,320	753478	42,19	0,18296	0,37	13,145	1,20	0,5210	1,08	0,90	2680	12	2703	48	2690	23	-0,88
013-ZR8	0,467	1163089	16,47	0,17543	0,38	11,629	1,16	0,4807	1,03	0,89	2610	12	2530	43	2575	21	3,05
058-ZR41	0,269	138325	12,27	0,17800	0,82	12,064	1,48	0,4915	1,17	0,79	2634	27	2577	50	2609	28	2,17
056-ZR39	0,305	178722	16,11	0,18059	0,63	12,624	1,12	0,5069	0,85	0,76	2658	21	2644	37	2652	21	0,56
055-ZR38	0,278	189053	17,61	0,17302	0,81	10,482	1,51	0,4394	1,21	0,81	2587	27	2348	48	2478	28	9,25
054-ZR37C	0,324	135685	13,51	0,18022	0,71	11,309	1,40	0,4551	1,15	0,82	2655	23	2418	46	2549	26	8,93
053-ZR36	0,256	220553	17,53	0,16370	0,76	9,154	1,19	0,4055	0,84	0,71	2494	25	2194	31	2353	22	12,02

ADE-18P	Th/U	$^{206}Pb/^{204}Pb$	1s%	$^{207}Pb/^{206}Pb$	1s %	$^{207}Pb/^{235}U$	1s %	$^{206}Pb/^{238}U$	1s %	Rho	$^{207}Pb/^{206}Pb$	2s abs	$^{206}Pb/^{238}U$	2s abs	$^{207}Pb/^{235}U$	2s abs	% U-Pb disc[4]
050-ZR35	0,474	796624	15,70	0,17399	1,05	12,024	1,58	0,5012	1,13	0,71	2596	35	2619	48	2606	29	-0,86
048-ZR33	0,290	134781	18,18	0,18078	0,64	12,308	1,09	0,4937	0,80	0,74	2660	21	2587	34	2628	20	2,75
046-ZR31	0,496	490951	27,30	0,18149	0,57	12,744	1,36	0,5092	1,18	0,87	2667	19	2653	51	2661	26	0,49
045-ZR30	0,414	316069	16,09	0,18046	0,93	12,742	1,46	0,5121	1,07	0,73	2657	31	2665	46	2661	27	-0,32
044-ZR29	0,427	1627654	63,56	0,17417	0,73	12,402	1,22	0,5164	0,91	0,74	2598	24	2684	40	2635	23	-3,30
037-ZR26C	0,408	544929	17,42	0,17608	0,54	12,429	1,27	0,5119	1,09	0,86	2616	18	2665	48	2637	24	-1,85
036-ZR25	0,296	103496	14,38	0,18436	0,68	12,660	1,17	0,4980	0,88	0,75	2692	22	2605	38	2655	22	3,24
035-ZR24	0,413	404663	19,09	0,17921	0,43	12,163	1,06	0,4922	0,90	0,85	2646	14	2580	38	2617	20	2,47
034-ZR23	0,326	90433	16,92	0,18135	0,70	12,107	1,16	0,4842	0,84	0,73	2665	23	2545	35	2613	22	4,50
033-ZR22	0,434	1005132	25,07	0,17602	0,50	12,642	0,98	0,5209	0,76	0,78	2616	17	2703	34	2653	18	-3,33
029-ZR20	0,386	201334	15,18	0,18180	0,71	12,309	1,19	0,4910	0,88	0,74	2669	24	2575	37	2628	22	3,53
028-ZR19	0,418	191721	14,10	0,18322	0,58	12,868	1,08	0,5094	0,84	0,77	2682	19	2654	36	2670	20	1,06
024-ZR15	0,181	121175	19,17	0,15103	1,60	7,705	2,11	0,3700	1,33	0,63	2358	54	2029	46	2197	38	13,93
019-ZR13B	0,372	445018	85,40	0,18609	1,29	12,045	1,79	0,4694	1,17	0,66	2708	42	2481	48	2608	33	8,38
018-ZR13C	0,128	426854	65,75	0,15428	0,75	7,949	1,25	0,3737	0,93	0,74	2394	25	2047	32	2225	22	14,51
016-ZR11	0,242	862579	23,41	0,17223	0,49	11,749	1,03	0,4947	0,82	0,80	2579	16	2591	35	2585	19	-0,45
015-ZR10	0,086	539967	14,41	0,15685	1,31	7,966	1,68	0,3683	0,98	0,59	2422	44	2022	34	2227	30	16,53
014-ZR9	0,349	172807	23,53	0,17952	0,62	13,026	1,11	0,5262	0,84	0,76	2648	21	2726	37	2682	21	-2,91
013-ZR8	0,301	805400	21,86	0,17465	0,66	12,496	1,00	0,5189	0,66	0,66	2603	22	2694	29	2642	19	-3,52
010-ZR7	0,215	753028	20,53	0,17118	0,65	11,108	1,04	0,4706	0,73	0,70	2569	22	2486	30	2532	19	3,23
008-ZR5	0,487	660430	19,94	0,16273	1,18	8,938	1,65	0,3983	1,10	0,66	2484	39	2161	40	2332	30	13,00
007-ZR4	0,409	349442	15,86	0,17958	0,50	12,977	0,97	0,5241	0,75	0,77	2649	17	2716	33	2678	18	-2,54
006-ZR3	0,133	783760	17,86	0,16736	0,93	10,100	1,41	0,4377	1,00	0,71	2531	31	2340	39	2444	26	7,56
005-ZR2	0,382	311129	15,06	0,18024	0,55	12,195	1,21	0,4907	1,01	0,84	2655	18	2574	43	2620	23	3,07
004-ZR1	0,287	186334	13,77	0,18417	1,41	12,527	1,74	0,4933	0,96	0,55	2691	46	2585	41	2645	32	3,93
047-ZR32	0,345	1221664	15,69	0,15241	0,73	8,186	1,28	0,3895	0,99	0,77	2373	25	2121	36	2252	23	10,64
026-ZR17	0,080	745848	18,74	0,16193	0,53	9,713	1,00	0,4350	0,75	0,76	2476	18	2328	29	2408	18	5,96

ADE-18P	Th/U	$^{206}Pb/^{204}Pb$	1s%	$^{207}Pb/^{206}Pb$	1s %	$^{207}Pb/^{235}U$	1s %	$^{206}Pb/^{238}U$	1s %	Rho	$^{207}Pb/^{206}Pb$	2s abs	$^{206}Pb/^{238}U$	2s abs	$^{207}Pb/^{235}U$	2s abs	% U-Pb disc[4]
009-ZR6	0,114	1392995	17,10	0,15993	0,56	9,244	1,03	0,4192	0,78	0,76	2455	19	2257	30	2362	19	8,08
049-ZR34	0,369	24603455	96,49	0,16337	0,69	10,060	1,32	0,4466	1,07	0,81	2491	23	2380	42	2440	24	4,45
020-ZR14	0,301	337389	22,52	0,16246	0,85	10,195	1,33	0,4551	0,96	0,72	2481	29	2418	39	2453	25	2,55
039-ZR29B	0,321	417726	20,95	0,16780	0,90	11,085	1,62	0,4791	1,30	0,80	2536	30	2523	54	2530	30	0,49
019-ZR14	0,441	554167	25,35	0,16863	0,80	8,865	1,70	0,3813	1,45	0,85	2544	27	2082	51	2324	31	18,16
008-ZR5B	0,298	1179726	25,20	0,16600	0,51	10,471	1,50	0,4574	1,36	0,91	2518	17	2428	55	2477	28	3,55
005-ZR2	0,373	329473	15,59	0,16689	0,40	9,704	1,59	0,4217	1,49	0,94	2527	14	2268	57	2407	29	10,24
004-ZR1	0,245	427724	24,05	0,16650	0,84	7,766	1,94	0,3383	1,71	0,88	2523	28	1878	56	2204	35	25,54
016-ZR11B	0,040	323623	47,01	0,13787	0,74	8,172	1,08	0,4298	0,69	0,64	2201	26	2305	27	2250	19	-4,74
018-ZR13B	0,022	1036766	17,01	0,14216	0,60	7,999	1,09	0,4081	0,83	0,76	2254	21	2206	31	2231	20	2,11
017-ZR12	0,015	902285	12,63	0,13259	1,02	7,116	1,69	0,3892	1,30	0,77	2133	35	2119	47	2126	30	0,63
038-ZR26B	0,017	883570	15,92	0,11971	0,65	6,003	1,07	0,3637	0,77	0,71	1952	23	2000	26	1976	19	-2,44
025-ZR16	0,013	210003	23,19	0,11877	1,12	5,227	1,52	0,3192	0,97	0,63	1938	40	1786	30	1857	26	7,86
027-ZR18	0,048	558429	14,05	0,11784	0,75	5,851	1,21	0,3601	0,87	0,72	1924	27	1983	30	1954	21	-3,06
ADE-12L	**Th/U**	$^{206}Pb/^{204}Pb$	**1s%**	$^{207}Pb/^{206}Pb$	**1s %**	$^{207}Pb/^{235}U$	**1s %**	$^{206}Pb/^{238}U$	**1s %**	**Rho**	$^{207}Pb/^{206}Pb$	**2s abs**	$^{206}Pb/^{238}U$	**2s abs**	$^{207}Pb/^{235}U$	**2s abs**	**% U-Pb disc[4]**
012-ZR34B	0,506	884	6,26	0,13893	1,43	4,228	3,26	0,2207	2,90	0,89	2214	49	1286	67	1679	53	41,93
028-ZR42C	0,470	854	3,52	0,13459	0,50	4,253	1,68	0,2291	1,56	0,93	2159	17	1330	37	1684	27	38,39
019-ZR38	0,553	1497	5,13	0,12995	0,77	4,572	1,83	0,2552	1,62	0,88	2097	27	1465	42	1744	30	30,14
018-ZR13	0,315	1184	7,22	0,12484	0,92	5,073	1,45	0,2947	1,05	0,73	2027	32	1665	31	1832	24	17,85
013-ZR8	0,188	13525	4,84	0,12379	0,57	5,772	1,08	0,3381	0,84	0,78	2012	20	1878	27	1942	19	6,66
015-ZR10	0,266	22822	12,33	0,12298	0,84	5,751	1,24	0,3391	0,84	0,68	2000	30	1883	27	1939	21	5,87
010-ZR7	0,175	25689	44,21	0,12291	0,98	5,430	2,75	0,3204	2,55	0,93	1999	35	1792	79	1890	47	10,36
039-ZR29B	0,138	5736	9,70	0,12228	0,84	5,181	1,26	0,3073	0,85	0,68	1990	30	1727	26	1849	21	13,19
006-ZR32C	0,424	4561	4,29	0,12124	1,59	5,086	2,16	0,3042	1,42	0,66	1975	56	1712	43	1834	36	13,28
009-ZR6	0,020	121702	50,22	0,12052	0,58	5,818	1,04	0,3501	0,78	0,75	1964	20	1935	26	1949	18	1,48
036-ZR45C	0,443	8167	16,10	0,11902	0,57	5,986	1,27	0,3647	1,07	0,85	1942	20	2005	37	1974	22	-3,24
027-ZR41B	0,413	10733	12,39	0,11881	0,48	5,931	1,38	0,3620	1,23	0,90	1938	17	1992	42	1966	24	-2,75

ADE-18P	Th/U	$^{206}Pb/^{204}Pb$	1s%	$^{207}Pb/^{206}Pb$	1s %	$^{207}Pb/^{235}U$	1s %	$^{206}Pb/^{238}U$	1s %	Rho	$^{207}Pb/^{206}Pb$	2s abs	$^{206}Pb/^{238}U$	2s abs	$^{207}Pb/^{235}U$	2s abs	% U-Pb disc[4]
023-ZR39B	0,697	4998	5,89	0,11861	1,37	5,462	1,76	0,3340	1,03	0,59	1935	49	1858	33	1895	30	4,02
016-ZR36B	0,282	4870	7,93	0,11810	0,97	5,654	2,51	0,3472	2,29	0,91	1928	35	1921	76	1924	43	0,35
014-ZR9	0,342	262509	47,11	0,13284	0,74	7,000	1,15	0,3821	0,81	0,70	2136	26	2086	29	2111	20	2,32
033-ZR23	0,857	6109	19,43	0,12813	1,23	7,183	2,07	0,4066	1,63	0,79	2073	43	2199	61	2134	37	-6,11
025-ZR40B	0,342	781	4,22	0,12558	0,59	3,917	2,49	0,2262	2,39	0,96	2037	21	1315	57	1617	40	35,46
016-ZR11	0,201	1586	10,53	0,14490	0,63	1,800	3,88	0,0901	3,81	0,98	2287	22	556	41	1046	50	75,68
018-ZR37B	0,290	536	5,62	0,12723	1,90	3,357	3,05	0,1914	2,35	0,77	2060	66	1129	49	1495	47	45,20
019-ZR14	0,332	4985	24,64	0,12661	1,96	5,524	2,39	0,3164	1,33	0,56	2051	68	1772	41	1904	41	13,62
024-ZR16	0,509	6022	5,12	0,12674	0,43	5,606	1,60	0,3208	1,49	0,93	2053	15	1794	47	1917	27	12,65
027-ZR19	0,432	1005	17,13	0,12752	1,30	5,829	1,64	0,3315	0,92	0,56	2064	46	1846	29	1951	28	10,58
ADE-18Li	**Th/U**	$^{206}Pb/^{204}Pb$	**1s%**	$^{207}Pb/^{206}Pb$	**1s %**	$^{207}Pb/^{235}U$	**1s %**	$^{206}Pb/^{238}U$	**1s %**	**Rho**	$^{207}Pb/^{206}Pb$	**2s abs**	$^{206}Pb/^{238}U$	**2s abs**	$^{207}Pb/^{235}U$	**2s abs**	**% U-Pb disc[4]**
049-ZR22B	0,296	93944	81,06	0,19329	2,24	10,361	2,67	0,3887	1,39	0,52	2770	73	2117	50	2468	49	23,59
048-ZR22C	0,462	10077	16,05	0,20756	0,52	15,251	1,13	0,5329	0,93	0,82	2887	17	2753	42	2831	21	4,61
046-ZR21C	0,223	243099	60,86	0,20410	1,53	14,006	1,66	0,4977	0,52	0,71	2859	49	2604	22	2750	31	8,94
047-ZR21B	0,275	1446018	19,48	0,20692	0,39	14,927	0,81	0,5232	0,61	0,75	2882	13	2713	27	2811	15	5,86
040-ZR18C	0,132	210659	45,47	0,20570	1,69	14,023	3,81	0,4944	3,40	0,89	2872	54	2590	144	2751	71	9,83
037-ZR16C	0,516	35152	83,40	0,19606	1,95	9,976	4,32	0,3690	3,83	0,89	2794	63	2025	132	2433	78	27,52
030-ZR13C	0,089	26388	5,26	0,20685	0,89	12,409	2,54	0,4351	2,35	0,93	2881	29	2328	91	2636	47	19,18
029-ZR12C	0,383	915919	19,24	0,20966	0,55	13,768	1,57	0,4762	1,42	0,91	2903	18	2511	59	2734	29	13,51
028-ZR11B	0,158	3641	3,45	0,17729	1,38	7,280	2,61	0,2978	2,18	0,84	2628	46	1680	64	2146	46	36,05
026-ZR10B	0,314	2636	7,30	0,18937	0,43	7,803	3,63	0,2988	3,59	0,99	2737	14	1686	106	2209	64	38,41
025-ZR10C	0,309	1122563	22,75	0,21005	0,41	14,950	0,99	0,5162	0,82	0,83	2906	13	2683	36	2812	19	7,67
024-ZR9B	0,313	15877	9,76	0,19717	1,08	11,685	3,03	0,4298	2,80	0,93	2803	35	2305	108	2580	56	17,77
020-ZR9C	0,267	7782	5,12	0,19029	1,09	9,662	2,75	0,3682	2,49	0,91	2745	36	2021	86	2403	50	26,37
018-ZR8C	0,211	27281	7,96	0,18511	0,70	9,913	1,21	0,3883	0,91	0,76	2699	23	2115	33	2427	22	21,64
016-ZR7C	0,548	24598	10,18	0,19276	0,80	10,908	3,12	0,4104	2,99	0,96	2766	26	2217	112	2515	57	19,86
015-ZR6B	0,199	11476	24,37	0,19680	0,85	11,053	1,43	0,4073	1,09	0,76	2800	28	2203	41	2528	27	21,33

ADE-18P	Th/U	$^{206}Pb/^{204}Pb$	1s%	$^{207}Pb/^{206}Pb$	1s %	$^{207}Pb/^{235}U$	1s %	$^{206}Pb/^{238}U$	1s %	Rho	$^{207}Pb/^{206}Pb$	2s abs	$^{206}Pb/^{238}U$	2s abs	$^{207}Pb/^{235}U$	2s abs	% U-Pb disc[4]
014-ZR6C	0,353	11392	10,65	0,20689	0,58	14,612	1,45	0,5122	1,28	0,88	2881	19	2666	56	2790	27	7,47
010-ZR5C	0,655	5581	11,53	0,21277	1,16	10,523	2,70	0,3587	2,41	0,89	2927	37	1976	82	2482	50	32,49
009-ZR4C	0,522	8044	5,27	0,19815	0,78	9,854	3,21	0,3606	3,09	0,96	2811	25	1985	105	2421	58	29,38
007-ZR2C	0,438	19439	17,52	0,20942	0,41	16,053	1,27	0,5559	1,15	0,90	2901	13	2850	53	2880	24	1,77
008-ZR3C	0,404	760206	19,33	0,13688	0,42	6,899	0,82	0,3655	0,60	0,73	2188	15	2008	21	2098	15	8,22
004-ZR1C	0,037	596854	27,26	0,12061	2,50	4,241	5,37	0,2550	4,73	0,88	1965	88	1464	123	1682	86	25,49
038-ZR17C	0,120	2469	5,42	0,14089	3,26	3,816	3,64	0,1964	1,58	0,43	2238	111	1156	33	1596	58	48,34
006-ZR1BB	0,048	240307	84,68	0,05794	0,68	0,755	0,90	0,0945	0,44	0,49	528	30	582	5	571	8	-10,26
039-ZR17B	0,119	111250	56,15	0,05990	0,69	0,766	1,14	0,0927	0,83	0,73	600	30	572	9	577	10	4,73
005-ZR1B	0,183	39839	5,40	0,05971	0,38	0,753	0,83	0,0914	0,64	0,77	593	16	564	7	570	7	4,87
036-ZR15C	0,069	334390	20,32	0,05781	1,97	0,713	3,21	0,0895	2,51	0,78	523	85	552	27	547	27	-5,69
ADE-29	**Th/U**	**$^{206}Pb/^{204}Pb$**	**1s%**	**$^{207}Pb/^{206}Pb$**	**1s %**	**$^{207}Pb/^{235}U$**	**1s %**	**$^{206}Pb/^{238}U$**	**1s %**	**Rho**	**$^{207}Pb/^{206}Pb$**	**2s abs**	**$^{206}Pb/^{238}U$**	**2s abs**	**$^{207}Pb/^{235}U$**	**2s abs**	**% U-Pb disc[4]**
006-ZR3	0,570	419605	17,66	0,22280	0,69	18,809	1,12	0,6122	0,80	0,72	3001	22	3079	39	3032	22	-2,59
036-ZR26	0,476	220317	19,98	0,21823	0,60	16,966	1,21	0,5638	0,99	0,82	2968	19	2882	46	2933	23	2,88
040-ZR30	0,842	173700	48,93	0,22274	0,73	17,665	1,63	0,5751	1,41	0,86	3001	23	2929	66	2972	31	2,39
039-ZR29	0,412	146252	31,14	0,20045	0,74	10,482	1,73	0,3792	1,52	0,88	2830	24	2073	54	2478	32	26,76
041-ZR31	0,393	139083	17,13	0,15141	0,90	5,513	1,66	0,2640	1,34	0,81	2362	31	1511	36	1903	28	36,05
038-ZR28	0,159	193114	16,02	0,17762	0,66	11,231	1,42	0,4585	1,20	0,85	2631	22	2433	48	2542	26	7,51
037-ZR27	0,435	281967	16,53	0,16540	0,59	7,503	1,25	0,3290	1,04	0,83	2512	20	1833	33	2173	22	27,00
035-ZR25	0,343	244616	17,40	0,17386	0,63	10,346	1,29	0,4316	1,07	0,82	2595	21	2313	41	2466	24	10,88
034-ZR24	0,399	28642	28,20	0,16963	0,85	8,781	1,61	0,3754	1,32	0,82	2554	28	2055	46	2316	29	19,54
030-ZR22	0,480	313935	14,56	0,15755	1,17	6,161	1,64	0,2836	1,08	0,66	2430	40	1609	31	1999	28	33,76
029-ZR21	0,537	755972	16,19	0,16169	0,85	6,823	1,47	0,3060	1,14	0,78	2473	29	1721	34	2089	26	30,42
028-ZR20	0,539	117929	31,02	0,17204	0,69	9,234	1,28	0,3892	1,01	0,79	2578	23	2119	36	2361	23	17,78
027-ZR19	0,116	195554	17,97	0,18108	0,68	11,870	1,31	0,4754	1,06	0,81	2663	22	2507	44	2594	24	5,84
026-ZR18	0,233	299866	38,55	0,17872	1,16	11,199	2,36	0,4545	2,02	0,86	2641	38	2415	81	2540	44	8,56
025-ZR17	0,259	1713420	93,24	0,15025	0,73	5,377	1,40	0,2595	1,14	0,81	2349	25	1488	30	1881	24	36,67

ADE-18P	Th/U	$^{206}Pb/^{204}Pb$	1s%	$^{207}Pb/^{206}Pb$	1s %	$^{207}Pb/^{235}U$	1s %	$^{206}Pb/^{238}U$	1s %	Rho	$^{207}Pb/^{206}Pb$	2s abs	$^{206}Pb/^{238}U$	2s abs	$^{207}Pb/^{235}U$	2s abs	% U-Pb disc[4]
024-ZR16	0,243	320129	16,86	0,17904	0,85	11,087	2,13	0,4491	1,92	0,90	2644	28	2391	77	2530	39	9,56
019-ZR14	0,170	301371	13,99	0,17490	0,99	10,894	1,52	0,4517	1,10	0,72	2605	33	2403	44	2514	28	7,76
018-ZR13	0,422	354686	16,89	0,15330	0,72	5,734	1,61	0,2712	1,39	0,87	2383	24	1547	38	1936	28	35,08
017-ZR12	0,190	333691	15,85	0,16684	0,58	8,271	1,40	0,3595	1,21	0,87	2526	20	1980	41	2261	25	21,62
015-ZR10	0,303	92127	31,60	0,17226	0,62	8,259	1,64	0,3477	1,48	0,90	2580	20	1924	49	2260	30	25,43
014-ZR9	0,233	310069	29,88	0,17785	0,59	11,158	1,30	0,4550	1,10	0,85	2633	19	2417	44	2536	24	8,19
013-ZR8	0,302	211690	43,77	0,16780	0,97	8,828	1,60	0,3815	1,22	0,76	2536	32	2083	43	2320	29	17,84
010-ZR7	0,417	526604	14,71	0,17421	0,72	9,960	1,29	0,4146	1,01	0,78	2599	24	2236	38	2431	24	13,95
009-ZR6	0,382	218719	21,99	0,15570	0,74	6,842	1,40	0,3187	1,13	0,81	2409	25	1783	35	2091	25	25,99
008-ZR5	0,195	447680	12,99	0,16884	0,58	8,536	1,34	0,3667	1,15	0,86	2546	19	2014	40	2290	24	20,91
007-ZR4	0,587	348591	22,29	0,16100	0,58	7,192	1,54	0,3240	1,37	0,89	2466	20	1809	43	2136	27	26,65
005-ZR2	0,407	351330	16,28	0,16045	0,80	7,019	1,34	0,3172	1,01	0,75	2460	27	1776	31	2114	24	27,81
004-ZR1	0,587	405253	19,61	0,16400	0,70	8,013	1,22	0,3543	0,93	0,76	2497	24	1955	31	2232	22	21,71
016-ZR11	0,460	91016	16,52	0,05960	0,94	0,784	1,54	0,0955	1,17	0,76	589	40	588	13	588	14	0,22
AP-17	**Th/U**	$^{206}Pb/^{204}Pb$	**1s%**	$^{207}Pb/^{206}Pb$	**1s %**	$^{207}Pb/^{235}U$	**1s %**	$^{206}Pb/^{238}U$	**1s %**	**Rho**	$^{207}Pb/^{206}Pb$	**2s abs**	$^{206}Pb/^{238}U$	**2s abs**	$^{207}Pb/^{235}U$	**2s abs**	**% U-Pb disc[4]**
016-ZR11	0,017	73006	16,30	0,05998	0,90	0,831	1,50	0,1005	1,14	0,76	603	39	617	13	614	14	-2,44
015-ZR10	0,387	201178	23,68	0,10430	0,56	3,986	1,17	0,2772	0,95	0,82	1702	21	1577	27	1631	19	7,34
014-ZR9	0,050	94726	18,89	0,06060	0,59	0,833	1,06	0,0997	0,79	0,75	625	25	613	9	615	10	1,99
013-ZR8	0,016	124898	17,51	0,06127	0,72	0,864	1,23	0,1023	0,92	0,75	649	31	628	11	632	12	3,20
010-ZR7	0,038	103104	33,03	0,06066	0,87	0,824	1,37	0,0985	0,99	0,72	627	37	606	11	610	13	3,46
009-ZR6	0,142	133371	23,49	0,06053	0,67	0,848	1,12	0,1016	0,82	0,73	623	29	623	10	623	10	-0,15
008-ZR5	0,018	106593	19,48	0,05925	0,77	0,807	1,30	0,0988	0,97	0,75	576	33	607	11	601	12	-5,35
007-ZR4	0,013	101356	14,06	0,05957	0,69	0,809	1,13	0,0985	0,82	0,72	588	30	606	9	602	10	-3,05
006-ZR3	0,217	101213	20,38	0,18246	0,62	12,004	1,14	0,4771	0,88	0,77	2675	21	2515	37	2605	21	6,00
005-ZR2	0,009	96965	18,34	0,05947	0,65	0,803	1,16	0,0980	0,88	0,76	584	28	602	10	599	10	-3,08
ADE-20	**Th/U**	$^{206}Pb/^{204}Pb$	**1s%**	$^{207}Pb/^{206}Pb$	**1s %**	$^{207}Pb/^{235}U$	**1s %**	$^{206}Pb/^{238}U$	**1s %**	**Rho**	$^{207}Pb/^{206}Pb$	**2s abs**	$^{206}Pb/^{238}U$	**2s abs**	$^{207}Pb/^{235}U$	**2s abs**	**% U-Pb disc[4]**
033-ZR23	0,084	17413	17,24	0,06095	2,38	0,828	3,64	0,0985	2,73	0,75	638	101	606	31	613	33	4,99

ADE-18P	Th/U	$^{206}Pb/^{204}Pb$	1s%	$^{207}Pb/^{206}Pb$	1s %	$^{207}Pb/^{235}U$	1s %	$^{206}Pb/^{238}U$	1s %	Rho	$^{207}Pb/^{206}Pb$	2s abs	$^{206}Pb/^{238}U$	2s abs	$^{207}Pb/^{235}U$	2s abs	% U-Pb disc[4]
017-ZR13	0,215	17741	15,33	0,06226	2,09	0,838	3,25	0,0976	2,46	0,76	683	88	600	28	618	30	12,10
014-ZR9	0,046	13967	20,10	0,05812	2,11	0,790	3,35	0,0985	2,57	0,77	534	91	606	30	591	30	-13,41
006-ZR3	0,015	15561	14,57	0,05879	2,68	0,804	3,85	0,0992	2,74	0,71	559	115	610	32	599	35	-9,04
005-ZR2	0,005	17373	25,00	0,05832	2,66	0,804	4,03	0,1000	3,00	0,75	542	114	614	35	599	36	-13,39
ADE-16	Th/U	206Pb/204Pb	1s%	207Pb/206Pb	1s %	207Pb/235U	1s %	206Pb/238U	1s %	Rho	207Pb/206Pb	2s abs	206Pb/238U	2s abs	207Pb/235U	2s abs	% U-Pb disc4
049-ZR36	0,461	118344	20,19	0,22362	0,79	18,142	1,35	0,5884	1,04	0,76	3007	25	2983	49	2997	26	0,80
048-ZR35	0,171	91234	23,65	0,17521	0,68	9,496	1,35	0,3931	1,11	0,82	2608	23	2137	40	2387	25	18,06
047-ZR34	0,185	126434	21,30	0,17766	0,63	11,674	1,30	0,4765	1,07	0,82	2631	21	2512	44	2579	24	4,53
046-ZR33	0,163	27521	44,06	0,15707	0,64	3,495	2,09	0,1614	1,95	0,94	2424	22	964	35	1526	33	60,22
045-ZR32	0,230	252276	19,43	0,17568	0,60	10,407	1,28	0,4296	1,07	0,83	2612	20	2304	41	2472	24	11,81
044-ZR31	0,268	220465	16,95	0,17384	0,66	9,833	1,19	0,4102	0,92	0,77	2595	22	2216	34	2419	22	14,61
040-ZR30	0,290	25745	24,35	0,17434	1,43	8,458	1,91	0,3518	1,21	0,63	2600	47	1943	41	2281	34	25,25
039-ZR29	0,616	26698	19,82	0,06070	2,23	0,806	3,10	0,0963	2,11	0,68	629	95	593	24	600	28	5,67
038-ZR28	0,200	216673	16,63	0,17742	0,58	10,966	1,33	0,4482	1,14	0,86	2629	19	2387	45	2520	25	9,18
037-ZR27	0,230	156080	15,88	0,17993	0,59	12,095	1,18	0,4875	0,96	0,81	2652	20	2560	40	2612	22	3,48
036-ZR26	0,301	138840	23,85	0,17796	0,69	9,075	2,38	0,3698	2,25	0,94	2634	23	2029	78	2346	43	22,98
035-ZR25	0,240	183123	17,10	0,17816	0,53	10,885	0,99	0,4431	0,76	0,76	2636	17	2364	30	2513	18	10,30
034-ZR24	0,226	147758	28,42	0,17834	0,59	11,285	1,11	0,4589	0,87	0,78	2638	20	2435	35	2547	21	7,69
033-ZR23	0,228	303263	16,36	0,17615	0,65	11,282	1,15	0,4645	0,87	0,76	2617	22	2459	36	2547	21	6,02
030-ZR22	0,176	217145	14,59	0,17619	0,74	10,248	1,16	0,4218	0,81	0,70	2617	25	2269	31	2457	21	13,32
029-ZR21	0,213	205779	15,32	0,17904	0,68	11,600	1,19	0,4699	0,90	0,76	2644	22	2483	37	2573	22	6,09
028-ZR20	0,247	170920	21,35	0,16840	0,69	8,531	1,13	0,3674	0,81	0,72	2542	23	2017	28	2289	20	20,64
027-ZR19	0,226	237843	17,66	0,17753	0,94	11,102	1,45	0,4535	1,04	0,72	2630	31	2411	42	2532	27	8,32
026-ZR18	0,204	98345	15,58	0,17400	0,84	9,571	1,58	0,3989	1,29	0,82	2597	28	2164	47	2394	29	16,66
025-ZR17	0,150	141345	21,15	0,16520	0,52	7,679	1,08	0,3371	0,87	0,81	2510	17	1873	28	2194	19	25,37
024-ZR16	0,326	158057	19,58	0,16929	1,25	7,138	2,09	0,3058	1,64	0,78	2551	42	1720	49	2129	37	32,57
020-ZR15	0,131	90129	21,36	0,16961	0,74	9,718	1,39	0,4155	1,12	0,81	2554	25	2240	42	2408	25	12,29

ADE-18P	Th/U	$^{206}Pb/^{204}Pb$	1s%	$^{207}Pb/^{206}Pb$	1s %	$^{207}Pb/^{235}U$	1s %	$^{206}Pb/^{238}U$	1s %	Rho	$^{207}Pb/^{206}Pb$	2s abs	$^{206}Pb/^{238}U$	2s abs	$^{207}Pb/^{235}U$	2s abs	% U-Pb disc[4]
019-ZR14	0,171	253890	15,54	0,17742	0,69	11,115	1,21	0,4544	0,93	0,77	2629	23	2415	37	2533	22	8,15
018-ZR13	0,244	159208	17,79	0,16947	0,69	8,834	1,68	0,3780	1,49	0,88	2552	23	2067	52	2321	30	19,02
017-ZR12	0,205	199382	21,64	0,18148	0,55	12,233	1,06	0,4889	0,83	0,78	2666	18	2566	35	2622	20	3,77
016-ZR11	0,223	270726	18,02	0,17938	0,58	11,241	1,14	0,4545	0,91	0,80	2647	19	2415	37	2543	21	8,77
015-ZR10	0,225	226244	14,71	0,17325	2,02	8,810	2,42	0,3688	1,27	0,53	2589	67	2024	44	2318	44	21,85
014-ZR9	0,261	497473	56,80	0,16715	1,01	7,621	2,35	0,3307	2,09	0,89	2529	34	1842	67	2187	42	27,19
013-ZR8	0,241	278638	14,00	0,16766	0,77	7,973	1,54	0,3448	1,28	0,83	2534	26	1910	42	2228	28	24,64
010-ZR7	0,202	146549	19,96	0,17644	1,07	10,750	1,53	0,4419	1,03	0,67	2620	35	2359	41	2502	28	9,95
009-ZR6	0,228	176781	21,29	0,17967	0,82	11,693	1,23	0,4720	0,84	0,68	2650	27	2492	35	2580	23	5,95
008-ZR5	0,230	37658	38,55	0,14385	0,81	3,886	2,43	0,1959	2,26	0,93	2274	28	1153	48	1611	39	49,28
007-ZR4	0,236	177168	22,00	0,17196	0,57	9,096	1,44	0,3836	1,27	0,88	2577	19	2093	45	2348	26	18,77
006-ZR3	0,121	122527	29,61	0,14507	0,80	4,504	1,39	0,2252	1,08	0,77	2289	28	1309	26	1732	23	42,80
005-ZR2	0,209	274098	22,98	0,17820	0,38	12,009	1,01	0,4887	0,86	0,85	2636	13	2565	36	2605	19	2,70
004-ZR1	0,272	22082	28,24	0,15512	0,48	5,930	1,21	0,2773	1,05	0,86	2403	16	1578	29	1966	21	34,35
ADE-09	**Th/U**	$^{206}Pb/^{204}Pb$	**1s%**	$^{207}Pb/^{206}Pb$	**1s %**	$^{207}Pb/^{235}U$	**1s %**	$^{206}Pb/^{238}U$	**1s %**	**Rho**	$^{207}Pb/^{206}Pb$	**2s abs**	$^{206}Pb/^{238}U$	**2s abs**	$^{207}Pb/^{235}U$	**2s abs**	**% U-Pb disc[4]**
048-ZR33C	0,033	77960	19,47	0,11080	0,95	3,446	1,59	0,2255	1,22	0,77	1813	34	1311	29	1515	25	27,68
045-ZR31B	0,078	69397	46,60	0,12173	0,61	5,932	1,11	0,3534	0,85	0,77	1982	22	1951	29	1966	19	1,56
040-ZR30C	0,147	100904	14,63	0,17830	1,20	11,687	1,71	0,4753	1,15	0,67	2637	40	2507	48	2580	32	4,94
039-ZR29C	0,318	187983	14,11	0,18023	0,82	12,089	1,34	0,4864	1,00	0,74	2655	27	2555	42	2611	25	3,75
038-ZR28C	0,001	21140	17,23	0,05842	1,96	0,775	2,66	0,0962	1,76	0,66	546	85	592	20	583	23	-8,54
037-ZR27C	0,002	43314	25,47	0,05790	2,10	0,789	2,79	0,0988	1,81	0,65	526	91	608	21	591	25	-15,49
035-ZR25C	0,050	118219	12,28	0,12150	1,00	4,019	2,62	0,2399	2,40	0,91	1978	35	1386	60	1638	42	29,94
034-ZR24C	0,149	109520	19,07	0,16250	0,81	9,780	1,48	0,4365	1,18	0,80	2482	27	2335	46	2414	27	5,92
030-ZR22C	0,053	44865	14,73	0,09871	1,31	1,972	2,16	0,1449	1,68	0,78	1600	49	872	27	1106	29	45,47
029-ZR21C	0,133	109790	15,07	0,14317	1,17	6,330	1,91	0,3206	1,46	0,77	2266	40	1793	46	2023	33	20,88
028-ZR20C	0,162	32803	20,48	0,14149	1,34	4,369	2,04	0,2240	1,50	0,73	2246	46	1303	35	1707	34	41,98
027-ZR19C	0,323	128845	12,99	0,17757	1,23	10,947	1,70	0,4471	1,12	0,66	2630	41	2382	44	2519	31	9,43

ADE-18P	Th/U	$^{206}Pb/^{204}Pb$	1s%	$^{207}Pb/^{206}Pb$	1s %	$^{207}Pb/^{235}U$	1s %	$^{206}Pb/^{238}U$	1s %	Rho	$^{207}Pb/^{206}Pb$	2s abs	$^{206}Pb/^{238}U$	2s abs	$^{207}Pb/^{235}U$	2s abs	% U-Pb disc[4]
025-ZR17C	0,032	25681	20,85	0,11581	1,86	2,523	2,71	0,1580	1,94	0,72	1892	66	945	34	1279	39	50,04
024-ZR16C	0,175	86330	15,66	0,16788	0,93	9,869	1,59	0,4263	1,24	0,78	2537	31	2289	48	2423	29	9,75
020-ZR15C	0,003	17868	15,55	0,06302	2,65	0,813	3,70	0,0935	2,56	0,69	709	111	576	28	604	33	18,67
019-ZR14C	0,292	54730	14,31	0,18234	1,24	11,655	1,74	0,4635	1,16	0,67	2674	41	2455	47	2577	32	8,20
017-ZR12C	0,001	22338	15,99	0,06118	1,95	0,811	2,80	0,0962	1,97	0,71	646	83	592	22	603	25	8,30
016-ZR11C	0,011	20221	16,29	0,09332	2,34	1,560	3,51	0,1212	2,60	0,74	1494	87	738	36	955	43	50,63
015-ZR10C	0,002	16956	16,99	0,06178	2,67	0,799	3,64	0,0938	2,45	0,67	667	112	578	27	596	33	13,27
014-ZR9C	0,310	135152	33,18	0,17468	0,80	9,606	1,62	0,3988	1,35	0,84	2603	27	2164	50	2398	30	16,88
013-ZR8C	0,023	113642	23,13	0,12098	0,81	5,021	1,42	0,3010	1,10	0,78	1971	29	1696	33	1823	24	13,93
010-ZR7C	0,292	65296	16,30	0,18438	1,00	13,038	1,75	0,5128	1,39	0,79	2693	33	2669	61	2682	33	0,89
009-ZR6C	0,062	192438	15,40	0,17092	1,26	11,078	1,68	0,4700	1,04	0,62	2567	42	2484	43	2530	31	3,23
008-ZR5C	0,013	25918	18,02	0,11900	2,42	2,700	3,67	0,1646	2,73	0,74	1941	85	982	50	1329	54	49,41
006-ZR3C	0,092	88590	11,05	0,14867	1,34	5,713	2,24	0,2787	1,75	0,78	2331	46	1585	49	1933	38	32,01
005-ZR2C	0,267	77931	12,57	0,18437	1,88	13,192	3,32	0,5189	2,71	0,82	2693	61	2695	119	2693	62	-0,07
ADE-24	**Th/U**	$^{206}Pb/^{204}Pb$	**1s%**	$^{207}Pb/^{206}Pb$	**1s %**	$^{207}Pb/^{235}U$	**1s %**	$^{206}Pb/^{238}U$	**1s %**	**Rho**	$^{207}Pb/^{206}Pb$	**2s abs**	$^{206}Pb/^{238}U$	**2s abs**	$^{207}Pb/^{235}U$	**2s abs**	**% U-Pb disc[4]**
048-ZR35C	0,042	56992	15,89	0,11612	0,94	3,722	1,60	0,2324	1,23	0,77	1897	34	1347	30	1576	25	28,99
047-ZR34C	0,012	99474	20,81	0,12510	0,56	6,226	1,17	0,3610	0,97	0,82	2030	20	1987	33	2008	20	2,14
045-ZR32C	0,029	34551	17,82	0,11860	1,05	4,606	1,56	0,2816	1,10	0,70	1935	37	1600	31	1750	26	17,34
040-ZR30C	0,022	27783	16,31	0,12516	1,22	5,741	2,57	0,3326	2,23	0,87	2031	43	1851	71	1938	44	8,86
039-ZR29C	0,146	180638	27,87	0,12387	0,85	6,150	1,34	0,3601	0,97	0,72	2013	30	1983	33	1997	23	1,49
038-ZR28C	0,161	120463	21,47	0,12527	0,55	5,969	1,13	0,3456	0,92	0,81	2033	20	1913	30	1971	20	5,86
033-ZR23C	0,029	89672	23,20	0,12701	0,56	6,168	1,41	0,3522	1,25	0,88	2057	20	1945	42	2000	25	5,45
029-ZR21C	0,068	62318	19,77	0,11776	0,51	5,308	1,57	0,3269	1,44	0,92	1923	18	1823	46	1870	27	5,16
028-ZR20C	0,034	120130	12,80	0,12657	0,81	5,575	1,34	0,3195	1,00	0,74	2051	28	1787	31	1912	23	12,86
019-ZR14C	0,078	72239	28,70	0,11959	1,14	5,556	2,31	0,3369	1,97	0,85	1950	41	1872	64	1909	39	4,01
018-ZR13C	0,135	150117	19,89	0,12454	0,65	6,463	1,46	0,3764	1,26	0,86	2022	23	2059	44	2041	26	-1,83
014-ZR9C	0,015	231734	57,25	0,12435	0,78	6,244	1,32	0,3642	1,00	0,76	2019	28	2002	34	2011	23	0,87

ADE-18P	Th/U	$^{206}Pb/^{204}Pb$	1s%	$^{207}Pb/^{206}Pb$	1s %	$^{207}Pb/^{235}U$	1s %	$^{206}Pb/^{238}U$	1s %	Rho	$^{207}Pb/^{206}Pb$	2s abs	$^{206}Pb/^{238}U$	2s abs	$^{207}Pb/^{235}U$	2s abs	% U-Pb disc[4]
010-ZR7C	0,051	48613	20,00	0,12235	1,09	5,688	1,77	0,3371	1,35	0,76	1991	39	1873	44	1930	30	5,92
009-ZR6C	0,033	76288	31,27	0,12056	0,44	5,227	0,92	0,3144	0,72	0,78	1964	16	1763	22	1857	16	10,28
008-ZR5C	0,025	101461	12,90	0,11396	0,44	4,745	0,76	0,3020	0,50	0,66	1863	16	1701	15	1775	13	8,71
007-ZR4C	0,176	85487	19,80	0,12125	0,88	5,485	2,12	0,3280	1,89	0,89	1975	31	1829	60	1898	36	7,38
006-ZR3C	0,104	27987	4,62	0,11892	0,55	5,304	0,86	0,3235	0,54	0,63	1940	20	1807	17	1870	15	6,87
004-ZR1C	0,060	92294	58,40	0,12027	1,06	5,537	1,41	0,3338	0,85	0,60	1960	38	1857	27	1906	24	5,27
011-ZR6C	0,052	53188	16,02	0,12033	0,96	5,792	1,46	0,3491	1,03	0,71	1961	34	1930	34	1945	25	1,58
006-ZR3C	0,004	138851	9,54	0,12490	0,57	6,237	0,94	0,3621	0,65	0,69	2027	20	1992	22	2010	16	1,73
005-ZR2C	0,012	61171	19,14	0,12439	0,85	5,899	1,37	0,3439	1,01	0,74	2020	30	1905	33	1961	24	5,68
048-ZR35	0,224	692032	60,60	0,21261	1,51	15,619	2,26	0,5328	1,64	0,72	2926	49	2753	73	2854	43	5,89
047-ZR34	0,540	289747	18,72	0,21204	0,51	17,400	1,18	0,5951	1,00	0,85	2921	16	3010	48	2957	23	-3,04
046-ZR33	0,578	501395	21,91	0,21295	0,44	17,150	1,00	0,5841	0,82	0,82	2928	14	2965	39	2943	19	-1,27
045-ZR32	0,583	336071	17,69	0,21339	0,46	16,715	1,11	0,5681	0,94	0,85	2931	15	2900	44	2919	21	1,08
044-ZR31	0,125	157120	47,26	0,20965	0,53	16,073	1,13	0,5560	0,92	0,82	2903	17	2850	42	2881	21	1,82
043-ZR30	0,258	77210	36,81	0,19035	0,79	10,841	1,86	0,4130	1,64	0,88	2745	26	2229	62	2510	34	18,81
042-ZR29	0,415	56331	31,00	0,20984	0,68	16,270	1,37	0,5623	1,14	0,83	2904	22	2876	53	2893	26	0,97
039-ZR28	0,303	79718	46,65	0,21023	1,08	16,230	2,10	0,5599	1,76	0,84	2907	35	2866	81	2890	40	1,41
038-ZR27	0,238	456441	15,09	0,20944	0,74	14,764	1,85	0,5112	1,66	0,89	2901	24	2662	72	2800	35	8,25
037-ZR26	0,174	122112	53,18	0,21831	1,28	16,445	2,14	0,5463	1,67	0,78	2968	41	2810	76	2903	40	5,34
036-ZR25	0,306	152044	41,54	0,21025	1,09	14,888	2,10	0,5135	1,75	0,84	2908	35	2672	77	2808	40	8,11
035-ZR24	0,172	196193	55,07	0,20127	0,57	13,374	1,44	0,4819	1,27	0,88	2837	19	2536	53	2706	27	10,61
034-ZR23	0,322	18639	14,93	0,20515	0,91	14,142	1,47	0,4999	1,10	0,75	2868	29	2614	47	2759	28	8,86
031-ZR22	0,394	316641	15,72	0,20519	0,81	13,617	1,44	0,4813	1,13	0,79	2868	26	2533	47	2723	27	11,68
028-ZR20	0,557	409625	15,84	0,21154	0,46	17,377	1,02	0,5957	0,83	0,81	2917	15	3013	40	2956	20	-3,27
026-ZR18	0,182	16561	6,91	0,19486	0,88	10,548	1,66	0,3926	1,35	0,82	2784	29	2135	49	2484	30	23,31
025-ZR17	0,228	9198	9,11	0,18758	0,96	8,824	3,35	0,3411	3,19	0,95	2721	31	1892	104	2320	60	30,46
023-ZR15	0,151	390068	65,19	0,21264	0,49	16,573	1,16	0,5652	0,98	0,85	2926	16	2888	46	2910	22	1,29

ADE-18P	Th/U	$^{206}Pb/^{204}Pb$	1s%	$^{207}Pb/^{206}Pb$	1s %	$^{207}Pb/^{235}U$	1s %	$^{206}Pb/^{238}U$	1s %	Rho	$^{207}Pb/^{206}Pb$	2s abs	$^{206}Pb/^{238}U$	2s abs	$^{207}Pb/^{235}U$	2s abs	% U-Pb disc[4]
022-ZR14	0,337	44218	14,37	0,21246	0,57	15,376	2,40	0,5248	2,30	0,96	2924	19	2720	102	2839	45	7,00
019-ZR13	0,515	369945	51,99	0,21232	1,06	15,835	1,47	0,5409	0,94	0,64	2923	34	2787	43	2867	28	4,66
018-ZR12	0,307	69758	73,55	0,21023	0,91	16,300	2,57	0,5623	2,38	0,92	2907	29	2876	110	2895	49	1,08
016-ZR10	0,360	658708	14,80	0,21120	0,40	16,680	0,98	0,5727	0,82	0,83	2915	13	2919	38	2917	19	-0,15
015-ZR9	0,343	61045	75,09	0,20462	1,24	14,781	1,95	0,5239	1,45	0,75	2863	40	2715	64	2801	37	5,17
014-ZR8	0,283	678856	37,25	0,20929	0,32	16,549	0,93	0,5734	0,79	0,85	2900	10	2922	37	2909	18	-0,76
013-ZR7	0,243	53197	69,31	0,20323	1,28	10,886	2,78	0,3885	2,44	0,88	2852	41	2116	88	2513	51	25,83
ADE-14	**Th/U**	$^{206}Pb/^{204}Pb$	**1s%**	$^{207}Pb/^{206}Pb$	**1s %**	$^{207}Pb/^{235}U$	**1s %**	$^{206}Pb/^{238}U$	**1s %**	**Rho**	$^{207}Pb/^{206}Pb$	**2s abs**	$^{206}Pb/^{238}U$	**2s abs**	$^{207}Pb/^{235}U$	**2s abs**	**% U-Pb disc[4]**
006-ZR2B	0,141	4473	4,89	0,13504	1,09	5,251	2,40	0,2820	2,11	0,88	2165	38	1601	60	1861	41	26,02
025-ZR9B	0,022	20097	9,57	0,12921	1,02	2,987	3,70	0,1677	3,54	0,96	2087	36	999	65	1404	56	52,13
054-ZR21C	0,152	3064	9,91	0,14416	1,95	6,256	4,53	0,3147	4,07	0,90	2278	66	1764	125	2012	78	22,55
048-ZR19C	0,220	8410	20,40	0,14083	0,96	6,656	1,71	0,3428	1,36	0,80	2237	33	1900	45	2067	30	15,08
042-ZR15C	0,171	132696	58,46	0,14276	0,35	7,156	1,13	0,3635	1,00	0,89	2261	12	1999	34	2131	20	11,59
035-ZR12C	0,214	3980	14,17	0,14231	1,54	6,413	3,60	0,3268	3,23	0,90	2255	53	1823	102	2034	62	19,18
031-ZR11C	0,566	9456	4,77	0,14151	0,36	7,498	0,74	0,3842	0,54	0,72	2246	12	2096	19	2173	13	6,67
024-ZR9C	0,123	13641	2,66	0,13289	0,28	4,524	3,62	0,2469	3,59	0,99	2137	10	1422	91	1735	59	33,43
017-ZR6C	0,194	6287	4,12	0,13964	0,20	5,764	3,55	0,2993	3,53	0,99	2223	7	1688	104	1941	61	24,05
009-ZR3C	0,408	1922	2,18	0,13595	1,39	3,949	3,69	0,2106	3,40	0,92	2176	48	1232	76	1624	59	43,38
034-ZR11B	0,553	5444	9,65	0,13888	1,74	7,433	2,56	0,3881	1,84	0,72	2213	60	2114	66	2165	45	4,47
043-ZR16C	0,045	131652	13,04	0,11790	1,07	2,752	1,99	0,1693	1,63	0,82	1925	38	1008	30	1343	29	47,61
023-ZR8C	0,323	261557	41,52	0,13545	0,38	6,560	1,08	0,3513	0,95	0,87	2170	13	1941	32	2054	19	10,56
019-ZR7C	0,127	3307	6,88	0,13174	0,35	5,980	2,39	0,3292	2,34	0,98	2121	12	1835	74	1973	41	13,52
055-ZR22C	0,076	18248	7,84	0,12881	0,46	6,118	0,82	0,3444	0,57	0,69	2082	16	1908	19	1993	14	8,35
018-ZR6B	0,056	25400	3,51	0,12707	0,63	4,494	2,13	0,2565	2,00	0,94	2058	22	1472	52	1730	35	28,48
004-ZR1C	0,267	93805	52,62	0,13390	0,66	6,789	1,11	0,3677	0,80	0,73	2150	23	2018	28	2084	19	6,11
010-ZR4C	1,598	20253	7,20	0,11891	0,22	4,011	2,05	0,2446	2,01	0,98	1940	8	1411	51	1636	33	27,28
049-ZR20C	0,758	28193	16,45	0,12087	0,38	3,960	1,78	0,2376	1,69	0,95	1969	14	1374	42	1626	29	30,21

ADE-18P	Th/U	$^{206}Pb/^{204}Pb$	1s%	$^{207}Pb/^{206}Pb$	1s %	$^{207}Pb/^{235}U$	1s %	$^{206}Pb/^{238}U$	1s %	Rho	$^{207}Pb/^{206}Pb$	2s abs	$^{206}Pb/^{238}U$	2s abs	$^{207}Pb/^{235}U$	2s abs	% U-Pb disc[4]
047-ZR18C	0,801	25475	7,01	0,12171	0,31	4,725	1,19	0,2815	1,09	0,91	1981	11	1599	31	1772	20	19,30
056-ZR23C	0,597	38465	18,81	0,12337	1,17	6,670	4,00	0,3921	3,80	0,95	2006	41	2133	137	2069	69	-6,33
053-ZR20B	0,140	14403	17,96	0,12207	1,16	5,779	1,55	0,3433	0,97	0,62	1987	41	1903	32	1943	27	4,23
022-ZR7B	0,050	31706	19,13	0,11818	0,53	5,334	0,91	0,3273	0,64	0,70	1929	19	1826	20	1874	16	5,36
016-ZR5B	0,069	4834	15,61	0,11932	0,93	5,266	1,40	0,3201	0,98	0,70	1946	33	1790	31	1863	24	8,01
011-ZR4B	0,814	21932	10,33	0,12131	0,21	5,509	1,08	0,3294	1,00	0,92	1976	7	1835	32	1902	19	7,10
ADE-01	**Th/U**	**$^{206}Pb/^{204}Pb$**	**1s%**	**$^{207}Pb/^{206}Pb$**	**1s %**	**$^{207}Pb/^{235}U$**	**1s %**	**$^{206}Pb/^{238}U$**	**1s %**	**Rho**	**$^{207}Pb/^{206}Pb$**	**2s abs**	**$^{206}Pb/^{238}U$**	**2s abs**	**$^{207}Pb/^{235}U$**	**2s abs**	**% U-Pb disc[4]**
040-ZR30	0,296	381622	17,60	0,14034	0,48	7,268	0,90	0,3756	0,67	0,74	2231	16	2056	23	2145	16	7,87
039-ZR29	0,231	1082334	20,69	0,13776	0,42	7,116	0,83	0,3746	0,61	0,74	2199	15	2051	21	2126	15	6,75
038-ZR28	0,249	91876	50,09	0,13690	1,22	6,782	4,61	0,3593	4,43	0,96	2188	42	1979	150	2083	80	9,58
036-ZR26	0,250	36404	11,16	0,13977	0,45	7,603	1,65	0,3945	1,55	0,94	2224	16	2144	56	2185	29	3,63
035-ZR25	0,238	233211	41,06	0,14190	0,32	7,818	0,78	0,3996	0,60	0,78	2251	11	2167	22	2210	14	3,71
034-ZR24	0,320	254306	51,91	0,13910	0,35	8,260	1,02	0,4306	0,89	0,87	2216	12	2309	34	2260	18	-4,17
033-ZR23	0,360	26958	13,64	0,14449	0,68	8,960	2,08	0,4497	1,93	0,93	2282	23	2394	77	2334	38	-4,92
030-ZR22	0,287	899720	33,09	0,13856	0,43	8,091	0,83	0,4235	0,60	0,73	2209	15	2276	23	2241	15	-3,03
029-ZR21	0,240	538490	19,91	0,14152	0,39	8,539	1,03	0,4376	0,88	0,85	2246	14	2340	34	2290	19	-4,19
028-ZR20	0,294	391993	28,04	0,14068	0,48	8,011	0,94	0,4129	0,71	0,76	2236	16	2228	27	2232	17	0,32
027-ZR19	0,257	959448	15,91	0,13993	0,32	7,510	0,92	0,3892	0,78	0,85	2226	11	2119	28	2174	16	4,81
026-ZR18	0,219	134394	39,61	0,13717	0,31	7,787	0,83	0,4117	0,67	0,81	2192	11	2223	25	2207	15	-1,41
024-ZR16	0,298	30256	16,18	0,13921	0,41	8,306	1,13	0,4327	0,99	0,87	2217	14	2318	38	2265	20	-4,53
020-ZR15	0,307	453954	18,28	0,13918	0,55	7,913	0,91	0,4123	0,62	0,68	2217	19	2225	23	2221	16	-0,38
017-ZR12	0,254	341344	56,77	0,14318	0,90	9,588	2,44	0,4856	2,24	0,92	2266	31	2552	94	2396	44	-12,61
016-ZR11	0,330	1208369	36,58	0,13970	0,30	8,261	1,17	0,4288	1,07	0,91	2223	10	2301	41	2260	21	-3,47
013-ZR8	0,180	180886	43,46	0,13864	0,71	8,889	1,83	0,4650	1,64	0,90	2210	24	2461	67	2327	33	-11,36
009-ZR6	0,137	8214	9,08	0,13798	0,99	6,744	2,09	0,3544	1,81	0,86	2202	34	1956	61	2078	37	11,18
008-ZR5	0,252	210724	29,58	0,14460	0,99	9,082	2,86	0,4555	2,65	0,93	2283	34	2420	107	2346	52	-5,99
007-ZR4	0,291	1014628	21,99	0,13946	0,33	8,325	1,20	0,4329	1,09	0,91	2220	11	2319	42	2267	22	-4,43

ADE-18P	Th/U	$^{206}Pb/^{204}Pb$	1s%	$^{207}Pb/^{206}Pb$	1s %	$^{207}Pb/^{235}U$	1s %	$^{206}Pb/^{238}U$	1s %	Rho	$^{207}Pb/^{206}Pb$	2s abs	$^{206}Pb/^{238}U$	2s abs	$^{207}Pb/^{235}U$	2s abs	% U-Pb disc[4]
005-ZR2	0,208	768275	22,37	0,13753	0,35	6,998	1,06	0,3690	0,93	0,88	2196	12	2025	32	2111	19	7,82
004-ZR1	0,219	830003	28,37	0,14000	0,31	7,541	1,05	0,3906	0,94	0,89	2227	11	2126	34	2178	19	4,55
ADE-03	**Th/U**	**$^{206}Pb/^{204}Pb$**	**1s%**	**$^{207}Pb/^{206}Pb$**	**1s %**	**$^{207}Pb/^{235}U$**	**1s %**	**$^{206}Pb/^{238}U$**	**1s %**	**Rho**	**$^{207}Pb/^{206}Pb$**	**2s abs**	**$^{206}Pb/^{238}U$**	**2s abs**	**$^{207}Pb/^{235}U$**	**2s abs**	**% U-Pb disc[4]**
048-ZR35	0,451	347850	23,94	0,21804	0,60	18,519	1,18	0,6159	0,94	0,80	2966	19	3094	46	3017	23	-4,30
016-ZR11	0,939	439991	21,83	0,21527	0,56	18,233	1,17	0,6143	0,95	0,82	2946	18	3087	47	3002	22	-4,80
036-ZR26	0,084	522000	29,84	0,17925	0,61	11,269	1,21	0,4559	0,97	0,81	2646	20	2421	39	2546	22	8,48
049-ZR36	0,307	1687	5,25	0,11017	0,81	2,186	1,26	0,1439	0,90	0,71	1802	29	867	15	1176	17	51,92
047-ZR34	0,513	11990	39,56	0,12526	0,81	4,486	1,56	0,2597	1,27	0,82	2032	29	1488	34	1728	26	26,77
046-ZR33	0,429	913	4,11	0,12951	0,72	5,622	1,20	0,3148	0,89	0,74	2091	25	1764	27	1919	21	15,64
044-ZR31	0,242	1030	3,18	0,10665	0,87	1,891	1,33	0,1286	0,94	0,70	1743	32	780	14	1078	18	55,26
040-ZR30	0,223	938	2,10	0,09261	1,04	1,341	1,61	0,1050	1,16	0,72	1480	39	644	14	864	19	56,51
037-ZR27	0,368	1414	4,20	0,10294	0,90	1,995	1,47	0,1406	1,11	0,75	1678	33	848	18	1114	20	49,46
035-ZR25	0,150	909	2,50	0,09283	1,29	1,485	1,64	0,1160	0,94	0,57	1484	49	707	13	924	20	52,34
034-ZR24	0,092	851	2,77	0,10330	1,10	1,608	2,00	0,1129	1,63	0,81	1684	40	690	21	973	25	59,06
029-ZR21	0,214	736	2,33	0,08279	1,27	1,159	1,76	0,1015	1,15	0,66	1264	49	623	14	782	19	50,69
028-ZR20	0,171	536	4,57	0,08062	0,94	1,108	1,88	0,0997	1,59	0,84	1212	37	613	19	757	20	49,46
027-ZR19	0,193	1739	4,40	0,10963	0,77	2,429	1,22	0,1607	0,86	0,71	1793	28	961	15	1251	17	46,43
026-ZR18	0,222	569	1,93	0,12213	0,69	2,676	1,41	0,1589	1,17	0,83	1988	25	951	21	1322	21	52,16
024-ZR16	0,182	733	3,03	0,12700	0,97	3,310	1,48	0,1890	1,06	0,71	2057	34	1116	22	1483	23	45,74
020-ZR15	0,047	1654	4,76	0,10172	1,71	2,057	2,26	0,1466	1,43	0,63	1656	63	882	24	1135	31	46,73
019-ZR14	0,146	831	4,37	0,09529	1,67	1,546	2,33	0,1177	1,57	0,68	1534	62	717	21	949	29	53,24
018-ZR13	0,224	654	2,89	0,09487	1,49	1,421	1,85	0,1086	1,03	0,56	1525	56	665	13	898	22	56,43
015-ZR10	0,123	583	2,03	0,09450	0,92	1,293	1,48	0,0992	1,09	0,74	1518	35	610	13	842	17	59,84
010-ZR7	0,129	872	2,25	0,08003	1,35	1,135	2,00	0,1029	1,43	0,71	1198	53	631	17	770	22	47,30
009-ZR6	0,190	723	2,23	0,09095	1,16	1,307	1,68	0,1042	1,16	0,69	1446	44	639	14	849	19	55,80
007-ZR4C	0,224	858	5,48	0,08810	1,43	1,383	2,29	0,1139	1,75	0,76	1385	54	695	23	882	27	49,80
005-ZR2	0,168	553	3,09	0,10123	1,47	1,770	2,10	0,1268	1,46	0,70	1647	54	770	21	1035	27	53,27

ADE-18P	Th/U	$^{206}Pb/^{204}Pb$	1s%	$^{207}Pb/^{206}Pb$	1s %	$^{207}Pb/^{235}U$	1s %	$^{206}Pb/^{238}U$	1s %	Rho	$^{207}Pb/^{206}Pb$	2s abs	$^{206}Pb/^{238}U$	2s abs	$^{207}Pb/^{235}U$	2s abs	% U-Pb disc[4]
004-ZR1	0,272	1266	6,03	0,10897	0,86	2,197	1,62	0,1462	1,33	0,82	1782	31	880	22	1180	23	50,63
038-ZR28	0,192	1108	2,28	0,10360	1,24	2,076	1,69	0,1454	1,09	0,64	1690	45	875	18	1141	23	48,22
027-ZR19	0,087	871	3,01	0,08427	0,87	1,164	1,28	0,1002	0,87	0,68	1299	34	615	10	784	14	52,62
019-ZR14	0,126	2574	6,54	0,11427	1,57	2,656	2,29	0,1686	1,62	0,71	1868	56	1004	30	1316	34	46,25
010-ZR7	0,268	623	1,02	0,11041	1,04	2,021	1,88	0,1327	1,52	0,81	1806	38	803	23	1122	25	55,52
009-ZR6	0,278	1020	2,22	0,12567	0,95	3,175	2,14	0,1832	1,88	0,88	2038	33	1085	37	1451	33	46,79
008-ZR5	0,222	1824	6,78	0,11941	0,74	2,844	1,47	0,1727	1,22	0,83	1947	26	1027	23	1367	22	47,26
017-ZR12	0,129	1773	7,61	0,06483	0,78	0,922	1,32	0,1031	1,00	0,76	769	33	633	12	663	13	17,72
006-ZR3	0,031	11445	12,27	0,05971	0,41	0,868	1,24	0,1054	1,11	0,90	593	18	646	14	634	12	-8,89
ADE-04	**Th/U**	**$^{206}Pb/^{204}Pb$**	**1s%**	**$^{207}Pb/^{206}Pb$**	**1s %**	**$^{207}Pb/^{235}U$**	**1s %**	**$^{206}Pb/^{238}U$**	**1s %**	**Rho**	**$^{207}Pb/^{206}Pb$**	**2s abs**	**$^{206}Pb/^{238}U$**	**2s abs**	**$^{207}Pb/^{235}U$**	**2s abs**	**% U-Pb disc[4]**
040-ZR30	0,452	21283	34,70	0,14264	0,89	6,620	2,19	0,3366	1,96	0,90	2260	31	1870	64	2062	38	17,23
039-ZR29	0,477	111175	16,41	0,13948	0,88	7,321	1,65	0,3807	1,35	0,82	2221	30	2079	48	2151	29	6,36
037-ZR27	0,345	38881	41,49	0,13990	0,51	6,901	1,26	0,3577	1,09	0,87	2226	18	1971	37	2099	22	11,44
036-ZR26	0,438	53534	21,31	0,14123	0,74	7,871	1,43	0,4042	1,16	0,81	2242	25	2188	43	2216	26	2,41
035-ZR25	0,448	46891	25,24	0,14072	0,78	7,912	1,46	0,4078	1,18	0,81	2236	27	2205	44	2221	26	1,41
034-ZR24	0,504	43181	26,58	0,14390	1,04	5,833	2,09	0,2940	1,77	0,85	2275	36	1661	52	1951	36	26,96
033-ZR23	0,373	65054	15,15	0,14131	0,87	7,598	1,55	0,3899	1,23	0,79	2243	30	2123	44	2185	28	5,39
030-ZR22	0,460	70544	17,08	0,14075	0,98	7,876	1,70	0,4058	1,34	0,79	2236	34	2196	50	2217	30	1,83
029-ZR21	0,382	38777	20,03	0,14381	0,92	7,371	1,69	0,3717	1,37	0,81	2274	32	2037	48	2157	30	10,39
028-ZR20	0,470	46557	22,05	0,14040	0,93	7,724	1,74	0,3990	1,43	0,82	2232	32	2164	52	2199	31	3,04
027-ZR19	0,441	68794	18,62	0,13869	0,90	7,915	1,58	0,4139	1,25	0,79	2211	31	2233	47	2221	28	-0,99
026-ZR18	0,454	101551	19,21	0,13844	0,77	7,178	1,33	0,3760	1,01	0,76	2208	27	2058	36	2134	23	6,80
025-ZR17	0,414	71234	15,80	0,14031	0,86	7,764	1,41	0,4013	1,05	0,75	2231	30	2175	39	2204	25	2,51
024-ZR16	0,443	84890	17,19	0,13989	0,96	7,562	1,65	0,3920	1,28	0,78	2226	33	2132	46	2180	29	4,20
019-ZR14	0,433	78300	15,03	0,14267	0,81	7,889	1,41	0,4010	1,09	0,77	2260	28	2174	40	2218	25	3,82
018-ZR13	0,401	74715	42,26	0,14234	0,76	7,865	1,38	0,4007	1,09	0,79	2256	26	2172	40	2216	25	3,70
016-ZR11	0,452	25176	27,84	0,14035	1,02	8,630	2,14	0,4459	1,84	0,86	2232	35	2377	73	2300	39	-6,52

ADE-18P	Th/U	$^{206}Pb/^{204}Pb$	1s%	$^{207}Pb/^{206}Pb$	1s %	$^{207}Pb/^{235}U$	1s %	$^{206}Pb/^{238}U$	1s %	Rho	$^{207}Pb/^{206}Pb$	2s abs	$^{206}Pb/^{238}U$	2s abs	$^{207}Pb/^{235}U$	2s abs	% U-Pb disc[4]
015-ZR10	0,500	51394	20,82	0,14082	0,91	8,279	1,57	0,4264	1,22	0,78	2237	31	2289	47	2262	28	-2,32
014-ZR9	0,392	78392	15,35	0,13985	0,96	7,378	1,66	0,3826	1,30	0,78	2225	33	2088	46	2158	29	6,15
013-ZR8	0,439	62390	19,86	0,14073	0,99	7,994	1,70	0,4119	1,32	0,78	2236	34	2224	50	2230	30	0,55
010-ZR7	0,464	56565	17,13	0,14140	0,99	7,869	1,57	0,4036	1,17	0,74	2244	34	2186	43	2216	28	2,62
009-ZR6	0,416	45606	24,38	0,14338	0,95	6,963	1,59	0,3522	1,22	0,77	2268	33	1945	41	2107	28	14,26
005-ZR2	0,500	104354	21,50	0,14256	0,52	8,181	0,98	0,4162	0,74	0,76	2259	18	2243	28	2251	18	0,69
004-ZR1	0,434	67032	24,72	0,14154	0,65	8,148	1,15	0,4175	0,88	0,76	2246	22	2249	33	2248	21	-0,13
ADE-13	**Th/U**	$^{206}Pb/^{204}Pb$	**1s%**	$^{207}Pb/^{206}Pb$	**1s %**	$^{207}Pb/^{235}U$	**1s %**	$^{206}Pb/^{238}U$	**1s %**	**Rho**	$^{207}Pb/^{206}Pb$	**2s abs**	$^{206}Pb/^{238}U$	**2s abs**	$^{207}Pb/^{235}U$	**2s abs**	**% U-Pb disc[4]**
039-ZR2	0,211	80860	37,18	0,06060	0,82	0,846	1,29	0,1012	0,92	0,71	625	35	622	11	622	12	0,54
038-ZR3	0,318	5609	11,75	0,06254	0,80	0,843	1,33	0,0978	0,99	0,75	693	34	601	11	621	12	13,19
037-ZR4	0,179	7916	32,47	0,06213	0,66	0,837	1,14	0,0977	0,85	0,75	678	28	601	10	617	11	11,47
036-ZR20	0,302	37373	52,70	0,06107	0,87	0,817	1,91	0,0970	1,66	0,87	642	37	597	19	606	17	7,01
035-ZR18	0,160	1152	5,99	0,06987	1,22	0,927	1,66	0,0962	1,07	0,64	925	50	592	12	666	16	35,95
033-ZR8	0,310	5891	45,28	0,06843	1,13	0,879	1,81	0,0932	1,36	0,75	882	46	574	15	641	17	34,84
030-ZR30	0,310	53654	37,02	0,06057	0,76	0,849	1,27	0,1017	0,95	0,75	624	33	624	11	624	12	-0,03
027-ZR24	0,161	178753	17,84	0,05969	0,55	0,839	1,06	0,1019	0,83	0,78	592	24	626	10	619	10	-5,67
026-ZR15	0,405	158887	22,89	0,05993	0,57	0,828	1,08	0,1002	0,84	0,78	601	25	615	10	612	10	-2,39
024-ZR21	0,210	14909	52,20	0,06910	0,50	0,909	1,07	0,0954	0,87	0,81	902	21	588	10	657	10	34,82
019-ZR7	0,121	795809	94,54	0,06010	0,72	0,802	1,41	0,0968	1,15	0,82	607	31	595	13	598	13	1,95
016-ZR41	0,325	1759	9,53	0,06275	1,10	0,877	1,43	0,1014	0,83	0,58	700	47	623	10	640	13	11,03
015-ZR40	0,237	1976	3,69	0,06968	0,67	0,952	1,18	0,0991	0,90	0,76	919	27	609	10	679	12	33,72
014-ZR39	0,236	4206	6,86	0,06450	0,88	0,900	1,31	0,1012	0,89	0,68	758	37	621	11	652	13	18,02
013-ZR38	0,303	57614	20,96	0,05969	0,89	0,809	1,43	0,0983	1,06	0,74	592	38	604	12	602	13	-2,00
010-ZR37	0,320	1099	5,67	0,06728	1,27	0,861	1,70	0,0928	1,06	0,63	846	52	572	12	630	16	32,44
008-ZR35	0,252	2118	4,64	0,06724	1,08	0,921	1,46	0,0993	0,92	0,63	845	45	610	11	663	14	27,78
ADE-06	**Th/U**	$^{206}Pb/^{204}Pb$	**1s%**	$^{207}Pb/^{206}Pb$	**1s %**	$^{207}Pb/^{235}U$	**1s %**	$^{206}Pb/^{238}U$	**1s %**	**Rho**	$^{207}Pb/^{206}Pb$	**2s abs**	$^{206}Pb/^{238}U$	**2s abs**	$^{207}Pb/^{235}U$	**2s abs**	**% U-Pb disc[4]**
048-ZR29C	0,325	99503	25,92	0,13997	0,64	7,556	1,34	0,3915	1,11	0,83	2227	22	2130	40	2180	24	4,36

ADE-18P	Th/U	$^{206}Pb/^{204}Pb$	1s%	$^{207}Pb/^{206}Pb$	1s %	$^{207}Pb/^{235}U$	1s %	$^{206}Pb/^{238}U$	1s %	Rho	$^{207}Pb/^{206}Pb$	2s abs	$^{206}Pb/^{238}U$	2s abs	$^{207}Pb/^{235}U$	2s abs	% U-Pb disc[4]
047-ZR28B	0,195	81859	37,42	0,13502	1,31	6,781	1,76	0,3642	1,12	0,64	2164	45	2002	39	2083	31	7,49
045-ZR27B	0,223	135278	17,38	0,13704	0,83	7,486	1,42	0,3961	1,10	0,77	2190	29	2151	40	2171	25	1,78
044-ZR27C	0,373	41935	32,07	0,13929	0,62	7,661	1,20	0,3989	0,96	0,80	2218	21	2164	35	2192	21	2,45
043-ZR26C	0,249	108736	28,47	0,13805	1,17	6,967	1,90	0,3660	1,44	0,76	2203	41	2010	50	2107	33	8,74
040-ZR25C	0,191	81962	18,21	0,13868	0,79	7,612	1,34	0,3981	1,02	0,76	2211	27	2160	37	2186	24	2,28
039-ZR24B	0,277	204694	18,81	0,13588	0,63	7,397	1,28	0,3948	1,05	0,82	2175	22	2145	38	2161	23	1,38
038-ZR24C	0,269	96497	27,29	0,13619	1,23	7,362	1,62	0,3920	0,99	0,61	2179	43	2132	36	2156	29	2,16
037-ZR23C	0,250	68111	19,36	0,13905	0,77	7,471	1,28	0,3896	0,96	0,75	2215	27	2121	35	2169	23	4,26
035-ZR21C	0,263	44681	23,72	0,14025	0,80	6,919	1,80	0,3578	1,57	0,87	2230	27	1972	53	2101	32	11,60
030-ZR19C	0,248	30623	23,72	0,13972	0,86	7,406	1,35	0,3844	0,97	0,72	2224	30	2097	35	2162	24	5,71
028-ZR17C	0,337	81738	20,33	0,13988	0,71	7,709	1,21	0,3997	0,91	0,75	2226	25	2168	33	2198	22	2,61
027-ZR16C	0,321	512879	83,58	0,13895	0,64	7,629	1,14	0,3982	0,86	0,76	2214	22	2161	32	2188	20	2,42
026-ZR15C	0,277	96740	19,72	0,13655	0,71	6,713	1,17	0,3565	0,86	0,73	2184	25	1966	29	2074	21	9,99
025-ZR14C	0,267	57299	17,06	0,13931	0,89	7,372	1,37	0,3838	0,97	0,71	2219	31	2094	35	2158	24	5,62
023-ZR12C	0,318	139316	36,71	0,13680	0,70	7,024	1,27	0,3723	0,99	0,78	2187	24	2040	35	2114	22	6,71
020-ZR11C	0,450	119450	23,29	0,13672	0,77	7,367	1,37	0,3908	1,07	0,78	2186	27	2126	39	2157	24	2,73
019-ZR10C	0,147	60973	71,11	0,12844	1,63	5,084	2,47	0,2870	1,81	0,73	2077	57	1627	52	1833	41	21,67
014-ZR5B	0,141	422608	30,55	0,13461	0,71	7,237	1,28	0,3899	1,00	0,78	2159	25	2122	36	2141	23	1,69
013-ZR5C	0,284	166987	19,38	0,13673	0,86	6,995	1,44	0,3710	1,09	0,76	2186	30	2034	38	2111	25	6,94
010-ZR4B	0,122	4565	7,42	0,13577	1,07	6,585	1,45	0,3517	0,90	0,62	2174	37	1943	30	2057	25	10,63
009-ZR4C	0,313	4246	9,95	0,13883	1,13	7,471	1,49	0,3903	0,90	0,60	2213	39	2124	33	2170	27	4,00
007-ZR3C	0,371	229858	15,30	0,13926	0,55	7,789	1,08	0,4056	0,85	0,79	2218	19	2195	32	2207	19	1,04
006-ZR2C	0,272	66946	18,13	0,13905	0,75	7,249	1,16	0,3781	0,81	0,70	2215	26	2067	29	2143	21	6,68
005-ZR1B	0,208	188855	19,22	0,13623	0,67	7,247	1,13	0,3858	0,83	0,74	2180	23	2103	30	2142	20	3,51
004-ZR1C	0,291	156507	38,29	0,13863	0,65	7,476	1,12	0,3911	0,83	0,74	2210	23	2128	30	2170	20	3,72
AT-25	**Th/U**	**$^{206}Pb/^{204}Pb$**	**1s%**	**$^{207}Pb/^{206}Pb$**	**1s %**	**$^{207}Pb/^{235}U$**	**1s %**	**$^{206}Pb/^{238}U$**	**1s %**	**Rho**	**$^{207}Pb/^{206}Pb$**	**2s abs**	**$^{206}Pb/^{238}U$**	**2s abs**	**$^{207}Pb/^{235}U$**	**2s abs**	**% U-Pb disc[4]**
066-ZR31C	0,358	928541	20,44	0,17561	0,27	10,889	0,98	0,4497	0,87	0,88	2612	9	2394	35	2514	18	8,35

ADE-18P	Th/U	$^{206}Pb/^{204}Pb$	1s%	$^{207}Pb/^{206}Pb$	1s %	$^{207}Pb/^{235}U$	1s %	$^{206}Pb/^{238}U$	1s %	Rho	$^{207}Pb/^{206}Pb$	2s abs	$^{206}Pb/^{238}U$	2s abs	$^{207}Pb/^{235}U$	2s abs	% U-Pb disc[4]
064-ZR29C	0,357	1000385	76,74	0,18224	0,37	12,210	0,91	0,4859	0,74	0,82	2673	12	2553	31	2621	17	4,51
068-ZR33C	0,339	425556	16,94	0,18421	0,30	13,078	0,68	0,5148	0,49	0,72	2691	10	2677	22	2685	13	0,52
029-ZR13A	0,264	236283	14,55	0,18541	0,46	13,066	1,70	0,5111	1,60	0,94	2702	15	2661	69	2684	32	1,51
027-ZR12C	0,334	375771	22,00	0,18518	0,32	13,024	0,69	0,5100	0,48	0,70	2700	11	2657	21	2681	13	1,60
006-ZR3C	0,096	460040	19,09	0,17167	0,29	10,348	0,85	0,4372	0,71	0,83	2574	10	2338	28	2466	16	9,17
008-ZR4B	0,146	317287	23,83	0,18186	0,73	12,104	1,01	0,4827	0,59	0,59	2670	24	2539	25	2612	19	4,91
048-ZR22C	0,357	218546	11,26	0,18201	0,41	13,732	1,30	0,5471	1,18	0,91	2671	14	2813	54	2731	25	-5,31
046-ZR21C	0,304	149488	17,54	0,18070	0,36	13,111	1,76	0,5262	1,69	0,96	2659	12	2725	75	2688	33	-2,48
047-ZR21B	0,060	8800	12,15	0,16482	1,12	7,818	1,63	0,3440	1,12	0,69	2506	37	1906	37	2210	29	23,94
056-ZR26A	0,190	32820	57,04	0,17686	0,67	10,126	1,29	0,4152	1,03	0,80	2624	22	2239	39	2446	24	14,67
007-ZR4C	0,340	52843	6,68	0,17851	0,28	11,844	0,75	0,4812	0,59	0,79	2639	9	2532	25	2592	14	4,04
039-ZR18C	0,411	343714	19,39	0,17946	0,38	11,843	1,54	0,4786	1,44	0,94	2648	13	2521	60	2592	29	4,79
050-ZR23C	0,450	662905	16,92	0,17827	0,44	12,905	1,41	0,5250	1,29	0,91	2637	14	2720	57	2673	26	-3,16
038-ZR17C	0,429	584504	23,46	0,17297	0,34	12,461	1,20	0,5224	1,09	0,91	2587	11	2710	48	2640	22	-4,75
020-ZR10C	0,255	663970	43,22	0,17398	0,51	12,053	0,87	0,5024	0,60	0,69	2596	17	2624	26	2609	16	-1,08
036-ZR16C	0,337	796798	57,84	0,17345	0,36	11,777	0,95	0,4924	0,80	0,84	2591	12	2581	34	2587	18	0,39
054-ZR24C	0,085	9809	3,27	0,17208	0,26	9,751	1,66	0,4109	1,60	0,96	2578	9	2219	60	2412	30	13,92
014-ZR7C	0,254	365791	26,81	0,16898	0,36	10,346	1,23	0,4440	1,11	0,91	2548	12	2369	44	2466	23	7,03
065-ZR30C	0,038	298080	34,85	0,17265	0,42	7,359	1,33	0,3091	1,20	0,91	2584	14	1736	37	2156	24	32,79
018-ZR9C	0,476	3450	6,70	0,17307	0,29	6,052	1,45	0,2536	1,37	0,95	2588	10	1457	36	1983	25	43,69
009-ZR5C	0,409	957	3,98	0,16425	1,02	2,421	2,66	0,1069	2,43	0,91	2500	34	655	30	1249	38	73,81
034-ZR15A	0,213	167737	17,16	0,16174	0,82	10,313	3,27	0,4624	3,14	0,96	2474	28	2450	127	2463	60	0,97
010-ZR5B	0,257	5306	8,01	0,16035	0,64	9,107	2,92	0,4119	2,83	0,97	2459	22	2223	106	2349	53	9,59
005-ZR2C	0,219	40430	15,75	0,15944	1,13	5,530	4,72	0,2515	4,57	0,97	2450	38	1446	118	1905	80	40,95
016-ZR8C	0,121	80596	37,81	0,16070	0,63	7,366	1,59	0,3324	1,41	0,89	2463	21	1850	45	2157	28	24,89
033-ZR14C	0,182	643488	18,84	0,14216	1,54	8,020	2,36	0,4091	1,75	0,74	2254	53	2211	65	2233	42	1,90
049-ZR22B	0,147	498791	16,10	0,14312	0,84	7,637	2,30	0,3870	2,11	0,92	2265	29	2109	76	2189	41	6,91
053-ZR23B	0,003	620037	16,50	0,13128	0,35	7,045	0,76	0,3892	0,56	0,74	2115	12	2119	20	2117	13	-0,18

ADE-18P	Th/U	$^{206}Pb/^{204}Pb$	1s%	$^{207}Pb/^{206}Pb$	1s %	$^{207}Pb/^{235}U$	1s %	$^{206}Pb/^{238}U$	1s %	Rho	$^{207}Pb/^{206}Pb$	2s abs	$^{206}Pb/^{238}U$	2s abs	$^{207}Pb/^{235}U$	2s abs	% U-Pb disc[4]
069-ZR33B	0,019	88593	51,88	0,13119	0,62	7,045	1,01	0,3894	0,70	0,70	2114	22	2120	25	2117	18	-0,30
026-ZR11B	0,002	620703	21,19	0,13131	0,30	6,710	0,67	0,3706	0,47	0,70	2115	11	2032	16	2074	12	3,94
019-ZR9B	0,003	508731	28,08	0,12995	0,35	6,527	1,01	0,3643	0,88	0,86	2097	12	2002	30	2050	18	4,53
017-ZR8B	0,062	715990	13,78	0,12109	0,63	5,218	0,91	0,3125	0,55	0,60	1972	22	1753	17	1856	16	11,11
028-ZR12B	0,003	674053	19,11	0,12056	0,34	5,608	0,72	0,3373	0,52	0,72	1965	12	1874	17	1917	12	4,61
040-ZR18B	0,002	894736	12,34	0,12681	0,32	6,683	0,99	0,3822	0,86	0,87	2054	11	2086	31	2070	17	-1,57
AT-02	**Th/U**	**$^{206}Pb/^{204}Pb$**	**1s%**	**$^{207}Pb/^{206}Pb$**	**1s %**	**$^{207}Pb/^{235}U$**	**1s %**	**$^{206}Pb/^{238}U$**	**1s %**	**Rho**	**$^{207}Pb/^{206}Pb$**	**2s abs**	**$^{206}Pb/^{238}U$**	**2s abs**	**$^{207}Pb/^{235}U$**	**2s abs**	**% U-Pb disc[4]**
019-ZR10C	**0,269**	**143070**	**18,11**	**0,18656**	**0,94**	**13,644**	**2,75**	**0,5304**	**2,56**	**0,93**	**2712**	**31**	**2743**	**114**	**2725**	**51**	**-1,15**
018-ZR9C	0,014	14180	14,75	0,15559	2,36	10,093	3,58	0,4704	2,66	0,74	2408	79	2486	109	2443	65	-3,21
016-ZR7B	0,155	205078	52,51	0,12250	1,29	5,272	3,60	0,3121	3,34	0,93	1993	45	1751	102	1864	61	12,13
015-ZR7C	0,032	113935	9,10	0,12671	1,80	5,064	3,80	0,2898	3,32	0,87	2053	63	1641	96	1830	63	20,07
014-ZR6C	0,200	780253	15,15	0,16685	0,62	10,743	1,25	0,4669	1,02	0,82	2526	21	2470	42	2501	23	2,23
010-ZR5B	0,213	67131	60,10	0,16470	0,45	9,747	2,11	0,4292	2,03	0,96	2504	15	2302	78	2411	39	8,08
009-ZR5C	0,142	59918	74,47	0,16638	1,74	7,395	2,92	0,3223	2,32	0,79	2522	58	1801	73	2160	52	28,57
008-ZR4B	0,002	491095	22,11	0,12318	0,32	5,047	0,98	0,2971	0,85	0,87	2003	11	1677	25	1827	17	16,26
007-ZR4C	0,031	147447	33,17	0,12947	0,97	3,799	1,69	0,2128	1,33	0,79	2091	34	1244	30	1593	27	40,51
006-ZR3	0,047	1302231	45,92	0,15273	0,38	8,599	0,99	0,4083	0,83	0,84	2377	13	2207	31	2296	18	7,13
004-ZR1	0,242	260720	19,75	0,17271	0,86	10,747	1,76	0,4513	1,49	0,85	2584	29	2401	60	2501	33	7,09
AP-09	**Th/U**	**$^{206}Pb/^{204}Pb$**	**1s%**	**$^{207}Pb/^{206}Pb$**	**1s %**	**$^{207}Pb/^{235}U$**	**1s %**	**$^{206}Pb/^{238}U$**	**1s %**	**Rho**	**$^{207}Pb/^{206}Pb$**	**2s abs**	**$^{206}Pb/^{238}U$**	**2s abs**	**$^{207}Pb/^{235}U$**	**2s abs**	**% U-Pb disc[4]**
036-ZR27C	0,538	76571	13,15	0,14656	0,74	8,662	1,37	0,4286	1,09	0,80	2306	25	2300	42	2303	25	0,28
035-ZR26C	0,472	102687	48,21	0,13409	0,33	7,000	1,10	0,3786	0,98	0,89	2152	11	2070	35	2111	19	3,84
034-ZR25C	0,414	71321	15,04	0,14820	0,55	8,579	1,09	0,4198	0,87	0,80	2325	19	2260	33	2294	20	2,82
031-ZR22C	0,383	51332	17,72	0,14637	0,99	8,163	1,60	0,4045	1,20	0,75	2304	34	2190	45	2249	29	4,97
028-ZR21C	0,477	48922	19,83	0,14751	0,96	8,413	1,47	0,4136	1,05	0,72	2317	33	2231	40	2277	27	3,70
027-ZR20C	0,109	1602	12,32	0,15495	1,09	8,189	1,83	0,3833	1,42	0,78	2401	37	2092	51	2252	33	12,89
024-ZR17C	0,484	68106	12,89	0,14677	0,83	7,841	1,50	0,3874	1,19	0,79	2309	28	2111	43	2213	27	8,57
022-ZR15C	0,521	76023	19,34	0,14735	0,76	8,204	1,45	0,4038	1,17	0,81	2315	26	2186	43	2254	26	5,57
019-ZR14C	0,417	24501	28,41	0,15159	1,27	9,003	1,92	0,4307	1,39	0,72	2364	43	2309	54	2338	35	2,33

ADE-18P	Th/U	$^{206}Pb/^{204}Pb$	1s%	$^{207}Pb/^{206}Pb$	1s %	$^{207}Pb/^{235}U$	1s %	$^{206}Pb/^{238}U$	1s %	Rho	$^{207}Pb/^{206}Pb$	2s abs	$^{206}Pb/^{238}U$	2s abs	$^{207}Pb/^{235}U$	2s abs	% U-Pb disc[4]
017-ZR12C	0,546	2471	8,83	0,14897	0,83	7,320	1,71	0,3563	1,45	0,85	2334	28	1965	49	2151	30	15,83
016-ZR11C	0,519	48069	23,06	0,14921	0,63	8,615	1,02	0,4187	0,71	0,69	2337	22	2255	27	2298	18	3,51
015-ZR10C	0,510	111994	70,91	0,14834	1,03	7,916	1,56	0,3870	1,11	0,71	2327	35	2109	40	2222	28	9,36
014-ZR9C	0,608	33809	28,59	0,14569	1,16	8,325	1,95	0,4144	1,53	0,78	2296	39	2235	58	2267	35	2,66
013-ZR8B	0,643	118847	12,90	0,14852	0,53	8,758	1,05	0,4277	0,82	0,79	2329	18	2295	32	2313	19	1,45
012-ZR8C	0,685	164932	13,39	0,14687	0,55	7,698	1,72	0,3801	1,59	0,92	2310	19	2077	56	2196	31	10,09
010-ZR7C	0,435	50822	21,95	0,14756	0,67	9,142	1,25	0,4493	0,99	0,79	2318	23	2392	40	2352	23	-3,20
008-ZR5C	0,473	63789	14,38	0,14408	0,82	8,142	1,44	0,4098	1,12	0,78	2277	28	2214	42	2247	26	2,76
006-ZR3C	0,349	6368	36,82	0,14000	1,00	5,546	2,47	0,2873	2,23	0,90	2227	34	1628	64	1908	42	26,90
005-ZR2C	0,523	33795	33,78	0,14828	0,85	8,117	1,31	0,3970	0,92	0,70	2326	29	2155	34	2244	24	7,35
004-ZR1C	0,520	95915	44,00	0,14639	0,57	8,054	1,24	0,3990	1,04	0,84	2304	20	2164	38	2237	22	6,07
AP-22	**Th/U**	**$^{206}Pb/^{204}Pb$**	**1s%**	**$^{207}Pb/^{206}Pb$**	**1s %**	**$^{207}Pb/^{235}U$**	**1s %**	**$^{206}Pb/^{238}U$**	**1s %**	**Rho**	**$^{207}Pb/^{206}Pb$**	**2s abs**	**$^{206}Pb/^{238}U$**	**2s abs**	**$^{207}Pb/^{235}U$**	**2s abs**	**% U-Pb disc[4]**
049-ZR22C	0,378	178606	38,16	0,18841	3,45	7,674	3,83	0,2954	1,63	0,42	2728	111	1668	48	2194	68	38,85
048-ZR21B	0,307	10406	14,75	0,20980	1,98	7,878	9,62	0,2723	9,40	0,98	2904	63	1553	257	2217	166	46,54
047-ZR21C	0,396	3364	6,14	0,19679	2,47	9,532	7,89	0,3513	7,48	0,95	2800	80	1941	248	2391	140	30,69
046-ZR20B	0,168	3614	7,80	0,18478	0,79	2,243	12,08	0,0880	12,05	1,00	2696	26	544	125	1195	163	79,83
045-ZR20C	0,313	1748	8,05	0,17656	0,90	1,876	9,12	0,0771	9,07	0,99	2621	30	479	83	1073	117	81,74
039-ZR18B	0,168	5158	10,40	0,20793	3,04	5,444	8,93	0,1899	8,39	0,94	2890	97	1121	172	1892	148	61,21
038-ZR18C	0,445	4501	11,45	0,20102	1,40	8,455	8,70	0,3050	8,57	0,99	2834	45	1716	256	2281	152	39,45
037-ZR17C	0,233	73962	25,05	0,19630	1,02	7,925	10,94	0,2928	10,89	1,00	2796	33	1655	314	2222	188	40,79
026-ZR11B	0,263	1535	12,01	0,21815	1,96	1,854	35,50	0,0616	35,44	1,00	2967	63	386	263	1065	421	87,00
018-ZR8B	0,129	2461	13,32	0,19954	1,43	0,123	126,47	0,0045	126,46	1,00	2822	46	29	72	118	264	98,98
016-ZR7B	0,225	3040	40,80	0,21004	1,97	6,501	8,04	0,2245	7,79	0,97	2906	63	1305	183	2046	137	55,07
009-ZR5C	0,306	7273	10,77	0,20366	1,18	7,050	6,86	0,2510	6,75	0,98	2856	38	1444	173	2118	119	49,44
008-ZR4C	0,218	13025	21,51	0,18403	0,96	7,283	7,55	0,2870	7,47	0,99	2690	32	1626	213	2147	130	39,52
005-ZR1B	0,282	15551	23,02	0,20270	0,43	5,484	8,94	0,1962	8,92	1,00	2848	14	1155	187	1898	148	59,45
004-ZR1C	0,444	8412	13,70	0,19342	0,60	3,394	19,88	0,1273	19,87	1,00	2771	20	772	286	1503	290	72,14
006-ZR2C	0,294	9939	29,01	0,20047	2,03	10,979	4,55	0,3972	4,06	0,89	2830	65	2156	148	2521	83	23,82

ADE-18P	Th/U	$^{206}Pb/^{204}Pb$	1s%	$^{207}Pb/^{206}Pb$	1s %	$^{207}Pb/^{235}U$	1s %	$^{206}Pb/^{238}U$	1s %	Rho	$^{207}Pb/^{206}Pb$	2s abs	$^{206}Pb/^{238}U$	2s abs	$^{207}Pb/^{235}U$	2s abs	% U-Pb disc[4]
051-ZR23C	0,535	298562	45,18	0,21223	0,41	15,109	0,88	0,5163	0,68	0,78	2923	13	2683	30	2822	17	8,18
050-ZR22B	0,515	486990	11,07	0,20867	0,37	15,308	0,83	0,5320	0,64	0,77	2895	12	2750	28	2835	16	5,02
033-ZR14B	0,416	1408	4,59	0,21847	0,39	9,091	3,05	0,3018	3,01	0,98	2969	13	1700	90	2347	55	42,75
030-ZR14C	0,424	20696	13,16	0,20988	0,41	11,623	3,86	0,4016	3,82	0,99	2905	13	2177	140	2575	71	25,07
029-ZR13B	0,472	352115	29,35	0,20223	0,41	14,406	1,33	0,5166	1,21	0,91	2844	13	2685	53	2777	25	5,61
028-ZR13C	0,384	2215	17,22	0,20557	0,60	15,008	3,37	0,5294	3,30	0,98	2871	19	2739	146	2816	63	4,59
027-ZR12C	0,060	19586	9,53	0,20500	0,70	14,839	1,26	0,5249	0,98	0,78	2866	23	2720	43	2805	24	5,11
024-ZR10C	0,487	674612	15,05	0,19902	0,27	14,115	1,08	0,5144	0,98	0,91	2818	9	2675	43	2757	20	5,07
020-ZR9B	0,449	276479	19,74	0,20758	0,34	16,624	1,48	0,5808	1,39	0,94	2887	11	2952	66	2913	28	-2,26
019-ZR9C	0,530	411815	17,36	0,19748	1,32	11,140	2,85	0,4091	2,50	0,88	2805	43	2211	93	2535	52	21,19
015-ZR7C	0,465	21345	5,16	0,21140	0,24	14,899	1,70	0,5111	1,64	0,97	2916	8	2661	71	2809	32	8,74
012-ZR5B	0,406	937	5,61	0,21102	0,38	3,043	4,80	0,1046	4,77	0,99	2913	12	641	58	1419	72	77,99
036-ZR16C	0,562	309330	37,44	0,19208	1,21	12,374	2,20	0,4672	1,80	0,82	2760	39	2471	74	2633	41	10,47
035-ZR15C	0,308	7677	4,57	0,18415	0,37	8,771	3,05	0,3454	3,01	0,99	2691	12	1913	99	2315	55	28,91
007-ZR3C	0,338	41202	25,30	0,19083	0,86	10,831	2,09	0,4116	1,86	0,89	2749	28	2222	70	2509	38	19,17
014-ZR6B	0,552	12800	14,94	0,18955	0,75	13,592	1,86	0,5200	1,66	0,89	2738	25	2699	73	2722	35	1,43
013-ZR6C	0,785	6919	8,06	0,19445	0,50	8,840	3,59	0,3297	3,53	0,98	2780	16	1837	112	2322	64	33,93
041-ZR19B	0,230	96055	30,40	0,05928	0,46	0,789	0,95	0,0966	0,75	0,78	577	20	594	8	591	8	-2,96
040-ZR19C	0,986	63083	25,26	0,06389	0,72	0,828	1,16	0,0940	0,83	0,72	738	30	579	9	612	11	21,56
ADE-25B	**Th/U**	**$^{206}Pb/^{204}Pb$**	**1s%**	**$^{207}Pb/^{206}Pb$**	**1s %**	**$^{207}Pb/^{235}U$**	**1s %**	**$^{206}Pb/^{238}U$**	**1s %**	**Rho**	**$^{207}Pb/^{206}Pb$**	**2s abs**	**$^{206}Pb/^{238}U$**	**2s abs**	**$^{207}Pb/^{235}U$**	**2s abs**	**% U-Pb disc[4]**
031-ZR16	0,417	200229	58,34	0,20163	0,55	14,275	1,50	0,5134	1,34	0,90	2839	18	2671	59	2768	28	5,92
013-ZR8	0,147	383328	20,62	0,16081	0,77	8,388	1,90	0,3783	1,69	0,89	2464	26	2068	60	2274	34	16,07
023-ZR12	0,079	438477	27,01	0,16027	1,54	10,103	2,63	0,4572	2,10	0,80	2459	51	2427	85	2444	48	1,28
030-ZR15	0,308	334036	22,52	0,15677	1,00	8,619	1,69	0,3987	1,31	0,77	2421	34	2163	48	2299	31	10,66
025-ZR13B	0,396	86773	43,26	0,14146	0,34	7,199	1,08	0,3691	0,95	0,88	2245	12	2025	33	2136	19	9,81
024-ZR13C	0,493	146970	40,32	0,14211	0,34	7,586	1,09	0,3872	0,97	0,89	2253	12	2110	35	2183	20	6,37
019-ZR10B	0,018	4425	4,13	0,12175	0,37	5,111	1,31	0,3044	1,20	0,92	1982	13	1713	36	1838	22	13,57
018-ZR10	0,027	2397	3,33	0,11792	0,44	3,561	1,95	0,2190	1,87	0,96	1925	16	1277	43	1541	31	33,68

ADE-18P	Th/U	$^{206}Pb/^{204}Pb$	1s%	$^{207}Pb/^{206}Pb$	1s %	$^{207}Pb/^{235}U$	1s %	$^{206}Pb/^{238}U$	1s %	Rho	$^{207}Pb/^{206}Pb$	2s abs	$^{206}Pb/^{238}U$	2s abs	$^{207}Pb/^{235}U$	2s abs	% U-Pb disc[4]
032-ZR17	0,182	757806	26,93	0,12247	0,34	5,890	0,92	0,3488	0,77	0,84	1992	12	1929	26	1960	16	3,19
026-ZR14	0,008	1206110	17,19	0,12067	0,51	5,199	1,18	0,3124	1,00	0,85	1966	18	1753	31	1852	20	10,86
017-ZR9	0,047	2074645	20,09	0,11699	0,45	5,424	1,29	0,3362	1,15	0,89	1911	16	1868	37	1889	22	2,21
007-ZR4	0,077	401372	33,31	0,11584	1,52	4,879	2,43	0,3055	1,87	0,77	1893	54	1718	56	1799	41	9,22
012-ZR7	0,286	326736	23,07	0,11542	0,52	4,334	1,58	0,2723	1,44	0,91	1886	19	1553	40	1700	26	17,69
020-ZR11	0,060	2517933	24,99	0,10222	1,18	5,192	1,84	0,3683	1,37	0,74	1665	43	2022	47	1851	31	-21,43
011-ZR6	0,054	3300584	44,48	0,10452	1,07	5,123	1,51	0,3555	1,00	0,66	1706	39	1961	34	1840	25	-14,94
010-ZR5	0,053	3078788	23,57	0,10729	0,58	5,407	1,23	0,3655	1,02	0,83	1754	21	2008	35	1886	21	-14,49
033-ZR3C	0,055	1629942	23,93	0,10968	0,42	3,914	1,37	0,2588	1,25	0,91	1794	15	1484	33	1617	22	17,30
006-ZR3	0,055	1300416	29,38	0,10939	0,78	4,845	2,04	0,3212	1,85	0,91	1789	28	1796	58	1793	34	-0,35
005-ZR2	0,039	2450889	24,58	0,10714	1,59	6,377	2,92	0,4316	2,42	0,83	1751	58	2313	94	2029	51	-32,07
004-ZR1	0,036	1898010	27,91	0,10163	1,20	5,261	2,83	0,3754	2,53	0,90	1654	44	2055	89	1863	48	-24,22
ADE-26A	**Th/U**	$^{206}Pb/^{204}Pb$	**1s%**	$^{207}Pb/^{206}Pb$	**1s %**	$^{207}Pb/^{235}U$	**1s %**	$^{206}Pb/^{238}U$	**1s %**	**Rho**	$^{207}Pb/^{206}Pb$	**2s abs**	$^{206}Pb/^{238}U$	**2s abs**	$^{207}Pb/^{235}U$	**2s abs**	**% U-Pb disc[4]**
046-ZR28	0,067	1299148	27,65	0,12061	0,41	5,619	1,35	0,3379	1,23	0,91	1965	14	1876	40	1919	23	4,52
045-ZR27	0,118	509429	20,32	0,10676	0,88	3,530	1,98	0,2398	1,73	0,88	1745	32	1385	43	1534	31	20,60
044-ZR26	0,054	624443	20,47	0,12169	1,89	5,167	4,36	0,3079	3,91	0,90	1981	67	1731	118	1847	73	12,65
043-ZR25	0,680	507884	16,79	0,12235	0,44	6,182	2,51	0,3664	2,44	0,97	1991	16	2012	84	2002	43	-1,09
025-ZR15	1,061	53841	17,09	0,05944	0,94	0,783	1,91	0,0955	1,62	0,85	583	41	588	18	587	17	-0,83
017-ZR9	0,123	152569	33,61	0,06872	1,17	1,000	3,32	0,1055	3,09	0,93	890	48	647	38	704	33	27,36
037-ZR22	0,399	50117	21,78	0,06118	1,64	0,915	2,26	0,1084	1,50	0,67	645	70	664	19	660	22	-2,84
036-ZR21	0,285	166704	12,44	0,05989	0,53	0,818	1,03	0,0990	0,80	0,78	600	23	609	9	607	9	-1,51
031-ZR18	0,105	487297	22,98	0,17685	1,35	12,093	3,74	0,4959	3,47	0,93	2624	45	2596	147	2612	69	1,04
030-ZR17	0,326	22960	46,64	0,18894	1,43	15,310	2,27	0,5876	1,73	0,76	2733	47	2980	82	2835	43	-9,03
026-ZR16	0,329	690262	25,40	0,18222	0,58	13,042	1,37	0,5191	1,18	0,86	2673	19	2695	52	2683	26	-0,82
012-ZR7	0,308	129606	56,93	0,18085	1,24	10,960	3,64	0,4395	3,40	0,93	2661	41	2348	133	2520	67	11,73
010-ZR5	0,432	95106	40,09	0,18717	0,60	14,190	1,57	0,5498	1,41	0,89	2717	20	2824	64	2762	30	-3,93
019-ZR11	0,252	303793	21,91	0,20267	0,73	12,245	2,71	0,4382	2,58	0,95	2848	24	2342	101	2623	50	17,74
007-ZR4	0,455	6633	5,22	0,19771	1,47	10,157	2,71	0,3726	2,24	0,83	2807	48	2041	78	2449	49	27,28

ADE-18P	Th/U	$^{206}Pb/^{204}Pb$	1s%	$^{207}Pb/^{206}Pb$	1s %	$^{207}Pb/^{235}U$	1s %	$^{206}Pb/^{238}U$	1s %	Rho	$^{207}Pb/^{206}Pb$	2s abs	$^{206}Pb/^{238}U$	2s abs	$^{207}Pb/^{235}U$	2s abs	% U-Pb disc[4]
005-ZR2	0,059	11672	37,46	0,13112	3,00	2,946	4,13	0,1630	2,81	0,68	2113	103	973	51	1394	62	53,94
004-ZR1	0,271	384383	95,19	0,21576	0,94	15,996	2,43	0,5377	2,21	0,91	2949	30	2774	99	2877	46	5,96
ADE-28A	**Th/U**	$^{206}Pb/^{204}Pb$	**1s%**	$^{207}Pb/^{206}Pb$	**1s %**	$^{207}Pb/^{235}U$	**1s %**	$^{206}Pb/^{238}U$	**1s %**	**Rho**	$^{207}Pb/^{206}Pb$	**2s abs**	$^{206}Pb/^{238}U$	**2s abs**	$^{207}Pb/^{235}U$	**2s abs**	**% U-Pb disc[4]**
005-ZR2	0,075	494697	35,31	0,15959	0,77	8,471	1,65	0,3849	1,42	0,86	2451	26	2099	51	2283	30	14,36
032-ZR19	0,909	1245	7,00	0,07194	1,20	0,995	2,60	0,1003	2,28	0,88	984	48	616	27	701	26	37,41
031-ZR18	0,729	742	12,23	0,08103	1,28	1,094	2,04	0,0979	1,54	0,76	1222	50	602	18	750	21	50,75
030-ZR17	0,854	1957	45,81	0,07509	1,43	1,141	3,21	0,1102	2,86	0,89	1071	57	674	36	773	34	37,06
029-ZR16	0,810	1193	6,73	0,06563	1,87	0,924	2,98	0,1021	2,29	0,77	795	77	627	27	664	29	21,15
026-ZR16	0,805	3319	37,38	0,07187	1,81	1,008	2,97	0,1017	2,32	0,78	982	73	624	28	708	30	36,43
025-ZR15	0,758	1938	40,66	0,07614	3,91	1,115	4,65	0,1062	2,49	0,54	1099	153	650	31	760	49	40,80
025-ZR14	0,697	1907	6,64	0,06903	0,67	0,863	1,23	0,0907	0,97	0,79	900	27	560	10	632	12	37,78
023-ZR13	0,855	1504	3,47	0,07869	0,71	1,125	1,19	0,1037	0,87	0,74	1164	28	636	11	765	13	45,38
020-ZR12	0,663	1534	6,53	0,07606	1,13	1,069	1,55	0,1019	0,99	0,64	1097	45	626	12	738	16	42,94
018-ZR10	0,882	1844	12,76	0,07064	0,69	0,918	1,87	0,0943	1,70	0,91	947	28	581	19	661	18	38,66
017-ZR9	0,831	3177	30,50	0,06991	2,46	0,989	3,51	0,1025	2,47	0,71	926	99	629	30	698	35	32,01
013-ZR8	0,835	2256	31,60	0,07624	2,06	1,110	3,10	0,1056	2,29	0,74	1101	81	647	28	758	33	41,26
012-ZR7	0,707	4180	29,57	0,07082	2,92	1,117	4,33	0,1143	3,18	0,73	952	117	698	42	761	46	26,71
011-ZR6	0,720	1395	3,31	0,08290	0,71	1,211	1,29	0,1060	1,01	0,78	1267	28	649	12	806	14	48,75
010-ZR5	0,760	2530	32,90	0,06994	0,68	1,045	3,48	0,1084	3,39	0,97	926	28	663	43	726	36	28,41
006-ZR3	0,786	1356	38,84	0,07621	3,28	1,021	4,46	0,0971	3,00	0,67	1101	128	597	34	714	45	45,71
004-ZR1	0,769	1568	4,98	0,06699	0,67	0,897	2,76	0,0972	2,65	0,96	837	28	598	30	650	26	28,63

Supplementary Table 6.2. Itajá U-Pb zircon data.

AP-23	Th/U	$^{206}Pb/^{204}Pb$	1σ%	$^{207}Pb/^{206}Pb$	1σ %	$^{207}Pb/^{235}U$	1σ %	$^{206}Pb/^{238}U$	1σ %	Rho	$^{207}Pb/^{206}Pb$	2σ abs	$^{206}Pb/^{238}U$	2σ abs	$^{207}Pb/^{235}U$	2σ abs	% U-Pb disc[4]
039-ZR21C	0,787	5681	8,95	0,14507	1,39	9,108	3,79	0,4553	3,51	0,92	2289	48	2419	141	2349	68	-5,69
038-ZR20C	0,591	139878	43,57	0,14675	1,88	8,359	3,06	0,4131	2,38	0,78	2308	64	2229	89	2271	55	3,45
037-ZR19B	0,659	254955	35,98	0,14015	0,83	7,736	1,21	0,4003	0,80	0,66	2229	29	2170	30	2201	22	2,63
036-ZR19C	0,538	5743	6,76	0,14015	0,42	5,412	3,76	0,2800	3,72	0,99	2229	14	1592	105	1887	63	28,60
034-ZR17C	0,720	77723	49,16	0,14136	2,68	8,008	3,22	0,4108	1,75	0,54	2244	91	2219	66	2232	57	1,12
033-ZR16C	0,745	330994	43,59	0,15050	0,55	9,205	1,01	0,4436	0,77	0,76	2352	19	2367	30	2359	18	-0,64
030-ZR15B	0,607	453315	16,28	0,14727	0,74	8,515	1,24	0,4193	0,92	0,74	2314	25	2257	35	2287	22	2,47
029-ZR15C	0,577	608740	31,86	0,14778	0,58	8,587	0,90	0,4214	0,57	0,64	2320	20	2267	22	2295	16	2,31
028-ZR14B	0,660	555181	22,14	0,14877	0,55	8,998	0,85	0,4386	0,54	0,63	2332	19	2345	21	2338	16	-0,55
026-ZR13B	0,425	81033	35,69	0,14437	0,51	8,598	1,10	0,4319	0,91	0,82	2280	18	2314	35	2296	20	-1,49
024-ZR12B	0,874	7939	8,86	0,14779	0,49	8,031	0,98	0,3941	0,77	0,78	2321	17	2142	28	2234	18	7,71
020-ZR12C	0,573	549092	32,35	0,14927	0,56	8,981	0,81	0,4363	0,45	0,56	2338	19	2334	18	2336	15	0,15
019-ZR11B	0,149	106724	17,89	0,13559	0,52	7,048	1,07	0,3770	0,85	0,80	2172	18	2062	30	2118	19	5,04
018-ZR11C	0,262	14182	7,69	0,14128	0,80	8,212	1,54	0,4216	1,26	0,82	2243	28	2268	48	2255	28	-1,10
017-ZR10B	0,595	18205	13,30	0,15333	0,67	7,841	1,55	0,3709	1,35	0,87	2383	23	2034	47	2213	28	14,68
015-ZR9C	0,842	16518	12,44	0,14810	0,36	9,351	2,50	0,4579	2,44	0,98	2324	12	2430	99	2373	45	-4,56
014-ZR8C	0,794	5128	6,90	0,14812	0,47	7,043	1,23	0,3448	1,08	0,88	2324	16	1910	36	2117	22	17,84
013-ZR7C	0,952	707557	26,59	0,14969	0,38	8,728	0,85	0,4229	0,67	0,78	2342	13	2273	26	2310	15	2,94
007-ZR3C	0,257	272561	34,48	0,13430	0,29	6,878	0,83	0,3714	0,68	0,82	2155	10	2036	24	2096	15	5,51
006-ZR2B	0,902	21993	42,91	0,15629	0,80	7,699	2,68	0,3572	2,53	0,94	2416	27	1969	86	2196	48	18,50
005-ZR2C	0,985	18035	20,15	0,14247	0,53	7,593	2,69	0,3865	2,62	0,97	2257	18	2106	94	2184	48	6,69
004-ZR1C	0,382	559997	18,37	0,14596	0,44	8,690	1,59	0,4318	1,48	0,93	2299	15	2314	57	2306	29	-0,63
AP-36	**Th/U**	$^{206}Pb/^{204}Pb$	**1σ%**	$^{207}Pb/^{206}Pb$	**1σ %**	$^{207}Pb/^{235}U$	**1σ %**	$^{206}Pb/^{238}U$	**1σ %**	**Rho**	$^{207}Pb/^{206}Pb$	**2σ abs**	$^{206}Pb/^{238}U$	**2σ abs**	$^{207}Pb/^{235}U$	**2σ abs**	**% U-Pb disc[4]**
037-ZR20C	0,468	8925	7,31	0,15056	0,41	5,855	2,72	0,2820	2,66	0,98	2352	14	1602	75	1955	47	31,91
036-ZR19C	0,612	76384	73,21	0,14580	0,66	6,711	2,74	0,3338	2,63	0,96	2297	23	1857	85	2074	48	19,17

AP-23	Th/U	$^{206}Pb/^{204}Pb$	1σ%	$^{207}Pb/^{206}Pb$	1σ %	$^{207}Pb/^{235}U$	1σ %	$^{206}Pb/^{238}U$	1σ %	Rho	$^{207}Pb/^{206}Pb$	2σ abs	$^{206}Pb/^{238}U$	2σ abs	$^{207}Pb/^{235}U$	2σ abs	% U-Pb disc[4]
035-ZR18C	0,395	8606	19,66	0,14490	1,48	7,868	2,55	0,3938	2,04	0,80	2287	50	2140	74	2216	45	6,39
029-ZR15C	0,582	229473	40,33	0,15192	0,48	8,168	1,15	0,3899	0,97	0,85	2368	16	2122	35	2250	21	10,36
026-ZR13C	0,796	61599	43,41	0,14758	1,82	8,677	2,20	0,4264	1,18	0,54	2318	62	2289	45	2305	40	1,24
020-ZR10C	0,329	57764	89,29	0,15176	1,38	6,422	2,09	0,3069	1,53	0,73	2366	47	1725	46	2035	36	27,07
018-ZR9M	0,615	538868	27,66	0,14999	0,56	8,926	1,09	0,4316	0,87	0,79	2346	19	2313	34	2330	20	1,41
017-ZR9C	0,704	24444	9,19	0,14865	0,49	8,772	1,35	0,4280	1,21	0,89	2330	17	2297	47	2315	25	1,45
015-ZR7C	0,576	71617	47,31	0,14856	1,75	6,404	2,07	0,3126	1,04	0,50	2329	59	1754	32	2033	36	24,72
014-ZR6B	0,751	26104	3,74	0,14849	0,99	8,536	1,29	0,4169	0,75	0,58	2329	34	2246	29	2290	23	3,54
013-ZR6C	0,724	129673	77,48	0,14451	1,87	9,058	2,22	0,4546	1,13	0,51	2282	64	2416	46	2344	40	-5,85
009-ZR5C	1,276	27588	7,76	0,14596	1,03	7,836	3,02	0,3893	2,82	0,93	2299	35	2120	101	2212	54	7,80
007-ZR3C	0,501	101665	56,78	0,14757	2,01	9,128	2,44	0,4486	1,34	0,55	2318	68	2389	53	2351	44	-3,07
006-ZR2C	0,559	5171	23,25	0,15031	0,65	8,539	1,29	0,4120	1,05	0,81	2349	22	2224	39	2290	23	5,33
005-ZR1B	0,585	444615	25,87	0,15201	0,51	9,578	1,31	0,4569	1,15	0,88	2369	17	2426	46	2395	24	-2,42
004-ZR1C	0,698	18466	6,40	0,14955	0,49	8,320	1,11	0,4035	0,92	0,83	2341	17	2185	34	2266	20	6,65
AT-36A	**Th/U**	$^{206}Pb/^{204}Pb$	**1σ%**	$^{207}Pb/^{206}Pb$	**1σ %**	$^{207}Pb/^{235}U$	**1σ %**	$^{206}Pb/^{238}U$	**1σ %**	**Rho**	$^{207}Pb/^{206}Pb$	**2σ abs**	$^{206}Pb/^{238}U$	**2σ abs**	$^{207}Pb/^{235}U$	**2σ abs**	**% U-Pb disc[4]**
040-ZR22C	0,366	177335	31,39	0,13720	0,36	7,012	0,73	0,3707	0,51	0,71	2192	12	2032	18	2113	13	7,28
039-ZR21C	0,344	823909	22,15	0,13793	0,32	7,102	0,75	0,3734	0,57	0,76	2201	11	2045	20	2124	13	7,09
038-ZR20B	0,350	519039	14,31	0,13686	0,29	7,148	0,75	0,3788	0,59	0,78	2188	10	2071	21	2130	13	5,36
037-ZR20C	0,137	16067	8,66	0,12928	0,36	3,089	2,60	0,1733	2,55	0,98	2088	12	1030	48	1430	40	50,66
036-ZR19C	0,534	734510	16,34	0,13725	0,31	7,062	0,71	0,3731	0,52	0,73	2193	11	2044	18	2119	13	6,78
035-ZR18C	0,438	829771	12,34	0,13764	0,62	7,574	1,34	0,3990	1,13	0,84	2198	22	2165	41	2182	24	1,51
034-ZR17B	0,376	556647	15,36	0,13616	0,36	7,022	0,73	0,3740	0,51	0,71	2179	12	2048	18	2114	13	5,99
033-ZR17C	0,554	599125	18,41	0,13729	0,40	7,046	0,81	0,3722	0,60	0,74	2193	14	2040	21	2117	14	7,00
030-ZR16C	0,359	468104	16,84	0,13720	0,56	7,318	1,34	0,3868	1,16	0,87	2192	19	2108	42	2151	24	3,83
029-ZR15B	0,373	696809	16,80	0,13464	0,43	6,262	0,75	0,3373	0,49	0,65	2159	15	1873	16	2013	13	13,24
028-ZR15C	0,529	318266	32,15	0,13724	0,58	7,088	0,95	0,3746	0,66	0,69	2193	20	2051	23	2123	17	6,47
027-ZR14C	0,369	528446	12,77	0,13676	0,33	6,670	0,70	0,3537	0,50	0,71	2187	11	1952	17	2069	12	10,72

AP-23	Th/U	$^{206}Pb/^{204}Pb$	1σ%	$^{207}Pb/^{206}Pb$	1σ %	$^{207}Pb/^{235}U$	1σ %	$^{206}Pb/^{238}U$	1σ %	Rho	$^{207}Pb/^{206}Pb$	2σ abs	$^{206}Pb/^{238}U$	2σ abs	$^{207}Pb/^{235}U$	2σ abs	% U-Pb disc[4]
026-ZR13C	0,388	12245	11,98	0,13748	0,31	6,711	0,67	0,3540	0,46	0,69	2196	11	1954	16	2074	12	11,02
025-ZR12C	0,306	85331	14,33	0,13341	0,28	5,795	1,88	0,3150	1,82	0,97	2143	10	1765	56	1946	32	17,63
024-ZR11C	0,489	9788	6,76	0,13821	0,34	6,808	0,77	0,3572	0,58	0,75	2205	12	1969	20	2087	14	10,70
020-ZR10C	0,428	13298	19,80	0,13616	0,51	6,730	0,92	0,3585	0,67	0,73	2179	18	1975	23	2077	16	9,36
019-ZR9B	1,247	25947	9,20	0,13452	0,41	4,939	1,89	0,2663	1,81	0,96	2158	14	1522	49	1809	32	29,47
018-ZR9C	0,508	652900	27,08	0,13662	0,30	6,421	0,86	0,3408	0,71	0,83	2185	11	1891	23	2035	15	13,46
017-ZR8C	0,362	558584	14,21	0,13736	0,32	6,870	0,68	0,3627	0,48	0,70	2194	11	1995	16	2095	12	9,08
016-ZR7B	0,377	647600	18,18	0,13380	0,28	6,071	0,65	0,3291	0,46	0,70	2148	10	1834	15	1986	11	14,65
014-ZR6C	0,366	674993	30,33	0,13746	0,31	7,335	0,99	0,3870	0,86	0,87	2195	11	2109	31	2153	18	3,95
013-ZR5C	0,411	424769	19,40	0,13708	0,34	7,064	0,74	0,3737	0,54	0,73	2191	12	2047	19	2120	13	6,57
010-ZR4B	0,291	24149	60,69	0,13219	0,45	5,693	0,83	0,3123	0,59	0,71	2127	16	1752	18	1930	14	17,63
008-ZR3C	0,627	163451	47,92	0,13666	0,35	6,946	2,01	0,3686	1,95	0,97	2185	12	2023	67	2105	35	7,43
007-ZR2B	0,423	749040	17,26	0,13572	0,29	6,853	0,64	0,3662	0,44	0,68	2173	10	2011	15	2093	11	7,45
006-ZR2C	0,417	20096	8,61	0,13730	0,27	6,828	0,76	0,3607	0,60	0,80	2193	9	1985	21	2089	13	9,48
005-ZR1B	0,349	435562	22,58	0,13530	0,34	6,671	1,10	0,3576	0,98	0,89	2168	12	1971	33	2069	19	9,10
004-ZR1C	0,438	275890	27,07	0,13764	0,33	7,506	1,14	0,3955	1,03	0,90	2198	11	2148	37	2174	20	2,25
AP-05B	**Th/U**	$^{206}Pb/^{204}Pb$	**1σ%**	$^{207}Pb/^{206}Pb$	**1σ %**	$^{207}Pb/^{235}U$	**1σ %**	$^{206}Pb/^{238}U$	**1σ %**	**Rho**	$^{207}Pb/^{206}Pb$	**2σ abs**	$^{206}Pb/^{238}U$	**2σ abs**	$^{207}Pb/^{235}U$	**2σ abs**	**% U-Pb disc[4]**
039-ZR20C	1,083	272198	35,94	0,14360	0,41	7,564	0,82	0,3820	0,61	0,74	2271	14	2086	22	2181	15	8,16
038-ZR19C	1,090	583883	17,20	0,14406	0,30	7,708	0,72	0,3880	0,54	0,75	2277	10	2114	19	2198	13	7,16
037-ZR18C	0,726	11441	8,09	0,14070	0,37	7,346	1,23	0,3786	1,11	0,91	2236	13	2070	39	2154	22	7,42
036-ZR17B	0,522	587225	18,14	0,13719	0,22	6,901	0,72	0,3648	0,57	0,80	2192	8	2005	20	2099	13	8,55
035-ZR17C	0,548	14913	18,00	0,13342	0,68	6,994	1,66	0,3802	1,46	0,88	2143	24	2077	52	2111	29	3,10
034-ZR16C	0,985	86981	34,48	0,14404	0,29	7,676	0,88	0,3865	0,75	0,84	2276	10	2106	27	2194	16	7,46
033-ZR15C	0,621	112494	60,35	0,14274	0,30	7,871	0,83	0,3999	0,69	0,82	2261	10	2169	25	2216	15	4,07
030-ZR14B	1,028	672295	30,54	0,13920	0,31	7,237	0,68	0,3770	0,48	0,70	2217	11	2062	17	2141	12	6,99
029-ZR14C	0,713	10011	8,29	0,13838	0,44	7,163	0,92	0,3754	0,72	0,78	2207	15	2055	25	2132	16	6,90
028-ZR13CV	0,436	17669	4,61	0,13878	0,26	6,575	1,20	0,3436	1,11	0,93	2212	9	1904	37	2056	21	13,93

AP-23	Th/U	$^{206}Pb/^{204}Pb$	1σ%	$^{207}Pb/^{206}Pb$	1σ %	$^{207}Pb/^{235}U$	1σ %	$^{206}Pb/^{238}U$	1σ %	Rho	$^{207}Pb/^{206}Pb$	2σ abs	$^{206}Pb/^{238}U$	2σ abs	$^{207}Pb/^{235}U$	2σ abs	% U-Pb disc[4]
025-ZR11C	0,236	61710	35,30	0,13769	0,29	6,637	0,69	0,3496	0,51	0,74	2198	10	1933	17	2064	12	12,09
024-ZR10B	0,429	1410	2,21	0,14825	0,37	6,812	1,06	0,3333	0,92	0,87	2326	13	1854	30	2087	19	20,28
020-ZR10C	0,690	9372	13,09	0,14580	0,41	7,500	0,76	0,3730	0,52	0,69	2297	14	2044	18	2173	14	11,04
019-ZR9B	0,850	272806	15,38	0,14491	0,36	7,725	0,73	0,3866	0,51	0,70	2287	13	2107	18	2200	13	7,86
017-ZR8B	0,599	1046220	20,61	0,14369	0,23	7,544	0,66	0,3808	0,49	0,74	2272	8	2080	17	2178	12	8,46
015-ZR7C	0,714	111588	41,14	0,14265	0,30	7,348	0,68	0,3735	0,48	0,71	2260	10	2046	17	2155	12	9,45
014-ZR6C	0,782	420679	17,88	0,14446	0,29	7,758	0,69	0,3895	0,51	0,74	2281	10	2120	18	2203	12	7,06
013-ZR5C	0,591	844307	21,80	0,13979	0,29	7,243	0,71	0,3758	0,53	0,75	2225	10	2056	19	2142	13	7,56
010-ZR4B	0,491	1206970	34,42	0,13922	0,30	7,165	0,68	0,3732	0,48	0,71	2218	11	2045	17	2132	12	7,80
008-ZR3C	1,017	744301	19,91	0,14397	0,35	7,633	0,84	0,3845	0,67	0,80	2276	12	2097	24	2189	15	7,84
007-ZR2B	0,558	756137	20,39	0,14006	0,22	7,212	0,66	0,3734	0,49	0,75	2228	8	2046	17	2138	12	8,19
006-ZR2C	0,932	13088	13,95	0,13645	1,17	7,644	2,15	0,4063	1,76	0,82	2183	41	2198	66	2190	38	-0,70
005-ZR1B	0,557	9804	14,12	0,14563	0,76	7,331	1,29	0,3651	0,98	0,76	2295	26	2006	34	2153	23	12,60
004-ZR1C	0,670	1272580	19,47	0,14015	0,29	7,508	1,15	0,3885	1,05	0,91	2229	10	2116	38	2174	20	5,07
AP-07A	**Th/U**	$^{206}Pb/^{204}Pb$	**1σ%**	$^{207}Pb/^{206}Pb$	**1σ %**	$^{207}Pb/^{235}U$	**1σ %**	$^{206}Pb/^{238}U$	**1σ %**	**Rho**	$^{207}Pb/^{206}Pb$	**2σ abs**	$^{206}Pb/^{238}U$	**2σ abs**	$^{207}Pb/^{235}U$	**2σ abs**	**% U-Pb disc[4]**
049-ZR30C	0,420	155005	30,43	0,12381	2,27	6,238	3,43	0,3654	2,54	0,74	2012	79	2008	87	2010	59	0,20
048-ZR29C	0,448	956755	23,45	0,13640	2,10	7,525	3,01	0,4001	2,12	0,71	2182	72	2170	78	2176	53	0,57
047-ZR28C	0,811	516139	26,74	0,13559	0,26	6,619	1,38	0,3540	1,30	0,94	2172	9	1954	44	2062	24	10,03
046-ZR27C	0,405	431206	17,13	0,12227	0,33	5,607	0,72	0,3326	0,52	0,72	1990	12	1851	17	1917	12	6,97
045-ZR26C	0,657	456003	15,01	0,13328	0,23	5,872	0,72	0,3195	0,58	0,80	2142	8	1787	18	1957	12	16,54
044-ZR25B	0,267	419338	12,94	0,12060	0,30	5,503	0,69	0,3309	0,51	0,73	1965	11	1843	16	1901	12	6,23
040-ZR25C	0,313	353169	14,44	0,12381	0,36	5,838	0,77	0,3420	0,57	0,74	2012	13	1896	19	1952	13	5,75
038-ZR23C	0,700	263037	21,42	0,13760	0,34	6,999	0,80	0,3689	0,62	0,78	2197	12	2024	22	2111	14	7,87
037-ZR22C	0,232	289033	58,99	0,13499	1,64	7,218	2,59	0,3878	1,97	0,76	2164	57	2112	71	2139	46	2,38
035-ZR20C	1,177	34558	11,52	0,13622	2,25	7,102	3,63	0,3781	2,82	0,78	2180	77	2067	99	2124	64	5,15
034-ZR19B	0,170	490510	25,29	0,13808	0,29	7,068	2,59	0,3712	2,55	0,98	2203	10	2035	89	2120	46	7,63
030-ZR18C	0,651	554149	23,66	0,13837	0,97	7,507	2,14	0,3935	1,87	0,88	2207	33	2139	68	2174	38	3,08

AP-23	Th/U	$^{206}Pb/^{204}Pb$	1σ%	$^{207}Pb/^{206}Pb$	1σ %	$^{207}Pb/^{235}U$	1σ %	$^{206}Pb/^{238}U$	1σ %	Rho	$^{207}Pb/^{206}Pb$	2σ abs	$^{206}Pb/^{238}U$	2σ abs	$^{207}Pb/^{235}U$	2σ abs	% U-Pb disc[4]
029-ZR17C	0,317	138168	55,18	0,13423	2,63	6,700	3,07	0,3620	1,54	0,50	2154	90	1992	53	2073	54	7,54
028-ZR16C	0,366	358837	21,91	0,12480	1,80	6,162	2,76	0,3581	2,06	0,75	2026	63	1973	70	1999	48	2,61
025-ZR14C	0,505	674665	27,86	0,13772	0,42	7,810	2,66	0,4113	2,60	0,98	2199	15	2221	97	2209	47	-1,00
024-ZR13C	0,513	352716	19,57	0,13674	0,39	6,774	1,17	0,3593	1,03	0,89	2186	14	1979	35	2082	21	9,50
020-ZR12B	0,441	553035	30,33	0,13783	0,53	6,977	1,03	0,3671	0,80	0,78	2200	18	2016	28	2108	18	8,39
019-ZR12C	0,898	535069	19,88	0,13933	0,36	7,492	1,09	0,3900	0,96	0,88	2219	12	2123	35	2172	19	4,34
018-ZR11C	0,945	169818	39,75	0,13562	0,36	4,934	1,44	0,2639	1,35	0,93	2172	12	1510	36	1808	24	30,50
017-ZR10B	0,463	399601	16,70	0,14012	0,39	8,846	3,79	0,4579	3,75	0,99	2229	13	2430	151	2322	68	-9,04
016-ZR10C	0,352	435765	17,96	0,13693	0,33	7,779	3,96	0,4120	3,93	0,99	2189	11	2224	147	2206	70	-1,61
015-ZR9C	0,804	1170286	17,82	0,13944	0,24	7,177	0,72	0,3733	0,56	0,79	2220	8	2045	20	2134	13	7,90
014-ZR8C	0,858	12535	2,02	0,13095	0,27	4,385	1,44	0,2428	1,37	0,95	2111	9	1401	34	1709	24	33,60
013-ZR7C	0,819	20222	44,75	0,14144	1,01	6,970	1,54	0,3574	1,09	0,71	2245	35	1970	37	2108	27	12,25
010-ZR6C	0,644	1399888	19,62	0,13935	0,34	7,509	1,08	0,3908	0,96	0,88	2219	12	2126	35	2174	19	4,18
009-ZR5C	0,255	699362	24,24	0,13052	0,32	6,275	0,73	0,3487	0,54	0,74	2105	11	1928	18	2015	13	8,39
008-ZR4C	0,341	669485	29,60	0,13531	0,27	8,612	4,22	0,4616	4,19	0,99	2168	10	2446	170	2298	75	-12,84
007-ZR3C	0,383	387621	20,21	0,13467	1,14	6,668	2,60	0,3591	2,31	0,89	2160	39	1978	79	2068	45	8,42
005-ZR2C	0,665	59271	27,03	0,13797	0,23	6,881	0,93	0,3617	0,82	0,88	2202	8	1990	28	2096	16	9,62
004-ZR1C	0,459	471720	19,89	0,13267	0,36	6,559	0,88	0,3586	0,71	0,81	2134	13	1975	24	2054	15	7,41

Supplementary Table 6.3. Nd isotope data and U-Pb zircon age for the Campo Grande and Itajá block.

Block	Sample	UTM X	UTM Y	Rock	Sm (ppm)	Nd (ppm)	$^{147}Sm/^{144}Nd$	$^{143}Nd/^{144}Nd \pm 2SE$	$\varepsilon_{Nd(0)}$	T_{DM}(Ga)	U-Pb zircon age (Ga)					(Ma)
Campo Grande	ADE-09	679495	9355415	Amphibolite	3,30	12,75	0,156692	0.512121+/-3	-10,09	2,46		2.69			2.0	593
Campo Grande	ADE-16	687186	9367246	Amphibolite	4,33	16,95	0,154564	0.511773+/-8	-16,88	3,33	3.01	2.65				593
Campo Grande	ADE-20	685014	9362028	Amphibolite	2,23	9,50	0,141955	0.512116+/-5	-10,19	1,95						599
Campo Grande	ADE–24A	687678	9361941	Amphibolite	4,50	16,94	0,160752	0.511780+/-20	-16,74	3,75					2.0	
Campo Grande	ADE-24B	687678	9361941	Amphibolite	4,24	16,43	0,156052	0.512077+/-2	-10,95	2,55						
Campo Grande	ADE-29	682062	9359773	Amphibolite	3,57	12,70	0,170028	0.512416+/-13	-4,32	2,17	2.99	2.66				589
Campo Grande	At-10	694967	9361572	Amphibolite	5,90	24,53	0,145492	0.511922+/-19	-13,97	2,50						
Campo Grande	At-14a	683321	9360722	Amphibolite	4,45	19,78	0,135880	0.511189+/-4	-28,27	3,70						
Campo Grande	At-16	682499	9360150	Amphibolite	5,34	20,71	0,155846	0.512099+/-12	-10,51	2,48						
Campo Grande	At-24	687154	9358978	Amphibolite	4,76	18,70	0,153968	0.511907+/-6	-14,25	2,92						
Campo Grande	At-26	685121	9359016	Amphibolite	3,60	12,53	0,173462	0.512187+/-12	-8,81	3,34						
Campo Grande	At-32	683195	9351556	Amphibolite	3,98	14,96	0,160949	0.512125+/-15	-10,00	2,66						
Campo Grande	AP-10	689429	9365786	Amphibolite	5,31	19,65	0,163452	0.512011+/-4	-12,23	3,19						
Campo Grande	AP-17	683241	9360032	Amphibolite	9,59	39,16	0,148096	0.512104+/-3	-10,42	2,17						614
Campo Grande	ADE-23	688721	9359183	Migmatite	17,43	93,43	0,112748	0.511325+/-4	-25,60	2,59		2.65	2.46	2.23	2.13	1.93	
Campo Grande	ADE-08	692208	9353364	Amph-Bt gneiss	2,31	10,51	0,133022	0.511755+/-3	-17,22	2,42							
Campo Grande	AP-09	687408	9350474	Amph-Bt gneiss	3,78	19,70	0,115932	0.511536+/-4	-21,51	2,34				2.33			
Campo Grande	At-06	695271	9358884	Hbl migmatite	30,87	138,08	0,135130	0.511592+/-10	-20,41	2,82							
Campo Grande	At-02	696541	9353516	Hbl migmatite	4,60	19,02	0,146310	0.511909+/-11	-14,23	2,56		2.71	2.4			1.99	
Campo Grande	At-13b	683328	9360094	Bt migmatite	4,66	22,82	0,123469	0.511388+/-10	-24,38	2,80							
Campo Grande	At-28	691307	9368206	Bt migmatite	3,17	19,14	0,100057	0.510589+/-19	-39,97	3,31							
Campo Grande	ADE-10	679434	9355088	Bt migmatite	5,56	33,21	0,101138	0.510677+/-8	-38,25	3,22	2.92						
Campo Grande	ADE-14	680057	9353112	Bt migmatite	5,05	32,01	0,095451	0.511166+/-4	-28,72	2,41				2.23	2.15	1.98	
Campo Grande	ADE-15	691730	9370171	Bt migmatite	9,09	55,32	0,099317	0.511019+/-1	-31,57	2,69	2.91					1.96	611
Campo Grande	ADE-18	683347	9364136	Bt migmatite	4,86	27,78	0,105862	0.510976+/-8	-32,42	2,93	2.98						

Campo Grande	ADE-01	719922	9374303	Orthogneiss	14,38	64,85	0,134007	0.511418+/-8	-23,80	3,13				2.23			
Campo Grande	ADE-03	710259	9362444	Orthogneiss	6,09	36,57	0,100681	0.511149+/-9	-29,05	2,55	2.96	2.64		2.19			640
Campo Grande	ADE-04	698901	9351772	Orthogneiss	5,01	31,62	0,095842	0.511032+/-17	-31,33	2,59				2.23			
Campo Grande	ADE-06	690941	9347540	Orthogneiss	4,94	24,38	0,122628	0.511509+/-6	-22,02	2,56				2.22			
Campo Grande	ADE-12	672348	9357353	Orthogneiss	3,52	24,36	0,087379	0.510997+/-11	-32,01	2,46						1.95	
Campo Grande	AT-14B	683321	9360722	Pegmatite	1,95	6,96	0,169067	0.511395+/-14	-24,24		2.91			2.18		1.96	568
Campo Grande	AT-23	690837	9359006	Granite	26,93	169,75	0,095909	0.511189+/-13	-28,27	2,39							566
Campo Grande	ADE-13	666358	9360156	Orthogneiss	12,48	70,90	0,106444	0.511554+/-9	-21,15	2,10							603
Campo Grande	ADE-27	686696	9361990	Supracrustal	1,68	8,59	0,118218	0.511341+/-10	-25,30	2,72							
Campo Grande	At-22	685228	9366806	supracrustal	4,46	20,18	0,133481	0.511153+/-20	-28,98	3,65							
Campo Grande	At-25	685737	9359296	supracrustal	4,55	20,10	0,136809	0.511411+/-8	-23,94	3,27		2.65	2.46	2.25	2.11	2.03	
Campo Grande	AP-12	688179	9362230	Supracrustal	1,67	7,66	0,131808	0.511478+/-14	-22,63	2,92							
Campo Grande	AP-16	682735	9358176	Supracrustal	21,45	112,19	0,115598	0.511401+/-3	-24,13	2,55							
Campo Grande	AP-18B	686983	9361480	Supracrustal	0,56	2,64	0,129098	0.511321+/-11	-25,69	3,12							
Campo Grande	ADE-17	682759	9366783	Ultramafic	1,87	8,00	0,141493	0.511950+/-18	-13,41	2,29							
Campo Grande	ADE-22	686715	9362241	Ultramafic	1,78	35,40	0,030348	0.511331+/-2	-25,50	1,42							
Campo Grande	ADE-25A	687089	9362507	Ultramafic	0,69	3,58	0,117281	0.511341+/-9	-25,29	2,69							
Campo Grande	ADE-25B	687089	9362507	Ultramafic							2.83		2.44	2.25		1.99	
Campo Grande	ADE-26A	686780	9362179	Ultramafic	1,00	4,71	0,128430	0.511413+/-13	-23,90	2,92	2.95	2.68				1.99	600
Campo Grande	ADE-26C	686780	9362179	Ultramafic	0,68	3,40	0,121110	0.511288+/-13	-26,33	2,90							
Campo Grande	ADE-28A	686279	9361529	Ultramafic	3,74	18,82	0,120027	0.511076+/-43	-30,47	3,22							627
Campo Grande	AP-18A	686983	9361480	Ultramafic	2,28	13,99	0,098428	0.511302+/-4	-26,06	2,29							
Campo Grande	At -09	695051	9361072	ultramafic	6,51	36,71	0,107176	0.511378+/-6	-24,58	2,37							
Campo Grande	AP-22	683311	9354674	Ultramafic	3,56	23,80	0,090438	0.511410+/-4	-23,94	2,01	2.87	2.74					594
Itajá	ADE 31	743726	9380744	Amphibolite	2,821	12,212	0,1396	0.511946+/-6	-13,50	2,25							
Itajá	ADE-30B	749233	9369998	Ultramafic	0,711	2,874	0,1496	0.511928+/-9	-13,86	2,66				2.19			
Itajá	AP-05B	748379	9367658	Orthogneiss	13,904	103,507	0,0812	0.510843+/-6	-35,01	2,52				2.23			
Itajá	AP-06	749296	9370562	Ultramafic	0,626	4,046	0,0936	0.511330+/-6	-25,51	2,16				2.23			

Itajá	AP-07A	750140	9372398	Ultramafic	2,098	10,244	0,1238	0.511419+/-4	-23,77	2,75	2.19
Itajá	AP-23A	750245	9377268	Ultramafic	2,704	14,141	0,1156	0.511479+/-5	-22,61	2,42	2.29
Itajá	AP-23B	750245	9377268	Ultramafic	2,876	14,141	0,1229	0.511479+/-5	-22,61	2,62	2.29
Itajá	AP-24A	749348	9379584	Ultramafic	3,714	34,332	0,0654	0.510820+/-2	-35,47	2,27	
Itajá	AP-24B	749348	9379584	Ultramafic	4,103	34,332	0,0722	0.510819+/-3	-35,49	2,39	
Itajá	PC-36	756328	9380004	Orthogneiss	3,675	25,248	0,0880	0.511081+/-3	-30,37	2,37	2.32

7. CONCLUSÃO

A história evolutiva do Bloco Campo Grande começa com intenso magmatismo cálcio-alcalino de 2,9 Ga, gerado em ambiente de arco magmático, com contribuições de fontes juvenis de 2,9–3,0 Ga, e principalmente reciclagem de crosta mais antiga, de 3,25 Ga. A existência dessa crosta paleoarqueana também é indicada por idades modelo T_{DM} de Nd e Hf entre 3,3 e 3,7 Ga. Leucossomas alcalinos de 2,69–2,65 Ga indicam que a crosta tonalítica de 2,9 Ga foi retrabalhada e quimicamente diferenciada no Neoarqueano. Ainda no Neoarqueano, é documentada a geração de crosta oceânica de composição toleítica em 2,65 Ga. Cristais de zircão com idades entre 2,52 e 2,42 Ga são localmente registrados, sugerindo restrita atividade magmático-termal na transição Neoarqueano-Paleoproterozoico. Nas margens do complexo núcleo arqueano, com duas fases de retrabalhamento, são instalados e acrescionados arcos magmáticos de composição cálcio-alcalina de alto K, entre 2,23 e 2,18 Ga. O calor remanescente dos arcos magmáticos riacianos possivelmente promoveu anatexia com geração de leucossomas graníticos de 1,95 Ga. Metamorfismo de alto-grau em 2,0 Ga é registrado em rochas de origem oceânica de 2,65 Ga, indicando condições de alta-pressão antes da fusão parcial na base da crosta arqueana tonalítica. Assim, entre 2,2 e 1,9 Ga provavelmente houve a instalação de distintos e diacrônicos arcos magmáticos. A quiescência tectônica entre 1,9 Ga e 0,6 Ga indica que o bloco permaneceu estável por cerca de 1,2 Ga, durante todo o Mesoproterozoico. Um novo ciclo de metamorfismo de alta pressão (14–16 kbar), entre 630 e 590 Ma, registrado em rochas toleiticas, seguido da geração de veios injetados de leucossoma de composição alcalina, entre 580 e 520 Ma, em níveis crustais mais rasos (4–6 kbar), comprovam que o Bloco Campo Grande foi retrabalhado durante a Orogenia Brasiliana-Panafricana.

REFERÊNCIAS

Albarède, F., 1998. The growth of continental crust. Tectonophysics 296, 1–14.

Almeida, F.F.M., Brito Neves, B.B., Fuck, R., 1981. Brazilian structural provinces: an introduction. Earth Science Reviews 17, 1–29.

Angelim, L. A. A.; Medeiros, V. C.; Nesi, J. R., 2006. Programa Geologia do Brasil (PGB). Projeto Geologia e Recursos Minerais do Estado do Rio Grande do Norte. Mapa geológico do Estado do Rio Grande do Norte. Escala. 1:500.000. Recife: CPRM/FAPERN.

Barker, F., Arth, J.G., 1976. Generation of trondhjemite-tonalite liquids and Archean bimodal trondhjemite-basalt suites. Geology 4, 596–600.

Bedard, J.H., 2006. A catalytic delamination-driven model for coupled genesis of Archaean crust and sub-continental lithospheric mantle: Geochimica et Cosmochimica Acta, v. 70, p. 1188–1214, doi:10.1016/j.gca.2005.11.008.

Brito Neves, B. B., 1975. Regionalização geotectônica do Pré-Cambriano Nordestino. Tese de Doutorado. Inst. Geoc. USP, 198p.

Brito Neves, B. B., Van Schmus, W.R., Santos, E. J., Campos Neto, M. C., Kozuch, M., 1995. O Evento Cariris Velhos Na Província Borborema: Integração De Dados, Implicações E Perspectivas. Revista Brasileira de Geociências 25, 279-296.

Brito Neves, B. B., Dos Santos, E. J., Van Schmus, W. R., 2000. Tectonic history of the Borborema Province, Northeastern Brazil. In: Cordani, U., Milani, E. J., Thomaz Filho, A., Campos, D. A., (Eds.). Tectonic evolution of South America. 31st International Geological Congress, Rio de Janeiro, Brazil, 151–182.

Brito Neves, B.B., 2011. The Paleoproterozoic in the South-American continent: Diversity in the geologic time. Journal of South American Earth Sciences 32, 270–286.

Caby, R., 1989. Precambrian terranes of Benin-Nigeria, and Northeast Brazil and Late Proterozoic South Atlantic fit. Geol. Soc. America, Spec. Paper 230, 45-158.

Caby, R., Sial, A.N., Arthaud, M., Vauchez, A., 1991. Crustal evolution and the Brasiliano Orogeny in Northeast Brazil, in: Dallmayer, R.D., Lécorché, J.P. (Eds.), The West African Orogens and Circum-Atlantic Correlatives. Berlin, Springer-Verlag, 373-397.

Condie, K.C., 1981. Archean Greenstone Belts. Elsevier, Amsterdam, 434 pp.

Condie, K.C., 1998. Episodic continental growth and supercontinents: a mantle avalanche connection? Earth and Planetary Science Letters 163, 97-108.

Condie, K.C., 2000. Episodic continental growth models: afterthoughts and extensions. Tectonophysics 322, 153–162.

Condie, K.C., Aster, R.C., 2010. Episodic zircon age spectra of orogenic granitoids: the supercontinent connection and continental growth. Precambrian Research 180, 227–236.

Condie, K. C., O'NEILL, C., 2010. The Archean-Proterozoic Boundary: 500 My gf Tectonic Transition in Earth History. American Journal of Science, Vol. 310, P. 775–790.

Dantas, E. L., 1992. Evolução tectono-magmática do maciço polidiapírico São Vicente/Florânia - RN. 1992. 272 p. Dissertação (Mestrado) - Instituto de Geociências e Ciências Exatas, Universidade Estadual Paulista, Rio Claro.

Dantas, E.L., Negrão, M.M., Buhn, B., 2008. 2.3 Ga continental crust generation in the Rio Grande do norte terrane, NE-Brazil, in: 6th South American Symposium on Isotope Geology, Abstract Volume, pp. 40.

Dantas, E. L., Souza, Z. S., Wernick, E., Hackspacher, P. C., Martin, H., Xiaodong, D., & Li, J. W., 2013. Crustal growth in the 3.4-2.7 Ga São José de Campestre Massif, Borborema Province, NE Brazil. Precambrian Research, 227, 120–156.

Dantas, E.L., Van Schmus W.R., Hackspacher P.C., Fetter A.H., Neves B.B.B., Cordani U.G., Nutman A.P., Williams S., 2004. The 3.4-3.5 São José do

Campestre Massif, NE Brazil: remnants of the oldest crust in South America. Precambrian Research 130, 113-137.

Diwu, C., Sun, Y., Lai, Y. Z. S., 2014. Early Paleoproterozoic (2.45–2.20 Ga) magmatic activity during the period of global magmatic shutdown: Implications for the crustal evolution of the southern North China Craton. Precambrian Research 255, 627–640.

Evans, D.A.D., Mitchell, R.N., 2011. Assembly and breakup of the core of Paleoproterozoic–Mesoproterozoic supercontinent Nuna. Geology 39, 443–446.

Ferreira, A. C. D., 2015. Intrusões máficas-ultramáficas do Domínio Rio Grande do Norte, Província Borborema: ambiente tectônico e potencial para depósitos magmáticos. 86 p. Dissertação Nº 354 (Mestrado) - Instituto de Geociências, U Bloco Arqueano Campo Grande, Domínio Rio Grande do Norte, Província Borborema: dados preliminares

Ferreira, A.C.D., Ferreira Filho, C.F., Dantas, E.L., Souza, V.S., 2019. Paleoproterozoic Mafic-Ultramafic Magmatism in the Northern Borborema Province, NE Brazil: Tectonic Setting and Potential for Deposits. The Journal of Geology, 127. 483-504. (doi.10.1086/704256)

Ferreira, J. A. & Albuquerque, J. P. T., 1969. Sinopse da geologia da folha Seridó. SUDENE/DRN/DG, Ser. Geol. Reg. 18:47p.

Fetter, A.H., Van Schmus, W.R., Santos, T.J.S., Arthaud, M., J.A.N., Nogueira Neto, J.A., 2000. U-Pb and Sm-Nd geochronological constraints on the crustal evolution and basement architecture of Ceará State, NW Borborema Province, NE Brazil: implications for the existence of the Paleoproterozoic supercontinent Atlantica. Revista Brasileira de Geociências 30, 102-106.

Flament, N., Coltice, N. & Rey, P. F. 2008. A case for late-Archaean continental emergence from thermal evolution models and hypsometry. Earth and Planetary Science Letters 275, 326–336.

Foley, S.F., Tiepolo, M., and Vannucci, R., 2002, Growth of early continental crust controlled by melting of amphibolite in subduction zones: Nature 417, 837–840.

Galindo, A. C. Petrologia dos granitoides brasilianos da região de Caraúbas e Umarizal, oeste do Rio Grande do Norte. Natal, 1993. 370p. Tese (Doutorado) - Centro de Geociências, Universidade Federal do Pará.

Goodwin, A.M., 1991. Precambrian Geology. Academic Press, New York, 666 pp.

Griffi n, W.L., O'Reilly, S.Y., Afonso, J.C., and Begg, G.C., 2009, The composition and evolution of lithospheric mantle: A re-evaluation and its tectonic implications: Journal of Petrology 50, 1185–1204.

Hackspacher P.C., Van Schmus W.R., Dantas E.L. 1990. Um embasamento Transamazônico na Provincia Borborema. Congresso Brasileiro de Geologia, 36, Natal, Anais, 6, 2683-2696.

Hawkesworth, C.J., Cawood, P.A., Dhuime, B., Kemp, A.I.S., 2017. Earth's continental lithosphere through time. Annu. Rev. Earth. Sci. 45, 169–198.

Hawkesworth, C., Cawood, P.A., Dhuime, B., 2019. Rates of generation and growth of the continental crust. Geoscience Frontiers 10, 165-173.

Herzberg, C., Condie, K., and Korenaga, J., 2010, Thermal history of the Earth and its petrological expression: Earth and Planetary Science Letters 292, 79–88.

Holder, R.M., Viete, D.R., Brown, M. Johnson, T.E., 2019. Metamorphism and the evolution of plate tectonics. Nature 572, 378–381.

Hollanda, M.H.B.M., Archanjo, C.J., Souza, L.C., Dunyi, L., Armstrong, L., 2011. Long-lived Paleoproterozoic granitic magmatism in the Seridó-Jaguaribe domain, Borborema Province-NE Brazil. Journal of South American Earth Sciences 32, 287-300.

Hollanda, M.H.B.M., Archanjo, C.J., Bautista, J.R., Souza, L.C., 2015. Detrital zircon ages and Nd isotope compositions of the Seridó and Lavras da Mangabeira basins (Borborema Province, NE Brazil): Evidence for exhumation and recycling associated with a major shift in sedimentary provenance. Precambrian Research 258, 186–207.

Hurley, P.M., Rand, J.R., 1969. Pre-drift continental nucleii. Science 164, 1229–1242.

Jardim de Sá, E.F., 1994. A Faixa Seridó (Província Borborema, Ne Brasil) e o seu Significado Geodinâmico na Cadeia Brasiliana/Pan-Africana. Tese de Doutorado, Universidade De Brasília, 803pp

Jayananda, M., Martin, H., Peucat, J.-J., Mahabaleswar, B., 1995. Late Archean crust-mantle interactions: geochemistry of LREE-enriched mantle derived magmas. Example of the Closepet batholith, southern India. Contributions to Mineralogy and Petrology 119, 314–329.

Johnston, A.D., Wyllie, P.J., 1988. Constraints on the origin of Archean trondhjemites based on phase relationship of Nuk gneiss with H2O at 15 kbars. Contributions to Mineralogy and Petroloy 100, 35–46.

Lauri, L. S., Mikkola, P., Karinen, T., 2012. Early Paleoproterozoic felsic and mafic magmatism in the Karelian province of the Fennoscandian shield. Lithos 151, 74–82.

Legrand, J. M., Dantas, E. L., Liegeois, J. P., 1997. Definição e caracterização do embasamento da porção Oeste da Faixa Seridó (Província Borborema, NE-Brasil). In: SIMPÓSIO DE GEOLOGIA DO NORDESTE, 17, Fortaleza. Resumos expandidos. Fortaleza: SBG. Núcleo Nordeste, 1997. 537pp. il. (Boletim do Núcleo Nordeste da SBG, 15), 50-55.

Legrand, J. M., Liegeois, J. P., Deutsch, S., 1991. Datação U/Pb e Rb/Sr das rochas pré-cambrianas da região de Caicó. Reavaliação da definição de um embasamento arqueano. In: SIMPÓSIO DE GEOLOGIA DO NORDESTE, 14, 1991, Recife. Atas. Recife: SBG. v. 12, 276-279.

Lima, E. A. M., Wanderley, A. A., Vieira, A. T., Medina, A. M., Barbosa, A. J., Vasconcelos, A. M., Amaral, C. A., Sato, E. Y., Silva, E. H., Rocha, O., Leite, J. F, Moraes, J. F. S., Ribeiro, J. A., Nesi, J. R., Angelim, L. A. A., Calheiros, M. E. V., 1980. Projeto scheelita do Seridó. Recife, DNPM/CPRM. Unpubl. (Relatório Final e Mapas).

Martin, H., 1986. Effect of steeper Archean geothermal gradient on geochemistry of subduction-zone magma. Geology 14, 753–756.

Martin, H., 1994. The Archean grey gneiss and the genesis of continental crust. In: Condie, K.C. (Ed.), The Archean Crustal Evolution. Amsterdam: Elsevier, 205–259.

Martin, H., Moyen, J.F., Rapp, R., 2010. The sanukitoid series: magmatism at the Archaean–Proterozoic transition. Earth and Environmental Science Transactions of the Royal Society of Edinburgh 100, 15–33.

Martin, H., Smithies, R.H., Rapp, R., Moyen, J.-F., Champion, D., 2005. An overview of adakite, tonalite-trondhjemite-granodiorite (TTG), and sanukitoid: relationships and some implications for crustal evolution. Lithos 79, 1–24.

Medeiros, V.C., Nascimento, M. A. L., Galindo, A. C., Dantas, E. L., 2012. Augen gnaisses riacianos no Domínio Rio Piranhas-Seridó – Província Borborema, Nordeste do Brasil. Revista do Instituto de Geociências – USP. Geol. USP 12, 3-14.

Moyen, J.F., 2009. High Sr/Y and La/Yb ratios: the meaning of the adakitic signature. Lithos 112, 556–574.

Moyen, J.F., Martin, H., 2012. Forty years of TTG research. Lithos 148, 312-336. (doi: 10.1016/j.lithos.2012.06.010)

Moyen, J.F., Martin, H., Jayananda, M., 2001. Multi-element geochemical modelling of crust-mantle interactions during late-Archean crustal growth: the Closepet granite (South India). Precambrian Research 112, 87–105.

Moyen, J.F., Martin, H., Jayananda, M., Auvray, B., 2003. Late Archean granites: a typology based on the Dharwar Craton (India). Precambrian Research 127, 103–123.

Nance, R.D., Murphy, J.B., Santosh, M., 2014. The supercontinent cycle: A retrospective essay. Gondwana Research 25, 4-29.

Nebel, O., Capitanio, F. A., Moyen, J. F., Weinberg, R. F., Clos, F., Nebel-Jacobsen, Y.J., Cawood, P.A., 2018. When crust comes of age: on the chemical

evolution of Archaean, felsic continental crust by crustal drip tectonics. Phil. Trans. R. Soc. A 376, 20180103.

Rapp, R.P., Watson, E.B., 1995, Dehydration melting of metabasalt at 8–32 kbar: Implications for continental growth and crust-mantle recycling: Journal of Petrology 36, 891–931.

Reddy, S. M., Evans, D.A.D., 2009. Paleoproterozoic supercontinents and global evolution: Correlations from core to atmosphere. Geological Society, London, Special Publications 323, 1-26.

Rogers, J.J.W. 1996. History of Continents in the Past Three Billion Years. Journal of Geology 104, 91-107.

Rogers, J. J. W., Santosh, M. 2002. Configuration of Columbia, a Mesoproterozoic supercontinent. Gondwana Research, 5, 5–22.

Rollinson, H., 2006. Crustal generation in the Archean. In: Brown, M., Rushmer, T. (Eds.), Evolution and Differentiation of the Continental Crust. Cambridge, Cambridge University Press, 173–230.

Rollinson, H., 2010, Coupled evolution of Archean continental crust and subcontinental lithospheric mantle: Geology 38, 1083–1086.

Santos, E.J., 1996. Ensaio preliminar sobre terrenos e tectônica acrescionária na Província Borborema, in 39º Congresso Brasileiro de Geologia, Anais, v 1, pp. 47-50.

Smithies, R.H., Champion, D.C., 2000. The Archean high-Mg diorite suite: links To Tonalite-Trondhjemite-Granodiorite magmatism and implications for Early Archean crustal growth. Journal of Petrology 41, 1653–1671.

Souza, Z.S., Martin, H., Peucat, J.J., Jardim de Sá, E. F., Macedo, M.H.F., 2007. Calc-Alkaline Magmatism at the Archean-Proterozoic Transition: The Caicó Complex Basement (Ne Brasil). Jounal of Petrology 48, 2149-2185.

Souza, Z. S., Kalsbeek, F., Deng X. D., Frei, R., Kokfelt, T. F., Dantas, E. L., Li, J.W., Pimentel, M., Galindo, A. C., 2016. Generation of continental crust in the northern part of the Borborema Province, northeastern Brazil, from Archaean to Neoproterozoic. Journal of South American Earth Sciences 68, 68-96.

Stern, R.A., Hanson, G.N., 1991. Archean high-Mg granodiorite: a derivative of light rare earth element-enriched monzodiorite of mantle origin. Journal of Petrology 32, 201–238.

Sylvester, P.J., 1994. Archean granite plutons. In: Condie, K.C. (Ed.), The Archean Crustal Evolution. Amsterdam, Elsevier, 261–314.

Tappe, S., Smart, K. A., Pearson, D. G, Steenfelt, A., Simonetti, A., 2011. Craton formation in Late Archean subduction zones revealed by first Greenland eclogites. Geology 39, 1103–1106.

Taylor, S. R., McLennan, S. M., 1985. The Continental Crust: its Composition and Evolution. Oxford: Blackwell, 312 pp.

Terentiev, R. A., Skryabin, V. Y., Santosh, M., 2016. U–Pb zircon geochronology and geochemistry of Paleoproterozoic magmatic suite from East Sarmatian Orogen: Tectonic implications on Columbia supercontinent. Precambrian Research 273, 165–184.

Trindade, R. I. F., Dantas, E. L., Babinski, M., & Van Schmus, W. R. (1999). Short-lived granitic magmatism along shear zones: evidence from U-Pb zircon and sphene ages of Caraúbas and Tourão granites. In Actas. Cordoba: SEGEMAR.

Toteu, S.F., Van Schmus, W.R., Penaye, J., Michard, A., 2001. New U-Pb and Sm-Nd data from north-central Cameroon and its bearing on the pre-Pan African history of Central Africa. Precambrian Research 108, 45–73.

Toteu, S.F., Van Schmus, W.R., Penaye, J., Nyobe, J.B., 1994. U-Pb and Sm-Nd evidence for Eburnian and Pan-African high-grade metamorphism in cratonic rocks of southern Cameroon. Precambrian Research 67, 321–347.

Trompette, R., 1997. Neoproterozoic (~ 600 Ma) aggregation of Western Gondwana: a tentative scenario. Precambrian Research 82, 101-112.

Van Schmus, W. R., Dantas, E., Fetter, A., Brito Neves, B. B.; Hackspacher, P. C., Babinsk, M., 1995. Neoproterozoic Age for Seridó Group, NE Borborema Province, Brazil. Anais do XXXIX Cong. Bras. Geol. 6, 152-155.

Van Schmus, W. R., Brito Neves, B.B., Williams, I. S., Hackspacher, P. C., Fetter, A. H., Dantas, E. L., Babinski, M., 2003. The Seridó Group of NE Brazil, a late Neoproterozoic pre- to syn-collisional basin in West Gondwana: insights form SHRIMP U-Pb detrital zircon ages and Sm-Nd crustal residence (TDM) ages. Precambrian Research 127, 287-327.

Van Schmus, W.R., Kozuch, M., Brito Neves, B.B. 2011. Precambrian history of the Zona Transversal of the Borborema Province, NE Brazil: insights from Sm–Nd and U–Pb geochronology. Journal of South American Earth Sciences 31, 227-252.

Vauchez, A., Neves, S., Caby, R., Corsini, M., Egydio-Silva, M., Arthaud, M., Amaro, V.E., 1995. The Borborema shear zone system, NE Brazil. Journal of South American Earth Sciences 8, 247–266.

Wei, C., Qiana, J., Zhou, X., 2014. Paleoproterozoic crustal evolution of the Hengshan–Wutai–Fuping region, North China Craton. Geoscience Frontiers 5, 485–497.